

ALPHA PARTICLE DETECTION IN NUCLEAR REACTORS
USING SOLID STATE TRACK RECORDERS

by

Adnan Y.K. Qaqish

B.Sc. (Eng) (High Energy Physics)
Faculty of Mechanical and Electrical Engineering
The University of Michigan

Member of the American Nuclear Society
Member of the Jordanian Mechanical
Engineering Society

A thesis submitted for the degree of
Doctor of Philosophy (Ph.D.)
in the Faculty of Engineering of the
University of London
and for the
Diploma of Membership of Imperial College

Nuclear Power Section
Department of Mechanical Engineering
Imperial College of Science and Technology
London SW7 2BX

September 1977

To my dear wife, Daid, and our lovely son,

Ihab

ACKNOWLEDGEMENTS

The author is deeply indebted to Professor P.J. Grant, Head of the Nuclear Power Section of the Mechanical Engineering Department at the Imperial College of Science and Technology for his support, encouragement and criticism on the theoretical and experimental aspects of this work.

The author wishes to express his gratitude to his supervisor, Dr. C.B. Besant, who has taken a close interest in the work, for his moral support, help, advice and correction of the manuscript.

Sincere thanks are due to Dr. J.G. Williams and Mr. M. Kerridge of the University of London Reactor Centre (Silwood Park) for their advice and comments with respect to the experiments on the reactor CONSORT.

The author acknowledges with gratitude the cooperation of the Accelerator Group at the Atomic Energy Research Establishment (Harwell) in particular Dr. G. Dearnaley and Mr. E. Sparrow, and the Accelerator Group at Oxford University for the use of the accelerators and their support for the project.

Many thanks go to the following, for their advice and helpful discussions: Dr. A. Windle of Cambridge University; Professor J.H. Fremlin, Professor of Applied Radioactivity at Birmingham University; Professor E.V. Benton of University of San Francisco (USA); Dr. M. Monnin and B.B. Varga of the Institute of Nuclear Physics, France; Dr. H. Schmidt of the Institute of Nuclear Research (West Germany) and V. Perelygin of the Institute of Nuclear Research (USSR).

Sincere thanks are due to many colleagues at Imperial College, in particular, Mr. G.H. Briers of the Metallurgy and Materials Science Department, Mr. L. Eggleston and Mr. J. Lawrence of the Nuclear Power Laboratory, Mr. G. Tindall and Mr. S. Bedley of the Reprographics Department (Department of Mechanical Engineering), Miss P. Martins and the Reprographics Department of the Metallurgy and Materials Science Department.

The author wishes to express his appreciation of the patient and talented effort of Mrs. E.M. Noel and Miss C.E. Todorovitch in the typing of his manuscript into a legible and presentable form.

Last, but not least, I am deeply grateful to my wife, Mrs. D. Qaqish, for her constant support and total involvement in this project, without which this thesis would not have been possible; also to my parents for their moral and financial support and encouragement during my studies.

ERRATA

<u>Page</u>	<u>Figure</u>	
xxi	5.3b	2.5 N NaCl should read 2.5 N NaOH.
xxvii	6.57	(25 K x 31) should read (25 K x 3).
xxviii	6.62	V_G should read V_B (bulk etching rate).
101		Should be 102 not 101
102		Should be 101 not 102
156		r_T should be V_T
172c	6.16b	Should be 16 N KOH not KO
208		Should be in section 6.6.4 not 6.64
194		Should be in sections 6.7.1 , 6.7.2 and 6.7.3 not 6.71 , 6.72 and 6.73
210c	6.62	V_G should read V_B (bulk etching rate).

ABSTRACT

Both experimental and theoretical contributions are presented on the topic of dielectric charged particle track recorders. The track registration properties of the most sensitive known solid state track recorder, cellulose nitrate, have been investigated. The study covers five areas:-

(1) Track Formation Mechanism

The understanding of the track formation phenomena is basic to the knowledge of which particles register latent (etchable) tracks in a given solid and which particles can be revealed by chemical etching. It is also essential to the practical utilization of these track recorders in quantitative measurements.

Three parameters are of major importance to track formation, namely:

- (a) the particle energy per nucleon;
- (b) the particle atomic number;
- (c) the stopping properties of the material of concern (target material) defined by its density, atomic weight, atomic number and mean ionisation potential.

These parameters determine the average rate of energy loss per unit path length, the particle experiences in traversing the matter. This is directly involved with the extent of the damage to be left by the passage of the particle.

Detailed experiments were performed to study the basic phenomena of track formation in solids using an accelerator to provide charged particles at discrete energies covering a wide energy range.

Direct experimental evidence has proved the validity of the thermal spike model of track formation for high LET charged particles. Other experiments indicate that fast chemical reactions take place in the high temperature environment created by fission fragment tracks in condensed media. In all experiments tracks were only observed in specimens of resistivity $\geq 1 \text{ m } \Omega\text{-cm}$. Clarity of tracks increased with increasing resistivity which confirms the dependence of track formation on the electric conductivity of solids.

(2) The Chemical Etch Development of Tracks

Part of this research is an investigation of the effects of the

different constituents of cellulose nitrate plastic on the chemical etching of tracks. The dependence of track etching on certain etching solution parameters is also discussed.

It has been found that the degree of preferential etching of the particle damage trails can be significantly increased by reducing the chemical attack rate (V_B) of the undamaged bulk material. The quantity V_B is lower for the more highly nitrated and higher degree of polymerization of nitro-cellulose. The presence of plasticizers also greatly reduces V_B . Preferential etching can also be increased by etching at lower temperatures and etchant concentrations due to preferential swelling.

The thermal stability of tracks is discussed. The geometry of tracks is examined and useful relationships between track parameters are derived.

Experimental observations of etched tracks in several types of cellulose nitrate plastic are reported.

(3) Charged Particle Detection and Range-Energy Measurements

The shape of the etched tracks is often far from conical, which indicates that the ratio of track to bulk etching rates varies along the track as a function of the energy loss of the charged particle.

An empirical formula relating the track etching rate (V_T) to the particle restricted energy loss (REL) is derived for optimum etching conditions. This formula enables us to identify incident charged particles with a charge resolution (Δz) of 0.2 electron charge units, to resolve energies better than 42 keV, to separate isotopes of small mass differences with mass resolution (Δm) of 0.4 amu and to measure particle incident angle ($\Delta\theta$) better than 0.5° for a beam from the accelerator. The method is based on the measurements of etched track portions produced by incident charged particles penetrating layers of plastic.

The efficiency of detection and the range of alpha particles of various energies were measured in cellulose nitrate, as well as the critical angle for the revelation of a track by chemical etching.

Not only the variation of charged particle energy has been studied but also the effect of varying the angle of incidence of the particle with the surface of the plastic detector.

We have succeeded in shifting the threshold of track registration down (from A to B as shown in Figure 3.4) so as to reveal protons. This results in decreasing the minimum detector threshold for track registration

by about twofold. This improvement was accomplished by a preferential swelling technique.

(4) Reactor Physics Applications

The Solid State Track Recorder (SSTR), consisting of a source material covered with a plastic, has been found to be an excellent detector for measuring fission rates in reactors. Measuring these reaction rates usually necessitates a detector which is small, so that it can be inserted into the reactor in the required position without causing perturbation in the neutron flux. In this case the source is a fissile material and when the SSTR is irradiated, fission fragments leave damage trails or tracks in the plastic cover. These tracks can be counted using an optical microscope technique, or automatic counting techniques.

Part of the present work is concerned with the detection of α and ${}^7\text{Li}$ particles from (n,α) reactions, where the particle energy and atomic number are very much lower than that of fission fragments. Measurements of (n,α) reaction rates have been made in boron rods, which are used as fast reactor control rods, to an accuracy of $\pm 3\%$.

Our investigations of the influences of the nuclear reactor environment on the basic parameters of these detectors resulted in the development of a gamma dosimeter.

(5) New Techniques of Track Revelation

Our detailed study and understanding of the different track formation mechanisms made the following developments possible:-

- (i) A heavy particle dosimetry capable of discriminating between different linear energy transfer (LET).
- (ii) A neutron spectrometer (to be developed).
- (iii) Reactor reaction rate measurements.
- (iv) A gamma ray dosimetry for absorbed doses above 1 Mrad.
- (v) New techniques of track revelation based on the nature of the latent tracks. These include:-
 - (a) Base-exchange,
 - (b) Free-radicals (scavengers), and,
 - (c) Colouring of acidic groups by methylene blue.

These techniques are still in their infancy. The colouring of acidic groups by methylene blue has been found very successful for revealing a charged-particle radiograph and for fission rate measurements in the reactor core. But this technique still needs better understanding

and more quantitative data.

(6) Nuclear Medicine Applications

Medical diagnostic applications of nuclear tracks, such as tracks made by protons, alphas, neons and carbons, in CA 80-15 cellulose nitrate have been investigated for non-destructive charged particle radiography of the human body. The success of this technique in investigating and locating regions of tissue abnormality and tumours is attributed to the high registration sensitivity of cellulose nitrate to incident charged particles of low restricted energy loss; to the new track revelation techniques which have been developed at Imperial College of Science and Technology; to the small electron density changes which are reflected in measurable charge particle energy and range changes of the penetrating particle, and to the smaller radiation dose delivered to the human body compared to that delivered by the present techniques such as the EMI scanner and x-ray radiography.

We have in fact carried SSTRs from the experimental stages to the research and application stages and made incident particle identification, energy resolution and mass measurements possible within statistical and experimental errors. Further applications include measurements of reactor fluxes, reactor reaction rates, reaction cross-sections and neutron spatial distribution in the reactor core.

In nuclear medicine we have contributed towards the evaluation of cellulose nitrate track recorders for use in charged particle radiography, and have shown that it can be applied successfully for the investigation and location of tumours and regions of abnormal density in soft tissues, and as a radiation dosimeter.

SUMMARY

Nuclear Radiation Measurement Devices

Measurements in nuclear and reactor physics tend to differ rather considerably from measurements in sciences dealing with microscopic objects. It follows from the quantum-mechanical uncertainty principle that a single observation on a submicroscopic physical system yields at best an approximate picture of the system. If a precise description of a nuclear reaction is desired, it is necessary to make a large number of observations and to draw conclusions on the basis of a statistical analysis of large quantities of data. As physicists attempt more sophisticated experiments demanding higher standards of statistical accuracy, they require measuring instruments capable of recording and classifying very considerable quantities of data.

In many cases, conventional pulse-counting circuits capable of storing these large quantities of data are too costly to build and maintain or too full of fallible components to operate reliably.

Nuclear instruments are being built with acoustic delay-line memories, with magnetic-core and magnetic-drum memories, with cathode-ray tube electrostatic memories, with magnetic tape, punched paper tape and punched card storage systems, and it is likely that, as new computer memory devices are developed, they will be employed in nuclear instruments.

Research in nuclear and reactor physics makes use of a relatively small number of basic measuring tools, most of which can be grouped into four general classes:-

1. Track-recording devices: Included in this class are cloud chambers of the expansion and diffusion type, bubble chambers, photographic emulsions and solid-state track recorders (SSTRs).
2. Magnetic and electrostatic deflection devices: These devices separate charged particles according to their momenta, and include magnetic lens and electrostatic beta-ray spectrometers as well as several types of spectrometers.
3. Diffraction devices: Neutron diffraction spectrometers sort neutrons according to their energies. They make use of regular crystal lattices to diffract neutrons, much as a diffraction grating is used in an optical spectrometer.
4. Counter and ionization chamber devices: This class includes radio-assay and radiation-dose measuring devices that use Geiger counters, proportional counters, scintillation counters and ionization chambers.

Also included are two types of spectrometric devices that take advantage of relations between pulse amplitude or pulse detection time in these counters and incident particle energy.

The four classes of nuclear devices are not, of course, distinct and unrelated, counters, for example, are commonly used in association with all of the other devices mentioned.

A serious difficulty in working with a number of nuclear detectors, namely photographic emulsions, bubble chambers and scintillation counters is that these detectors have a response that is considerably affected by the low energy delta-rays generated by the incident heavy charged particles. The blob density along a higher energy particle track in a photographic emulsion as well as the drop counts in a cloud chamber have been found to parallel closely the restricted energy loss w_0 (the energy of the *delta* ray) to within a few keV.

Experimental costs are high and discrimination against gamma rays is difficult with scintillation counters. Low efficiency at energies of about 1 eV, poor relative resolution time and difficult reproducibility of observed pulse height (observed pulse height is a function of how far from the collection electrode ionization takes place) are difficulties with BF_3 counters. Finally, complications with proportional counters arise from the formation of negative ions produced by the leakage of gas into the counter at atmospheric pressure when dealing with weak (alpha particle and proton) sources.

These above-mentioned difficulties and the below-listed possible sources of inefficiency in nuclear detectors, which, if not recognized and taken into account, may lead to errors in the interpretation of the results, contributed towards the superseding *by* solid-state track recorders *OF* the conventional nuclear detectors in certain nuclear applications.

Possible sources of inefficiency are as follows:-

1. There is the efficiency of the counter itself to be considered. This is defined as the probability that, when the ionizing event to be studied actually occurs, the counter discharges. The counter may fail to discharge for several possible reasons. The event to be detected may not produce an ion in the sensitive volume. The sensitivity of various positions of the counter's volume may be different. Finally, the event may occur before the counter has recovered from the previous count.

2. Particles to be counted may not reach the sensitive volume, i.e. they are absorbed into the wall of the detector.
3. The coincidence counting, when the particle passing through the coincidence arrangement may not be detected because of an inefficiency in the system and some event other than that to be detected causes the counter to discharge simultaneously.
4. The efficiency of the proportional counter due to:
 - (a) the range of the particle not lying entirely in the sensitive volume, or being interrupted by the particle striking the wall of the counter;
 - (b) the background of large pulses due to alpha particles and giant showers, and,
 - (c) any effects such as electron capture which cause an apparent decrease in the amplification factor measurement of reaction rate, not flux.

Radiation Damage to Conventional Nuclear Detectors

Detectors such as the ones containing $^{10}\text{BF}_3$ or ^{10}B coating, when tested prior to and after being subjected to higher neutron or gamma radiation show marked changes in characteristic curves. Experience shows that the effect is noticeable in neutron fluxes of 10^6 and in gamma fluxes of 10^2 r/hr. The neutron flux varies by a factor of 10^8 or more in power reaction applications and in normal installations may go well above 10^8 .

It is, therefore, necessary to shield the chamber or detector from both gamma rays and neutrons after the start up period, either by moving the shield in around the detector, or by drawing the detector out of the field which is quite inconvenient for ideal experimental procedure and may induce geometrical perturbation to the experimental arrangement.

Track Recorders

A direct and permanent microscopic observation of the phenomenon of nuclear radiation in the form of tracks is established by these nuclear track recorders, otherwise, this phenomenon would remain purely conceptual. Without such observations, many hypotheses would have only been statistical substantiations through observations of great numbers of events instead of finding their direct verification through observations of single events. A variety of information can be obtained from a study of tracks, which is not possible to be established by the conventional detector, i.e. a study of detailed structure of the tracks leads to the determination of the mass, charge and energy of the particle. A detailed analysis can be made of an extremely complicated event involving several

particles and spatial distribution of these particles. Also, radiation fluxes can be simply obtained, which is impossible to obtain with a conventional detector. Thus, photographic emulsions along with SSTRs serve a unique function in nuclear radiation detection. These track recorders actually measure the integral flux, i.e. the dose received, so it is not necessary to know exactly the time elapsed after irradiation and before etching (developing) or measurements, also the flux need not be constant during irradiation as is the case when making measurements with foils. The major difficulty in the foil activation method arises when dealing with large numbers of measurements taken simultaneously and also when foils are in a highly active assembly and therefore difficult to retrieve quickly, which is a major problem especially when gamma counting foils are with absolute short half lives or short relative gamma counting time.

Naturally, each of these track recorder devices has certain advantages and disadvantages over the conventional detectors.

Photographic Emulsions

When charged particles pass through photographic emulsions, they can produce latent images along their paths. Upon development of the film, the grain of silver appears along the tracks of the particles. A variety of information can be obtained from a study of nuclear track plates, and it is prominent in nuclear physics because it provides the following advantages:-

- (a) A lasting record of individual particle trajectories is made, which can be examined subsequently with relatively simple equipment.
- (b) The sensitivity time is arbitrary, it may be exposed within a fraction of a second to particles in an accelerator experiment or over many weeks in cosmic ray work.
- (c) Its high stopping power frequently permits containment of the ranges of energetic particles within small volumes available to study.
- (d) Its sensitivity may be adjusted within limits to favour desired particles, and to suppress background.
- (e) Within limits the grain density of the tracks may be related to specific ionization.

The chief disadvantages inherent in the emulsion are:-

- (a) Time relationships of events are unknown.
- (b) Use of magnetic field for momentum determinations on particle tracks has not been achieved.
- (c) The atomic heterogeneity of an emulsion is frequently undesirable.

- (d) Data are not quite available, e.g. range energy data.
- (e) Nuclear emulsions should be kept in a cool, dry place until they are used.
- (f) Caution is necessary as the times involved in handling are often long; there are several materials, and they should be kept in total darkness.
- (g) They do not withstand high temperatures.
- (h) Perturbations in the system under investigation will exist due to extra care taken not to expose the film to light.
- (i) Gamma and x-ray interferences may affect their sensitivity and discrimination against background.

Solid-State Track Recorders (SSTRs)

Although a large amount of energy is needed to produce a track in SSTRs as compared to other types of detectors as shown in Table S1, SSTRs

TABLE S1

Energy Necessary to Produce a Signal in Various Particle Detectors

Detector	Energy Necessary to Produce a Signal
Scintillator	10^2 eV/scintillation
Photograph Emulsion	10^3 eV/blob
Bubble Chamber	$3-5 \times 10^3$ eV/bubble
CA 80-15 } LR-115 Type-II } Cellulose Nitrate	150×10^3 eV/micron of track

are becoming increasingly important in the reactor physics field, where they are already used for measuring reaction rates in the determination of fission ratios, angular distribution, neutron spectrum measurements and neutron cross-section measurements; in science and technology, investigation of the physics of high velocity impact is currently of great importance; in medicine, selectively etched tracks in thin layers of plastic have been used as fine sieves for the filtration of cancer blood cells. This is due to the track registration efficiency of these films to particles such as alpha particles, protons, heavy ions and particles from nuclear fission, which is superior to that of the best detector at present known, but is nevertheless highly selective to different charged particles in the presence of high background radiation fields of almost any variety. The preferential etching phenomenon is the key to the use of SSTRs as fine sieves for medical purposes. SSTRs

possess considerable geometric flexibility, and can be shaped and mounted to detect charged particles over an extended solid angle, or can be reduced in size to eliminate flux depression or flux perturbation without upsetting the experimental arrangement. They can be subjected to environmental perturbations without detrimental effect to their performance, and are therefore stable for arbitrary long periods. Their advantage over nuclear emulsions is that they do not contain silver material in them, so they are easy to handle and darkroom conditions and special storage are not required. They withstand high temperatures better than most conventional detectors, can be placed in direct contact with the source so that very high efficiency and sensitivity can be obtained.

In addition to the above, they provide the same advantages as that of the photographic emulsion, and, moreover, they can be used for monitoring personnel for radiation dose (dosimeters). The choice of the type of film will always depend on the radioactive substance being studied, and the discrimination required. Their chief disadvantages are the following:-

- (a) Time relationships of events are unknown;
- (b) Quantitative measurements such as bulk etching rate (V_B), track etching rate (V_T) and their variation as a function of the corresponding particle restricted energy loss (REL) at optimum etching conditions are not yet available. These measurements are necessary to enable incident particle and energy identification, and to allow the progression of SSTRs from the experimental stages to nuclear and reactor physics applications.

Fission rates and power distribution measurements in critical assemblies which will increase in relative precision and absolute accuracy have a significant bearing on in-core geometry or spatial distribution, and also on the upward in-core neutron energy distribution respectively. Increased precision coupled with the unmatched spatial resolution available with SSTRs will permit investigations of spatial gradients of these distributions. In addition, high spatial resolution studies of fission rate distributions across boundaries will also be possible. This is performed by loading the SSTRs with such elements as Li, B, Bi, U and Th either by vacuum evaporation or by soaking them in solutions of certain compounds of the desired element to allow the quantitative study and measurements of reaction rates, neutron fluxes and fluences, etc., via (n,α) and (n,f) reactions. The use of boron-loaded film for neutron detection through the $^{10}\text{B}(n,\alpha)\text{Li}^7$ reaction is an example which was

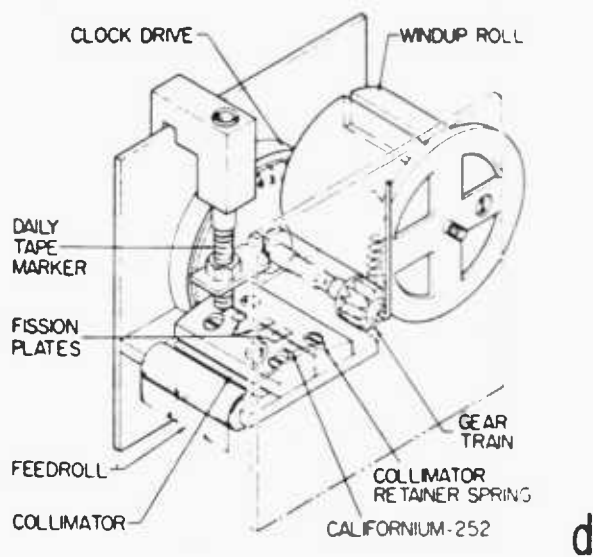
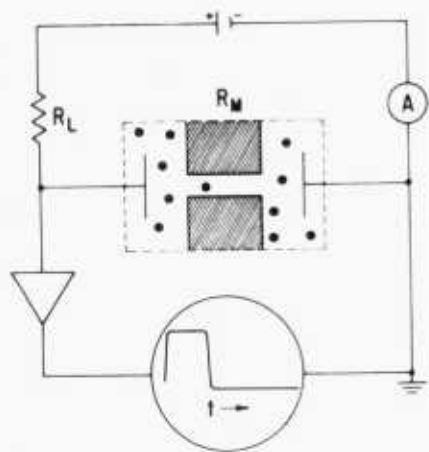
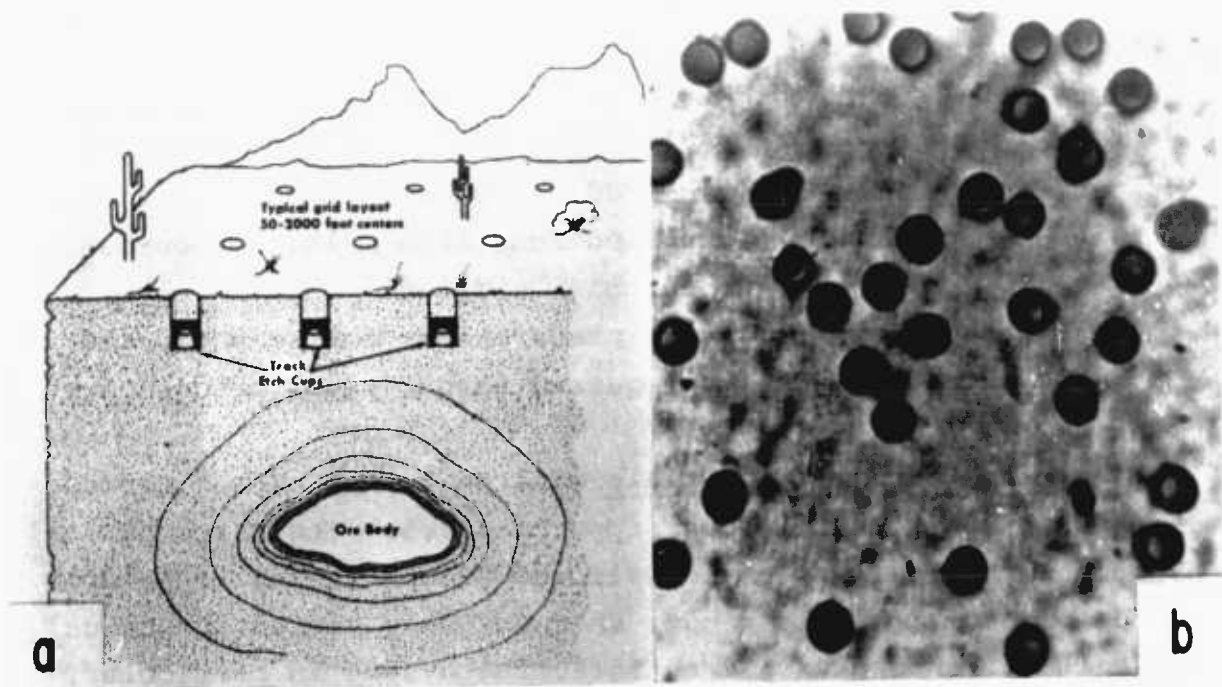


Figure 6. Technological uses of track etching: (a) A uranium exploration technique uses cellulose nitrate to sense the alpha decays arising from Rn, which emanates from uranium ore. (b) Filters can be produced by irradiation and etching of thin sheets of detector materials. (c) Using a membrane with a single etched hole a virus counter can be made. (d) A safeguards device with a moving tape records as an array of fission tracks the neutron energy spectrum at nuclear reactors.

considered during the present work, and using this reaction, the reaction rates in several neutron spectra from thermal up to that similar to fast reactors were measured.

SSTRs can be successfully used in nuclear medicine and the resulting tracks can be revealed by dyeing with high efficiency. The major advantage of the method is the high contrast achieved between irradiated and unirradiated regions of the radiograph, which permits easy revelation of a beam profile of a diagnostic beam and the low radiation dose delivered to the human body compared to the technique used at present. This shows that techniques of histological staining can be useful when applied to SSTRs for charged particle radiography.

The advantage of solid-state track recorder technique is its simplicity, higher accuracy, compactness and maximum information is obtained. The measured track parameters, i.e. track length and diameter, depend on the energy loss of the incident particle ((dE/dx) or (REL)), on the chemical composition of the detector, on the ratio between the bulk etching rate and the track etching rate (V_B/V_T) and on the threshold of track registration of the detector (REL critical); while the efficiency of the detector depends on additional parameters, such as the nature of the etchant and the etching conditions.

TABLE OF CONTENTS

	<u>Page</u>
ABSTRACT	i
TABLE OF CONTENTS	v
LIST OF ILLUSTRATIONS	xi
 <u>CHAPTER ONE - RESEARCH ON TRACKS IN SOLIDS</u>	
1.1 Introduction	1
1.2 History of Tracks in Solids	2
1.3 Methods of Track Revelation in Solids - General Considerations	4
1.3.1 Transmission Electron Microscopy	6
1.3.2 Decoration Technique	6
1.3.3 Chemical Etching	7
1.4 Applications of Solid State Track Recorders	8
1.4.1 Radiation Dosimetry	10
1.4.2 Reactor Physics Applications	14
1.5 Radiation Damage Along Tracks	15
1.6 Program of Investigation	17
1.6.1 Objectives of the Present Investigations	20
 <u>CHAPTER TWO - CELLULOSE NITRATE: RADIATION CHEMISTRY</u>	
2.1 Introduction	21
2.2 Cellulose and its Properties	22
2.3 Cellulose Nitrate: Chemical Composition	24
2.3.1 Physical Properties of Cellulose Nitrate	24
2.3.2 Cellulose Nitrate Plasticisation	26
2.4 Degradation of Cellulose Nitrate	28
2.4.1 Thermal Degradation of Cellulose Nitrate	29
2.4.2 Radiative Degradation of Inorganic Nitrates	31
2.4.3 UV Degradation of Cellulose Nitrate	31
2.4.4 Radiative Degradation of Cellulose	32
2.4.5 Oxidative Degradation of Cellulose	35
2.4.6 Alkaline Erosion and Scission of Cellulose	36
2.5 Degradation of Cellulose Nitrate by High-Energy Radiation	38
2.6 Alkaline Etching of Cellulose Nitrate	39
2.7 Hydrolytic Degradation of Cellulose Nitrate by Acids ..	41
2.8 Swelling in Cellulose and Cellulose Nitrate and its Effect on Chemical Reactions	44

<u>CHAPTER THREE - REVIEW OF THEORETICAL MODELS</u>		Page
	Introduction	48
3.1	The Energy Loss Processes	49
3.1.1	Energy Losses by Radiation	50
3.1.2	Nuclear Collision Losses	50
3.1.3	Electronic Energy Losses	53
3.2	Etchable Track Formation Criteria	56
3.2.1	Total Energy Loss Criterion	58
3.2.2	The Primary Ionisation Criterion	59
3.2.3	The Restricted Energy Loss Criterion	60
3.2.4	The Delta-Ray Criterion	62
3.3	Mechanism of Track Formation	62
3.3.1	Atomic Displacement and Displacement Cascades	63
3.3.2	Thermal Spike Model	64
3.3.3	The Ion Explosion Spike Model	67
3.4	Conclusions	69
<u>CHAPTER FOUR - TRACK FORMATION IN SOLIDS</u>		
4.1	Introduction	72
4.2	General Conceptual Framework	75
4.3	Radiation Damage in Latent Tracks	77
4.4	The Initial Energy Deposition	79
4.4.1	Energy Partition of Heavy Charged Particle between the Core of the Track and the Surroundings	81
4.5	Damage Produced by Fission Fragment Irradiation of Heat-Sensitive Solids	82
4.5.1	Observed Characteristics of Tracks	83
4.5.2	The Effect of Heat	85
4.5.3	Comparison of Observed and Calculated Track Width	87
4.6	Energy Degradation around Tracks	89
4.6.1	Resistivity Dependence of Track Registration	95
4.7	Conclusions	96
<u>CHAPTER FIVE - DESCRIPTION OF INSTRUMENTS AND EXPERIMENTAL TECHNIQUES FOR TRACK RECORDING AND REVELATION</u>		
5.1	Introduction	97
5.2	Specimen Preparation	97
5.2.1	Preparation of Cellulose Nitrate Plastic in the Laboratory	98
5.2.2	Commercial Cellulose Nitrate	99
5.3	Radiation Exposure	102

	<u>Page</u>
5.3.1	Protons 102
5.3.2	Alpha Particles 102
5.3.3	Alpha Particle Production using Boron 103
5.3.4	Alpha Particle Irradiation using the Van de Graaff Accelerator 104
5.3.5	Fission Fragments from a Cf-252 Source 104
5.3.6	Fission Fragments from the Reactor 105
5.3.7	Experiments on the Reactor "Consort" 105
5.4	The Development of Charged Particle Tracks 113
5.4.1	Transmission Electron Microscopy (TEM) 113
5.4.2	Scanning Electron Microscopy (SEM) 114
5.4.3	The Decoration Method 114
5.4.4	The Graft-and-Dye Method 115
5.4.5	Base-Exchange and Scavengers 116
5.5	Latent Track Revelation by Chemical Etching: Introduction 116
5.5.1	Required Properties of the Etchant 117
5.5.2	Etching Precautions 117
5.5.3	Starting Material 117
5.5.4	Irradiation Environment 118
5.5.5	Steady State Reactivity of Latent Track 118
5.5.6	Sensitization Methods: Direct Photolysis 119
5.5.7	Latent Track Etching Techniques 120
5.5.8	Latent Track Revelation by Electrochemical Etching ... 120
5.6	Instruments and Techniques for Etched Track Observation and Measurement 121
5.6.1	Ozalid Method 122
5.6.2	Light Scattering 122
5.6.3	Spark Scanning 123
5.6.4	Diffraction Technique Using Laser Light 123
5.7	Optical Microscope Technique for Track Analysis 126
5.7.1	Bright-Field, Transmitted Light Illumination 126
5.7.2	Dark-Field Illumination 127
5.7.3	Phase Contrast Microscopy 130
5.7.4	Interference Contrast Microscopy 130
5.7.5	Incident Light Illumination (Reflection) 131
5.8	Automatic Scanners 132
 <u>CHAPTER SIX - TRACK DEVELOPMENT BY MEANS OF CHEMICAL ETCHING</u>	
6.1	Introduction 134
6.2	Geometry of Etched Tracks 135

	<u>Page</u>
6.2.1	Mathematical Evaluation of Track Parameters 136
6.2.2	Mathematical Evaluation for Track Parameters with Dip Angle $\delta = 90$ deg. 141
6.2.3	Track Specifications and Measurement of Parameters ... 142
6.2.4	Measurement Optimization 143
6.2.5	Computation of the Track Etch Rate 147
6.2.6	Track Measurement 147
6.3	Preliminary Experiments 148
6.3.1	Low Background Counts and Measurements 148
6.3.2	Reproducibility of Tracks 149
6.3.3	Clarity of Tracks and Ability to Count and Measure Tracks 149
6.3.4	Relative Sensitivity and Registration Efficiency of the Detectors 149
6.3.5	Effect of Oxygen and Humidity on the Relative Sensitivity of the Detector 151
6.3.6	Effect of Ultraviolet and Radiation Pre- and Post- Treatment on the Relative Sensitivity of the Detectors 153
6.4	Experimental Observations 154
6.5	Effects of the Specimen Composition 154
6.6	Etching Technique and the Effect of the Etching Solution Parameters 158
6.6.1	Description of Experiments 160
6.6.2	Electron Microscope Study of Track Parameters 161
6.6.3	Optical Microscope Study of Track Parameters and Track Counting 161
6.6.4	Specimen Preparation for Electron and Optical Microscopy 163
6.7	Effect of Etchant Temperature, Concentration and Agitation on Track Formation 166
6.7.1	Measurements of Bulk Etching Rate 166
	Discussion 170
6.7.1.1	Method for Determining Alkali Absorbed in Cellulose Nitrate and its Effect on Bulk Etching 173
6.7.1.2	Swelling of Cellulose Nitrate in Alkali Hydroxide Solutions and its Effect on Bulk Etching 174
6.7.2	Measurement of Track Etching Rates 175
6.7.3	Comparison of Track and Bulk Etching Rates 176
6.8	Latent Track Annealing 179
6.9	Critical Angle of Etching and its Effect on the Detection Efficiency of Cellulose Nitrate 180
6.9.1	Critical Angle of Etching 181

	<u>Page</u>
6.9.2	Detection Efficiency and Counting Techniques 183
6.9.3	Effect of Temperature and Ultra-Violet Light on Detection Efficiencies 189
6.9.4	Modifications in Geometry Factors for SSTR's 192
6.10	Particle Identification and Energy Measurement 194
6.10.1	Dependence of the Track Etching Rate on the Restricted Energy Loss 195
6.10.2	Information Content of Particle Etched Tracks 198
6.10.3	Particle Identification Techniques and Particle Energy Measurements 200
6.10.4	Evaluation of z and E for Particles whose Entire Registration Range is contained within the Plastic Film 201
6.10.4.1	Determination of Range-Energy Relation in Cellulose Nitrate 202
6.10.5	Evaluation of z for Particles whose Entire Registration Range is not contained within the Stack ... 206
6.10.6	Isotopic Mass Separation of Particles 207
6.10.7	Particle Identification by Measurements of Induction Time and Etched Pit Diameter 208
	Discussion 215
6.11	Reactor Physics Applications 223
6.11.1	The Effect of High Gamma Doses on the Etching Characteristics of Cellulose Nitrate Plastic 223
6.11.2	Measurement of Fast Reactor Reaction Rates using Solid State Track Recorders 225
6.11.2.1	Relative (n, α) Reaction Rate Ratios 226
6.11.2.2	Reaction Rate Ratios in Several Neutron Spectra 228
6.11.2.3	Absolute Reaction Rates and Absolute Neutron Fluxes ... 231
6.11.2.4	Counting Techniques 232
6.11.2.5	Statistical Analysis of the Counting 233
	Results 237

CHAPTER SEVEN - TRACK REVELATION BY BASE-EXCHANGE AND FREE RADICAL
TECHNIQUES

7.1	Introduction 244
7.1.1	The Base-Exchange Phenomenon 244
7.1.2	Base-Exchange in the Latent Track: Swelling and Etching 247
7.1.3	Revelation by Etching and Swelling 248
7.1.4	Revelation by Base-Exchange Alone 250
7.1.5	Increasing the Sensitivity of Track Revelation 251
7.2	Free Radicals in Nuclear Tracks 253
7.2.1	Scavengers 254

	<u>Page</u>
7.2.2 Free Radicals in Latent Tracks	255
7.2.3 Track Revelation via Free Radicals	256
<u>CHAPTER EIGHT - SOLID STATE TRACK RECORDERS IN NUCLEAR MEDICINE</u>	
8.1 Introduction	258
8.2 Charged Particle Radiography	258
8.3 The Technique	260
8.4 Radiograph Development by Methylene Blue	260
Conclusions	262
<u>CHAPTER NINE - SUMMARY OF CONCLUSIONS AND PROPOSALS FOR FUTURE WORK</u>	
9.1 Summary of Conclusions	263
9.2 Proposals for Further Study	266
REFERENCES	268
<u>APPENDICES</u>	
A-I The Energy Interchange between Electrons and Lattice ..	A1
A-II The Ranges of Secondary Electrons in the Lattice	A4
B-I Etching Conditions for Alpha Particles and Fission Fragments	B1
B-II Track Annealing Characteristics	B11
B-III Chemical Effects on Particle Tracks	B16
B-IV Photo-Oxidation Effects on Particle Tracks	B18
B-V Irradiation Effects on Particle Track Etching	B19
B-VI Methods of Locating or Enlarging Tracks	B21
B-VII Automated or Integrating Scanning Methods	B22
C a) Alpha Tracks (Particles Incident at Angle $\theta = 90^{\circ}$ to the Surface of the Semi Conductor Detector)	C1
b) Alpha Tracks (Particles Incident at Angle $\theta = 90^{\circ}$ 5° to the Surface of the Plastic Detector)	C4
D-I Energy-Loss Rate in Cellulose Nitrate (in $\text{MeV mg}^{-1} \text{cm}^2$) .	D1
D-II Range in Cellulose Nitrate (in μm)	D3

LIST OF ILLUSTRATIONS

Figure

- 1.1 Photomicrograph of a typical Fe calibration track in emulsion with adjacent ultra heavy cosmic ray primary in both emulsion and plastic.
- 2.1 Diagram of the structural formula for cellulose. Three hydroxyl groups are present in each of the anhydroglucose rings; these are joined by ether linkages. In the middle picture is shown the puckered "chair" shape of the rings, oxygen atoms being represented by O's. The bottom picture shows a path along the backbone of the chain, projected on a plane perpendicular to the rings. The carbon atoms are numbered.
- 2.2 Diagram of the unit cell of native cellulose (Cellulose I). Chains in alternate planes are antiparallel; the chains in the right hand front and left hand rear corners are not shown. Oxygen atoms are represented by black circles. The angle β is 84° .
- 2.3 Diagrams of: a) The structural formula of cellulose trinitrate; b) The resonant structure of cellulose nitrate.
- 2.4a Proposed mechanisms for pyrolytic cis-eliminations of acetic acid from cellulose triacetate. Depolymerization would involve other monomeric units.
- 2.4b Proposed mechanisms for the decomposition of cellulose nitrate.
- 2.5 Diagram of the degradation of cellulose acetate and cellulose nitrate in the presence of ultraviolet light at 60°C . Samples of cellulose acetate (38.0% acetyl content) and cellulose nitrate (11-10% N) cast as 0.005-in. films were exposed to ultraviolet light in alternate atmospheres of nitrogen and oxygen.
- 2.6 Diagram of a summary of the effects of various oxidizing agents on cellulose. The carbon atoms of the glucose ring are numbered the standard way.
- 2.7 Diagram showing alkaline erosion and stabilization of cellulose.
- 2.8a Diagram of alkaline scission of cellulose.
- 2.8b Diagram of β alkoxy carbonyl groups in carbonyl-containing oxidized cellulose.
- 2.8c Diagram of alkaline degradation of carbonyl-containing oxidized cellulose.
- 2.9 Diagram of a summary of the possible effects of ionizing radiation on the anhydroglucose unit of the cellulose molecule.
- 2.10 Diagram of a summary of the possible effects of ionizing radiation on the ring unit of the cellulose trinitrate molecule. Double dashed lines denote same effects as in preceding case of the cellulose ring unit.
- 2.11 Graph of rates of acetolysis at 25°C for ethyl cellulose, cellulose acetate and cellulose nitrate. Acetolysis was carried out in an anhydrous medium, 95:5 acetic acid:acetic anhydride, which was 0.78 N with respect to HCl and 0.105 N with respect to LiCl.

Figure

- 3.1 Graph showing: a) Total energy loss rate;
b) Primary ionization rate in muscovite mica of various charged particles of varying energy. Regions of (i) complete tracks, (ii) partial tracks and (iii) no tracks, based on total energy loss rate and primary ionization rate.
- 3.2a Diagram of a model for the formation of intermittent tracks in crystals with a layer structure such as molybdenum disulphide. Intense electronic excitation is produced at successive low-angle intersections with the high-density atomic planes such as AB.
- 3.2b The lower diagram shows a latent damage trail of a fission fragment in crystals, and the upper shows the intensity of damage as a function of radial distance in the same crystals.
- 3.3 Graph showing the restricted energy loss rate, $(dE/dx)_{\omega < 10^3}$ eV, as a function of energy per nucleon for a number of heavy ions in Lexan polycarbonate resin ($I_{adj} = 69.5$ eV).
- 3.4 Graph showing the restricted energy loss rate, $(dE/dx)_{\omega < 10^3}$ eV, as a function of energy per nucleon for a number of heavy ions in cellulose ($I_{adj} = 81.1$ eV).
- 3.5a Models showing the formation of latent trails in: a) plastics;
b) crystals.
- 3.5b Diagram of the ion explosion spike model. Different parts of the figure show the following: (a) passage of a charged particle, (b) ionization of medium atoms along its path, (c) Coulombic repulsion and (d) formation of a latent trail.
- 3.6a Trajectories of the ions for the case of triple ionization of four chlorine ions up to a time of 8×10^{-13} sec.
- 3.6b-e Consecutive configurations of the central lattice as a function of time (triple ionization).
- 3.7 Schematic representation of the fission spike.
a) The fragment enters the crystal at X and comes to rest at the point Y. The intensity of the thermal spike at any point along this 'track' is given by the radius of a right circular cone (seen here in section) at that point.
b) Diagram showing the formation of a displacement spike by an energetic knock-on deriving from a collision between the fragment and a lattice atom. When the mean-free-path for atomic displacement falls below an inter-atomic distance a displacement spike is formed.
c) The frequency of displacement spike formation increases as the fragment slows down and there is a gradual transition from "Rutherford" to "hard sphere" collisions. The statistical nature of the frequency of collision events is considered to be understood and is omitted from the diagram.
- 3.8a Schematic representation of interstitial atoms around a multiple vacancy during production of a Brinkman displacement spike.
- 3.8b Schematic two-dimensional representation of the Seeger depleted zone and its environment in a face-centred cubic crystal. A primary knock-on impinges from the left and comes to rest on the site P.

Figure

- 4.1 Electron micrograph of a fission fragment track in lead iodide, showing characteristic branching.
- 4.2 Schematic description of the partition of energy deposit as a function of time t , in sec. The vertical dimension of a given region is proportional to the fraction of the deposited energy which is in a particular form. This figure is intended to describe the situation for an average energy deposit. Note that, in exothermal reactions, the line showing low-grade heat can terminate above the level of total energy absorbed. This situation is the same even when luminescence occurs, because the amount of heat loss in such processes is rarely significant.
- 4.3a Diagram of a typical fission fragment track in water. Secondary electrons densely overlap to form the "sheath". Their LET is about two orders of magnitude smaller than that of the core.
- 4.3b Schematic view of a track of an O^{8+} ion in water projected in a plane through the track axis. Secondary electron tracks are shown shaded in the diagram.
- 4.3c Diagram showing a section of a typical track due to protons in water having energy 1-2 MeV/amu. The secondary electrons have roughly the same LET as in the core; they are spaced by $\sim 300 \text{ \AA}$ on the track axis.
- 4.4 Graph showing the partition of energy loss between the core and emergent secondary electrons plotted as a function of incident energy. At a given incident energy variation with respect to particle quality is small.
- 4.5 Electron micrograph of a discontinuous fission fragment track formed due to thermal decomposition and evaporation of the crystals along the path of the particle, followed by recrystallization.
- 4.6 Electron micrograph of a thin crystal of lead iodide showing tracks which have 'spikes' at points where the width increases by a factor of two or more. Note that the arrowed track is thinner than those produced by the fission fragments, and is outside the angle of collimation.
- 4.7 Electron micrograph of a fission fragment track in lead iodide showing the recrystallization of the lead, which was released by the decomposition of the crystals along the path of the particle, as indicated by the arrow.
- 4.8 Electron micrograph of fission fragment tracks in C-UO₂-Pb film of electrical resistivity $\sim 10^3 \mu\Omega\text{-cm}$.
- 4.9 Electron micrograph of variation of fission fragment track properties in C-UO₂-Pb film as a function of electrical resistivity.
Electron micrograph of latent damage of fission fragments (non-etched) in CA 80-15 cellulose nitrate.
- 5.1 Electron micrograph of cellulose nitrate detector, LR 115 type-II (Kodak-Pathe, France), unirradiated and unetched (25 K x 3).
- 5.2 Electron micrographs of cellulose nitrate detector, CA 80-15 (available from Kodak-Pathe, France), unirradiated and unetched (25 K x 3).

Figure

- 5.3a Photomicrograph of 2.5 MeV alpha tracks in cellulose nitrate (Daicel, Japan) at 90° incidence, etched in 2.5 N sodium hydroxide at 18°C for 20 hours.
- 5.3b Electron micrograph of 0.8 MeV alpha tracks in LR 115 type-II (Kodak-Pathe, France) at 90° incidence, etched in 2.5 N sodium hydroxide at 18°C for 2 hours (100 K x 1.5)*.
- 5.3c Electron micrograph of 0.8 MeV alpha tracks in LR 115 type-II (Kodak, Pathe, France) at 30° incidence, etched in 2.5 N sodium hydroxide at 18°C for 2 hours (100 K x 1.5).
- 5.3d Electron micrograph of 4 MeV alpha tracks in cellulose nitrate (Daicel, Japan) at 90° incidence, etched in 2.5 N sodium hydroxide at 18°C for 26 hours (25 K x 2).
- 5.3e Electron micrograph of 4 MeV alpha tracks in cellulose nitrate (Daicel, Japan) at 45° incidence, etched in 2.5 N sodium hydroxide at 18°C for 26 hours (25 K x 2).
- 5.3f Electron micrograph of 4 MeV alpha tracks in cellulose nitrate (Nixon-Baldwin, USA) at 90° incidence, etched in 2.5 N sodium hydroxide at 18°C for 26 hours (25 K x 2).
- 5.3g Electron micrograph of 4 MeV alpha tracks in cellulose nitrate (Nixon-Baldwin, USA) at 45° incidence, etched in 2.5 N sodium hydroxide at 18°C for 26 hours (25 K x 2).
- 5.3h Electron micrograph of 3 MeV alpha tracks in cellulose nitrate (Dynamit-Nobel, Germany) at 90° incidence, etched in 2.5 N sodium hydroxide at 18°C for 26 hours (25 K x 2).
- 5.3i Electron micrograph of 3 MeV alpha tracks in cellulose nitrate (Dynamit-Nobel, Germany) at 45° incidence, etched in 2.5 N sodium hydroxide at 18°C for 26 hours (25 K x 2).
- 5.3j Electron micrograph of 5 MeV alpha tracks in cellulose nitrate (laboratory made) at 90° incidence, etched in 2.5 N sodium hydroxide at 18°C for 26 hours (25 K x 2).
- 5.3k Electron micrograph of 5 MeV alpha tracks in cellulose nitrate (laboratory made) at 45° incidence, etched in 2.5 N sodium hydroxide at 18°C for 26 hours (25 K x 2).
- 5.4a Diagram of an apparatus designed in order to vary the alpha energies and incident angles. This apparatus consists of an evacuable metal chamber which houses a movable system containing the americium source and a rotating disc containing the specimen.
- 5.4b Graph showing a calibrated curve for alpha energies of the americium source versus the pressure in the vacuum chamber.
- 5.5 Photomicrograph of a beam tube assembly terminating in the rotator system containing specimen foils and semi-conductor particle detector.
- 5.6a Diagram showing target layout on the 6 MV Van de Graaff.
- 5.6b Scale diagram showing the accelerator vacuum box.
- 5.7 Photograph of a SSTR rotator system showing rotator with 12 recorders, back-plate with motor and semi-conductor and housing with beam entrance hole.

* The detector was etched in 2.5 N NaOH not 2.5 N NaCl as stated on the illustration.

Figure

- 5.8 Photograph of the scaler for counting the signal from the semi-conductor detector due to passage of alpha particles.
- 5.9a Diagram showing the installation of the NISUS facility on the reactor CONSORT.
- 5.9b Photograph showing the hollow boron carbide shell positioned inside the lower hemisphere of the NISUS facility on the reactor CONSORT.
- 5.9c Photograph showing the proton recoil proportional counter positioned inside the uranium shell of the NISUS facility on the reactor CONSORT, as used in the experiments.
- 5.9d Photograph of the foil holder of the NISUS facility on the reactor CONSORT. The solid State Track Recorder was held in position next to the foil.
- 5.10 Diagram of the cross-sectional side elevation on the thermal column extension surrounding the NISUS facility on the reactor CONSORT.
- 5.11 Diagram showing details of the demountable SSTR holder and the uranium-cadmium plug to simulate the closed-shell configuration when performing experiments inside the NISUS facility.
- 5.12 Electron micrograph of 5 MeV alpha tracks in CA 80-15 (Kodak-Pathe, France) at 90° incidence, etched in 2.5 N sodium hydroxide at 18°C for 26 hours (3 K x 2).
- 5.13 Scanning electron micrograph of 5 MeV alpha tracks in CA 80-15 (Kodak-Pathe, France) at 70° incidence, etched in 2.5 N sodium hydroxide at 18°C for 26 hours (50 K x 2).
- 5.14 Photomicrographs of 0.60 MeV overlapping proton tracks in CA 80-15 (Kodak-Pathe, France) at 90° incidence, pre-swollen in 65% zinc chloride solution for two hours at 18°C , then treated with calcium hydroxide (base-exchange) for 26 hours.
- 5.15 Photomicrograph of 0.60 MeV overlapping proton tracks in LR 115 type-II (Kodak-Pathe, France) at 90° incidence, pre-swollen in 65% zinc chloride solution for two hours at 18°C , then treated with calcium hydroxide (base-exchange) for 26 hours.
- 5.16 Photomicrograph of fission fragment tracks in soda lime glass, in 2π geometry.
- 5.17 Photomicrograph of fission tracks in soda lime glass at 90° and 70° incidence.
- 5.18a Diagram of the experimental arrangement used for the track parameter measurements.
- 5.18b Graph showing the diameters of the 1st and 2nd corrected dark rings (in mm) as a function of track diameter. The solid curves were calculated using equation 5.6.
- 5.18c Graphs showing the D-d relation. The diameters D were calculated from the 1st and 2nd dark rings (see text), the d values were measured by microscope. The error bar d gives the halfwidth of the track diameter distributions.
- 5.19 Optical diagram of the interface contrast device.

Figure

- 5.20 Photomicrographs of alpha tracks incident normal to the surface of the detector (CA 80-15 cellulose nitrate) taken with colour interface. The energies of the incident alpha particles were: (a) 1 MeV, (b) 2 MeV, (c) 3 MeV, (d) 4 MeV.
- 5.21 Block diagram of the Quantimet 720.
- 6.1 Diagram showing the damage trail and track etching on a sub-microscopic scale.
- 6.2 Partially etched particle damage trails seen on the scale of an optical microscope. Both tracks are etching toward the right-hand side of the figure. It should be noted that the diameter of the damage trail has been exaggerated.
- 6.3 Sequential stages of track etching for a particle damage trail of finite length.
- 6.4 Pointed tracks and their parameters ($B < L_r \sin\theta$).
- 6.5 Rounded tracks and their parameters ($L_r \sin\theta < B < L_r \left\{ \sin\theta + \frac{\sin\frac{1}{2}(\delta-\theta)}{\cos\frac{1}{2}(\delta+\theta)} \right\}$).
- 6.6 Tracks with no undercutting and their parameters ($\delta < \pi/2 - \theta$).
- 6.7 Nonundercutting tracks with partially circular track openings and their parameters ($L_r \sin\delta < B < L_r (\sin\delta + \sin\theta)$).
- 6.8 Graph showing track density ρt (arbitrary units) versus etching time, t (minutes), etched in 6 N KOH at $(50 \pm 0.1)^\circ\text{C}$, for several different plastic detectors.
- Photograph showing the Talysurf 4 machine used for measuring the bulk etching rates of CA 80-15 and LR 115 type-II cellulose nitrate plastic.
- Photograph showing the universal measuring machine SIP 214 used for measuring the bulk etching rates of CA 80-15 and LR 115 type-II cellulose nitrate plastic.
- 6.9 Graph showing the difference in detector thickness and track diameter measurements versus etching time for CA 80-15 cellulose nitrate etched in 2.5 N NaOH at 50°C .
- 6.10a Graphs showing the bulk etching rate (V_B) of CA 80-15 cellulose nitrate versus NaOH concentration (normals) at different temperatures without etchant agitation or interruption of the etching process.
- 6.10b Graphs showing the bulk etching rate (V_B) of CA 80-15 cellulose nitrate versus KOH concentration (normals) at different temperatures without etchant agitation or interruption of the etching process.
- 6.11 Graphs showing: a) Bulk etching rate of CA 80-15 (V_B) versus normality for KOH at 50°C ;
b) Bulk etching rate of CA 80-15 (V_B) versus normality for LiOH at 50°C .
- 6.12 Graph showing the bulk etching rate (V_B) of CA 80-15 cellulose nitrate versus NaOH concentration (normals) at 50°C with varying interruption periods and stirring speeds.
- 6.13 Graph showing the bulk etching rate of unplasticised cellulose nitrate versus NaOH concentration (normals) at 40°C .

Figure

- 6.14 Graph showing the bulk etching rate of CA 80-15 cellulose nitrate partly plasticized (stored in high vacuum) versus normality for NaOH at 40°C.
- 6.15 Graph showing the bulk etching rate of CA 80-15 cellulose nitrate partly plasticized (stored in high vacuum) versus normality of NaOH at 15°C.
- 6.16a Graph showing the bulk etching rate of CA 80-15 cellulose nitrate versus temperature at different concentrations of NaOH, without interruption or agitation.
- 6.16b Graph showing the bulk etching rate of CA 80-15 cellulose nitrate versus temperature at different concentrations of KOH, without interruption or agitation.
- 6.17 Graph showing the bulk etching rate of partly plasticized CA 80-15 and LR 115 type-II (stored in high vacuum) as a function of temperature, without interruption or agitation.
- 6.18 Graph showing the effect of temperature and concentration on the total alkali and water absorbed by CA 80-15 plasticized and un-plasticized cellulose nitrate.
- 6.19 Graph showing the NaOH and H₂O absorbed by cellulose nitrate at 25°C. Curves: 1. total alkali; 2. preferentially absorbed alkali; 3. water absorbed.
- 6.20 Graph comparing (A) the alkali absorbed by the (B) the swelling produced in cellulose nitrate on treatment with solutions of various alkali metal hydroxides.
- 6.21 Electron micrograph of cellulose nitrate detector CA 80-15 (Kodak-Pathe, France), unirradiated, etched with 2.5 N sodium hydroxide at 18°C, for 20 hours (25 K x 3).
- 6.22 Electron micrograph of cellulose nitrate detector CA 80-15 (Kodak-Pathe, France), unirradiated, etched with 5 N sodium hydroxide at 50°C, for 1 hour (25 K x 3).
- 6.23 Photomicrograph of 2.0 MeV alpha tracks in LR 115 type-II (Kodak-Pathe, France) at 90° incidence, etched in 5 N sodium hydroxide at 50°C, for 1 hour.
- 6.24 Photomicrograph of 2.0 MeV alpha tracks in LR 115 type-II (Kodak-Pathe, France) at 90° incidence, etched in 2.5 N sodium hydroxide at 18°C, for 20 hours.
- 6.25 Photomicrograph of 2.0 MeV alpha tracks in LR 115 type-II (Kodak-Pathe, France) at 90° incidence, pre-swollen in 65% zinc chloride solution for two hours at 18°C, then etched in 5 N sodium hydroxide at 50°C, for 1 hour.
- 6.26 Photomicrograph of 2.0 MeV alpha tracks in LR 115 type-II (Kodak-Pathe, France) at 90° incidence, pre-swollen in 65% zinc chloride solution for two hours at 18°C, then etched in 2.5 N sodium hydroxide at 18°C, for 18 hours.
- 6.27 Diagram showing a plot of the measurements of the cone-coordinates.
- 6.28 Graph showing the time required to etch out fission fragment tracks in CA 80-15 cellulose nitrate plastic as a function of NaOH concentration (normals), without interruption or agitation.

Figure

- 6.29 Graph showing the track etching rate (V_T) of CA 80-15 cellulose nitrate as a function of NaOH concentration (normals) at a temperature of 15°C , without interruption or agitation.
- 6.30 Photomicrograph of 2.0 MeV alpha tracks in LR 115 type-II (Kodak-Pathe, France) at 30°C incidence, etched in 5 N sodium hydroxide at 50°C , for 1 hour.
- 6.31 Photomicrograph of 2.0 MeV alpha tracks in LR 115 type-II (Kodak-Pathe, France) at 30° incidence, pre-swollen in 65% zinc chloride solution for 2 hours, then etched in 5 N sodium hydroxide at 50°C for 1 hour.
- 6.32 Photograph of 2.0 MeV alpha tracks in LR 115 type-II (Kodak-Pathe, France) at 30° incidence, etched in 2.5 N sodium hydroxide at 18°C , for 20 hours.
- 6.33 Photomicrograph of over etched 2.0 MeV alpha tracks in LR 115 type-II (Kodak-Pathe, France) at 30° incidence, pre-swollen in 65% zinc chloride solution for 2 hours, then etched in 2.5 N sodium hydroxide at 18°C , for 18 hours.
- 6.34 Graph showing V_T/V_B of CA 80-15 cellulose nitrate as a function of temperature for 2.5 N NaOH, without interruption or agitation.
- 6.35 Graph showing V_T/V_B of CA 80-15 cellulose nitrate as a function of NaOH etchant concentration (normals) at 15°C , without interruptions or agitation.
- 6.36 A free energy diagram of irradiated and unirradiated CA 80-15 cellulose nitrate.
- 6.37 Graph showing the temperature dependence of latent track fading for 2.5 MeV alpha particles in CA 80-15 cellulose nitrate plastic etched for 15 hours in 2.5 N NaOH solution at 18°C , without interruption or agitation. The degree of fading is represented by the fraction of the circle that is filled.
- 6.38 Diagram showing the critical angle of etching (θ_c), and its importance on the efficiency of solid state track recorders.
- 6.39 Diagrammatic representation of an etched track and its importance on the determination of the parameters of the etched track.
- 6.40 Diagram showing profiles of the "effectively etchable" portions of the damage trails.
- 6.41 Diagram showing the importance of the critical angles of etching in the determination of solid angles subtended by SSTRs on a point source.
- Graph showing the variation of the detection efficiency of CA 80-15 cellulose nitrate as a function of the angle of incidence of the alpha particles, which have an energy of 2.5 MeV.
- 6.42 Graph showing the variation of the critical angle of track revelation (θ_c) with annealing temperature for CA 80-15 cellulose nitrate etched in 2.5 N NaOH at 18°C for 16 hours without interruptions or stirring. The critical angle of track revelation (θ_c) was $5^\circ \pm 2^\circ$. No change in θ_c took place when the CA 80-15 cellulose nitrate was annealed between 25°C and 40°C , at 5°C intervals, for an annealing time of ten minutes at each temperature.

Figure

- 6.43 Diagram showing the importance of the critical angles of etching in the determination of the efficiency of SSTRs on a point source.
- 6.44 Graph showing the comparison of the frequency histogram of observed number of tracks per strip with the Poisson distribution P_n , corresponding to the observed mean value ($m=17.622$). (The strips are CA 80-15 cellulose nitrate irradiated with charged particles using a cyclotron.)
- 6.45 Graph showing measurements of the track etching rates and the ratio of the track etching rates to the bulk etching rates as a function of the particle restricted energy loss rates (REL) and Δ REL (REL of the incident particle - REL critical of the detector) for CA 80-15 cellulose nitrate etched in 2.5 N NaOH at 15°C and 18°C, without interruptions or stirring.
- 6.46 Diagram showing the primary specific ionization corresponding to the full range and etchable range of the incident charged particle (note the threshold of track registration, i.e. REL critical, and the volume of the damage profile in relation to the detector surface).
- 6.47a Graph showing the measurements of the average track etching rate, V_T , as a function of Δ REL (the difference between the particle average REL and the detector's critical REL (REL_{crit})) in CA 80-15 cellulose nitrate plastic etched with various concentrations of NaOH and at different etching temperatures, without interruptions or stirring.
- 6.47b Graph showing the measurements of track etching rate (V_T) versus REL for CA 80-15 cellulose nitrate plastic pre-treated in a concentrated solution of zinc chloride (swelling agent) and etched with different etchant concentrations and temperatures, without interruptions or stirring.
- 6.47c Graph showing the measurements of the particle average \overline{REL} as a function of the average track etching rate, V_T , in CA 80-15 cellulose nitrate plastic etched with various concentrations of NaOH at different etching temperatures, without interruptions or stirring, except where indicated (by V_{BS}).
- 6.48 Electron micrograph of 1.1 MeV proton track in CA 80-15 (Kodak-Pathe, France) at 90° incidence, pre-swollen in 65% zinc chloride solution for 2 hours, then etched in 2.5 N sodium hydroxide at 18°C, for 4 hours (25 K x 3).
- 6.49 Electron micrograph of 1.1 MeV underetched proton tracks in CA 80-15 (Kodak-Pathe, France) at 60° incidence, pre-swollen in 65% zinc chloride solution for 2 hours, then etched in 2.5 N sodium hydroxide at 18°C, for 4 hours (25 K x 3).
- 6.50 Diagrammatic representation of alpha particle tracks in CA 80-15 at various particle energies for etching in 2.5 N NaOH for 20 hours at 18°C.
- 6.51 Diagram showing the various observed categories of etched tracks in a stack of cellulose nitrate plastic layers.
- 6.52 The predicted maximum registration range, R_{reg} , in CA 80-15 cellulose nitrate (density of CA 80-15 cellulose nitrate is 1.54 gm/cm³).

Figure

- 6.53a Graph showing alpha particle ranges in CA 80-15 using 2.5 N NaOH at 18°C.
- 6.53b Graph showing the ranges of various charged particles in CA 80-15 using 2.5 N NaOH at 18°C.
- 6.54 Graph showing the measurements of the rate of change of etched track length with respect to particle residual range as a function of the particle charge (z) for stacks of CA 80-15 cellulose nitrate irradiated with ions of maximum energy 12.6 MeV/amu and etched in 2.5 N NaOH at 18°C for 100 hours, without interruptions or stirring.
- 6.55a Graph showing the measurements of true track length (L_1) as a function of residual range (R) for stacks of CA 80-15 cellulose nitrate irradiated with ions of maximum energy 12.6 MeV/amu and etched in 2.5 N NaOH at 18°C for 100 hours without interruptions or stirring.
- 6.55b Graph showing the measurements of the true track length (L_1) as a function of residual range (R) for CA 80-15 cellulose nitrate films irradiated with charged particles of maximum energy 0.70 MeV/amu and etched in 2.5 N NaOH at 18°C for 6 hours, with no interruptions or stirring.
- 6.55c Graph showing the measurements of the rate of change of etched track length with respect to particle range as a function of the particle charge (z) for CA 80-15 cellulose nitrate films irradiated and etched as in 6.55b.
- 6.56 Histogram showing the measured charge distribution of cosmic ray particles in CA 80-15 cellulose nitrate at an altitude of 145,000 ft over Manitoba, Canada. The peaks observed in the figure indicate that charge discrimination is being achieved. The precision in the z determination varies from approximately ± 0.3 for $z = 18$ to ± 3 for some of the particles measured at $z = 7$.
- 6.57 Electron micrograph of 0.8 MeV alpha track in LR 115 type-II (Kodak-Pathe, France) at 90° incidence, etched in 2.5 N sodium hydroxide at 18°C for 2 hours (25 K x 3)*.
- 6.58 Electron micrograph of 0.8 MeV alpha track in LR 115 type-II (Kodak-Pathe, France) at 30° incidence, etched in 2.5 N sodium hydroxide at 18°C for 2 hours (25 K x 3).
- 6.59 Electron micrograph of 1.1 MeV proton track in CA 80-15 (Kodak-Pathe, France) at 90° incidence, pre-swollen in 65% zinc chloride solution for 2 hours, then etched in 2.5 N sodium hydroxide at 18°C, for 16 hours (25 K x 2).
- 6.60 Electron micrograph of 1.1 MeV proton track in CA 80-15 (Kodak-Pathe, France) at 60° incidence, pre-swollen in 65% zinc chloride solution for 2 hours, then etched in 2.5 N sodium hydroxide at 18°C, for 16 hours (25 K x 2).
- 6.61a Diagram showing the continuous etch apparatus for induction time measurements.
- 6.61b The induction time (T_{in}) versus the particle's $|\Delta(\text{REL}) \times z^*|$. These measurements were obtained using the apparatus shown above.

* The magnification should be (25 K x 3), not (25 K x 31) as shown in the text.

Figure

- 6.62 Diagram showing the successive etched surfaces and their effect on the geometry of the track and the cone angle θ^* .
- 6.63 Diagram showing the track geometry: (a) with V_T constant, the cone angle is $\sin^{-1}(V_0/V_T)$. (b) with V_T decreasing as etching continues, the shape of the etched track is more complicated.
- 6.64a Graph showing the variation of etched track diameters in relation to the etching time for H^1 , D^2 , T^3 , 3_2He , 4_2He particles normal to the CA 80-15 cellulose nitrate detector surface.
- 6.64b Graph showing track diameter as a function of etching time in CA 80-15 cellulose nitrate for particles of energies 1.5 and 6.0 MeV with an angle of incidence of 90° , etched in 2.5 N NaOH at $18^\circ C$.
- 6.65 Graph showing the variation of track diameters with the corresponding particle energy and charge.
- 6.66 Histograms showing the diameter distribution of etch pits initiated by protons of different energies (in keV). Values for the removed layer thickness are noted in each right upper corner.
- 6.67 Graph showing a few optimum values for the full width at half-maximum (fwhm) as a function of proton energy, as shown in Figure 6.66.
- 6.68 Histogram summary of different spectra obtained from alpha particles. Distribution of etch pit radii versus sum of residual thickness and etch pit radius. All the etchings were carried out at the rear of the detector sheets.
- 6.69 Graph showing the maximum etchable track length distributions initiated by alpha particles normal to the surface of the CA 80-15 cellulose nitrate detector.
- 6.70 Graph showing the full width at half-maximum of the range (lower curve) and the energy determination (upper curve) as a function of particle range and energy. The error of etching and microscopic measurement is given at 0 MeV.
- 6.71 Electron micrograph of etched alpha tracks in CA 80-15 cellulose nitrate (2π geometry).
- 6.72 Photomicrograph of 4.0 MeV alpha tracks in CA 80-15 (Kodak-Pathe, France) at 90° incidence, pre-swollen in 65% zinc chloride solution for 2 hours at $18^\circ C$, then etched in 2.5 N sodium hydroxide at $18^\circ C$ for 20 hours.
- 6.73 Photomicrograph of 4.0 MeV alpha tracks in CA 80-15 (Kodak-Pathe, France) at 30° incidence, pre-swollen in 65% zinc chloride solution for 2 hours at $18^\circ C$, then etched in 2.5 N sodium hydroxide at $18^\circ C$ for 20 hours.
- 6.74 Photomicrograph of 6.0 MeV alpha tracks in CA 80-15 (Kodak-Pathe, France) at 40° , 45° , 55° , 70° , 80° and 90° incidence, etched in 2.5 N sodium hydroxide at $18^\circ C$ for 26 hours.

* V_G shown on this diagram should read V_B (bulk etching rate).

Figure

- 6.75 Photomicrograph of 1.50 MeV proton tracks in CA 80-15 (Kodak-Pathe, France) at 30°, 40°, 50°, 60°, 75° and 90° incidence, pre-swollen in 65% zinc chloride solution for 2 hours, then etched in 2.5 N sodium hydroxide at 18°C for 22 hours.
- 6.76 Electron micrograph of 1.1 MeV proton track in CA 80-15 (Kodak-Pathe, France) at 90° incidence, pre-swollen in 65% zinc chloride solution for 2 hours, then etched in 2.5 N sodium hydroxide at 18°C for 24 hours (25 K x 2).
- 6.77 Electron micrograph of 1.1 MeV proton track in CA 80-15 (Kodak-Pathe, France) at 60° incidence, pre-swollen in 65% zinc chloride solution for 2 hours, then etched in 2.5 N sodium hydroxide at 18°C, for 16 hours (25 K x 2).
- 6.78 Photomicrograph of 3.90 MeV alpha tracks in CA 80-15 (Kodak-Pathe, France) at 90° incidence, etched in 2.5 N sodium hydroxide at 18°C, for 26 hours.
- 6.79 Photomicrograph of 3.90 MeV alpha tracks in CA 80-15 (Kodak-Pathe, France) at 30° incidence, etched in 2.5 N sodium hydroxide at 18°C for 26 hours.
- 6.80 Graphs showing the ratio of \bar{w}_D/\bar{w}_0 (the average width of etched fission fragment tracks at gamma doses of "D-megarads" and "zero-megarads") of CA 80-15 cellulose nitrate versus gamma dose, etched in 2.5 N and 6 N NaOH at (a) 18°C and (b) 50°C, without interruptions or stirring.
- 6.81 Graphs showing the ratio of \bar{w}_D/\bar{w}_0 (the average width of etched fission fragment tracks at gamma doses of "D-megarads" and "zero-megarads") of CA 80-15 cellulose nitrate versus gamma dose, etched in 2.5 N and 6 N KOH at (a) 18°C and (b) 50°C, without interruptions or stirring.
- 6.82 Graphs showing the bulk etching rate of CA 80-15 cellulose nitrate versus gamma dose (a) etched in 2.5 N and 6 N NaOH at 18°C without interruption or stirring, and (b) etched in 2.5 N and 6 N NaOH at 50°C without interruption or stirring.
- 6.83 Graphs showing the bulk etching rate of CA 80-15 cellulose nitrate versus gamma dose (a) etched in 2.5 N and 6 N KOH at 18°C without interruptions or stirring, and (b) etched in 2.5 N and 6 N KOH at 50°C without interruption or stirring.
- 6.84 Graphs showing the ratio of $V_{B,D}/V_{B,0}$ (the ratio of the bulk etching rate at gamma doses of "D-megarads" and "zero-megarads") of CA 80-15 cellulose nitrate versus gamma doses, etched in 2.5 N and 6 N NaOH at (a) 18°C, and (b) 50°C, without interruptions or stirring.
- 6.85 Graphs showing the ratio of $V_{B,D}/V_{B,0}$ (the ratio of the bulk etching rate at gamma doses of "D-megarads" and "zero-megarads") of CA 80-15 cellulose nitrate versus gamma doses, etched in 2.5 N and 6 N KOH at (a) 18°C, and (b) 50°C, without interruptions or stirring.
- 6.86 Diagram showing the experimental geometry used in the irradiation of boron carbide pellets for the measurement of $^{10}\text{B}(n,\alpha)$ reaction rates.

Figure

- 6.87 Three-dimensional diagram showing the functions assumed for the variation of particle detection efficiency as a function of particle energy and angle of incidence. E_L , E_U are the lower and upper energy limits for track registration respectively, C_{eff} is the counting efficiency, E is the particle energy and θ is the particle angle of incidence relative to the SSTR surface. a. Sinusoidal efficiency, b. Flat efficiency between the sensitivity-energy range limits of 100%.
- 7.1 Diagram of the aldehyde groups produced by radiation damage in cellulosic materials which can be revealed using Schiff's reagent.
- 7.2 Diagram showing how the "dialdehyde" cellulose of Figure 7.1 is converted by mild oxidation via chlorous acid, acidic sodium chlorite or barium hypiodite into the corresponding "dicarboxyl" cellulose.
- 8.1 Photograph showing details of a long tailed rodent, (a) with x-rays and (b) with 400 MeV/nucleon neon ions.
- 8.2 Photographs showing: (a) an EMI Scan of the brain consisting of 180 views and requiring a 1600 mrad dose to the subject.
(b) a helium ion image of the same subject on SSTR consisting of 64 sheets of CA 80-15 cellulose nitrate plastic, requiring only a 30 mrad dose.
- 8.3 Schematic diagram of helium ion transverse section imaging (charged particle radiography).
- 8.4 Photograph showing: (a) A plane intersecting the ventricles in the human brain for imaging the cross-section.
(b) Reconstructed image of the brain.
(c) Densities of the brain and the surrounding bones and tissues.

CHAPTER ONE

RESEARCH ON TRACKS IN SOLIDS

1.1 Introduction

Solid state track recorders (SSTR's) have been used in an astonishing variety of ways in the natural sciences and in technology over the last eighteen years since the discovery of the track etching method. The detecting principle is based on the delineation of individual paths of heavily ionised charged particles in a number of dielectric solids, including minerals, glasses and polymers. Delineation is accomplished through the selective etching of the radiation damaged material along the particle trajectory. This results in an etch pit, or in some cases a narrow channel, referred to as a track. Further etching enlarges tracks to a convenient size for direct viewing with an ordinary optical microscope. The field has now reached a certain maturity, but it is still evolving and much useful work remains to be done both on the nature of charged particle tracks in insulating solids, and on their applications.

SSTR's are becoming increasingly important in radiation dosimetry and nuclear reactor physics. Among their useful characteristics the following are worth mentioning: ability to permanently record tracks of particles which ionize above a certain level while excluding a very high background of other radiation; convenience due to small size and weight; low cost of detectors, track processing and counting; huge range of dose amenable to study; ubiquity of track recording in insulators permitting selection of a detector with particular characteristics. The general applicability of this technique in the study of fission phenomena is based upon the following properties:

- (i) They are insensitive to light and weakly ionizing radiations (β , γ , X-ray) and simple to use, unlike nuclear emulsions.
- (ii) They are not affected by environmental influences (temperature, humidity, etc.) and therefore are stable for a long time, unlike nuclear emulsions.
- (iii) The source of fission fragments can be placed in direct contact with the solid state track recorder, so that very high efficiency and sensitivity can be obtained.
- (iv) Solid state track recorders possess considerable geometric flexibility, and can be shaped to detect fragments over an extended

solid angle, or can be reduced in size to eliminate flux depression or flux perturbation.

(v) Solid state track recorders actually measure the integral flux; it is not necessary to know exactly the time elapsed before measurements, nor the time elapsed after measurements and before etching of the detector. In fact the detector can be stored for a long time without losing any of its efficiency and sensitivity - but it is necessary to know the exact time of irradiation when fission rate and cross-section measurements are required. Moreover, the flux need not be constant during irradiation as is the case when making measurements with activated foils.

This chapter contains a sketch of the history of tracks in solids and several of the important track revelation methods. A summary of applications to radiation dosimetry and nuclear reactor physics is presented and the usefulness of increasing the sensitivity of plastic detectors is pointed out. The nature of the damage trail in both inorganic and organic insulators is then discussed. Finally, the research carried out on properties of tracks in cellulose nitrate is motivated in terms of extending our knowledge about the damage trail and the sensitivity of track revelation.

1.2 History of Tracks in Solids

Since the first observation of the radioactivity of uranium by Becquerel, track registration in photographic emulsions has been a major tool in nuclear science, as the first available method for the permanent recording of tracks of ionizing particles. However nuclear emulsions have a number of drawbacks: fogging by background radiation, fading (especially under conditions of high temperature and humidity), limited shelf life, need for darkroom processing, shrinking of the sensitive layer during processing, and often tedious microscopic evaluation. Therefore alternative methods of permanent nuclear track registration in solids are highly desirable, whence the utility of SSTR's.

One of the great advantages of SSTR's is their insensitivity to β , γ , and X radiation which makes nuclear track counting possible in high radiation environments such as inside nuclear reactors. Each detector has its particular sensitivity, i.e. a level of particle energy loss (LET) below which no tracks are seen and above which almost all particles create tracks. For example, mica registers tracks of ions which

are more ionizing than ^{20}Ne ; in fission studies, tracks of fission fragments are seen, but not those of alphas.

An extremely simple technique for revealing particle impact locations in insulators was first described by Young in 1958. He observed microscopic etch pits in the surface of a lithium fluoride crystal which had been irradiated with uranium fission fragments and subsequently etched in a mixture of hydrofluoric and acetic acids and ferric fluoride (1). He reasoned that the damage trail of a fission fragment is similar to that of a dislocation; the free energy of the trail should be higher than that of the surrounding undamaged material and thus should be preferentially attacked by a suitable etchant. The usefulness of etching techniques for the study of surface emergent crystal defects was already recognised; the first direct proof that dislocations could be revealed under the microscope by means of etching had been given in 1952 (2).

At about the same time, the first photographs of damage trails (latent tracks) created by heavy ions were made by Silk and Barnes (3). These were transmission electron micrographs of fission tracks in mica observed by diffraction contrast (due to the strain field produced around the damage trail).

Rather surprisingly, Young's discovery remained unexploited for several years until the study of track etching was intensively taken up again by Price and Walker (1962) and by Fleischer and Price (1963). These workers showed that tracks could be enlarged and made visible by etching in a wide variety of dielectrics, including minerals such as mica (4), natural and artificial inorganic glasses (5), and organic polymers (6). The last category proved to be the most sensitive, permitting the detection not only of heavy, densely ionizing particles, but also of light particles such as alphas and protons. Only if the stopping power is greater than $\sim 15 \text{ MeV cm}^2/\text{mg}$ can tracks be detected by etching in inorganic media. By contrast, all organic polymers which have been tested record particles of stopping power less than $\sim 4 \text{ MeV cm}^2/\text{mg}$ and some cellulose derivatives record as low as $\sim 1 \text{ MeV cm}^2/\text{mg}$.

Since 1962, nuclear track registration has burgeoned as a field of fundamental research and especially as a field of applied research having wide implications for nuclear physics and chemistry, earth and space sciences, biology and dosimetry; these wide-ranging applications have been the subject of a recent book (7).

A survey was made in 1972 of work on nuclear track recorders. In this survey, questionnaires were sent to more than 550 researchers at approximately 220 laboratories where work with track recorders had been reported. These laboratories represented 29 countries. Replies about work in progress were received from 118 laboratory groups in 20 countries; their national distribution is shown in Table 1.1 reflecting a widespread geographic interest in track work. Subsequently there has been a dramatic increase in the number of laboratories using techniques for the registration of nuclear particles in dielectric materials. In this period, there has been additional published work on solid state track recorders from countries other than those in Table 1.1, including Brazil, Republic of China, Czechoslovakia, German Democratic Republic, Pakistan and U.S.S.R. (7). It is probable that at present more than 300 laboratories throughout the world are using these techniques.

It is interesting to compare the rate of development of nuclear emulsions and of solid state track recorders. Alpha tracks from radioactive decay were studied as early as 1910 in ordinary photographic emulsion, however no attempts to improve their sensitivity and stability were made for a long time. It was not until 1946 that emulsions with a high concentration of silver halide grains were produced and intensively applied to elementary particle and cosmic ray research. By contrast, important nuclear physics experiments were done very soon after the discovery of track etching in solids, and relatively little effort has gone into modifying the structure of detectors, because of the wide range of available SSTR's with different sensitivities. The favourite detectors today are ordinary glass, muscovite mica and commercial plastic films.

1.3 Methods of Track Revelation in Solids - General Considerations

The quality and quantity of information which can be acquired about the tracks left by the passage of charged particles in a dielectric depend on the methods of revelation and observation. Different revelation techniques have different sensitivities (i.e. for charged particles of differing stopping power or linear energy transfer, LET) as well as different efficiencies (fraction of existing tracks which are observable). Each method of revelation has its particular advantages and disadvantages; a detailed discussion is given in Chapter Five.

TABLE 1.1

THE NATIONAL DISTRIBUTION OF LABORATORIES USING
SOLID-STATE TRACK RECORDERS

Country	Number of Laboratories
United States	53
West Germany	18
France	8
Japan	6
England	5
Australia	3
Belgium	3
Canada	3
Italy	3
Switzerland	3
Hungary	2
Ireland	2
Netherlands	2
Austria	1
India	1
Israel	1
Poland	1
Romania	1
Sweden	1
Trinidad	1

1.3.1 Transmission electron microscopy

This technique has a number of severe limitations: extremely thin specimens are required with large track densities; only a small track length can be examined; observations are limited to tracks of heavy particles; track fading due to the electron beam occurs in certain substances. However, since electron microscopy is a direct method, it provides fundamental information on latent track structure unobtainable by other means. In addition, it is of advantage when very large track densities ($> 10^5 \text{cm}^{-2}$) are to be measured.

Since the original experiments of Silk and Barnes, a number of different systems have been studied (8). The observations fall into two classes: (1) tracks in ultra thin ($< 100 \text{ \AA}$) polycrystalline layers and thin polymer films (2) tracks in bulk insulating monocrystals. In the first case the tracks are visible by enhanced transmission due to the removal of material by evaporation along a line $50\text{-}100 \text{ \AA}$ wide. A furrow is formed along the track, the removed material being deposited on both sides as small particles of $\sim 50 \text{ \AA}$ diameter. In the second case the contrast is due to diffraction effects, suggesting a radial displacement field of cylindrical symmetry; the track core of diameter $\sim 100 \text{ \AA}$ is probably rich in vacancies and interstitials are shot out radially.

1.3.2 Decoration technique

Various methods have been used to nucleate precipitates of a second phase along the damage tracks. These methods allow tracks to be displayed throughout a large volume, even when they do not intersect the surface. Often, however, the efficiency varies in an erratic manner, depending sensitively on a few impurities in the detector material. In crystals the precipitation is caused by the strain field along the track, which favours the presence of either over or undersized atoms near the track centre. An analogous phenomenon is observed in the strain field of dislocations.

The most successful decoration procedure involves the deposition of silver along tracks in silver chloride (9), which renders them visible in the optical microscope. Ultra-violet light creates free photoelectrons, which are pulsed through the crystal via an electric field and react with silver ions to convert them into silver atoms. The sensitivity of cadmium doped silver chloride detectors is greater

than any of the etched track detectors so far developed, which is not surprising since the process involved is similar to photography (sensitive nuclear emulsion can reveal even the weakest ionizing electron track). Latent tracks in these AgCl detectors are unstable and fade with time; they can be stabilized for months by illumination in light during or just after the passage of a particle (10). This feature offers a simple method of switching the detector "on" or "off".

In polymers, tracks can be decorated by the grafting method, which utilizes the high concentration along damage trails of free radicals and reactive groups (such as peroxy groups) to initiate graft copolymerization (11). Fission fragment tracks in cellulose triacetate have been revealed by grafting with acrylic acid and subsequent dyeing of the graft to improve optical contrast. The technique needs more development before it can be reliably applied.

1.3.3 Chemical etching

By far the most widely used technique for observing charged particle tracks in solids is the method of preferential etching which enlarges tracks large enough to be easily visible with the optical microscope. The etchant attacks the damage trail faster than the detector surface. The technique is very simple; ordinary acids and bases are used as etchants. Moreover, it is the only procedure that has succeeded in revealing tracks of extremely low-energy heavy nuclei (down to ~ 0.3 keV/nucleon) such as solar wind ions and recoil nuclei from alpha decay (7).

The etching of particle tracks is more of an art than a science. Optimized etching conditions have to be established empirically for each detector material. More for convenience than for scientific reasons, simple etchants such as KOH, NaOH and HF have dominated etching work for a long time. Only in recent years have more sophisticated procedures such as multistep treatments and more complex etchants (e.g. oxidizing agents) been studied. Much remains to be done along this line.

The etching rate along the track depends mainly on the following variables: (i) charge and velocity of the particle, (ii) etchant composition, (iii) nature of etchant (temperature and concentration), (iv) detector pre- and post-irradiation treatments, (v) the environment of the detector foil during irradiation. Under point (iii) should be

included the fluid motion of the etchant around the detector; stirring and agitation often increase the surface etching rate. As an example of point (v), the presence of oxygen during irradiation of cellulose nitrate foils increases the sensitivity substantially (12).





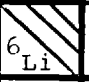

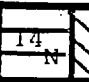

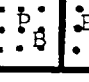
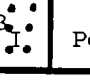

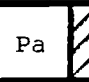

If only track densities are required, the etching conditions do not have to be precisely controlled; however, accurate measurements of track dimensions require reproducibility of etching conditions and control of changes in etchant activity during etching. Precise measurements of the track dimensions have been used for particle type and energy identification. The high resolution of the method permits close neighbours like ^{10}B and ^{11}B to be distinguished (13).

1.4 Applications of Solid State Track Recorders

The applications of SSTR's to pure and applied science are too manifold to even treat briefly here. Among the most important applications are fission track dating (geochronology, geophysics, palaeontology, archaeology), cosmic ray and solar flare studies, tracks in meteorites and lunar rocks and soil, nuclear fission studies and element mapping and isotopic analysis in various specimens. These applications as well as many others are extensively treated in a recent book (7). Here I confine myself to a discussion of some of the closely related applications of SSTR's to radiation dosimetry and nuclear reactor physics. However, two interesting applications fall outside these categories. The first is the use of solid state track recorders to determine the concentration of various elements in a specimen; these elements are shown in Table 1.2. This application is based on the fact that the number of tracks produced per unit area is proportional to the concentration of the element emitting the particles which produce the tracks. With the proper choice of detector and etching conditions, it is possible to make sensitive chemical analyses in a variety of specimens. The second is the technique of heavy ion radiography which involves shooting a monoenergetic beam of charged particles (e.g. ^{16}O ions) through the object to be imaged and bringing the beam to rest in a stack of plastic sheets. Particles traverse about the same mass thickness (g/cm^2) before coming to rest in a particular sheet, which gives information about the mass density along their path. The technique seems capable of becoming a practical tool for tumour diagnosis (14). Proton and alpha radiography may also be of interest, however, because of smaller straggling and scattering, radiographs of

TABLE 1.2

Elements that can be determined by SSTR

		 (n, α) Reaction		 (n,p) Reaction													
		 (γ ,f) Reaction															
		 (n,f) Reaction (thermal and fast)															
H																	
 ⁶ Li	Be																
Na	Mg																
				 ¹³ B	 ¹⁴ N												
				Al	Si												
					P												
					S												
					Cl												
					Ar												
K	Ca	Sc	Ti	V	Cr	Mn	Fe	Co	Ni	Ca	Zn	Ga	Ge	As	Se	Br	Kr
Rb	Sr	Y	Zr	Nb	Mo	Tc	Ru	Rh	Pd	Ag	Cd	In	Sn	Sb	Te	I	Xe
Cs	Ba	La*	Hf	Ta	W	Re	Os	Ir	Pt	Au	Hg	 ²⁰³ Tl	 ²⁰⁹ Pb	 ²¹⁰ Bi	Po	At	Rn
Fr	Ra	Ac**															
			* Ce Pr Nd Pm Sm Eu Gd Tb Dy Ho Er Tm Yb Lu														
			**  ²³¹ Th  Pa  ²³⁷ Np Pu Am Cm Bk Cf Es Fm Md No Lw														

higher resolution can be produced with heavy ions. The application of this technique is restricted by the need for high energy particles (several hundreds of MeV/nucleon).

1.4.1 Radiation dosimetry

Neutron detection and neutron fluence measurements have been made mainly by using tracks from (n, fission) reactions. The neutron fluence is measured by counting the fission tracks recorded in a thin detector foil in contact with a foil of fissionable material. The technique has a number of advantages over the older methods of counting recoil protons in nuclear emulsions or measuring the radioactivity of a fissile foil or other neutron absorber; insensitivity to γ , X and β radiation; permanent recording with no deterioration, storage or fading problems; ease of "development" and evaluation; high sensitivity of detector to fission fragments; wide range of doses amenable to measurement; small detector gives small flux perturbation; detectors can be easily switched "on" or "off". The main problem is in preparing uniform, thin layers of fissionable materials; this problem can be avoided by using a layer thicker than the range of fission fragments so that fragments from zero to the maximum energy strike the detector. The sensitivity of a plastic detector in contact with a thick fission foil is given by (15) $\rho(\text{tracks/cm}^2) = 1.6 \times 10^{-5} \Phi(\text{neutrons/cm}^2) \sigma$ (barns), because all fissionable isotopes emit fission fragments with roughly the same range and the same detection efficiency in sensitive plastics.

A variety of particles and radiations can be readily counted by their property of inducing fission as shown in Tables 1.3 and 1.4; high-energy charged particles including protons, electrons of a few hundred MeV and γ 's of more than about 20 MeV can be detected. Such dosimetry is particularly important around high-energy accelerators and is also applicable for recording doses of the lightly ionizing nucleonic portion of the cosmic rays that are encountered at high altitudes or in space. Often detector-foil combinations with different fissionable nuclei will be needed if neutron effects are to be separated from those of the charged particles of interest (16).

It is easy to obtain a histogram of the neutron energy distribution by employing either fissionable materials with different thresholds or the same material encapsulated in different neutron shields. For example, a ^{10}B spherical shell eliminates thermal and

TABLE 1.3

PARTICLE TRACK DETECTORS

Type of Radiation	Mode of Observation	Detector Material	Sensitivity Track/Particle	Notes
Fission fragments	Direct	Any dielectric solid	1.0	
Heavy cosmic rays; Heavy ions from accelerator	Direct	Most plastic detectors	1.0	For ions at sufficiently low energies
Alpha particles	Direct	Cellulose plastic or U.V. irradiated Lexan	0.1 - 1.0	Most efficient at energies below 4 MeV
Protons	Direct	Cellulose nitrate or acetate	0.1 - 1.0	Only at low energy (0.55 MeV)
Protons	Induced fission	Any dielectric solid	$\sim 10^{-5}$	High energy; depends on fission cross section of fissioned nuclide
Fast neutrons	Induced fission	Any dielectric solid	$\sim 10^{-5}$	"

TABLE 1.4

PARTICLE TRACK DETECTORS

Type of Radiation	Mode of Observation	Detector Material	Sensitivity Tracks/Particle	Notes
Thermal neutrons	Induced fission	Any dielectric solid	$\sim 5 \times 10^{-3}$	Via ^{235}U fission foil
Thermal neutrons	Reaction (n, α)	Cellulose nitrate or acetate	$\sim 2 \times 10^{-2}$	^{10}B layer or deposit
Fast neutrons	Recoil nuclei	Cellulose Derivatives or Polycarbonate	$\sim 3 \times 10^{-5}$	Energy > 0.5 MeV
High-energy electrons	Induced fission	Any dielectric solid	10^{-8} to 10^{-7}	Energy > 200 MeV
High-energy γ	Induced fission	Any dielectric solid	$\sim 2-3 \times 10^{-6}$	Energy > 20 MeV

resonance neutrons and provides a cut-off of ~ 10 keV for the neutron spectrum (17). By using foils of ^{235}U , ^{239}Pu , ^{237}Np , ^{238}U and ^{232}Th , the neutron flux can be determined in the following five energy intervals (in MeV) (18): 0-0.1; 0.1-0.6; 0.6-1.5; 1.5-3; 3-6. For personnel dosimetry of fast neutrons ^{237}Np has the best characteristics because of its low threshold, high cross-section and absence of high-energy γ sensitivity.

Thermal and epithermal neutrons can be best measured by employing the (n,α) reactions of ^{10}B or ^6Li whose cross-sections go as v^{-1} . For a thermal neutron distribution the cross-sections are 3840 barns for ^{10}B and 950 barns for ^6Li , both of which are significantly higher than the fission cross-section of ^{235}U . A sensitivity of 0.013 tracks/neutron has been attained using a thick ^{10}B layer with a cellulose nitrate detector (19). The technique is attractive as it avoids the disadvantages of fissionable materials.

Alpha particle dosimetry is important in certain environments. Alphas represent a hazard at very high altitudes and also in uranium mines where radon gas and its daughters emit high energy alphas (5.5 to 7.7 MeV). Sensitive plastic detectors such as cellulose nitrate are in present use in personnel dosimeters (7).

Fast neutrons can produce tracks by causing nuclei to recoil elastically and also by (n,α) and other reactions. In the most general detector geometry there is a triple sandwich of a radiator of track-forming particles, an energy degrading foil and the SSTR. Spectral information on high-energy neutrons can be obtained from the manner in which the track density changes with varying degrader thickness (20). Measurements consist of track counting and do not involve the relatively complex procedures of track dimension measurements. The maximum recoil energies due to 14 MeV neutrons (e.g. from a fusion reaction) are: ^9Be (5.04 MeV); ^{12}C (4.0 MeV); ^{16}O (3.1 MeV). The radiator and detector can be the same sensitive plastic film, resulting in a somewhat lower sensitivity; the sensitivity of cellulose nitrate detectors is $(1-3) \times 10^{-5}$ tracks/neutron depending on the neutron energy, which is comparable to that of a natural uranium radiator (enclosed in cadmium) next to a fission track detector (21). The sensitivity of plastic films can be increased by a factor of ~ 12 by employing a helium atmosphere as the radiator. Neutrons of energy greater than 10 MeV can be distinguished from lower energy neutrons by detecting three-prong stars

from the breakup reaction $^{12}\text{C}(n,n')3\alpha$; the sensitivity is $\sim 4 \times 10^{-8}$ tracks/neutron at 14 MeV (22). SSTR's based on direct interaction are by far the least expensive and simplest fast neutron detectors available.

1.4.2 Reactor physics applications

Fission rate, neutron flux and nuclear fission cross-section measurements are all simplified by using SSTR's which do not register the background of β and γ radiation and perturb neutron fluxes minimally. The fission reaction, so basic in nuclear science and engineering, is very important in reactor physics measurements. Use is made either of the kinetic energy of the fission fragments, or their resulting γ -activity, or as already discussed their ability to produce tracks in nuclear emulsions and solid state track recorders.

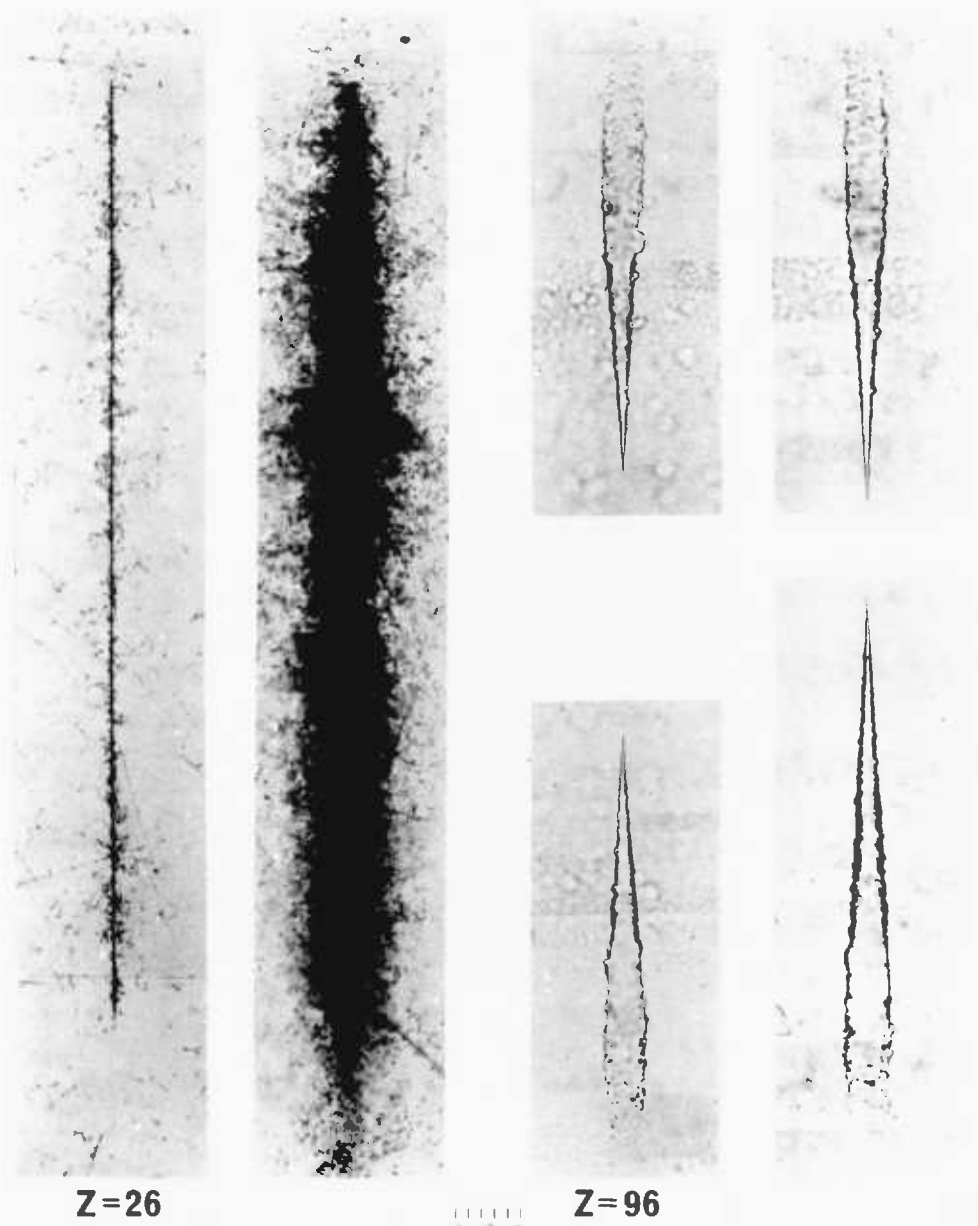
A few remarks on these different techniques are appropriate. In measurements of neutron fluxes using fission chambers, the ionization produced as the fission fragments are brought to rest is utilised. A particular problem with their use is the perturbation introduced by the fission chamber material on the neutron flux. To reduce neutron absorption and scattering effects, the electrodes and structural elements are usually made of aluminium, and the insulators are made of a hydrogen-free polymer.

In the γ -counting technique, use is made of the fission product activity in the foil detectors. If the fission yield of the product is known, the number of the fission events can, therefore, be deduced from the γ -activity. The time of irradiation and the time elapsed to the γ -activity measurement must be accurately known, as shown in Figure 1.1.

When charged particles pass through sensitive nuclear photographic emulsions they produce latent images along their paths. Upon development of the film, grains of silver appear along the tracks of the charged particles. A detailed examination of the structure of the tracks leads to determination of the mass, charge and energy of the charged particle.

SSTR's have been used inside reactors for fission density distribution measurements inside fuel elements and near interfaces. Intracell and axial fast neutron flux distributions have been measured via recoil and (n,α) reaction tracks in a Makrofol (poly-carbonate)

Figure 1.1



Typical Fe calibration track in emulsion with adjacent ultra heavy cosmic ray primary in both emulsion and plastic.

film (23). Mica has been used extensively for flux measurements via fission tracks (24). The neutron flux distribution near boron containing "grey" control rods and the microscopic distribution of boron in steel were investigated by recording alphas from the $^{10}\text{B}(n,\alpha)^7\text{Li}$ reaction (25). The fast advantage factor was calculated from measurements of the fast neutron flux inside fuel elements and in the moderator. The $^{238}\text{U} : ^{235}\text{U}$ fission ratio was measured in a fast neutron reactor using fission tracks in Lexan (polycarbonate) plastic film (26). When the track density is greater than 10^5 cm^{-2} , it has been measured directly in very thin Lexan films with an electron microscope, without preliminary etching (27). This technique also permits very high spatial resolution.

When reactor fluxes are measured via fission tracks from a uranium radiator, the use of plastics rather than mica improves visibility because of the longer track lengths in organic material. However, sometimes mica is more reliable; track fading in plastics may occur under conditions of high temperature and very high background radiation (α , β , and γ).

Improving sensitivity is one of the main problems in extending the use of SSTR's for registering light particles at higher energies. For example, it has been proposed to design an SSTR as a small neutron spectrometer using the (n, α) reaction, which could be inserted in a fast reactor fuel element (28). For neutron energy measurements above 100 keV, it would be a clear advantage to use recoil protons: the (n,p) elastic cross-section is particularly high and slowly decreasing with energy, (thus giving a fairly uniform response); the recoiled energy is the highest of any nucleus; the proton recoil track is long, permitting accurate measurement of its energy. Thus one would like to measure the tracks of protons up to about 2 MeV, while the present sensitivity of cellulose nitrate corresponds to protons of only several hundred keV. More sensitive organic detectors or improved revelation techniques to permit the registration of recoil protons over a larger range of energies would also be of great advantage in fast neutron dosimetry (21).

1.5 Radiation Damage Along Tracks

Compared to the widespread interest in seeking new applications of the track etching technique, research on the mechanism of latent

track formation has been relatively neglected. Part of the difficulty is that dielectric detectors fall into two distinct categories: inorganic crystals and glasses, and organic polymers. As mentioned previously, these two categories have quite different sensitivities, which can be related to their structural differences (see Chapter Four). A better understanding of the processes of track formation and revelation could lead to finding improved detectors and revelation techniques.

Nearly twenty years after the observation of fission fragment tracks in mica, the detailed atomic structure of heavy ion tracks in insulating minerals is still poorly understood. Experiments on mica have shown that 1 MeV/nucleon Ar ions create not only dispersed point defects, but also large defects of diameter $\sim 30 \text{ \AA}$ (29). Later studies by low angle X-ray scattering of various heavy ion tracks showed that point defects and large defects are formed along the ion path; the latter have diameters between 20-60 \AA depending on the incident particle (30). These large defects comprise the latent track which becomes visible after etching. Low LET particles form only point defects. The spacing between the large defects must be sufficiently small in order that a visible track may be etched.

In organic polymers, the most plausible theory for latent track formation is based on a radiochemical damage mechanism (21). Etchable tracks are formed by radiolytic scission of long polymer chains into shorter fragments, and the production of reactive, low molecular weight species which etch faster than the surrounding undamaged plastic. All particle impacts that create a sufficient number of "chemical activation centers" in a certain minimum volume appear to lead to visible etch pits. The exact threshold concentration of altered chemical species depends on the detector, its pre- and post-irradiation treatments, the type of etchant and the etching conditions. There is no way at present of predicting the sensitivity of a polymeric material.

Experiments support the concept that the radiation dose along a track determines the rate of preferential etching. Irradiation by a beam of β -rays causes localised etchable damage in cellulose nitrate at the megarad dose level (31). Studies of the bulk etching rate of various plastics as a function of the β -ray dose demonstrate its similarity to the behaviour of the track etching rate versus the local dose (in a region around the ion path) (32). However, this correlation does not much simplify the search for sensitive detectors.

1.6 Program of Investigation

It was decided to investigate the properties of charged particle tracks in cellulose nitrate, the most sensitive detector presently known, with a view to understanding the nature of the latent tracks and extending the sensitivity of track recording and revelation. The present work represents a first step in this direction.

(i) Cellulose Nitrate: Radiation Chemistry

Chemical processes play an important role in the radiolysis of polymers, a sketch of relevant parts of the complex subject of cellulose chemistry is presented.

The reactions of cellulose chemistry are known to be greatly facilitated by the use of swelling agents, therefore their effects on latent tracks and track etching are investigated.

(ii) Review of Theoretical Models

The specific problem of understanding the damage processes and mechanisms which occur when a charged particle penetrates a medium is dealt with in this chapter.

(iii) Track Formation in Solids

In this chapter a general discussion of various competing theories of track formation is presented. An attempt is made to evaluate the competing theories and to point out their limitations in explaining the track formation mechanism.

Our preferred model of the track formation mechanisms is presented. Some of the special structural characteristics of polymers are discussed, which are considered to be important in explaining their high sensitivity.

(iv) Track Recording and Revealing Techniques

The experimental techniques used to produce and to reveal the tracks and the instruments used to observe the tracks are discussed. The purpose of these experiments is to fulfil the objectives set forth in this chapter as well as substantiating the theoretical ideas discussed in this research.

The various irradiations performed with the detectors are discussed and listed in Table 1.5.

TABLE 1.5

LIGHT AND HEAVY IONS USED IN THIS STUDY

Particle	Source of Irradiation	Particle Energy in MeV/Nucleon	Angle of Incidence
Protons	Oxford van de Graaff Harwell Tandem Accelerator	0.2 - 1.4 1.4 - 4.5	10°, 20°, 30°, 40°, 50° 60°, 70°, 80°, 90°
Alpha	Americium-241 Californium-252	0.1 - 1,35 0.1 - 1.5	2π geometry 2π geometry
Alpha	Harwell 6 MeV van de Graaff	0.15 - 1.5	5° - 90° at 5° step
Alpha	(n,α) reaction $^{10}\text{B In, } ^7\text{Li}$ Silwood Park Experimental Consort Reactor, University of London Reactor Centre -	0.37 and 0.45	2π geometry
Chlorine-35	Harwell Tandem Accelerator	0.1 - 1.0	~ 45°, ~ 30°, ~ 90°
Fission Fragments	Silwood Park Experimental Consort Reactor, University of London Reactor Centre -	0.1 - 1.0	~ 45°, ~ 60°, ~ 90°
Fission Fragments	Californium-252	~ 0.8 - 1.0	2π geometry

(v) Track Development by means of Chemical Etching

Different commercial and laboratory-made plastic films are studied in order to determine their sensitivity and reproducibility on etching. The Kodak-Pathé plastic films CA 80-15 and LR-115 Type II cellulose nitrate films are used in these studies, due to their superior characteristics; high sensitivity; uniformity of different sheets; homogeneity; stability against environmental effects. However, the exact composition of these plastics such as the plasticizer, the colouring agent and the degree of polymerization is regarded by the manufacturer as a trade secret and this caused considerable difficulties.

The nature of the track etching process, geometry and the important parameters of etched tracks are studied by varying the concentration and temperature of the etchant. An etching condition is established in order to improve the efficiency and sensitivity of the detector.

Thermal neutron dosimetry and high gamma dosimetry are studied from the $^{10}\text{B}(n,\alpha)^7\text{Li}$ reaction and the bulk etching rates for detectors irradiated in odd locations like a reactor core (33,34).

Counting and measurement of track parameters such as the length and cone angle are often necessary, this led to a search for automatic data analysing and recording equipment. An optical digitizer was designed and interfaced with a PDP 11/45 digital computer via CAMAC, capable of counting tracks and measuring parameters of tracks. This invention is described in another publication.

(vi) Track Revelation by Base-Exchange and Free Radicals Technique

The study of cellulose and its derivatives suggested that some of the "chemical activation centres" which are important in etching are acidic (carboxyl) groups. These groups can be studied by base-exchange processes. A new technique of track revelation is found which involves the base-exchange of calcium and barium ions with the hydrogen ions of acidic groups. Since this technique reveals the tracks by visible deposits of calcium or barium, it may be considered to be another decoration method for the tracks. However, since the ions diffuse inwards along the latent tracks, only those tracks which intersect the surface are revealed. An advantage of base-exchange as a revelation technique is that the detector surface is not removed by chemical attack. The sensitivity of this technique remains to be elucidated in further experiments, but it seems that proton tracks of ~ 1 MeV can be revealed without difficulty.

Ionization and excitation of molecules lead to breaking of bonds and the formation of free radicals, which play the role of intermediates in many degradation process of cellulose and its derivatives. Scavengers such as DPPH and iodine react with free radicals to form relatively stable compounds. These scavengers can be dissolved in organic solvents, and then are able to penetrate into cellulose nitrate by solvent action. When the DPPH radical reacts with a free radical inside a latent track it loses its characteristic of light colour in a dark background. Some recent partial results on this method of revelation are given; this method is particularly interesting for elucidating the nature of "chemical activation centres" in latent tracks.

Energetic charged particles from an accelerator may be used to produce radiographs with high contrast and high depth resolution. Small differences in the stopping power of objects can be detected and permanently recorded by using stacks of plastic track detectors. The combination of technique 4 - with this method should aid in the diagnosis of soft-tissue abnormalities, including some tumors, and make possible quantitative reconstruction of the internal density structure of objects.

1.6.1 Objectives of the Present Investigations

The objectives of the present work are:

- 1 - To develop a high resolution SSTR technique capable of accurate quantitative detection and identification of charged particles.
- 2 - To extend the use of this technique to accurate quantitative measurements of (n,α) reaction rate ratios in several neutron spectra.
- 3 - To investigate the feasibility of SSTR techniques in the field of neutron spectroscopy and in-core gamma dosimetry.
- 4 - To develop a new and more sensitive technique of track revelation (other than etching) such as base-exchange and scavengers.
- 5 - To investigate the feasibility of SSTR techniques in the field of diagnostic radiography.

CHAPTER TWO

CELLULOSE NITRATE: RADIATION CHEMISTRY

2.1 Introduction

This chapter is included in order to provide background and to familiarise the reader with cellulose nitrate and the other useful cellulose derivatives with a view to understanding the effects of radiation and the important process of latent track formation as well as the alkaline chemical etching mechanism for track revelation.

In order to discuss the effect of high-energy radiation on cellulose nitrate, it is important to define the starting material as clearly as possible. The composition, morphology, chemical properties, and chemical and physical modifications of the cellulose are important factors in determining the energy-transfer processes in the cellulose molecule. These processes, particularly the localisation of energy, determine the observed chemical and physical effects of radiation on cellulose nitrate.

Cellulose itself has been used as the common standard for the comparison of radiation effects because it is the starting material in the manufacturing of cellulose nitrate plastic, because many properties of cellulose and cellulose nitrate are similar, and because the great majority of physical and chemical studies have been performed on cellulose rather than on cellulose nitrate.

A brief description of the origin, the chemical composition, and the physical structure of this extensive and very complex family of materials is presented. Also included is a short discussion about the effects of thermal decomposition, of oxidative degradation, of ionising radiations, of alkaline degradation and hydrolytic degradation on each of the molecular structures, the chemical properties and the bulk properties of these materials. Since some properties of cellulose and cellulose nitrate are strikingly different, special care has been taken in using the results on cellulose to understand the properties of cellulose nitrate. Preferential etching depends on the relative rate of alkaline degradation of cellulose nitrate in the damaged (i.e. irradiated) and undamaged states. Since irradiated cellulose undergoes oxidative degradation, a discussion is presented of the alkaline degradation process of oxidised cellulose, which proceeds primarily through the scission of chains.

2.2 Cellulose and its Properties

Cellulose (polyanhydroglucose) is a naturally occurring carbohydrate which is present as the chief constituent of the cell wall in all plants. The chief sources of commercial cellulose are cotton hairs and linters, spinners' waste, and specially treated wood pulp which is first freed from lignin by treatment with alkali or acid bisulphate.

Purified cellulose is prepared by utilising a solution of purified cotton linters in cuprammonium hydroxide, from which cellulose is regenerated by spinning into a setting bath of warm water, followed by an acid wash. The empirical formula can be written as $(C_6H_7O_2(OH)_3)_n$. Although the structure of cellulose shown in Figure 2.1 can serve to explain many of its properties, in order to understand its behaviour more fully, it is necessary to consider the spatial arrangement of each atom in a glucopyranose (anhydroglucose) unit. The spatial distribution of these units within the polymer demonstrates how long thread-like chains are possible.

Cellulose is thus composed of a large number of anhydroglucose units joined together by ether linkages. The molecular weight of the anhydroglucose unit is taken as 162, with end groups and trace substituents in the cellulose assumed to be negligible. The average number of anhydroglucose units in a molecule is several thousands for most native celluloses and ranges from 500 to 2,500 for chemically purified celluloses. Thus the length of the polymer chain is specified by the number of repeating units in the chain. This is called the degree of polymerization (\overline{DP}); for a given sample it depends on both the starting material and the method of preparation.

Further information about the nature of forces which hold the lattice structure together in the crystalline form of cellulose as shown in Figure 2.2 has been established by Mark (35). In the direction of the b-axis, the glucose units are held together by strong 1,4 - glucosidic primary valence bonds. Along the a-axis, the glucose rings are separated by only $2.5 \overset{O}{\text{Å}}$ and this suggests that relatively strong forces are acting in this plane, so it is reasonable to assume that hydrogen bonds are formed between oxygen atoms of adjacent molecules. Along the c-axis, the nearest distance between atomic centres is $3.1 \overset{O}{\text{Å}}$ which corresponds closely to the distance

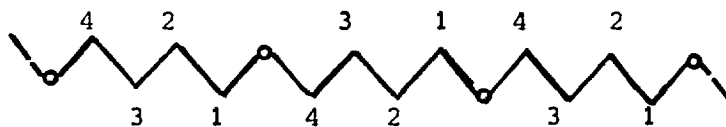
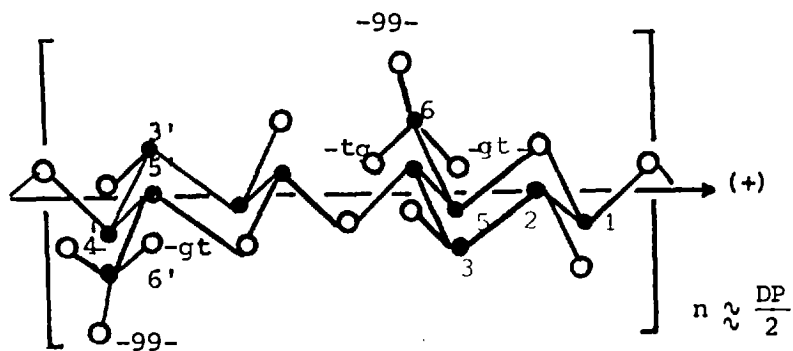
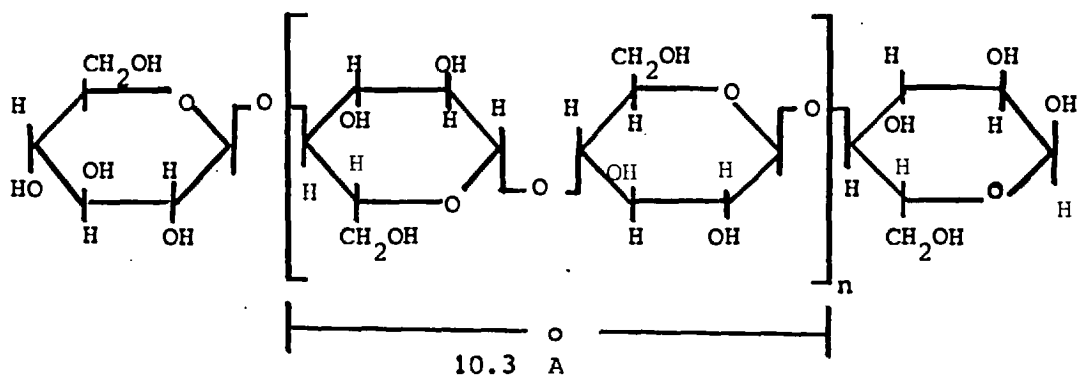


Figure 2.1 The structural formula for cellulose. Three hydroxyl groups are present in each of the anhydroglucose rings; these are joined by ether linkages. In the middle picture is shown the puckered "chair" shape of the rings, oxygen atoms being represented by O's. The bottom picture shows a path along the backbone of the chain, projected on a plane perpendicular to the rings. The carbon atoms are numbered.

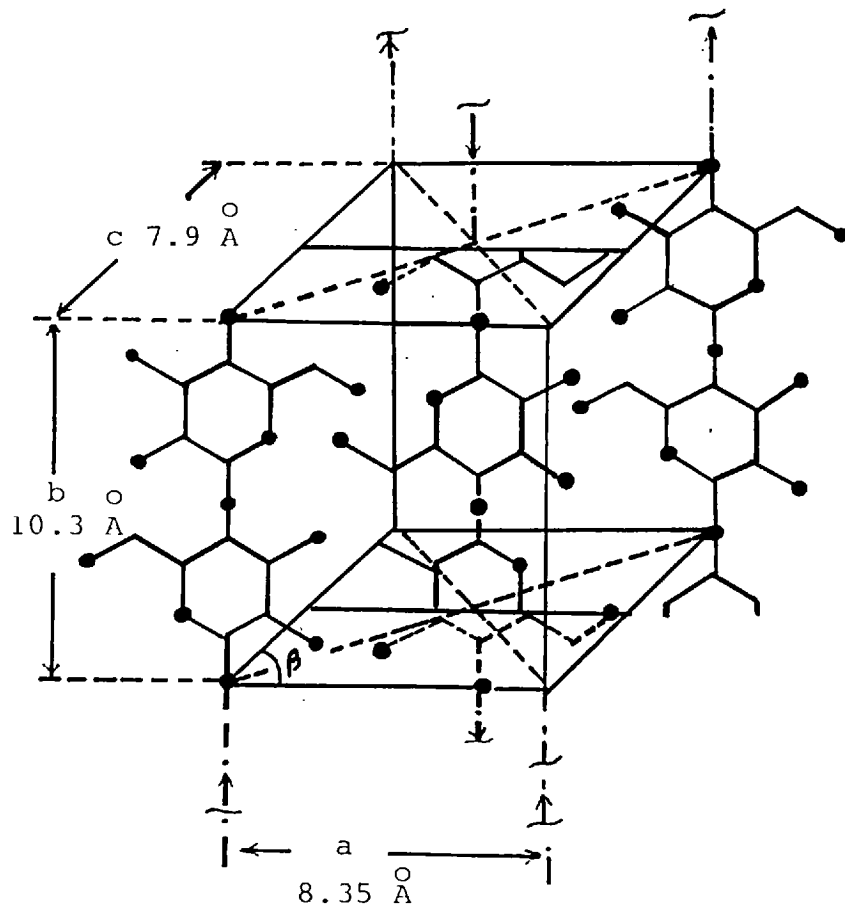


Fig.2.2. The unit cell of native cellulose (Cellulose I). Chains in alternate planes are antiparallel; the chains in the right hand front and left hand rear corners are not shown. Oxygen atoms are represented by black circles. The angle β is 84°.

expected if van der Waals forces hold the lattice together in this direction. No two carbons from each net approach each other closer than 3.1 Å. No two oxygen atoms are closer than 3.8 Å. Thus, cellulose may be regarded as a combination of a chain lattice and a layer lattice, composed of primary valence forces along the b-axis, relatively strong hydrogen bond network in the ab-plane, and weaker van der Waals forces perpendicular to the ab-plane. These three different forces acting in three different directions may be responsible in part for many of the properties of cellulose and its sensitivity as a detector for charged particles.

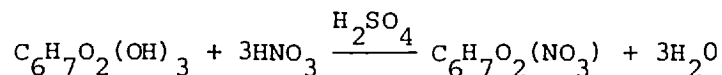
The covalent atomic bonds confer electrical and thermal resistance, rigidity and hardness.

Cellulose occurs in a fibrous form having a specific gravity of about 1.50 - 1.55, and an index of refraction of 1.599 along the fibre and 1.532 perpendicular to it. Cellulosic fibres are built up of bundles of long molecules, held together in a more or less parallel alignment by intermolecular secondary valence forces (hydrogen bonds) due to the highly polar hydroxyl groups. The electric field configuration between neighbouring chains is conducive to their parallel orientation. The crystallites are called micelles and the minimum dimensions of the micelle are thought to be 60-70 Å wide and 600 Å long. Individual chain molecules may traverse many micelles, resulting in an interlocking assembly of mostly parallel micelles or submicroscopic crystallites. According to X-ray measurements, cellulose is from 30% to 70% crystalline depending on the source and regeneration treatment.

Cellulose is insoluble in all organic solvents, has no melting point, and is fairly resistant to thermal degradation. In polymers swelling agents are necessary to facilitate the progress and the speed of various chemical reactions (36) by supplying the necessary energy to break or stretch the hydrogen bonds (which then reform with the swelling agent), but not enough to bring the cellulose into solution. Thus the sodium and zinc ions with their sheaths of water molecules (hydrated ions) can penetrate even into the crystallites and cause intra-crystalline swelling. In general the swelling of the amorphous regions is more rapid and easier (35). In Chapters Seven and Eight it is shown that swelling plays an important role in the alkaline etching of charged particle tracks in cellulose nitrate.

2.3 Cellulose Nitrate: Chemical Composition

Cellulose nitrate is a condensation polymer produced by the esterification of cellulose with nitric acid in the presence of a catalyst, usually sulphuric acid. The hydroxyl ions are replaced by the nitrate ions, according to the following formula for complete nitration



The most important function of sulphuric acid is its role as a dehydrating agent for the additional undesirable water formed in the nitration reaction. Sulphuric acid also functions as a swelling agent allowing initial entry of the nitrate groups and influences the degree of substitution or nitrogen content (37). The concentration of the sulphuric acid governs the degree of nitration obtainable: nearly anhydrous conditions and a low temperature must be maintained if minimum degradation is required. After washing the product, to ensure that traces of acid do not at a later stage initiate its decomposition, it is stabilised by boiling in alcohol or very dilute acid, to remove residual sulphate groups.

The structural formula of cellulose nitrate is shown in Figure 2.3. The degree of substitution is defined as the average number of hydroxyl groups replaced per anhydroglucose unit and varies between 0 and 3. In principle, it should be possible to replace all hydroxyl groups in each anhydroglucose unit with nitrate groups to give cellulose trinitrate. Such a product, having a degree of substitution of 3, would contain 14% nitrogen. In practice, the upper limit for substitution is about 2.9 corresponding to a nitrogen content of 13.8%. To provide properties most valuable for industrial uses, the nitrogen content is maintained between 10.9% and 13.6%. Cellulose nitrate with a nitrogen content of about 11% is used in plastics, 12% in lacquers and 13% in explosives. Cellulose nitrate with nitrogen content less than about 10% is quite insoluble and hence not useful.

2.3.1 Physical Properties of Cellulose Nitrate

Although considerably less crystalline than the parent cellulose, cellulose nitrate possesses, in general, short range order. X-ray and electron diffraction studies amply support this view. They show the existence of short range order extending to about 20-40 Å. The

extent of crystallinity depends on many factors, such as the degree of nitration and the exact conditions and manner of sample preparation. Cellulose nitrate is more naturally crystalline in the trinitrate state than in the less nitrated states. However, as the degree of nitration is decreased towards the pure cellulose form, the polymer becomes more crystalline again. The two properties of a batch of cellulose nitrate which have the greatest influence on its behaviour as a charged particle detector are:

(i) its degree of nitration (which is effected with complete retention of the original fibre structure, the chief superficial changes being an increase in hardness of the fibre and, in the case of cotton, an untwisting of the convoluted fibres), and

(ii) its solution viscosity (which is a function of the molecular weight or degree of polymerisation of the cellulose nitrate. The degree of polymerisation is related to the viscosity of the solution formed when cellulose nitrate is dissolved at a given concentration in a particular solvent. The viscosity of commercial cellulose nitrate is generally expressed in terms of either centipoises (cps) or in the time, expressed in seconds, required for a metal ball of specified size and density to fall through a measured distance in a solution of specific formulation at 25°C. A viscosity of 1 second is equal to about 370 cps. Commercially available cellulose nitrate varies in viscosity from 18 cps = .049 seconds to about 200,000 seconds. The approximate relation between viscosity, molecular weight and the degree of polymerisation is given in Table 2.1.

TABLE 2.1

APPROXIMATE RELATION BETWEEN THE VISCOSITY,
MOLECULAR WEIGHT AND THE DEGREE OF POLYMERISATION
OF CELLULOSE NITRATE

Viscosity	Molecular Weight	Degree of Polymerisation
1/4 sec	22,000	74
30- 40 sec	68,000	229
600-1000 sec	140,000	471

The extent of crystallinity has a definite influence on the mechanical properties of the material. As is the case with many polymers, this material has a viscoelastic response to an applied stress.

Infrared absorption spectrum measurements of cellulose nitrate lead to the proposal that the nitrate group in cellulose nitrate has the resonant structure of Figure 2.3b.

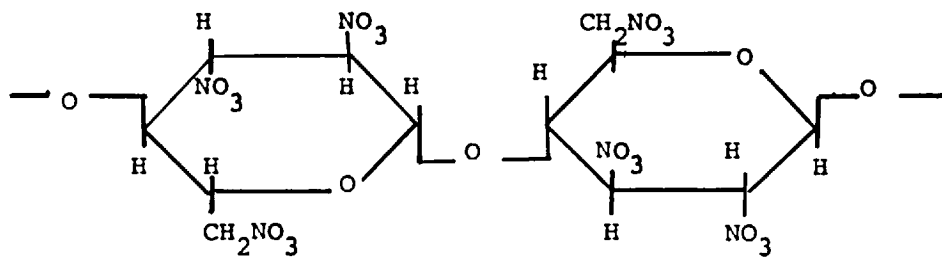
2.3.2 Cellulose Nitrate Plasticisation

The application of plasticisers is of great value in many aspects of polymer technology. In general terms, plasticisers are substances, which mixed with polymers, improve their flow during processing and reduce the brittleness of the end product. The effect of a plasticiser, which is in both physical and chemical contact with a polymer, is to reduce the interchain forces and increase the mobility and flow of the chains, and hence to lower the glass transition temperature below room temperature. Thus, the properties of the polymer change from glassy to rubbery.

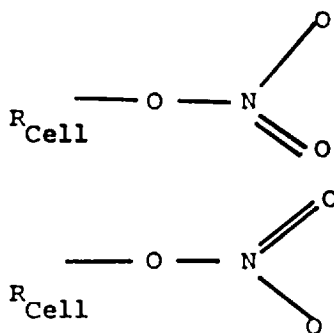
A wide variety of materials find use as plasticisers. The choice for any particular polymer may be limited because the function of plasticisers is based on the fact that they contain groups capable of solvating particular polymer groups. The polar bond from the plasticiser is capable of neutralising or sufficiently weakening the van der Waals forces and hydrogen bonds that exist between the polymer chains. Plasticisers have limited compatibility with highly crystalline polymers, and therefore their use is generally restricted to the more easily soluble amorphous polymers with a low degree of crystallinity.

The addition of plasticisers which are of lower molecular weight (generally organics) to high polymers, also produces swelling; the secondary valence forces are relaxed, permitting flexing of the long linear polymer chains.

There are basically four different types of plasticisers used with cellulose nitrate; they are classified as solvent, non-solvent, monomeric, or polymeric types. Solvent type plasticisers are defined as those which exhibit complete miscibility with cellulose nitrate in all proportions. They act as non-volatile solvents which remain in the treated film. Dibutyl phthalate (DBP) is a typical example. Non-solvent type plasticisers neither dissolve nor form a colloid with



(a)



(b)

Figure 2.3 (a) The structural formula of cellulose trinitrate
 (b) The resonant structure of cellulose nitrate

nitrocellulose, but are compatible with cellulose nitrate in the dry film. They also contribute flexibility to the film; castor oil is a typical example. Monomeric plasticisers such as dioctyl phthalate are generally of low molecular weight. The polymeric types of plasticisers have a relatively low volatility, and do not leave the film even at high temperatures; paraplex G-41 is a typical example.

Cellulose nitrate is soluble in ketones, esters, amides, nitro-paraffins, and ethyl ether/ethyl alcohol mixtures (38). These liquids are usually referred to as true, active or primary solvents. Another group of liquids such as ethyl, isopropyl, and butyl alcohols, and others, are not true solvents in that they alone do not dissolve cellulose nitrate. However, when used in combination with a primary solvent, they improve its dissolving power resulting in solutions with appreciably lower viscosities. These liquids are called co-solvents or secondary solvents. The original plasticiser, camphor, remains standard and the most widely used. The combination of camphor with cellulose nitrate is said to be ideal in the sense that the nitrate group of the latter and the ketone groups of the former interact with the formation of a molecular complex. This interpretation is derived from studies from which it was concluded that cellulose nitrate has the ability to form crystalline complexes with various substances such as acetone, cyclohexanone, fenchone, m-xylene, and camphor (39). The theory is that the camphor molecule, being itself rigid, enforces a high degree of separation between the polymer chains. The effect obtained is proportional to the amount of plasticiser employed. Another effect is to reduce the bulk etching rate of cellulose nitrate films in alkali hydroxides (40).

Often several primary and secondary solvents, each having a specific desirable characteristic, are used in the preparation of films. A proper combination of primary and secondary solvents is needed in order to achieve uniform evaporation through the bulk, and thus a uniform plastic film. Some of the physical properties of plasticised cellulose nitrate film are listed in Table 2.2.

TABLE 2.2

MECHANICAL, PHYSICAL AND ELECTRICAL PROPERTIES
OF PLASTICISED CELLULOSE NITRATE FILM

Specific Gravity	1.35 - 1.60
Refractive Index	1.5
Thermal conductivity in cal/sec cm ^o C	(3.1-5.1) x 10 ⁻⁴
Electrical resistivity (volume) at 30 ^o C in ohm-cm	(0.106-0.32) x 10 ¹⁰
Specific heat in cal/ ^o C gm	0.34 - 0.38
Softening Point	70 ^o - 90 ^o C
Effect of Heat	Decomposition at 100-150 ^o C
Burning Rate	Very High
Effects of ultra-violet light	Discoloration and Embrittlement
Effect of Water	Very Slight Swelling

2.4 Degradation of Cellulose Nitrate

For charged particle track formation the radiative degradation of cellulose nitrate is of primary concern. The precise nature of this process is complex and remains mostly to be elucidated by future experiments. At this time, one can make only conjectures on the basis of extensive studies on cellulose, since similar detailed studies of cellulose nitrate are lacking. We shall make the assumption that the radiative degradation of cellulose nitrate may be understood by combining results on the radiative degradation of inorganic nitrates, UV and thermal degradation of cellulose nitrate, and radiative and oxidative degradation of cellulose. Free radicals provide a common thread between the initial stages of these different modes of degradation. The importance of free-radical intermediates in reactions initiated by heat, light, high-energy radiation and oxidation-reduction systems has often been suggested by cellulose chemists (41); all these reactions are of interest for the track formation mechanism. The susceptibility of cellulose derivatives to degradative processes is a reflection both of the chemical nature of the cellulose chain molecule and of that of the substituents along the chain. The most common manifestation of degradation is a decrease in \overline{DP} , evidenced by a loss

of tensile strength of the material as well as marked changes in solubility properties (42).

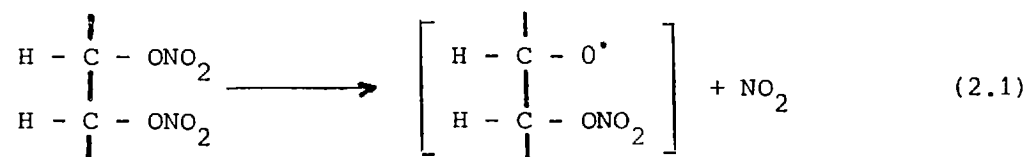
The first stage of radiative degradation involves the creation of free radicals, many of which subsequently react to form new chemical species. In this chapter, attention is focussed on these new species; the long-lived free radicals formed by radiation are discussed in Chapter Seven in connection with track revelation techniques which make use of their presence in the latent track.

2.4.1 Thermal Degradation of Cellulose Nitrate

Fission fragments are well known to lead to thermal spike phenomena due to the high rate of energy loss via fragment-atom collisions to atomic motions. These high temperatures developed along the trajectory of the fission fragments will create local thermal damage and decomposition of the matter penetrated.

Cellulose nitrate is the only one of the cellulose derivatives to undergo extensive thermal degradation. This thermal degradation is a spontaneous reaction whose initial rate is temperature dependent, and which cannot be prevented by antioxidants.

The presence of a weak bond in cellulose nitrate linking the NO₂ group to a CO group in the ring, as shown in Figure 2.3b with an activation energy of approximately 1.7 eV or less, appears to play an important role in the degradation processes (38). This leads to considerable thermal decomposition of cellulose nitrate at moderate temperatures. (1% per hour at 135°C), although at room temperature the decomposition rate is negligible. This may account for the superior sensitivity of cellulose nitrate for nuclear track registration over all other solid state track recorders, including other derivatives such as cellulose acetate. The proposed mechanism for the decomposition is shown in Figure 2.4.



The organic free radical formed in reaction 2.1 together with an NO₂ group is many times more reactive than the NO₂ group itself. The reactivity is such that all these processes occur simultaneously to

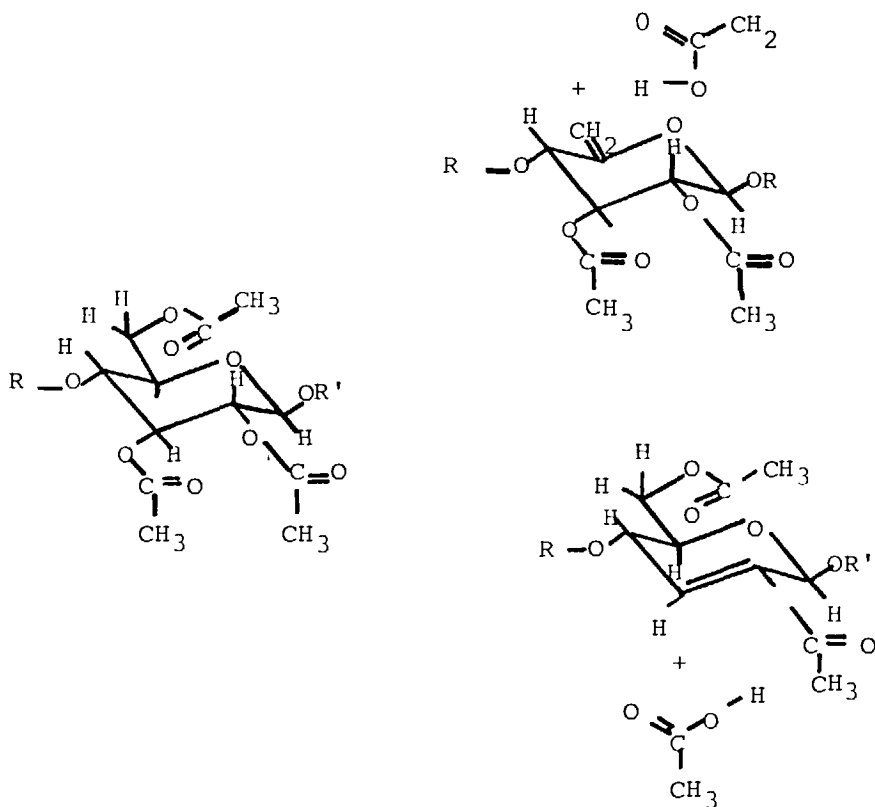


Figure 2.4a Proposed mechanisms for pyrolytic cis-eliminations of acetic acid from cellulose triacetate. Depolymerization would involve other monomeric units.

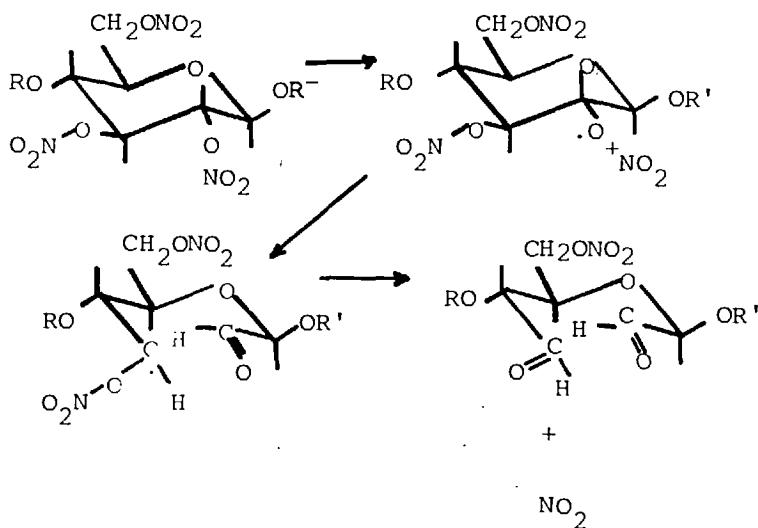
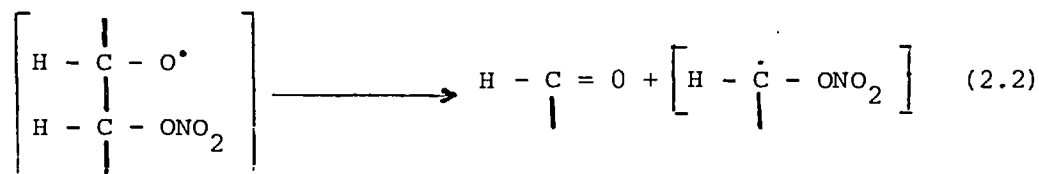


Figure 2.4b Proposed mechanisms for the decomposition of cellulose nitrate.

bring about carbon-carbon bond cleavage and the production of aldehyde groups at position C₆, and ketone groups at C₂ or C₃ or both:



The C-C cleavage shown above between the neighbouring 2,3-dinitrated groups leads to the elimination of another molecule of nitrogen dioxide, $\left[\text{H} - \overset{\cdot}{\text{C}} - \text{ONO}_2 \right] \rightarrow \text{H} - \overset{\cdot}{\text{C}} = \text{O} + \text{NO}_2$, and the resulting dialdehyde reacts with nitrogen dioxide to give carbon dioxide, formic acid and other molecules. In the final stage an accelerated decomposition of the nitrate group at C₆ into nitrogen dioxide and formaldehyde is accompanied by the decomposition of the cellulose chains into smaller fragments. This cleavage reaction can result also in some cross-linking with subsequent insolubilisation in some systems.

From a study of the decomposition rate, one concludes that the stability of the - O - N bond decreases as the number of nitrate groups in the molecule increases, which is in accordance with the observed sensitivity of track formation versus degree of nitration.

The formation of carbonyl groups on the cellulose chain, as a result of thermal denitration, sensitises the chain to alkaline cleavage which could explain the preferential etching by alkalis. The denitration reaction accompanying thermal decomposition produces NO₂ and HNO₃, which are strong oxidising agents and which convert the primary alcohol groups (those which have not been nitrated) into carboxyl groups (43), hydroxyl groups into aldehyde groups, as well as oxidising aldehyde groups into carboxyl groups (44). These oxidative reactions cause further decomposition and chain scission, and still further liberation of nitrogen oxides, instigating thus an auto-catalytic process. The stabilisation of cellulose nitrate against such a process depends upon the addition of substances which consume NO₂ and HNO₃ by nitration reactions, forming inactive products (38). It should be noted that these stabilisers do not slow down the initial decomposition reaction of the nitrate, but rather prevent the occurrence of a self-accelerating reaction.

2.4.2 Radiative Degradation of Inorganic Nitrates

Inorganic nitrates in the form of ionic crystals show a strong tendency to decompose when exposed to ionising radiation (45). Irradiated barium nitrate yields nitrite ions and oxygen upon dissolution in water; the gas is trapped in the crystal as oxygen atoms or oxygen molecules. Reactor-irradiated sodium and potassium nitrate yield oxygen gas not only on dissolution but also on heating to the melting point. It is clear that the gas evolution results from electronic displacement rather than from atomic displacement (which would disappear on annealing). In irradiated sodium nitrate the presence of stable NO_2^- ions is indicated by the optical absorption spectrum. X-rays give about the same yield per dose as reactor radiation (45).

2.4.3 UV Degradation of Cellulose Nitrate

In the case of cellulose nitrate, one would not expect an oxygen atom or NO_2^- ion to remain trapped, since these strong oxidising agents immediately attack the cellulose chains and create a whole range of new molecular species. In fact, over 95% of the gas evolved on irradiating cellulose nitrate appears as hydrogen (46), although this depends to some extent on the atmosphere in which the irradiation is carried out. Hydrogen is the main gaseous product from the irradiation of polymers because of the ease with which hydrogen can diffuse away from a broken C-H bond and the rapidity with which H_2 is formed.

The breakdown of cellulose nitrate film under UV irradiation is greatly accelerated by the presence of oxygen, as shown in Figure 2.5, however the action of oxygen is probably secondary (42). This can be best illustrated by examining the data in Figure 2.5. In this example, cellulose acetate and cellulose nitrate films are compared under the same conditions. The greatly increased rate of viscosity change in an atmosphere of oxygen is readily apparent. The radiative denitration reaction produces NO_2 and HNO_3 as well as organic reducing materials: the latter convert NO_2 to NO . The oxygen probably acts to reconvert NO to NO_2 and HNO_3 ; these cause further degradation of the cellulose nitrate and liberation of nitrogen dioxides, instigating an auto-catalytic process (42). Inorganic peroxides also have a catalytic effect on cellulose nitrate degradation similar to that of oxygen.

The common oxidation and polymerisation inhibitors of the neutral type, such as hydroquinone are effective in retarding the rate of decomposition.

The stability characteristics of cellulose nitrate can be summarised by the following:

1. Thermal degradation of cellulose is a spontaneous reaction whose rate is temperature dependent and which cannot be prevented by anti-oxidants.
2. The products of decomposition, NO_2 and HNO_3 , unless removed, will initiate a further autocatalytic phase of the decomposition.
3. The formation of carbonyl groups on the cellulose chain as a result of thermal denitration sensitises the chain to alkaline cleavage.
4. Oxygen plays only a very minor part in the degradation of cellulose nitrate in contrast to its importance with the other cellulose derivatives.
5. Cellulose nitrate is subject to photochemical decomposition which is accelerated in air or oxygen.
6. Cellulose nitrate solutions, on standing in the dark, show a decrease in viscosity.
7. The decrease in viscosity is accelerated by standing in strong light.
8. The decrease in relative viscosity is more marked the more concentrated the solution.
9. The decrease in viscosity is more marked in the early than in the late stages of the ageing process.
10. The decrease in viscosity has been observed with solutions in acetone and in many other solvents.

2.4.4 Radiative Degradation of Cellulose

The interaction of radiation with a polymer and the subsequent events that occur can be chronologically divided into three distinct periods (47). The first period, lasting less than 10^{-15} sec, is that of energy dissipation by the incident radiation, and the absorption of this energy by matter. There are three ways to absorb energy in a solid:

- (a) electron displacement (both ionisation and excitation are included under this heading),

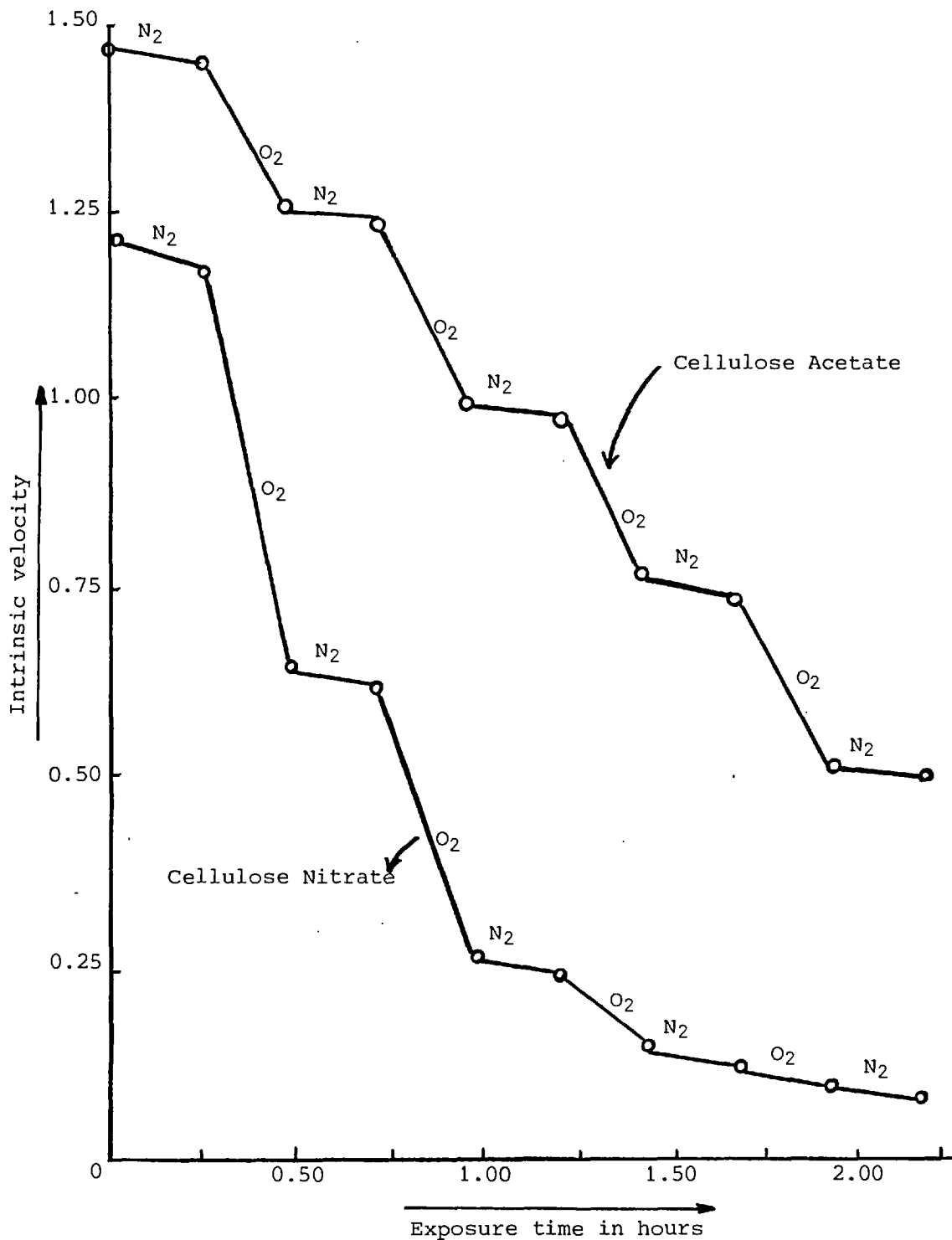


Figure 2.5 Degradation of cellulose acetate and cellulose nitrate in the presence of ultraviolet light at 60°C. Samples of cellulose acetate (38.0% acetyl content) and cellulose nitrate (11-10% N) cast as 0.005-in. films were exposed to ultraviolet light in alternate atmospheres of nitrogen and oxygen

- (b) atomic displacement,
- (c) generation of an impurity atom as a result of a nuclear reaction.

The second period, lasting anywhere up to 10^{-12} to 10^{-9} sec, involves the transport and dissipation of absorbed energy by the molecular motion as the thermal equilibrium within the solid is established.

Again, there are three alternatives:

- (a) energy can be emitted as luminescence,
- (b) it can be dissipated as heat,
- (c) energy can be stored as potential energy in the form of chemically reactive species.

The path followed depends strongly on the structure of the polymer molecules and the environmental conditions.

The third and final period is that of the establishment of chemical equilibrium. Here, the potential energy stored in the form of chemically reactive species is dissipated. Diffusion processes and reaction rates extend the duration from a minimum of about 10^{-8} sec up to months or years. To recapitulate, from the absorber point of view, it is convenient to think of three distinct phases:

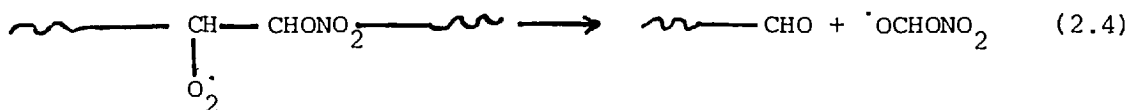
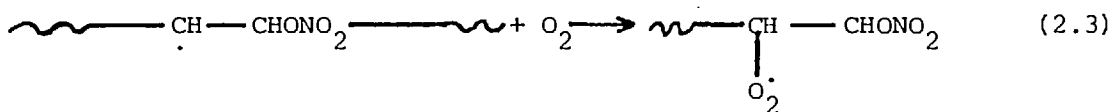
- (a) energy absorption,
- (b) establishment of a thermal equilibrium,
- (c) the establishment of a chemical equilibrium.

The primary mechanism for the absorption of the energy deposited by charged particles is electronic and atomic displacements. The probability of a nuclear reaction is generally low, and the energy transfer resulting from this process can generally be neglected. Except at very low velocities of the incident particle, the predominant mechanism of energy absorption is through electronic displacement, i.e. through ionisation and excitation of electrons of the absorbing medium. Since cellulose nitrate does not readily luminesce, the bulk of the absorbed energy goes either into heat or is stored as potential energy of reactive species. The manner in which the energy is divided between ionisation and excitation depends upon the type of particle, its velocity and the state of the absorbing medium. Very little is known of the number, types or distribution of the chemically reactive species that are formed. Even less is known of the manner in which these species react with each other or with substance present in the matrix of the bulk material (such as oxygen or water). It is in this

area, the approach to chemical equilibrium, that our knowledge of the subject is least satisfactory.

In the studies of irradiated polymers, the major reactions depend primarily on the total absorbed energy (dose) rather than on dose rate, the type of radiation, or its sources (48). Fast electrons, alpha rays, gamma rays or mixed radiation from a reactor, including neutrons, all produce approximately the same effect for a given dose. Polymers containing a high percentage of aromatic rings have been found to be resistant to radiation (for example, the polycarbonate resins); those with highly aliphatic structure are the least resistant (49). There is also a general trend for polymers with the largest molecular size to be more susceptible to radiation damage. This arises from the fact that a small number of chain scissions or cross links can change a large percentage of the molecules. In agreement with these observations, cellulose nitrate is found to be one of the most sensitive of all polymers to high energy radiation.

The resulting conclusion is that the interaction of radiation with the cellulose molecule causes scission at a relatively high rate, about 13.5 scissions per 100 eV of dose (50). The scission reaction breaks the molecule into smaller fragments, decreasing the molecular weight, increasing the solubility, and lowering the softening point. Scission is often accompanied by gas evolution, leading to an oxidative degradation of the solid residue of irradiated cellulose. With increasing dosage there is an increase formation of reducing groups and acid groups. When the cellulose is irradiated in an atmosphere of oxygen, the yields of these groups are slightly greater than those obtained in an atmosphere of nitrogen. The reaction of oxygen with the free radicals formed in the amorphous or more accessible regions of the fibrous cellulose could lead to the formation of reducing groups, as follows:



the formation of OCHONO_2 would also probably cause additional cleavage of anhydroglucose ring, further depolymerisation of the cellulose molecule and formation of acid groups.

Removal of water during irradiation increases the number of trapped radicals; with 0.5% moisture, three times as many radicals are observed as with 7%. The radicals which do not decay on exposure to moisture or oxygen are long-lived, presumably because they are trapped in crystallites where accessibility is decreased. Solvents such as zinc chloride (swelling agents) open the fibrous structure, making some of the radicals available to react (51).

2.4.5 Oxidative Degradation of Cellulose

The interaction of radiation with the cellulose molecule to cause scission and evolution of gases, leads to an oxidative degradation of the solid residue (52). The degradation of cellulose by sunlight also gives an oxidised cellulose (oxycellulose) with a large number of reducing groups (53). This is accompanied by a loss of tensile strength of the fibre (i.e. reduced \overline{DP}) and the production of carbonyl and carboxyl groups. Chain scission and functional group formation results to a large extent during the post irradiation oxidation of long-lived radicals (53). Thus it is relevant to study oxidative degradation in order to understand the radiative degradation of cellulose and especially cellulose nitrate.

A summary (54) of the effects of oxidising agents is given in Figure 2.6. A number of reagents bring about random oxidation; these include oxygen, ozone, H_2O_2 , chlorine and its oxygen acids. The periodates and NO_2 differ from other oxidising agents in that they are able to penetrate and react with the crystalline as well as the amorphous portions of cellulose without causing so much damage that the material loses its fibrous form (55).

The action of many different oxidising agents on cellulose results in the introduction of acidic as well as reducing groups in the chain. According to the nature of the oxidant, the oxycellulose may be predominantly acidic or reducing, or display both characteristics simultaneously.

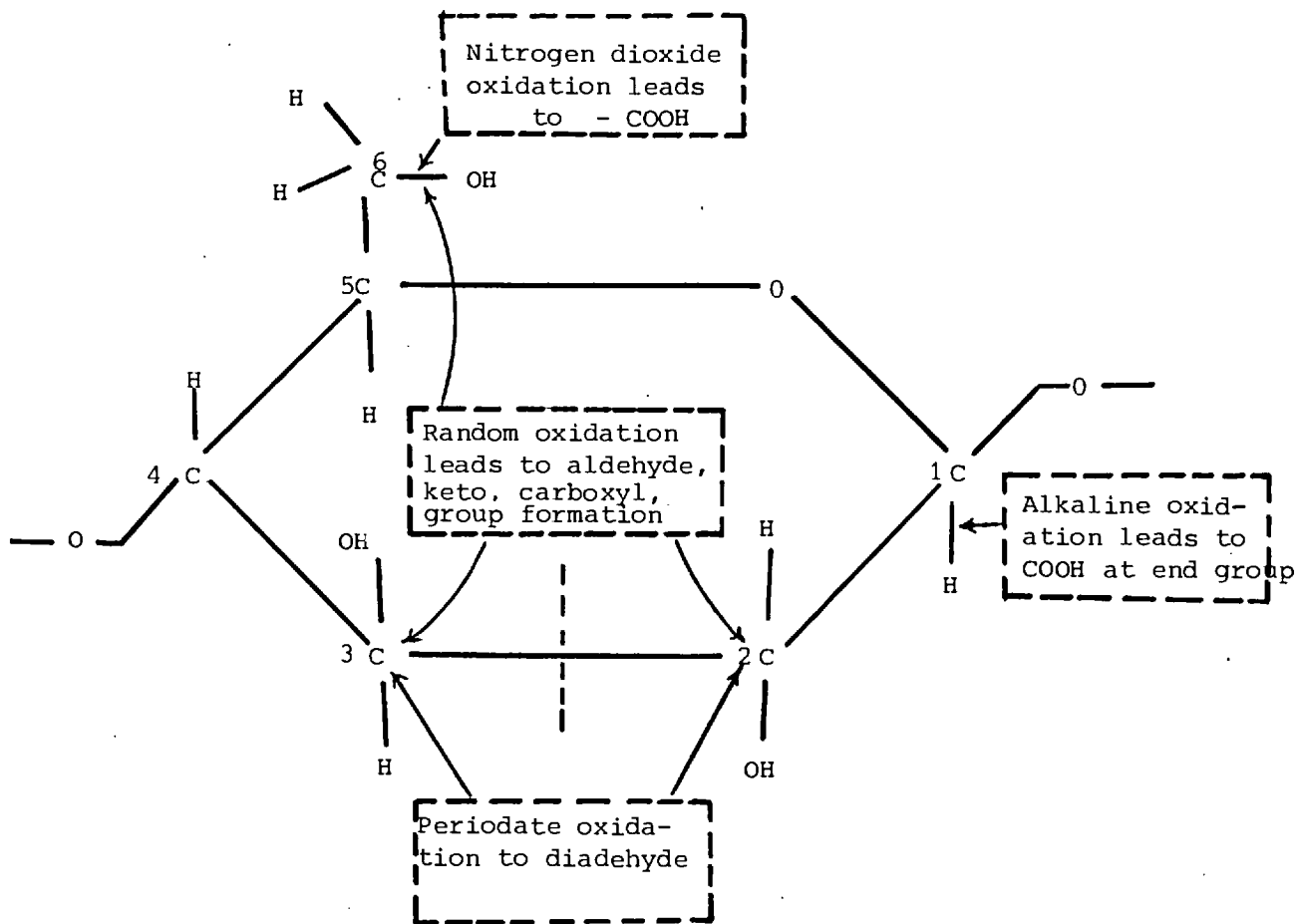


Figure 2.6 A summary of the effects of various oxidizing agents on cellulose. The carbon atoms of the glucose ring are numbered the standard way.

2.4.6 Alkaline Erosion and Scission of Cellulose

The reactions with which we are concerned in this section are those that occur between alkali or the hydroxyl ion and cellulose or an oxidized cellulose. Oxidation by molecular oxygen in alkaline conditions is not considered here, but it should be emphasised that such autoxidation may, as a first step, produce carbonyl-containing oxidized celluloses, which are subsequently degraded by alkali as described.

(i) Mechanism of alkaline erosion reactions

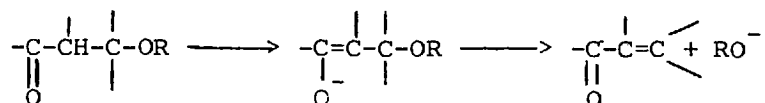
The cellulose erosion reaction proceeds predominantly by a mechanism based on the formation of the intermediate compound 3 in model systems (see Figure 2.7). The reducing end group thus becomes converted predominantly to D-glucoisosaccharinic acid, but at higher temperatures the soluble products become quite complex, as increasing amounts of other acids, and especially formic acid are also produced. This may explain the advantage of revealing tracks by cold etching. The mixture of reaction products is simplified in the presence of calcium ions, which appear to catalyze the re-arrangement of compound 3 to compound 5.

(ii) Alkaline scission of cellulose

The nonoxidative scission of cellulose by 1.0 N sodium hydroxide at 170°C may be postulated as occurring either by intramolecular displacement (route A) or by addition of hydroxyl ion (route B). This is shown in Figure 2.8a. Either mechanism could yield a new reducing end group at the point of scission, and would be followed by alkaline erosion.

(iii) Alkaline scission of oxidized cellulose

It has been established that, in any situation where a β-alkoxycarbonyl group is present in alkali, a rapid elimination of the alkoxyl group will occur as follows:



the β-alkoxycarbonyl grouping occurs in all possible situations where a carbonyl group is introduced into a cellulose molecule (see Figure 2.8b), and in all such circumstances it may be assumed that rapid scission will occur by the above mechanism in dilute alkali. The only type of carbonyl-containing oxidized cellulose that has been isolated in the pure state is

periodate-oxidized cellulose, and the alkaline degradation of this material itself, and also of model compounds, has been shown to proceed predominantly as shown in Figure 2.8c. This type of degradation occurs rapidly at room temperature in very dilute alkali (0.05 N), (which explains the advantage of revealing tracks by dilute and cold etching), and if the cellulose sample has been extensively oxidized, it will be completely dissolved by the alkali.

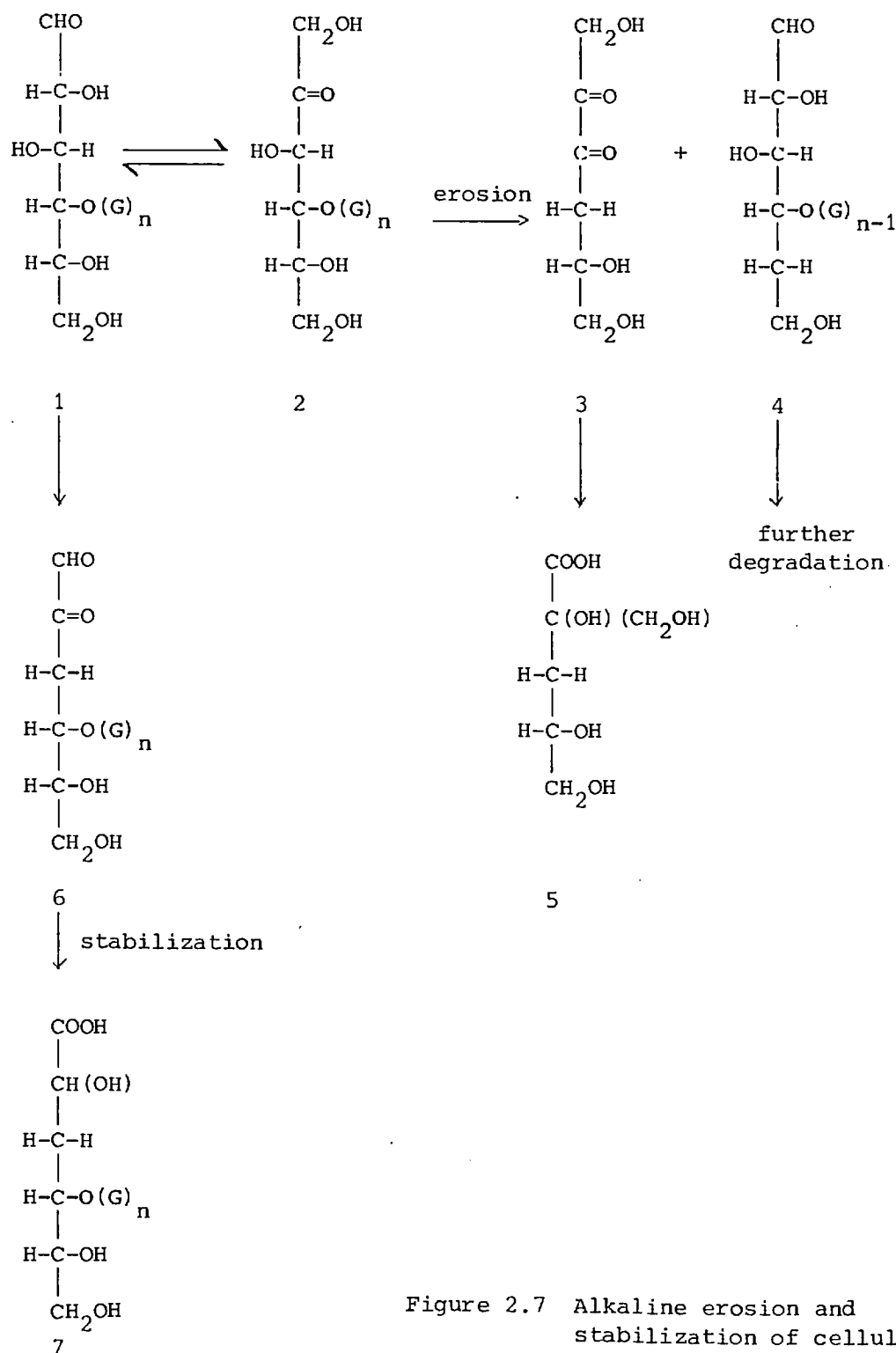


Figure 2.7 Alkaline erosion and stabilization of cellulose

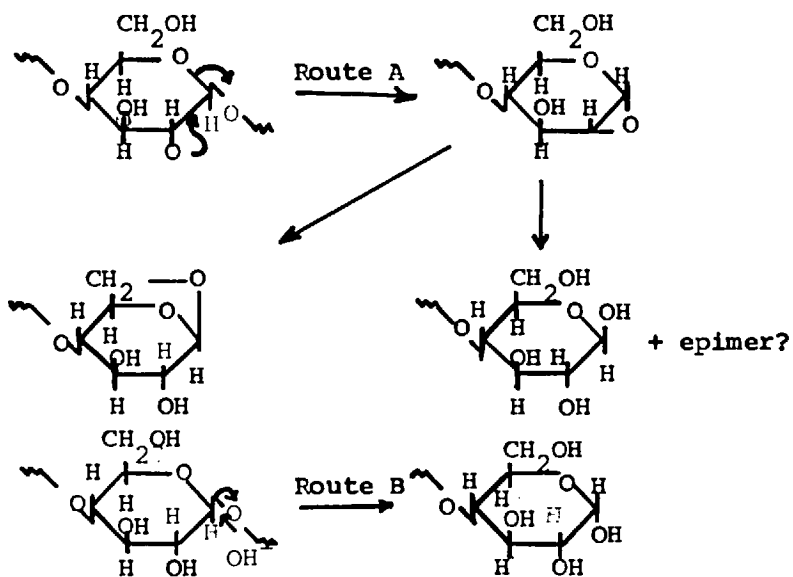


Figure 2.8a Alkaline scission of cellulose

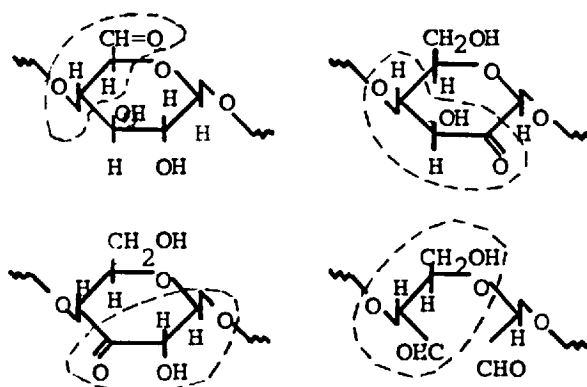


Figure 2.8b β Alkoxycarbonyl groups in carbonyl-containing oxidized cellulose

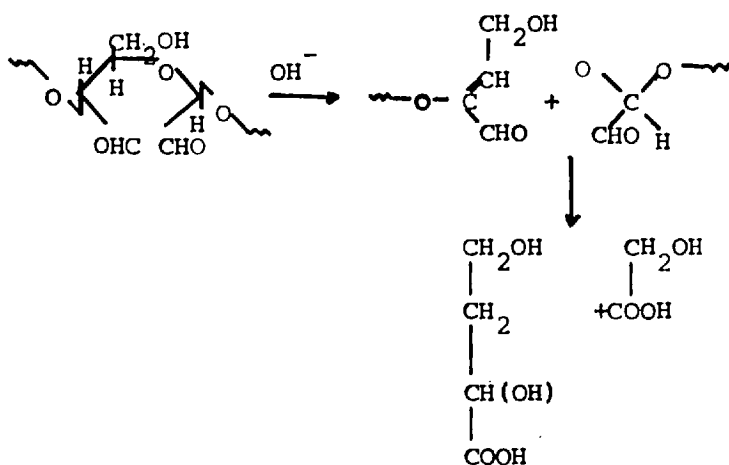


Figure 2.8c Alkaline degradation of carbonyl-containing oxidized cellulose

2.5 Degradation of Cellulose Nitrate by High-Energy Radiation

It is now possible to sketch the nature of the degradation caused by charged particle tracks in cellulose nitrate and answer the question raised at the beginning of Section 2.4. Undoubtedly the substituent nitrate groups play a major role and the splitting of the weak O-NO₂ bond releases NO₂, a powerful oxidising agent, just as in the case of inorganic nitrates. The sequence of events then becomes similar to those during UV and thermal degradation, where an autocatalytic process of oxidation and liberation of NO₂ is set up. As a consequence a rapid degradation of \overline{DP} occurs in the irradiated region, with a loss of tensile strength. The presence of oxygen hastens this decomposition, and also reduces the number of free radicals along the tracks. As evidence for this sequence of events, it is known that the addition of stabilisers to the cellulose nitrate film (which reduce thermal degradation) also reduces the track registration sensitivity (56). The particular susceptibility of cellulose chains to cleavage also plays an important role. Since the degree of substitution is incomplete, some of the hydrogen producing processes which occur in cellulose (52) also occur in cellulose nitrate; broken C-H bonds explain the hydrogen gas evolved.

In cellulose nitrate about 25% of the energy is deposited around the core of the track of a charged particle as ionisation, about 12% as vibration and the remainder as (unionised) electronic excitation (52). The energy which is vibrational (or quickly converted into vibrational) becomes ordinary thermal motion energy, so the resulting process of degradation will be similar to the ordinary thermal degradation already described. The excitation energy of a molecule will break various bonds within the molecule with different probabilities, however, reformation of the bonds can occur due to cage effects, except when light gases such as hydrogen and NO₂ are liberated and escape easily from the molecule by diffusion. The effect of radiation on the plasticiser (camphor) is also very important, in view of its protective role in etching. It seems reasonable to conclude that an important degree of denitration occurs along the particle track, although for example other processes such as direct scission without denitration will also occur. Cellulose is particularly susceptible to radiative degradation as shown in Figure 2.9. The scission yield is particularly high.

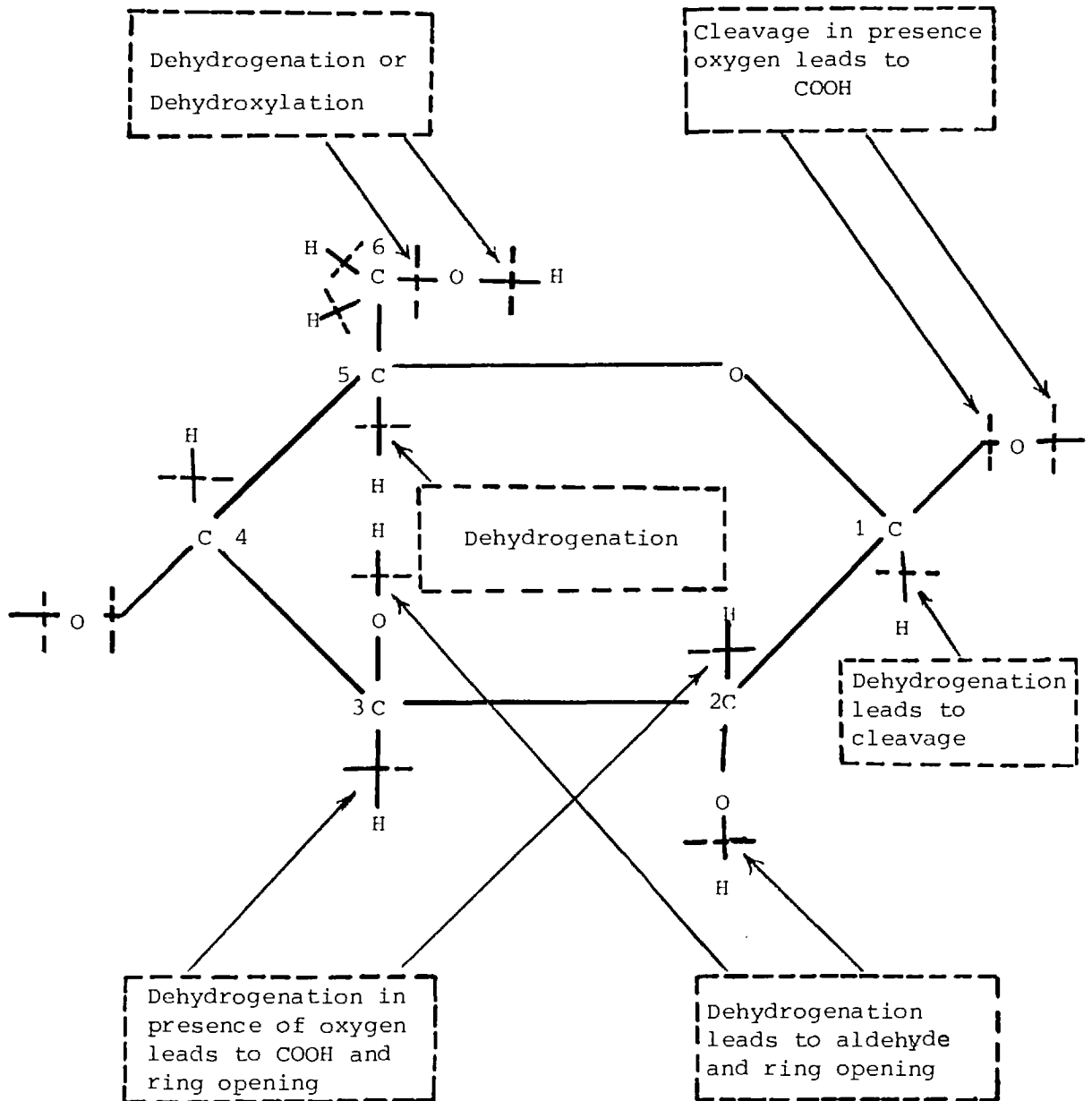


Figure 2.9 A summary of the possible effects of ionizing radiation on the anhydroglucose unit of the cellulose molecule.

It is not known exactly how the nitrate groups will affect the scission rate, but the above discussion suggests that they increase it considerably; this may explain the greater sensitivity of cellulose nitrate as a track recorder, as compared to other cellulose derivatives (see Figure 2.9 and Figure 2.10).

The superior sensitivity of cellulose nitrate towards track registration is probably related to its property of thermal degradation. High temperatures are attained in fission fragment tracks and other high LET tracks (Chapter Four). Electronic energy deposited on the passage of a charged particle (ionisation or excitation) is rapidly converted into vibrational energy. The same phenomenon would also occur in low LET tracks, however without the attainment of a local thermal equilibrium; nevertheless as pointed out in Chapter Four, the loss of vibrational energy out of a cellulose nitrate ring unit occurs rather slowly.

The radiative degradation creating the damage trail of a charged particle may be summarised as follows: denitration occurs in the ionised or excited molecules followed by an autocatalytic oxidation process which rapidly degrades the cellulose chains. The oxidation leads to reducing (aldehyde) and acidic (carboxyl) groups. The latter play an important role in chemical etching and base-exchange (Chapters Seven and Eight). The processes involve the creation of free-radical intermediates, some of which are long-lived and trapped in the damage trails; track revelation via free radicals is discussed in Chapter Eight.

2.6 Alkaline Etching of Cellulose Nitrate

It is also of importance to understand the alkaline degradation of cellulose nitrate in order to explain the phenomenon of preferential track etching.

Irradiated cellulose nitrate exhibits base-exchange properties, (base exchange is treated in Chapter Eight), probably due to the acid groups formed. By the use of radioisotopes, the exchange of H^+ by Ca^{+2} was observed to be proportional to the radiation dosage and to be dependent on the pH of the solution. The Ca^+ absorbed in the irradiated cellulose increased to a maximum as the solution was made alkaline and decreased to a minimum as the solution was made acid. The relative

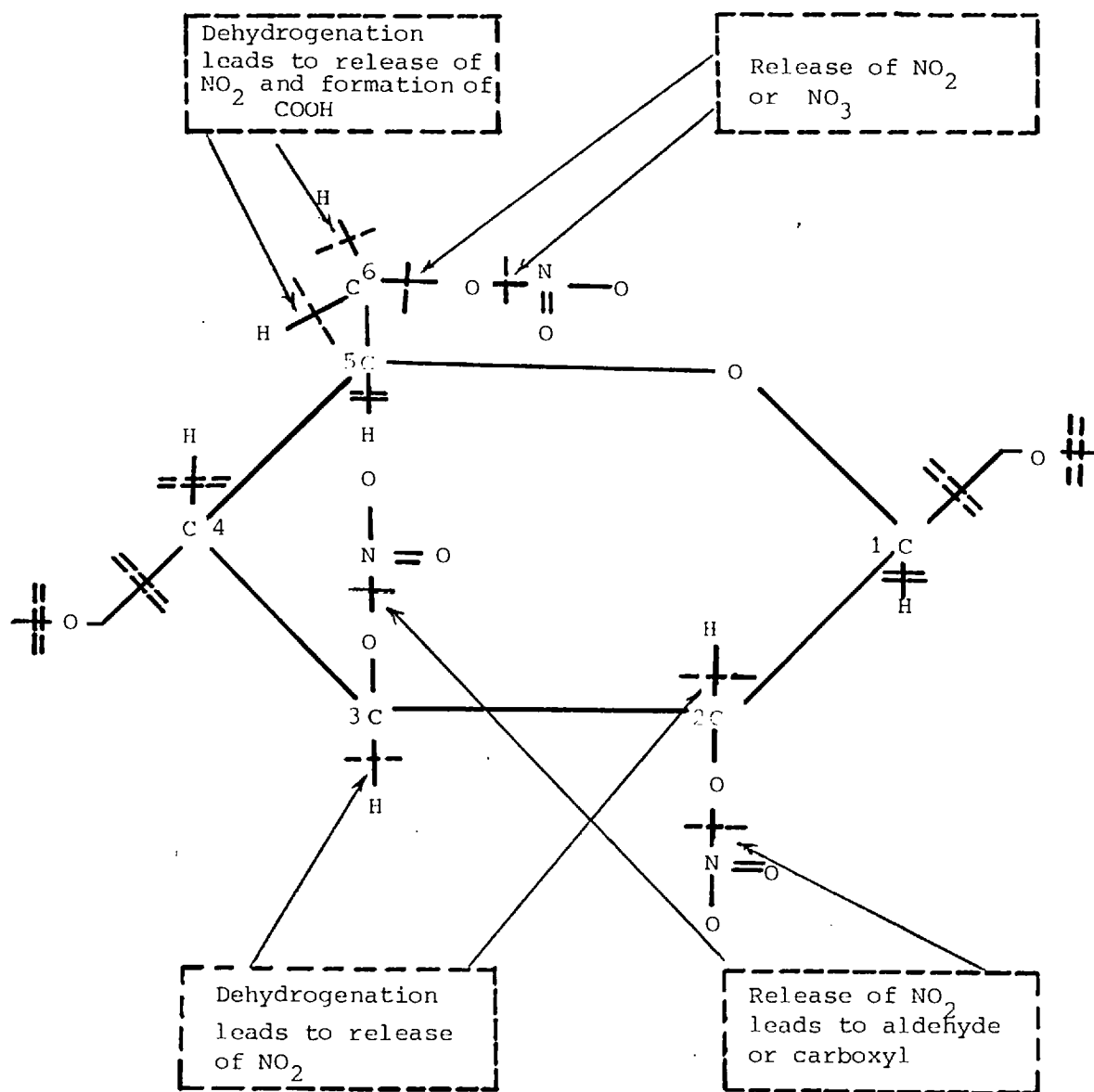
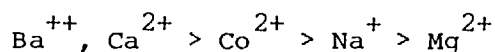


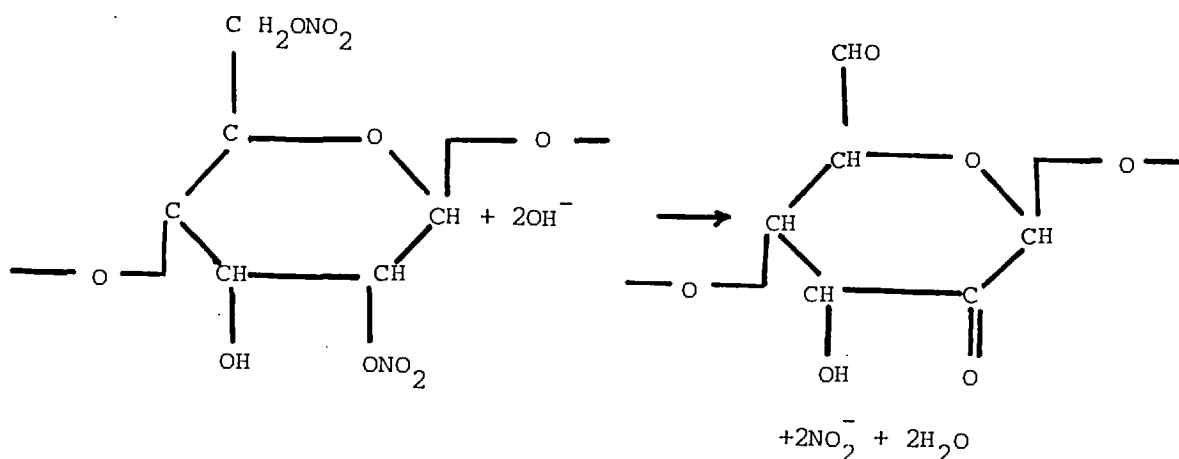
Figure 2.10 A summary of the possible effects of ionizing radiation on the ring unit of the cellulose trinitrate molecule. Double dashed lines denote same effects as in preceding case of the cellulose ring unit.

affinity of irradiated cellulose for metal-ions was found to be



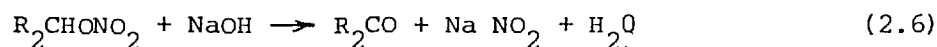
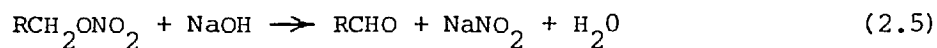
If the pH is sufficiently high, the concentration of OH^{-} ions will initiate the process of preferential attack (Alkaline Etching).

It is believed that the base-catalysed decomposition of cellulose nitrate proceeds by a chain of events similar to the previously treated thermal degradation (38). The OH^{-} ion reacts with cellulose nitrate ring as follows (taking as an example a ring with one primary nitrate group and one secondary group).

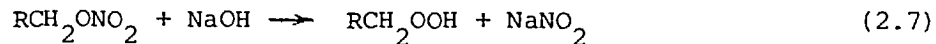


The resulting intermediate compound ring would be extremely sensitive to alkaline cleavage, and in the above example the left hand side glucosidic link would be cut. With the secondary nitrate group in the other possible position, both glucosidic links would be cut after removal of this nitrate group, so that the oxidised glucose unit is effectively chopped out of the chain (38).

The above sequence of events is consistent with the fact that alkali hydroxides are known to convert primary and secondary nitrate groups to aldehyde and ketone groups respectively, according to the reactions (57).



An alternative possibility is the following reaction:



In the ordinary course of events, the peroxide will decompose into aldehyde and water



The oxycelluloses which are formed by these reactions (RCHO and R_2CO) are rapidly degraded by the alkali, as explained above, or according to other more complicated sequences of events (57), the end results being scission somewhere in the chain. This reduces the DP rapidly and the small molecules are readily dissolved.

It has been noted that the presence of plasticisers in the matrix of the cellulose nitrate reduces the bulk etching rate substantially (58). It is thought that this occurs as a result of reduction of the penetration of OH^- ions in the plasticised material. Cellulose nitrate appears to form a swelling compound of definite structure with camphor, and the resulting solvation effect appears to protect the cellulose nitrate by restricting the accessibility of the OH^- ions, preventing the initiation of the above degradation reactions.

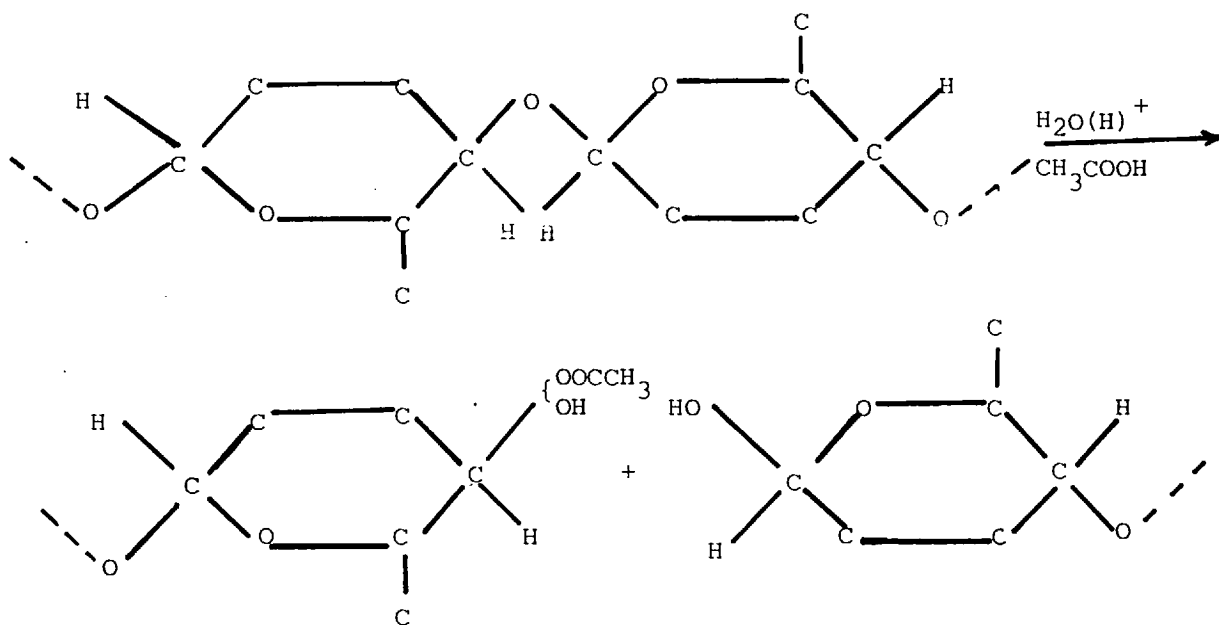
Chemical etching along the track is expected to occur to a large extent through the alkaline degradation of the denitrated and cleaved oxycellulose and the damaged plasticizer. The penetration of the OH^- ions is a crucial factor in increasing the etching rate to well above that of bulk etching, and is aided by the damaged plasticizer and the gaps in the broken cellulose chains which are initially present before etching. The penetration also depends on the ability of the alkali hydroxide to swell the crystalline regions of cellulose nitrate. This occurs best at a specific alkali hydroxide concentration, and is greater at a low temperature, leading to a maximum in track etching rate at a certain concentration.

2.7 Hydrolytic Degradation of Cellulose Nitrate by Acids

It has been observed in the course of this work that tracks can be revealed in cellulose nitrate by treatment in acids, such as hydrofluoric acid and especially nitric acid. This alternative etching technique is due to acid hydrolysis (cleavage) of the cellulosic chains, which is particularly rapid in the damaged material along the particle tracks.

Degradation of organosoluble cellulose derivatives by hydrolytic reaction can be attributed to acid cleavage of the glucosidic links in the polymer molecule. The chain cleavage is accompanied by de-esterification with the esters and by de-etherification with the ethers.

Under homogeneous conditions, depolymerization can occur either by acetolysis or by hydrolysis as illustrated in the accompanying reaction scheme:



In a homogeneous system containing both acetic acid and water, degradation will occur as a result of the medium effect (acetic acid hydrolysis) and can be greatly accelerated by the presence of strong acids such as sulfuric acid (59). The reaction appears to obey the kinetic laws for the random degradation of polymers and the rate of reaction is shown to be temperature dependent, increasing with temperature as would be anticipated. The reaction rates are recorded in Table 2.3. From these data it is apparent that sulfuric acid accelerates the degradation to a marked degree.

TABLE 2.3

REACTION RATE CONSTANTS FOR DEGRADATION OF CELLULOSE ACETATE

Temperature °C	Reaction rate constant x 10 ⁶ hr ⁻¹
Uncatalysed Reaction	
84.4	0.77
94.2	2.1
104.4	8.1
115.1	20
Sulfuric Acid-catalyzed Reaction	
46.0	22
54.8	64
65.7	177

The loss in viscosity which organosoluble cellulose derivatives may undergo under acidic conditions is the direct consequence of the acid lability of the β -glucosidic bond joining the anhydroglucose units in the cellulose chain. It would be anticipated, therefore, that organosoluble esters and ethers of cellulose would be equally susceptible to acid degradation if they were exposed under conditions of a homogeneous reaction, where all of the β -glucosidic bonds would be equally available for attack. Experimental investigation has shown the above conclusion to be an oversimplification since it has neglected the possible role of the substituents in modifying the rate of cellulose chain cleavage under identical homogeneous reaction conditions.

Change in intrinsic viscosity versus time, as shown in Figure 2.11 was compared under identical acetolysis conditions for samples of ethyl cellulose, cellulose acetate, and cellulose nitrate (60). It is apparent from the curves in Figure 2.11 that ethyl cellulose is the least stable and cellulose acetate the most stable, with cellulose nitrate occupying an intermediate position. The extreme difference in the rate of loss of intrinsic viscosity between ethyl cellulose and cellulose acetate is a striking example of how substituents can modify the basic characteristics of the cellulose molecule. Cellulose

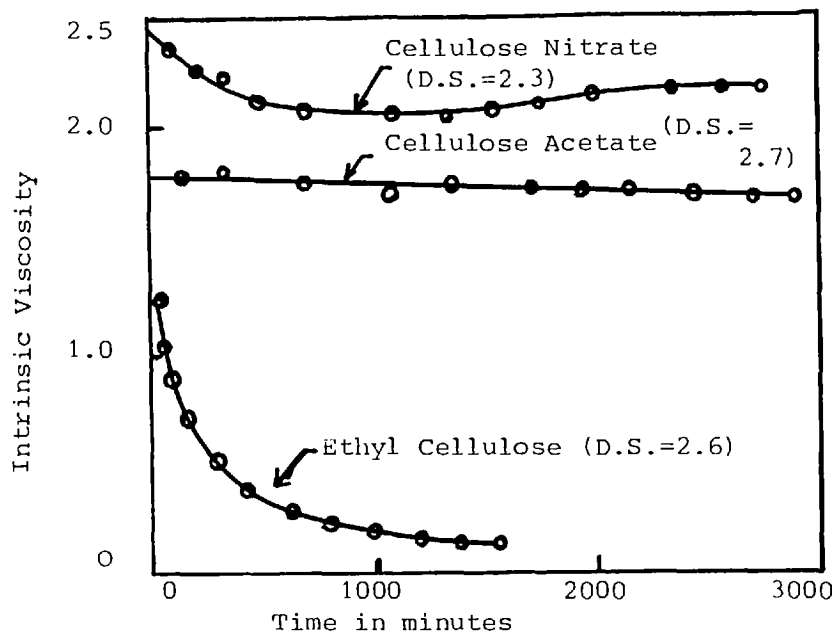


Figure 2.11 Rates of acetolysis at 25°C. for ethyl cellulose, cellulose acetate, and cellulose nitrate. Acetolysis was carried out in an anhydrous medium, 95:5 acetic acid:acetic anhydride which was 0.78 N with respect to HCl and 0.105 N with respect to LiCl.

nitrate shows a somewhat ambiguous behaviour which can be attributed to the complex nature of the denitration reaction.

This discussion serves to point up a serious gap in knowledge of cellulose derivative behaviour, namely, the development of a sound theory to explain the substituent effect on the hydrolytic sensitivity of such compounds. It would be of great help to understand the effect of substituent size, polarity, extent of substitution, and uniformity of substitution on the activation energy and frequency factor in these cases, moreover it will explain the role of a buffer solution in the alkaline etching mechanisms.

2.8 Swelling in Cellulose and Cellulose Nitrate and its Effect on Chemical Reactions

Cellulose and its derivatives consist of long-chain polymer molecules, with hydroxyl groups located along the chains. The hydroxyl groups give rise to hydrogen bonding between the chains, which lead to local crystalline order in certain regions (crystallites) and a consequent rigidity of the structure. Because of the limited accessibility of reagents due to this rigidity, many reactions which occur rapidly with glucose, the cellulose monomer, do not occur to a measurable extent with cellulose under the same conditions. A few chemical solvents will dissolve or at least soften cellulose by breaking the inter-chain hydrogen bonds and inserting their molecules between the cellulose chains, thus causing swelling of the cellulose. As a general rule cellulose derivatives act in a similar manner to cellulose itself, although they have fewer hydroxyl groups depending on the degree of substitution.

Swelling agents supply the necessary energy to break the hydrogen bonds, but not enough to bring the cellulose molecules into solution. These hydrogen bonds reform with the swelling agent. The reactivity of cellulose and its derivatives increases as the degree of swelling increases. The rate of diffusion of small molecules in gels with an open structure similar to that of swollen cellulose, is little less than in ordinary water. As an example of increased diffusibility on swelling, one may cite the diffusion of water vapour through cellophane, which increases by 10 orders of magnitude as the relative humidity is raised from 0% to 100%.

The use of swelling agents to increase the penetration of reagents in cellulose and its derivatives is well-known. However, the nature and extent of swelling depends sensitively on the fine (for microscopic) structure of the cellulose or derivative specimen. A basic model for the fine-structure of cellulose is similar to that for many other natural or high polymers, namely a system of small, microfibrillar crystallites surrounded by and embedded in a matrix consisting of amorphous and semi-crystalline regions. This sub-division of the fine-structure leads to a corresponding subdivision of swelling processes into intra- and inter-crystalline and amorphous or disordered regions also has a great influence on the course of most cellulose reactions, and it is generally agreed that the amorphous material is always attacked more rapidly than the crystalline. In inter-crystalline swelling, the swelling agent penetrates only the inter-crystalline, disordered regions. There is no change of the X-ray diagram except for the superposition of the diagram of the swelling agent on that of cellulose. In intra-crystalline swelling the agent penetrates the crystallites as well, beginning at the crystallite ends, thus swelling the lateral interchain distance and forming a new X-ray diagram.

The facility of inter-crystalline swelling versus intra-crystalline is easy to understand. A crystalline arrangement permits close contact via bonding of chains over a length of hundreds of Ångströms. A disordered, entangled arrangement gives a more open structure, and many of the chains will not have their attractive forces satisfied. This permits easy motion into and bonding of swelling agents in the amorphous regions. The best example of intercrystalline swelling is the swelling of cellulose fibres in water. The total volume of the system increases with swelling in such a manner that each water molecule contributes approximately its normal molecular volume to the system. The magnitude of the swelling varies from fibre to fibre as shown by the fact that the maximum increase in cross-sectional area on swelling is 20-35% in natural fibres and 55-70% in regenerated fibres. A much greater degree of intercrystalline swelling occurs in dilute NaOH (caustic soda), as well as most other dilute bases, acids and salts. There is a concentration threshold at which intracrystalline swelling begins to take place. For example, at such a concentration, the sodium ion with its sheath of water molecules enters the crystalline regions and forms new crystalline compounds.

These swelling phenomena are exploited in cellulose chemistry. Thus, cellulose alone does not react appreciably with etherifying agents; if the cellulose is to be reactive it must be treated with a swelling agent and a solvating agent, the usual agents being NaOH and H₂O respectively. Similarly, in cellulose formate manufacture, the use of inert swelling agents such as zinc chloride, calcium bromide and magnesium perchlorate is useful. In practically all useful reactions the cellulose is swollen either by the reactant, by the solvent, or pre-swelling with a third component which may be subsequently replaced. In alkali cellulose preparation, the addition of certain salts to dilute alkali greatly increases the rate of reaction with cellulose at the expense of reagent consuming side effects. Typical among these salts are sodium thiocyanate, potassium iodide and sodium perchlorate, when used as nearly saturated aqueous solutions, to achieve intra-crystalline swelling. In addition, the type of interaction of a catalyst with a reagent and a hydroxyl group that leads to a more rapid reaction, will also lead to a partial solvation of the cellulose and an increased tendency for it to swell. This indicates the close relationship between catalysis of reactions and swelling phenomena. The course of reactions is usually divided into an initial rapid rate (penetration into amorphous regions), followed by a slower rate (penetration into crystallites).

The above considerations on the swelling of cellulose are generally applicable to its derivatives as well, although obviously the details will be different. As a general rule, solvents for cellulose derivatives act first as swelling agents and then as a dispersing agent. Swelling may be divided into limited and unlimited types, the latter leading to dispersion into solution. As with cellulose fibres, the swelling phenomena may be divided into intra- and inter-crystalline, the latter occurring first.

Cellulose trinitrate is capable of forming "swelling compounds" (analogous to alkali cellulose) with a number of organic solvents without losing its fibre structure. These solvents are cyclohexane, acetone, fenchone, m-xylene and camphor.

For a complete theory of swelling, the structure of the ions in aqueous solution is as important as the structure of cellulose itself. The ability of alkalis and of inorganic salt solutions to swell and dissolve cellulose has been attributed to the degree of hydration of

the ions, and their fixation by cellulose. In the hydrates the water is strongly contracted (by electrical forces) so that by its liberation on reaction with the cellulose chains an explosive swelling can take place. Penetration into the crystalline regions of cellulose depends on the appropriate hydrated ion being small enough, less than about 8 \AA diameter. This size depends on the concentration. It is shown in Chapter Six that for the hydroxides of Li, Na, K and Rb, the swelling maxima of cotton fibres (highly crystalline) corresponded to alkali concentrations at which fully hydrated cations are known to exist. In lower concentrations of NaOH it is considered that ion hydrates of diameter $15\text{--}20 \text{ \AA}$ are more frequent. As the concentration increases, dipole hydrates of $5\text{--}8 \text{ \AA}$ diameter are formed, and at still higher concentrations undissociated, unhydrated molecules of NaOH can exist.

The absorption of alkali hydroxides by cellulose varies inversely with temperature and undergoes a higher maximum versus concentration at a lower concentration as the temperature is lowered.

Finally let us discuss on the base of purely structural considerations the outstanding sensitivity of cellulose derivatives among all plastic detectors. We suppose that an important role is played here by the following factors:-

- (a) conjugation of monomers with each other through a relatively weak acetal bond;
- (b) presence of oxygen in the six-member ring, leading to a displacement of electron densities and thus decreasing the bond-break energy;
- (c) a significantly greater number of easily substituted hydroxyl groups in cellulose monomers than in monomers of any other plastic used for detecting ionizing particles;
- (d) correspondingly greater possibilities for introducing various groups of high reactivity into macromolecules through substituting hydrogen in hydroxyl groups;
- (e) the possibility of introducing such groups, whose great polarizability enables an easier main-chain break as well as groups, whose products of oxidizing and decomposition possess an oxidizing action themselves. The first applies to nitrogroups to the greatest degree, but to acetyl groups too, while the second applies to nitrogroups only, thus making clear why cellulose nitrate is the first in sensitivity among all cellulose derivatives and cellulose acetate comes next.

CHAPTER THREE

REVIEW OF THEORETICAL MODELS

Introduction

In this chapter we deal with the specific problem of understanding the damage processes and mechanisms which occur when a charged particle penetrates a medium.

A number of attempts have been made to predict theoretically the nature of the processes which occur when a charged particle falling on a material makes an etchable track, and how this track is enlarged and modified on immersing the medium in some etchant, i.e. the mechanism of etching the damaged area; unfortunately, they have not yielded a clear and universally accepted picture as yet. Similarly, some work on pre- and post-irradiation treatment of samples has been done, but it has left many unanswered questions of a very basic nature. Also, the results of almost all the efforts made until now to predict the etched track parameters show poor agreement with the ones experimentally obtained.

In order to introduce in Chapter Four our theoretical model of the track formation mechanism, a very brief account of the energy-loss processes and some of the important work being done on other track formation mechanisms is given here. The main emphasis has been placed on the discussion of the various theories and criteria of track formation.

Our model is based on observations of highly ionising particles of high mass, energy and charge, such as fission fragments, which produce a dense concentration of point defects and dislocations, observable under an electron microscope as a continuous black straight line. This continuous straight line is called a latent track.

The passage of a highly ionising charged particle forms a latent track easily in insulators, but only with difficulty in semi conductors and metals. Formation is easier with increasing resistivity; latent tracks are observed in media with resistivity greater than about $1 \text{ m}\Omega \text{ cm}$

In the present chapter, therefore, it is our purpose to provide qualitative answers to the following questions:

- (i) By what processes does a fission fragment lose energy to the constituents of the material in which it is travelling?
- (ii) To what extent do these processes depend on the energy and effective charge of the fragment?
- (iii) How is the energy lost by the fragment dissipated in the environment of its trajectory in the material?
- (iv) What, in general terms, is the form of the permanent damage in a solid through which a fission fragment has passed?
- (v) What is the eventual fate of a fission fragment brought to rest in a solid?

3.1 The Energy Loss Processes

A heavy charged particle moving through a medium composed of atomic nuclei and electrons can lose energy by three main processes. The principal mode of energy loss is due to interaction with the atomic electrons by Coulomb excitation or ionization. A fragment may lose energy by direct collisions with nuclei of the stopping medium, though such events are rare until the particle nears the end of its path. The third energy loss is due to emission of 'bremsstrahlung' and Cerenkov radiation which is small compared to either of the first two processes. For any energy E , therefore, the total rate of energy loss (the absolute stopping power) is the sum of the rates of energy loss due to each of the three processes, and may be written in the form:

$$\left(-\frac{dE}{dx}\right)_{\text{total}} = \left(-\frac{dE}{dx}\right)_{\text{electronic}} + \left(-\frac{dE}{dx}\right)_{\text{nuclear}} + \left(-\frac{dE}{dx}\right)_{\text{radiation}}$$

The problem is then decoupled and each of the three contributions may be examined separately.

The rate of energy loss of the fission particle to radiation, to bremsstrahlung, is in fact negligible though we include it here since a very small amount of energy is dissipated by this means. The rate of energy loss in nuclear collision events, however, is certainly not negligible. Various estimates have been made of the contribution which these processes make to the arresting of a fission particle before it is deposited as an impurity atom, and they range from less than 1% up to 10%, according to the model which is chosen for the interaction potential. Such treatments are based on the assumption that collision events between moving ions like fission fragments and

lattice atoms at rest are describable at high energies in terms of Rutherford scattering dynamics, which favours low energy transfers, and at low energies in terms of hard sphere scattering. The importance of the above term is therefore greatest at the lower values of the energy E ; at the higher energies, the third term, which accounts for energy given to electrons in the crystal, dominates. We do not, of course, mean to imply that the energy which is communicated to struck atoms in the crystal is not stored in lattice defects, and we do indeed suggest that, in all crystals, displacement and plasticity spikes or modern modifications of these concepts such as the depleted zone must lead to the introduction of Frenkel pairs. This is especially the case for metals, as the electron microscopy of gold and the alloy copper/gold has shown. It remains true, however, that, in all crystals, over 90% of the energy of each fission particle is dissipated in the energization of electrons, or delta particles, and we need to know how efficiently and how quickly these excited electrons, these waves of delta rays, communicate their energy to the lattice.

3.1.1 Energy Losses by Radiation

Because of its relative unimportance in contributing to the total energy loss, we shall mention this process only briefly. 'Bremsstrahlung', or braking radiation, is emitted when a charged particle is rapidly accelerated or retarded in the field of a nucleus. The intensity of the radiation is, according to classical electrodynamics, inversely proportional to the square of the mass of the incident particle and consequently the phenomenon is of much less importance in the case of heavy ions than it would be for lighter particles such as electrons. Cerenkov radiation arises from the polarization of a crystal along the path of a charged particle when the velocity of the latter exceeds the phase velocity of light in the medium. This polarization is time-dependent owing to the moving electric field of the particle, and can produce a radiation field. The effect is, of course, quite small in the case of a fission fragment, since the particle velocity is very much less than the velocity of light in any medium.

3.1.2 Nuclear Collision Losses

Retardation of a heavy charged particle by collisions with atoms in the medium only takes precedence near the end of the fragment range,

where electronic excitation becomes small. Such two-body 'nuclear' collisions may be described classically (61) provided that the collision diameter b , the distance of the nearest approach in a head-on collision, is very much greater than the de Broglie wavelength λ . For scattering of a charged particle by a Coulomb field of force (62), this condition may be written:

$$k = b/\lambda = (Z_1 Z_2 e^2)/(hv) \gg 1 \quad (3.1)$$

where Z_1 and Z_2 are the atomic numbers of the moving and struck particles respectively and v is the velocity.

The most simple way classically to describe a 'nuclear' collision between two heavy ions is to employ the Rutherford scattering law. The differential cross-section for scattering through an angle θ into a solid angular increment $d\omega$ is given by:

$$d\sigma_{\text{nuclear}} = \left\{ \frac{Z_1 Z_2 e^2}{2M_0 v^2} \right\}^2 \text{cosec}^4 \left(\frac{\theta}{2} \right) d\omega \quad (3.2)$$

where M_0 is the reduced mass. Alternatively, in terms of the energy transfer T , for collision between two particles specified by (M_1, Z_1, E) and $(M_2, Z_2, 0)$ it is given by:

$$d\sigma(E, T)_{\text{nuclear}} = \frac{\pi Z_1^2 Z_2^2 e^4}{E} \left(\frac{M_1}{M_2} \right) \frac{dT}{T^2} \quad (3.3)$$

This description, however, assumes that the collision is occurring between two point charges and masses with central fields of force. In the case of a collision between a fission fragment and an atom, the picture is complicated by the presence of bound electrons on each nucleus, and the problem is essentially a many-body collision process. It is possible to approximate a real situation by considering the screening effect of the bound electrons, replacing the simple Coulomb potential of Rutherford scattering by

$$V(r) = (Z_1 Z_2 e^2/r) \exp(-r/a) \quad (3.4)$$

where a is a screening parameter.

In these circumstances the conditions under which we must replace the Rutherford scattering law by one which allows for screening are determined by the value of the ratio:

$$\zeta = b/a \quad (3.5)$$

Thus, only if the collision diameter is small compared to the screening parameter ($\zeta \ll 1$) will the Rutherford Law be valid (weak screening). This corresponds to high fragment velocities.

We note, for completeness, that the condition for the validity of a classical approximation to two-body collisions in crystals is modified by the introduction of the general concept of screening. To the requirement that $\lambda \ll b$ must be added the condition that $\lambda \ll a$, so that

$$\kappa \gg \xi \quad (3.6)$$

This condition is evidently satisfied for the fission fragment, whatever the velocity. The classical approximation is therefore also sufficient for strong screening, when $\xi \gg 1$. In this regime the screening parameter "a" is small, so that collisions may effectively be considered as occurring between rigid spheres. Giving the hard spheres radii $R(E)$, which depend on the energy, the differential scattering cross-section is then given by the formula

$$d\sigma(E,T)_{\text{nuclear}} = 4\pi[R(E)]^2 (dT/T_{\text{max}}) \quad (3.7)$$

where

$$T_{\text{max}} = \frac{4M_1 M_2}{(M_1 + M_2)^2} \cdot E \quad (3.8)$$

In the case of weak screening (Rutherford scattering), therefore, the differential cross-section depends on the inverse square of the energy transfer T ; so, at high fragment velocities, low energy transfers are preferred. For strong screening (hard sphere scattering), which is clearly the situation at low fragment velocities, all energy transfers up to T_{max} are equally probable.

The differential cross-section $d\sigma(E,T)$ is very simply related to the specific rate of energy loss of the fission fragment by the following:

$$\left(-\frac{dE}{dx}\right)_{\text{nuclear}} = n_0 \int_{T_{\text{min}}}^{T_{\text{max}}} T d\sigma(E,T) \quad (3.9)$$

where n_0 is the spatial density of available nuclei and T_{min} is a lower limit of the order of 0.1 eV. We may illustrate the determination

of T_{\min} for the case of weak screening. By a simple geometric treatment of the scattering process, since the deflection angle θ_{\min} for transfer of energy T_{\min} is small, it may be shown that

$$\theta_{\min} = b/p_{\min} \quad (3.10)$$

and

$$T_{\max}/T_{\min} = (2/\theta_{\min})^2 \quad (3.11)$$

where p_{\min} is the corresponding impact parameter. Now the Rutherford scattering law will clearly hold only for values of θ for which p is small in comparison with the screening radius a . This this as the limit, therefore:

$$\theta_{\min} = \xi \quad (3.12)$$

so that:

$$T_{\max}/T_{\min} = (2/\xi)^2 \quad (3.13)$$

where:

$$T_{\min} = \frac{Z_1 Z_2 e^4}{a^2} \left(\frac{M_1}{M_2} \right) \frac{1}{E} \quad (3.14)$$

The specific rate of nuclear energy losses then becomes:

$$\begin{aligned} \left(- \frac{dE}{dx} \right)_{\text{nuclear}} &= \left(\frac{2\pi Z_1^2 Z_2^2 e^4}{M_2 v^2} \right) n_o \log_e \left(\frac{T_{\max}}{T_{\min}} \right) \\ &= \left(\frac{\pi Z_1^2 Z_2^2 e^4}{E} \right) \left(\frac{M_1}{M_2} \right) n_o \log_e \left[\frac{2aE}{Z_1 Z_2 e^2} \left(\frac{M_2}{M_1 + M_2} \right) \right] \end{aligned} \quad (3.15)$$

3.1.3 Electronic Energy Losses

If it is also assumed, in a first approximation, that energy loss collisions which the moving fragment makes with atomic electrons are also to be considered within the framework of classical mechanics, then the differential scattering cross-section is again given by the Rutherford law:

$$d\sigma(E, T)_{\text{electronic}} = \frac{\pi Z_1^2 e^4}{E} \left(\frac{M_1}{m_e} \right) \frac{dT}{T^2} \quad (3.16)$$

where m_e is the electronic mass. Choosing I , the ionizing energy of the electron from the atom, as a suitable lower limit T_{\min} , and defining the maximum energy transfer T_{\max} in the normal manner:

$$T_{\max} = \frac{4M_1 m_e}{(M_1 + m_e)^2} \cdot E \approx \frac{4m_e}{M_1} \cdot E \quad (3.17)$$

the appropriate classical equation for the specific electronic energy loss rate becomes:

$$\left(-\frac{dE}{dx}\right)_{\text{electronic}} = \left(\frac{\pi Z_1^2 e^4}{E}\right) \left(\frac{M_1}{m_e}\right) n_o \sum_i \log_e \left(\frac{4m_e}{M_1} \cdot \frac{E}{I_i}\right) \quad (3.18)$$

where the summation extends over the i electrons in each of n_o atoms, using appropriate values of the ionization potential I_i . This formula is, of course, strictly approximate. In the general case of passage of a charged particle through a medium it is necessary to differentiate between 'resonance' and 'free' collision contributions to the electronic stopping power, the former being quantum mechanical in every way, and the latter being classical. The way in which (61) takes care of this in terms of the old quantum theory is referred to in Ref.(63).

Bethe (64) and Bloch (65) have also derived appropriate expressions for the electronic energy loss rate. Based on the Born approximation, Bethe's formula is the following:

$$\left(-\frac{dE}{dx}\right)_{\text{electronic}} = \left(\frac{2\pi Z_1^2 e^4}{E}\right) \left(\frac{M_1}{m_e}\right) Z_2 n_o \log_e \left(\frac{4m_e}{M_1} \cdot \frac{E}{\bar{I}}\right) \quad (3.19)$$

where \bar{I} is a suitable average of the ionization potential taken over all atomic electrons, which may be approximated thus:

$$\bar{I} = kZ_2 \quad (k \approx 11.5 \text{ eV}) \quad (3.20)$$

It is to be noted that, in the Bethe formula, the effect of including the small energy transfer processes - the 'resonance' processes of Bohr - is merely to double the rate of energy loss whilst retaining the same dependence on the fundamental physical parameters associated with stopping. The Bloch formula, however, contains the quantum-theoretical formula of Bethe, and an early classical formula of Bohr (66), as limiting cases for small and large values of the parameter $\kappa = (Z_1 e^2)/(hv)$. This equation has the following form:

$$\left(-\frac{dE}{dx}\right)_{\text{electronic}} = \left(\frac{2\pi Z_1^2 e^4}{E}\right) \left(\frac{M_1}{m_e}\right) Z_2 n_o \left\{ \log_e \left(\frac{2m_e v^2}{\bar{I}}\right) + \psi(1) - R \psi(1 + i\kappa) \right\} \quad (3.21)$$

where ψ is the logarithmic derivative of the Γ -function and $R\psi$ denotes the real part of ψ . For $\kappa = 0$, it is the Bethe formula (now familiarly referred to as the Bethe-Bloch formula), and for $\kappa \gg 1$, since $\psi(1) = -0.577$ and $R\psi(1 + i\kappa) \approx \log_e \kappa$, it is the Bohr formula:

$$\left(-\frac{dE}{dx}\right)_{\text{electronic}} = \left(\frac{2\pi Z_1^2 e^4}{E}\right) \left(\frac{M_1}{m_e}\right) Z_2 n_o \log_e \left(\frac{1.123m_e v^2}{\kappa \bar{I}}\right) \quad (3.22)$$

where $\omega = \bar{I}/h$ is an average oscillation frequency for the electrons in the atom.

It should be emphasised here that the difficulties associated with a proper accounting of all of the possible eventualities in high energy collisions with an atom are profound. Thus the quantum mechanical treatment assumes that the collision is over before the electrons respond to the field of the moving fragment, which cannot be the case. Furthermore, the charge on the fragment fluctuates and falls as it penetrates into the crystal. To some extent it is possible to allow for the fall of the charge on the fragment by assuming that the particle only carries along those electrons whose orbital velocities are greater than the fragment velocity itself. Utilising this hypothesis and the Thomas-Fermi model of the atom, the effective fragment charge becomes:

$$Z_1^{\text{eff}} = Z_1^{1/3} h\nu/e^2$$

Likewise, the number of electrons of a target atom which may be removed by a fragment of velocity v is given by:

$$n = Z_2^{1/3} h\nu/e^2 \quad (3.23)$$

so that the electronic stopping power may be apportioned in some crude fashion to the various electronic shells. By proceeding in this fashion the energy loss rate to electrons assumes the following form:

$$\left(-\frac{dE}{dx}\right)_{\text{electronic}} = \frac{2Z_1^{2/3} Z_2^{1/3} h^3 n_o}{\pi^2 e^2 m_e} \left(\frac{2E}{M_1}\right)^{1/2} \quad (3.24)$$

For a fuller treatment, refer to the original work of Bohr (61).

3.2 Etchable Track Formation Criteria

The minimum energy loss of an incident charged particle in a target medium needed to form a linear damaged area, i.e. a latent track in the medium which can be observed by the electron microscope or by Moire patterns, or upon enlarging by the optical microscope, is called the threshold energy loss criterion or the latent track registration threshold for the medium. Below this registration threshold, no latent track is registered.

The latent track registration threshold depends on the following parameters:

- (i) the bombarding particle charge, mass and velocity,
- (ii) the bombarded material, its chemical composition, molecular weight, type of chemical bonding between atoms, size of atoms, etc.,
- (iii) temperature and nature of atmosphere at the time of irradiation (especially for polymers),
- (iv) the nature of the revelation technique.

It is well understood that the charged particle breaks certain molecular chains in the bombarded medium by ionization and excitation. These broken chain-ends form new species which are chemically highly reactive and can be observed optically as tracks upon etching. But this does not necessarily lead to an observable etched track upon development for every damaged area above the registration threshold. This is because the chemical etching is a very harsh and insensitive treatment for track revelation. It reveals only the highly damaged area where the track etching rate V_T is much larger than the bulk (non-damaged area) etching rate V_B . In order to observe a damaged area as an etched track, not only should V_T be larger than V_B , but also all of the following conditions should be fulfilled.

- (i) The incident charged particle energy should be greater than the track registration minimum so that V_T/V_B is sufficiently greater than 1 (in practice, at least 2 for electron microscopy and 4 for optical microscopy).
- (ii) The projected length ℓ_p or the diameter of the etched track D should be sufficiently large for optical or electron microscope resolution, i.e.

$$(a) \qquad \qquad \qquad \geq \qquad 0.28 \mu\text{m for optical microscope resolution}$$

$$l_p = (V_T - V_B) t \cos \theta$$

$$\geq \qquad 5 \times 10^{-3} \mu\text{m for electron microscope resolution}$$

where t is the time needed to etch the full length of the track,
 θ is the angle the charged particle makes with the surface
(dip-angle),

and l_p is the length of track projected on the surface.

or

$$(b) \qquad \qquad \qquad \geq \qquad 0.28 \mu\text{m for optical microscope resolution}$$

$$D = 2V_B t \sqrt{(V_T - V_B)/(V_T + V_B)}$$

$$\geq \qquad 5 \times 10^{-3} \mu\text{m for electron microscope resolution}$$

where D is the diameter of the etched track.

Then we may define the minimum energy loss of a charged particle needed to form a linear damaged region in a medium (which can then be etched into an observable track) as the etchable track formation threshold for a given incident charged particle and target medium.

Temperature, concentration and nature of etchant are the important variables for etchable track formation. The etchable track formation threshold for a given incident particle and target medium can be greatly improved by varying the etchant and the etching conditions. For this reason, the etchable track formation threshold for a given incident particle and target medium is experimentally determined. During the present research our electron microscope observations confirmed the existence of latent tracks for some incident particles and target media which could be revealed only by employing improved etching techniques.

Most of the attempts made up to now to calculate etchability of particle tracks in a material assume a certain fixed etching condition for different values of charge, mass and velocity of incoming particles. During the last decade, new criteria have been put forward concerning the registration of etchable tracks. A brief account of some of these criteria (in chronological order) is given below. Also, various experimental observations are discussed and compared with these criteria whenever necessary.

3.2.1 Total Energy Loss Criterion

This criterion is based on the total energy loss, as was put forward by Fleisher et al (67) in 1964. According to them, there exists a certain critical rate of energy loss for each track-detecting material. All those particles having appreciably less energy loss than $(\frac{dE}{dx})_{crit}$ will not be able to produce etchable tracks. On the other hand, particles with appreciably higher rates of energy loss than $(\frac{dE}{dx})_{crit}$ will be registered with a 100% efficiency.

The total rate of energy loss $(\frac{dE}{dx})_{tot}$ can be calculated from the following expression for the total energy loss (TEL),

$$TEL = (\frac{dE}{dx})_{tot} = \frac{2\pi n (Z^*)^2 R_o^2 m_o c^2}{\beta^2} \left[\log_e \frac{(2m_o c^2 \beta^2 \gamma^2 W_{max})}{I_{adj}} \right] \left[2\beta^2 - \frac{2c}{Z} - \delta \right] \quad (3.25)$$

where n = electron density in the stopping material,

$$R_o = \text{the classical electron radius} = \frac{e^2}{m_o c^2}$$

$$m_o c^2 = \text{the rest energy of electron} = 0.511 \text{ MeV}$$

$$\beta = \text{the ratio of the velocity of the particle to the velocity of light (c)} = v/c$$

$$\gamma = (1 - \beta^2)^{-\frac{1}{2}} \text{ and}$$

$$Z^* = \text{effective charge of the bombarding particles (68,69)} \\ = Z(1 - \exp(-125 \beta/Z^{2/3}))$$

$$W_{max} = (2\beta^2/(1 - \beta^2)) m_o c^2$$

$$I_{adj} = \text{mean excitation potential of the target material}$$

$$c/Z = \text{tight binding shell correction}$$

$$\delta = \text{correction for density effect.}$$

Fleischer et al (67) used various particles of different masses and energies in their investigations on muscovite mica, Lexan polycarbonate and cellulose nitrate. The curves of rate of energy loss dE/dx vs particle energy (energy/nucleon) were drawn. On displaying the experimental results on these dE/dx curves for each material, they discovered the existence of a narrow range of dE/dx values over which the etchable track registration efficiency varies from zero to unity (Figure 3.1.a).

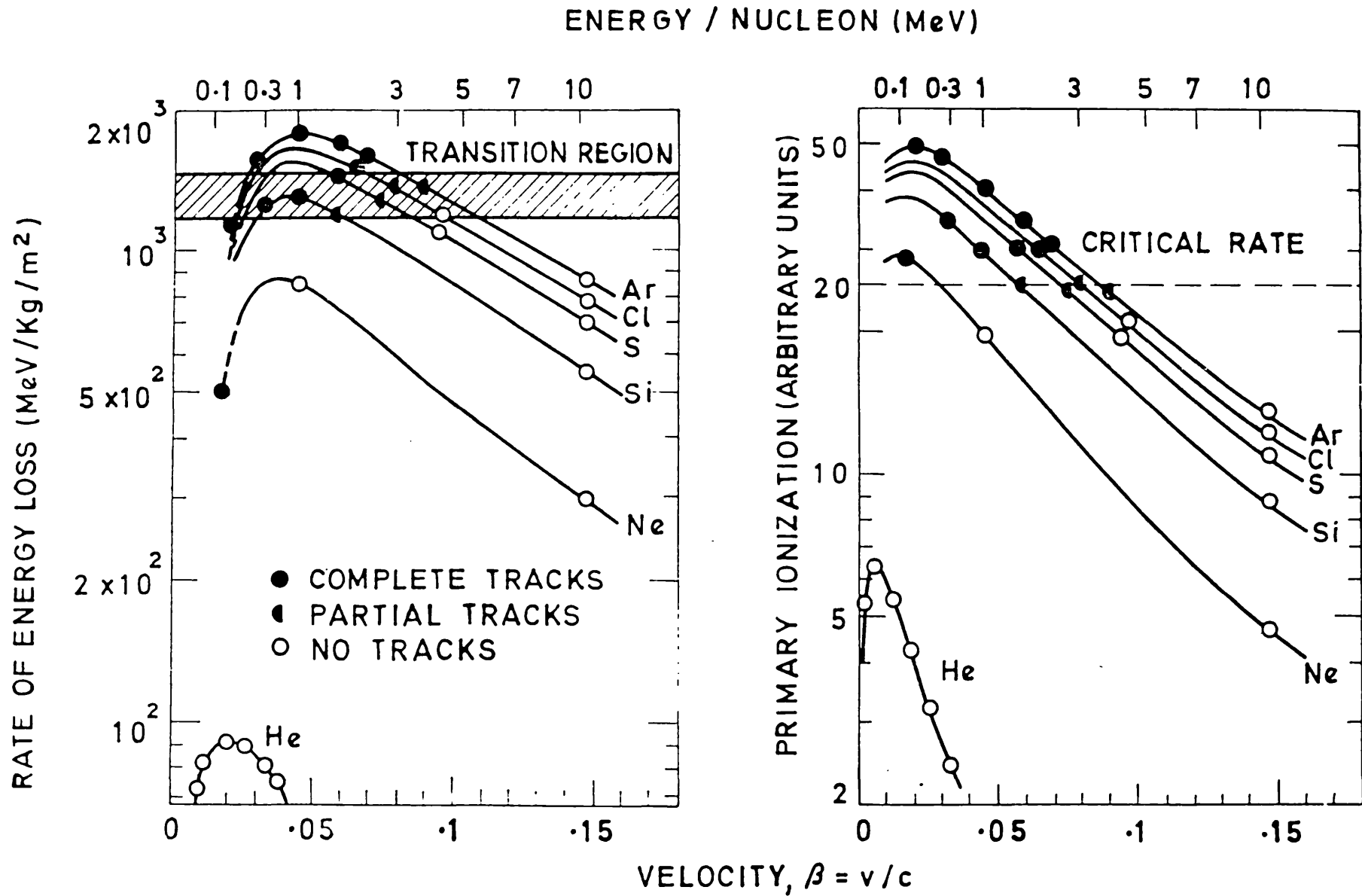


Figure 3.1

(a)

(b)

The criterion failed when applied to relativistic particles and could not explain some of the experimental results.

3.2.2 The Primary Ionisation Criterion

In 1967, Fleischer et al (68) themselves reported that their new data collected on track registration in various materials were inconsistent with their early criterion based on total energy loss. They gave a new criterion which was based on the "ion-spike model". According to this model, as already discussed, a charged particle passing through the material creates a narrow cylinder of net positive charge. The mutual coulomb repulsion of the positive ions making up this region subsequently produces catastrophic atomic displacements, leading to a dense cloud of interstitial atoms and vacancies along the original particle trajectory. Thus, they concluded that a quantity somewhat different from $(dE/dx)_{total}$ should determine the presence or absence of tracks. This is the primary ionization rate.

The primary ionization PI, is defined by Bethe as the average number of collisions (per g cm⁻²) that results in an ejection of the least tightly bound electron from an atom.

$$PI = \frac{dJ}{dx} = \frac{2\pi n(Z^*)^2 R_o^2 m_o c^2 R}{\beta^2 I_o} \times \left[\log_e \frac{2m_o c^2 \beta^2 \gamma^2}{I_o} + S - \beta^2 \right] \quad (3.26)$$

where PI = the primary ionization

I_o = the ionization potential of the outmost shell of the target material atom

Z^* = the effective charge of the bombarding particle

R and S are two dimensionless parameters.

$n, R_o, m_o, c^2, \beta, \gamma$ and Z^* have the same meaning as in Equation (3.25).

This criterion is in good agreement with most of the existing experimental data and thus proved to be considerably successful in predicting the track formation in different materials for different particles of varying energies (Figure 3.1.b).

However, a certain confusion arose regarding the physical nature of the criterion.

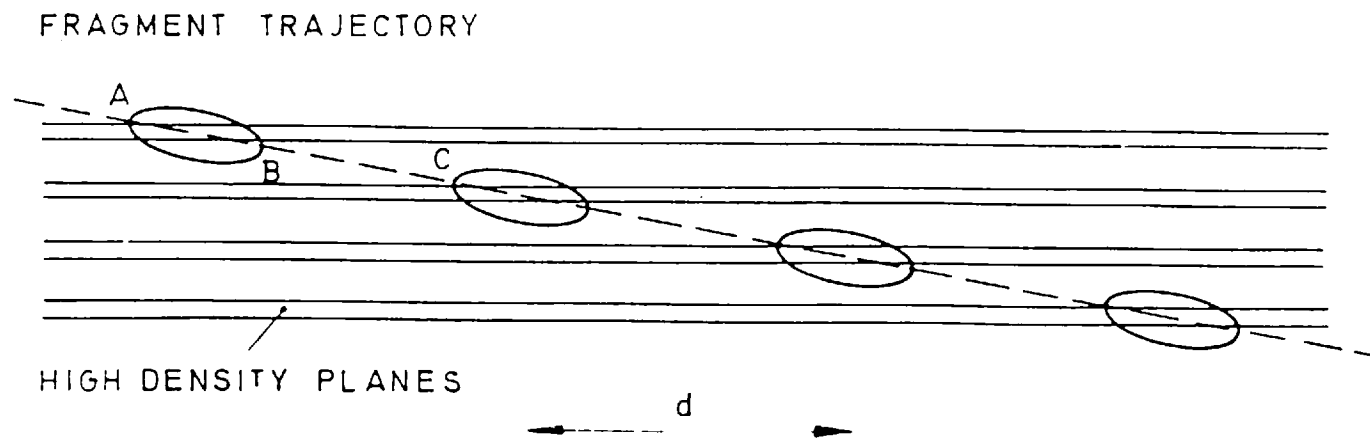


Fig. 3.2a Model for the formation of intermittent tracks in crystals with a layer structure such as molybdenum disulphide. Intense electronic excitation is produced at successive low-angle intersections with the high-density atomic planes such as AB .

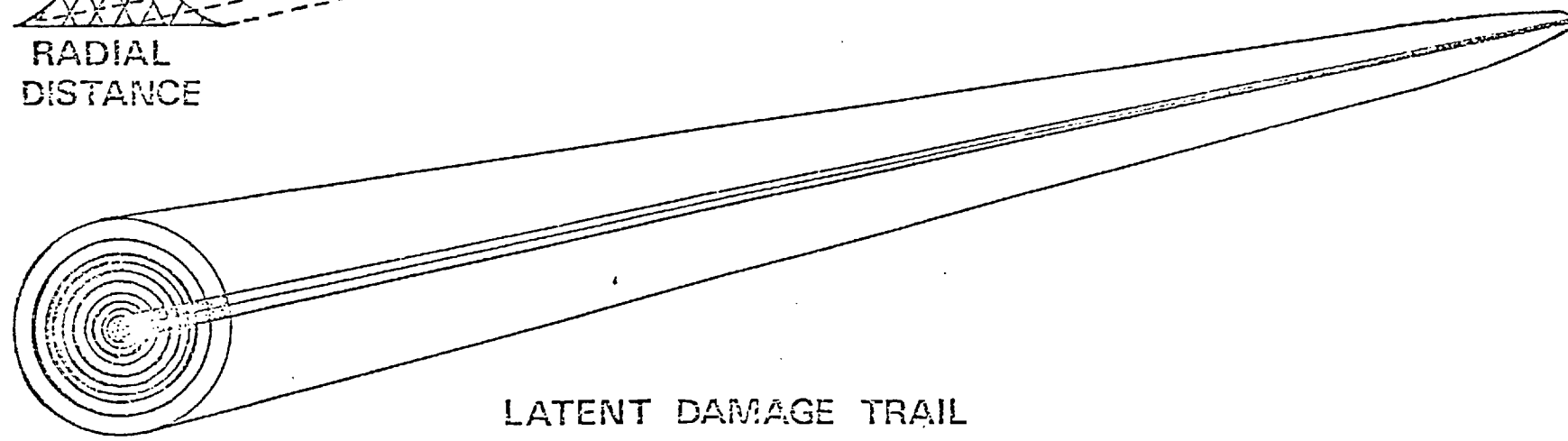
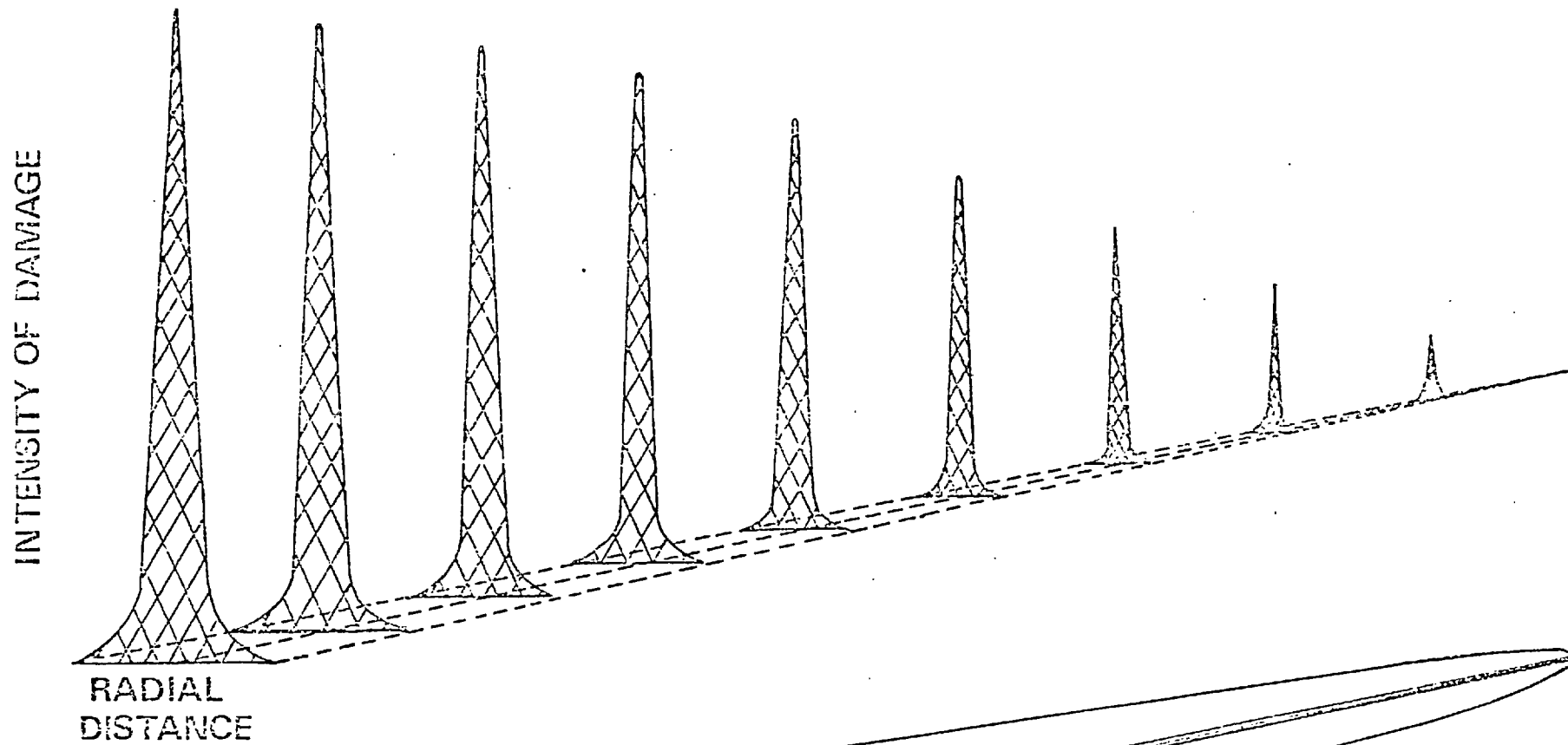


Figure 3.2b

One of the unexplained phenomena observed is the previously mentioned sudden change in the registration efficiency of materials. A number of experiments (71,72) were carried out to explain this phenomenon by studying the behaviour of a certain fixed registering material for different particles. It was concluded that the total rate of production of defects does not decrease sharply, but that discontinuities appear along the damage trail, separating the small regions of defects and thereby slowing down the track etching rate.

Similar experiments were carried out to study the track registration sensitivity of different materials for certain incoming particles (mainly fission fragments) showing that the values of $(PI)_{crit}$ are different for different materials and fewer defects are produced in less sensitive materials. There is little variation in the critical spacing (Figure 3.2) of the defect areas.

Moreover, this criterion is also subject to the following criticisms (73).

- (i) The Bethe formula used in the (PI) calculations contains two parameters R and S , the values of which are not known for any material other than hydrogen. Thus absolute values of PI cannot be calculated.
- (ii) The value of I_0 (the ionization potential of the outermost shell of the stopping atoms) used by Fleischer et al (70), in order to fit the experimental data, is equal to 2 eV. This value of I_0 is too low considering its physical meaning. The value as deduced by Benton from experimental evidence is about 4.4 eV. Moreover, an energy of 2 eV as chosen by Fleischer et al (70) may be sufficient to excite the atom, but to ionize an atom, such as those present in plastics, one usually needs 8 - 15 eV. This indicates that even the name 'primary ionization' is not as suitable as 'primary excitation'.
- (iii) The criterion assumes that all the higher orders of ionization can be neglected, which again is controversial.

3.2.3 The Restricted Energy Loss Criterion

In 1969 Benton and Nix (74) put forward a new criterion for the registration of charged particle tracks in plastics. Their criterion is free from the objections raised against the PI criterion of Fleischer et al (70).

The new criterion is based on restricted energy loss REL. REL is defined by Benton and Nix (74) as the rate of energy loss of the bombarding particle in collisions with the electrons of the stopping material which result in the ejection of electrons of energy W less than some predetermined value W_0 .

According to the criterion, the formation of the etchable tracks is possible only when the restricted energy loss rate exceeds the REL_{crit} which is a characteristic of the detecting material.

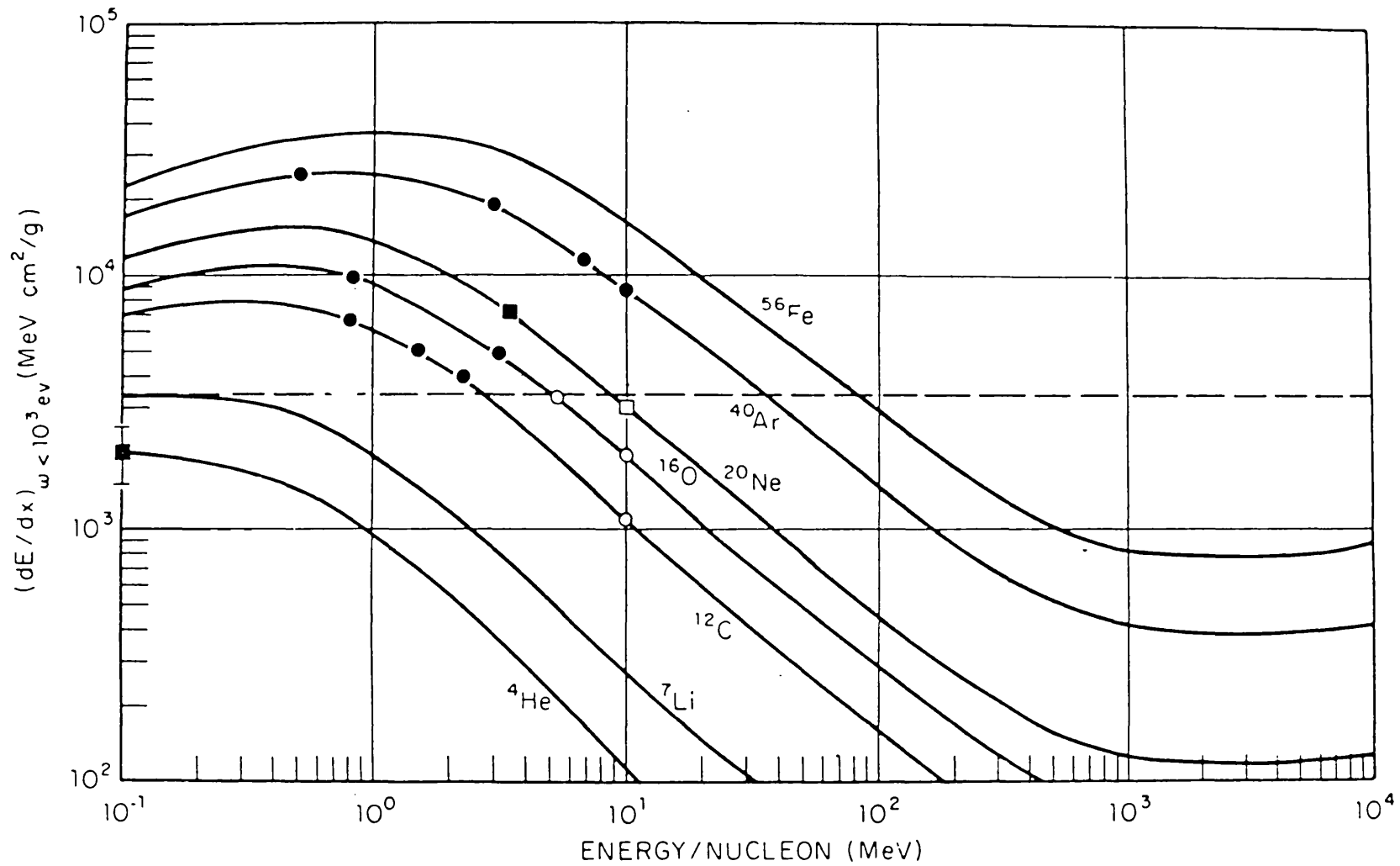
Restricted energy loss can be calculated from the following equation:

$$REL = \frac{dE}{dx} W < W_0 = \frac{2\pi n(Z^*)^2 R_0^2 m_0 c^2}{\beta^2} \times \left[\log_e \left(\frac{2 m_0 c^2 \beta^2 \gamma^2 W_0}{I_{adj}^2} \right) - \beta^2 - 2 \frac{c}{Z} - \delta \right] \quad (3.27)$$

where the symbols, n , Z^* , R_0 , $m_0 c^2$, β , γ , I_{adj} , $\frac{c}{Z}$ and δ have the same meaning as given for Equations 3.25 and 3.26 for total energy loss calculations. REL values for a number of heavy ions in Lexan and cellulose nitrate are shown in Figures 3.3 and 3.4.

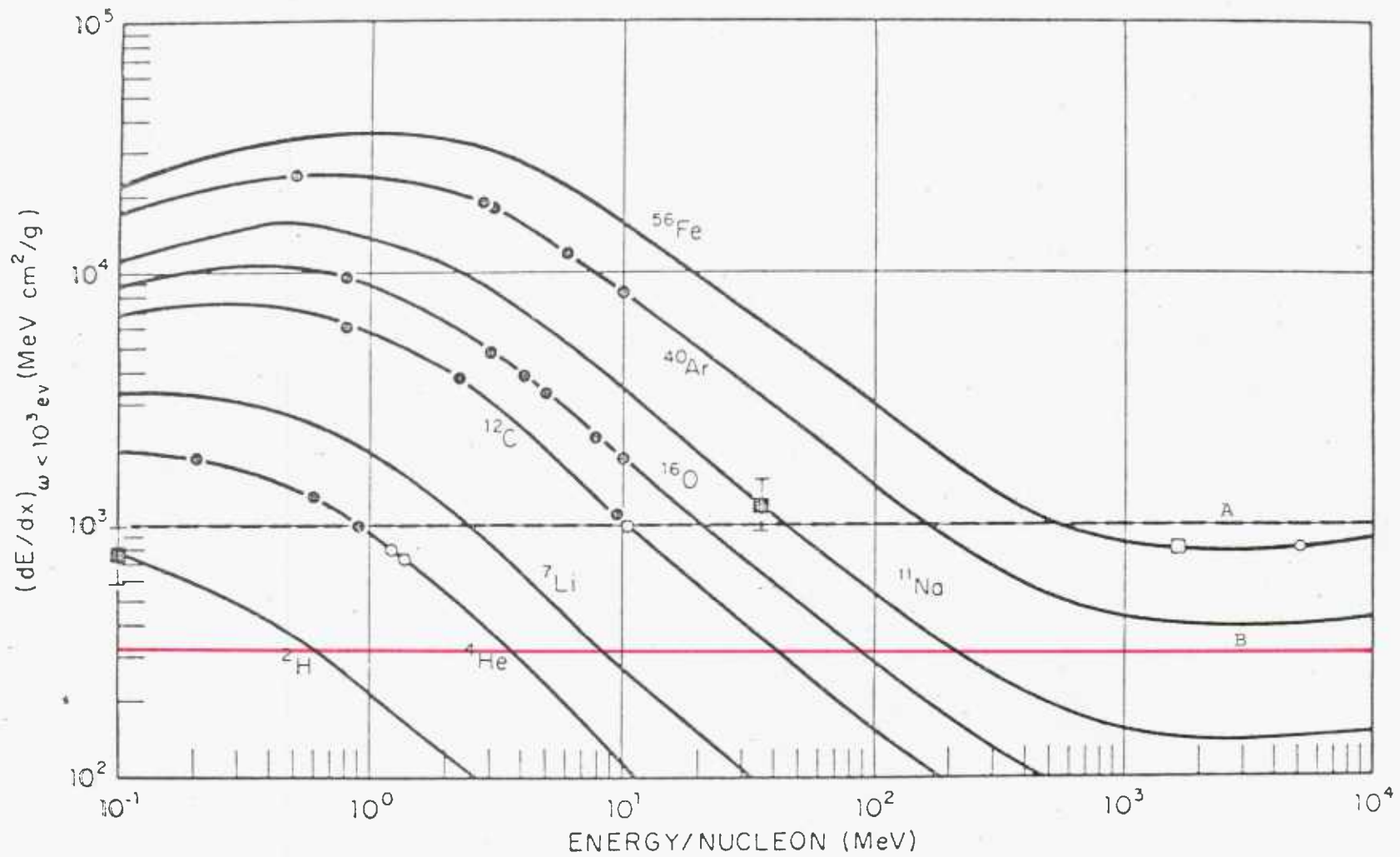
The criterion includes both energy going into primary and higher order ionizations. But it neglects the contribution of all delta rays with $W > W_0$. It employs two adjustable parameters, W_0 , the average energy of the recoil electrons below which they can contribute to track formation, and $(REL)_{crit}$ the critical rate of energy loss. Using this criterion, absolute values of sensitivity of different plastics can be calculated, and they are found to be in considerable agreement with the existing experimental data.

However, the criterion is not fully acceptable. Firstly, since the value of c/Z has not been calculated below 8 MeV/nucleon, REL values below this energy are difficult to calculate. Secondly it was found that the value of $W_0 = 10^3$ eV used by Benton and Nix (31) is rather high.



Restricted energy loss rate, $(dE/dx)_{\omega < 10^3 \text{ eV}}$, as a function of energy per nucleon for a number of heavy ions in Lexan polycarbonate resin ($I_{\text{adj}} = 69.5 \text{ eV}$).

Figure 3.3



Restricted energy loss rate, $(dE/dx)_{\omega < 10^3 \text{ eV}}$, as a function of energy per nucleon for a number of heavy ions in cellulose nitrate ($I_{\text{adj}} = 81.1 \text{ eV}$).

Figure 3.4

3.2.4 The Delta-Ray Criterion

Katz and Kobetich (75) and Monnin (76) emphasize that the major role in track formation is not played by the primary but rather by the secondary electrons.

They have calculated the spatial energy distribution around the trajectory of the penetrating particle and proposed that an etchable track can be formed if the dose deposited by the secondary electrons at a critical distance from the particle's trajectory is more than a critical dose. The main difference between Katz's (75) and Monnin's (76) calculations is the choice of the effective radius. Katz and Kobetich (75) have taken a fixed cylinder of radius 20 \AA (which according to them is the appropriate radius for etchant movement and the diffusion of the etch products back to the surface). On the other hand, Monnin (76) has calculated doses deposited within cylinders of different radii. Also, Katz and Kobetich (75) postulate that the doses required at the critical radius for etchable track formation can be approximated to the gamma ray dose producing a certain level of damage of the bulk material.

These criteria also agree with most of the experimental results presently available.

However, the correctness of the basic assumptions made in the calculations is questionable, on the basis that the contributions of the primary excitations are completely negligible and that the exact form of the angular distribution of the ejected electrons and that of the range-energy curve in the low energy range (particularly in the eV region) are completely unknown.

3.3 Mechanism of Track Formation

Having investigated the processes of energy transfer from the charged incident particle to a stopping-medium, it is appropriate to consider the general ways in which this energy is dissipated in a medium, and the general types of damage produced. We have divided collision events initiated by the energetic fragment into electronic and nuclear and into inelastic and elastic collisions. Let us now examine the processes which take place in the solid subsequent to each type of collision in order to establish which effects might be likely to be observable on a microscopic scale. It will be appropriate to

assume a 'general' solid, although a charged particle produces quite different types of damage in the different classes of materials.

An energetic charge particle can hand over its energy to the target medium, according to the following modes.

- (a) Atoms can be displaced in the target medium during elastic and inelastic interactions of the incident particle with the constituent atoms of the target material.
- (b) A nuclear interaction with the atoms of the medium can take place.
- (c) Electrons can be displaced in the medium during ionization and excitation of the atoms of the target medium by the incident particle.

On the other hand, the absorbed energy by the target medium can be transported or disposed of as follows:

- (i) it can be dissipated as heat,
- (ii) it can be emitted in the form of radiation,
- (iii) it can be stored as chemical energy.

A detailed study of the above incident particle/target medium interaction has yielded the following track formation theories.

3.3.1 Atomic Displacement and Displacement Cascades

A number of theories of displacement and displacement cascades have been established in order to explain both the dissipation of energy in the material and the resultant permanent effects (77).

An atom of the target medium as a complete entity may receive kinetic energy from the incident charged particle, leading to a number of atoms being displaced. This may also occur via secondary processes arising from the electronic part of the energy loss of the incident charged particle. Such an atom will undergo elastic scattering and, if the energy is sufficient, subsequent elastic or inelastic collisions with neighbours, initiating further secondary and higher order displacements. A cascade of displaced atoms will build up until the maximum energy of any atom falls below the appropriate displacement threshold E_d . The value of E_d depends on the binding energy and characteristics of the material, and is normally about 25 eV. If the atom of the target medium receives energy in excess of its displacement threshold, but insufficient for it to displace another, this atom

will eventually either return to its lattice site or come to rest in an interstitial position of metastable equilibrium, creating a Frenkel pair (assuming that a replacement collision does not occur). A statistical treatment of the energy distribution among initial and succeeding displacements should be employed, if the energies involved are high and a large cascade is produced.

Apparently, the process seems to play some part in track formation. However, the model lost its significance in view of the following considerations:

(i) atoms can be displaced by both elastic and inelastic scattering, but the cross-section for inelastic recoil is extremely small compared to that for elastic recoil. Calculations for 3 MeV argon ions in mica produced 300 recoils (78), the energy of which would exceed the lattice displacement energy, (25 eV),

(ii) latent tracks should be formed in metals and all semi-conductors but there is no experimental evidence of such tracks,

(iii) the tracks should be more easily formed near the end of the particle trajectory, where the number density of elastically recoiled atoms is greatest. Actually, in contrast to this prediction, the damage in this region is found to be very difficult to etch.

3.3.2 Thermal Spike Model

A temperature pulse is initiated in the lattice of the target medium by the incident charged particle and as it travels out and away from the trajectory of the incident particle, the intensity of this pulse decreases. In this model, all the energy which is carried by the electrons of the target medium liberated by the incident charged particle is assumed to appear quickly in rapid heating and subsequent quenching of a small volume of the target material, and subsequently to diffuse according to the macroscopic laws of heat conduction. The temperature distribution in time t and distance r from the axis of the spike is as follows:

The heat conduction equation

$$\nabla^2 T = \left(\frac{1}{D}\right) (\partial T / \partial t) \quad (3.28)$$

giving the solution for the excess temperature

$$T(r, t) = \frac{Q}{4\pi c_p D t} \exp(-r^2/4Dt) \quad (3.29)$$

where K is the thermal conductivity, c is the heat capacity, ρ is the mass density (diffusivity $D = K/c\rho$), and Q is the energy delivered per unit length of the spike.

It has been shown that in certain heat-sensitive crystals, the energy which is carried off by the delta-rays is very rapidly communicated to the lattice, so there is no reason to discard the thermal spike as being without significance (79). Moreover, the computer simulation studies, made by Vineyard (80) and his associates of the dynamic motions of atoms in an irradiated lattice reveal that after 10^{-12} of 10^{-11} sec the concept of a spherical thermal spike (81), can be shown to have very real validity.

In considering the course of events, the characteristic time is

$$t_o = r_s^2/4D \quad (3.30)$$

where r_s , the mean atomic radius (81), is defined by the equation

$$4/3\pi r_s^3 = 1/n_o \quad (3.31)$$

for the charged particle and for a typical solid with a melting temperature of T_m , the distance r_m from the axis to which the high temperature boundary has diffused when the temperature has dropped down to T_m is determined approximately by using the ideal gas specific heat:

$$\pi r_m^2 \cdot n_o = Q/3kT_m \quad (3.32)$$

Hence, substituting for n_o from (3.31)

$$r_m = 2/3 (Q/kT_m)^{1/2} r_s^{3/2} \quad (3.33)$$

If we neglect the exponential part of Equation (3.29) and consider a disordering process with an activation energy E' , then the probability n_j with which the process may be expected to occur in the centre zone of the spike during the period of duration (per unit length of spike) is given by:

$$n_j = \int_0^{\infty} N dt = \int_0^{\infty} N \exp(-E'/kT(t)) dt \quad (3.34)$$

which may be shown to become

$$r_j = \Lambda r_s N_a / 9 \quad (3.35)$$

where $\Lambda = v_o r_s^2 / D$, and $N_a = Q/E'$ is an 'activation number'. The critical radius r' within which the probability that a given atom participates in the disordering process is unity becomes:

$$r' = 2/3 r_s^{3/2} \left[N_a \log_e r_j \right]^{1/2} \quad (3.36)$$

and the number of atoms which actually participate per unit length of the spike (some of them more than once) is

$$n_a = \frac{n_j N_a}{3} \exp \left\{ - \frac{9r'^2}{4N_a r_s^3} \right\} + \frac{3r'^2}{4r_s^3} \quad (3.37)$$

According to the thermal spike model, there are two essential conditions for track formation. Firstly, the state of high temperature should exist for appreciable times, which requires that electron-phonon coupling should be stronger than electron-electron coupling in the material. Secondly, the normal heat conductivity in the material should be low. These conditions quite rightly predict that the probability of track formation is very high in insulators and very low in good conductors like metals.

In spite of predicting correctly some features of track forming material, the thermal spike alone does not appear to be sufficient, for the following reasons:

(i) This simple treatment of the thermal spike model omits any consideration of the fundamental differences in the electron-lattice energy transfer process for the different types of target media. This model has therefore to be modified to include these differences.

(ii) Even carefully conducted experiments show signs of a very high temperature phase in heavily irradiated insulators. But the above model does not give any valid predictions. A theoretical model which should involve the resistivity of the target medium and relate it to the track formation cut-off resistivity for that medium, below which the target medium will not register any tracks for any incident charged particle irrespective of energy will be introduced in Chapter Four.

(iii) The dependence of track parameters such as track widths on the decomposition temperature of the material were calculated via the

thermal spike model by Bonfiglioli et al (82) but these calculated values did not show a good agreement with the values obtained by Price and Walker (4) and others. This may be because equilibrium never exists within the spike so we should use the time dependent perturbation theory and the deformable atom model (45).

(iv) Sensitivities of different track forming materials are not related in any regular manner to their known melting, softening or transformation temperatures. On the other hand, because of the short duration of the thermal spike, the spike region does not attain a true liquid state, and may be more accurately described as a super-heated solid.

3.3.3 The Ion Explosion Spike Model

This model is essentially an extension of the ideas of the Varley mechanism (83) to all solids. It is assumed in Figure 3.5 that in the trajectory of the incident charged particle, there is a small dense core of positive charge on account of multiple ionization processes induced by Coulomb interactions with the passing charged particle, and that this core has a sufficiently long lifetime so that explosive Coulomb repulsion can eject ions into the surrounding lattice to produce Frenkel defects. Serious difficulties with this proposal, however, arise out of doubts about the lifetime of the excited ions on which the model crucially depends, and from misunderstandings concerning the dynamic influence of the atomic 'lens' which border the charged particle trajectory (84). Furthermore, one can never be certain what parts the processes of 'focussing' and 'channelling' in crystals will play (85) in such complicated dynamic events.

The dynamics of this problem had been conveniently simulated for a planar crystal of KCl (20 x 20 ions without any initial lattice vibrations) on a high-speed digital computer (84). Four chlorine ions near the centre of the array were multiply ionized and the subsequent motions of ions in the array were calculated by varying both the degree of ionization of the chlorine ions (between one and four) and the lifetime of these ions (each ionic state having a corresponding lifetime).

The general pattern emerging from a set of typical computations is illustrated in Figure 3.6a which shows trajectories of the ions for the case of triple ionization up to a time of 8×10^{-13} sec, and the final relaxation of the lattice is not shown since it makes the diagram

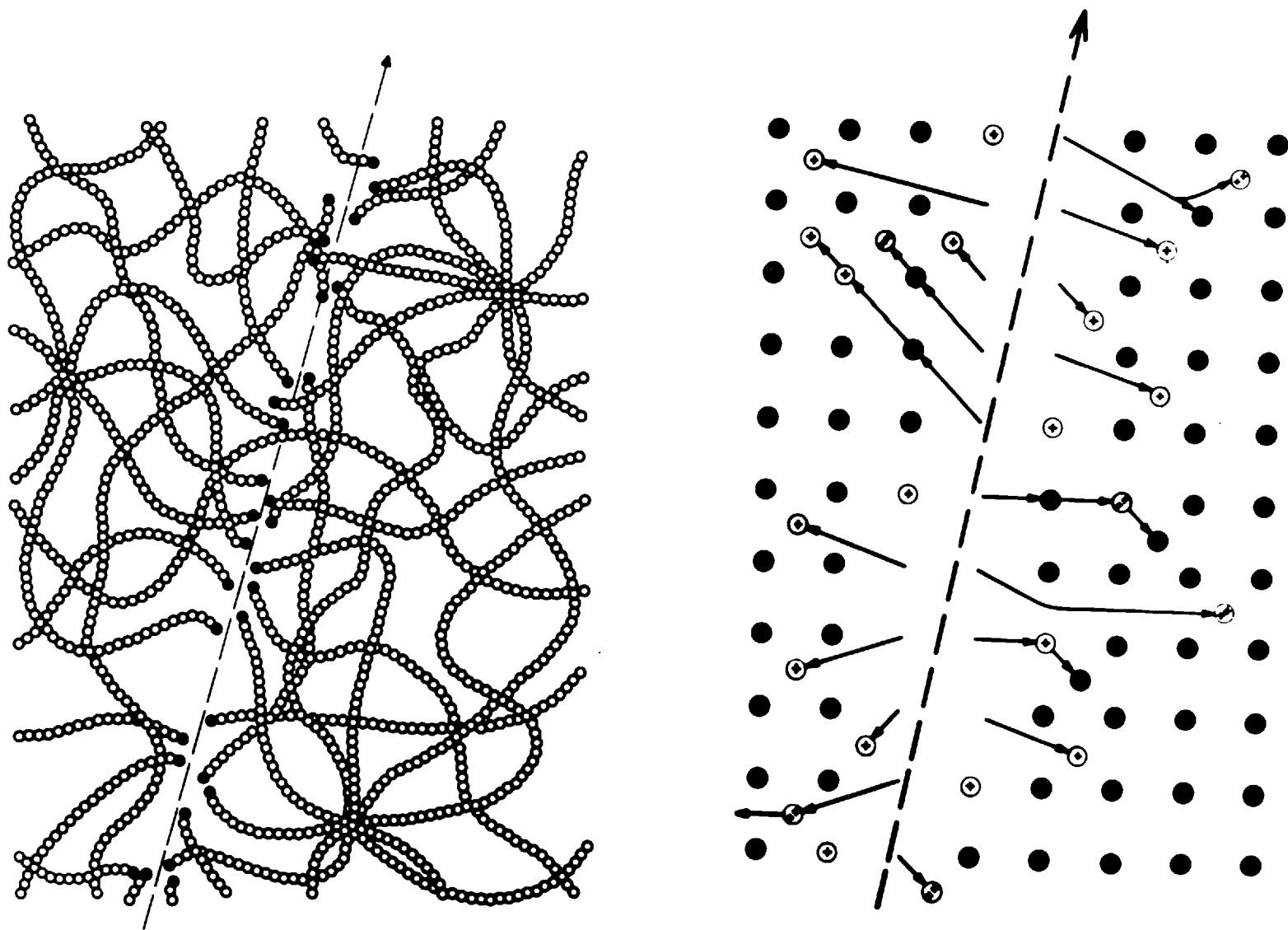


Figure 3.5a Models showing the formation of latent trails in (a) plastics, (b) crystals.

Ion Explosion Spike Model

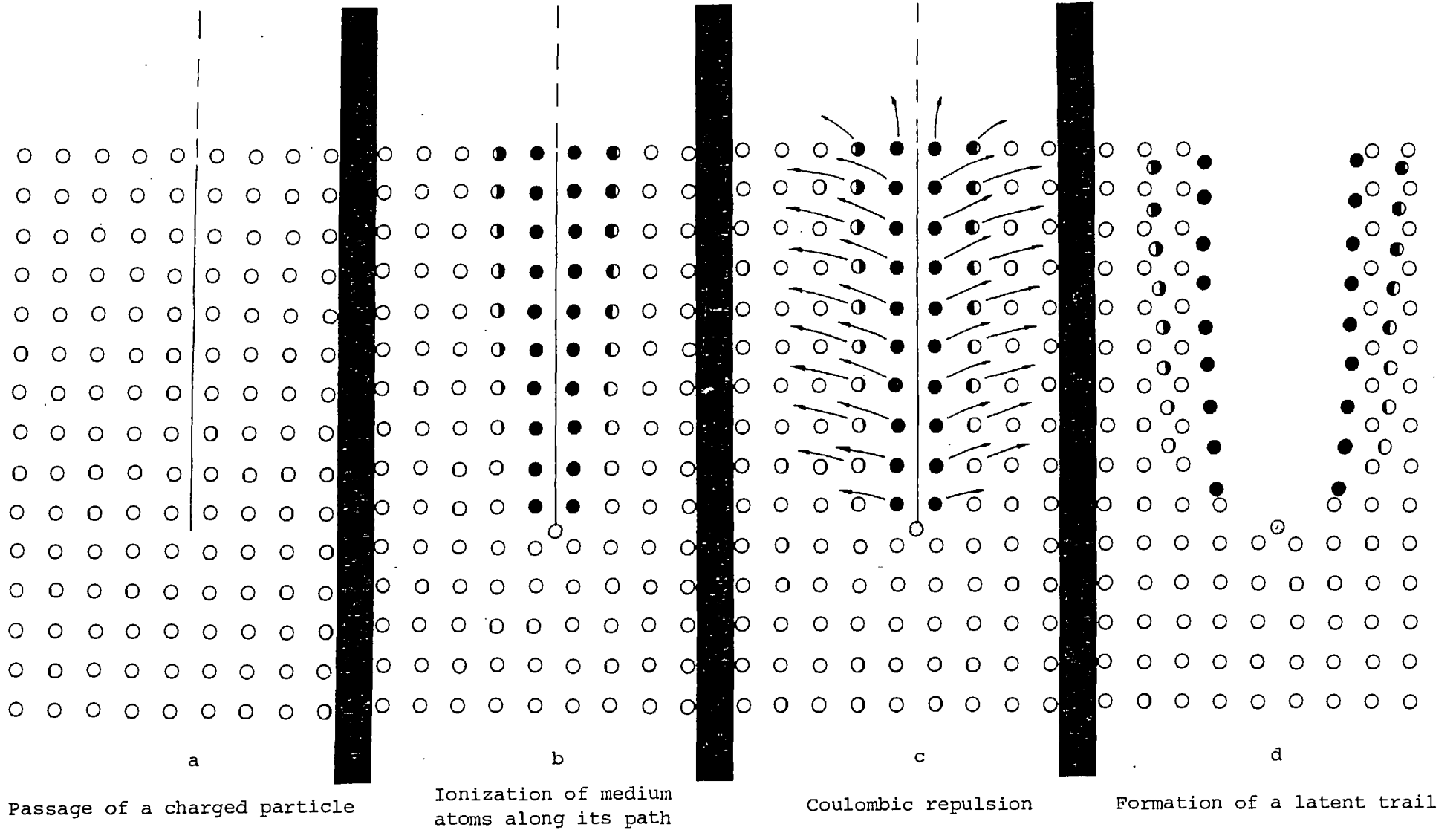


Figure 3.5b

over-complicated. Figure 3.6b shows consecutive configurations of the lattice as the disturbance progressed towards equilibrium. The results may be summarised as follows:

- (i) An outward movement of all the positive ions in the central region takes place (this includes the K^+ as well as Cl^{+n} ions, where n is the number of electrons removed).
- (ii) Very pronounced $\langle 100 \rangle$ focussed collisions are generated which transmit energy outwards many lattice spacings, in the case of the triply ionized case the disturbance travels some 10 lattice parameters in 3×10^{-13} sec. This is a highly efficient means of dispersing a considerable proportion of the initial electrostatic energy. The subsequent motion of the ions indicates an oscillation about their mean positions which are placed outward from the original equilibrium lattice sites.
- (iii) The next nearest Cl^- neighbours move inwards under the attractions of the positive core. In the triply and quadruply ionized cases, some of these Cl^- ions move into the vacancy core left by the outgoing positive ions. This is illustrated for the triply ionized case (Figure 3.6c).
- (iv) There is a great deal of re-arrangement of the central ions. For the case of triple ionization the following events develop in 10^{-12} sec.
 - (i) interstitials are produced by the outward expanding positive ions,
 - (ii) the Cl^- ions gather in the partially vacated central region left by the expanding core,
 - (iii) ions interchange lattice sites.
- (v) A secondary 're-arrangement explosion' occurs after electron capture as the central core, now predominantly filled with Cl^- ions, tries to regain its electrical neutrality (Figure 3.6d) and (e). A type of electrostatic annealing occurs. The ions seek to arrange themselves so that the Cl^- ions settle on sites originally occupied by Cl^- ions, and similarly for K^+ . Thus, although some atoms have travelled as much as two or three lattice spacings, they come to rest on sites which are environmentally identical to those which they left, thereby reducing the visible damage.

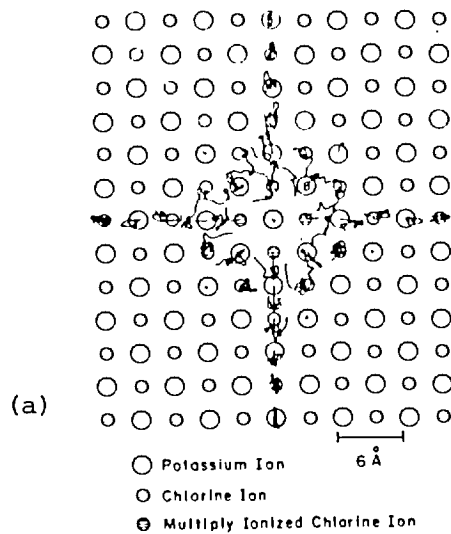


Figure 3.6a Trajectories of the ions for the case of triple ionization of four chlorine ions up to a time of 8×10^{-13} sec.

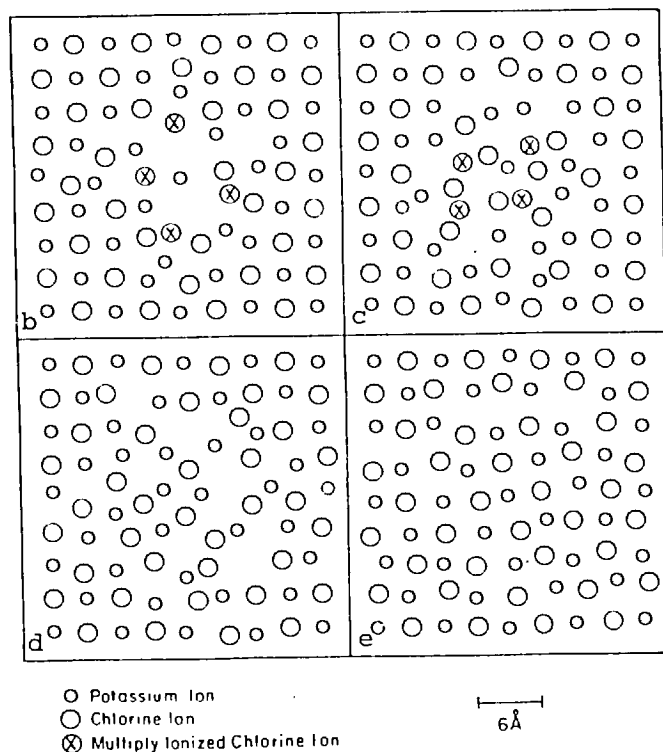


Figure 3.6b,c,d,e Consecutive configurations of the central lattice as a function of time (triple ionization).

- (b) After 5×10^{-13} sec. Showing the outward movement of positive ions.
- (c) After 5×10^{-12} sec. This is just before the ions start their process of electron capture. Chlorine ions have moved into the partly vacant central core.
- (d) After 1.5×10^{-12} sec. The electrostatic annealing is now taking place.
- (e) After 3×10^{-12} sec. Ions have now re-arranged themselves so that no visible damage remains. (Perturbations of ions from their lattice sites is due to their oscillations, which in turn transmits energy outwards).

These results do not take any account of the thermal vibrations initially present in the lattice, nor of the lattice 'thermal spike' due to electron-phonon interactions, which is estimated to be considerable in insulating compounds. It is therefore possible that a combined 'thermal ion explosion spike' could result in an outward thermal activation, and a more permanent production of stable positive ion interstitials, particularly with larger positive cores (produced by more energetic heavy charged particles).

We must therefore conclude from this present model that the ion-explosion spike alone is not sufficient to produce large numbers of defects in ionic solids, since although damage occurs, it is unstable and electrostatic annealing returns the lattice to its normal state after electron capture. In covalent solids, provided the lifetime criterion is satisfied, the thermal spike might thermally activate some of the ions participating in the ion explosion to more stable positions. A minimum time required for this would be $\sim 5 \times 10^{-13}$ to 10^{-12} sec depending on the degree of ionization.

3.4 Conclusions

Thermal spike effects can be caused by collisions of the incident charged particle with the atoms of the target lattice as well as by electronic excitation subsequently heating the lattice; the atoms of the target that have been hit just hard enough to vibrate with large amplitude without being actually displaced will rapidly transfer energy to their neighbours which become excited. Thus a region of the target medium around the track of the charged particle will contain knock-on atoms which will heat it to a high temperature. The region of the lattice thermal excitation expands rapidly via thermal conduction and at the same time there is a drastic decrease of temperature. Calculations indicate that a cylindrical volume of radius about 100 \AA and several microns in length may attain a temperature of the order of $10^4 \text{ }^\circ\text{K}$ for a duration of 10^{-10} to 10^{-11} secs.

There is a readily available estimate of the variation of the effective fission fragment charge with its energy, which determines the energy communicated to the electrons and hence the effective radius of the cylindrical thermal spike. Since the average charge decreases as the fragment energy falls, this radius will also decrease; the thermal

spike can be approximated as a right circular cone with its apex at the final resting place of the fragment. In Figure 3.7a the fragment enters the crystal at X and comes to rest at Y. The intensity of the thermal spike at any point along the track is represented by the radius of the right angle cone at that point. To include the effect of atomic displacements it will be recalled that collisions with atoms become more frequent as the fission fragment slows down, so that the frequency of displacement cascade production will increase as the particle comes to rest, each knock-on atom creating a spike according to the schematic representation of Figure 3.7b. When the mean free-path for atomic displacement falls below an interatomic distance, a displacement spike is formed. The displacement spike production shown in Figure 3.7c increases in frequency up to the end of the track, which itself takes the form of one large spike caused by the fission fragment as it comes to rest as an impurity atom in the lattice. As the fragment slows down there is a gradual transition from "Rutherford" to "hard sphere" collisions. The statistical nature of the frequency of collision events is considered to be understood and is omitted from the diagram.

The situation at the end of the track is complicated by the large number of atomic displacements and displacement cascades, which in turn produce more thermal excitation. In particular, many neighbouring atomic displacements will be created in many small volumes adjacent to the trajectory of the fragment. This multiple displacement idea leads to the concept of the displacement spike, first suggested and developed by Brinkman (86,87). Brinkman hypothesized that a multiple vacancy would be created at the end of the path of an incident fission fragment or an energetic primary knock-on, the configuration immediately following each event being a shell of interstitial atoms surrounding a vacancy core (Figure 3.8a). It is doubtful if such a configuration is stable, however, since the high density of interstitials exerts a high pressure on the central region. Most likely some collapse of the spike will occur, with interstitial-vacancy annealing, but in the final configuration, dislocation loops and small regions of misorientation are highly probable.

Seeger (63) proposed a modification of the displacement spike which included the propagation of focussed collision sequences along close-packed rows of lattice atoms. These sequences present a very

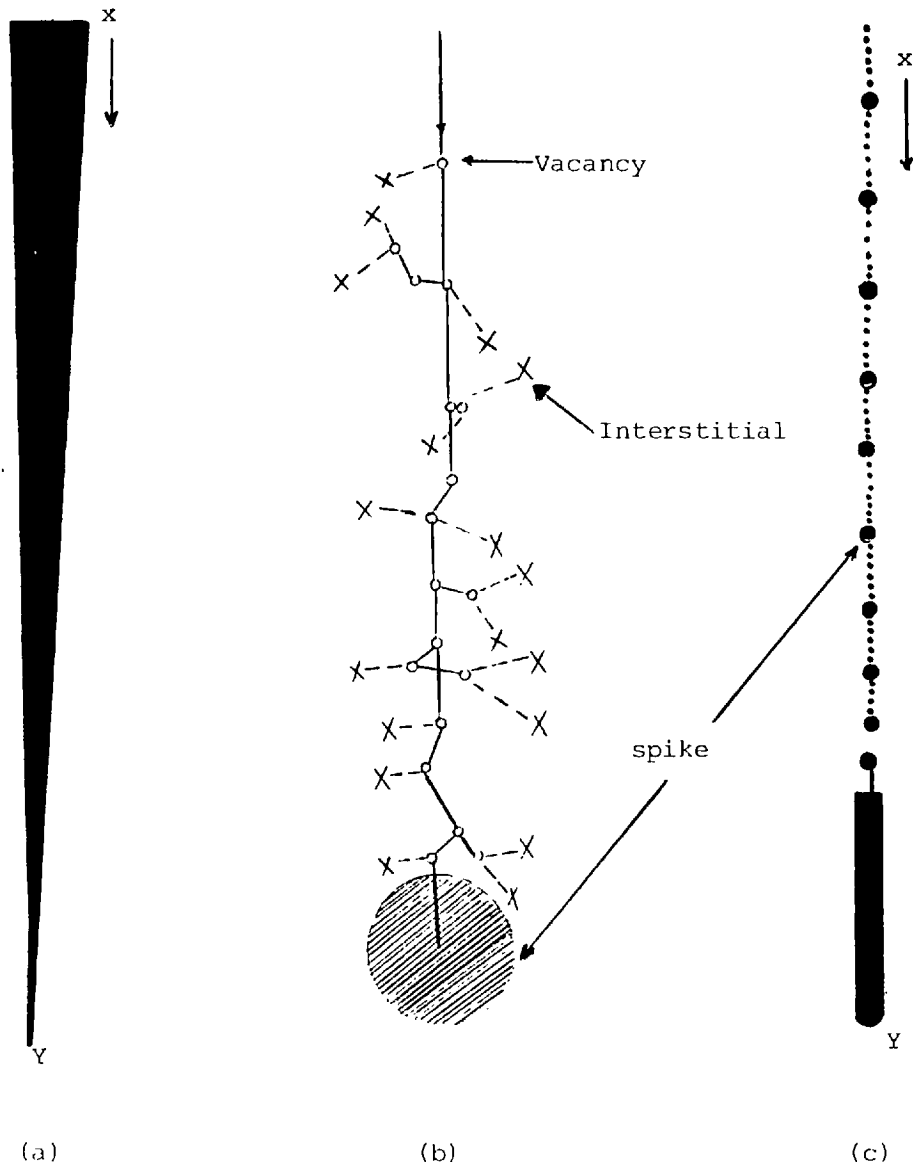


Figure 3.7 Schematic representation of the fission spike.

- (a) The fragment enters the crystal at X and comes to rest at the point Y. The intensity of the thermal spike at any point along this 'track' is given by the radius of a right circular cone (seen here in section) at that point.
- (b) Diagram showing the formation of a displacement spike by an energetic knock-on deriving from a collision between the fragment and a lattice atom. When the mean-free-path for atomic displacement falls below an inter-atomic distance a displacement spike is formed.
- (c) The frequency of displacement spike formation increases as the fragment slows down and there is a gradual transition from "Rutherford" to "hard sphere" collisions. The statistical nature of the frequency of collision events is considered to be understood and is omitted from the diagram.

effective mechanism for the separation of an interstitial at the end of the sequence from the corresponding vacancy at its beginning. The result is a high local density of vacancies in the region where the primary energetic particle is brought to rest, surrounded by only a few nearby interstitials, the so-called depleted zone (Figure 3.8b).

In the case of the ion-explosion spike mechanism, as discussed in Section 3.3.3, objections centre on the fact that the fraction of the total LET contained in the electrostatic energy of ions is very small (75); these ions are probably neutralized before they can be ejected into the lattice as interstitials (90); even if they were ejected, electrostatic annealing heals a large fraction of the initial damage (88).

On the basis of the previous considerations it may be concluded that none of the previous models is sufficient by itself for the production of a large number of point defects in charged-particle irradiated solids.

A model is constructed in Chapter Four to explain the fission fragment track observations in certain semi-conducting layer compounds. This model discusses the resistivity dependence of track formation in the target medium.

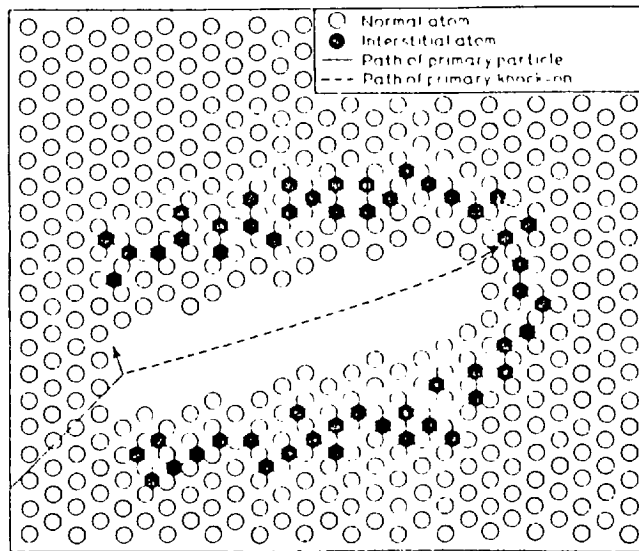


Figure 3.8a Schematic representation of interstitial atoms around a multiple vacancy during production of a Brinkman displacement spike.

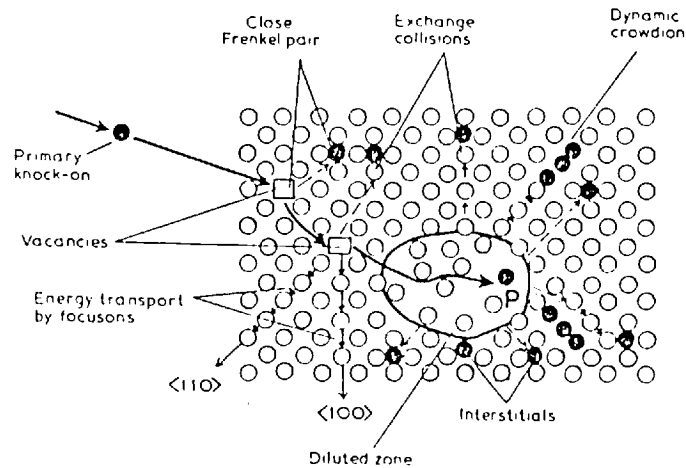


Figure 3.8b Schematic two-dimensional representation of the Seeger depleted zone and its environment in a face-centred cubic crystal. A primary knock-on impinges from the left and comes to rest on the site P.

CHAPTER FOUR

TRACK FORMATION IN SOLIDS

4.1 Introduction

The study of latent tracks is conveniently divided in Chapter Three into two general categories. The first contains various interaction phenomena from the point of view of the impinging particle and concerns itself with such aspects regarding the physical properties of the incident particle as its charge, mass, momentum, range and rate of energy loss, etc. In the second category are included physical and chemical transformations of the medium which the incident particle traverses. Because all chemical reactions depend strongly on the nature and proximity of the reactive intermediates, the study of this category is intimately connected with that of the first. However, there is usually a cascade of changes involving several generations of intermediates separating the initial energy loss to the medium and the first recorded chemical effect. For example, it may be pointed out that even in the fastest observed radiation-induced luminescence, the light is rarely emitted from the state first produced, even though this possibility is not ruled out in principle. Similarly, the various products observed in radiolysis are frequently the result of a sequence of chemical reactions. We are, therefore, obliged to make some theoretical assumptions regarding the state of the medium immediately following the absorption of energy. Many of these assumptions cannot be verified by experiments at the present time.

A sound theoretical latent track formation model should include stopping power, range-velocity relations, ionisation along the tracks and particle identification by the nature of its track, etc. Sophisticated observations such as latent track branchings as shown in Figure 4.1, nuclear deflections, latent track annealings and even energy-loss localisation events, should be satisfactorily explained.

There is a large body of known physical and chemical phenomena that require a track model for their existence or explanation. Most of the physical evidence with the possible exception of yield of escaped ions has been compiled by Fano (89) in an excellent review. Only a short description is given here and the reader is referred to the original article for further details.

(i) Particle Identification

Most charged particles can be identified uniquely by the nature of the tracks they leave. The density of ionisation in the track is characteristic of the specific rate of energy loss of a given particle in a medium. Use of kinematic principles can be used to compute particle energy after the particle has been identified.

(ii) Restricted and Unrestricted Energy Loss Phenomena

Restricted energy loss belongs to energy losses resulting from primary excitations and ionizations brought about by the incident particle as well as those brought about by secondary electrons of low energy. Unrestricted energy loss belongs to phenomena by which the loss of energy is removed from the vicinity of the track in a time period comparable to the physico-chemical time scale (Table 4.1).

TABLE 4.1

APPROXIMATE TIME SCALE OF EVENTS IN RADIATION CHEMISTRY

$-\log t(\text{sec})$ $\equiv pt$	Events	Stage
18	Fast electron traverses molecule.	
17	MeV proton traverses molecule; time for energy loss to fast secondary electrons	
16	Time for energy loss to electronic states. (Vertical excitation)	
14	Fast ion-molecule reactions involving H-atom transfer. Molecular vibration. Fast dissociation.	
12	Electron thermalizes. Self-diffusion time scales for liquids of low molecular weight.	
11	Dielectric relaxes in water. Basic neutralization time for polar media.	
10)	Spur formed.	
9)	Spur reactions.	
8)	Intratrack reactions completed.	
7)	Neutralization times in media of low viscosity and dielectric constant.	
6)		
4)	Escape time for electrons in media of low viscosity and dielectric constant.	
3)		
0)	Radiative lifetime of triplets.	
-2)	Neutralization times for media of high viscosity and low dielectric constant.	
-4)		

Basically two kinds of unrestricted energy loss: Cerenkov light and energetic δ -rays.

(iii) Yield of Escaped Ions

It has been observed that insulating and low dielectric liquids exhibits a transient conductivity induced by radiation. Obviously, this conductivity is a manifestation of ions created by the radiation escaping geminate recombination under the influence of Brownian motion, often enhanced by an external field when the latter is present. A detailed track model has been found to be able to provide a quantitative estimate of the yield of escaped ions (90). It also gives correctly the trend of change with the change of temperature and of radiation quantity. As a consequence of this study a concept of "thermalization length" is gradually emerging and it is likely that in this and similar studies this concept will replace that of the range obtained by integrating the electronic stopping power only.

(iv) Inter- and Intratrack Effects

It is conceivable that most of the molecular yield is a result of intratrack reactions between radicals. Use of the term "radical" is extended to ionic intermediates such as the solvated electron. The radicals escaping from a track may react with a scavenger in a first-order process or may react with other radicals or even molecular products arising out of other tracks in the proximity in a second-order. Secondary reactions which can be attributed to intertrack effect are presumably homogeneous but should be expected to be dose-dependent because the average distance between neighbouring tracks is inversely proportional to the square root of the dose, if the latter is delivered in a time small compared to the lifetime of the track.

(v) Channelling

Channelling is observed at high and low incident proton energies and is not a characteristic of nuclear collision. In a certain sense, channelling is an extreme form of track effect in crystalline media.

(vi) Energy Flow as a Function of Time

Figure 4.2 demonstrates, schematically, the distribution of deposited energy among various degrees of freedom as a function of time. In the earliest time scale, consistent with the uncertainty principle, all the energy is in electronic form. In the characteristic

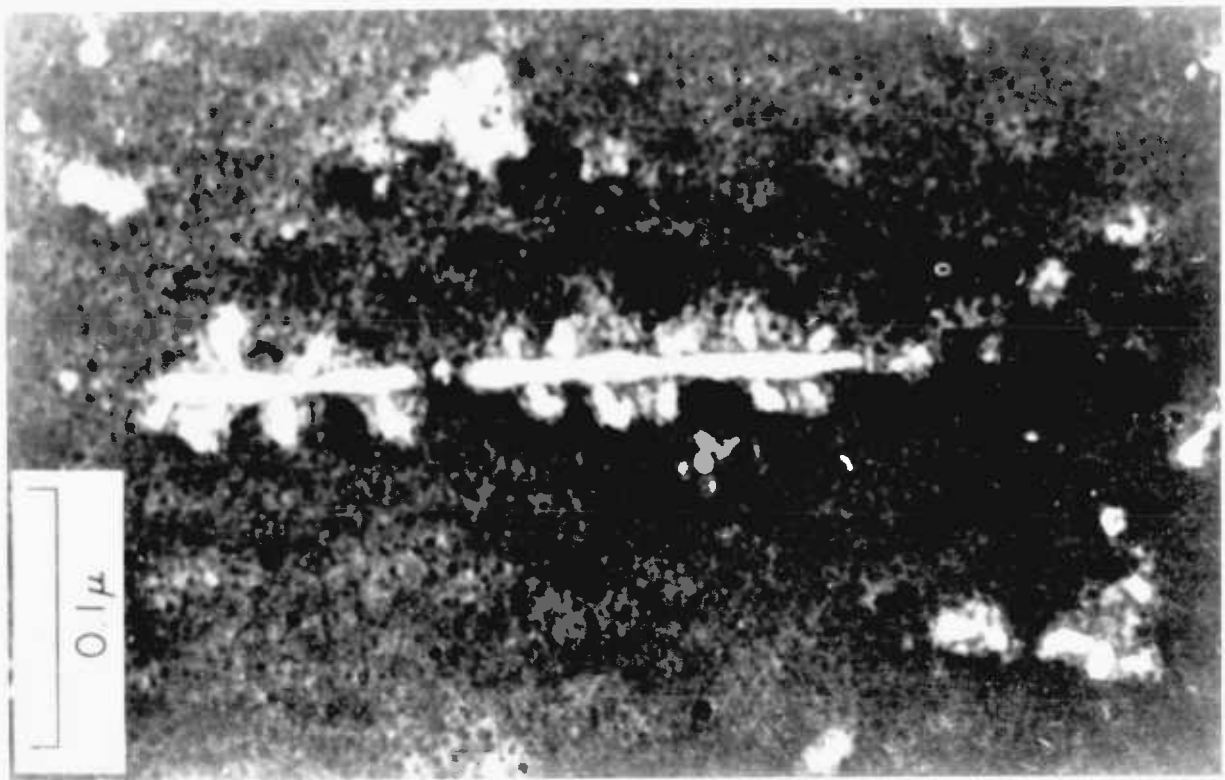


Figure 4.1 Electron micrograph of a fission fragment track in lead iodide, showing characteristic branching

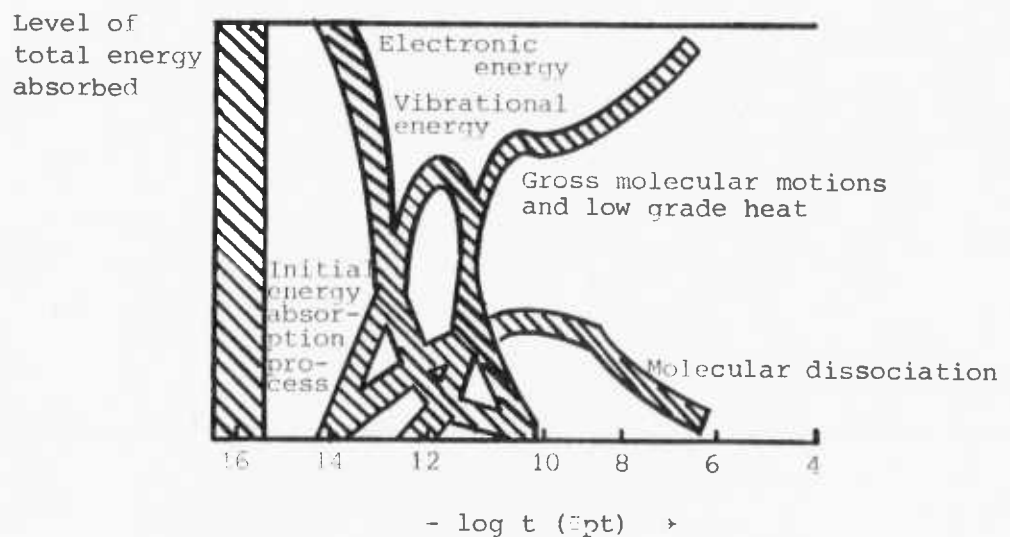


Figure 4.2 Schematic description of the partition of energy deposit as a function of time t , in sec. The vertical dimension of a given region is proportional to the fraction of the deposited energy which is in a particular form. This figure is intended to describe the situation for an average energy deposit. Note that, in exothermal reactions, the line showing low-grade heat can terminate above the level of total energy absorbed. This situation is the same even when luminescence occurs, because the amount of heat loss in such processes is rarely significant.

time of molecular vibration, most of the energy appears in that degree of freedom with a small part shared with low-grade heat and products of any ensuing molecular dissociation. After a local temperature is established, a large fraction of the energy has been transformed into heat. Ultimately, on a much longer time scale, all the energy appears in the form of heat. For low-LET radiation, significant increase of local temperature is not expected except in sensitive heat and explosive crystals.

The description given here is valid only in an approximative way and much detail remains to be filled in.

For the purpose of understanding chemical transformations and the operation of detectors, etc., it is imperative to consider that the energy must be localised in a molecule before its bonds are broken or it is ionized. Also, the localisation must occur in a reasonably short time or else preferential funnelling of energy into minor components may result.

4.2 General Conceptual Framework

It is difficult to theoretically analyse the many-body processes which lead to the degradation and distribution of the particle energy over more and more degrees of freedom, and also difficult to perform experiments to delineate the nature of these rapid processes. Here we shall content ourselves with sketching the probable main factors of importance in the formation of a latent track. The ideas which are described here are sufficiently general to apply to most types of solids in which tracks are registered, including covalent and ionic-bonded insulators and semi-conductors, small-grain thin metallic films as well as chain-like polymers such as plastics and glasses, although there are obvious differences in the nature of radiation damage in these different materials.

In a detailed analysis of the creation of latent tracks we shall also consider the traditional approach to the problem of the "thermal spike". Kinetic energy received by the electrons is passed to the lattice at a rate which depends upon the fundamental properties of the target medium, and then appears as heat. Thus the concept of a "spike" in the terminology of radiation damage physics is intimately associated with the release of energy. When delta particles are energized in a solid by a passing fission fragment, not all of the

energy which the fragment loses appears immediately in the kinetic form. Some is consumed in overcoming the binding energy of the electrons to their respective nuclei and is stored for a somewhat longer period as electrostatic potential energy or chemical energy. It is just as important for us to consider the fate of this energy and to assess its effectiveness in the creation of latent tracks. Is the energy diffused away, or is there a rapid and efficient conversion to the more damaging form of heat and decomposition? Experimental verifications are presented at the end of this chapter to confirm the chosen model of latent track formation.

Roughly speaking there are two important factors in track formation: (i) the amount of energy deposited by the passing charged particle which depends on the electron density and ionization energy of the material, and (ii) the susceptibility of the medium to "damage" due to this deposited energy. Materials which register tracks generally require a certain minimum LET (linear energy transfer) before a latent track can be revealed, although this minimum will depend to a large extent on the revelation technique employed, as discussed in Chapters One and Three.

The energy deposited on the passage of an energetic charged particle goes into the form of both electronic and atomic displacements. Electronic displacements are divided into excitation and ionization events while atomic displacements are divided into elastic and inelastic events. A small number of new nuclear species (including the incident particle) may also be present in a track, as is shown in Table 4.2, but this number is negligible for track formation (47). The electronic part of the energy loss can be further subdivided into hard and soft collisions. The energy transfer in a hard collision is large compared to the binding energy of the struck electron and gives a high-energy primary or δ -ray which forms a branching track off the main track. Soft collisions cover the remaining energy spectrum down to the minimum excitation energy of the molecules. Bethe obtained an expression for the electronic part of the stopping power (LET) by treating the hard collisions classically and the soft ones via the Born approximation (91).

$$\frac{dE_e}{dx} = \frac{4\pi Z^2 e^4}{mv^2} nB$$

Here Z_e is the effective charge of the charged particle passing through the material, v is its velocity, m and n the electron mass and number density respectively and $B = \ln(2mv^2/I)$ for a non-relativistic charged particle ($v \ll c$), where I is the average excitation potential of the atoms or molecules of the medium.

TABLE 4.2

MODES OF ENERGY DISSIPATION IN A HYDROCARBON MATERIAL

Incident Particle	Displaced Electrons	Displaced Atoms	New Nuclei
0.5 MeV neutron	1.4×10^4	100	1 deuteron
10 MeV deuteron	3×10^5	~ 1	$\sim 0.003 \text{ C}^{13}$ $\sim 0.003 \text{ N}^{14}$ 1 deuteron
5 MeV alpha	1.5×10^5	~ 1	1 helium
2 MeV electron	6×10^4	< 1	0

The energy loss to direct atomic displacements (via Rutherford or hard-sphere collisions) is not important for most charged particle tracks except in the case of heavy and slowly moving particles. Even in the case of fission fragments, electronic stopping power dominates the slowing down process in a medium like water down to about 10-20 MeV and then stopping via atomic displacements takes over. A fission fragment leaves about 5% of its energy in direct atomic displacements. For low LET particles such as protons and alphas, the contribution of direct atomic displacement to track formation is negligible over the entire track length (92).

4.3 Radiation Damage in Latent Tracks

One of the main difficulties faced by a theory of track formation in solids is the large number of possibilities for damage in a solid structure as described in Chapter Three. In crystalline solids this damage includes defects of various kinds, (vacancies, interstitials, defect loops, edge dislocations) as well as a long-range strain field around the track, (which facilitates its observation via the electron microscope). In polymers the possibilities include chemical changes (increased number of polymeric chain ends, new chemical species

including trapped gases and smaller molecules, unsaturated bonds, free radicals) as well as physical changes (lower physical density, lower degree of local crystallinity). The distribution of this damage away from the track axis is difficult to describe and adds greatly to the complexity of the situation. Before such a plethora of possibilities, one is forced to make a simplified picture of the latent track and of the processes which formed it.

It should be emphasised that the important structural differences between different types of solids must lead to different types of latent tracks and hence to greatly differing sensitivities towards track formation. Thus the nature of latent track formation appears to be quite different in inorganic crystalline solids and in polymers. In the former case strong bonds are usually formed in three spatial directions so that the breaking of a single bond is not enough to detach an atom from its site in the structure. In the latter case, strong bonds are formed only in one dimension, along the polymer chains. Strong bonds are ionic, covalent or metallic (strength in the eV range) while weak bonds are van der Waals, dipole or hydrogen bonds, which are a factor of ten or more weaker than strong bonds. This structural difference explains the much greater sensitivity of polymers for charged particle track registration: to create a displaced atom in an inorganic crystal requires about 25 eV of energy, whereas a polymer chain may be cleaved when about 2 eV is supplied to break the appropriate bond. In general, the irradiation of polymers produces either cross-linking or scission. Cellulose proper undergoes scission at a particularly high rate, at least 11 scissions occurring per 100 eV of absorbed dose (93) as pointed out in Chapter Two, while cellulose nitrate must degrade even faster, for reasons given below. The scission reaction breaks the molecule into smaller fragments, decreasing the molecular weight and increasing the solubility. The shortened chains and the larger number of chain ends lead to weakening and embrittlement, which facilitates penetration of the etchant. The end-groups and new chemical species lead to increased chemical reactivity along the track. Cellulose nitrate is expected to be the most sensitive of the cellulose derivatives towards degradation, as discussed in Chapter Two. The weak -NO_2 bond is broken by less than 2 eV of energy, and as in the case of other inorganic nitrates, radiation liberates nitrite ions and oxygen which cause extensive oxidative degradation of the cellulosic chains. Since cellulose

nitrate is the only cellulose derivative which undergoes extensive thermal degradation, its particular chemical nature makes the molecule unstable whenever external energy is localised within it; a large fraction of the deposited charged particle energy therefore causes chemical changes in the latent track.

4.4 The Initial Energy Deposition

The primary mechanism for energy deposition, i.e. electronic displacement, (both primary and secondary), takes place in $< 10^{-15}$ sec (47). The second time period, lasting anywhere from 10^{-12} to 10^{-9} sec, involves the transport and disposition of absorbed energy by molecular motion as thermal equilibrium is established. The majority of this energy ends up as heat which is dissipated over the entire solid, but a small part ends up as more or less permanently stored energy in the latent track (defects, new chemical species, etc.). The third time period lasts from a minimum of about 10^{-2} sec up to years in certain solids ("ageing of the latent track"). It involves the approach to a chemical equilibrium of the new species formed: excited molecules, free electrons, radicals, ions. Although excited states decay in about 10^{-8} sec, electrons may be held for long times in "traps" while radicals and ions are stabilised for long times, by the "cage effect". The presence of "impurity" species in the solids, especially oxygen in the case of polymers, leads to important effects on the latent track through reactions with the chemical species created by the radiation. Note that it is in the approach to chemical equilibrium that knowledge and understanding are least satisfactory.

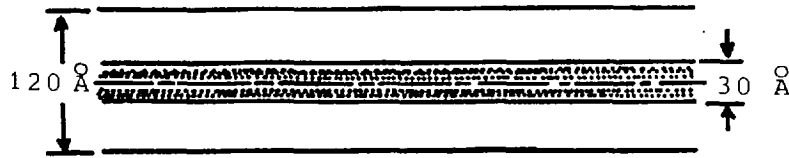
In principle, it should be possible to reveal a latent track (the most sensitive technique is probably electron microscopy) when the concentration of radiation-formed defects exceeds the background level of such defects already present in the solid. Thus a relatively defect-free inorganic crystal which has been well-annealed should be more sensitive towards track formation. In the case of plastics, chemical purity could be quite important; if radiation leads to degradation (scission), detector material containing only long-chain molecules initially should be more sensitive than material in which many short chains are already initially present.

The initial electronic excitation on the passage of a charged particle forms a cylindrical region of free electrons together with

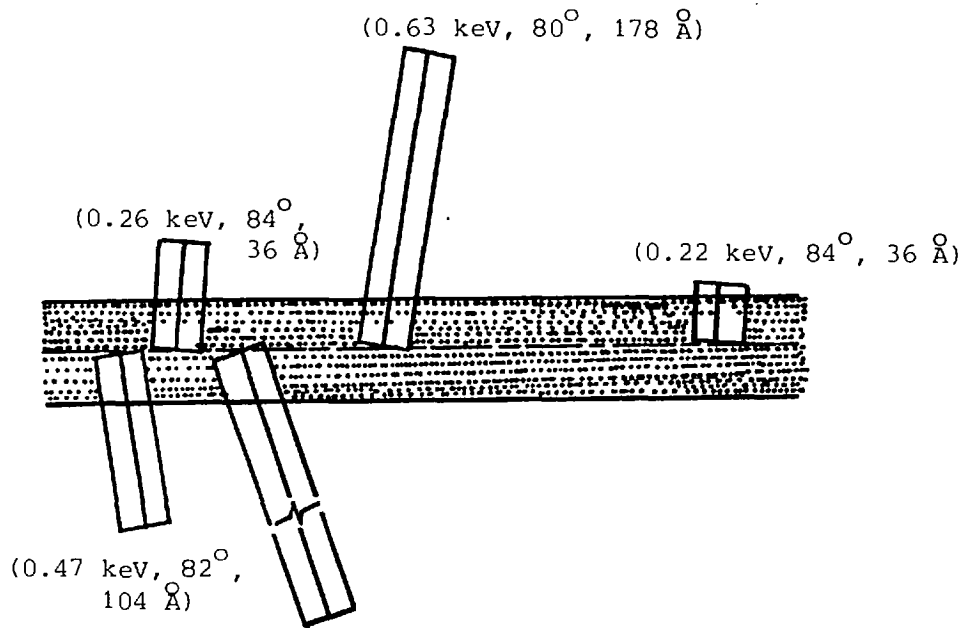
bound excited electrons and holes centred on the particle path. A typical fission fragment track (92) (representative of high LET radiation) in water is shown in Figure 4.3a and an O^{8+} ion in water is shown in Figure 4.3 b.

The majority of the primary ionization (and excitation) events occur within a few angstroms of the particle path; however, the energetic primaries then excite and ionize further secondary electrons, which may be energetic enough to continue this process to yet further stages. The "spurs" on the track overlap densely, creating a cylindrical core. A spur is formed when the primary or secondary electron loses all its energy in a small spatial region, leading to a small number of ionized or excited molecules and electrons weakly bound together. When the electron energy is less than several hundred eV a large spur is formed; this is sometimes called a "blob", the terminology coming from emulsion and cloud chamber physics (93). More precisely, a blob is generated by an electron which has insufficient energy to escape the attraction of its sibling hole (energy < 500 eV in water). Short tracks consist of overlapping spurs, formed by electrons between 500 eV and 5 keV, while branch tracks consist of isolated spurs, formed by electrons above 5 keV. High energy primaries (δ -rays) leave the track core and form their own branching tracks consisting of isolated spurs terminating in a blob. In the case of the fission fragment track, about half the energy is carried off by δ -rays some of which penetrate the core of Figure 4.3a and deposit most of their energy outside it. This energy is deposited as densely overlapping spurs in the sheath, where the ionization density is about two orders of magnitude lower than that in the core. Fission fragments display the highest LET at present obtainable, the initial stopping power in water being as high as 600 eV/\AA for the light fragment with the average being $\sim 250 \text{ eV/\AA}$ (92).

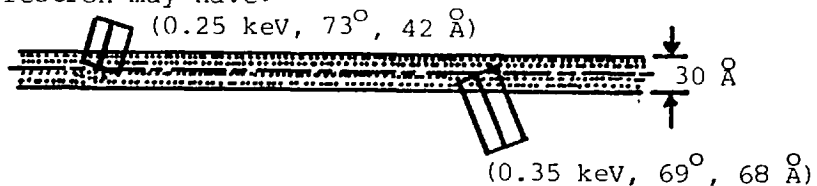
By way of contrast, a typical low LET track in water, that of a 1-2 MeV proton, is shown in Figure 4.3c. The branching tracks left by the δ -rays have roughly the same LET as the core itself; they are spaced by $\sim 300 \text{ \AA}$ on the track axis. Protons in water have a maximum LET of $\sim 10 \text{ eV/\AA}$ at ~ 100 keV, and a 1 MeV proton has an average LET of $\sim 5 \text{ eV/\AA}$ (in cellulose nitrate the corresponding figures are $\sim 12 \text{ eV/\AA}$ and $\sim 6 \text{ eV/\AA}$ respectively). The spur radius is somewhat smaller than the spur spacing in this case, so that the initial energy



- D Typical fission fragment track in water. Secondary electrons densely overlap to form the "sheath". Their LET is about two orders of magnitude smaller than that of the core



- b Schematic view of a track of an O^{8+} ion in water projected in a plane through the track axis. Secondary electron tracks are shown shaded in the diagram. Figures in parentheses denote respectively energy of ejected electron (ϵ), its direction of ejection (θ) with respect to the track axis and its range in water. The angle θ is given by $\cos^{-1}(\epsilon/\epsilon_{\max})^{1/2}$ where ϵ_{\max} is the maximum energy that the ejected electron may have.



- C Section of a typical track due to protons in water having energy 1-2 MeV/amu. The secondary electrons have roughly the same LET as in the core; they are spaced by $\sim 300 \text{ \AA}$ on the track axis.

Figure 4.3 (a,b,c)

deposition is on the borderline of being "continuous" i.e. overlapping spurs.

4.4.1 Energy Partition of Heavy Charged Particle between the Core of the Track and the Surroundings

It can be argued that energy loss in charge exchange is confined to the core of the track (94), however it is a small effect and in any case is taken into account numerically. Secondary electrons are the most important factor in the energy partition between the core and its surroundings. For convenience we divide the secondaries into two groups: (i) those that are stopped and (ii) those that are only partially stopped within the core. The electrons that are stopped are ejected almost normally to the track because their energies are small compared to 2 mv^2 . Knowing this and using the Rutherford cross section, we find that the energy deposited in the core by secondary electrons of group (i) over the entire track is given by

$$\epsilon_1 = \left(\frac{1}{2}\right) \int_{E_u}^{E_i} dE \log_e \{ \rho_1(R) / \epsilon_0 \} / \log_e (4E/\mu_1 \epsilon_0) \quad (4.1)$$

where E_i and E_u denote the energy per amu at start and at velocity u , respectively. Here ϵ_0 is the minimum energy of the secondary electrons (taken as 100 eV), μ_1 is the ratio of proton to electron mass and $\rho_1(R)$ is the energy of an electron with a range equal to the local core radius R . It is clear that for $E_i \leq E_u$, $\epsilon_1 = 0$.

Considering that appropriate ejection angle θ and using the Rutherford cross section again, we find that the energy deposited by partially stopped electrons in the core over the entire track is given by

$$\eta_1 = \frac{1}{2} \int_{E_f}^{E_i} dE \{ R / \log_e (4E/\mu_1 \epsilon_0) \} \int_{\rho(R)}^{4E/\mu} S(\epsilon) \text{cosec } \theta \, d\epsilon_1 / \epsilon_1^2 \quad (4.2)$$

where E_f is the final energy and $S(\epsilon_1)$ is the stopping power of an electron of energy ϵ_1 averaged over its path length within the core. The quantities ρ_1 and S are obtained from the low-energy electron range. There is a mild dependence of S and R which is neglected here; an average value is used. The procedure for obtaining this average is detailed elsewhere (94). Energy partition between the core and surroundings may now be obtained from Equations (4.1) and (4.2) and adding to them (i) half the total energy (equipartition principle)

and (ii) energy loss due to charge exchange. The numerical results so obtained are plotted in Figure 4.4, which shows a more or less universal curve. There is some slight difference between various particles at the same energy because of charge exchange.

At high energy there is a core expansion associated with Bohr's impulse principle (66). Therefore, more energy is deposited in the core. At low energies secondary electrons are also low in energy and cannot penetrate the core as effectively. Hence, the percentage energy deposited in the core is again large. We expect then that the core fraction of the deposited energy will show a minimum at an intermediate energy. Computation indeed reveals a minimum of $\sim 68.5\%$ at an incident energy of ~ 2.5 MeV/amu.

4.5 Damage Produced by Fission Fragment Irradiation of Heat-Sensitive Solids

In this section we describe the results of attempts to observe the damage produced by fission fragment irradiation of some heat-sensitive solids whose crystal lattices would not be expected to recover from such damage. The discussion considers whether the damage can be explained in terms of heat effects alone. Observations of this kind are of interest in connection with the concept of the minimum hot-spot size for the initiation of a thermal explosion (95), and with the problem of radiation-induced sensitivity to subsequent thermal decomposition (96).

It is necessary that the material, while being liable to thermal decomposition or evaporation, should withstand the beam of an electron microscope, and that thin crystals of about 300 \AA thickness should be used for direct transmission electron microscopy.

Fission fragment irradiations were carried out in both the thermal column of the Silwood Park experimental reactor for a period of 8 hours while it operated at ~ 100 Kw, as well as with a $1 \mu\text{Ci}$ californium-252 source for a period of 4 hours as explained in Chapter Five, Sections 5.3.5 and 5.3.6. The crystals were then examined on a Phillips E.M.301 microscope operated at 80 kV and at magnifications of up to 35,000. It is necessary to keep the electron beam below a certain level in order to prevent decomposition of the specimens, due to the heating effect of the electron beam. This means that sometimes the higher magnification ranges can only be used with difficulty.

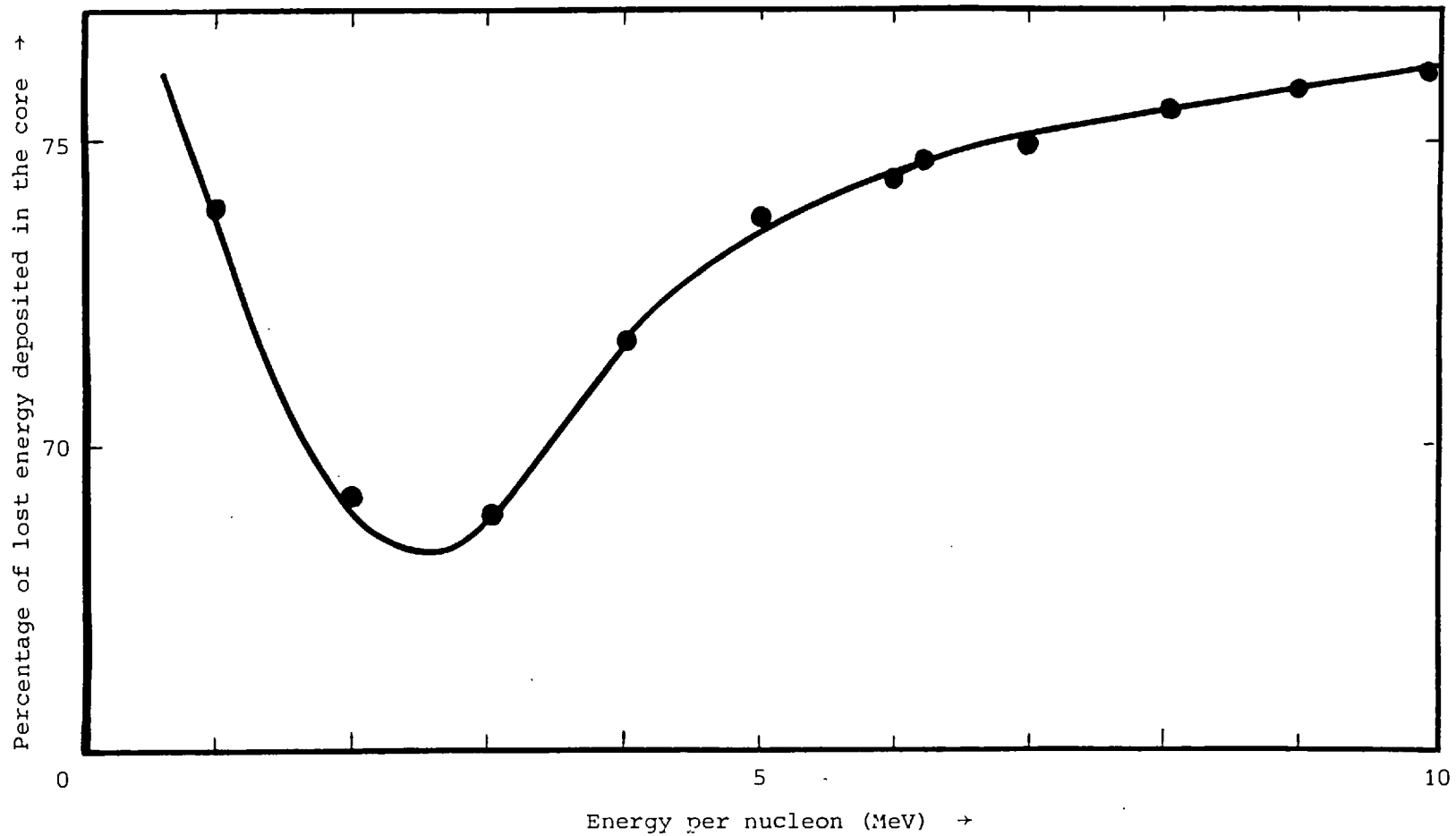


Figure 4.4 Partition of energy loss between the core and emergent secondary electrons plotted as a function of incident energy. At a given incident energy variation with respect to particle quality is small.

4.5.1 Observed Characteristics of Tracks

In some of the materials clearly defined tracks are visible on the electron microscope, and the number of tracks per unit flux of fission fragments does not appear to vary with the irradiated solid. The micrographs are consistent with the assumption that where tracks are seen, each track is produced by one fission fragment. Control specimens irradiated with neutrons and gamma-rays never showed tracks.

Continuous tracks of light contrast, representing paths of fission fragments travelling almost in the plane of the silver cyanamide crystal, and white dots representing fission fragments penetrating the silver cyanamide crystal vertically, or nearly so, are clearly observed. The mean track diameter is about 120 \AA . The visibility of the tracks decreases with increasing crystal thickness. With crystal thicknesses of up to 0.1 \mu m at least, there is no variation in track width as a function of distance from the crystal surface, or track dip-angle.

Fission fragment irradiated crystals of silver cyanamide contained specks of silver at large distances from the tracks. Most of this silver came from the decomposition of the crystal due to fission fragment damage. Control irradiation requires a dose of neutrons and γ -rays one hundred times as large as that deposited by fission fragments to give a comparable amount of silver (97).

Irradiated silver thiocyanate crystals showed continuous dark tracks. No clearly defined crystal thickness effects were found, though on some micrographs of very thin crystals the tracks tend to be of light contrast type.

Irradiated thin crystals of mercuric thiocyanate showed continuous tracks of light contrast. There was no variation in track length with crystal thickness, suggesting that continuous track registration does not occur below a certain depth from the crystal surface (the tracks obey the energy registration criterion involving $(\frac{dE}{dx})_{\text{crit}}$). The proportion of dots to continuous tracks, except those tracks making a small dip-angle which gave rise to slightly elongated dots, corresponding to points of entry or exit, was considerably higher than for silver cyanamide.

The width of all tracks, whether continuous or of dot form averages about 75 \AA , and the spacing between the dashes of a

discontinuous track appears to average 200 \AA - 300 \AA (see Figure 4.5 and Figure 3.2). A typical track of small dip-angle was observed to be continuous for a few hundred \AA from the point of entry or exit, and then either ceased to register or became discontinuous.

Continuous tracks of light contrast are visible in irradiated thallium picrate crystals. The track width decreased considerably with increasing crystal thickness.

No damage was visible on micrographs of irradiated potassium picrate or ammonium iodate crystals. The Bragg contours appeared to be irregular and broken into specks in some areas, in both un-irradiated and irradiated crystals. This was an effect of the electron beam (98).

In lead iodide crystals (Figure 4.6) fission fragment damage takes the form of distinct tracks whose contrast is dependent on the thickness of the crystals. At 100 \AA thickness or less the tracks are of light contrast due to the removal of material along the path of the fragment. At about 20μ thickness many unusual tracks are observed as seen in Figure 4.1. These track branchings are very similar to those reported by other workers (99) in cloud chamber photographs of fission fragment tracks are visible.

The lead that is released by the decomposition of the crystal in the trajectory of the incident fission fragment often crystallizes along the track and is oriented with respect to the matrix. Figure 4.7 shows an area of track containing recrystallized lead (shown by the arrow).

The average diameter of the normally incident fission fragment tracks are about 150 \AA and depend on the energy, charge and mass of the incident particle.

In sensitive explosive crystals (such as cadmium azide and nitrogen iodine) the growth of a thermal explosion from an incident charged particle is governed by simple physical considerations. If the rate of evolution of heat by chemical reaction within the small volume is greater than the rate at which it is lost to the surroundings by conduction and other means, it will grow. If not, it will die away. These experiments show that in general the activation of a small group of adjacent molecules is not enough to cause explosion. The diameter of the hot spot must be very much greater than this before

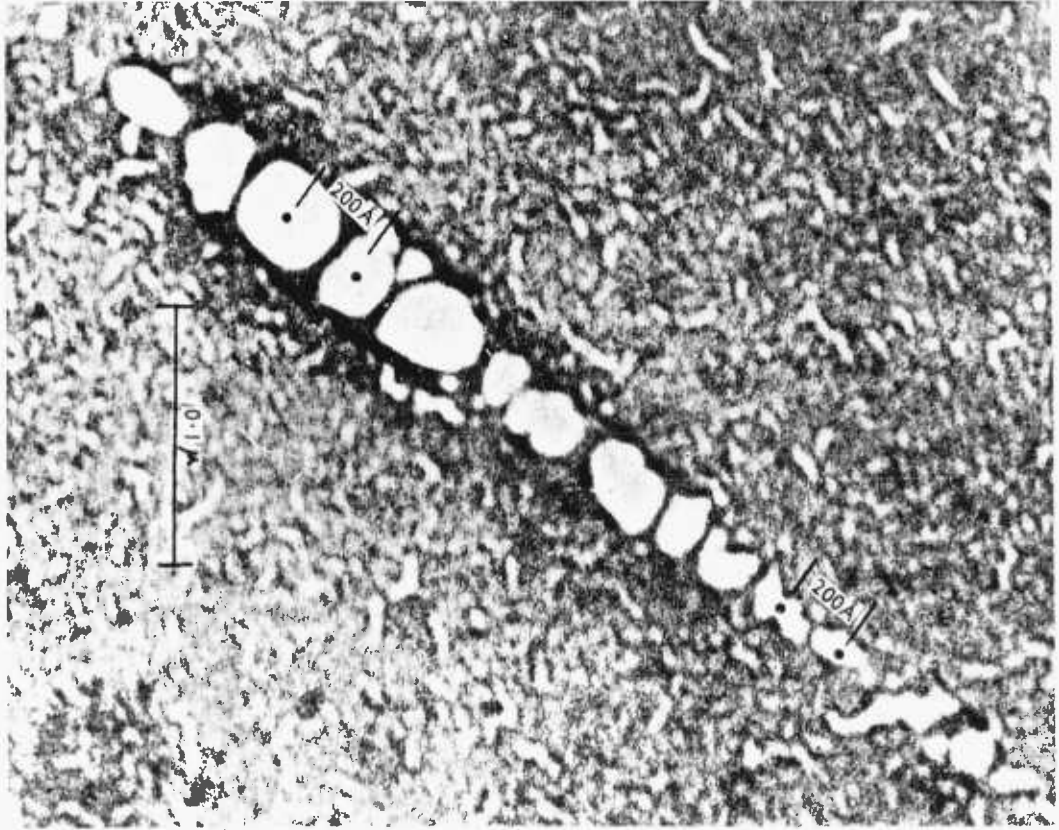


Figure 4.5 Electron micrograph of a discontinuous fission fragment track formed due to thermal decomposition and evaporation of the crystals along the path of the particle, followed by recrystallization

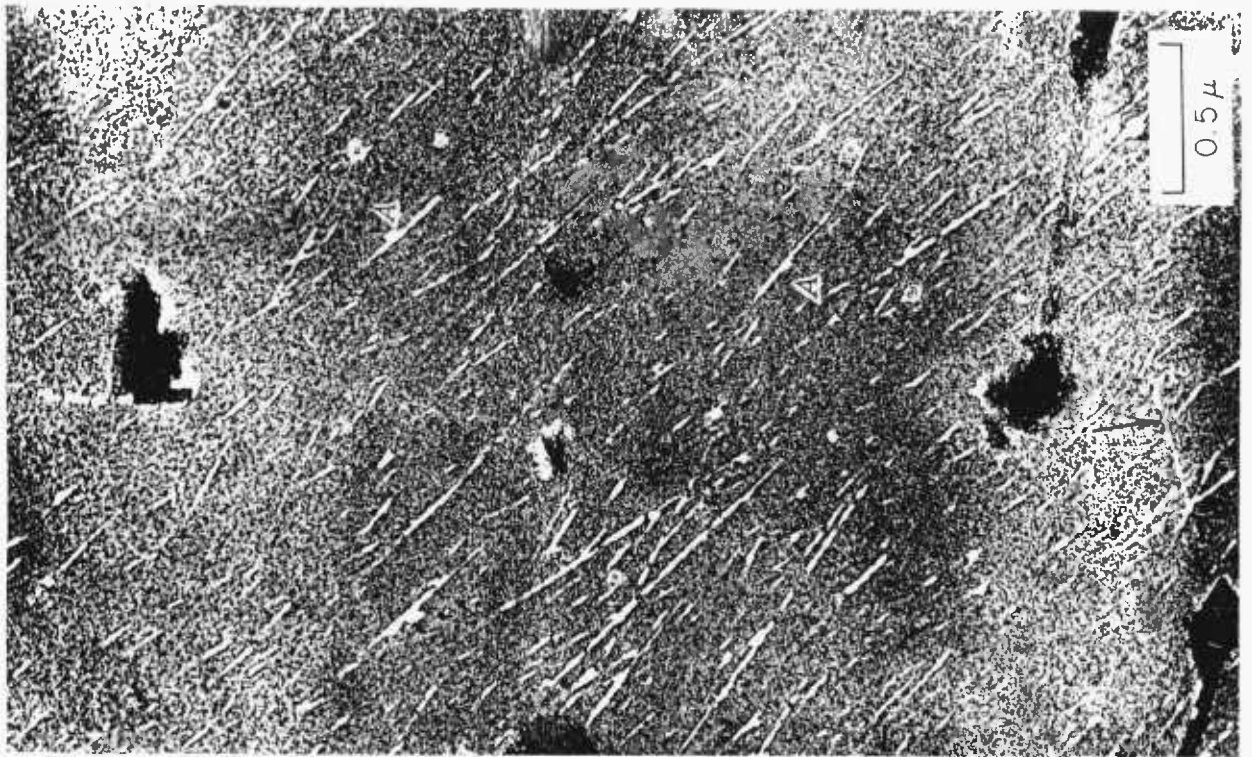


Figure 4.6 Electron micrograph of a thin crystal of lead iodide showing tracks which have 'spikes' at points where the width increases by a factor of two or more. Note that the arrowed track is thinner than those produced by the fission fragments, and is outside the angle of collimation.



Figure 4.7 A fission fragment track in lead iodide showing the recrystallization of the lead, which was released by the decomposition of the crystals along the path of the particle, as indicated by the arrow

it can lead to an explosion which spreads throughout the crystal. The limiting size of the "hot spot" depends upon "its temperature and duration". It is large on a molecular scale varying from 10^{-3} to 10^{-5} cm in diameter.

4.5.2 The Effect of Heat

The great variation, from one substance to another, in the type and amount of damage produced by fission fragment irradiation such as continuous and discontinuous tracks, dark or light contrast tracks and track diameter variation for different crystals, shall be accounted for. The volume of any missing material can be estimated with some precision from the dimensions of the light contrast tracks, which represent the amount of material evaporated and responsible for the light contrast effect. The dark tracks in silver thiocyanate showed regions of strained or disordered crystal (whether decomposed or not) which gave rise to diffraction contrast. With this type of track, the amount of material responsible for the diffraction effect cannot be reliably estimated.

In the case of energy loss in thin films one has true delocalized energy-loss events connected with the collective motion of electrons. These are produced by longitudinal excitations. The fate of the lost energy is not completely known; however, a significant process is radiation (Ferrel radiation). No chemical transformation of a medium is known to occur as a result of these "plasma" losses. It is, however, known that as long as the sample is thin ($\leq 500 \text{ \AA}$), the plasma losses dominate with no particular reference to atomic or molecular loss processes in the gas phase or in bulk solid form. As the thickness of the film is gradually increased, atomic excitation characteristics appear which explains the unusual tracks observed in Figure 4.2. Plasma losses in thin films are common to metals and non-metals, both crystals and amorphous.

In this section we consider the effect of the electronic energy loss for an average fission fragment of energy 80 MeV, as being about 10^3 eV/\AA for a target of low or medium atomic number. If the whole of this energy is to be effective in producing decomposition, then each incident fission fragment will produce a cylinder of linear damage at least 200 \AA wide penetrating the target crystal, which is much larger than the visible damaged area.

Calculation of the amount of damage produced in the target crystals is simplified by taking the electronic energy given to the target crystal by the incident fission fragment to appear as quantity of heat Q per \AA of track of radius (r_0). This calculation relies heavily on the law of thermal conductivity and the following approximations.

- (1) A molecule is assumed to be decomposed or sublimed if it is thermally activated at any time to an energy E .
- (2) Within a certain distance (r_1) from the track, if a molecule is excited just once to the activation energy, then r_1 is given by

$$1 = v_0 \int_{\text{all } t} \exp \left[- \frac{E}{kT(r_1, t)} \right] dt \quad (4.3)$$

provided that this gives $r_1 \geq r_0$; otherwise $r_1 = 0$. Where v_0 is the lattice vibration frequency of the target and $T(r, t)$ is the temperature at a distance r from the track at time t . At greater distances, the decomposition being taken as a zero order reaction, so that beyond $r = r_1$ the number of damaged molecules is proportional to r_2^2 where

$$r_2^2 = v_0 \int_{r_1}^{\infty} \int_{\text{all } t} 2\pi r \exp \left[- \frac{E}{kT(r, t)} \right] dr dt \quad (4.4)$$

- (3) The undamaged molecules will recrystallize, leaving a cylinder of damage equal in volume to the sum of the original volumes of all the damaged molecules. Its radius is thus given by R where:

$$R^2 = r_1^2 + r_2^2 \quad (4.5)$$

this assumption of a sharply defined cylinder of damage is consistent with the observed appearance of a fission fragment track, whose radius then corresponds to R .

- (4) The effect of any heat liberated by exothermic decomposition, in both parts, is neglected in comparison with Q . This approximation is expected to be fair for situations where the amount of decomposition is small.

A good approximation to this initially infinitesimally narrow thermal spike derived from the exact evaluation for the simple case $r_0 = 0$ shown in Equation (3.29) is:

$$\begin{aligned} T &= Q/8 \sqrt{\pi \lambda t} & \text{for } r < \sqrt{(Dt)} \\ T &= 0 & \text{for } r > \sqrt{(4Dt)} \quad \text{where } \lambda = C\rho D \end{aligned} \quad (4.6)$$

We then have from Equations (4.3) and (4.6):

$$r_1 = v_o \int_{t = r_1^2/4D}^{\infty} \exp \left(- \frac{E}{Q} \frac{8\sqrt{\pi\lambda t}}{k} \right) dt \quad (4.7)$$

giving

$$r_1^2 = \frac{k}{2\sqrt{\pi} c\rho} \frac{Q}{E} \log_e \left(\frac{v_o k}{8 \sqrt{\pi\lambda}} \frac{Q}{E} \right) \quad (4.8)$$

and from Equations (4.4) and (4.6)

$$r_2^2 = v_o \int_{t = r_1^2/4D}^{\infty} (4 Dt - r_1^2) \exp \left(- \frac{E}{Q} \frac{8 \sqrt{\pi\lambda t}}{k} \right) dt \quad (4.9)$$

which from (4.8) gives:

$$r_2^2 = \frac{k}{2 \sqrt{\pi c\rho}} \frac{Q}{E} \quad (4.10)$$

so that from (4.3):

$$R^2 = \frac{k}{2 \sqrt{\pi c\rho}} \frac{Q}{E} \left[\log_e \left(\frac{v_o k}{8 \sqrt{\pi\lambda}} \frac{Q}{E} \right) + 1 \right] \quad (4.11)$$

With the given temperature distribution equations (4.6) and (3.30), all the molecules within $r = r_o$ have the same thermal history, so that the only alternative to $r_1 \geq r_o$ is

$$R^2 = r_2^2 = v_o \int_{z = r_o^2/4D}^{\infty} 4Dt \exp \left(- \frac{E}{Q} \frac{8 \sqrt{\pi\lambda t}}{k} \right) dt \quad (4.12)$$

giving:

$$R^2 = \frac{v_o k}{8\sqrt{\pi\lambda}} \frac{Q}{E} \left(r_o^2 + \frac{k}{2\sqrt{\pi} c\rho} \frac{Q}{E} \exp \left(\frac{- r_o^2}{(k/2\sqrt{\pi} c\rho) (Q/E)} \right) \right) \quad (4.13)$$

4.5.3 Comparison of Observed and Calculated Track Width

Either Equation (4.11) or (4.13) can successfully give a value of R for silver cyanamide equal to the observed track diameter of 60 Å.

The following are the values of the thermal parameters should be used:

$$\begin{aligned}
 c &= 10^{-1} \text{ cal/gm.} \\
 \rho &= 5 \text{ gm/cm}^3 \\
 v_o &= 10^{13.5} (100), \\
 E &= 2 \text{ eV (97)}, \\
 Q &= 10^{11} \text{ eV/cm.}
 \end{aligned}$$

and Table 4.3 lists pairs of values of λ and r_o which give the correct value of R.

TABLE 4.3

λ cal/deg°C sec cm	Condition	r_o^2 (cm ²)
10^{-2}	$r_1 \geq r_o$	3×10^{-13}
	$r_1 = 0$	4×10^{-13}
10^{-3}	$r_1 = 0$	5×10^{-13}
10^{-4}	$r_1 = 0$	10^{-12}

Let us now compare the observed track radius in two materials of high and low sensitivity to irradiation. Silver cyanamide shows tracks of diameter 120 \AA , while no tracks are detectable in irradiated potassium picrate. On the basis of our model, since the observed diameter of silver cyanamide is 120 \AA , we may say that R_a^2 (of silver cyanamide) / R_b^2 (of potassium picrate) > 100 . Equation (4.11) will not fit the potassium picrate data unless c, E, Q, ρ, v_o , or λ differ from the values listed for silver cyanamide by a very large factor. It is evident that the difference between R_a and R_b is likely to arise from differing values of the exponential term of Equation (4.13). It is also evident that a difference in r_o alone is sufficient to account for the large R_a^2/R_b^2 . However the above arguments are enough to show that the amount of damage produced by a fission fragment depends very critically on the volume within which its energy appears as heat in the crystal (i.e. the radius r_o), and the absence of tracks in irradiated crystals suggests that in these materials r_o is large and the heat released by the fragment is not concentrated enough to produce visible decomposition.

In silver thiocyanate, r_o is not small enough to give the wide cylinder of decomposition seen in silver cyanamide, but is unlikely

to be greater than 100 \AA , since tracks are visible. For very thin crystals the change to light contrast may arise from the higher heat concentration: if the crystal thickness is less than r_0 , higher temperatures are expected, and material may sublime.

The discontinuity of tracks appears in irradiated crystals which sublime at temperatures of a few hundred degrees and it is proposed that r_0 can vary in diameter with the distance below the crystal surface, and can be discontinuous. Near the free surface, most of the molecules reaching the energy E will vaporize and escape. At somewhat greater depths, the pressure is higher and only a proportion of the activated molecules will escape. The remainder will cool and recrystallize before being able to do so, and the dashed appearance of the tracks shows that the material recrystallizes non-uniformly, and generally forms a single crystal with the surrounding material. At still greater depths, no material can escape since recrystallization is complete and the particle does not register.

It is necessary to invoke other mechanisms with the thermal spike mechanism of fission damage since the thermal spike mechanism by itself cannot account for the great difference between the observed damaged area or volume of tracks and the calculated damaged area of tracks due to "point heat" or local heating in the target medium.

4.6 Energy Degradation around Tracks

In considering how this electronic energy is transferred to the "lattice" (conceived in the general sense) to produce atomic motion and displacements, account must first be taken of a fundamental difference between electrical insulators on the one hand and conductors and semi-conductors on the other hand. In the case of insulators, the mobility of the final low-energy excited electrons at the end of the first stage of energy deposition is negligible, and excitation energy generally stays localized within the molecule where it was deposited just after the passage of a charged particle. One may neglect the transmission of energy by excitons or photons (luminescence) as being too slow or involving a negligible fraction of the energy (47). As a result this electronic energy is transformed into lattice energy without first undergoing any significant further spreading. On the contrary, in metals the very large mobility of conduction electrons

spreads out electronic energy rapidly before it can be transmitted to the lattice, while in semi-conductors the smaller electron and hole mobilities play a similar role on a reduced scale. This type of rapid diffusion of the energy away from the track axis reduces the possibility of radiation damage in good conductors.

The rate of transmission of electronic to lattice energy (i.e. energy of atomic motion, or vibrational energy), depends on the strength of the electron-phonon interaction, which is greatest in insulators, intermediate in semi-conductors, and least in metals (88). In metals this interaction also determines the high-temperature or non-impurity part of the resistivity - the greater the interaction the greater the resistivity - thus suggesting a connection between resistivity and ease of track formation. This appears to be the case in thin metallic films as discussed later. In semi-conductors the corresponding interaction determines the electron and hole mobilities.

Once the energy has been transferred to the lattice it starts to spread out by the processes of lattice thermal conductivity. If the initial lattice energy density is high, and the thermal conductivity low, this energy will remain localized for a relatively long time. In thermally unstable materials such as cellulose nitrate, this localized lattice energy can lead to a large amount of damage. In chain structures like polymers, the vibrational energy is much more rapidly transmitted in the direction of strong bonding along the chains than in the other directions of weak bonding. Thus in cellulose nitrate, the lattice energy tends to remain localized within a given chain, spreading more slowly to neighbouring chains via the weak hydrogen bonds and van der Waals forces. This means the lattice energy density remains higher than in a three-dimensionally bonded solid during the time it takes for the same distance of thermal spreading, i.e. a given lattice energy spread over twice the linear dimension halves the energy density in the one-dimensional case, while giving rise to one eighth the energy density in the three-dimensional case. Since the number of defects formed is roughly proportional to $\int_0^{\infty} \exp(-E_A/k_B T(t)) dt$ where E_A is the appropriate activation energy and $T(t)$ is the absolute temperature at time t after the passage of the charged particle, evidently one-dimensional spreading leads to a much greater number of defects.

One might expect to observe another consequence of the chain structure of polymers in track formation. When a charged particle passes parallel to the chains which are lined up locally (local crystallinity), a great number of electrons are excited or ionized within each chain along the particle path. The lattice energy will remain localized in these chains for a long time due to the reasons given above, leading to a great deal of damage within them. As a result, track registration should be easier (greater sensitivity) in this geometry than if the track were perpendicular to the chains. Such an effect may have already been observed in studying the track registration of 6 MeV alphas in cellulose nitrate (101). When the alphas entered at 90° to the surface, no particle tracks were revealed by etching, whereas at small dip-angles, they were revealed. During the manufacture of cellulose nitrate films the sheets are stretched in the plane of the surface (102). Thus tending to line up the chains in this plane. As a result, a particle entering the film at a small dip-angle has a better chance of passing parallel to chains along its path than a particle entering at 90° .

It may be useful to describe some of the preceding phenomena in a semi-quantitative form. In the case of high LET particles (e.g. fission fragments) the great number of excited and free electrons allows for a statistical treatment. When the primary electrons are energized by the passage of a charged particle, they begin a tortuous path through the medium undergoing multiple scattering collisions. In a simple model to describe this situation (88), one assumes a Maxwellian gas of electrons at a local temperature $T_1(x,t)$, homogeneously mixed with a second Maxwellian gas of heavy atoms of temperature $T_2(x,t)$. The rate of energy exchange within each system is assumed to be much greater than the exchange between them. The local energy density of the electrons ($C_1 \rho T_1$ where C_1 is the specific heat and ρ the material mass density) changes due to the heat flux $-K_1 \nabla T_1$ (where K_1 is the electronic thermal conductivity) and due to the energy loss to the lattice $b(T_1 - T_2)$, taken to be proportional to the temperature difference. The model is described by the equations

$$C_1 \rho \frac{\partial}{\partial t} T_1 = K_1 \nabla^2 T_1 - b(T_1 - T_2) \quad (4.14)$$

$$C_2 \rho \frac{\partial}{\partial t} T_2 = K_2 \nabla^2 T_2 + b(T_1 - T_2) \quad (4.15)$$

with the initial condition at $t = 0$ being $T_1 = T_0 + A\delta(r)$ and $T_2 = T_0$ where T_0 is the ambient temperature, $\delta(r)$ is the Dirac delta function in the two dimensions perpendicular to the track and $A = Q_1/C_1\rho$ is proportional to the electronic LET Q_1 of the charged particle. Actually a better initial condition would be to spread the electronic energy over the track core as indicated in Figure 4.3a, using for example a Gaussian function. For the present treatment this is not too important since only a dimensional analysis of the equations is presented here, because even these simple appearing equations do not have a solution simple enough for straightforward analysis.

If the exchange of energy between electrons and lattice were neglected, the electron temperature would obey a diffusion equation with diffusion constant $D_1 = K_1/C_1\rho$ i.e. the solution would be a Gaussian of width $2(D_1t)^{1/2}$ and height $(D_1t)^{-1}$. The electron-lattice coupling introduces the time-scale $\tau = c\rho/b = \mu^{-1}$ (now assume $C_1 = C_2$ for simplicity) for the transfer of energy from the electron to the lattice. Now let the latent track diameter be Δ (lying between 20 Å and 100 Å). In the case of "strong-coupling" $2(D_1\tau)^{1/2} \ll \Delta$, so that the spread of electronic energy by diffusion over the latent track region is negligible during the time τ for significant energy transfer to the lattice. Note that in insulators the electronic energy in the form of excitation (which is about equal to the energy in the form of ionization) does not spread significantly, so it belongs to this strong-coupling limit. There are two sub-cases of the strong-coupling case; if $2(D_2\tau)^{1/2} \ll \Delta$ then most of the electronic energy appears as lattice energy before it diffuses over the latent track region; if $2(D_2\tau)^{1/2} \gg \Delta$, the lattice energy spreads rapidly thus minimizing the lattice temperature rise and its duration. Evidently, track formation is favoured by a large value of the dimensionless parameter $\lambda_2 = \Delta(D_2\tau)^{-1/2} = \Delta(\mu/D_2)^{1/2}$. This is the case when electron-phonon coupling is strong compared to both electron-electron and phonon-phonon coupling.

In the case of "weak-coupling" $2(D_1\tau)^{1/2} \gg \Delta$, so that the electronic energy spreads over the latent track region rapidly, before significant energy transfer can occur to the lattice. Track formation is unlikely in this case. Thus in semi-conductors where the electron-phonon interaction is weak (high mobility) and where hot electrons diffuse rapidly, tracks are unlikely to be found.

The qualitative analysis presented here can be checked against the one case where a simple solution exists, namely when $D_1 = D_2$. In this case (letting $T_0 = 0$) $T_2 = Q_1/2C(4\pi D_2 t)^{1/2}\{\exp(-r^2/4D_2 t)\}\{1 - \exp(-2\mu t)\}$. The spreading of T_2 over the latent track region occurs over a time $\sim \Delta^2/4D_2$ during which the maximum temperature (at $r = 0$) becomes $(Q_1/2\pi d^2 C)\{1 - \exp(-2\mu\Delta^2/4D_2)\}$. Track formation is favoured by a large value of $\mu\Delta^2/D_2 = \lambda_2^2$, however, once $\lambda_2 > 2$ its size does not much matter in the exponent. Once this condition is fulfilled it is much more important that D_2 be as small as possible.

We may summarize the previous considerations on the ease of track formation. Track formation is favoured if (i) $\lambda_1 = \Delta(\mu/D_1)^{1/2}$ is greater than 1 ("strong-coupling") (ii) $\lambda_2 = \Delta(\mu/D_2)^{1/2}$ is much greater than 1. Once these conditions are met, it is the actual sensitivity of the material to the concentrated energy deposited in the lattice which determines the amount of damage in the latent track.

The above model omits an effect which should be important in those insulators where λ_1 is less than 1. There one has to contend with the fact that the primary ionization leaves behind ions at the center of the track whose lifetime is many orders of magnitude longer than that of an ion in a metal (103). Consequently, the electrons move in the attractive field of these ions, while at the same time the ions are pushed apart by their Coulomb repulsion. Merkle (104) has discussed a simplified model of this process in which the ions are treated as a column of positive charge in whose field the electrons move back and forth radially. Since the electrons are trapped in the ionic field, they do not spread much by diffusion and so the magnitude of D_1 is relatively unimportant. In this case only the parameter λ_2 is important for track formation.

Similar considerations are also of importance in the formation of tracks in thin metallic films where it is possible for hot electrons to play a role in track production via a mechanism that prevents rapid diffusion away of the electronic energy. These metallic films are composed of isolated crystallites in poor electrical contact with one another; their boundaries can reflect energetic electrons and prevent their escape into neighbouring crystallites. However, hot electrons are emitted from the surface of a crystallite by thermionic emission (which is the analogue of evaporation from a liquid drop). Since the hot electrons within a crystallite come into equilibrium

rapidly in about 10^{-15} sec., the electron-phonon interaction is spatially uniform within it. The crystallites become charged during the process of thermionic emission, which then cuts itself off rapidly due to the development of a potential barrier at the surface (which is maintained as long as the crystallites are electrically insulated). For a gold sphere (crystallite) of 100 \AA , Goland and Paskin (105) calculate that after the passage of a fission fragment the initial thermionic energy loss is $\sim 10^{18}$ eV/sec, while after the evaporation of 450 electrons (which carry away a very small fraction of the energy deposited) it is reduced to $\sim 2 \times 10^{16}$ eV/sec; the energy transfer rate from electrons to phonons is $\sim 4 \times 10^{17}$ eV/sec which is considerably higher than the final value of the surface energy loss rate. The electronic energy then causes the actual evaporation of spheres up to $\sim 170 \text{ \AA}$ in diameter in gold.

In a thin film the evaporated material can escape from the surface leaving behind a vacant region of low density. Note also that thermal energy loss via lattice conduction is very small since the crystallites are in poor thermal contact. The evaporation of the metallic crystallite is favoured by a strong electron-phonon interaction (high electrical resistivity).

Similar considerations probably play a role in the case of low-conductivity semi-conductors where hole-mobility is small. High-energy thermal secondary electrons from the tail of the Maxwellian "evaporate" from the track core leaving behind them a region of positive charge along the track; the resulting electric field restricts the outward diffusion of most of the hot electrons and thus reduces the effect of the diffusivity term. The extent of such an effect is difficult to estimate in a quantitative manner, however, it is clear that the field of the column of positive charge will be neutralized by the background conductivity in a time of $\sim \epsilon/\sigma$, where ϵ and σ are the electrical permittivity and conductivity respectively (in SI units). For the efficiency of the mechanism this characteristic time should therefore be long compared to the electron-phonon energy exchange time (i.e. $\epsilon\mu/\sigma > 1$). Note that low conductivity (σ) is correlated with strong electron-phonon interaction (μ). It is important to remark that such considerations do not affect the role and importance of the lattice energy diffusivity parameter D_2 in homogeneous material.

4.6.1 Resistivity Dependence of Track Registration

To establish a resistivity dependence of track registration, six crystals with similar layer structures (see Table 4.4) (each crystal contains basal planes of strong bonding and high density, separated by relatively large interplanar channels where bonding is mainly due to weak van der Waals forces) were irradiated with fission fragments under the same environmental conditions. Six more C-UO₂-Pb thin films of varying resistivity (by varying the concentration of Pb) were also irradiated with fission fragments under the same environmental conditions.

Tracks were only observed in specimens of resistivity $\geq 1\text{m } \Omega\text{-cm}$. Clarity of tracks increased with increasing resistivity (see Figures 4.8 and 4.9) which confirms the dependence of track formation on the electric conductivity of the crystals and the films. All those tracks registered, whether continuous or intermittent, show the same character which reflects the characteristic of layer structures. It is also observed that the average number of intermittent segments comprising each track is directly proportional to the specimen thickness.

TABLE 4.4

Compound	Structure	Distance between Layers(Å)	Electrical Resistivity (25°C) (mΩ-cm)	Damage
MoS ₂	MoS ₂	6.13	$\sim 10^5$	Clearly defined tracks
MoSe ₂	MoS ₂	6.45	3×10^3	Tracks
WSe ₂	MoS ₂ (modified)	6.47	5×10^2	Tracks
WTe ₂	MoS ₂	6.27	2.8	Tracks
TaSe ₂	MoS ₂	6.37	4×10^{-1}	Ill-defined surface tracks
NbTe ₂	related to CdCl ₂	6.26	2.8×10^{-1}	No tracks

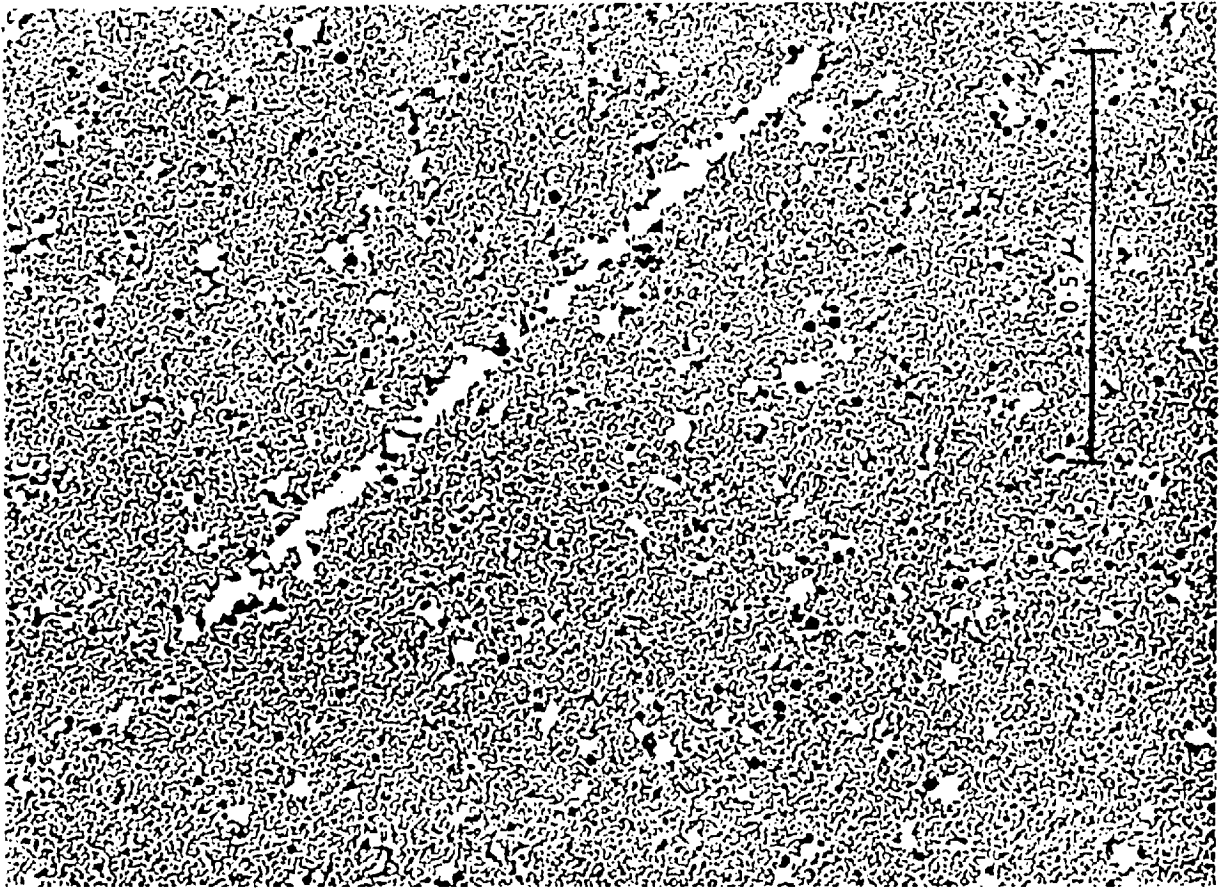


Figure 4.8 Fission fragment tracks in C-UO₂-Pb film of electrical resistivity $\sim 10^3 \mu\Omega\text{-cm}$

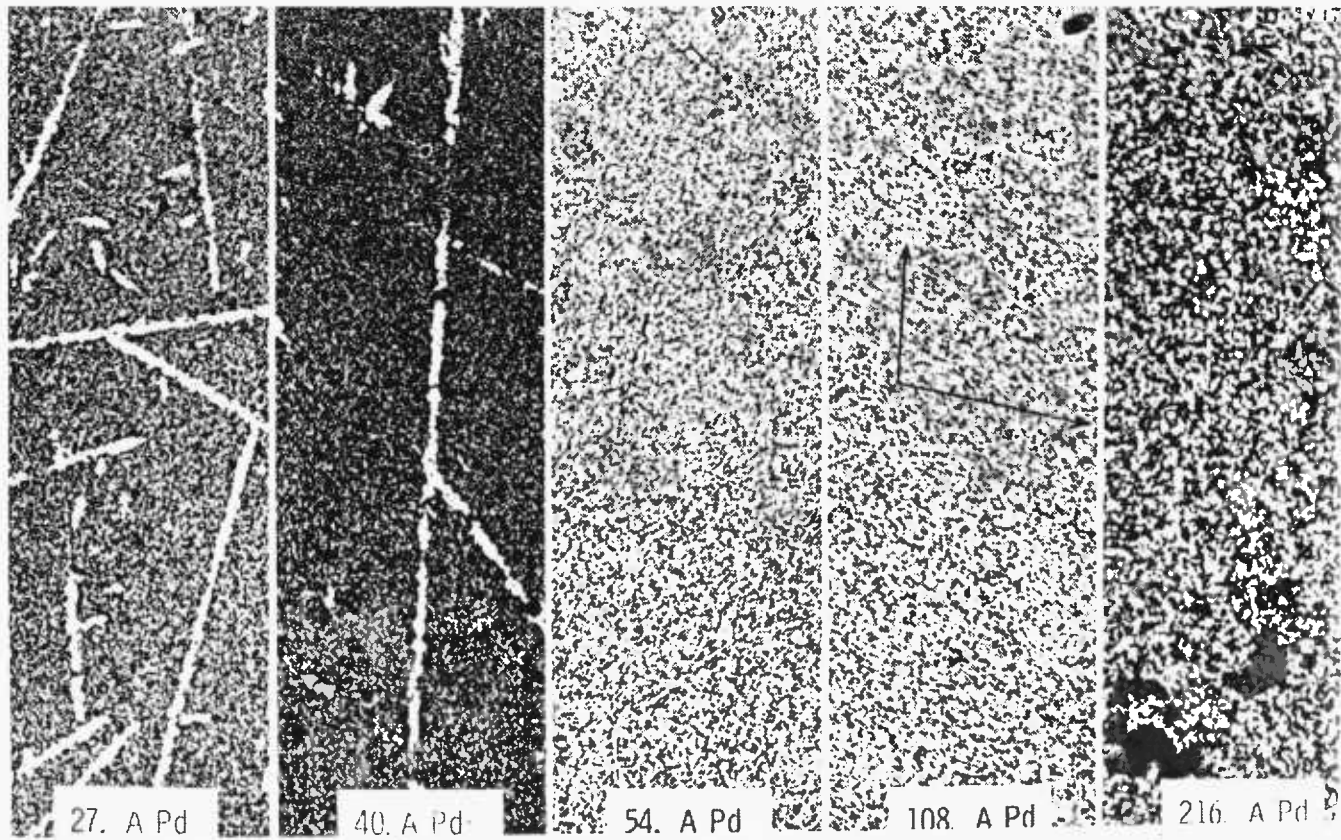
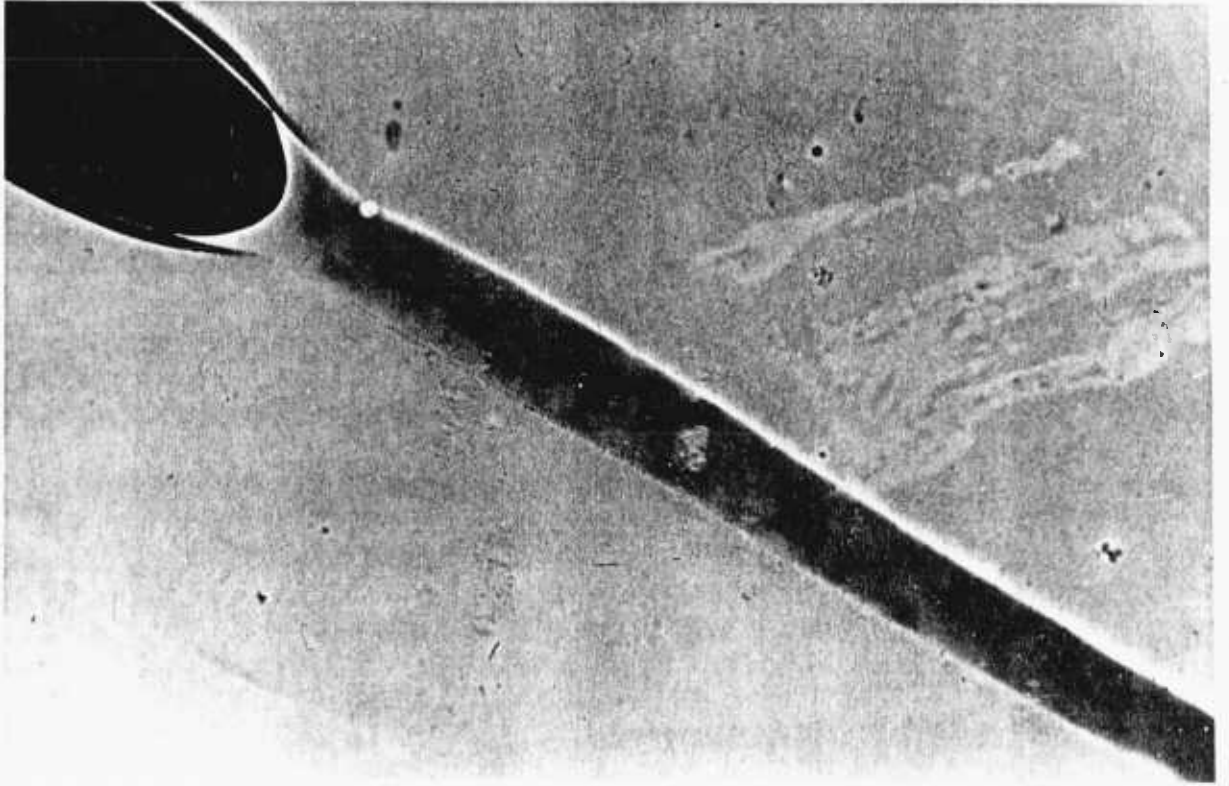


Figure 4.9 Variation of fission fragment track properties in C-UO₂-Pb film as a function of electrical resistivity



An electron micrograph of a non-etched fission fragment track in CA 80-15 cellulose nitrate

4.7 Conclusion

Strictly speaking, there are no real models for the process of track formation other than the already discussed thermal and ion-explosion spikes. However, certain "criteria" for "track formation" have been postulated and discussed in Chapter Three. Among these are the total energy loss (LET) criterion (67), the primary ionization criterion (70), the restricted energy loss criterion (31), and the various (75,106) δ -ray criteria. All these postulate a threshold or "critical" value of the mentioned quantities, above which value the charged particle forms a track which can be revealed; they take no account of the differing sensitivities of different track revelation techniques. The material properties enter only in determining the threshold or "critical" value. All of these criteria have had a fair amount of success in correlating data - indeed it is often hard to differentiate between them in their predictions. They should be regarded as phenomenological attempts to correlate data which may be useful for certain experimental purposes, but which do not yet rest upon a secure conceptual foundation.

Recently, direct experimental evidence has proved the validity of the thermal spike model of track formation for high LET charged particles (107). The velocity spectrum of Cs^+ and Br^- ions emitted from thin CsBr films irradiated with fission fragments shows that the ions are thermionically emitted with an average temperature of 6.6×10^4 °K. This indicates the existence of a transient hot thermal core within the fission fragment track. The radius of the hot central core of Figure 4.3a is estimated to be ~ 25 Å, giving 2×10^5 °K for the initial temperature, and the half-life of the thermal pulse is on the order of 10^{-11} sec (107). Other experiments indicate that fast chemical reactions take place in the high-temperature environment created by fission tracks in condensed media.

CHAPTER FIVE
DESCRIPTION OF INSTRUMENTS AND EXPERIMENTAL TECHNIQUES
FOR TRACK RECORDING AND REVELATION

5.1 Introduction

As has already been shown, an incident charged particle will do extensive physical and chemical damage along its trajectory upon penetrating a dielectric solid target. This narrow linear damage region has a maximum diameter of $\sim 100 \text{ \AA}$ and can be seen directly by the electron microscope or can be enlarged to be seen by an optical microscope.

In this chapter we discuss the experimental techniques used to produce and to reveal the tracks and the instruments used to observe the tracks. The purpose of these experiments is to fulfil the objectives set forth in Chapter One as well as substantiating the theoretical ideas discussed in this research.

Preliminary experiments were performed to select a dielectric material capable of recording the particles of interest and providing under certain etching conditions clear enough tracks for accurate counting and measurements. Experiments on the reactor and with an accelerator were performed as discussed in Chapter Six to study the registration and detection properties, reproducibility and response to reactor environments of the selected dielectric materials.

Four broad subject areas are considered; the instruments and the experimental techniques for specimen preparation, the radiation exposure of specimens, etching of specimens and the measurements of various track parameters.

5.2 Specimen Preparation

The preparation of uniform, thin cellulose nitrate films of large areas is a complicated and time-consuming procedure which requires large industrial equipment. Moreover the exact composition as well as the details of preparation of certain plastics are generally regarded by the manufacturer as trade secrets and are not available to the public.

Although commercially available cellulose nitrate plastics suitable for track recorders (see Table 5.1) have the advantage of being uniformly

thin over large areas and homogeneous, there are certain difficulties associated with their use. For example, since the exact composition is generally unknown, it is not possible to calculate accurate range-energy relations or to study the effects of the various constituents of the plastic on track registration.

Different batches of plastic usually have different particle and energy sensitivity, and even the two surfaces of a given sheet of plastic may vary in their track recording characteristics. The plastics are generally available in only a few thicknesses. The ageing plastic tends to pick up background tracks from the natural alpha particle emitting nuclides such as Rn-222 and Po-118.

5.2.1 Preparation of cellulose nitrate plastic in the laboratory

Many unsuccessful attempts have been made in our laboratory to produce a thin, uniform, homogeneous and more sensitive plastic than the ones commercially available. These attempts failed due to the technical difficulties and the unavailability of special equipment for mixing and casting the plastics. The samples which we prepared had superior energy response but inferior uniformity and homogeneity, so reproducibility of parameters of tracks was difficult and efficiency was never constant. As a consequence we had to abandon our attempts to manufacture our own detectors.

The recipe that was used for casting such films is given here for the benefit of other researchers:

To 24.3g of cellulose nitrate powder containing 30% ethyl alcohol, solvents, co-solvents and plasticizer are added sequentially: 124.7g ethyl acetate, 4g isopropyl alcohol, 5g butyl alcohol, 8g cellosolve acetate and 4g camphor. This resulted in a 10% cellulose nitrate solution, which should be stirred thoroughly until clear. After about 5 days at room temperature, a 10-20g aliquots. of the solution is diluted to 240ml with ethyl acetate. Then 40ml aliquots. of this are transferred to glass dishes 15cm in diameter and placed on a level surface in a clear area. The dishes are partially covered by a glass plate to obtain slow evaporation rate and to help prevent dust contaminations. After drying the foils at room temperature for two days, they are removed by stripping or by water flotation and dried between layers of blotting paper. Before use, the films are annealed at 80°C overnight to remove residual solvents and background tracks.

5.2.2 Commercial cellulose nitrate

The cellulose nitrate plastics which have been investigated are tabulated in Table 5.1. The Kodak-Pathé CA 80-15 plastic records alpha particles of energies up to well over 5 MeV, as was determined from the track length measurements. It is the most sensitive plastic tested, with about equal sensitivity for the two surfaces of a single sheet and little variation in track recording characteristics, and stable on storage, without decomposing or varying in sensitivity or changing colour on heating for long periods up to 75°C. The LR-115 (Figure 5.1) has the same ingredients as CA-80 (Figure 5.2) but is less sensitive and has only one sensitive surface on a single sheet. The Daicel material (Figure 5.3) records alpha particles of energy up to 5 MeV. The two surfaces of a single sheet of plastic as well as two different batches will differ in sensitivity. Sensitivity changes due to thermal decomposition upon storing the plastic above 30°C. Nobel and Rowland plastics are considered less sensitive and also have poor surface etching characteristics. The Nixon-Baldwin material, although it is less sensitive than the Kodak-Pathé CA-80 and the Daicel plastic, nevertheless is a satisfactory track recording material provided it is stored below 15°C. Unfortunately this material is no longer manufactured.

On our evaluation of all commercially available cellulose nitrate plastics, we have decided to use the Kodak-Pathé CA-80 and the LR-115 plastics for the major part of this research due to their superiority in uniformity, homogeneity, sensitivity, reproducibility and especially stability to environmental changes.

Moreover, since the manufacturer generally insists on a rather large minimum order, it was easier and faster to get the order from Kodak-Pathé in France rather than from Daicel in Japan.

The quality of tracks produced by each plastic is observed in Figures 5.3b up to 5.3k. Each detector was irradiated under the same environmental conditions and etched with the same etchant and etching conditions for different times. Notice the superiority of LR-115 type-II, where tracks of 0.8 MeV alpha particles observed (underetched) after etching for only two hours at 18°C.

TABLE 5.1 Commercially available cellulose nitrate plastics

Type of commercially available cellulose nitrate for track recording	Highest energy alpha particle recorded	Background etched feature density	Environmental stability	Variation in track recording characteristics for different batches
Daicel, Japan (250 μ , red)	\sim 5.0 MeV	fairly high	good	fairly high
Dynamit Noble, Germany (250 μ , clear)	\sim 3.0 MeV	very high	medium	low
Nixon-Baldwin, U.S.A. (500 μ , orange, clear)	\sim 4.0 MeV	low	bad	very high
Rowland, U.S.A.	\sim 3.0 MeV	high	bad	high
Kodak-Pathé LR-115 Type I France. (6 μ , strongly red coloured with 100 μ polyester backing)	\sim 2.1 MeV	low	excellent	low
Kodak-Pathé LR-115 Type II France. (10 μ , strongly red coloured with 100 μ polyester backing)	\sim 3.1 MeV	low	excellent	low
Kodak-Pathé CA 80-15, France (100 μ , light rose-tinted)	$>$ 5.0 MeV	very low	excellent	very low

Etching was performed in 2.5 N NaOH solution at 180°C and 20°C.

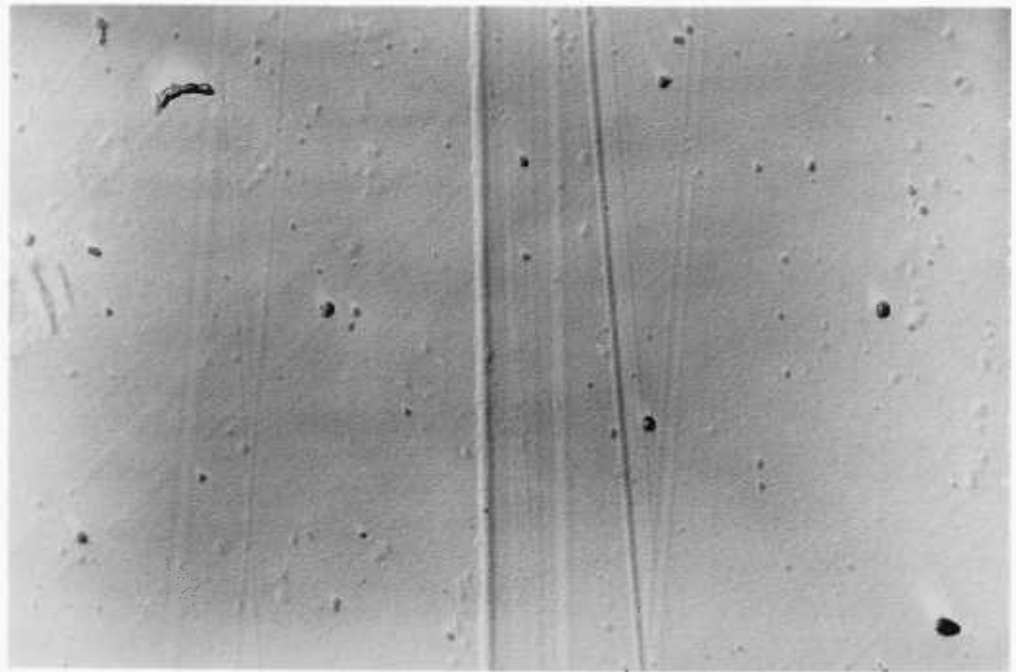


Figure Electron micrograph of cellulose nitrate detector, LR115 Type 2 (Kodak-Pathe, France) unirradiated, unetched (25 K x 3) .

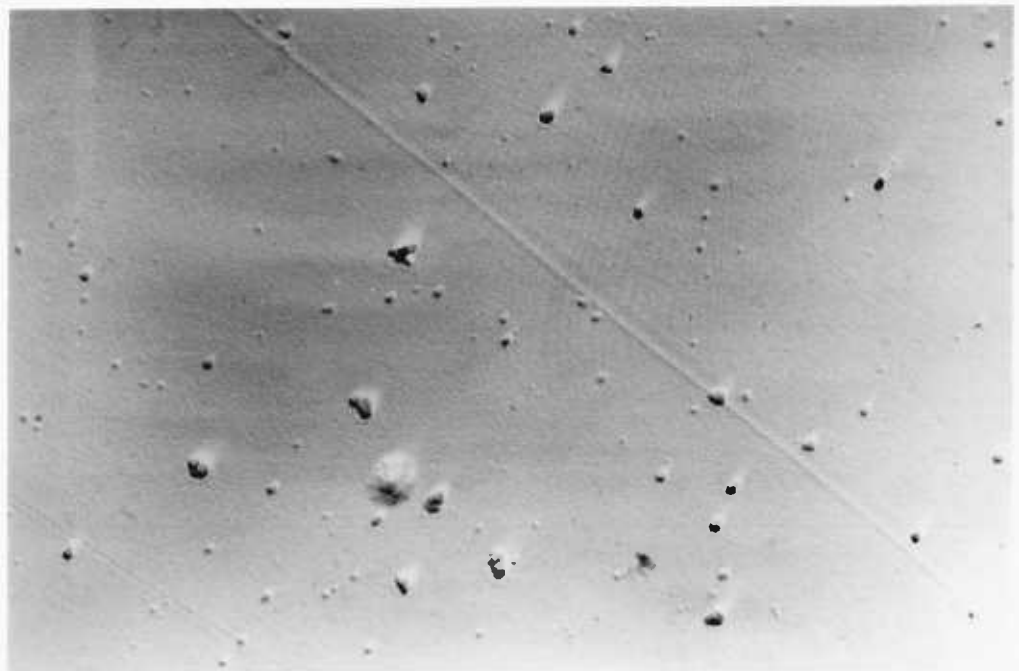


Figure 5.2 Electron micrographs of cellulose nitrate detector, CA80-15 (Kodak-Pathe, France) unirradiated, unetched (25 K x 3).

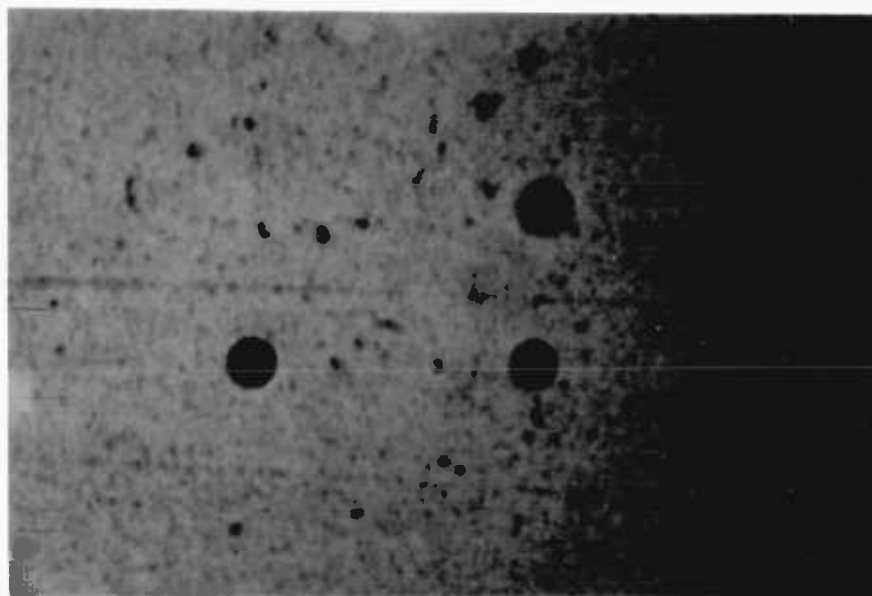


Figure 5.3 a Photomicrograph of 2.5 MeV alpha tracks in cellulose nitrate (Daicel, Japan) at 90° incidence, etched in 2.5 N sodium hydroxide at 18°C for 20 hours.

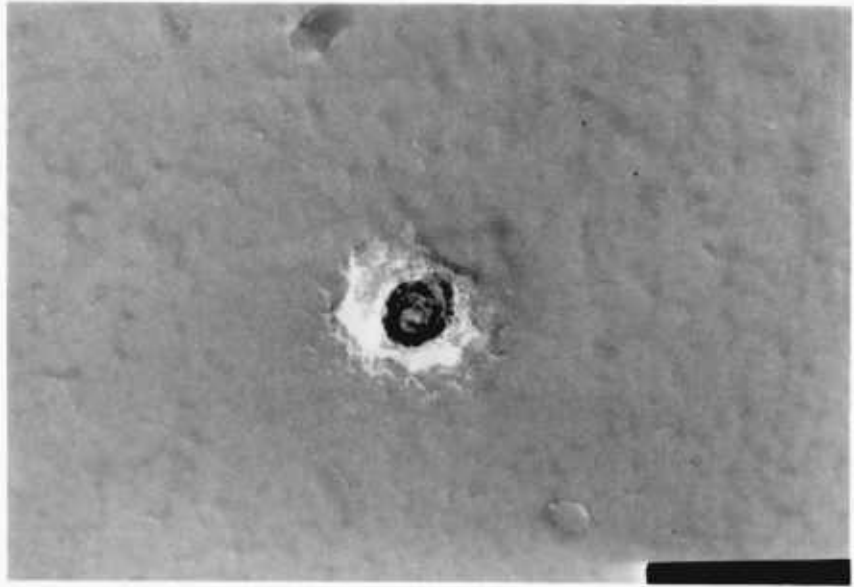


Figure 5.3 b Electron micrograph of 0.8 MeV alpha track in LR115 type 2 (Kodak-Pathe, France) at 90° incidence, etched in 2.5 N sodium chloride at 18°C for 2 hours (100 K x 1.5).

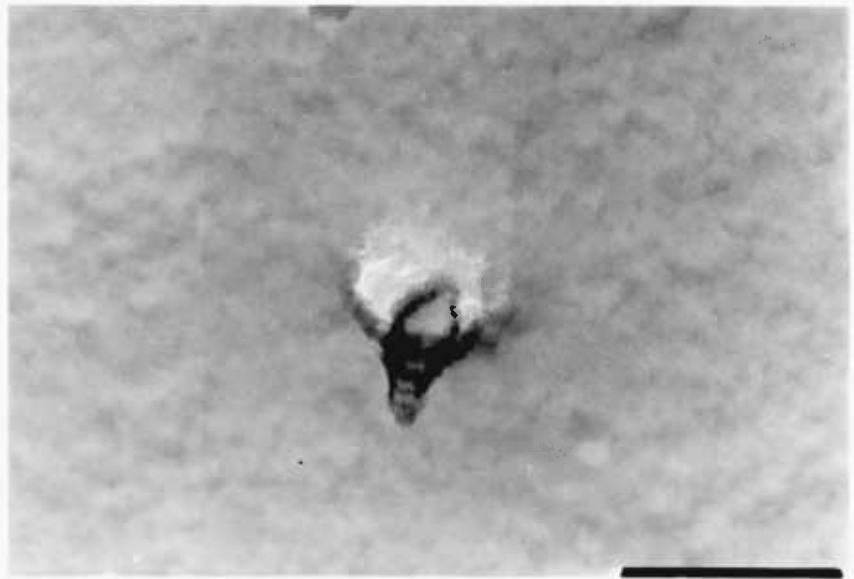


Figure 5.3 c Electron micrograph of 0.8 MeV alpha track in LR115 type 2 (Kodak-Pathe, France) at 30° incidence, etched in 2.5 N sodium hydroxide at 18°C for 2 hours (100 K x 1.5).

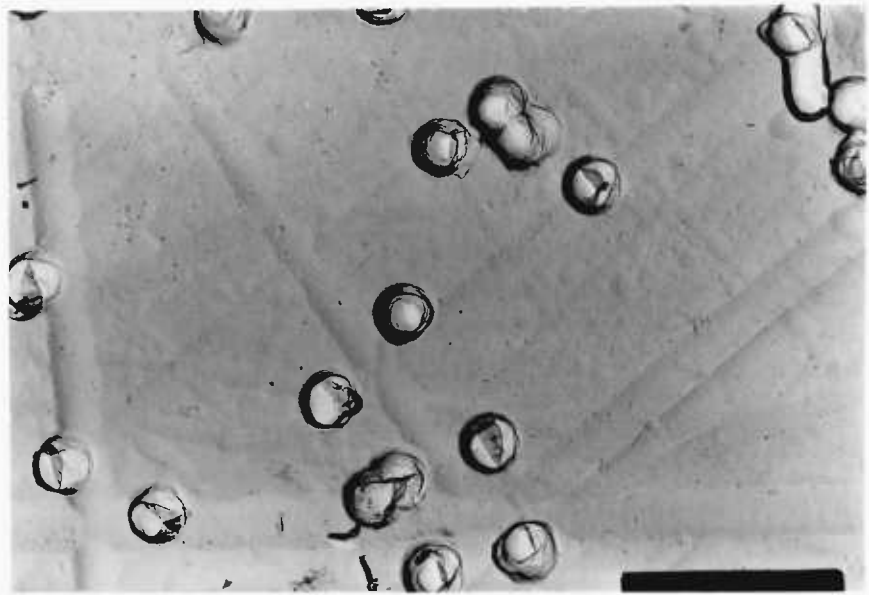


Figure 5.3 d Electron micrograph of 4 MeV alpha tracks in cellulose nitrate (Daicel, Japan), at 90° incidence, etched in 2.5 N sodium hydroxide at 18°C for 26 hours (25 K x 2).

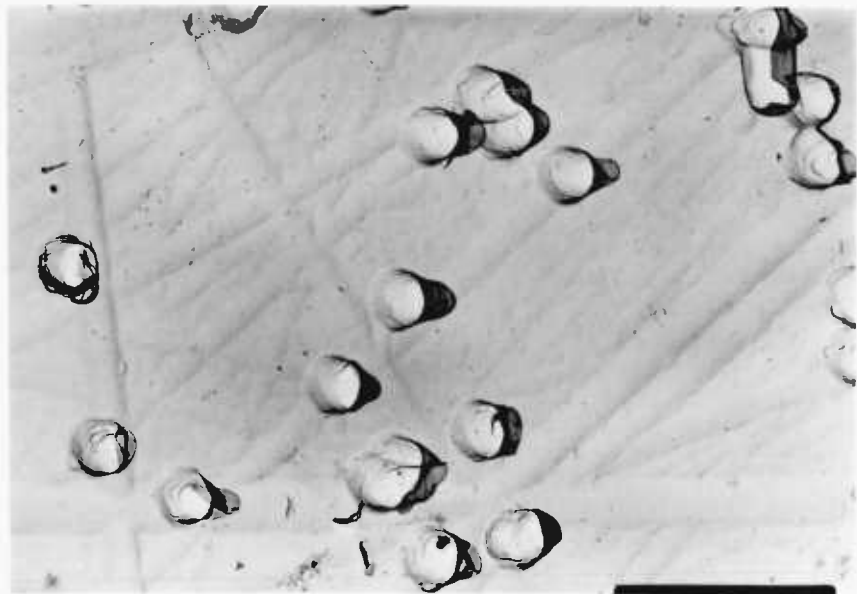


Figure 5.3 e Electron micrograph of 4 MeV alpha tracks in cellulose nitrate (Daicel, Japan) at 45° incidence, etched in 2.5 N sodium hydroxide at 18°C for 26 hours (25 K x 2).

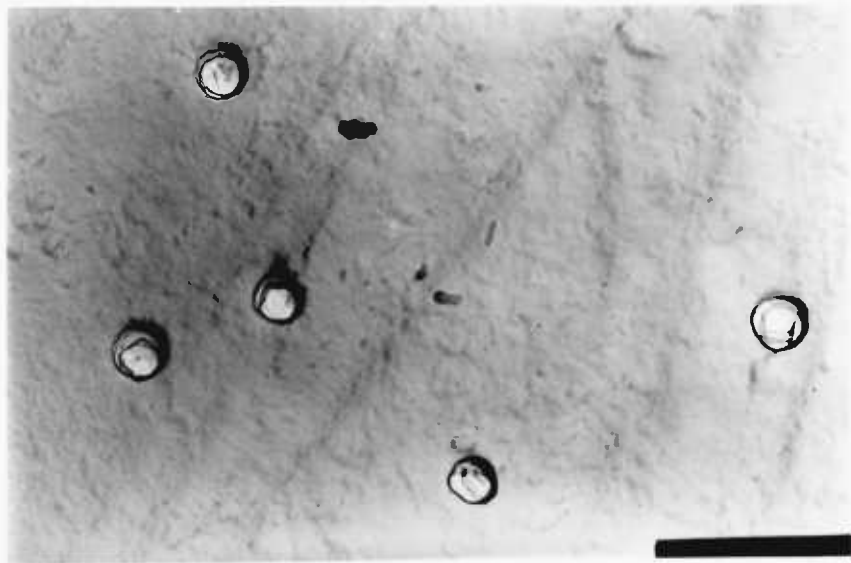


Figure 5.3 f Electron micrograph of 4 MeV alpha tracks in cellulose nitrate (Nixon-Baldwin, U.S.A.) at 90° incidence, etched in 2.5 N sodium hydroxide at 18°C for 26 hours (25 K x 2).



Figure 5.3 g Electron micrograph of 4 MeV alpha tracks in cellulose nitrate (Nixon-Baldwin, U.S.A.) at 45° incidence, etched in 2.5 N sodium hydroxide at 18°C for 26 hours (25 K x 2).

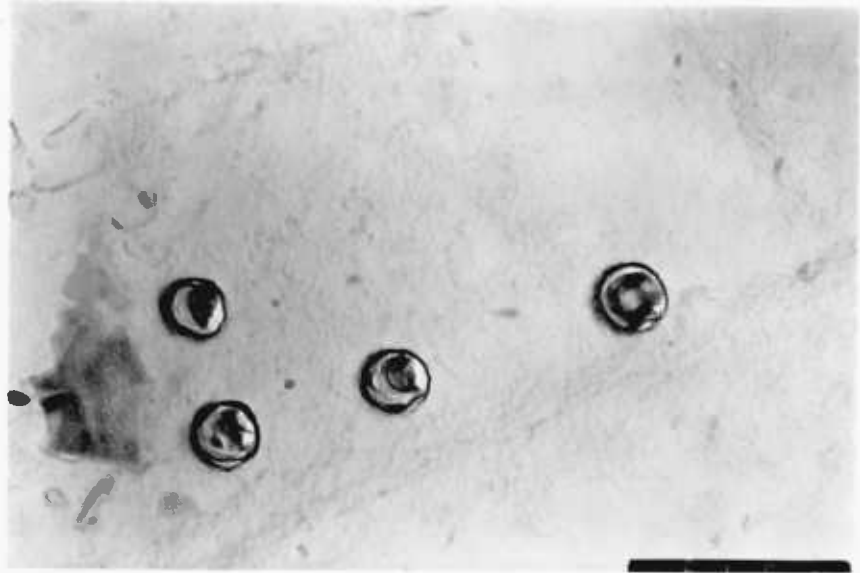


Figure 5.3 h Electron micrograph of 3 MeV alpha tracks in cellulose nitrate (Dynamit-Nobel, Germany) at 90° incidence, etched in 2.5 N sodium hydroxide at 18°C for 26 hours (25 K x 2).

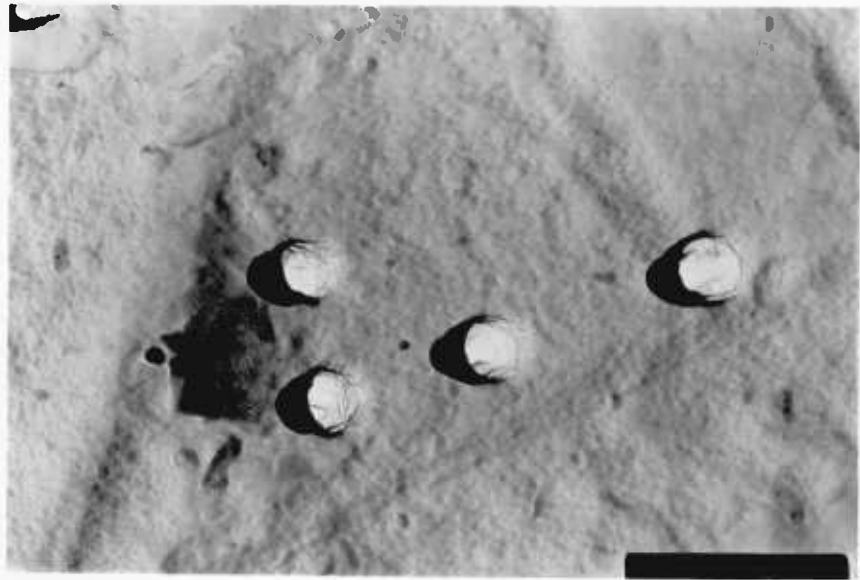


Figure 5.3 i Electron micrograph of 3 MeV alpha tracks in cellulose nitrate (Dynamit-Nobel, Germany) at 45° incidence, etched in 2.5 N sodium hydroxide at 18°C , for 26 hours (25 K x 2).

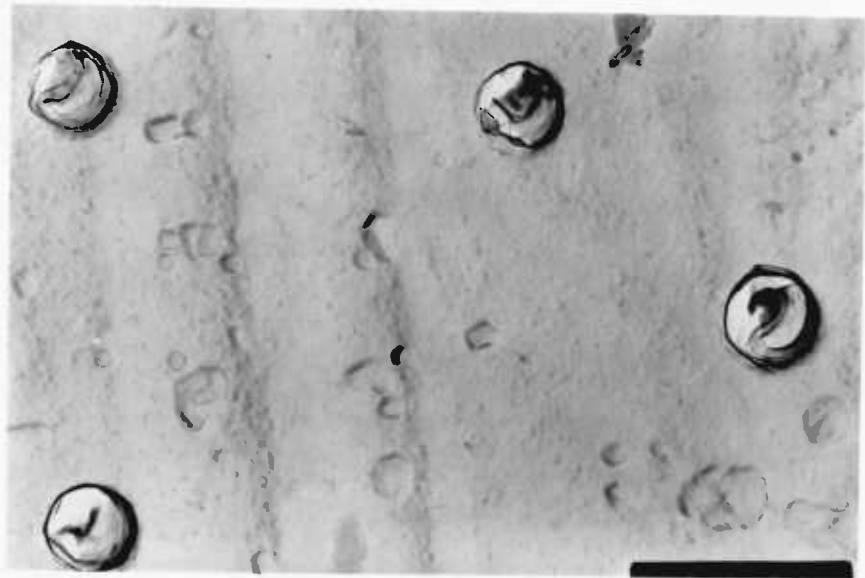


Figure 5.3 j Electron micrograph of 5 MeV alpha tracks in cellulose nitrate (laboratory made) at 90° incidence, etched in 2.5 N sodium hydroxide at 18°C for 26 hours (25 K x 2).



Figure 5.3 k Electron micrograph of 5 MeV alpha tracks in cellulose nitrate (laboratory made) at 45° incidence, etched in 2.5 N sodium hydroxide at 18°C for 26 hours (25 K x 2).

TABLE 5.2 Light and heavy ions used in this study

Particle	Source of Irradiation	Particle Energy in MeV/nucleon	Angle of Incidence
Protons	Oxford Van de Graaff Harwell Tandem Accelerator	0.2 - 1.4 1.4 - 4.5	10°, 20°, 30°, 40°, 50° 60°, 70°, 80°, 90°.
Alpha	Americium-241 Californium-252	0.1 - 1.35 0.1 - 1.5	2π geometry 2π geometry
Alpha	Harwell 6 MeV Van de Graaff	0.15 - 1.5	5° - 90° at 5° steps
Alpha	(n,α) reaction $^{10}\text{B}(n,\alpha)^7\text{Li}$ Silwood Park Experimental Consort Reactor, University of London Reactor Centre	0.37 and 0.45	2π geometry
Chlorine-35	Harwell Tandem Accelerator	0.1 - 1.0	~ 45°, ~ 30°, ~ 90°
Fission Fragments	Silwood Park Experimental Consort Reactor, University of London Reactor Centre	0.1 - 1.0	~ 45°, ~ 60°, ~ 90
Fission Fragments	Californium-252	~ 0.8 - 1.0	2π geometry

5.3 Radiation Exposure

The study called for exposure of cellulose nitrate plastic to a broad spectrum of heavy and light particle types, of various energies and incident angles: in Table 5.2 are listed the natural and artificial sources of particles used in these studies.

5.3.1 Protons

Protons with energies up to 4.5 MeV/nucleon and with varying incident angles, were obtained from a Van de Graaff at Oxford University and from the Tandem Generator at Harwell. The plastic detector was placed at one end of a shaft which could be rotated through 360° on an axis perpendicular to the incident proton beam.

5.3.2 Alpha particles

The principal sources of alpha particles were: (i) A 0.2 μ Ci calibrated Am-241 source in the form of a thin deposit by vacuum-sublimation on a lightly oxidised stainless steel disc of overall diameter 25 mm and thickness 0.5 mm. The diameter of the active area is approximately 17 mm. The half-life of the isotope is 433 years. The two modes of alpha decay have similar energies of 5.484 MeV (85.2%) and 5.442 MeV (12.5%). Calibration with nuclear emulsions showed that the alpha particles can be considered to be monoenergetic.

It is possible to vary the alpha particle energies by passing them through different thicknesses of a slowing down material before detection. They have a clearly defined range in a slowing down medium and straggling is very small. Thus the energy of the alpha beam decreases as distance travelled through the medium increases, but it remains sharply defined. It is possible also to vary the alpha energies by changing the distance between the source and the detecting film in air; the range of alphas of this energy in air is about 2.5 cm, but it is difficult to vary the distance with great precision. The same effect can be obtained by fixing the distance between the source and the detector and varying the air pressure. Alpha particles of any energy from 5.5 down to about 0.40 MeV could be readily obtained.

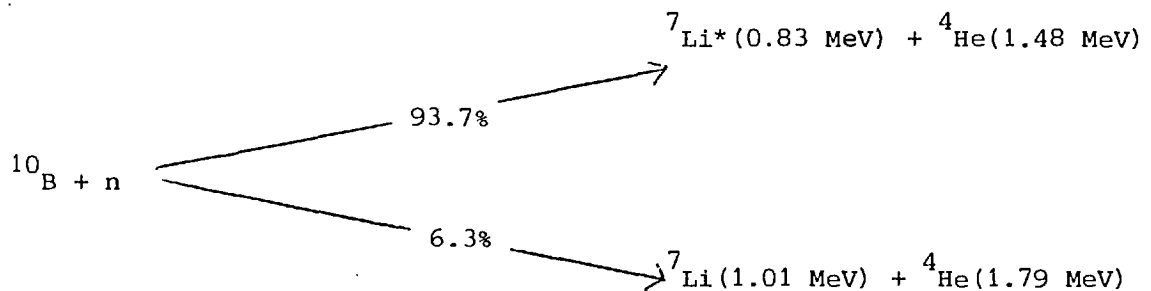
(ii) In order to vary the alpha energies and incident angles, an apparatus was built as shown in Figure 5.4a. This apparatus consists of an evacuable metal chamber which houses a movable system containing the americium source and, at a certain distance from this source a

shutter was fixed which could be operated remotely from outside of the vacuum chamber. On the other end of the vacuum chamber was fitted a brass disc machined to accept a cellulose nitrate film mounted on a $\frac{1}{2}$ " square glass slide. This disc could be rotated 360° around an axis from outside of the vacuum chamber. The disc had a $\frac{3}{8}$ " hole in the middle to allow the alpha particles to pass through and strike the film. The disc on the top of the inner cylinder was designed in such a way that it was possible to place, by means of an additional spacer, a scintillator detector within 0.02" of the position at which the cellulose nitrate film had been located. The energies of alpha particles were determined with a photomultiplier - scintillator light detector. A calibration curve was obtained for alpha energy versus pressure (Figure 5.4b).

Several films were irradiated in the above apparatus. No attention was given to the effect of the temperature on the air density and hence the alpha particle energy.

5.3.3 Alpha particle production using boron

The alpha particles produced in the boron (n, α) reaction have energies in the region of maximum sensitivity of cellulose nitrate film. The reaction details are shown below. It was decided to produce alpha tracks by neutron irradiation of cellulose nitrate plastics in contact with a uniformly thin layer of boron.



Boron and lithium have large (n, α) reaction cross-sections; the absorption cross-section is inversely proportional to the neutron velocity ($1/v$ law), in the neutron energy region from about 0.01 eV to 0.1 MeV. The $1/v$ law holds in an energy range well beyond that found for most other (n, α) reactions. Thus when boron or lithium is used as the neutron sensitive element, the interpretation of the data and calculations are much less complex than would be the case with a resonance absorber.

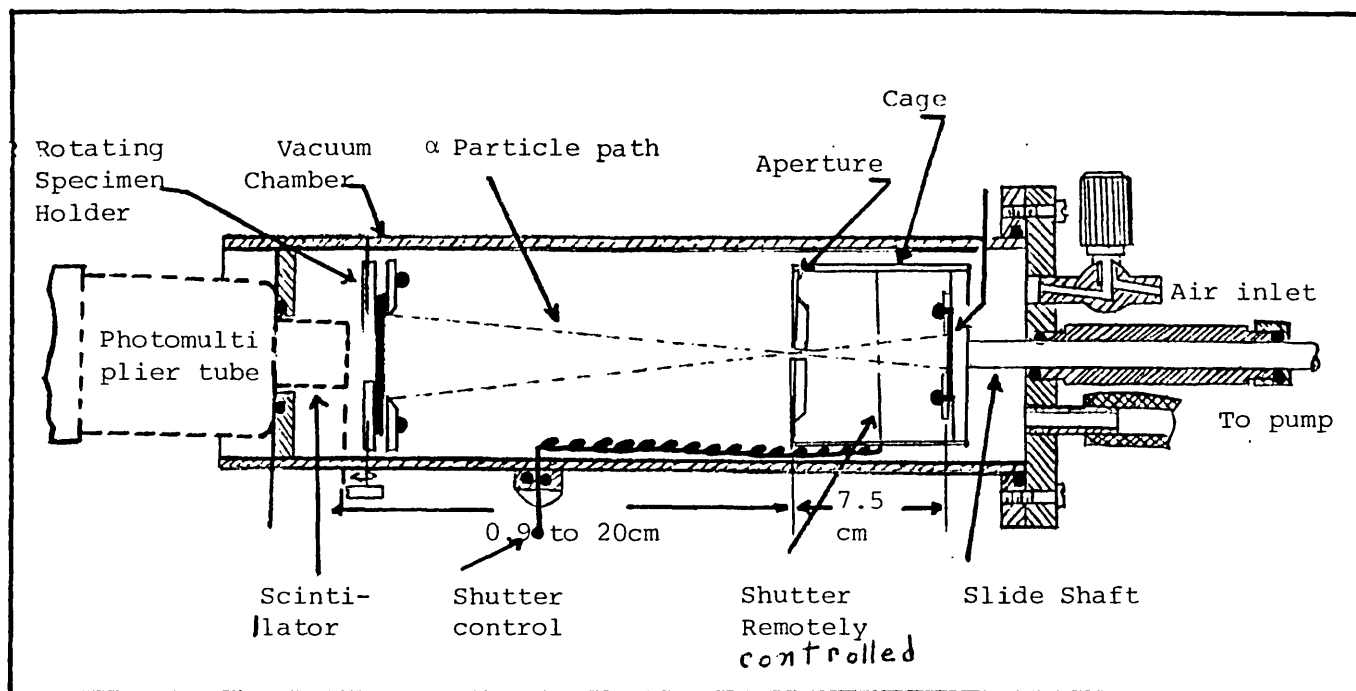


Figure 5.4 a. An apparatus designed in order to vary the alpha energies and incident angles. This apparatus consists of an evacuable metal chamber which houses a movable system containing the americium source and a rotating disc containing the specimen.

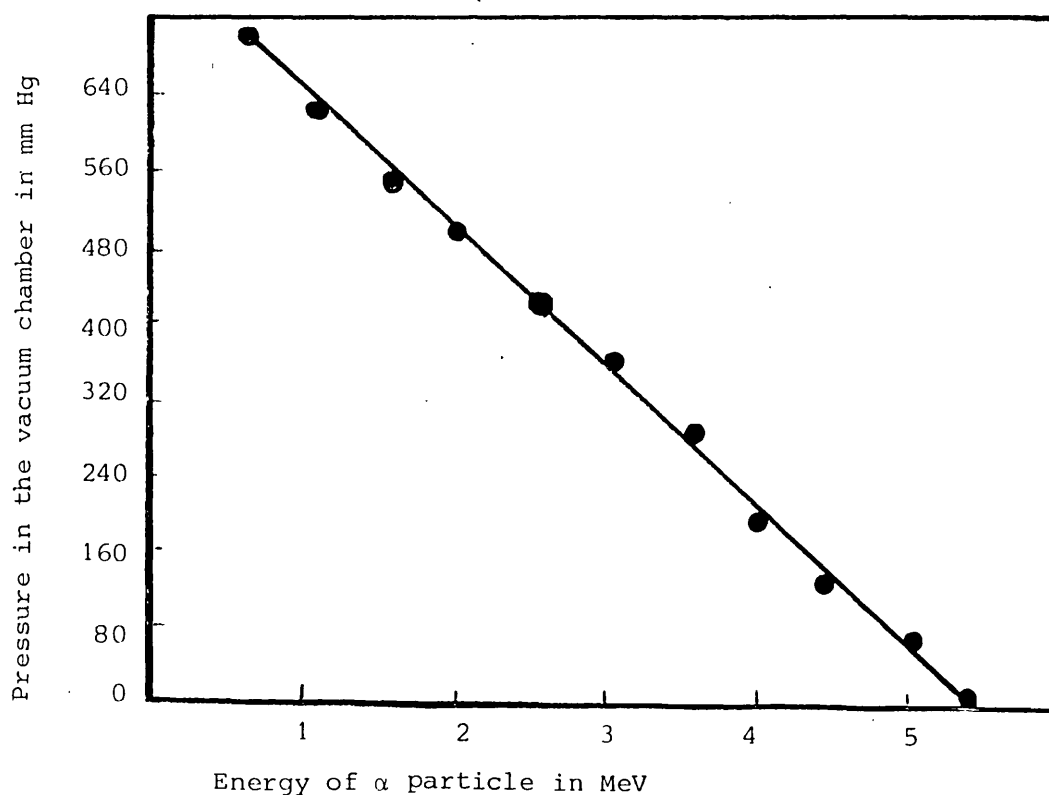
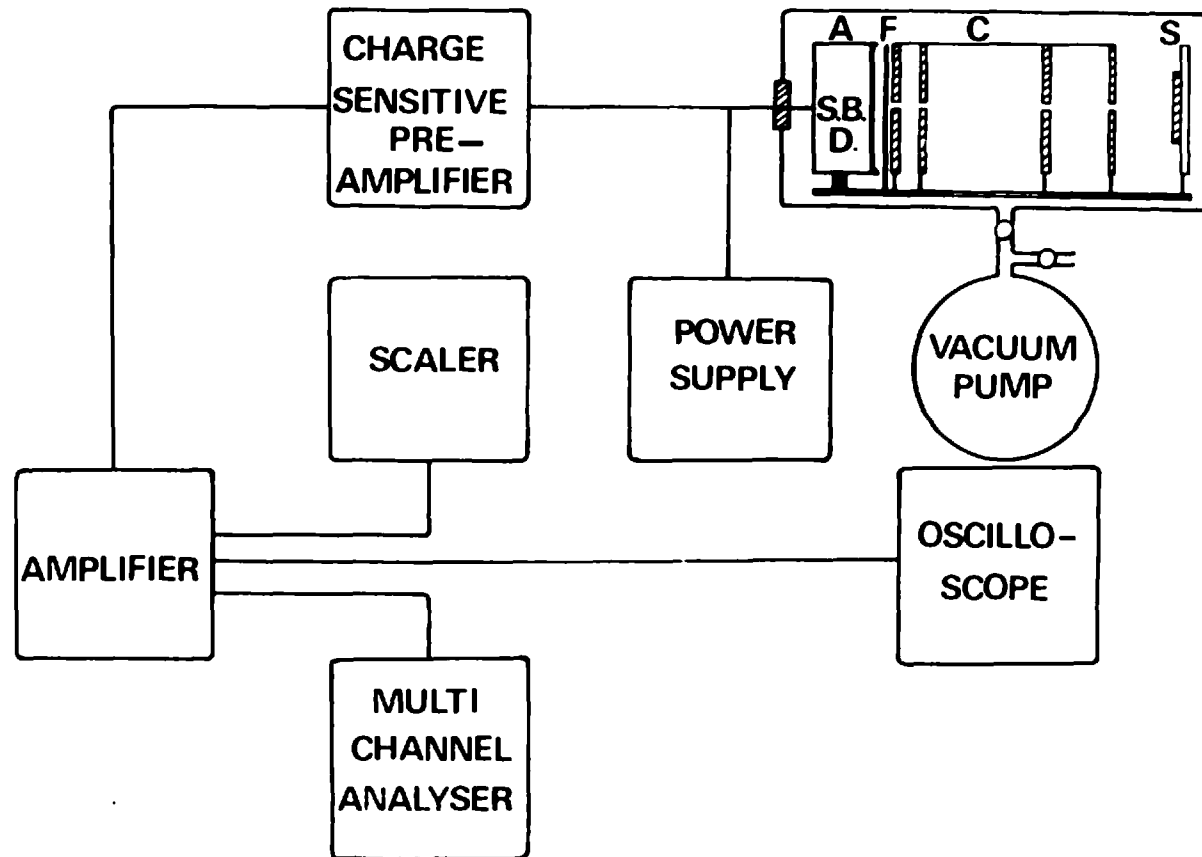


Figure 5.4 b A calibrated curve for alpha energies of the americium source versus the pressure in the vacuum chamber



The experimental set-up to count the particle tracks electronically. A silicon surface barrier detector (S.B.D.) counts collimated alpha particles emitted by a standard ^{241}Am source S and transmitted through a heavily etched plastic foil F previously exposed to fission fragments. The source-detector system is kept under vacuum while in operation.

It is convenient that the CA-80 type II is manufactured by Kodak-Pathé with a layer of a boron compound on its surface, which can be washed away prior to etching. Neutron irradiation of this film was done in the thermal column of the University of London reactor at Silwood Park.

5.3.4 Alpha particle irradiation using the Van de Graaff accelerator (Figure 5.5)

Recorders of LR-115 and CA-80 were bombarded with alpha particles at various energies and angles using the 6 MV Van de Graaff accelerator at Harwell. A schematic diagram of the experimental arrangement is shown in Figure 5.6. The recorders are mounted on aluminium supports which are in turn mounted onto a rotating plate. The plate is shown in detail in Figure 5.7 and it can be seen that there is a slot in the plate so that the beam can pass through onto a semiconductor detector once every revolution. The plate can contain 12 or more recorders and each recorder can be mounted at any desired angle to the beam. The plate rotates at 120 rpm. The beam energy can be varied from 0.6 up to 6 MeV and this energy together with the beam current is monitored by the semiconductor detector and pulse height analysis system.

The beam current was set together with the length of irradiation so that the track density, for 90° incident particles, was 5000 tracks per mm^2 . The track density was controlled and read in real time from the scaler in Figure 5.8. The 5000 tracks per mm^2 is a convenient density for both automatic or manual track counting since track overlapping is less than 5%.

5.3.5 Fission fragments from a Cf-252 source

A 1 μCi californium-252 source in the form of a thin deposit by vacuum sublimation onto a lightly oxidised stainless steel disc was used as a source of fission fragments. This isotope also emits alpha particles of energies 5.975 MeV and 6.119 MeV and spontaneous neutrons at the rate of approximately 4×10^3 neutron/sec. The half-life of the isotope is 2.65 years.

The mass and kinetic energy distributions of fission fragments emitted from californium-252 have been studied by Fraser et al (108).

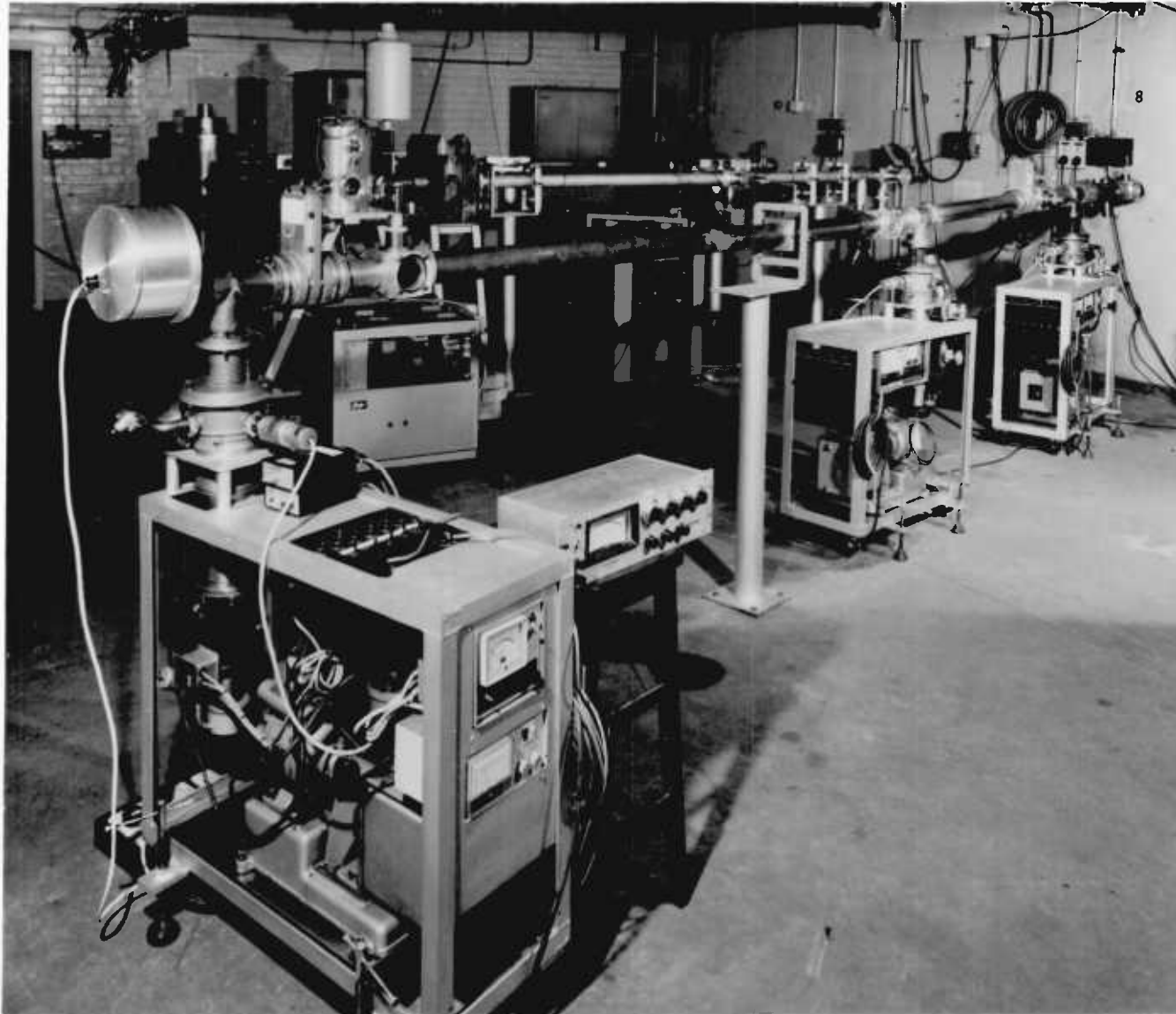


Figure 5.5 Beam tube assembly terminating in the rotator system containing specimen foils and semi-conductor particle detector.

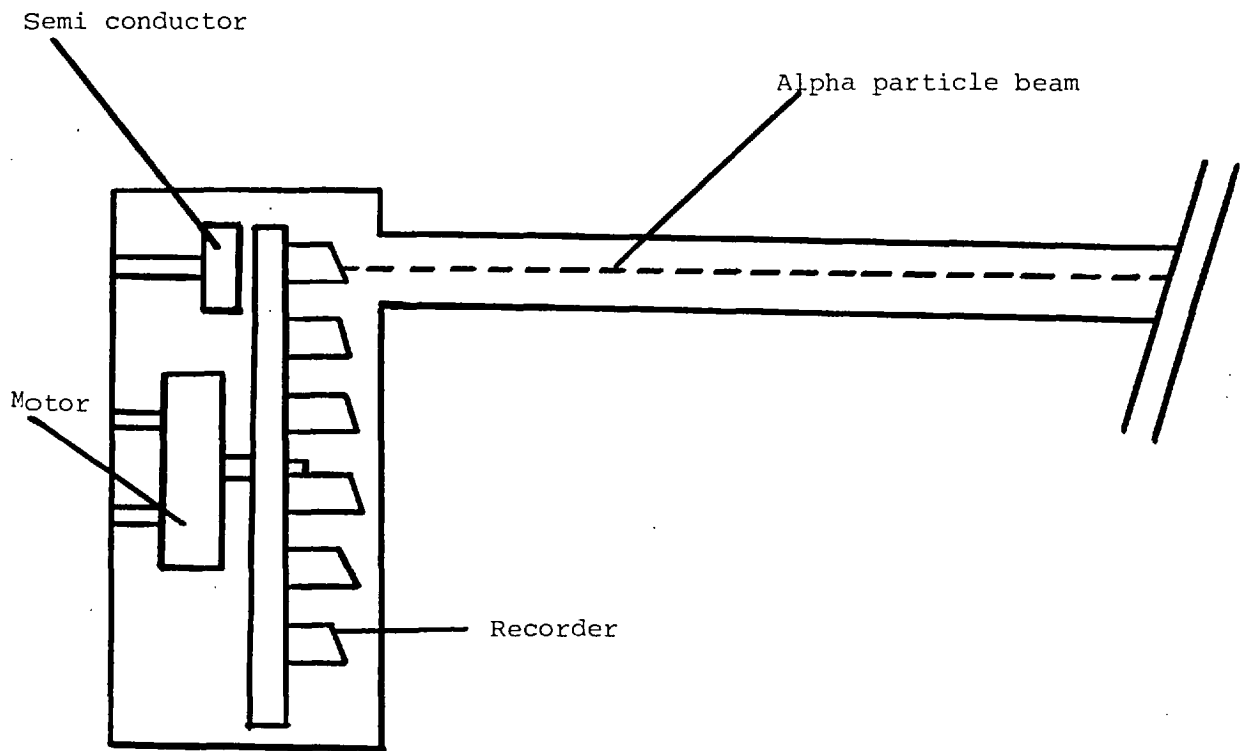
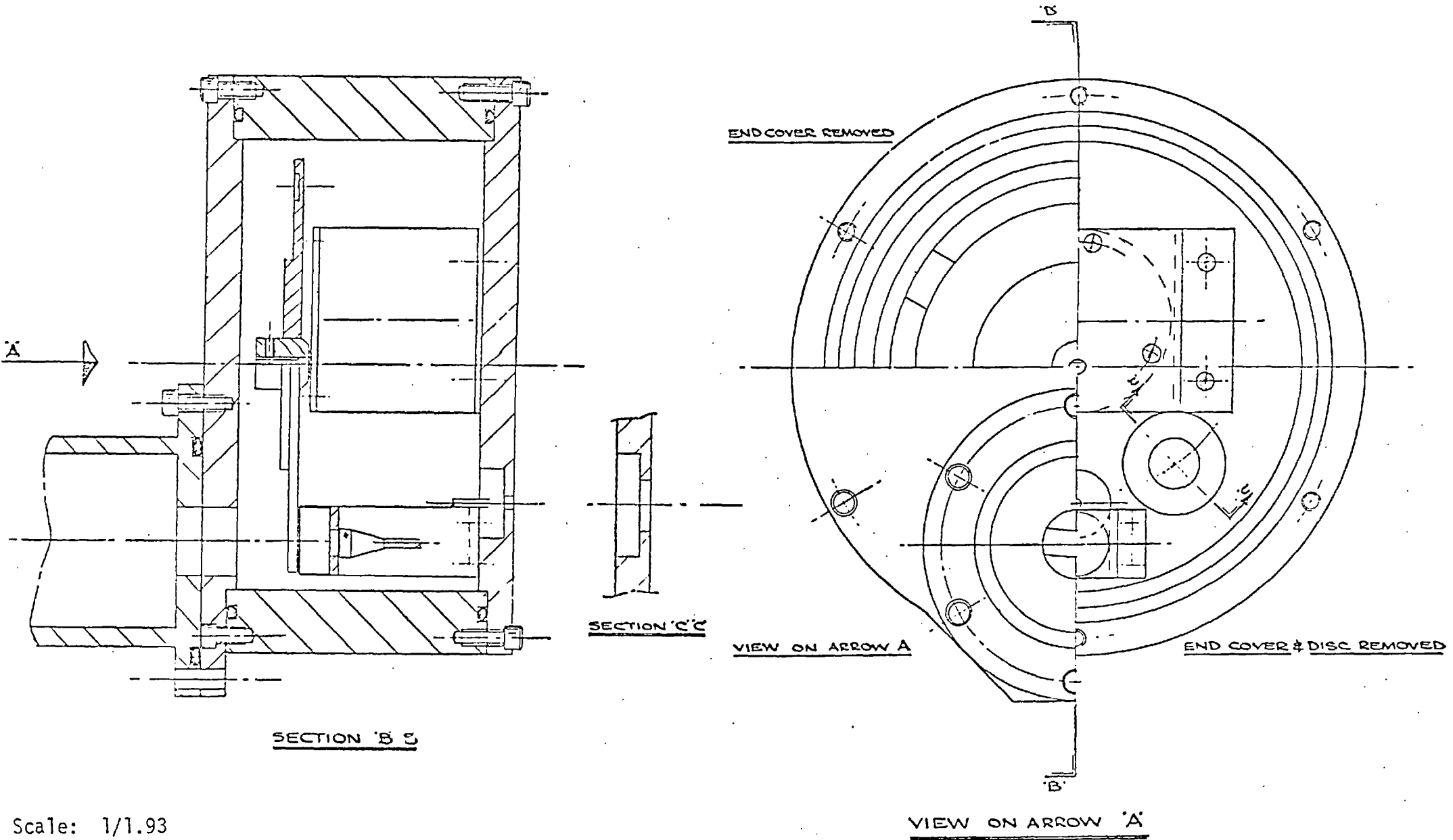


Figure 5.6a Diagram showing target layout on the 6 MV Van de Graaff



Scale: 1/1.93

Figure 5.6b. Accelerator vacuum box

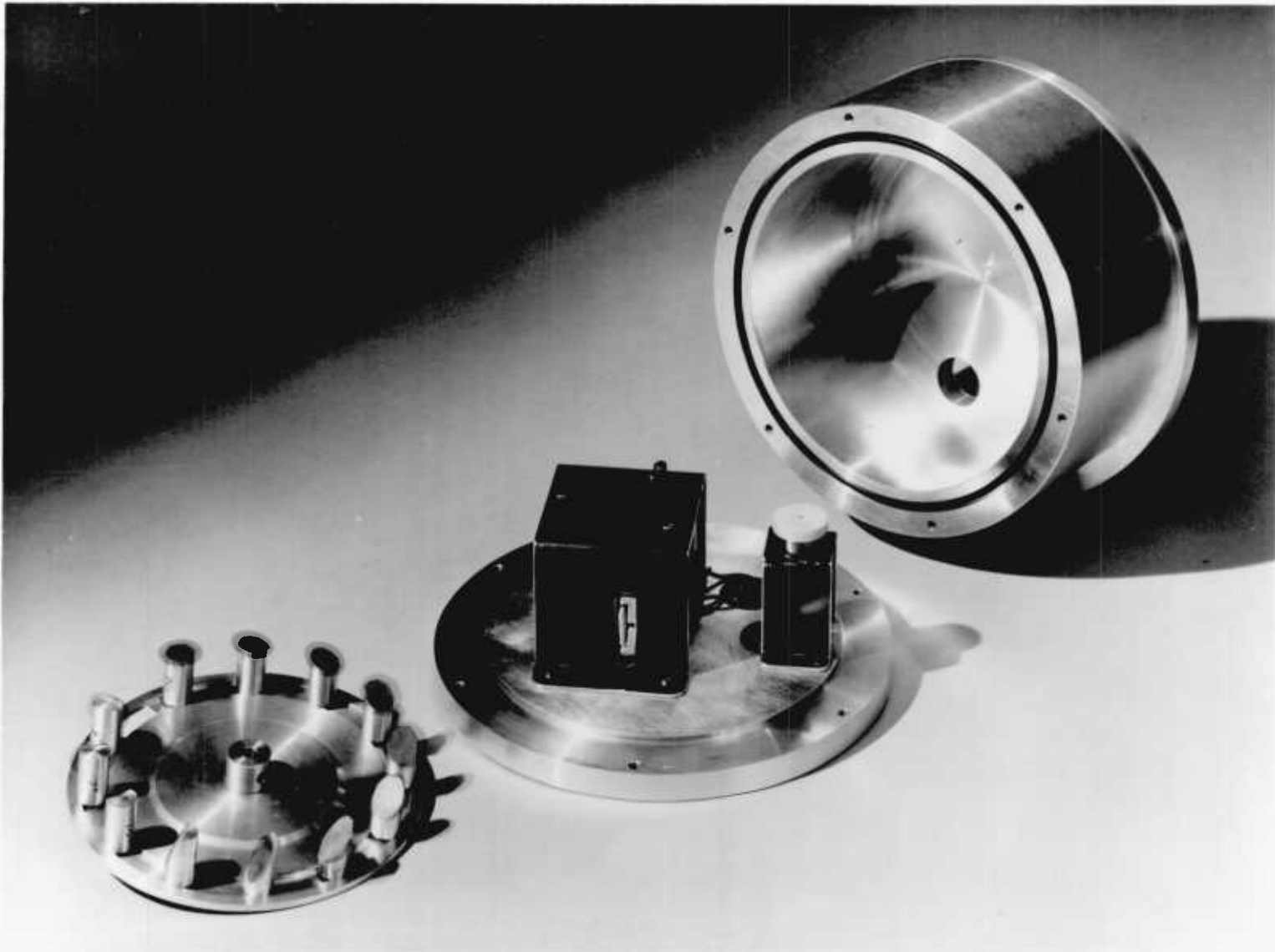


Figure 5.7 SSTR rotator system showing rotator with 12 recorders, back-plate with motor and semi-conductor detector and housing with beam entrance hole.

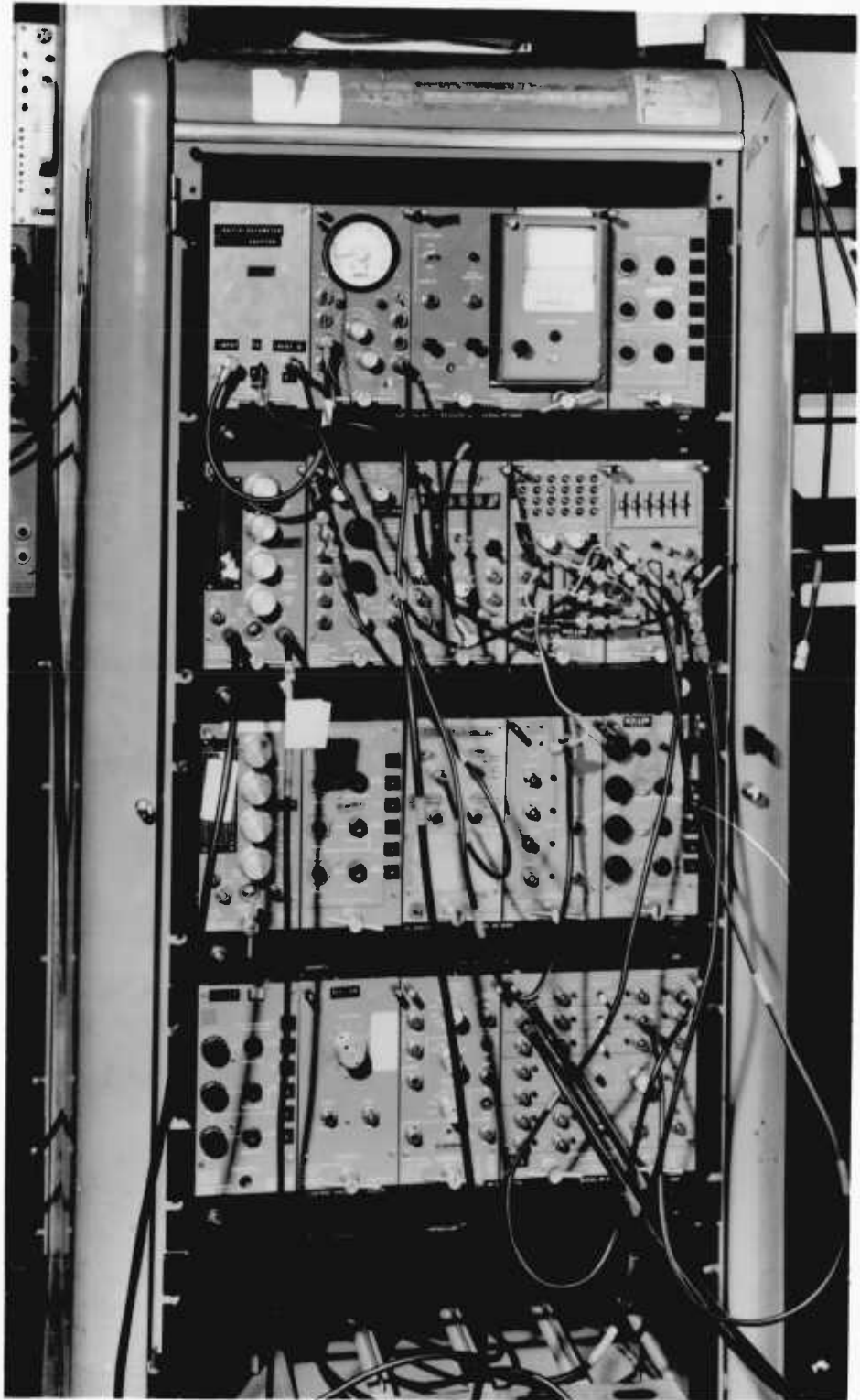


Figure 5.8 Scaler for counting the signal from the semi-conductor detector due to passage of alpha particles.

5.3.6 Fission fragments from the reactor

Thin foils of enriched uranium were placed in the thermal column of the Silwood Park experimental reactor (Consort) for 8 hours while it operated at ~ 100 kW. The neutron induced fission of U-235 produced fission fragments, which travelled several cm in an evacuated plastic chamber before entering the CA-80 plastic detector. The angle of the fragments from the surface was either around 90° or around 45° .

5.3.7 Experiments on the reactor "Consort"

These experiments consist of SSTR irradiations in thermal spectra existing in any part of the graphite stack of the thermal column extension on the reactor Consort, and SSTR irradiations in fast neutron spectra produced inside the NISUS facility.

The NISUS assembly was installed in the thermal column on the reactor Consort as a result of collaboration between C.E.N./S.C.K. Belgium, U.K.A.E.A., and Imperial College. The basic idea of this design was to build an assembly for generating a neutron spectrum which would simulate the neutron spectrum of the core and breeder of a fast reactor. The neutron energy range which is important in the study of fast breeder reactors goes from 50 eV to 5 MeV.

The design and basic requirements of NISUS are described in References (109) and (110), therefore, only details associated with the present measurements will be discussed here.

The original NISUS assembly consists of two concentric spherical shells, the outer shell being of natural uranium and the inner shell of boron carbide (B_4C). The shells are supported in the centre of a spherical cavity of 50 cm hollowed out of a 60 cm cube of graphite. The shell support is manufactured from aluminium and its height can be adjusted using aluminium spacers. The graphite block is mounted on an extension of a thermal column of the reactor. The assembly can be effectively shut off from the reactor by a remote controlled cadmium shutter, with a close/open operation time of ~ 46 seconds. The shutter, of total area 122 x 122 cm, has two parts which move apart horizontally. Each part is constructed of 1 mm thick cadmium sheet sandwiched between two 3 mm sheets of aluminium.

The neutron detectors are mounted on a graphite plug and can be loaded into the central cavity via an access hole of diameter 85.5 mm

on the central axis of the thermal column extension. A general view of the installation of NISUS on the Consort reactor is shown in Figures 5.9 and 5.10, while a view of the NISUS 1 assembly is shown in Figure 5.11.

The construction of the NISUS assembly allows the installation of concentric spherical shells of different thicknesses so that it is possible to generate spectra with a different degree of "hardness".

Eight natural uranium shells are available in total, and can be accommodated inside the cavity in several combinations. The details of these shells are given in Table 5.3.

The detectors were mounted on the graphite plug at the top of a miniature BF_3 -counter assembled together with a miniature fission chamber so that the centre of the BF_3 -counter active volume and the centre of the pellet were on the same radius and equidistant from the NISUS cavity centre. The detectors were irradiated in the neutron spectra 1 and 3 of Table 5.4. Spectrum 1 pertains approximately to the mid-point of the graphite stack, with the plug inserted by 19.5 cm, and is well thermalised. Spectrum 3 pertains to the centre of the NISUS assembly which consists of the uranium shells 5 and 6 and an inner iron shell. The detectors were placed inside Cd boxes of ~ 10 mm inner diameter and ~ 1 mm wall thickness to avoid the streaming of thermal neutrons through the hole which was made (~ 46 mm in diameter) to simulate the closed configuration.

The detectors were kept firm on the monitor by a special sticky tape. The B_4C -pellets were supplied by Winfrith Atomic and were polished at Imperial College. Their density of $\rho = 2.52$ g/cm³, with 19.76% abundance in ^{10}B .

The FC-counter was used in order to check the performance of the BF_3 -counter against spurious events from (n,p) reactions and γ -ray pile-up, and/or dead-time effects. Hence, the FC-monitor makes it easier to select the appropriate flux and time of irradiation to perform the experiments, as is seen in Table 5.5. For more details see Reference (109).

Key

1. Shielding Blades
2. Movable Graphite Plug
3. Graphite Stack
4. Spherical Cavity Block
5. Proton Recoil Proportional Counter
6. Boron Carbide Sheet
7. Uranium Sheet
8. Reactor Shielding
9. Cadmium Shutter (open position)
10. Graphite Thermal Column Extension
11. Graphite Thermal Column
12. Reactor Core

Scale: 1/75

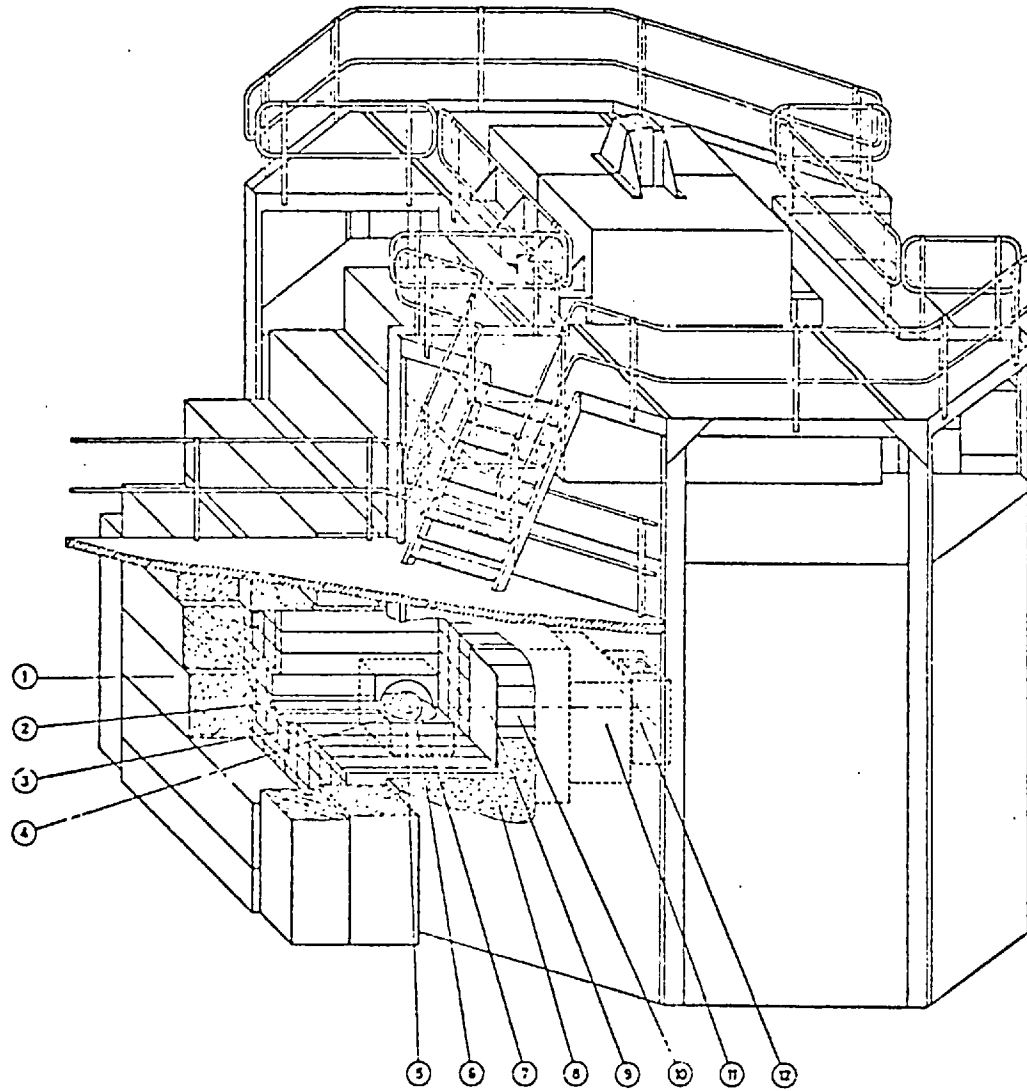


Figure 5.9 Installation of the NISUS facility on the reactor CONSORT

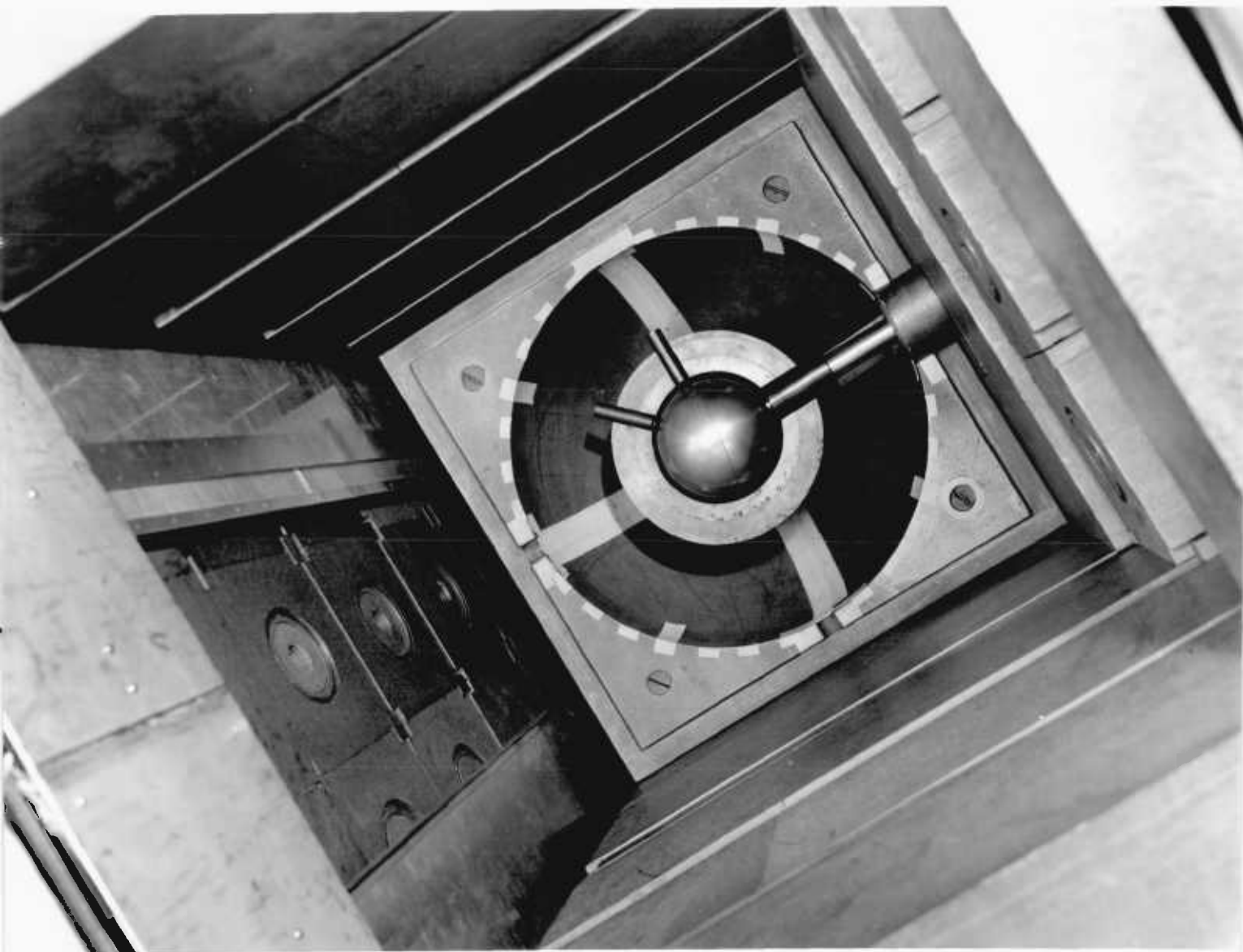


Figure 5.9b The Neutron Intermediate Standard Source (NISUS) which has been specifically designed and developed by AEE Winfrith in collaboration with Imperial College, London, to serve as an inexpensive fast neutron standard which could be adopted by a large number of laboratories as an international standard reference. It is driven by a thermal reactor and generates a neutron energy spectrum simulating that of the core and breeder of a fast reactor.

This photograph shows the hollow boron carbide shell positioned inside the lower hemisphere.

Reproduced by permission of United Kingdom Atomic Energy Authority and Imperial College.

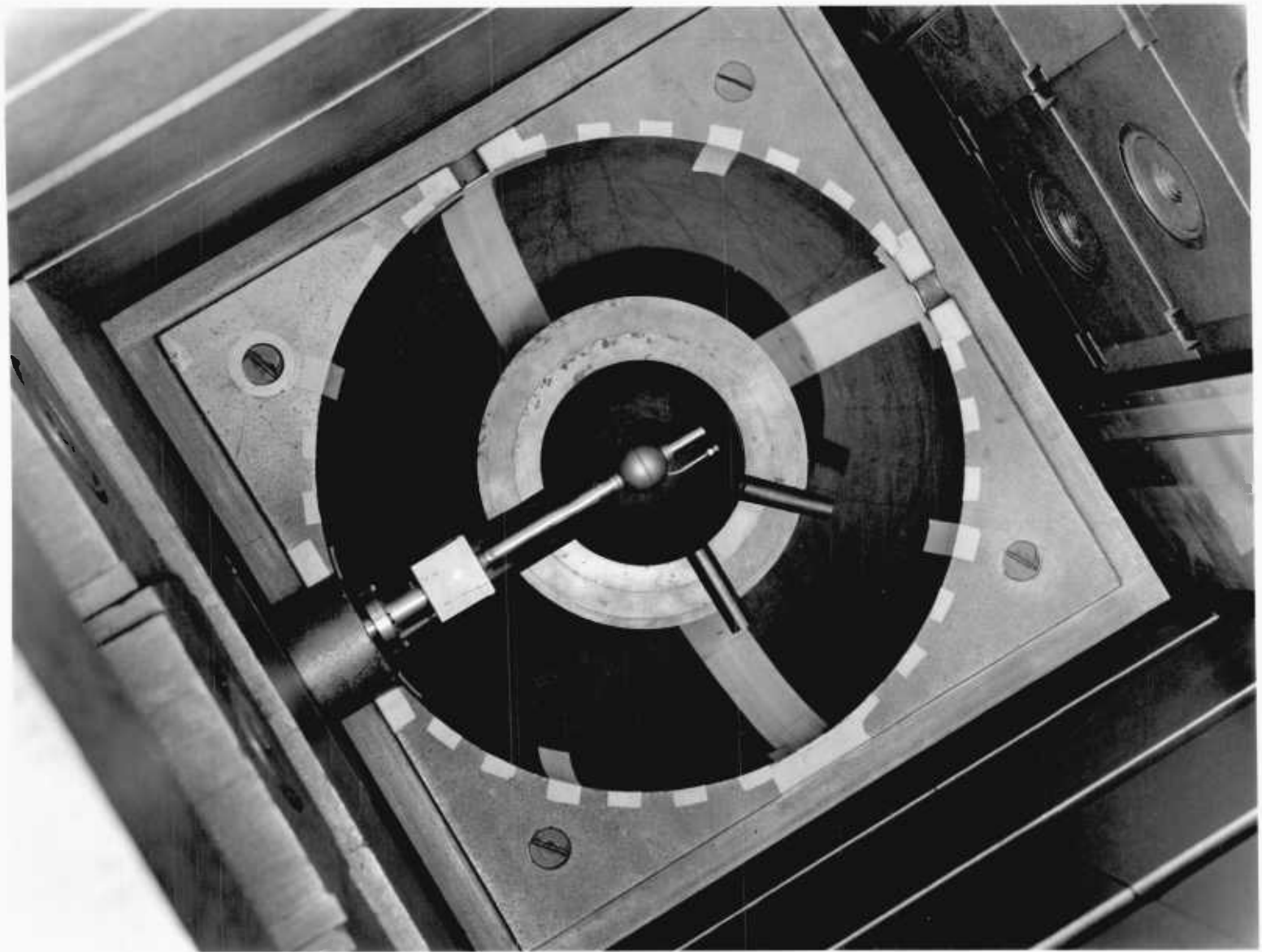


Figure 5.9c A photograph of the proton recoil proportional counter positioned inside the uranium shell, as used in the experiments

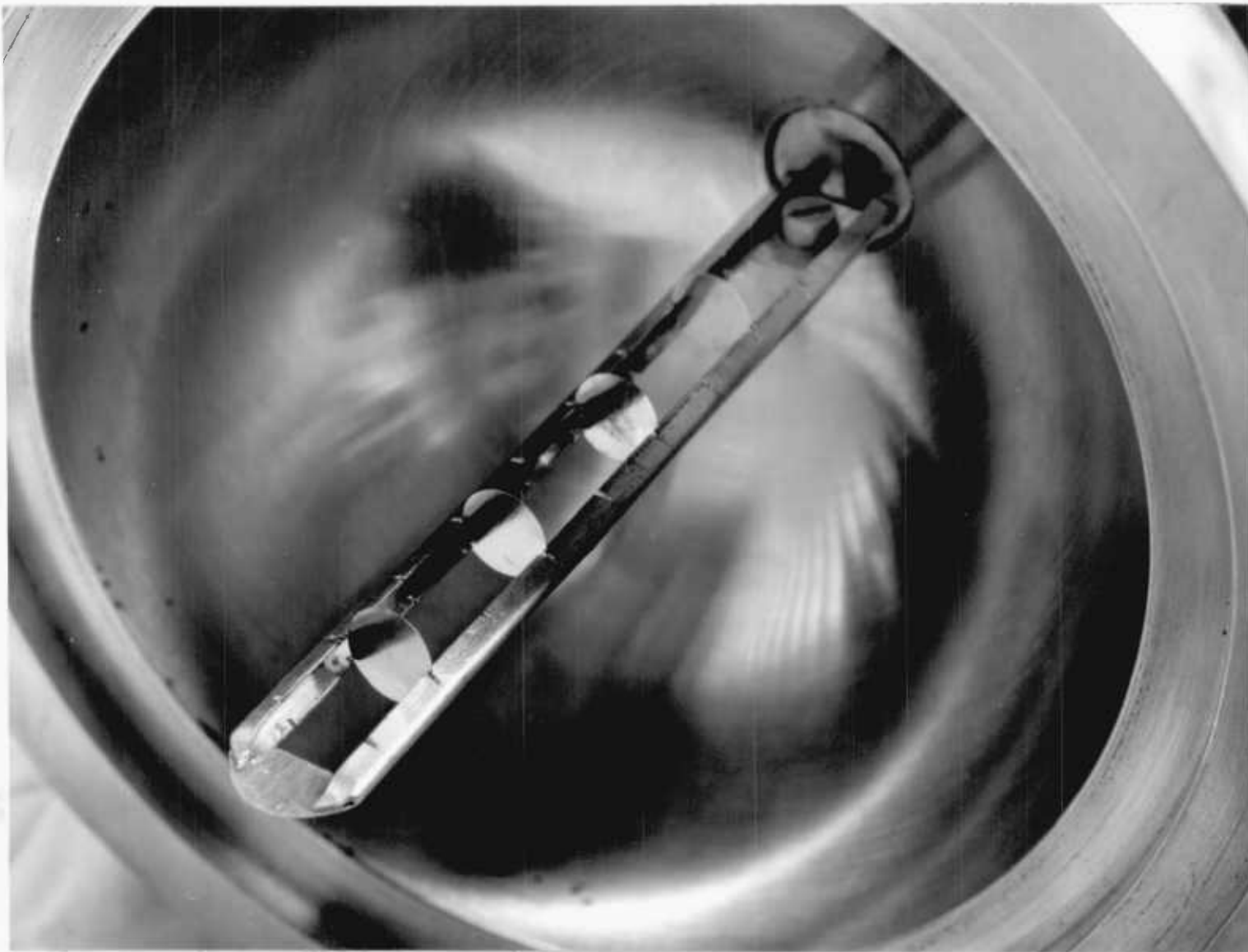


Figure 5.9 d A photograph of the foil holder. The Solid State Track Recorder was held in position next to the foil (i.e. one SSTR next to each foil)

Key:

1. Stackable Shielding Blocks
2. Graphite Stack
3. Movable Graphite Plug
4. Shielding Support Frame
5. NISUS Facility
6. Cadmium Shutter
7. Monolithic Reactor Shielding
8. Graphite Thermal Column Extension
9. Graphite Thermal Column
10. Reactor Core

Scale: 1/25

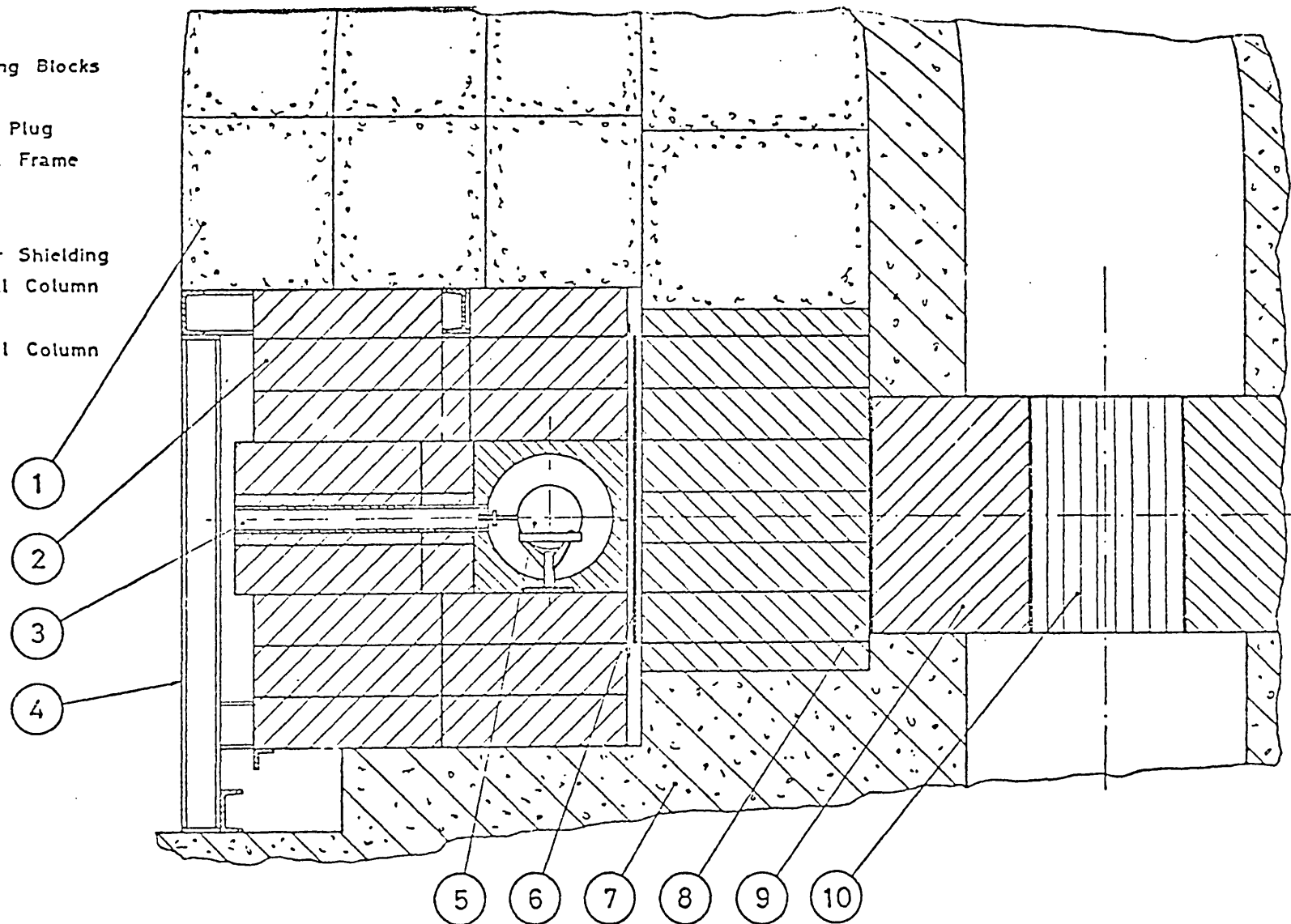
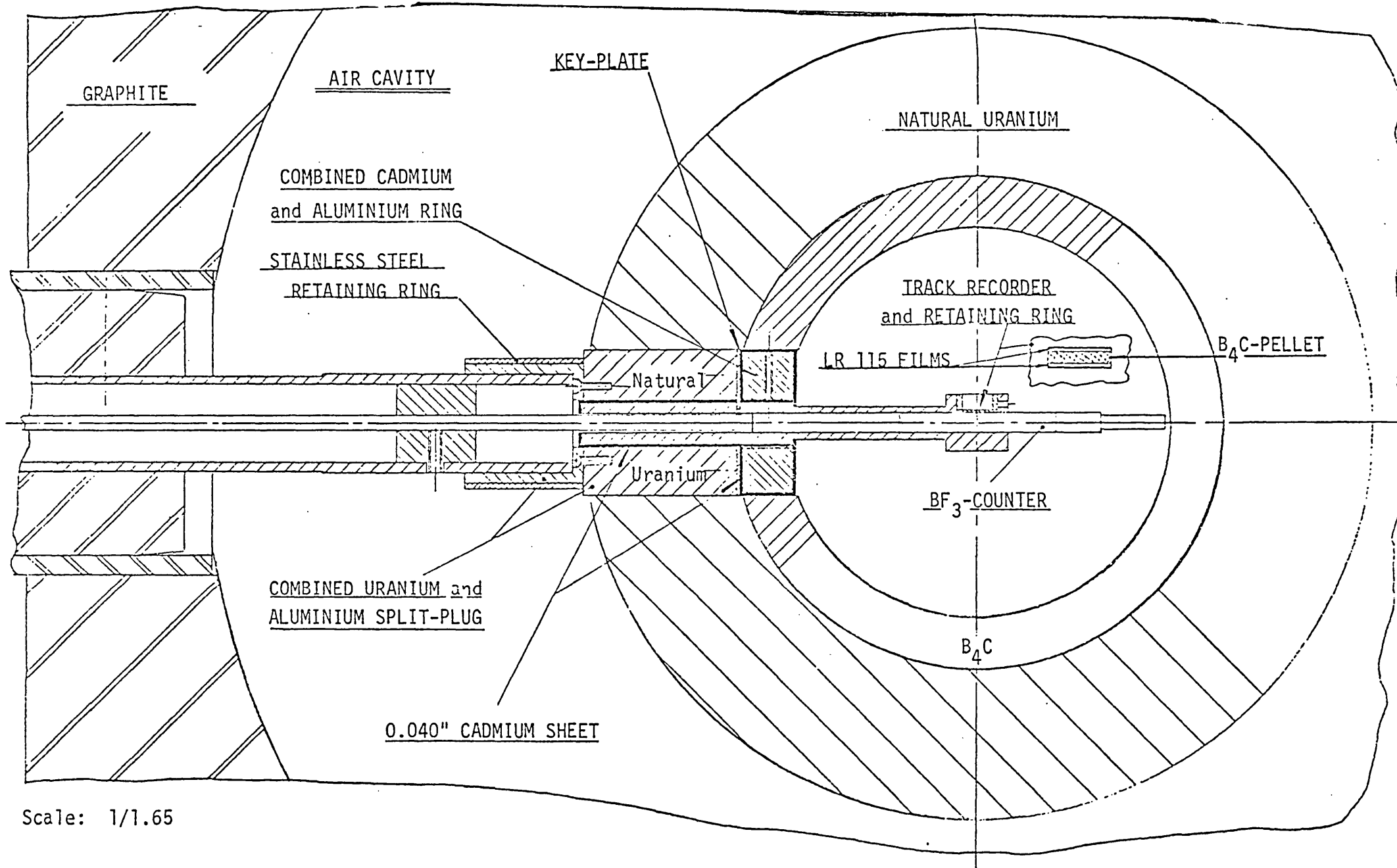


Figure 5.10 Cross-sectional side elevation on the thermal column extension



Scale: 1/1.65

Figure 5.11 A: Details of the demountable SSTR holder and the uranium-cadmium plug to simulate the closed-shell configuration when performing experiments inside the NISUS facility (i.e. NISUS 1b and NISUS 1a)

TABLE 5.4 a

AF = absolute neutron flux
 ME = mean neutron energy
 MEW = mean neutron energy weighed over the $^{10}\text{B}(\eta,\alpha)$ cross-sections
 \bar{R}_{th} (S) = theoretical response (i.e. not including the effects of the "critical angle for track detection" and counting efficiency)

Neutron Spectrum	AF (nv)	ME (MeV)	MEW (KeV)	\bar{R}_{th} (S) ⁻¹ (tracks.s ⁻¹ .cm ⁻² .RR ⁻¹)
1	5.075×10^4	0.253×10^{-9}	0.253×10^{-6}	0.4122×10^{-4}
2	2.30×10^8	0.908	3.222	0.4135×10^{-4}
3	2.50×10^8	1.327	6.109	0.4144×10^{-4}
4	2.50×10^8	1.358	43.65	0.4435×10^{-4}
5	3.0×10^9	0.507	121.4	0.4907×10^{-4}
6	3.0×10^9	0.537	149.1	0.4994×10^{-4}
7	3.0×10^9	0.580	201.1	0.5157×10^{-4}
8	2.1×10^8	0.928	255.8	0.5148×10^{-4}
9	2.1×10^8	0.926	258.2	0.5160×10^{-4}
10	1.896×10^5	0.253×10^{-9}	0.253×10^{-6}	0.4122×10^{-4}

where:

$$ME = \frac{\sum_{i=1}^G \phi_i (E_i + E_{i+1})/2}{\sum_{i=1}^G \phi_i}, \quad G = \text{number of energy groups}$$

$$MEW = \frac{\sum_{i=1}^G \phi_i \sigma_i (E_i + E_{i+1})/2}{\sum_{i=1}^G \phi_i \sigma_i}, \quad \bar{R}_{th} (S) = \bar{R}_{\alpha th} (S) + \bar{R}_{Li th} (S)$$

TABLE 5.4 b

CENTRAL NEUTRON SPECTRUM IN NISUS 3a ASSEMBLY (44)
SPECTRUM -3-

Group	Energy Boundaries (MeV)	Flux*
	0.100 x 10 ⁻⁸	
1	0.275 x 10 ⁻³	0.06500
2	0.454 x 10 ⁻³	0.01093
3	0.748 x 10 ⁻³	0.01157
4	0.123 x 10 ⁻²	0.01215
5	0.204 x 10 ⁻²	0.01353
6	0.335 x 10 ⁻²	0.01445
7	0.553 x 10 ⁻²	0.01586
8	0.912 x 10 ⁻²	0.01734
9	0.150 x 10 ⁻¹	0.01925
10	0.248 x 10 ⁻¹	0.02381
11	0.409 x 10 ⁻¹	0.02873
12	0.674 x 10 ⁻¹	0.03803
13	0.111	0.05378
14	0.183	0.07779
15	0.302	0.1105
16	0.498	0.1560
17	0.821	0.1934
18	1.350	0.1813
19	2.230	0.1601

TABLE 5.5 a

CHECKING OF BF₃-COUNTER PERFORMANCE, AND SELECTION OF REACTOR POWER DOMAIN TO PERFORM THE EXPERIMENTS

Thermal Stack - Mid Point - Shutter Open					
Counting Length (secs)	BF ₃ Dose (x 10 ²)	FC Dose (x 10 ²)	RP Reactor Power (W)	BF ₃ /FC	BF ₃ /RP (cps/W)
1000	32.33	10.88	1	2.97	3.23
100	27.80	8.24	10	3.37	2.78
100	109.35	31.00	40	3.53	2.73
100	193.15	55.13	70	3.51	2.76
100	286.07	78.95	100	3.62	2.86
100	414.39	116.24	150	3.56	2.76
100	602.00	156.55	200	3.85	3.01
100	842.11	237.86	300	3.54	2.81
100	1399.00	396.28	500	3.53	2.80
100	2761.57	795.55	1000	3.47	2.76
100	7684.42	2286.16	3000	3.36	2.56

* HSE = High Statistical Error

** OSE** = Out of Statistical Error

TABLE 5.5 b

CHECKING OF BF₃-COUNTER PERFORMANCE, AND SELECTION
OF REACTOR POWER DOMAIN TO PERFORM THE EXPERIMENTS

Thermal Stack - Mid Point Shutter Closed					
Counting Length (secs)	BF ₃ Dose (x 10 ²)	FC Dose (x 10 ²)	RP Reactor Power (kW)	BF ₃ /FC	BF ₃ /RP (cps/kW)
100	25.14	7.34	3	3.43	8.38
100	82.66	24.53	10	3.37	8.27
100	161.22	46.87	20	3.44	8.06
100	245.92	70.07	30	3.51	8.20
100	329.45	92.35	40	3.57	8.24
100	414.78	118.38	50	3.50	8.30
100	488.01	140.97	60	3.46	8.13
100	577.04	163.33	70	3.53	8.24
100	649.60	184.66	80	3.52	8.12
100	731.58	209.81	90	3.49	8.13
100	809.83	231.86	100	3.49	8.10

* HSE = High Statistical Error

TABLE 5.5. c

CHECKING OF BF₃-COUNTER PERFORMANCE, AND SELECTION
OF REACTOR POWER DOMAIN TO PERFORM THE EXPERIMENTS

NISUS 3a - Centre of Assembly - Shutter Open					
Counting Length (secs)	BF ₃ Dose (x 10 ²)	FC Dose (x 10 ²)	RP Reactor Power (kW)	BF ₃ /FC	BF ₃ /RP (cps/kW)
1000	646.92	278.73	1	2.32	64.7
100	687.00	287.69	10	2.39	68.7
100	990.51	417.41	15	2.37	66.0
100	1330.28	556.18	20	2.39	66.5
100	1662.51	701.92	25	2.37	66.5
100	2014.51	851.67	30	2.37	67.2
100	2697.07	1132.32	40	2.38	67.4
100	3389.84	1416.89	50	2.39	67.8
100	4070.96	1701.32	60	2.39	67.9
100	5414.07	2259.51	80	2.40	67.7
100	6742.24	2813.80	100	2.40	67.4

*HSE = High Statistical Error

TABLE 5.5 d

THERMAL STACK IRRADIATIONS - SHUTTER CLOSED

(Figures in parentheses correspond to counts per 100 kW seconds)

Film Number	Reactor Power (kW)	Irradiation Length (min)	BF ₃ Dose (x 10 ⁶)	FC Dose (x 10 ⁶)	BF ₃ /FC
501	100	40	1.690 (704)	0.473 (197)	3.573
503	100	20	0.849 (708)	0.236 (197)	3.597
505	50	20	0.428 (713)	0.112 (187)	3.821
507	100	30	1.290 (716)	0.342 (190)	3.772
503*	100	20	0.849 (708)	0.236 (197)	

TABLE 5.5 e

NISUS 3a IRRADIATION - SHUTTER OPEN

(Figures in parentheses correspond to counts per 100 kW seconds)

Film Number	Reactor Power (kW)	Irradiation Length (min)	BF ₃ Dose (x 10 ⁶)	FC Dose (x 10 ⁶)	BF ₃ /FC
309	100	5	1.960 (6533)	0.866 (2887)	2.263
407	50	10	2.020 (6733)	0.858 (2860)	2.354
307	100	10	3.920 (6533)	1.720 (2867)	2.279
409	50	20	3.900 (6500)	1.680 (2800)	2.321
307*	100	10	3.920 (6533)	1.720 (2866)	2.279

*Films for background measurements.

5.4 The Development of Charged Particle Tracks

There are several ways for revealing tracks in solid-state track recorders. Regions damaged by the charged particles cause electron diffraction and therefore they can be observed directly by transmission and scanning electron microscopy.

5.4.1 Transmission electron microscopy (TEM)

It is possible to view charged particle tracks with density $> 10^{10}$ tracks/cm² directly with a transmission electron microscope (Figure 5.12). Besant (111) had observed unetched fission fragment tracks in a polycarbonate known as Lexan. He prepared thin films of Lexan (less than 1 μ m) by dissolving the plastic in methylene chloride, which was a suitable solvent. A small drop of the solution was placed on the surface of some mercury in a watchglass. The Lexan solution spread over the surface, the solvent evaporated and a thin film of Lexan resulted. The thickness of the film depended on the original ratio of plastic to solvent.

The films, which were approximately 0.5 μ m thick were very delicate and it was difficult to avoid damage. A copper grid was laid on the Lexan film when the solvent had nearly all evaporated. The film attaches itself to the grid and this increases its strength. One of the main problems encountered in observation was due to electron scattering which resulted in a build-up of charge on the film; this led to a temperature rise which caused severe distortion and sometimes melting and breaking down of the film. Moreover with this technique the plastic film must be very thin (less than one micron) so that it can remain stable in the electron beam. The thin specimen should be supported on a fine copper wire grid to reduce charging in the film. Only a very small portion of the total range of an energetic heavy charged particle can be examined. Thus, this technique seems to be complicated and not useful for the majority of particle energy measurements for which less complicated methods should be used.

Examination of replicas taken from the surface of the detector demonstrated that this was a more reliable technique and more sensitive than the previous one, and gave good resolution down to 10 Angstroms. This latter technique is unique from the point of view of investigations of the structure of tracks and early stage of track revelation which is explained in Chapter Six.

5.4.2 Scanning electron microscopy (SEM)

Scanning electron microscopy is much more straightforward than the transmission electron microscopy, and is suitable for a high track density (Figure 5.13). The samples must be coated with a conducting layer before observation. This technique allows a detailed investigation of the tracks structure and the early stages of revelation of tracks when they intersect the surface.

In a scanning electron microscope a primary electron beam, emitted from a heated tungsten filament, is focussed into a fine electron probe on the specimen and made to scan and raster - similarly to television techniques - on the surface by a detection system. Electrons liberated from the specimen by the focussed primary beam are detected by a photomultiplier tube with a scintillator mounted on top.

The photomultiplier output signal is used to modulate the brightness of the electron beam in a cathode-ray tube, which is scanned in synchronism with the electron probe. The resolution depends upon the diameter of the electron probe, the accelerating voltage, the detector system and the type of specimen.

5.4.3 The decoration method

The crystal is exposed after irradiation, to a pulsed electric field of 4 kV/cm and to a simultaneous pulse of ultraviolet light with 10^9 photons per pulse at a repetition rate of about 1000 sec^{-1} . The photoconduction electrons and holes produced by absorption of the photons in a surface layer of several microns, are swept through the crystal by the electric field. Electrons trapped at defects that are along the path of the incident particle react with diffusion (+) ions of the target medium, thus producing the decoration of the track as a chain of metal atom spots as well as of other disturbed structures of the crystal such as dislocation lines. That is a visible second phase layer of material along the damaged region is preferentially formed which optically is distinguishable from the surrounding material. As can be seen this technique is highly effective for ionic crystals such as silver chloride and certain glasses doped with silver (in these cases the positive ion is the Ag^+ ion).

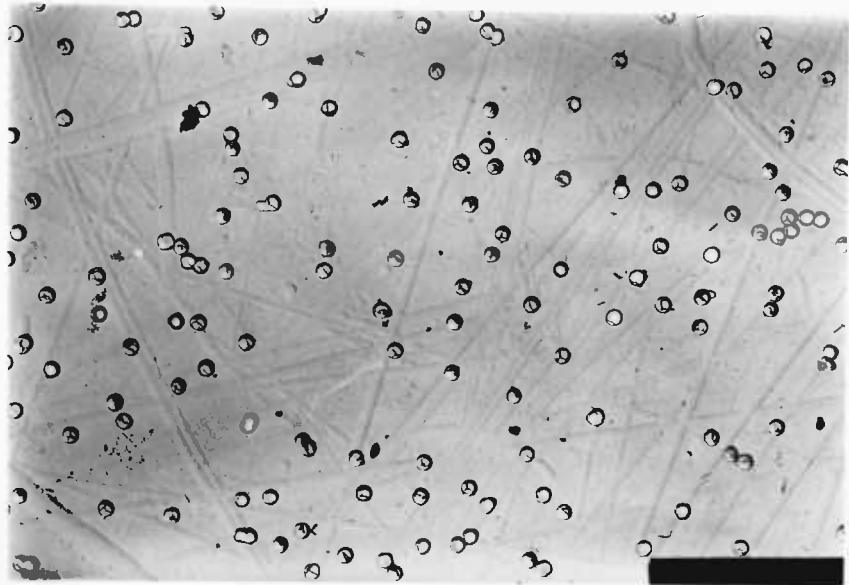


Figure 5.12 Electron micrograph of 5 MeV alpha tracks in CA80-15 (Kodak-Pathe, France) at 90° incidence, etched in 2.5 N sodium hydroxide at 18°C , for 26 hours (3 K x 2).

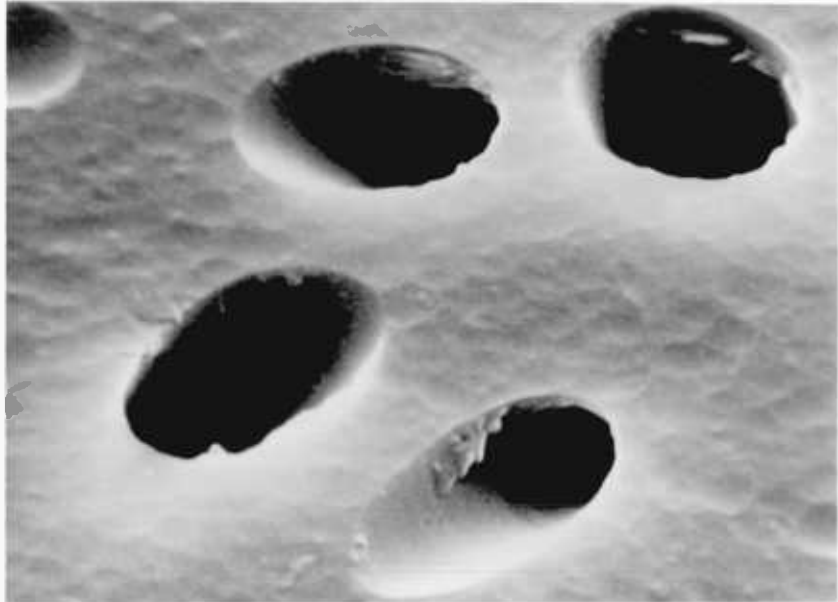


Figure 5.13 Scanning electron micrograph of 5 MeV alpha tracks in CA80-15 (Kodak-Pathe, France) at 70° incidence, etched in 1.5 N sodium hydroxide at 18°C for 26 hours (50 K x 2).

5.4.4 The graft-and-dye method

This technique is used to detect unetched tracks using an optical microscope. It is successful for open structure polymers which allow the grafting monomer to diffuse through the bulk material and graft onto the tracks originating from the inside of the detector but not necessarily intersecting the surface of the detector. The grafting molecules join onto the free radicals created by the radiation damage.

We have successfully grafted irradiated cellulose nitrate by swelling the cellulose nitrate in 75% concentrated zinc chloride solution, and then adding 15% acrylic acid solution degassed by freezing at liquid nitrogen temperature and pumping the system several times to 10^{-3} torr for 35 minutes.

The grafting was carried out at normal temperature (18°C) for five hours. To increase the contrast between bulk material and tracks, the grafted sample is dipped in a 100 ppm Rhodamine B solution in distilled water, with pH between 4 and 5, for 10 minutes at boiling water temperature, and finally the excess dye is washed out by boiling in soapy water.

Since Rhodamine B is a fluorescent phosphor we view the sample with an optical microscope equipped with an ultraviolet lamp.

The advantage of this technique is the ability to observe tracks originating inside the detector and not intersecting the surface, e.g. when energy loss at the surfaces of the detector is too small to create enough free radicals for grafting. But this method is quite complicated and not every grafting operation is successful.

However, track length measurements give the range of the particle in the medium only if the non-revealed part of the particle near the surface can be separately calculated, as in the case of etching where the amount of removed surface can be found from the bulk etching rate. In the case of grafting it is difficult to see how the non-revealed part of a particle track could be calculated when the grafted track does not reach the surface. For tracks originating in the medium itself via nuclear reactions, this criticism would not apply.

5.4.5 Base-exchange and scavengers

1. Base-exchange

Acidic groups are formed inside the latent track as a result of the chemical processes following the passage of a charged particle. These acidic groups can exchange their weakly bound hydrogen ions (protons) for cations in solution, which penetrate the latent track. Typical cations undergoing base exchange are Na^+ , K^+ , Ca^{++} and Ba^{++} . These cations diffuse into the track and replace the protons in the acidic groups. In the case of calcium and barium, the resulting white deposit renders the track visible under the microscope (see Figures 5.14 and 5.15).

2. Scavengers

Scavengers react with free radicals to form relatively stable compounds. Important scavengers include iodine, DPPH and ferric chloride. Iodine and DPPH (the stable free radical diphenylpicrylhydrazyl) can be dissolved in organic solvents such as hexane and dioxan, and then are able to penetrate into the cellulose nitrate due to the solvent action. When the DPPH radical reacts with a free radical inside a latent track, it loses its characteristic strong violet colour. Tracks are thus revealed as regions of light colour in a dark background.

These two techniques will be discussed in detail, with experimental procedures and results in Chapter Seven.

5.5 Latent Track Revelation by Chemical Etching: Introduction

A more general method of making visible the tracks intersecting the surface is by selective chemical etching in a suitable reagent, which permits direct study of tracks via the optical microscope, where densities of tracks and total ranges can be easily measured (see Figures 5.16 and 5.17).

The chemical etching effect was first discovered in synthetic mica by Young (1). When pre-thinned mica flakes containing fission fragment tracks were immersed in a suitable reagent, the volume of material composing the tracks was selectively attacked. The reagent etched fine hollow channels along the paths taken by the fission fragments and left the rest of the mica essentially untouched. With increasing immersion time the etchant enlarged the channels by dissolving the

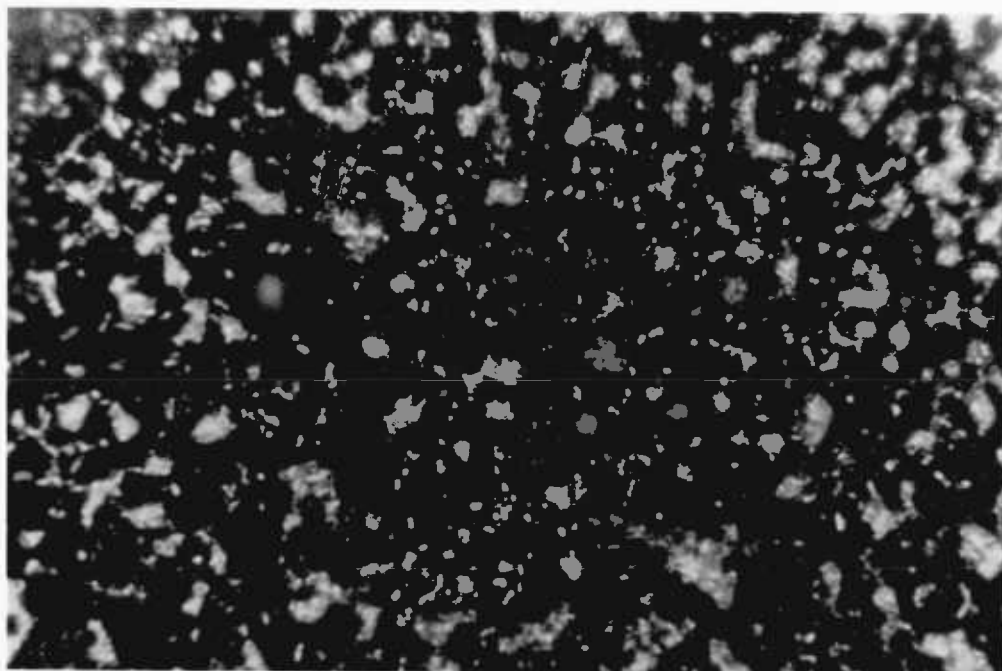


Figure 5.14 Photomicrograph of 0.60 MeV overlapping proton tracks in CA80-15 (Kodak-Pathe, France) at 90° incidence, pre-swollen in 65% zinc chloride solution for 2 hours at 18°C , then treated with calcium hydroxide (base-exchange) for 26 hours.

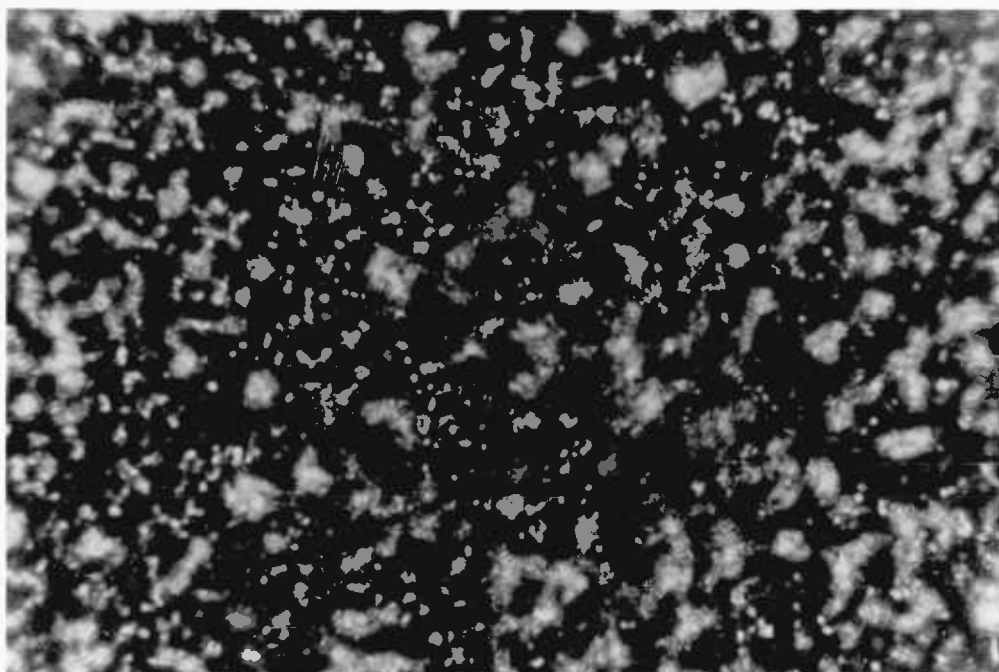


Figure 5.15 Photomicrograph of 0.60 MeV overlapping proton tracks in LR115 type 2 (Kodak-Pathe, France) at 90° incidence, pre-swollen in 65% zinc chloride solution for 2 hours at 18°C , then treated with calcium hydroxide (base-exchange) for 26 hours.



Figure 5.16 Photomicrograph of fission tracks in soda lime glass at 90° and 70° incidence.

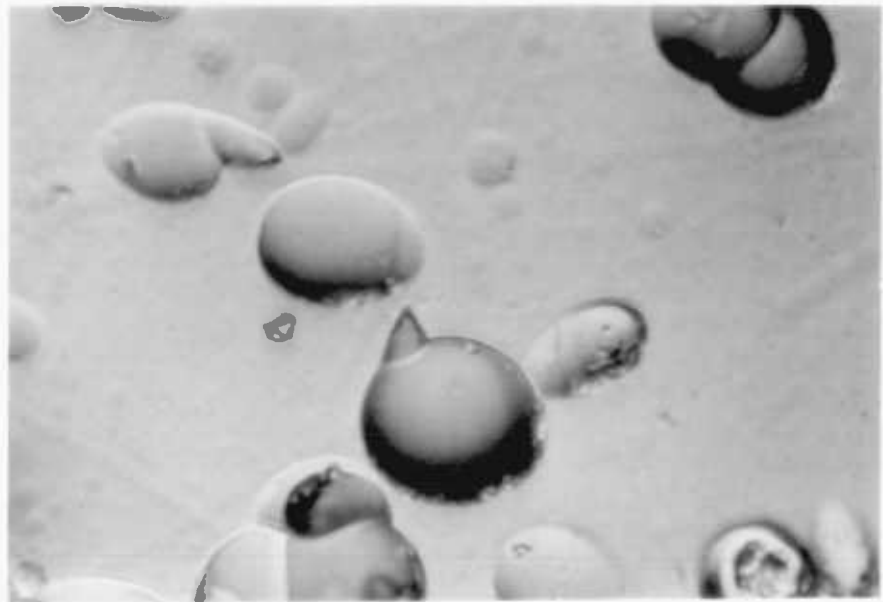


Figure 5.17 Photomicrograph of fission fragment tracks in soda lime glass in 2π geometry.

surrounding mica at a rate which varied with the type and temperature of the reagent.

The geometry of the etched tracks varies with the substance being examined, the solvent used, and the time and temperature of attack. There are only general guide lines to aid the experimenter in choosing the proper etching conditions for track development, and any new detector substance must still be approached empirically. Almost any insulator can be used as a charged-particle track detector, with track revelation achieved via a suitable etchant.

5.5.1 Required properties of the etchant

Following are some of the important requirements of the etching systems:

- (i) the reagent when used under suitable experimental conditions should be able to etch the general surface with a uniform velocity all along it and should produce the minimum number of background etch pits,
- (ii) the reagent must be able to etch the latent damage track with a preferential velocity V_T which is greater than the bulk etching velocity V_B and independent of the dip-angle θ between the latent track and the detector surface, or,
- (iii) the expected response of the detector has to be such that, with the use of a particular etchant, the variation of V_T with the ionization rate, J , of the particle should be able to yield the necessary resolution for the particular measurement for the purpose of charged particle identification.

5.5.2 Etching precautions

For accurate quantitative work in track analysis, it is not enough to know only about an appropriate etchant for the detector concerned, but also one must have a reasonable knowledge of the effects of certain environmental factors which play important parts before, during and after the irradiation and before and during the etching process itself. A very brief account of some of the important precautions is given below.

5.5.3 Starting material

It has been observed that the composition of a given plastic differs slightly even among different batches from the same manufacturer. Thus, for reproducibility, if possible the observations should be made

with plastics from the same batch kept under similar environmental conditions, preferably kept at low temperature and in ionization-free environments. It was found that a rapid change of the environment of samples of different batches will make them similar. In cellulose nitrate we found that if samples of different batches were soaked overnight in a bath of distilled water or a bath of 75% concentrated zinc chloride solution, and then dried with hot air at 80°C, the sensitivity of the different batches increases and becomes similar, especially if this procedure is repeated more than twice for the same samples.

5.5.4 Irradiation environment

The presence of oxygen and water vapours or the absence of these during irradiation yields entirely different results for the finally etched tracks (73,112). Even the sensitivities of various detectors change considerably. Thus a careful control of these environmental factors during the irradiation process is essential. In post-irradiation storage, trapped free radicals in the irradiated cellulose react with oxygen and water vapour, as these compounds slowly diffuse into the more ordered regions of the fibrous cellulose and react with the free radicals. The concentration of the long-lived free radicals decrease with increasing moisture content. Oxygen could also react with the free radical to form a peroxy radical (at C₅ to form C₅O); on the decomposition of this free radical, a carbonyl group would be formed and on breaking the anhydroglucose ring, depolymerization would occur. Also an oxygenated radical on C₅ could result, enhancing the formation of tracks by etching.

5.5.5 Steady state reactivity of latent track

Many authors have observed that after irradiation the reactivity of the damage trail in plastics increases with ageing time, first quite rapidly and then at a decreasing rate, reaching a steady state after a time which is a function of the plastic used and the ambient temperature (113). Thus, for reproducible results, either the samples should be etched after equal ageing times, or they should be allowed to attain the steady state reactivities before being etched.

The environmental effects and the reactivity changes can be minimized by creating a stable molecular species immediately after irradiation e.g. by soaking the sample in weak hydrogen peroxide

solution for about ten hours at room temperature, thus oxidizing the free radicals into a fairly stable reactive molecular species.

5.5.6 Sensitization methods: direct photolysis

When irradiated plastics are exposed to U.V. radiation in the presence of oxygen, an appreciable increase in the reactivity of the damage trail is observed (114). Similarly a slight reactivity increase is caused by other forms of ionizing radiation, such as X-rays and energetic electrons. This means that either the presence of these radiations should be totally excluded or, in case an enhanced sensitivity is desired, a uniform exposure to a controlled dose of U.V. radiations throughout the detector volume should be carried out.

Sensitizers initiating photo-oxidation include benzophenone (115) benzoquinone (116) hydrogen peroxide (117) and azo compounds (118). For each of these sensitizers the pattern of chemical change is similar. In the absence of oxygen primary and secondary alcohols are converted into the corresponding carboxyl compounds and the sensitizer is hydrogenated. In oxygenated solutions, primary alcohols yield hydrogen peroxide, the corresponding aldehyde, and carboxylic acid, secondary alcohols yield almost exclusively the ketone and hydrogen peroxide. From this brief consideration of the factors that control the photosensitization of model systems, it is clear that if a fundamental understanding of the processes that occur during the sensitization of cellulose nitrate under the influence of light is to be obtained, it is necessary to consider the following factors:

- (i) the wavelength of the radiation used
- (ii) the atmosphere surrounding the sample during exposure
- (iii) dampness of the sample during exposure.

Direct photolysis leads to rupture of the chemical bonds by the absorption of light. It is therefore necessary that the energy of the absorbed quanta be sufficient to achieve bond scission. For cellulose the cleavage of either carbon-carbon or carbon-oxygen bonds will require an energy of 80-90 kcal/mole. About 100 kcal per mole is needed to break a carbon-hydrogen bond (119) and about 40 kcal/mole is needed to break the weakest bond - NO_2 for cellulose nitrate.

During irradiation with monochromatic light of frequency ν , quanta of known energy ($h\nu$) are delivered. Generally the photochemist refers to a mole of quanta ($Nh\nu$, where N is Avogadro's number), and this is

called an einstein of radiation. The energy E per mole of quanta is given in kilocalories and can be evaluated from the following formula:

$$E = \frac{2.858 \times 10^5}{\lambda} \text{ kcal/einstein}$$

where λ is in angstrom units. Thus it can be seen that light of wavelength of 4000 Å wavelength is equivalent to 71 Kcal 3000 Å to 95 Kcal, and 2000 Å to 143 Kcal. Therefore, provided that light is absorbed by the cellulose molecule, the energy requirement for the sensitization of cellulose by direct photolysis is met by ultraviolet light with a wavelength of 3400 Å or shorter, and for cellulose nitrate this maximum wavelength is considerably longer ($\sim 7000 \text{ Å}$). The exact mechanism of photosensitized degradation is difficult to ascertain; the disruption of the bond between C_1 and C_2 will not necessarily cause immediate rupture of the cellulose chain. But C_1 , attached in this case to possibly three electronegative groups, could be sensitive to subsequent thermal oxidation, thus disrupting the chain.

5.5.7 Latent Track Etching Techniques

Irradiated specimens were etched in various concentrations of aqueous solution of NaOH and KOH at various temperatures up to 60°C. This will be discussed in detail in Chapter Six. Stirring the solution has been proven not useful since it favours the bulk etching rate V_B over the track etching rate V_T .

When measuring track etching rates, the removal of the specimens from the etching solution and return to the solution after measurements has been proven to alter the etching rates, since a freshly etched surface reacts with the atmosphere to produce a thin layer of material whose etching properties are different than that of the bulk material. Also extended rinsing in water of partially etched tracks may result in large increase in both V_T and V_B for the remainder of the track, so the number of specimens which have been used in such an experiment is equal to the number of points or measurements which are needed.

A technique was devised for the observation of tracks during the actual etching process, but this will be discussed later in Chapter Six under the heading of induction time.

5.5.8 Latent Track Revelation by Electrochemical Etching

The irradiated plastic foil is placed between two Teflon cells containing an etching reagent such as 2.5 N NaOH. The output of the

H.V. function generator (\sim 1000 volts) which gives sinusoidal or positive square pulse wave forms, is applied through the irradiated insulator by two platinum electrodes placed directly in the reagent. A good contact between the plastic detector and the dividing wall of the containers, ensures electrical isolation of the two electrolytes.

At the beginning of the etching, the reagent rapidly diffuses in the pre-existing fine channels resulting from the passage of the incident charged particles, producing a conductive path, which penetrates the insulating foil. The AC current produced in this conductive path delivers energy mostly along the track which increases the damaged area of the detector, producing elongated and well defined alpha tracks and allows the enlargement of the damaged tracks at will. Failure of this technique is due to thermal and electro-chemical breakdown which may effect reproducibility and cause microscopic damaged regions.

Compared with the chemical etching, the rate of attack of the surface is increased. The conduction currents due to the mobile ions, and other forms of dielectric loss generate heat continuously in the electrically stressed insulator, which raises the temperature of the dielectric foil, thus increasing the chemical action of the reagent.

5.6 Instruments and Techniques for Etched Track Observation and Measurement

Detection of etched tracks may be achieved either by eye, using the optical microscope, or automatically by means of automatic counters.

A major inconvenience of the SSTR method is the necessity of visual counting of tracks, a task which is expensive, tedious and time-consuming. This drawback is clearly evident in precise measurements where inherent statistical limitations require the observation of large numbers of tracks for adequate precision. Moreover, in precise measurements, elimination of the human element is highly desirable, since it permits the introduction of quantitative standards for track recognition. Such standards would obviate problems of personal bias in manual track counting, which can otherwise influence experimental data and therefore must be constantly guarded against. Consequently, considerable interest exists in the automation of this task. The

Ozalid method (120) and light scattering are two of the earliest attempts in semi-automatic track counting. A spark counting method (121) applicable with plastic SSTR's such as Makrofol, Lexan and cellulose nitrate has been successfully demonstrated but possesses several limitations for precision work. Recent investigations take advantage of digital computers linked to automatic scanners (122). Three commercially available instruments, the Quantimet (123) of Inanco, England, the Classimat (124) of Leitz, Germany, and the Leitz Texture-Analyzing system or Leitz-T.A.S., have been used in automatic fission track counting. Some of the most common etched track detection techniques are briefly discussed in the following paragraphs.

5.6.1 Ozalid method

A simple and fast method for detecting holes in polymer films and plastic track detectors has been described by Block et al (120) of the General Electric Research Centre. It consists of placing the polymer to be examined on a sheet of Ozalid paper and passing the pair through the second (ammonia) stage of a conventional Ozalid machine. The ammonia vapour passes through the holes and darkens the Ozalid paper, clearly revealing the location of etched holes. For example, a particle track that has been etched to form a 50 μm diameter hole through a 100 μm sheet of plastic will produce as its Ozalid image a dark spot approximately 1000 μm in diameter.

The limitation of this technique lies in the following:-

- (i) the Ozalid image will be produced for only those etched tracks which penetrate all the way through the SSTR
- (ii) ammonia vapour degrades and swells some polymers such as cellulose acetate and cellulose nitrate, so the accurate spatial distribution of tracks is perturbed
- (iii) this technique cannot handle high track densities.

5.6.2 Light scattering

Track densities in transparent SSTR's such as in glass, Lexan and cellulose nitrate have been measured using light scattered from the tracks as a measure of the track density (125). Scattered light was found to be proportional to track density up to the point where tracks begin to overlap. For the two track detector materials tested, a scattering angle was found at which an optimum signal-to-background ratio is obtained.

5.6.3 Spark scanning

A spark counting system has been developed by Congel et al (126) for counting etched holes in thin dielectric plastics. The etched film is placed between two metallic conductors. One of the conductors consists of an insulating material with a thin metallic coating, such as aluminium coated Mylar. When 200-1500 volts are applied between the two conductors, spark discharges will occur at the sites of etched holes. Heat from the spark will cause the aluminium to be evaporated at the point of discharge, thus exposing the insulator and preventing additional discharges through the same hole. Discharges continue until all holes are counted, at which time no more discharges can take place. The number of sparks, which corresponds to the number of etched holes, is determined by an electronic network and a signal channel analyzer.

The efficiency of such a system is a function of the incident angle of the tracks; normally incident tracks have an efficiency of about 80%.

The limitations of this technique are:

- (i) this technique can be applied only for track densities less than 100 tracks/cm², and accuracies of 10% are expected,
- (ii) this technique is applicable to tracks penetrating all the way through the plastic,
- (iii) day-to-day reproducibilities of about $\pm 10\%$ have been obtained under carefully controlled conditions,
- (iv) the performance of this apparatus is affected by humidity.

5.6.4 Diffraction technique using laser light

A monochromatic, parallel light beam penetrates a circular hole in the Fraunhofer-diffraction arrangement. The intensity distribution of the Airy diffraction pattern at a point P on a screen placed parallel to the circular hole target is

$$I(P) = \left(\frac{d^2 \Pi}{4\lambda}\right)^2 \left\{\frac{2J_1(x)}{x}\right\}^2 \quad (5.1)$$

where d is the diameter of the circle hole, λ the wavelength of the monochromatic light, $J_1(x)$ the first order Bessel-function of the first kind and

$$x = \frac{\Pi d \sin \theta}{\lambda} \quad (5.2)$$

where θ is the angle between the parallel and diffracted beam (see Figure 5.18a. The intensity $I(P)$ has its principal maximum at $x = 0$; the places of secondary maxima and minima can be calculated from the conditions

$$\frac{d}{dx} \left(\frac{J_1(x)}{x} \right) = 0 \quad (5.3)$$

and

$$J_1(x) = 0 \quad (5.4)$$

If a number N of randomly distributed circular holes are placed in the way of the beam, the pattern will remain the same and the places of maxima and minima can still be determined by equations (5.3) and (5.4) with the intensity N times higher. Values for the places of maxima and minima are in Table 5.6 obtained by solving equations (5.3) and (5.4).

TABLE 5.6

MAXIMA AND MINIMA OF $J_1(x)$

x/π
1.220 min
1.635 max
2.233 min
2.679 max
3.238 min
3.699 max
4.241 min
4.710 max
5.243 min

Let k_1 be the x/π value corresponding to the i th minimum. D_i the diameter of the i th dark ring. Then taking into account Figure (5.18a)

$$\sin \theta_i = \frac{D_i}{2L[1 + (D_i/2L)^2]^{1/2}} \quad (5.5)$$

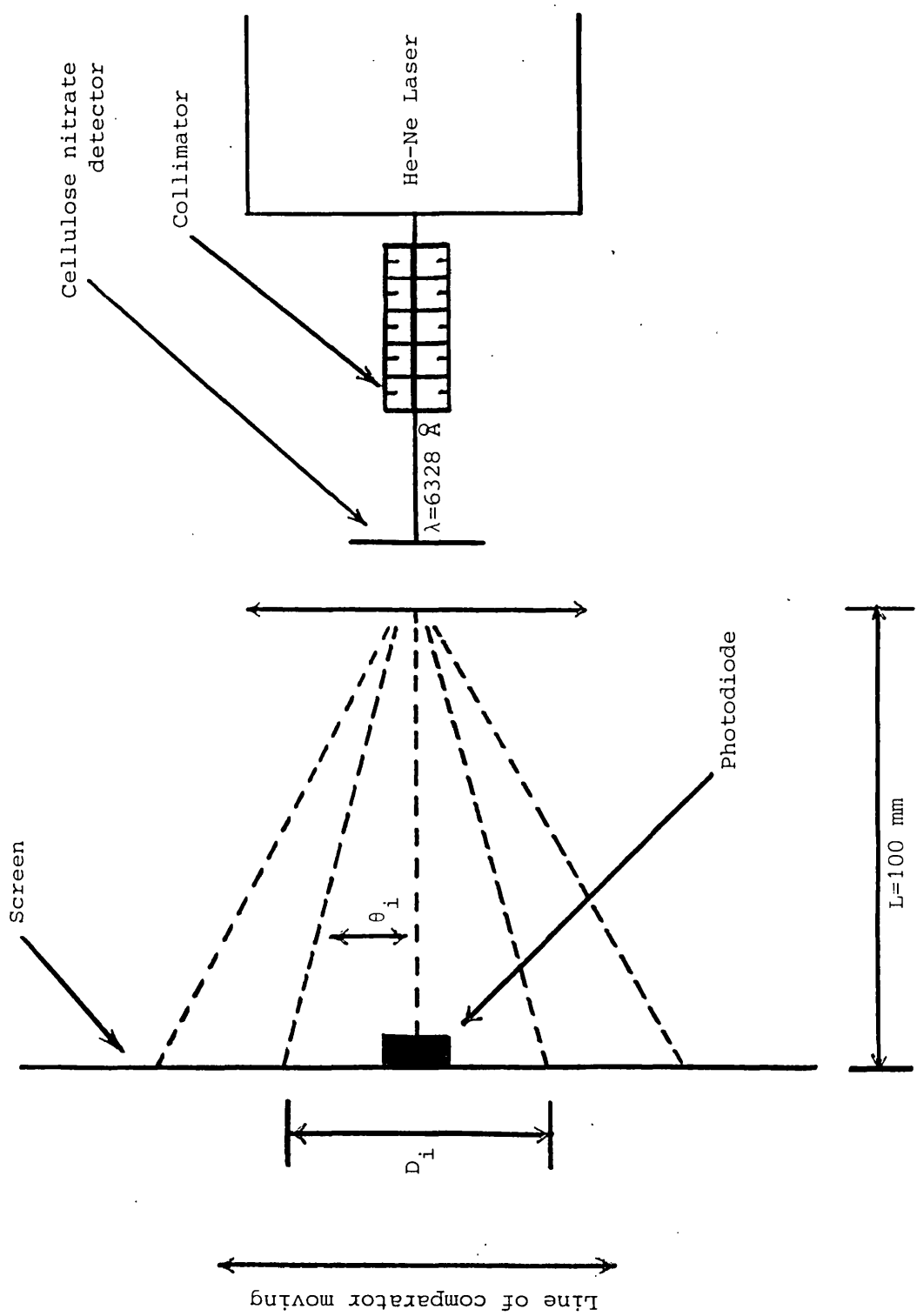


Figure 5.18a Experimental arrangement used for the track parameter measurements

from equation (5.2) and (5.5)

$$d = \frac{2 L \lambda K_i}{D_i} \{1 + (D_i/2L)^2\}^{1/2} \quad (5.6)$$

in a given arrangement (Figure 5.18a), by measuring the diameters of dark rings, knowing the wavelength of light and the focus distance of the lens (L), d can be determined.

(a) Experimental arrangement

A 5 mW He-Ne laser acting as a light source of $\lambda = 6328 \text{ \AA}$ was used with a cellulose nitrate track detector. The screen was set up into a comparator with an accuracy of 0.001 mm, which was moved in the line perpendicular to the laser beam; the screen was placed into the focal plane of a quartz lens of L; 100 mm focal distance (see Figure 5.18a). In such a way the Fraunhofer-diffraction arrangement was realized. A photodiode with an active surface of $0.3 \times 3.5 \text{ mm}^2$ was set up on the screen and its output was fed directly to a plotter. The comparator was moved by a motor with constant velocity. In such a way the intensity distribution and the diameters of dark rings (D_i) could be determined. More simply, D_i could be determined directly by visual measurement and the average diameter was calculated by equation (5.6) and with the slope of the line going through the origin, and fitted to the experimental points (D_i, k_i). The error of the slope and that of the diameter were estimated by the maximum likelihood method.

(b) Results and conclusions

Diffraction patterns with at least two well measurable dark rings were obtained; the track-area density interval $Nd^2/(4A)$ from 0.015 to 0.45, where "A" is the total area of the tracks on the detector surface (for N tracks).

The values of track diameters determined by the diffraction method were in good agreement with those measurements which were done with the microscope, provided that only two dark rings were considered. Taking into account higher order rings as well, the deviations were about 5-10% (see Figures 5.18b, 5.18c).

It can be seen clearly that this technique is tedious and that no advantage was obtained over the direct measurements via the microscope.

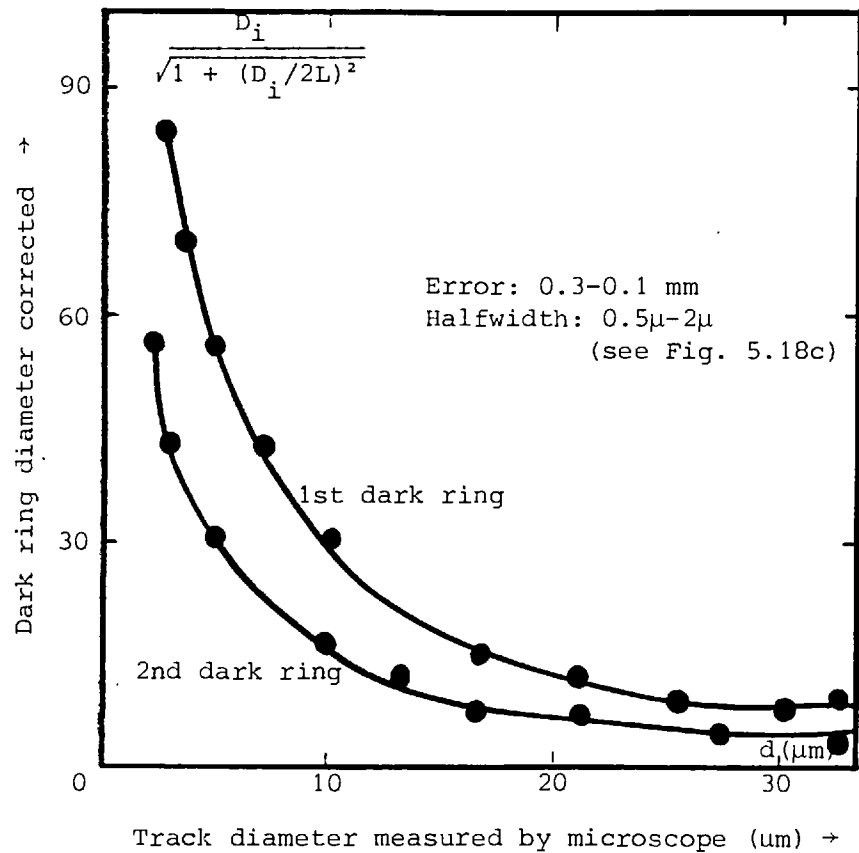


Figure 5.18b The diameters of the 1st and 2nd corrected dark rings (in μm) as a function of track diameter. The solid curves were calculated using equation 5.6

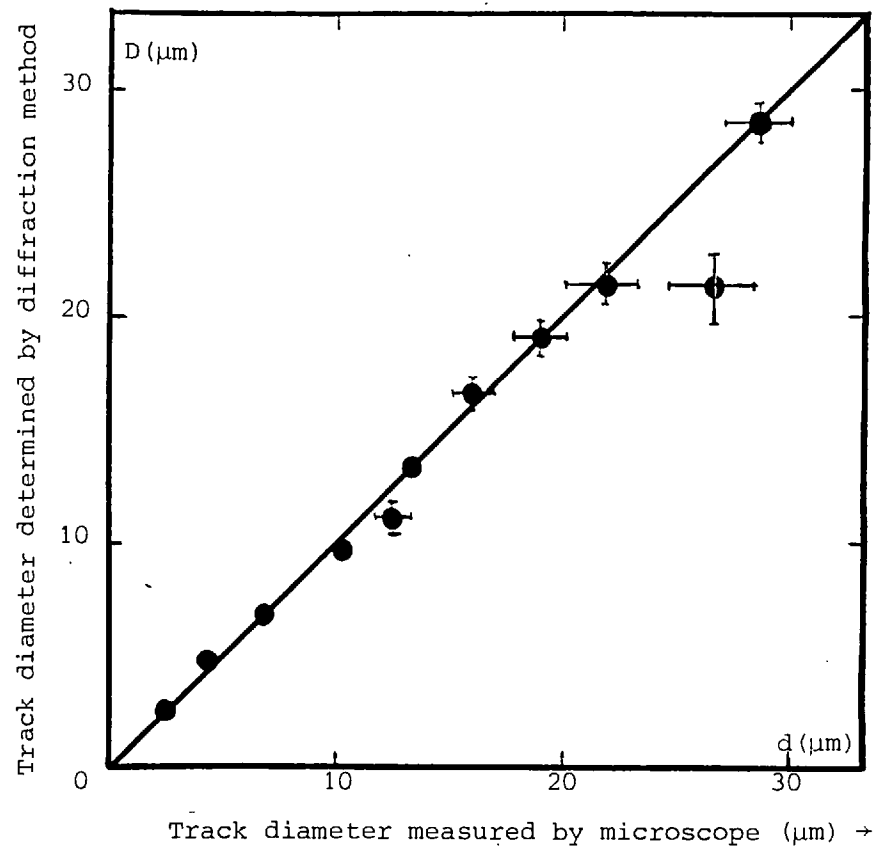


Figure 5.18c D-d relation. The diameters D were calculated from the 1st and 2nd dark rings (see text), the d values were measured by microscope. The error bar of d gives the halfwidth of the track diameter distributions

5.7 Optical Microscope Technique for Track Analysis

The dimensions of the chemically etched tracks may vary from a fraction of a micron to several microns. The observation and the measurement of the tracks requires the use of an optical microscope. The precision with which track parameters of interest (such as track length, cone angle, or surface openings) may be measured depending upon the optical resolution attainable as well as the ability to perform the actual measurements.

The microscopy of etched tracks has a number of unusual aspects that are generally not encountered in ordinary optical microscopy. The problem centres on the etched tracks being in the form of transparent cavities rather than opaque objects such as silver grains in nuclear photographic emulsions. Some of the major difficulties encountered are as follows:

- (i) The difference in the index of refraction of the track cavity and the bulk material is relatively small.
- (ii) Inhomogeneities and inclusions present in most commercial plastics cause a variation in the index of refraction of the bulk material.
- (iii) The often heavily pitted surfaces of the etched plastics degrade the quality of the optical image.
- (iv) Thick specimens may require objectives and condensers with larger working distances than usually available.
- (v) Thick cavities tend to fill up with liquids when immersion objectives are used, thus reducing track image contrast.
- (vi) Track dimensions may be small, requiring the use of high numerical aperture (N.A.) objective - condenser combinations.

Most of these difficulties can be overcome by the use of either one or a combination of the optical techniques that are described below.

5.7.1 Bright-field, transmitted light illumination

a. Dry objectives

Dry objectives are easy and convenient to use for many measurements at low magnifications. They facilitate easy access to track observations and rapid scanning of specimens. Their main attraction is that a few dry lenses, even of moderate magnifying power, have long working distances. This permits the observation of steeply dipping,

long tracks when tilting of the specimen is required. The Vickers-A.E.I. 651035, 40X, N.A. 0.57 objective having a working distance of 6mm is an excellent example of this type of lens. With this objective the observation of tracks during the actual etching process is possible.

The main limitation of dry objectives is the lack of high resolution. While dry objectives are available with N.A.'s of up to 0.95 most of the lenses with N.A.'s over about 0.60 require the use of a uniformly thick coverglass. This requirement decreases considerably their utility.

b. Immersion objectives

These are generally of two types, oil or water. These objectives are capable of higher resolution than the dry objectives with N.A. up to 1.40. The use of these objectives require procedures that are considerably more exacting than those necessary with the dry lenses. To achieve the full resolution of the objectives with N.A.'s of over 1.00 requires the use of an oil immersion condenser. However, the use of an oil immersion objective, without oiling the condenser, will still give greater resolution than that possible with the dry lenses.

The immersion objectives with practical resolution of 0.28 micron are extremely valuable for precise measurements, particularly the measurements of the vertical dimensions but have very small depth of field, which makes the oil immersion objectives less desirable for general scanning than the dry objectives. Table 5.7 shows the approximate limits of useful magnification and resolution for objectives and eyepieces of a microscope.

5.7.2 Dark-field illumination

A practical resolution of about 0.1 microns can be obtained with the use of oil immersion, dark field illumination. Although this type of dark field illumination requires a careful and a time consuming optical alignment, it is one of the few techniques available for the observation of very small tracks, such as low-energy recoil particles.

The lower power, dry, dark field techniques are very useful in the general and automatic scanning work. The depth of field is considerably greater than with bright field illumination, permitting the observation of large track segments. The considerable image contrast of track to background is also quite helpful. For accurate measurements, dark field is not particularly useful since track dimensions tend to be somewhat exaggerated.

TABLE 5.7a

CHARACTERISTICS OF MICROSCOPE OBJECTIVES

Focal Length		N.A.	Magnifi- cation	Working Distance mm	Diameter of Field mm	Depth of Field μ
ins.	mm					
1	25	0.15	x 5	23	3.2	20
2/3	16	0.28	x 10	7	1.6	10
1/6	4	0.74	x 40	1	0.4	2
1/12	2	1.3	x 100	0.25	0.15	1
1/16	0.16	1.4	x 130	0.20	0.12	0.75
1/18	0.14	1.4	x 160	0.18	0.10	0.50

TABLE 5.7b

MAGNIFICATION OF MICROSCOPE OPTICAL SYSTEMS

Objective		Primary Magnifi- cation	Final Magnification				
Focal Length			Eyepieces				
ins.	mm		x 6	x 8	x 10	x 15	x 20
1	25	x 5	30	40	50	75	150
2/3	16	x 10	60	80	100	150	200
1/6	4	x 40	240	320	400	600	800
1/12	2	x 100	600	800	1000	1500	2000
1/16	0.16	x 130	780	1040	1300	2150	2600
1/18	0.14	x 160	960	1280	1600	2400	3200

TABLE 5.7c

THE APPROXIMATE LIMITS OF USEFUL MAGNIFICATION
AND RESOLUTION

Objective		Objective Magnification	N.A.	Useful Magnification Limit	Resolution $1.22\lambda/2$ N.A.	
Focal Length					$\lambda \sim 0.425\mu$	$\lambda \sim 0.625\mu$
ins.	mm					
1	25	x 5	0.15	x 150	$\sim 1.73\mu$	$\sim 2.54\mu$
2/3	16	x 10	0.28	x 280	$\sim 0.93\mu$	$\sim 1.36\mu$
1/6	4	x 40	0.74	x 740	$\sim 0.35\mu$	$\sim 0.52\mu$
1/12	2	x 100	1.3	x 1300	$\sim 0.20\mu$	$\sim 0.29\mu$
1/16	0.16	x 130	1.4	x 2600	$\sim 0.19\mu$	$\sim 0.27\mu$
1/18	0.14	x 160	1.4	x 3200	$\sim 0.19\mu$	$\sim 0.27\mu$

5.7.3 Phase contrast microscopy

Phase contrast is available in the normal, or positive, and the negative types. For track observation the negative type was found to be more useful. In this case the track image is delineated by a sharp black border.

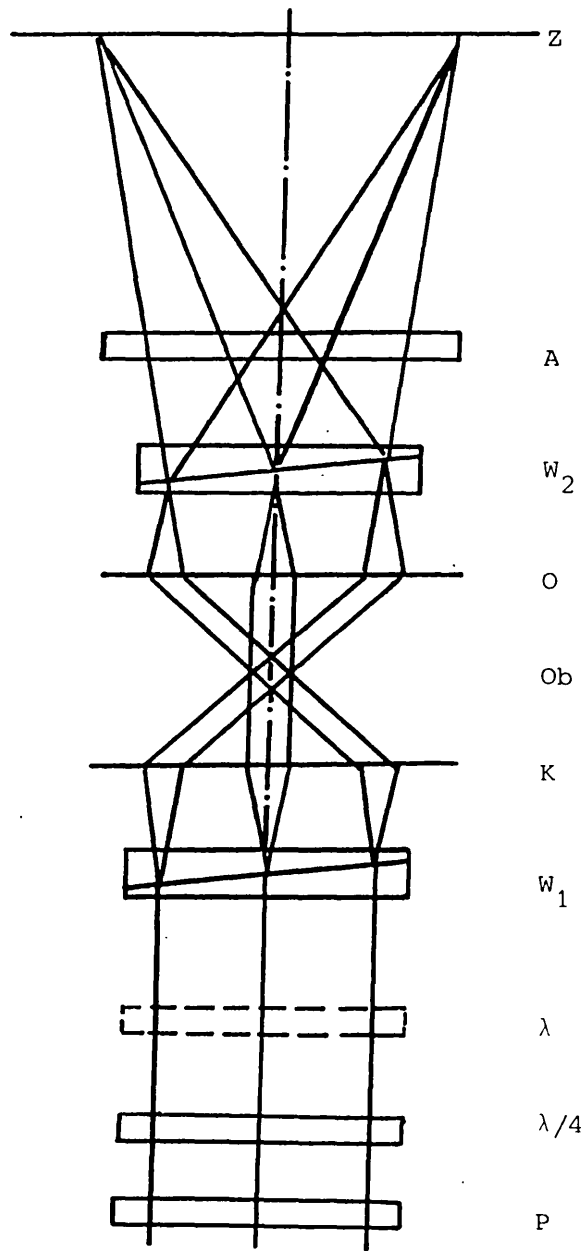
It is particularly useful for observation of small, low contrast tracks, such as shallow etch pits and recoil particle tracks, as well as long, narrow tracks where the retention of liquids has rendered the terminal ends of tracks invisible under bright field illumination.

5.7.4 Interference contrast microscopy

The use of an interference contrast equipment has improved the contrast of the transparent structures in comparison to the conventional back-and-white image obtained in the bright-field microscopy. This new technique shows several advantages for nuclear track counting: a brilliant relief image of etch pits, a good discrimination of the etch pits to the background, the possibility to improve the contrast by changing the colour of the image. The kind of colour and the contrast between the etch pits and the surface of the detector may be changed individually and adapted favourably to the corresponding detector surface. Therefore the interference contrast equipment facilitates direct counting of etch pits in the microscopy and is even advantageous for automatic track counting and measuring.

The interference contrast device used in the Reichert MEF2 microscope is based on the principle of two beam interference. The lateral separation between sample and interference beam is larger than or at least the same as the object size (total image separation), in the present device the beam separation has been chosen a little smaller than the resolving power of the objectives used in the microscope (differential image separation).

The splitting and recombination of the beams is carried out with optical crystal aids, according to the arrangement of Wollaston prisms in the front and rear focal plane of condenser and object. Figure 5.19 is a diagrammatic representation of the optical design of the interference contrast device. Here a linear polarized beam is split by means of a birefringent quartz prism ("Wollaston" prism, auxiliary prism) in the focal plane of the condenser into two mutually perpendicular polarized light wave components. After passing through the



Z = intermediate image plane

A = analyser

W_2 = Wollaston prism

O = objective

Ob = object plane

K = condenser

W_1 = Wollaston prism

λ = λ plate

$\lambda/4$ = $\lambda/4$ plate

P = polarizer

Figure 5.19 Optical diagram of the interference contrast device

transparent object, both the light wave components are combined in a second prism (main prism) in the focal plane of the objective and are tuned parallel in an analyzer so that the light can now interfere.

The $\lambda/4$ plate situated below the Wollaston prism W_1 acts as a phase-changing compensator in conjunction with the rotating polarizer P. By means of the λ -plate, which can also be inserted in the beam path, the brightness and colour differences between the background and the object can be varied. The interference contrast depends on the interference of two mutually perpendicular polarized light waves which suffered a phase shift in the object as well as in the birefringent quartz prism. Path differences arise between the ordinary and extraordinary waves in the following way:

(i) Light waves undergo path differences by a local variation of the thickness or by variations of the optical refraction index at the profiles and structures of the object.

(ii) Shifting of the main prism from the centre perpendicular to the direction of the incident light, a path difference arises from small differences in the refractive index of both the waves in case that there are optical path differences in front or behind the central areas of the prism. Using monochromatic light, this fact leads to a contrast image of the object (brightness interference), using white light it leads to a coloured illumination of the object and the image background (colour interference). Figure 5.20 shows the photomicrographs of alpha tracks in cellulose nitrate taken with colour interface.

5.7.5 Incident light illumination (reflection)

The resolution of the surface-reflected light system is somewhat inferior to the transmitted light system. This technique is useful for track observation in specimens that are very thick (> 2 mm), or specimens containing inhomogeneities or inclusions. Because of image degradation, observations are restricted to depths of less than about 50 microns into the volume of the specimen; with long working distances and dip cones available, incident light techniques can be used for observation of tracks in specimens that are still immersed in the etching solution (contained in opaque etching tanks).

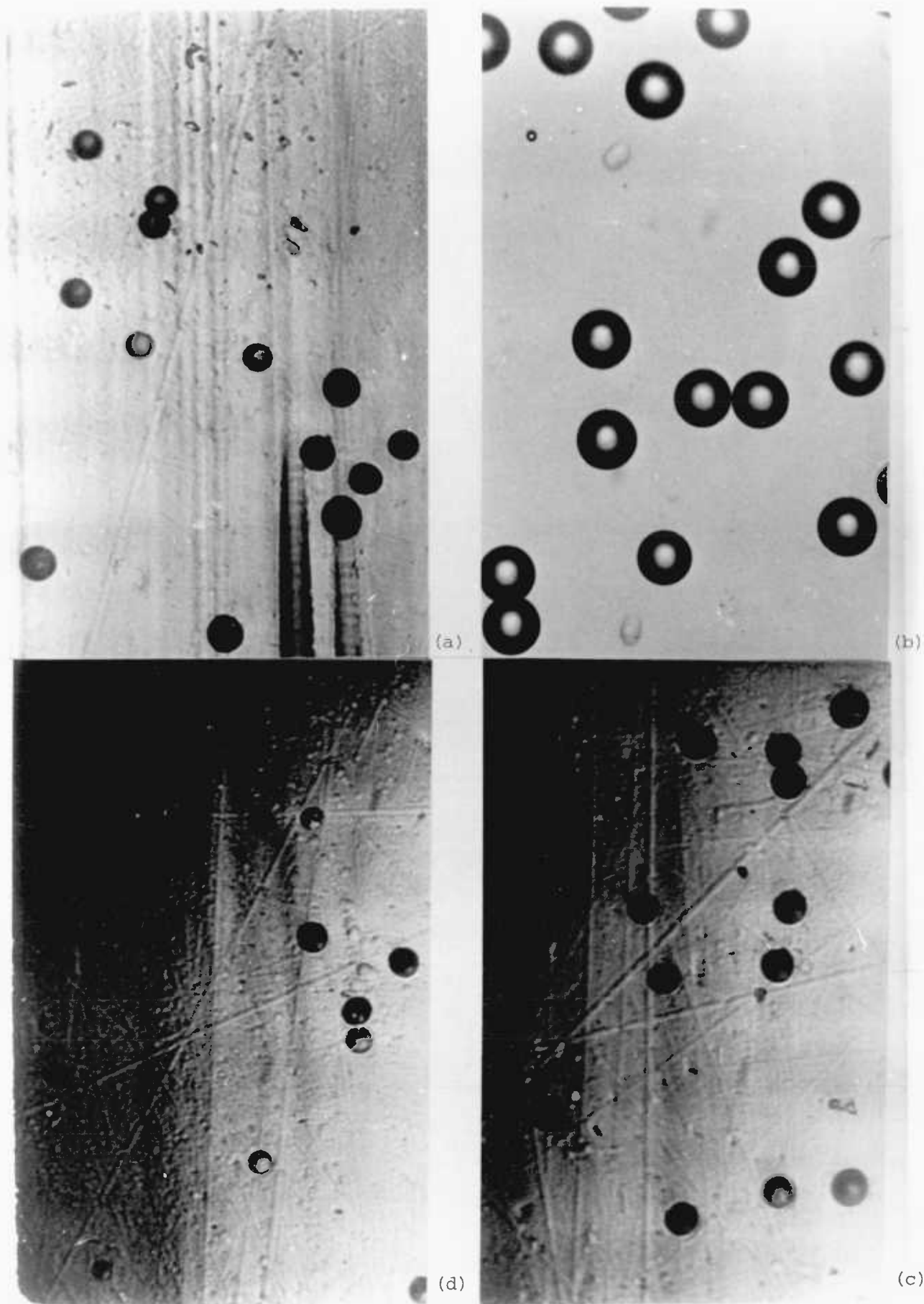


Figure 5.20 Photomicrographs of alpha tracks incident normal to the surface of the detector (CA 80-15 cellulose nitrate) taken with colour interface. The energies of the incident alpha particles were: (a) 1 MeV, (b) 2 MeV, (c) 3 MeV, (d) 4 MeV

5.8 Automatic Scanners

Several efforts to build automatic scanners have been reported so far. Most of these were specially built for nuclear track counting in emulsions.

An automatic scanning system for solid-state fission-track recorders was developed by Oosterkamp and Schaar (127) at Van Velze. They used a television camera as a scanning device, and a PDP-124 computer to analyse the data.

Cohn and Gold (122) developed an optical microscope having computer control of specimen motion in three dimensions, via stepping motors, and used for automatic scanning of solid-state nuclear track recorders. This computer-controlled microscope, which is called the automatic track scanner (ATS), affords the capability of full on-line computer control, thereby leading to improved precision, reliability and accuracy. The ATS system is the first to possess automatic focussing capability.

Image analysing computers make automatic assessments of selected features in photographs or in electron, X-ray or optical images, by recognising and isolating such features and then counting, measuring and classifying them. They do this much more quickly, accurately and reproducibly than human operators, and they have made valuable but previously impossible tasks in research and quality control both feasible and economic. Imanco (123) pioneered the development of image analysing computers with the introduction of the Quantimet A in 1963. The Quantimet B followed two years later. In 1970, the Quantimet 720 series was introduced. The Quantimet 720 is an advanced series of image analysis systems, each built on a modular design allowing the easy addition of many extra modules to an entirely compatible basic system. The Quantimet 720 offers a choice between radically new, low noise, high uniformity image scanners designed specifically for precision image analysis. It divides an image into the maximum number of discrete picture points, in this way giving optimal sampling and statistical accuracy. Figure 5.21 is a simplified block diagram of the Quantimet 720.

The Leitz-Texture-Analysing-System (Leitz T.A.S) (128) is the latest product of the extraordinarily fast improvements and developments of the instruments for quantitative image analysis during the

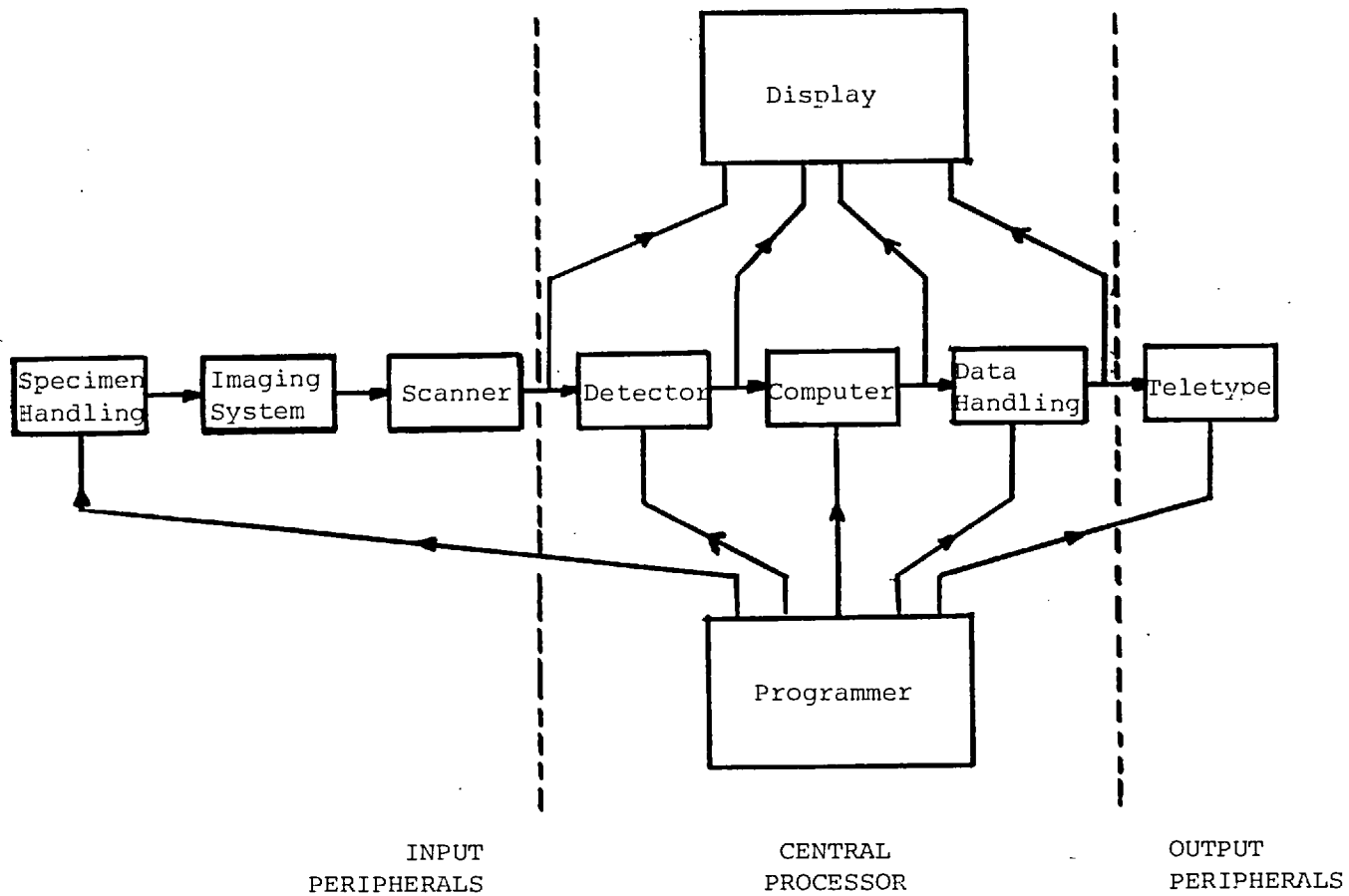


Figure 5.21 Block diagram of Quantimet 720

last few years. When the first electronic image analyzers appeared on the market, all the classical procedures of linear analysis were used, and only automatically controlled. With the Leitz-Texture-Analysing-System (Leitz T.A.S.) a new generation of image analyzers has been created, that make it possible to analyse images with two-dimensional scanning elements. The basis is an analysing concept which takes into account the practical work as well as the theoretical logical foundations, and employs new analytical procedures (for instance the generalization of the size concept).

CHAPTER SIX

TRACK DEVELOPMENT BY MEANS OF CHEMICAL ETCHING

6.1 Introduction

The studies reported in this chapter are motivated by a desire to understand the variables that control the track etching process. A criterion is established for the design and the modification of plastics in order to improve their sensitivity, reproducibility of tracks and suitability for track registration under most environmental conditions in research and reactor application.

The parameters that affect the chemical etch development of tracks are: the specimen composition, the etching solution parameters and the parameters associated with the charged particle.

Three of the most popular plastic detectors commonly used for the detection of light charged particles have been examined, together with cellulose nitrate detectors, with regard to their relative suitability for alpha particles and proton detection. Cellulose nitrate plastics were chosen for the major part of this study for reasons discussed later in this chapter. Kodak-Pathé LR 115 and CA 80-15 plastics were chosen because of their superior sensitivity and uniform homogeneity over other commercially available cellulose nitrate plastics (see Chapter Five). The exact composition of these plastics is not available; it is regarded by the manufacturers as a trade secret.

The parameters of etched tracks and the density of the target medium are the identity of the incident charged particle (charge, mass and energy of the incident charged particle). Accurate knowledge of the measurable etched tracks parameters and the relation between range-energy loss rate of incident charged particles, are essential, especially in the use of this kind of visual microscopic detectors.

The work on SSTR's can be divided into two categories: track fluences (number per cm^2) and track identification (charge, mass of incident-charged particle and range-energy measurement). In some applications only the fluences of tracks are desired; in these it is necessary only to distinguish the tracks from the background etch pits for count-rate measurements. In many studies, however, range-energy measurements and incident charged particle identification are required. This calls for measurements of track parameters such as the incident particle trajectory length, the dip angle and the diameter. These measurements can be then correlated to particle identification such as the particle ionization rate, energy, charge and mass.

The present work is confined to the use of the count-rate and range-energy measurements of the incident charged particles.

In these two categories, detailed knowledge of the track geometry is necessary in order to compute track parameters and distinguish them from other features that can be seen and measured with an optical microscope. The geometry of etched tracks and the range-energy relation for the incident charged particle are discussed and related, with mathematical evaluations and parameter measurements of etched tracks, to charge, energy and mass of the incident charged particle.

An etching criterion is established for producing a higher sensitivity and a maximum resolution of the detectors with better shaped tracks (close to perfect cones). The detection efficiency and range of alpha particles and protons were determined accurately with this criterion in cellulose nitrate.

6.2 Geometry of Etched Tracks

On a sub-microscopic scale, a particle damage trail and the subsequent formation of an etched track can be viewed in terms of the chemical attack of a narrow linear region, as shown in Figure 6.1. The tip of the track results from a chemical attack of the damage region. The degree of radiation damage is greatest in the immediate vicinity of the particle trajectory, where the etch rate has its greatest value V_T (the track etch rate). The degree of damage and the etch rate both decrease as the distance from the trajectory increases. At a certain distance estimated to be somewhere between 25 and 100 \AA , the damage falls off to some small value, and the etch rate normal to the interior of the track is then the etch rate of the undamaged bulk material, V_B . Since the advancing tip of the etch pit maintains its shape while moving forward at a rate V_T in the undamaged region, the angle made by the walls of the etch pit with the particle trajectory must be such that the projection of V_T in the direction of the normal to these walls will be V_B . This is shown in the vector diagram of Figure 6.1. Consequently the track cone angle θ is given by

$$\sin\theta = (V_B/V_T) \quad (6.1)$$

If one observes track formation on the scale of an optical microscope, the rounded tip shown in Figure 6.1 appears perfectly sharp. As the track tip proceeds past each point on the particle trajectory,

the track walls expand, carrying with them a cone angle characteristic of V_T at this particular point (Eqn. 6.1). It has been found (31) that V_T can be expressed as a monotonically increasing function of the particle restricted energy loss rate REL_{ω} , the rate of energy loss of electrons with energies less than ω . The function REL_{ω} is identical to the more commonly used function LET. Thus as LET varies along the particle damage trail, V_T and θ also vary. This is illustrated in Figure 6.2.

In Figure 6.2a is shown the formation of a track when etching proceeds from the direction of the particle stopping point. In Figure 6.2b the etching direction is the same as that of the particle travel. In both cases, the cone angle at point B is representative of the track etch rate at point A. As can be seen, the cone angle decreases towards the stopping end of the damage trail as both LET and the track etch rate increase.

Although nearly all tracks have continuously varying cone angles it is mathematically expedient to approximate track shape by geometric cones. In most cases this is a good approximation, since the deviations from conical track structure are usually beyond the measurement capability of the optical microscope. When the deviation from conical track structure can be seen, the conical approximation can be taken to give average values of parameters such as θ .

In practice, deviations of track shape from perfect cone are sometimes observed due to the following factors; if combined they produce a track considerably different from a perfect cone.

- (1) The bulk material may etch anisotropically.
- (2) The original surface of the plastic may have a different etch rate than the bulk material.
- (3) The charged particle may experience a rapid change of ionization along its trajectory.
- (4) For long tracks, etchant diffusion effects may become significant.
- (5) The copious number of low energy δ -rays produced by slow multi-charged particles may alter the bulk etch rate in the vicinity of the particular trajectory.

6.2.1 Mathematical Evaluation of Track Parameters

In the following mathematical treatment of track geometry we will neglect the above mentioned complicating factors and so assume

perfect cones, with LET constant, the detector homogeneous and isotropic, and the track and bulk etch rates are not affected by concentration gradients caused by the diffusion of either the etchant or the etch products (which is the case in ideal conditions).

The track quantities of the greatest interest are those that provide information with regard to the charged particle: the track length ℓ , and the track cone angle θ . These quantities and their variation as a function of etching time are used to determine the particle charge, mass and velocity. Also of interest is the particle range R in the plastic. This quantity, which is related to the particle kinetic energy E , is measured from the point of entry into the original surface before etching to the point where the particle came to rest.

In the measurement of track length, it is necessary to know which point in the ellipse, formed as a result of the intersection of the track cavity with the plastic surface, represents the point on the incident charged particle trajectory. Also, since the observation and measurement of tracks is performed with a microscope, measurements are made of the projected track quantities rather than actual track quantities. Thus we seek relationships between the projected and the actual parameters as well as other useful relations between the readily measurable track quantities and the track parameters of interest.

Figure 6.3 is a side view of a track with dip-angle δ degrees and cone angle θ degrees. The positions of the detector surface are labelled in a time sequence from 0 to 6. At time t_0 , the surface of the detector is coincident with the top of the damage trail. For damage trails completely contained within the detector, t_0 is the instant at which the etched detector surface just touches the end of the damage trail. The surface at t_0 is called the pre-etch surface, even for submerged tracks.

After t_0 , the detector surface is removed at a rate V_B while the rate of attack along the damage trail is V_T . At time t_1 , the vertex of the track cone is pointed. The etch length of the track (L), the distance to the cone vertex from the top of the damage trail, is given by

$$L = B \operatorname{cosec} \theta \quad (6.2)$$

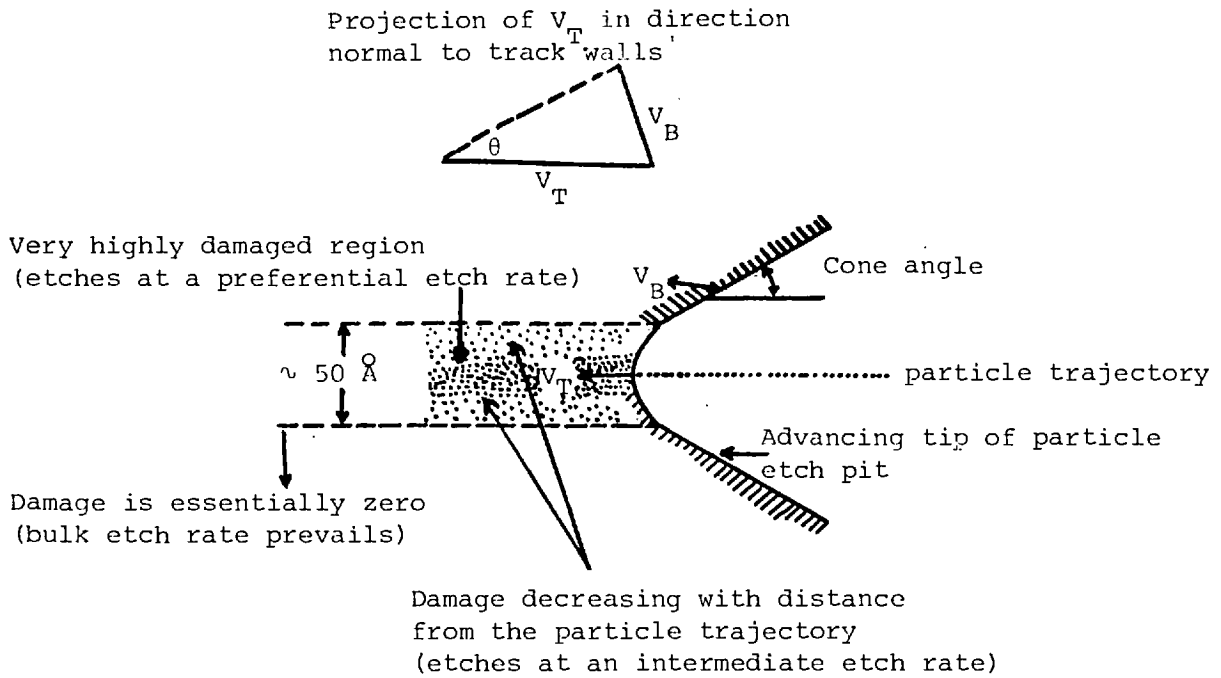


Figure 6.1 Damage trail and track etching on a sub-microscopic scale

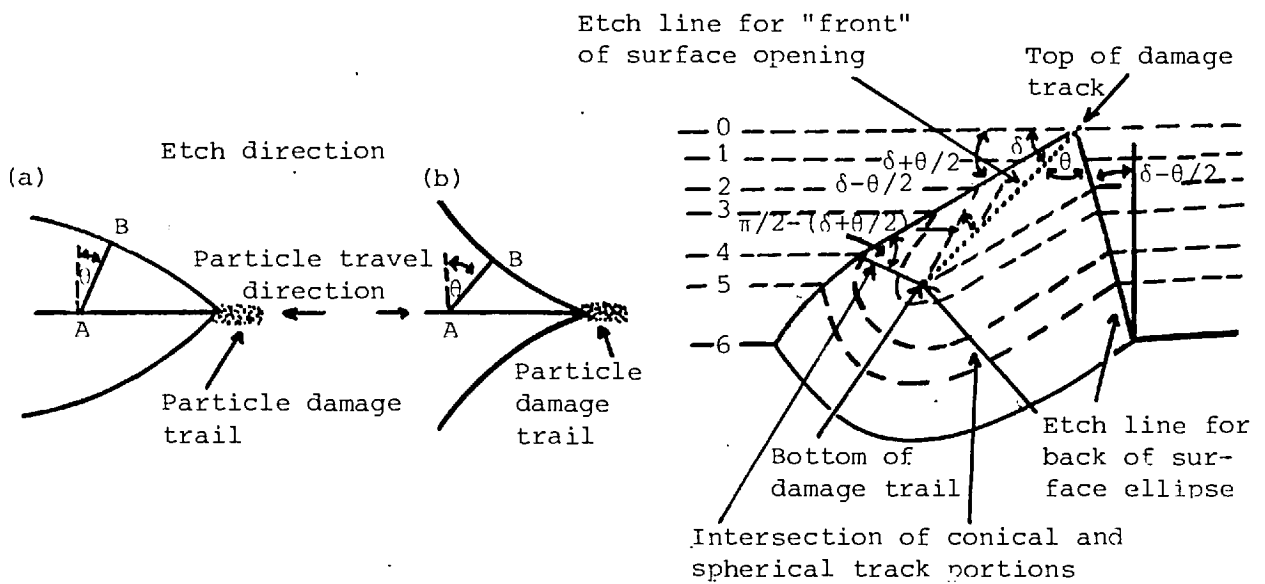


Figure 6.2 Partially etched particle damage trails seen on the scale of an optical microscope. Both tracks are etching toward the right-hand side of the figure. It should be noted that the diameter of the damage trail has been exaggerated

Figure 6.3 Sequential stages of track etching for a particle damage trail of finite length

where B is the bulk material removed since t_0 . (Figure 6.4 shows the parameters of pointed tracks.) Eqn.6.2 can be obtained by integrating Eqn. (6.1) with respect to time, realising that

$$L = \int_{t_0}^t v_T dt \quad (6.3)$$

then

$$B = \int_{t_0}^t v_B dt \quad (6.4)$$

The cone angle θ intersecting the surface at a dip angle $\delta (> \theta)$ produces an elliptical surface opening a conic section. Geometrical considerations give the semimajor axis of this surface ellipse a by

$$a = \frac{B \cos \theta}{\sin \delta + \sin \theta} \quad (6.5)$$

and its semiminor axis b by

$$b = B \left[\frac{\sin \delta - \sin \theta}{\sin \delta + \sin \theta} \right]^{\frac{1}{2}} \quad (6.6)$$

At time t_2 the preferential etching is just complete. The track vertex is still pointed and the track is of the same geometry as at t_1 so $a/b = \cos \theta / (\sin^2 \delta - \sin^2 \theta)^{\frac{1}{2}}$. At $t > t_2$, further etching proceeds at a rate v_B (normal to all surfaces). This results in the rounding of the track vertex. The vertex becomes a sphere of radius r, given by

$$r = v_B (t - t_2) \quad (6.7)$$

and joins smoothly with the conical part of the track. At times greater than t_2 , L continues to have the same value, which is called L_r , the length of the damage trail in this layer of the detector. This is shown in Figure 6.5 which shows the parameters of a rounded track.

At etch time t_3 (Stage 3 of Figure 6.3), the track has developed a spherical tip of radius r. Eqns.(6.5) and (6.6) are still valid, but Eqn.(6.2) has become

$$B = L_r \sin \theta + r \quad (6.8)$$

which reduces to Eqn.(6.2) if $r = 0$ and L_r is replaced by L. On the right-hand side of Eqn.(6.8), $L_r \sin \theta$ is the bulk etching that took place during the preferential etching, and r is the subsequent bulk etching. The depth from the surface to the bottom end of the damage

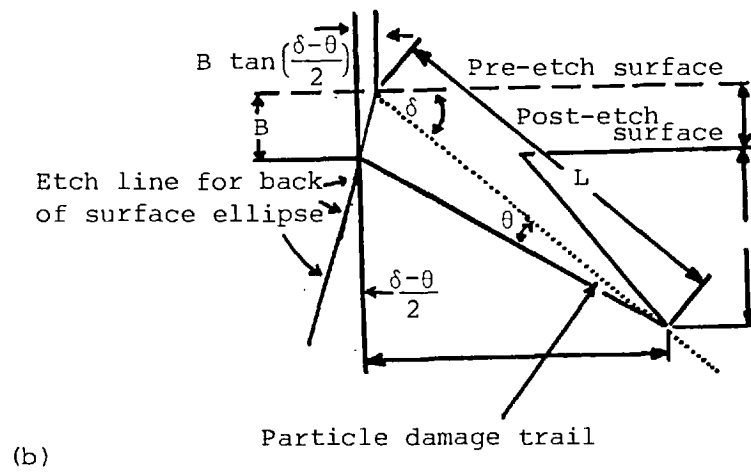
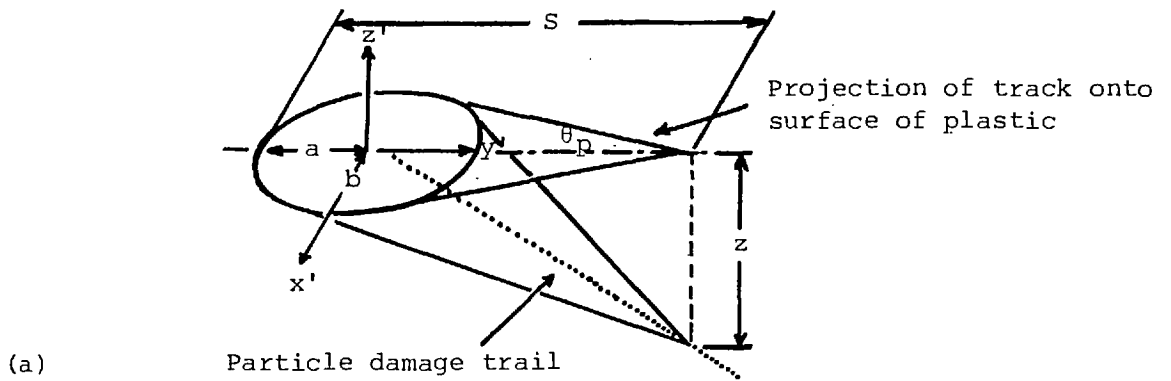


Figure 6.4a,b Pointed tracks and their parameters ($B < L_r \sin\theta$)

trail is z , which is also the centre of the vertex sphere (see Figure 6.5) and is given by

$$z = L_r \sin\delta - B \quad (6.9)$$

(For pointed tracks L_r in Eqn.6.9 is replaced by L , and in this case z is the depth of the track vertex.) The total projected length of the track s , as shown in Figure 6.5 is now given by

$$s = L_r \cos\delta + r + B \tan\frac{1}{2}(\delta - \theta) \quad (6.10)$$

Eqn.(6.10) follows directly from the geometry as seen in Figure 6.5a. Eqn.(6.10) can also be used for pointed tracks by setting $r = 0$. It should be noted that the horizontal displacement of the "back" of the surface ellipse from the top of the damage trail, $B \tan\frac{1}{2}(\delta - \theta)$, is small compared with a (Eqn.6.5), except for large values of $(\delta - \theta)$.

At this point it is appropriate to discuss a special case: tracks that are not undercut. A track is undercut if the detector surface overhangs some portion of the track. For a track etched to Stage (3), as shown in Figure 6.3, undercutting does not occur if $\delta > (\pi/2 - \theta)$; s is no longer defined, and z and r cannot be observed from above as with $\delta < (\pi/2 - \theta)$. Thus, in this case it is appropriate to define some new parameters, which are shown in Figure 6.6. The new parameters are d , the depth of the bottom of the track (directly below the particle stopping point) and ω , the horizontal distance from the bottom of the track to the "back" end of the surface ellipse. The new relations defining these parameters are

$$d = L_r \sin\delta + r - B = L_r (\sin\delta - \sin\theta) \quad (6.11)$$

and

$$\omega = L_r \cos\delta + B \tan\frac{1}{2}(\delta - \theta) \quad (6.12)$$

These can be derived by inspection of Figure 6.6. Of course, the parameters d and ω can be used in any case in which the bottom of the vertex sphere is visible from above, not just the non-undercut case. It can be seen that this is the case if $B > L_r \cos\delta \tan\frac{1}{2}(\delta + \theta)$; see Figure 6.3. It should also be noted that d does not change with etching.

When etching has proceeded to Stage (4), as seen in Figure 6.3, the character of the track is basically the same as after time t_3 , except that the vertex sphere portion of the track now just touches

the surface of the detector. The value of B necessary to establish this condition is given by

$$B_4 = L_r \left[\sin\theta + \frac{\sin\frac{1}{2}(\delta - \theta)}{\cos\frac{1}{2}(\delta + \theta)} \right] \quad (6.13)$$

As the detector is etched longer than t_4 (Stage 4 of Figure 6.3), the front portion of the surface opening is no longer an ellipse. Rather, it is a portion of a circle formed from the intersection of the vertex sphere with the detector surface.

At this point two new parameters should be defined. The radius of the circular portion of the surface opening is v . From Figure 6.7 it can be seen that v is given by

$$v^2 = 2 r d - d^2 \quad (6.14)$$

The total projected length of the opening is no longer $2a$. It is now the parameter u , shown in Figure 6.7. The figure shows that

$$u = L_r \cos\delta + v + B \tan\frac{1}{2}(\delta - \theta) \quad (6.15)$$

As etching proceeds, the circular portion of the surface opening becomes an increasingly greater fraction of the track opening. Before the circular portion becomes a semicircle, however, Stage (5) is reached. At etch time, t_5 all tracks even those with $\delta < (\pi/2 - \theta)$ cease to be undercut. As can be seen in Figure 6.3, this occurs because the etched detector surface has now reached the level of the bottom of the damage to trail. Thus B_5 is given by

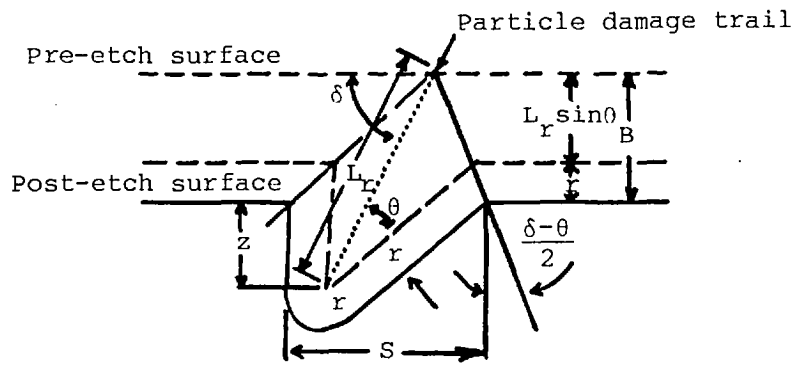
$$B_5 = L_r \sin\delta \quad (6.16)$$

As the etching continues again, the circular portion of the surface opening becomes a semicircle. The point at which this happens can be established by setting $b = v$ using Eqns. (6.6), (6.11) and (6.14) to eliminate b , r , d and v , one finds

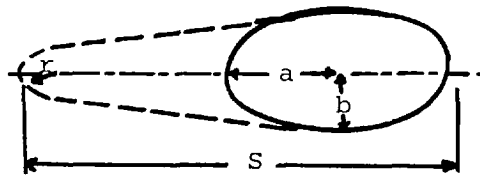
$$B_6 = L_r (\sin\delta + \sin\theta) \quad (6.17)$$

where B_6 is the value of B when the surface opening which is a semicircle joined to one half of an ellipse. The track now seen as Stage (6) in Figure 6.3.

As etching proceeds beyond Stage (6), the circular portion becomes greater than a semicircle and the width of the opening is $2v$, not $2b$.



(a)



(b)

Figure 6.5a,b Rounded tracks and their parameters

$$\left(L_r \sin \theta < B < L_r \left\{ \sin \theta + \frac{\sin \frac{1}{2}(\delta - \theta)}{\cos \frac{1}{2}(\delta + \theta)} \right\} \right)$$

Finally, with sufficient etching, the track becomes entirely spherical and its surface opening is a circle. This condition is just met when the detector surface has reached the intersection of the etch line for the back of the ellipse and the lower line in Figure 6.3, which is the focus of the intersection of the conical and spherical track portions. It can be shown that the value of B at this point, B_c , is given by

$$B_c = \frac{L_r \cos \theta}{\tan \frac{1}{2}(\delta - \theta)} \quad (6.18)$$

with $B \geq B_c$, the depth of the track is $d = L_r(\sin \delta - \sin \theta)$ and the radius of its circular opening is $= [d(2B - B_c)]^{\frac{1}{2}}$.

6.2.2 Mathematical Evaluation for Track Parameters with Dip Angle $\delta = 90$ deg.

With the growth of a track produced by a charged particle falling perpendicular to the surface of the detector, the etchant will penetrate along the track up to $V_T t$ and finally a conical pit will be formed. This etch pit will look circular, when viewed from the top, with diameter $D = 2R$ where R is the radius of the etch pit.

In this case the semimajor axis a and the semiminor axis b of the surface ellipse of Figure 6.4 becomes equal, i.e. $\delta = 90$ deg.

Then $\sin \delta = 1$

$$D/2 = R = a = b = \frac{B \cos \theta}{1 + \sin \theta} = B \left[\frac{1 - \sin \theta}{1 + \sin \theta} \right]^{\frac{1}{2}} \quad (6.19)$$

from Eqns. (6.1) and (6.4).

Then Eqn. (6.19) becomes

$$D/2 = V_B t \left[\frac{1 - V_B/V_T}{1 + V_B/V_T} \right]^{\frac{1}{2}} = B \left[\frac{(1 - V_B/V_T)}{(1 + V_B/V_T)} \right]^{\frac{1}{2}} \quad (6.20)$$

The etch pit diameter is

$$D = 2V_B t \left[\frac{(V_T - V_B)}{(V_B + V_T)} \right]^{\frac{1}{2}} = 2B \left[\frac{(V_T - V_B)}{(V_T + V_B)} \right]^{\frac{1}{2}} \quad (6.21)$$

In order to calculate the cone length in all stages we can substitute in all the previous formulae the value $\delta = 90$ deg.

6.2.3 Track Specifications and Measurement of Parameters

The situations shown in Figures 6.4 through 6.7 can be completely specified by not more than four parameters. The four parameters that are most useful are δ , θ , L_r and B . For pointed tracks L_r is replaced by L . All other quantities of interest can be computed quite easily and directly from these four parameters.

Since some (or in some cases all) of the above specification parameters cannot be measured directly, they must be computed from parameters that can be measured. The parameters that can be measured easily for a single track are: for undercut tracks, s , a , b , z and r ; and for non-undercut tracks, w , d , v and u .

In some cases one or two of the specification parameters can be measured. If the damage trails were produced by exposing the detector to a collimated particle beam of known dip-angle or if the two tracks produced by the same particle on the opposite surfaces of the detector can be measured, δ is known quite accurately. It is also possible to measure (for damage trails intersecting the surface of the detector prior to etching) by measuring the sample thickness or weight before and after etching and applying appropriate corrections for the edge effects.

With the two specification parameters described in the last paragraph there are seven possible measurement parameters - δ , B , s , a , b , z and r - that can be used to derive the four specification parameters δ , θ , L_r and B for undercut tracks. Since only four measurements are necessary to determine the specification parameters, the set of measurement variables yielding the greatest accuracy or possibly the greatest measurement facility should be chosen for each particular situation. The specification parameters are given in terms of seven different sets of measurement parameters. These seven sets are given in Table 6.1.

The sets are applicable to pointed tracks if r is set equal to zero and L_r is replaced by L . Of course if more than four parameters are measured, a least-squares fitting procedure can be used to obtain the best values of the specification parameters.

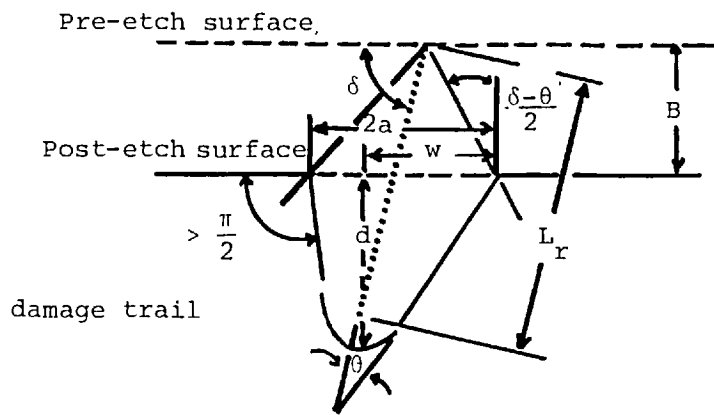


Figure 6.6 Tracks with no undercutting and their parameters
 $(\delta < \pi/2 - \theta)$

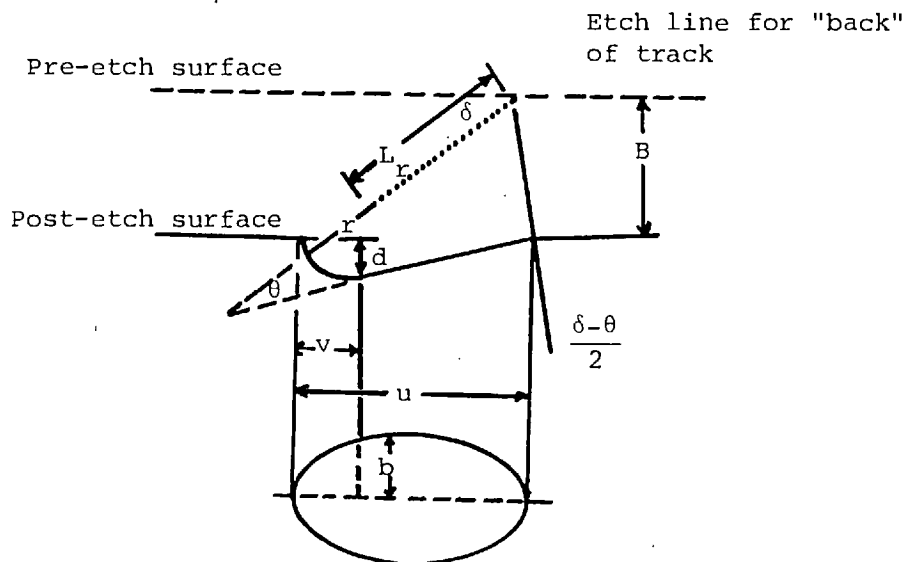


Figure 6.7 Nonundercutting tracks with partially circular track openings and their parameters
 $\{L_r \sin \delta < B < L_r (\sin \delta + \sin \theta)\}$

TABLE 6.1

SETS OF MEASUREMENT VARIABLES FOR UNDERCUT TRACKS

Set No.	Measurement Variables						
1	δ	B	s	-	-	-	r
2	δ	B	-	-	-	z	r
3	δ	-	s	-	b	-	r
4	δ	-	-	-	b	z	r
5	-	-	s	-	b	z	r
6	-	-	s	a	b	-	r
7	-	B	s	-	-	z	r

The specification parameters can also be computed from the measurement of tracks that are not undercut (Sets 8 and 9). Set 8 uses the measurement parameters a, b, w and d and is applicable for $L_r \cos\delta \tan\frac{1}{2}(\delta + \theta) < B < B_4$. Set 9 uses the measurement parameters u, v, b, and d and is applicable for $B_4 < B < B_6$.

6.2.4 Measurement Optimization

The accuracy of the computed specification parameters can be maximized by choosing the appropriate set of measurement parameters. The following discussion indicates the situation in which each of the measurement sets is most useful.

If δ is known accurately, one of the sets 1 through 4 should be used. Sets 1 and 2 are easy to use since it is only necessary to measure B once for a surface. Sets 3 and 4 are more accurate for tracks with small θ values because they allow for a variation of B over the detector surface, but when θ is large, b is small and thus subject to a greater measurement error. For large tracks, Sets 1 and 2 apply only to tracks produced by damage trails intersecting the surface prior to etching. For the greatest accuracy Sets 1 and 3 should be used for shallow tracks (small δ values) and Sets 2 and 4 for steep tracks (large values of δ). In fact since s is considerably easier to measure than z, Set 2 and 4 should be used only where tracks are quite steep.

When the value of δ is not known, Sets 5, 6 and 7 must be used. Set 6 is easier to measure because a is more easily measured than z,

but it should be noted that all the variables measured in Set 6 are in the horizontal plane. Thus it is possible to measure a track from a photograph. Set 7 has the advantages of not requiring the measurement of b for every track and of greater accuracy if θ is large.

For tracks that are not undercut, only one set of measurement parameters is available for each case. It should also be noted that although in principle Set 8 can always be used to obtain the specification parameters, in practice it is useful only for tracks with relatively large values of θ and values of δ somewhat different than $\pi/2$, so that $a \neq b$. However, if it can be seen that $r = 0$ (only a small point of light in the centre of the dark track as observed with an optical microscope), w and d become s and z , and Set 5 can be used with good accuracy for all values of δ and θ .

Sets of equations relating specification to measurement parameters

Eqns. (6.5), (6.6), (6.8), (6.9), (6.10), (6.11), (6.12), (6.14) and (6.15) can be used to derive the nine sets of relations for the specification parameters. In all cases except two these relations are explicit. The two implicit relations for θ can be solved by iteration. In most cases, four or five iterations suffice for the convergence of θ if the initial value is $\theta = 0$. In extreme cases (large θ), these relations must be solved by interpolation, or by Newton's method, in which case the convergence is more rapid.

However, the readily measureable parameters are θ_p , s , a and b . The relationship between the projected cone angle, θ_p and the actual cone angle, θ , can be shown to be

$$\sin\theta = \cos\delta \sin \theta_p \tag{6.22}$$

This relation is required when measurements of θ are made using an eyepiece-goniometer combination.

Set 1: δ , B , s and r . For this set δ and B are measured directly

$$\sin\theta = \frac{(B - r) \cos\delta}{s - r - B \tan \frac{1}{2}(\delta - \theta)} \tag{6.23}$$

is iterated for θ , and

$$L_r = \frac{s - r - B \tan \frac{1}{2}(\delta - \theta)}{\cos\delta} \tag{6.24}$$

Set 2: δ , B, z, and r. For this set δ and B are measured.

$$L_r = \frac{z + B}{\sin\delta} \quad (6.25)$$

and

$$\sin\theta = \frac{B - r}{L_r} \quad (6.26)$$

Set 3: δ , s, b and r. For this set δ is given,

$$\sin\theta = \frac{b \cos\delta \sin\delta - r \cos\delta [\sin^2\delta - \sin^2\theta]^{\frac{1}{2}}}{(s - r) [\sin^2\delta - \sin^2\theta]^{\frac{1}{2}} - b \cos\theta} \quad (6.27)$$

is iterated for θ , and B is obtained from Eqn.(6.6) and L_r from Eqn.(6.24). It should be noted that in Set 3 there are two possible solutions. Most probably in real cases the one with the smaller value of θ is correct. The computed value of B can be used as a test.

Set 4: δ , b, z and r. For this set δ is given,

$$\sin\theta = \left[\frac{b [z^2 + b^2 - r^2]^{\frac{1}{2}} - zr}{z^2 + b^2} \right] \sin\delta \quad (6.28)$$

$$L_r = \frac{z + r}{\sin\delta - \sin\theta} \quad (6.29)$$

and B is obtained from Eqn.(6.8).

Set 5: s, b, z and r. First $(\delta - \theta)$ and $\sin\theta/\sin\delta$ are given by

$$\sin(\delta - \theta) = \frac{r(s - r) + z[s^2 - 2sr + z^2]^{\frac{1}{2}}}{(s - r)^2 + z^2} \quad (6.30)$$

and

$$\frac{\sin\theta}{\sin\delta} = c = \frac{b [z^2 + b^2 - r^2]^{\frac{1}{2}} - zr}{z^2 + b^2} \quad (6.31)$$

Then the specification parameters are computed by

$$\tan\theta = \frac{c \sin(\delta - \theta)}{1 - c \cos(\delta - \theta)} \quad (6.32)$$

$$\delta = (\delta - \theta) + \theta \quad (6.33)$$

L_r is given by Eqn.(6.29), and B by Eqn.(6.8).

Set 6: s, a, b and r. For this

$$\tan\theta = \left[\frac{(a^2 - b^2)^{\frac{1}{2}}}{a} \right] \times \frac{[b^2(s-r-a)^2 - (a^2-b^2)(b^2-r^2)]^{\frac{1}{2}} - r(s-r-a)}{(s-r-a)^2 - (a^2 - b^2)} \quad (6.34)$$

$$\sin\delta = \left[a^2 \sin^2\theta + b^2 \cos^2\theta \right]^{1/2} / a \quad (6.35)$$

$$L_r = \frac{s - r - a + \left[a^2 - b^2 \right]^{1/2}}{\cos \delta} \quad (6.36)$$

and B is obtained from Eqn.(6.8).

Set 7: B, s, z and r. For this set B is known, $\sin(\delta - \theta)$ is obtained from Eqn.(6.30)

$$\frac{\sin\theta}{\sin\delta} = c = \frac{B - r}{B + z} \quad (6.37)$$

and $\tan \theta$, δ and L_r are respectively obtained from Eqn.(6.32), (6.33) and (6.25).

Set 8: a, b, w and d. For this set

$$\tan\theta = \frac{b^2 \left[w - a + (a^2 - b^2)^{1/2} \right]^2 - d^2 (a^2 - b^2)}{2ad(a^2 - b^2)^{1/2} \left[w - a + (a^2 - b^2)^{1/2} \right]} \quad (6.38)$$

and δ is obtained from Eqn.(6.35)

$$L_r = \frac{d}{\sin\delta - \sin\theta} \quad (6.39)$$

$$B = \frac{a(\sin\delta + \sin\theta)}{\cos\theta} \quad (6.40)$$

Set 9: u, v, b and d. If auxiliary variables are given by

$$r = (v^2 + d^2) / (2d) \quad (6.41)$$

$$h = d / (u - v) \quad (6.42)$$

$$\lambda = \frac{r(r - d) - b(b^2 + 2rd + d^2)^{1/2}}{b^2 + (r - d)^2} \quad (6.43)$$

and

$$\xi = \left[\lambda d + (1 - \lambda)r \right] / (u - v) \quad (6.44)$$

The specification parameters are given by

$$\tan\delta = \left\{ (1 + \lambda)h + \xi \left[1 + h^2(1 + \lambda) / (1 - \lambda) - 2\xi h / (1 - \lambda) \right]^{1/2} - \xi \right\} (1 - \lambda^2 - \xi^2)^{-1/2} \quad (6.45)$$

$$\sin\theta = \lambda \sin \delta \quad (6.46)$$

L_r is obtained from Equation (6.39) and B from Equation (6.8).

6.2.5 Computation of the Track Etch Rate

The most useful and important parameter that can be computed from the specification parameters is the track etching rate V_T . In terms of the bulk etch rate V_B , it is given by Eqn.(6.1). If a damage trail, known to have intersected the surface prior of etching is etched to form a track and the total surface etched is z , V_T is given more accurately if V_B in Eqn.(6.1) is given by

$$V_B = B/t \quad (6.47)$$

where B has the value consistent with the parameters of the particular track being measured.

6.2.6 Track Measurement

It has been assumed throughout this section that all the parameters used were the real physical parameters in a consistent set of units. Scale factors and the corrections for index of refraction in the z measurement are peculiar to the particular measurement situation and will not be discussed here. However, there are several pertinent points to be noted.

All the measurement parameters are defined in such a way that no "guesswork" is necessary to measure them. For example, it is not necessary to estimate the point of intersection of the particle trajectory and the surface (it is not the centre of the surface ellipse but lies a distance $a \tan\theta/\tan\delta$ towards the "front" end of the ellipse).

The parameters s , a , u and b are all measured between two track "boundaries". To obtain z , the microscope is alternately focussed on the detector surface and the very end of the vertex or tip, even if rounded. If θ is small, r can be taken to be half the diameter of the vertex. If θ is large (but $> \pi/4$) it can be measured by making two perpendicular reticule lines tangent to the vertex sphere (as projected onto the horizontal plane) and finding the distance from the point of tangency to the intersection of the reticule lines. This distance is r .

The parameters v and w are measured from a track boundary to the centre of the small circle of light seen at the bottom of the

track. This circle of light is the virtual image of the microscope condenser diaphragm formed by the track vertex sphere.

6.3 Preliminary Experiments

Three of the various plastic solid-state track recorders commonly used for the detection of light charged particles have been examined together with the selected cellulose nitrate (Kodak-Pathé CA 80-15), with regard to their relative suitability for alpha particle and proton detection:

- (a) Cellulose acetate butyrate (Bayer BN) dyed purple.
- (b) Cellulose triacetate (Triafol TN) dyed blue.
- (c) Polycarbonate (Makrofol E) clear.

All the above brands of plastics which are sold by the firm of Bayer A.G., in Leverkusen, W. Germany, have been used after having been thoroughly investigated because of their high sensitivity, their surface contains only very few "background" artifacts such as scratches, even after prolonged etching and because of their etching kinetics.

Various films including the Kodak-Pathé CA 80-15 were irradiated by 2.5 MeV alpha particles and 0.60 MeV protons at three angles (12° , 30° and 90° incidence to the surface of the detectors). After irradiation, all the detectors along with their unirradiated samples (for background) were etched simultaneously at a constant temperature of $(60 \pm 0.1)^\circ\text{C}$ in 5N KOH. The etching times were varied from one minute to many hours, and both interrupted and uninterrupted modes of etching were employed to study the relative reproducibility of tracks, clarity and ability to count, and the relative registration efficiency of the detectors.

The track visibility depends largely on the microscope technique used, in particular on magnification, resolution and illumination. In this study, the analyses were carried out using a Reichert (Model MEF2) microscope with an oil immersion objective of 140 X and $\sim 0.25 \mu\text{m}$ resolution together with 10 X ocular. This combination offers a useful magnification of 1400 X.

6.3.1 Low Background Counts and Measurements

Most commercially produced plastics (general purpose) were found to have too many scratches and imperfections to be used as quantitative

alpha particle and proton detectors, and consequently it was necessary to use specially manufactured plastic such as the ones mentioned in this section.

6.3.2 Reproducibility of Tracks

The low stopping powers of alpha particles and protons place them close to the limit of detectability for charged particles. Any change in material composition, mode of manufacture or environmental conditions during irradiation is likely to change the sensitivity of the detectors to the particles of interest. Cellulose acetate butyrate was found to be particularly prone to variability of this type and was rejected partly for this reason.

6.3.3 Clarity of Tracks and Ability to Count and Measure Tracks

Alpha particle tracks are about an order of magnitude smaller than fission tracks, and two orders of magnitude larger than proton tracks, which makes the observation, counting and measurement of both alpha and proton tracks difficult. The tracks in polycarbonate and cellulose triacetate were found to have insufficient contrast for reproducible track counting and measuring. In addition cellulose triacetate gave unsatisfactory definition of the etch pits, which made it difficult to distinguish between alpha and proton tracks; moreover the film had a tendency to buckle severely after etching.

6.3.4 Relative Sensitivity and Registration Efficiency of the Detectors

Figure 6.8 shows the growth and accumulation of etch pits in the detectors for the same dose ($\sim 10^6$ protons/cm²), energy (0.60 MeV) and incident angle (30° to the surface of the detectors). Each growth curve consists of three quite distinct regions. In the first region, the growth is quite slow due to the effect of the induction time, while the second region shows an almost linear rate of growth which is much greater than that of the first region. In the last region, the rate of growth has again fallen and is quite similar to region one, due to the disappearance of overetched tracks, which fall outside the narrow region of the range spread (i.e. cone length spread). Region one and two reflect the variation of density, uniformity and homogeneity of the plastic detectors; a proton has to travel a certain distance in the plastic detector in order to have a stopping power equal to the registration energy loss of the plastic before a latent track is revealable. The distance which the proton travels

is a function of the density of the plastic. Protons of equal energies will travel equal distances in uniform, homogeneous plastic detectors, provided the detectors have the same densities. In such an ideal homogeneous plastic detector, all tracks should be seen at the same time, immediately after the induction time and the necessary etching time (to a size compatible with the optical resolution of the objective used), and all should disappear at the same time immediately after overetching occurs to a size smaller than the optical resolution of the microscope. Any deviation from the above conditions could be due to straggling. In principle the curve of growth and accumulation of etch pits for charged particles of a specific incident angle and energy should consist of four regions (tracks observed in an ideal detector as shown in Figure 6.8). Region one, shows the effects of induction time and etching time of latent tracks on track growth to sizes just below optical resolution. This region should have a (slope) of $\sim \alpha^{-1}$ (i.e. very large), and the accumulation of observed etch pits should be zero (except for background). The second region shows the effect of the time necessary for latent tracks to reach a size compatible with optical resolution. The (slope) of this region should be about zero, when all tracks appear immediately. The number of tracks observed should be equal to the number of incident charged particles on the surface of the detector times the efficiency of registration of the detector. Region three manifests the etching period of tracks to pit sizes above the optical resolution, till they are overetched to a size equal to the optical resolution ($\sim 0.28 \mu$). In this region the number of tracks observed should be the same as in region two (since the ideal plastic is homogeneous and uniform in composition and density). The slope of this region is equal to the slope of region one (i.e. very large). Region four represents overetching of tracks to pit sizes below the optical resolution. This region is similar to region two and has a slope equal to the slope of region two.

It is clear from Figure 6.8 that the registration efficiency of cellulose nitrate detectors is superior to any of the other three plastic detectors. Also it is clear from comparison of the curves of Figure 6.8 that cellulose nitrate most closely approximates the curve of an ideal detector as in Figure 6.8, which suggests that cellulose nitrate is the most homogeneous of the detectors, with

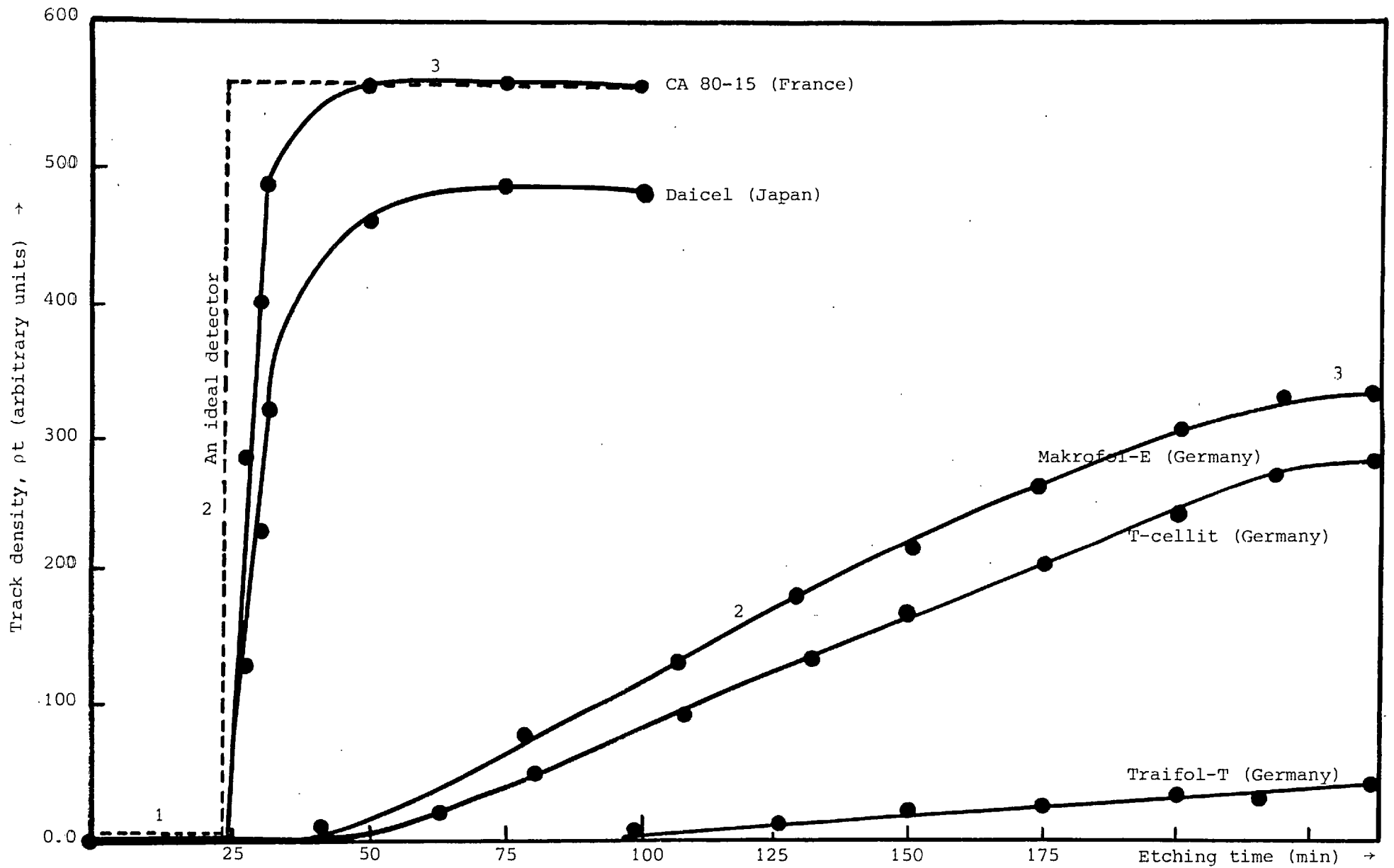


Figure 6.8 Track density ρt (arbitrary units) versus etching time, t (minutes) etched in 6 N KOH at $(50 \pm 0.1)^\circ\text{C}$

minimum range spread for equal energy protons and most capable of true range-energy reproducibility under these experimental conditions, with low noise ratio. Moreover, proton tracks of energy 0.60 MeV and incident angle of 12° to the surface of the detectors could not be revealed in any of the cellulose acetate butyrate, cellulose triacetate or polycarbonate detectors under these experimental and etching conditions. They could be revealed only in cellulose nitrate detectors with a high registration efficiency.

6.3.5 Effect of Oxygen and Humidity on the Relative Sensitivity of the Detector

It has been well established that the presence or absence of oxygen and/or humidity has a considerable effect on the type and number of chemical reactions taking place during and after irradiation in many organic systems, including living matter. The oxygen effect on living organisms makes them more sensitive to radiation damage in the presence than in the absence of oxygen. In this section, effects of oxygen and humidity on the latent track formation and etching kinetics are briefly described.

Detectors were kept in a vacuum of 10^{-4} torr for 120 hours in order to extract most of the chemically unbound oxygen from the outermost layer of the plastics, then kept for 120 hours in nitrogen prior to exposure, and exposed in a nitrogen environment. Reference plastics were also first kept in the vacuum chamber, and after this for 120 hours in dry air, and subsequently exposed in a dry air environment. A third batch of detectors were kept in pure oxygen at atmospheric pressure prior to and during exposure.

Remarkable differences in the number and size of visible tracks were found. In cellulose triacetate (Triafol TN) films after 72 minutes of etching no tracks were visible in the oxygen-free films, but 30 to 50 tracks per field were observed in the films exposed in air and in oxygen. Even after extended etching, differences in registration efficiency remained clearly visible.

The number of tracks visible in the cellulose triacetate films which had been kept and exposed in air are $\sim 14\%$ higher than the number of tracks visible in films kept in vacuum and exposed in air, $\sim 39\%$ higher than the number of tracks visible in films kept in vacuum and exposed in nitrogen, and $\sim 79\%$ higher than the number of tracks visible in films kept in vacuum and exposed in vacuum.

Evidently, there is a small difference in registration efficiency of several air-exposed cellulose triacetate detectors which could be explained by a nonsaturation of oxygen in the previously oxygen-free films. The reason for the difference between the vacuum-exposed and the nitrogen-exposed foils may be a small oxygen content in the unpurified nitrogen.

Not only the number but also the size of the etch pits depends on the presence of oxygen.

Evidently, for a given etching time the diameter of tracks visible in cellulose triacetate is approximately 25 to 30% larger for detectors exposed in oxygen than for detectors exposed in the absence of oxygen. Both the small size and the reduced number of the etch pits in the absence of oxygen contribute to the fact that they become visible only after a more extended etching time.

If the detectors which have been exposed in the absence of oxygen are kept in air or oxygen for different times between exposure and etching, they exhibit the same sensitivity as the foils which are kept free of oxygen between exposure and etching. Obviously, oxygen plays its role during exposure rather than after exposure. A drastic effect has been observed in cellulose acetate butyrate (Bayer BN) foils and a smaller effect in polycarbonate (Makrofol E) foils, but no oxygen effect has been observed in cellulose nitrate (Kodak-Pathé CA 80-15) foils which can probably be explained by the presence of loosely bound oxygen and strongly oxidizing nitrous oxides in this material.

Other batches of detectors which had been kept in dry air for 120 hours and in water for 120 hours prior to exposure were compared with foils which had been submerged for 120 hours in 15% H_2O_2 solution. The hydrogen peroxide treatment drastically increases the etching speed. In cellulose triacetate films pretreated in 15% H_2O_2 , for instance, an etch pit diameter of 4 micron is obtained after only 38 minutes of etching, as compared to 192 minutes required for a dry film and 148 minutes for films pretreated in H_2O . The effect of the H_2O_2 pretreatment was, to a small degree, still visible several days after the treatment, but it disappeared after extended storage in normal laboratory air. The maximum track count in H_2O -pretreated cellulose triacetate films was only about 10% and in H_2O_2 -pretreated films \sim 20% higher than in the dry films. Almost

the same results can be observed if treatment with humidity and H_2O_2 is done after exposure and before etching rather than before exposure. A larger effect has been observed in cellulose acetate butyrate (Bayer BN) films and polycarbonate (Macrofol E) films and a much lesser effect has been observed in cellulose nitrate (Kodak-Pathé CA 80-15) films especially if etching is carried out in concentration of $< 4N$. This could be explained partly by the experimental observation that cellulose nitrate detectors do not absorb water as much as the other detectors. The presence of water increases the etching speed but has only little effect, if any, on the sensitivity of any of the detectors. The saturation level of water is already obtained in humid air, and submersion of the detectors in water does not increase the effect. A much less pronounced oxygen enhancement was found under humid conditions. Hydrogen peroxide also increases the sensitivity only slightly, but has an even more pronounced softening effect than water on all the plastic detectors before or after exposure which accounts for the increase in etching speed.

It is obvious from the above discussion that cellulose acetate butyrate, cellulose triacetate and polycarbonate detectors are very much susceptible to oxygen and humidity effects. Reproducibility of tracks under different environmental conditions is difficult. A correction for oxygen and humidity is needed if these detectors have been exposed in vacuum inside the accelerator tube or under varying air pressures conditions.

6.3.6 Effect of Ultraviolet and Radiation Pre- and Post-Treatment on the Relative Sensitivity of the Detectors

Pre-irradiation of polymer films with ultraviolet or low LET ionizing radiation did not increase their registration sensitivity. In some cases, it even caused a reduction in sensitivity. Post-irradiation treatment with short wavelength UV has been found to considerably enhance the fission fragment track etching speed of all the detectors. Our results indicate that in all detectors, including cellulose nitrate, increase of the etching speeds, but no enhancement of the alpha and proton registration efficiency, occurs during UV-post-irradiation of the detectors.

The material found to meet most closely the required criteria is cellulose nitrate (Kodak-Pathé CA 80-15 films and LR-115 type II

films), having maximum registration efficiency, range-energy reproducibility under all environmental conditions with best signal to noise ratio and minimum change in sensitivity and registration efficiency of detectors due to mode of manufacture or environmental conditions during storage. Ultraviolet or low LET ionizing radiation did not improve the registration efficiency of any of the detectors but in all the detectors it increased the etching speed.

6.4 Experimental Observations

It was found that the geometry of tracks differs considerably from that of a perfect cone. The track shape was found to depend on the type of cellulose nitrate plastic used, on the etching conditions, on the LET of the incident charged particle and on the manner in which the LET varies along the trajectory. Etching performed at the higher temperatures ($\sim 50^{\circ}\text{C}$ and above) was found to result in imperfect tracks with a large variation in the observed track lengths and hence of the range deduced for the same initial energy. This is due to the uneven nature of the high temperature which proceeds too rapidly for uniformity in the etchant and without sufficient penetration into the latent track.

At low temperatures preferential swelling of the cellulose nitrate will facilitate an even and active diffusion of the etchant which will result in better shaped tracks which are close to perfect cones, and a higher sensitivity and resolution of track revelation.

It is important to investigate the variables that control the etching behaviour of cellulose nitrate plastic detectors.

6.5 Effects of the Specimen Composition

During the course of this investigation it was observed that the etching behaviour of a cellulose nitrate plastic is a function of a large number of variables including the degree of polymerization, the degree of nitration of the nitrocellulose, the nature of plasticizers and residual solvents and the effects of the etching solution parameters.

The etching reaction is a complex, heterogeneous process involving a solid-liquid interface. It is a three-step process, the steps being in series. Step one is associated with preferential swelling of the irradiated cellulose nitrate plastic by the etchant. Step 2 is

associated with the diffusion of the OH^- and the Na^+ ions to the interface and the diffusion of the products away from the interface; Step 3 is the actual interface reaction. If K_S is the rate of swelling K_D is the rate of the diffusion, and K_I is the rate of interface reactions, then the overall etch rate, K_T is given by

$$1/K_T = 1/K_S + 1/K_D + 1/K_I$$

The important variables that control the etching behaviour of a cellulose nitrate plastic include the following:

1. Degree of Polymerization

A heavily ionizing charged particle will produce the same degree of polymerization (DP) of the nitro cellulose, since practically all bonds in the path of the charged particle are broken. This implies that V_T should be independent of the degree of polymerization. On the other hand, the solubility of cellulose nitrate plastic in solvents has been observed to decrease with increasing degree of polymerization. From these conditions, we expect that V_T/V_B should increase for the higher molecular weight of cellulose nitrate plastic.

The results of measurements of cone angle θ is given below as a function of the viscosity of the cellulose nitrate. As it can be seen, there is a decrease of the cone angle with increasing degree of polymerization. This implies the existence of a trend of decrease in V_B for the higher degree of polymerization of cellulose nitrates which is clearly demonstrated in Table (6.2). It is clear that the decrease in V_B follows from the fact that in order to remove through chemical etching a given thickness of material from the specimen surface, a larger number of intra-chain bonds must be broken by the etchant.

Etching was performed in 5N NaOH at 27°C, and was terminated when easily measureable, short track segments appeared in all specimens. Measurements of θ were made using a goniometer/eyepiece combination.

TABLE 6.2

VARIATION OF θ , V_B WITH THE VISCOSITY
OF CELLULOSE NITRATE PLASTIC

Nitrocellulose Viscosity (sec)	Cone Angle θ (degrees)	Bulk Etching Rate $V_B = V_T \sin \theta$
~ 0.5	~ 40.7	$0.65 V_T$
~ 10	~ 29.6	$0.49 V_T$
~ 20	~ 13.4	$0.23 V_T$
~ 750	~ 10.8	$0.19 V_T$
~ 2000	~ 6.5	$0.11 V_T$

2. Effect of the Degree of Nitration

Again, for a heavily ionizing charged particle, the degree of radiation damage achieved along the trajectory appears to be independent of the degree of substitution of the NO_3 group for the OH group in the cellulose nitrate. Thus, the chemical reactivity of the latent track region, and hence of r_T remain approximately constant. However, V_B is found to decrease with increasing nitrogen content. The decrease in V_B may possibly result from the higher crystallinity of the higher nitrated specimens.

Measurements of tracks showed a decrease in θ for the more highly nitrated specimens. This increase in θ is compatible with the observation that the increase in V_T/V_B is achieved primarily through the reduction of V_B , because V_T remains essentially constant (see Table 6.3).

TABLE 6.3

VARIATION OF θ , V_B WITH THE PERCENTAGE BY WEIGHT
OF NITRATION OF CELLULOSE NITRATE PLASTIC

Percent N_2	Cone Angle θ (degrees)	Bulk Etching Rate $V_B = V_T \sin \theta$
$\sim 10.8 - 11.3$	~ 31.4	$0.52 V_T$
$\sim 11.4 - 11.9$	~ 16.8	$0.29 V_T$
$12.1 - 12.6$	~ 7.7	$0.13 V_T$

Etching was performed in 5N NaOH at 27°C.

3. Effect of Plasticizer and Solvents

A few remarks with regard to the function of the plasticizer in cellulose nitrate were given in Chapter Two. Here we will consider the influence of the concentration of the plasticizer in a cellulose nitrate on the chemical etching process.

The effect of the primary solvents will not be discussed, because of the complexity and difficulty in obtaining reliable quantitative results. Density measurements of solutions were performed at $(40 \pm 0.1)^{\circ}\text{C}$, with a hydrometer accurate to $\pm 0.002\text{g/ml}$, while measurements of solutions were determined also with Ostwald-type viscosity meters capable of 0.5% precision.

It was found that plasticizers with some volatility such as castor oil, if used alone, tend to gradually migrate out of the film. In time, the castor oil plasticizers tend to evaporate from the film, resulting in a gradual transition of the properties of the plastic back to the unplasticized state. Also we faced a difficult problem in reproducibility of parameter measurements for tracks in cellulose nitrate with volatile plasticizers. So we restricted our work to study the variation of concentration of one useful plasticizer with some degree of volatility (camphor) in cellulose nitrate.

The presence of plasticizers in the matrix of cellulose nitrate plastic has a profound effect in reducing the bulk etch rate. The degree of reduction depends on the amount and type of plasticizer and the viscosity of the cellulose nitrate used. This reduction is reflected in the very short induction times (etching times needed to develop an observable start of tracks in specimens) observed for unplasticized cellulose nitrate. Also the cone angle of the unplasticized cellulose nitrate was so large that these films are not considered useful as charged particle detectors. The presence of plasticizers in a cellulose nitrate plastic is effective in reducing cone angle θ . By varying the concentration ratio of plasticizer it is found that the optimum concentration of plasticizers appears to be less than about 28% of the weight of the dry nitrocellulose. The presence of excess quantities of plasticizer has been observed to have unfavourable effects by increasing the cone angle θ (see Table 6.4).

TABLE 6.4

VARIATION OF θ , V_B WITH THE PERCENTAGE BY WEIGHT OF CAMPHOR PLASTICIZER RELATIVE TO THE WEIGHT OF DRY NITROCELLULOSE

Camphor Concentration	Cone Angle θ (degrees)	Bulk Etching Rate $V_B = V_T \sin\theta$
0%	27	$0.45 V_T$
~ 10%	11	$0.19 V_T$
~ 25%	8	$0.14 V_T$
50%	41	$0.66 V_T$
80%	59	$0.86 V_T$
100%	very large (cannot be measured)	

Etching was performed in 2.5 N NaOH at 25°C.

At plasticizer concentration of over 50%, the plasticizer became the dominant component. The sensitivity of the detector is then reduced tremendously.

It is clear from Tables 6.2, 6.3 and 6.4 that the composition criteria of cellulose nitrate for optimal etched track conditions should consist of the following:

cellulose nitrate should have a viscosity of > 2000 , percentage of nitrogen by weight $> 11\%$ and percentage of plasticizer by weight between 15-35%.

6.6 Etching Technique and the Effect of the Etching Solution Parameters

The simplest and most general method of revelation of charged particle tracks is the chemical etching technique. However, the electron microscope observation technique is the only method used in direct track observation and for track structure studies of heavy charged particles of energy less than 1 MeV/nucleon.

The chemical etching is based on the principle that the rate of attack of a chemical reagent of the damaged area (track) of a track recorder is much greater than that of the bulk material, resulting in the tracks becoming visible under the optical microscope. There are several parameters involving the etching mechanism, and they will be discussed in the following paragraphs.

A. Etching Parameters

It is evident that the registration sensitivity of SSTR's and etched track parameters depend not only on the type of the detector but also on the etching conditions employed. For the characterization of the registration sensitivity and track geometry, several parameters should be taken into account. The criteria determining which particles leave revealable tracks by chemical etching are established in this chapter. The etching parameters which have important roles in the geometry of the etched tracks are: the etchant type, the concentration, the temperature, the agitation, the etching time, the type and concentration of impurities, and the geometrical position of the sample in the etching solution.

B. Etching Solution

The type of solution used as etchant depends on the type of the track recorder being examined. Even with one make of SSTR, different etching solutions result in appreciably different etching rates for a given etching time and temperature. The alkaline solutions (e.g. NaOH) and the acids (e.g. HF) are normally used as etchants for minerals and glasses, while for plastics, alcoholic alkaline solutions (e.g. NaOH + C₂H₅OH), oxidizing agents (e.g. KMnO₄), alkaline solutions and sometimes a mixture of all the above are recommended. A comprehensive list of etching conditions is given in Appendix (B-I).

In our experiments, the alkaline solutions were used. It was found that etching with ethyl alcohol has a drastic effect on the quantitative measurements of etched tracks, and a non-uniform bulk etching of the surface, which are probably due to variations of the parameters of the crystal-lattice (e.g. crystallinity) and of the polymer structure. The alcoholic alkaline etching solution was a mixture of 15% KOH and 40% C₂H₅OH diluted with 45% distilled water. The investigations showed that the etching times in alcoholic alkaline solution are much shorter than the etching times in an aqueous alkaline solution. On the other hand the tracks are more uniform, with better contrast and superior reproducibility in aqueous alkaline etching solution. The alcoholic alkaline etching solution was abandoned.

In addition to the above behaviour, it was determined that the alkali hydroxides had differing reactivities, the order being

$\text{KOH} > \text{NaOH} > \text{LiOH} > \text{Ba}(\text{OH})_2$. This order of reactivity is correlated with the sizes of the hydrated cations, potassium being the smallest and barium being the largest. Decreasing size of a hydrated cation allows for a faster reaction.

For optimal etching conditions, it was decided to etch with a relatively weak (2.5 N) solution of alkali hydroxides at a temperature of 18 °C. The accuracy of the alkali hydroxide solutions was controlled by titration to within ± 0.05 N, and the sample was completely immersed in a closed test tube of etchant which was maintained at (18.0 ± 0.01) °C in a water bath and monitored to within ± 0.01 °C at 15 minute intervals during etching, so that the etchant temperature remained constant. Etching with a weak etchant and low temperature gives precise control over the etching process, minimizes the surface damage of the detector and avoids partial annealing of the damaged area (tracks).

Experience with etching at various temperatures up to 70 °C and various concentrations of the alkali hydroxide etchants up to 12 normals has been obtained and the experiments are discussed in this chapter.

6.6.1 Description of Experiments

Cellulose nitrate films were irradiated with alpha particles and protons of several different energies on the Van de Graaff and the Tandem accelerators at Harwell and the University of Oxford accelerator at Oxford (see Table 5.2) to doses of about 10^3 up to 10^7 tracks per cm^2 (see Appendix C). Sheets of Kodak-Pathé LR 115 type II and CA 80-15 films were kept under normal environmental conditions before and after irradiation. In order to investigate the migration of the camphor plasticiser in the plastic and its effect on etching parameters and track geometry, other sheets were kept under a high vacuum of 10^{-5} torr for three months at room temperature before irradiation and one month after irradiation. This also permits the study of cellulose nitrate under difficult environmental conditions for absolute registration efficiency measurements and reproducibility purposes.

Etched films and carbon replicas of the etched films were prepared for optical and electron microscopy.

6.6.2 Electron Microscope Study of Track Parameters

In this study it became clear that the resolution of light optical system alone was insufficient to observe in detail the initial structures produced by etching the films for short times. A higher order of resolution was required in order that accuracy of determination of alpha particle and proton track parameters could be obtained with regard to the spatial distribution and growth characteristics during the initial stages of the etching process. One of the phenomena which is especially important during the initial stages of etching is the swelling of the cellulose nitrate by the alkali etchant.

Most light optical systems are limited to a spatial resolution of approximately 0.2μ due to systematic aberrations and the wavelengths of usable light. It was shown, however, that by utilising electron microscope techniques a considerable increase in resolution of spatial and structural detail could be obtained when observing etched alpha particle tracks in cellulose acetobutyrate films, irradiated by alpha particles produced by the $^{10}\text{B}(n,\alpha)^7\text{Li}$ reaction during thermal neutron irradiations (129). By applying similar techniques to etched films of cellulose nitrate (modified by addition of camphor), it was shown that a similar increase in resolution of structural details and measurable track parameters are possible.

Replicas of the etched alpha and proton tracks allow stereoscopic photography to be carried out at high magnification in the electron microscope, and hence the track length from the etched surface can be measured by using a measuring stereoscope (130), or calculated from the parallax between etch pit tips on a stereo pair. Stereo pair viewing of electron micrographs also enables an assessment of the quality of a replica to determine whether the features are truly replicated or whether the carbon film has collapsed during the replication procedure.

Electron microscope observations and recordings were carried out on a Philips EM 301 microscope operated at 100 KV and on an AE 1 EM 6G microscope operating at the same voltage.

6.6.3 Optical Microscope Study of Track Parameters and Track Counting

The optical microscope used along with the electron microscope for the present study was a Reichert (Model MFF 2) with oil-immersed

objective of 140 X or 150 X together with 12.5 X or 20 X oculars. The microscope stage and fine focus controls are equipped with micrometer dials so that the stage area can be scanned with precision for track counting purposes. In fact, track dimensions can be measured to an accuracy of better than $\pm 0.15 \mu$. One eye-piece is equipped with a Bausch and Lomb micrometer disc consisting of a square grid divided into 36 squares. The length of a side of the square was calibrated with a stage micrometer.

The microscope stage position is defined so that the same frame will not be counted more than once. At every frame position the tracks in the field of view bounded by the square are counted from the top row of squares to the bottom. If the tracks cross the left or top line they are not counted, whether they begin or end within the square. If they cross the right or bottom line they are counted, so that a proper statistical estimate of the track density can be obtained without deciding which is the beginning or end of the tracks. When the counting in one field is completed, the stage is moved so that a track or spot crossing one boundary is moved to the opposite boundary and the counting process is repeated. When counting tracks on the recorder, care is taken to move from one scanning path to another by displacing the scanning path by one field of view after a given path is completed and the counting process is repeated.

An automated technique for the quantitative detection of alpha track densities in LR 115 was recently developed by Lycos and Besant (131). This technique is based around the use of a Quantimet 720 Image Analysing Computer. This system utilises a Vidicon camera attached to a microscope, the camera being connected on-line to a processor with a video display.

The overall magnification from the microscope stage to the Vidicon camera screen was 1030 X and the full Quantimet frame size of $0.237 \times 0.185 \text{ mm}^2$ was used in the present work. A correction was applied for any overlapping tracks by setting two boundary numbers in the frame-separator corresponding to the track area in picture points (p.p.) and separating the track area universe into three regions. Region 1 covered single tracks up to a track area of 630 p.p., Region 2 covered double tracks up to an area of 1100 p.p. and Region 3 covered triple overlapping above an area of 1100 p.p. Hence the number of tracks per frame was:-

(Number of Singles) + 2 x (Number of Doubles) + 3 x (Number of Triples)

The region boundaries of 1100 p.p. and 630 p.p. were determined experimentally by comparisons with eye-counting and these numbers fit realistic requirements of track density with a better than 2% accuracy except for very high track densities where four and five tracks are overlapping.

Scanning of the film is automatic on the Quantimet 720 using the programmable stage control system. Repeatability of stage position was sufficiently accurate to give no observable change in track density.

The efficiency measurements at various energies were repeated using LR 115 as the SSTR and the Quantimet 720. The results showed that efficiency values measured using the Quantimet agree with the eye counted values to within the errors of $\pm 3\%$.

6.6.4 Specimen Preparation for Electron and Optical Microscopy

Films were prepared for electron and optical microscopy according to the following procedure.

Films were etched by complete immersion in alkali hydroxide solutions of various concentrations, temperatures, etchant agitation, and various lengths of etching time, then removed and worked with acidic water (acetic acid of normality half the normality of the alkali hydroxide etchant solution) for a period of half the etching time, washed in distilled water at room temperature and air-dried.

Films for optical microscopy were mounted on microscope glass slides of (0.8 - 1.0) mm thickness and glass cover slips of ~ 0.1 mm thickness.

Films for electron microscopy were studied by a one-stage and two-stage replication process according to the following procedure:

A. One-Stage Replication

(1) The dry etched plastic films were placed in an evaporator or sputtering apparatus and a layer of carbon ~ 100 angstroms thick deposited on the etched side.

(2) Shadowing of the replica may then be carried out using Pt/C at an angle of $\sim 30^\circ$ to assist in interpretation of the replica structure as necessary, or even the samples may be left unshadowed.

(3) The plastic films are then dissolved from the carbon replicas by the following method, using a solvent of composition 10 gms NaOH, 100 mls H_2O , 100 mls C_2H_5OH at room temperature. Since the backing is hard to dissolve, the procedure is different for the two types of film (LR 115 type II and CA 80-15).

(a) Kodak-Pathé LR 115 type II (backed film)

Pieces of film are cut large enough to cover electron microscope grids (2-3 mm square), immersed in the solvent for several days, avoiding vibration and movement until the cellulose nitrate films are dissolved. The carbon replicas which may now be in a folded state, are coaxed onto copper E.M. grids transferred to a bath of ethyl alcohol and then into distilled water. The replicas should then be flattened out and left floating on the water surface by this latter treatment where they can be collected on electron microscope grids, dried and examined.

(b) Kodak-Pathé CA 80-15 (unbacked film)

Pieces of film are cut as in (a) and placed carboned side up on electron microscope grids. These are then placed on a copper mesh bridge in a petri dish and solvent is carefully poured into the petri dish until the films and solvent come into contact. The action of evaporation and surface tension aids the dissolution and the working away of the plastic from the carbon replicas and after ~ half an hour all plastic should have been removed, leaving the carbon replicas on the microscope grids. These are now removed from the mesh bridge, placed on a similar bridge in ethyl alcohol for a few minutes, removed, allowed to dry in the atmosphere and examined.

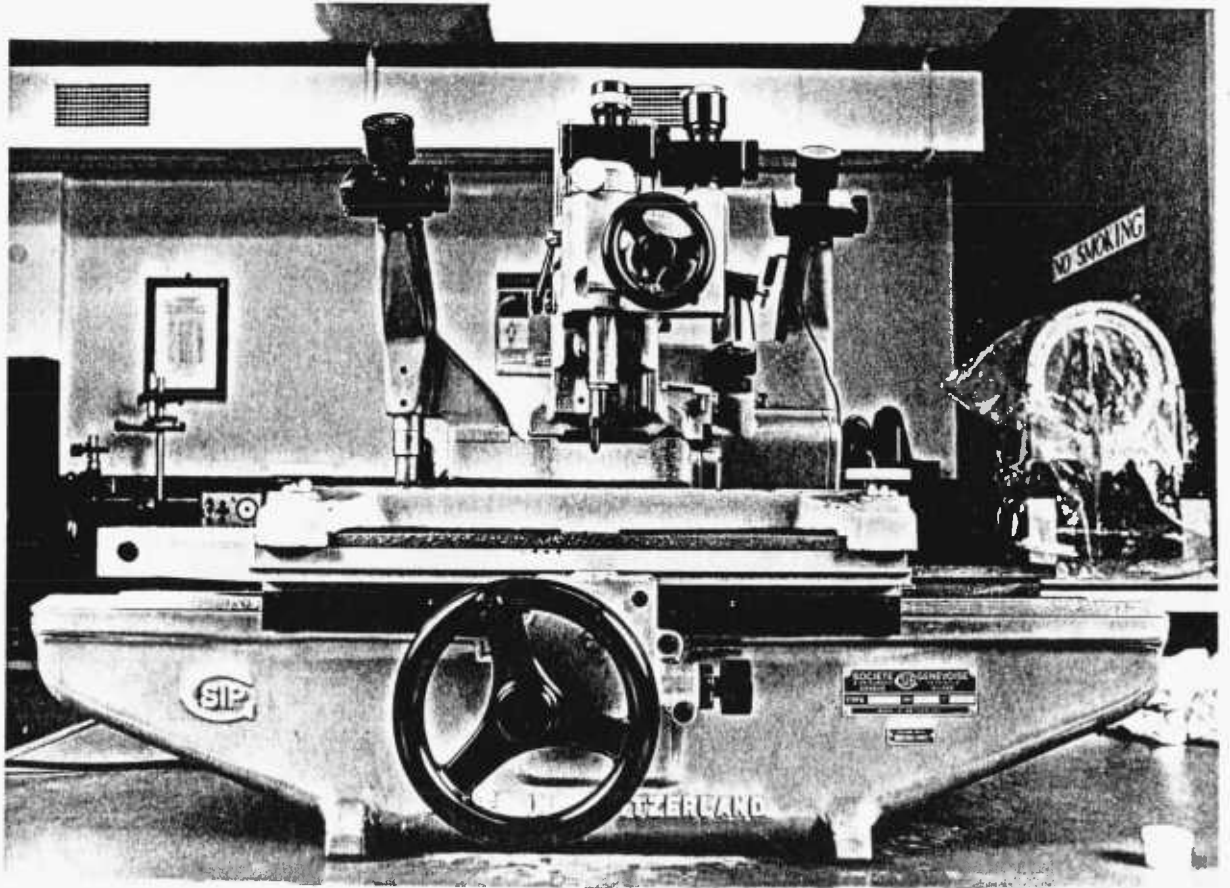
Technique (b) is to be preferred, as the result of technique (a) can lead to damaged replicas if it is not carried out with extreme care. Both one-stage replication, techniques are capable of yielding resolutions of the order of 25 Å.

(4) Examination of the replicas should be carried out in an electron microscope with specimen test facilities to allow stereo micrographs to be taken.

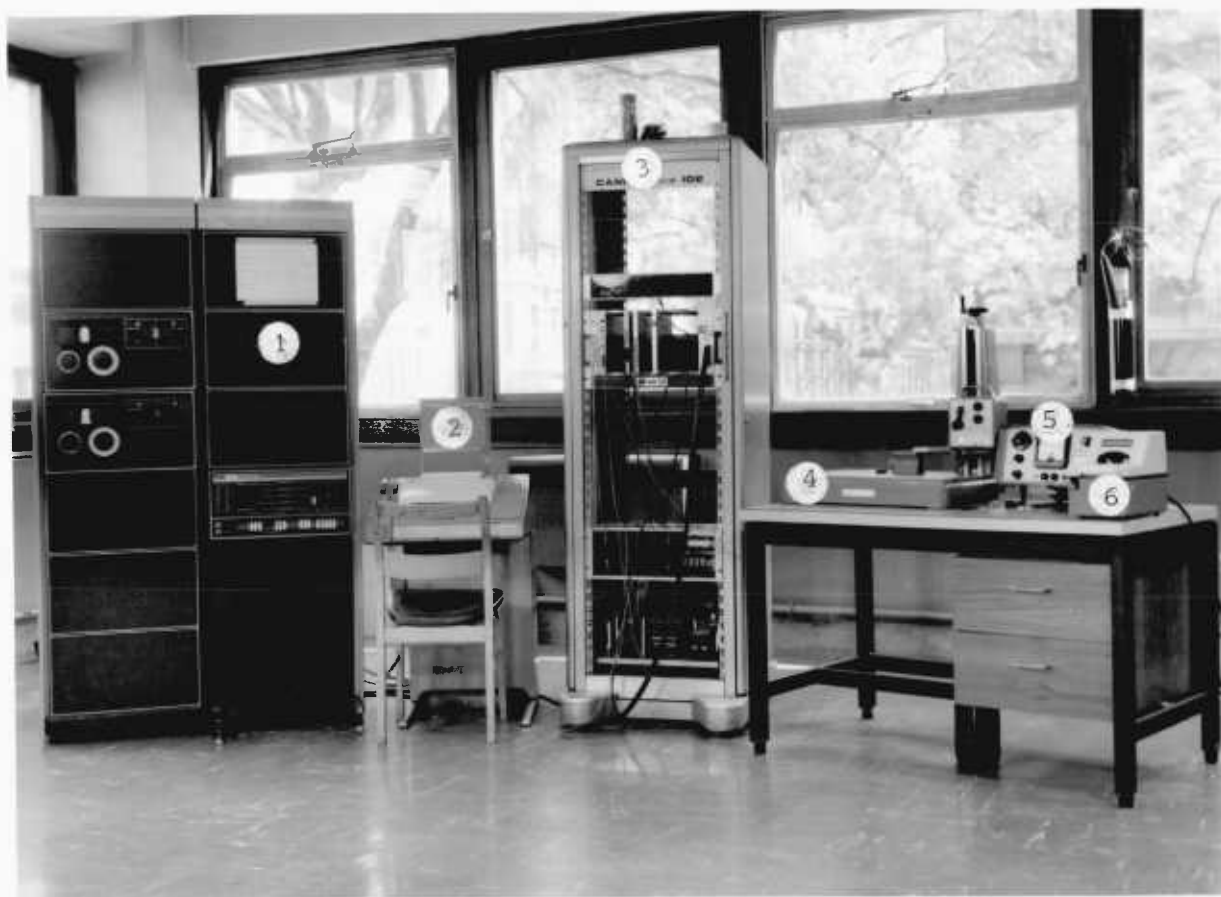
B. Two-Stage Replication

A film of polystyrene about 0.25 mm thick is made by coating a glass slide with a 5% solution of low-molecular-weight polystyrene in xylene containing 1% of dibutyl phthalate and allowing it to remain in the air for 1 hour until thoroughly hardened. The plastic detector sample is placed on the film with another glass slide placed on top of it to form a "sandwich". The two slides are clamped together with rubber tubing clamps so as to "sandwich" the sample between the two slides with enough tension so as just not to break the glass slides. The preparation is placed in an oven for 1 hour at 50°C. The "sandwich" is then removed from the oven and allowed to cool to room temperature, after which the sample can be removed from the polystyrene film with tweezers. Remaining fragments can be dissolved with cupriethylenediamine hydroxide without damaging the polystyrene replica. The polystyrene impression is transferred to a shadow casting device and carbon is evaporated on it from a vertical position, thereby forming a positive impression in carbon. Sufficient thickness of carbon has been deposited when the exposed surface of the glass slide shows a slight yellow colour. The replicas are then cut into squares which cover about eight electron screen grids. The grids are placed on small pieces of filter paper. The polystyrene replicas are arranged with the carbon face down on the screens, and a drop of xylene is placed at the edge of each of the small pieces of filter paper. These small pieces are mounted on a large piece of filter paper which is kept saturated with xylene in a covered dish for 24 hours. Gradual dissolution of the polystyrene is achieved by condensation of the xylene vapour, leaving the very thin positive replica of carbon necessary for examination with the electron microscope.

The positive carbon replicas are now placed on a glass slide, placed in the shadow casting unit, and coated with a thin layer of platinum (3 mg) deposited at whatever angle gives the best contrast to the fibre surface. A ratio of 3:1 with respect to the grids on the glass slide has been found a very satisfactory angle. This replica technique is capable of yielding resolutions of the order of 100 Å.



Photograph showing the universal measuring machine SIP 214 used for measuring the bulk etching rates of CA 80-15 and LR 115 type-II cellulose nitrate plastic



A photograph showing the Talysurf 4 machine used for measuring the bulk etching rates of CA 80-15 and LR 115 Type-II cellulose nitrate plastic

- (1) PDP 8/1 mini-computer
- (2) Teletype
- (3) CAMAC 102 interface (Talysurf-computer)
- (4) Gearbox and stand
- (5) Electronic unit
- (6) Recorder

6.7 Effect of Etchant Temperature, Concentration and Agitation on Track Formation

This preliminary set of experiments is performed with both CA 80-15 and LR 115 type II plastics in order to establish the effect of etchant concentration, temperature and agitation on the formation of tracks from the incident charged particle damage. The agitation of the etchant solution was mechanically performed with a small propeller and disc.

6.7.1 Measurements of Bulk Etching Rate

The bulk etching rates V_B were measured in two ways:

(a) Thickness measurements of the plastic sheet before and after etching were made with a high quality dial gauge micrometer and with a Talysurf 4 machine, a very high vertical resolution measuring device, which operates by dragging a stylus suspended from a pick-up across the surface at a fixed speed and with negligible lateral motion. A transducer in the pick-up translates the vertical motion of the stylus into an electrical signal which is fed to a recorder where the pen traces out the profile onto electrosensitive chart paper, or to a PDP-8/1 computer where the data is analysed and printed out (132).

(b) Diameter measurements of vertically incident 0.60 MeV alpha particles. Because $V_T \gg V_B$ the diameters of alpha particles can be treated as equal to $2 V_B t$ for a given etching time t .

The conformity of these two kinds of measurements was checked for 2.5 N NaOH at $(60.0 \pm 0.1)^\circ\text{C}$. Both methods give the same result with the same standard deviation of the measurements as shown in Figure 6.9 and below.

$$V_B \text{ (thickness)} = (5.35 \pm 0.1) \mu\text{m/h talysurf 4 machine}$$

$$V_B \text{ (thickness)} = (5.50 \pm 0.15) \mu\text{m/h micrometer}$$

$$V_B \text{ (diameter)} = (5.25 \pm 0.15) \mu\text{m/h microscope}$$

The thickness measurements are more convenient for high etching rates, while the diameter method is reliable only up to diameters of about $6 \mu\text{m}$.

The bulk etching rates at various normalities (1-12) N were measured at 15°C , 30°C and 50°C in NaOH (Figure 6.10), 50°C KOH and 50°C LiOH (Figure 6.11). All curves level out in individual

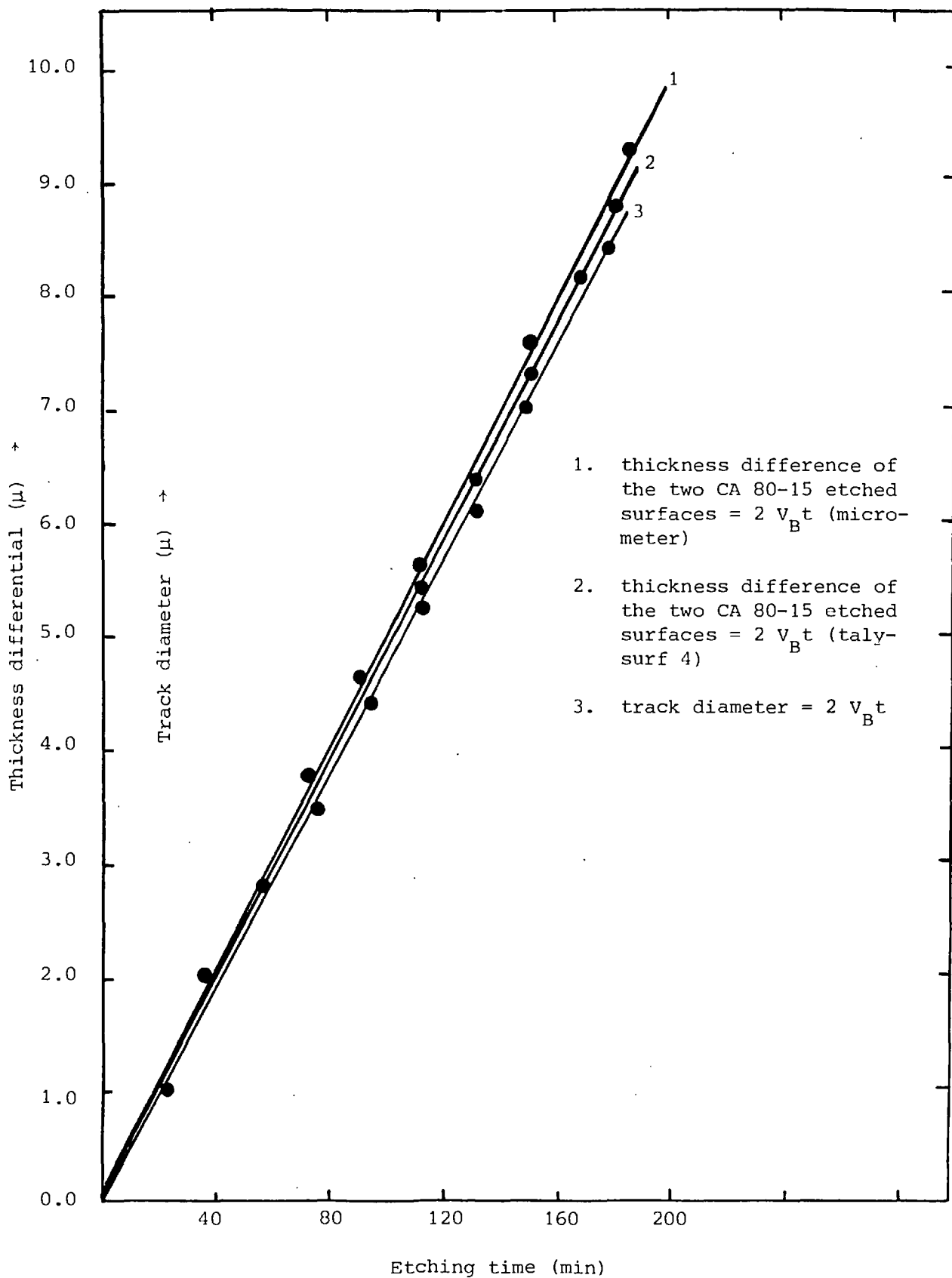


Figure 6.9 Difference in detector thickness and track diameter measurements versus etching time for CA 80-15 cellulose nitrate etched in 2.5 N NaOH at 50°C

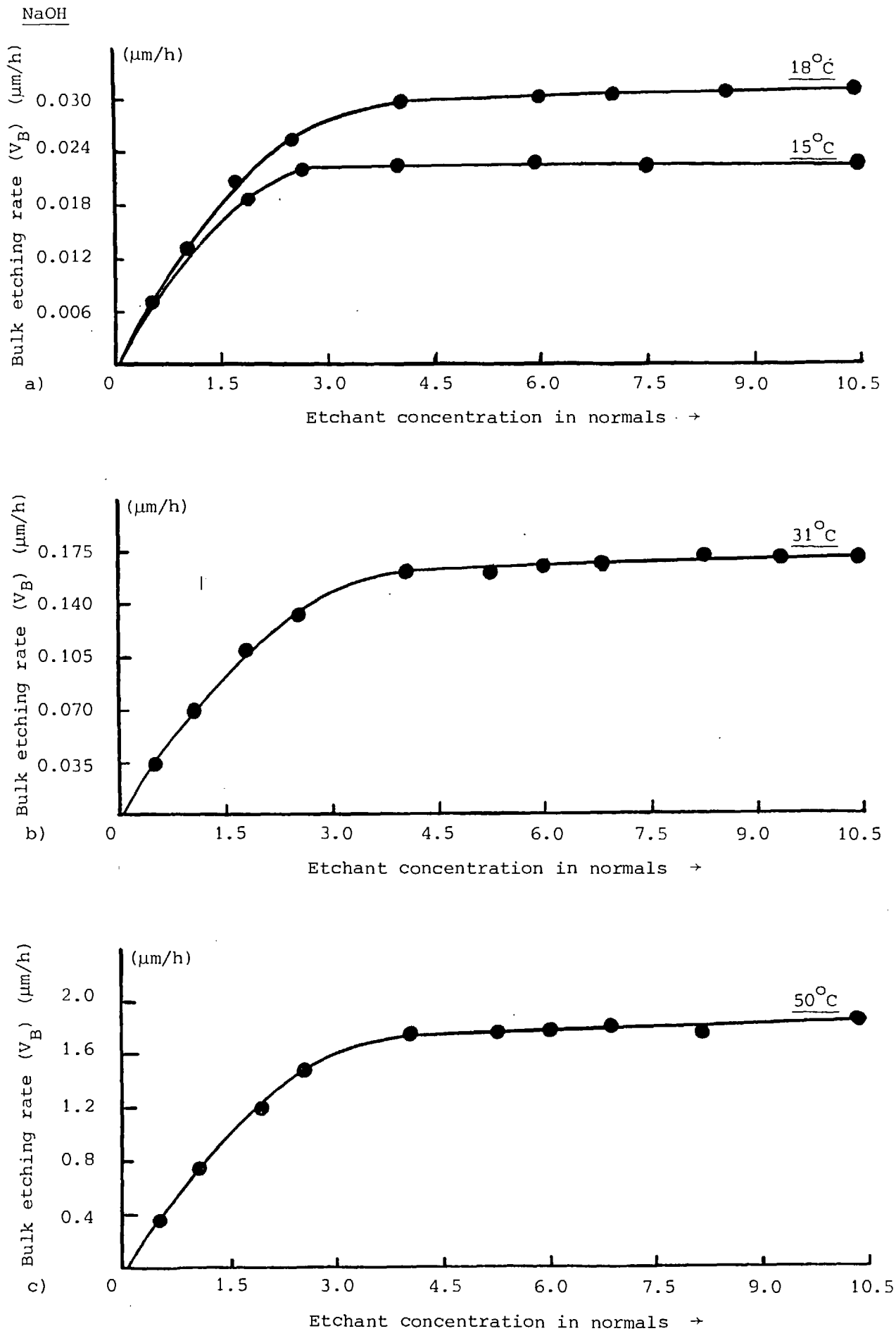


Figure 6.10 Bulk etching rate (V_B) of CA 80-15 cellulose nitrate versus NaOH concentration (normals) at different temperatures without etchant agitation or interruption of the etching process

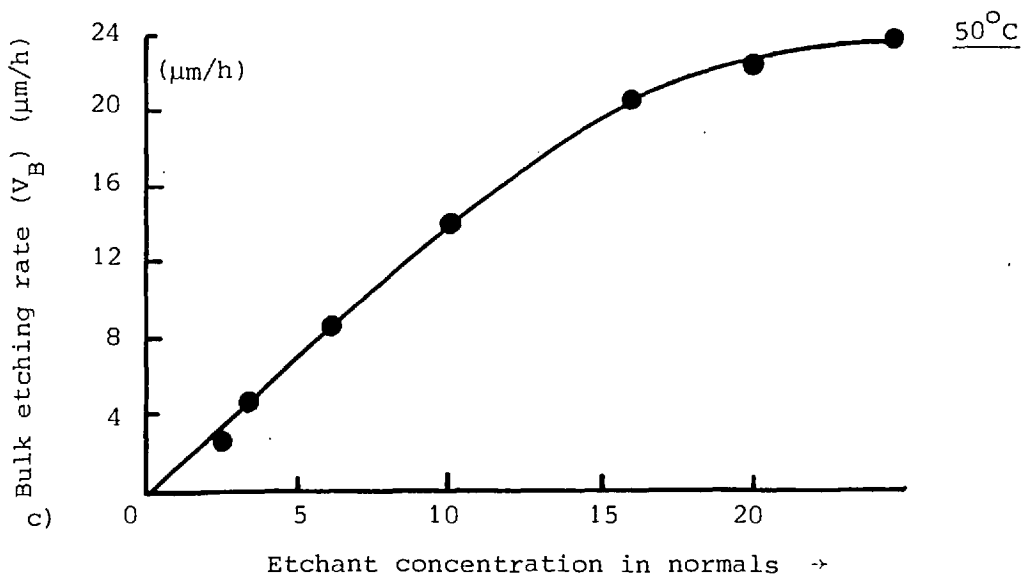
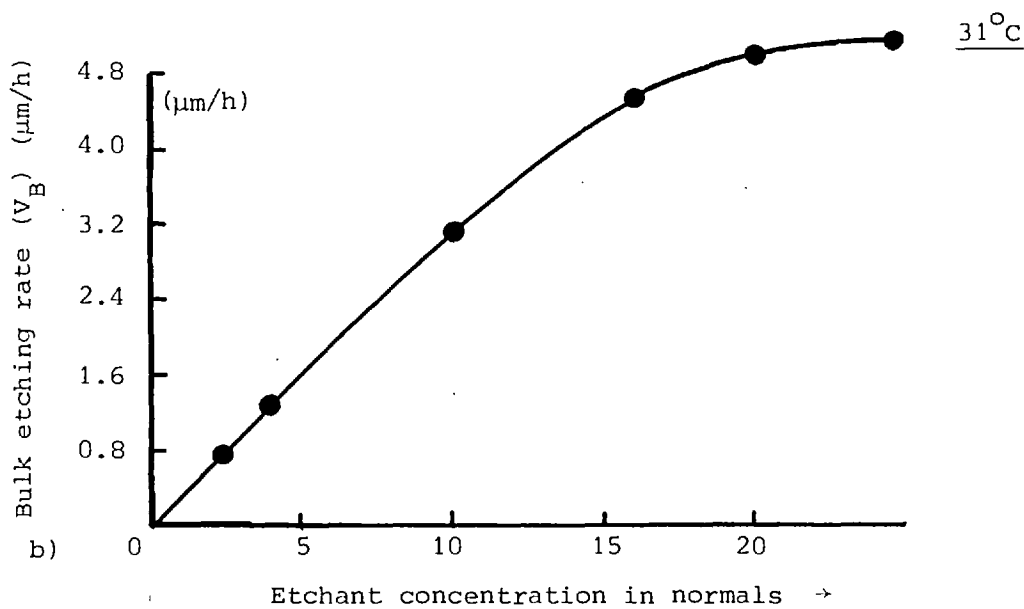
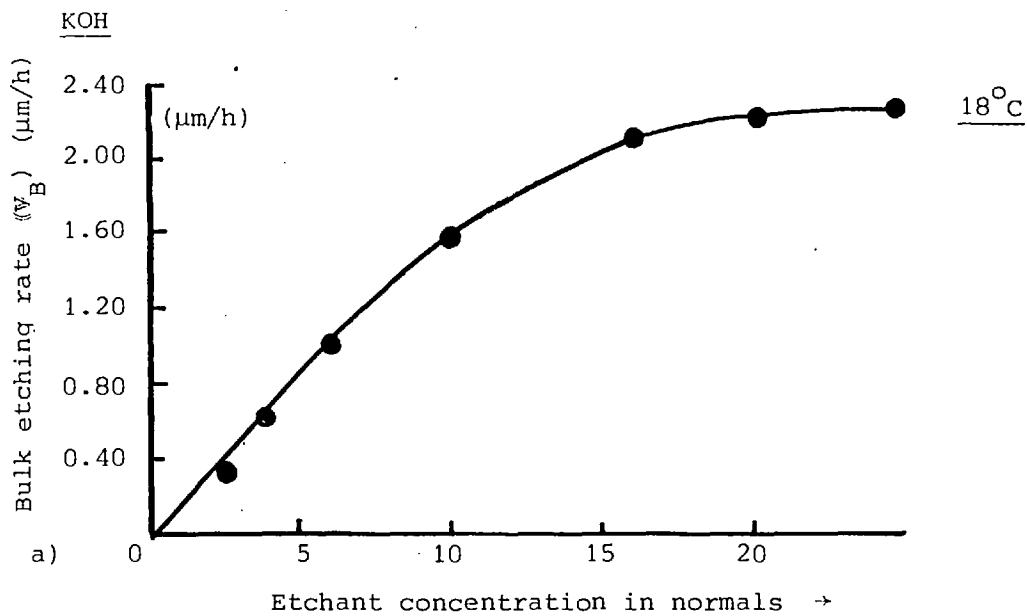


Figure 6.10b Bulk etching rate (V_B) of CA 80-15 cellulose nitrate versus KOH concentration (normals) at different temperatures without etchant agitation or interruption of the etching process

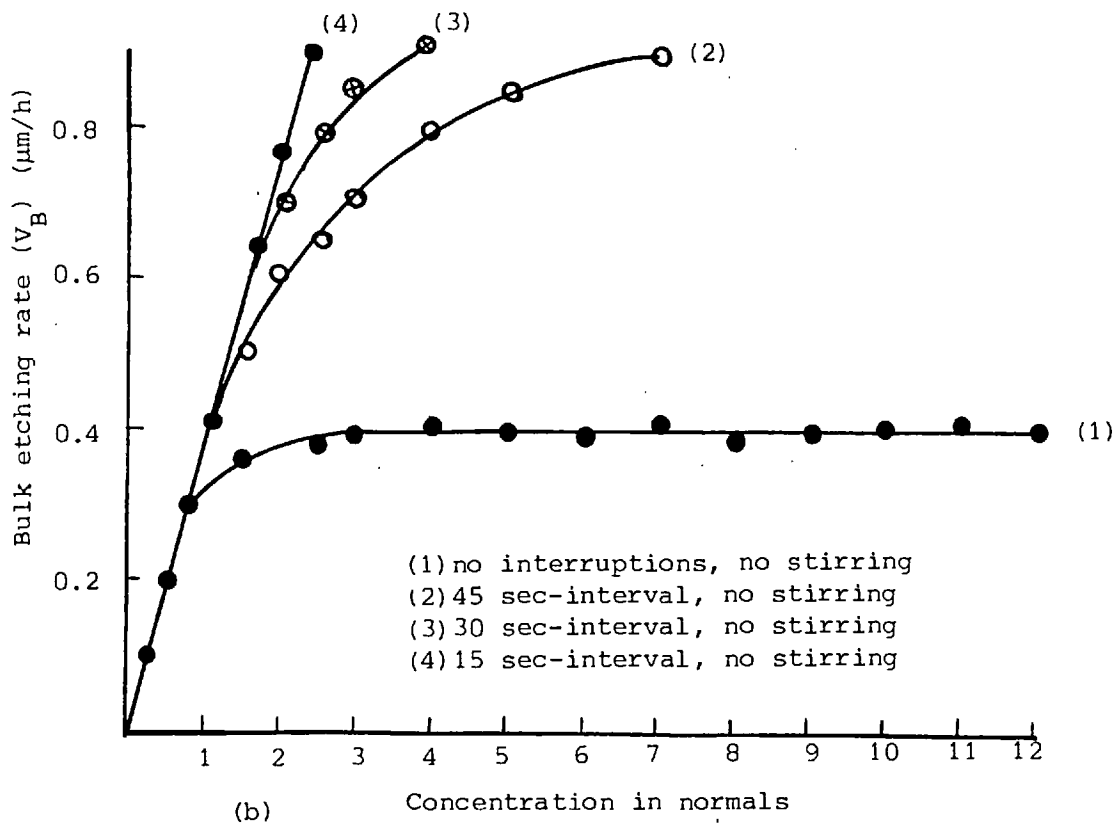
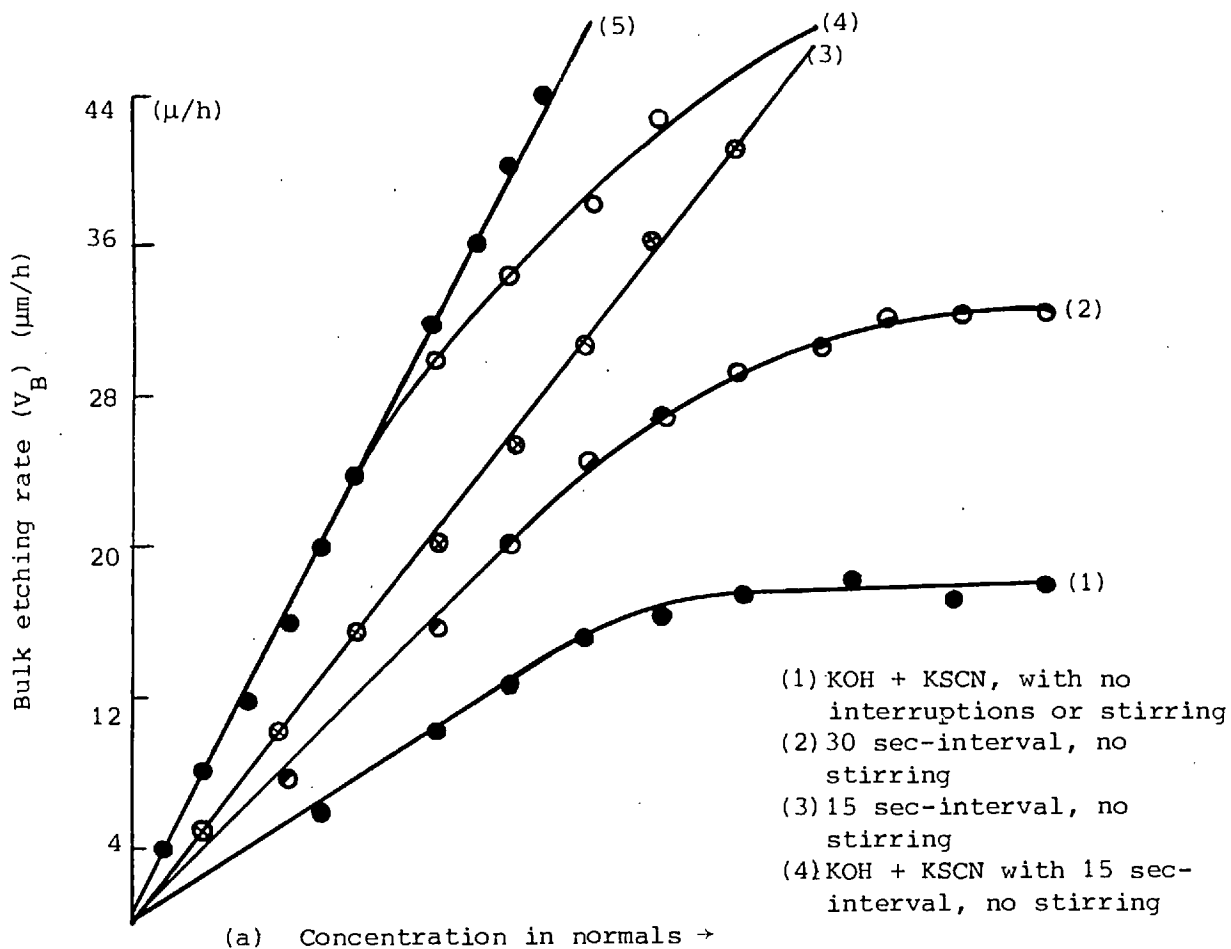


Figure 6.11 (a) Bulk etching rate of CA 80-15 (V_B) vs normality for KOH at 50°C

(b) Bulk etching rate of CA 80-15 (V_B) vs normality for LiOH at 50°C

plateaus at different concentrations. The lower the temperature the lower is the concentration where the curve starts levelling out. The beginning of this levelling out has the same temperature dependence as the maximum of the specific conductivity curve plotted versus the concentration.

The plateau bulk etching rates of LiOH is the lowest of the three plateaus for the same given temperature whereas the KOH plateau is the highest. (These plateaus were established under conditions of no stirring of the etchant.) This indicates that KOH etches better than LiOH or NaOH for the same etchant concentration (normality), and temperature. The normality, however, seems to be an unsuitable parameter for comparing the different bulk etching rate of the three etchants. Therefore, the bulk etching rates of the plastics versus the activity (the effective concentration of ions of the etchants were investigated for NaOH and KOH. NaOH and KOH solutions of different normalities at the same activity did not fall on the same curve, which indicates that the etching depends on further parameters; some of them are discussed in the following section.

A more qualitative explanation may be given by the different radii in aqueous solution of Li^+ , Na^+ and K^+ ions. These radii lead to different hydration numbers - that is the number of water dipoles around ions - and therefore to reactions of different strengths. The small K^+ ion with fewer water dipoles is more mobile than the other ions and therefore reacts faster (see Table 6.5).

TABLE 6.5

SEVERAL PARAMETERS OF Li^+ , Na^+ and K^+ IONS

<u>Ion</u>	<u>Li</u>	<u>Na</u>	<u>K</u>
Radius of the bare ion (A°)	0.6	0.95	1.33
Radius of the ion + water dipoles (A°)	3.40	2.76	2.32
Number of the water dipole per ion (No.)	6-7	3-4	2-3

It was observed that during etching of the plastics, a thin colloidal layer of partially dissolved and degraded cellulose nitrate molecules, together with components of the etching solution is formed on the surface of the plastic. This colloidal layer was found to dissolve in water, and its existence may affect the bulk etching rate of the plastic and contribute to the plateaus of Figures 6.10

and 6.11, or even the existing differences in the bulk etching rate curves using the activity as parameter.

Experiments were designed to investigate the effect of this colloidal layer on the bulk etching rate of cellulose nitrate. The simplest of these experiments was the removal of this colloidal layer either by washing the plastics with water at frequent intervals during etching, or washing away the colloidal layer by mechanical stirring of the etchant during etching. Both procedures were followed. In these experiments, it was assumed that the increase in bulk etching rates for a given temperature and normality due to any of the following procedures is a measure of the colloidal layer dissolution and vice versa.

Thickness measurements of the plastics were performed before etching in LiOH, NaOH and KOH at various normalities (1-12 N) in a temperature-controlled water bath at $(50.0 \pm 0.1)^\circ\text{C}$ for 45 seconds without stirring the etchant, rinsed in distilled water at $(50.0 \pm 0.1)^\circ\text{C}$ for 5 seconds and dried with tissue paper for 5 seconds. This cycle was repeated up to 90 minutes effective etching time and the thickness was measured again. Furthermore, etching periods of 30 seconds and 15 seconds within the cycle were also tried. The measured bulk etching rates for KOH, LiOH and NaOH are shown in Figures 6.11 (curve 1, 2, 3 of a and 1, 2, 3, 4 of b) and 6.12 (curve 1, 2, 3, 4), where the curves do not level out in plateaus. The etching rates of LiOH and NaOH obtained with intermediate rinsing are straight lines up to a definite point, depending on the intermediate rinsing frequency, at which a break occurs towards lower etching rate with increasing normality for lower rinsing frequency. Intermediate rinsing does not affect the bulk etching rate of either LiOH or NaOH at low normality (≤ 1 N), as shown in Figures 6.11 and 6.12. Whereas etching rates of KOH obtained with and without intermediate rinsing differ from each other even at low normalities (i.e. 3 N), the etching rates are one and half times larger with intermediate rinsing intervals of 30 seconds, and double with intermediate rinsing intervals of 15 seconds up to an etchant concentration of about 7 N. This means that the influence of the colloidal layer is very small at these normalities in LiOH and NaOH; however, it cannot be neglected in KOH.

Investigations of the effect of mechanical stirring of the etchant on the bulk etching rate were carried out using 0, 1.5 and

5 V voltage for the stirring motor. In Figure 6.12 (curves 1, 5, 6) show clearly the effects of different rotation speeds on bulk etching rate of the plastic samples.

To increase the effective agitation of the sample in the NaOH etchant, the plastic samples were fixed with a wire on a disk which was spinning with higher speed than the stirrer for the same voltage supply. The effects of different disk speeds on the bulk etching rate of the samples are shown in Figure 6.12 (curves 7, 8, 9). The small numbers of on these curves indicate the stirring rate in revolutions per minute of the disk. It is clear from Figure 6.12 that although the voltages were constant for each curve the bulk etching rates slow down for higher concentrations, after reaching a peak at 5 N. For low normalities and very high stirring speeds, the bulk etching rate approaches the value of the intermediate rinsing method as shown in Figure 6.12 (curves 4 and 9).

On the other hand, at a given temperature of $(40.0 \pm 0.1)^\circ\text{C}$ and stirring rate (≈ 100 rpm) the bulk etching rate of cellulose nitrate without plasticizer increases as the hydroxide concentration increases (up to approximately 5 N as in Figure 6.13 curve 1), till the increasing viscosity of the NaOH solution becomes effective in slowing down the etchant stirring rate. Figure 6.13 (curve 2) shows the etching rate of cellulose nitrate without plasticizer at $(40.0 \mp 0.1)^\circ\text{C}$ and without stirring (same as in curve 1 but without stirring). The bulk etching rates of partly plasticized (camphor has a high vapour pressure, so a large part of the plasticizer will escape due to storage under a high vacuum for a long period) CA 80-15 cellulose nitrate at $(40.0 \pm 0.1)^\circ\text{C}$ with stirring (≈ 100 rpm) and without are shown in Figure 6.14 (curves 1 and 2 respectively). Figure 6.15 is the same as Figure 6.14, but without stirring and with an etching temperature of $(15.0 \mp 0.1)^\circ\text{C}$.

Investigations were carried out in order to increase the KOH bulk etching rates by adding specific chemicals to the hydroxide. Curve 4 of Figure 6.11a shows the result after adding potassium thiocyanate KSCN to the KOH solution (KOH was mixed with 300 g KSCN). The samples were etched without interruption and the increase of the bulk etching rate V_B was observed to be greater than in the case of the intermediate rinsing method.

Discussion

The effect of the plasticizer in cellulose nitrate on the etching rate is quite important. Since camphor is neither attacked nor soluble in the etchants, (see Table 6.6), its buildup at the surface would be expected to increase with increasing hydroxide concentration, since the amount of camphor available at the surface per unit time would be greater, and its solubility would be less. If the layer inhibits etching, then one would expect either a levelling of the bulk etching rate or a maximum as the etchant concentration increases. Both have been observed.

TABLE 6.6

SOLUBILITY OF CAMPHOR AT 40 °C

<u>Solvent</u>	<u>Solubility (g/l)</u>
H ₂ O	2.13
4.00 N KSCN	2.01
3.00 N KOH	0.16
6.25 N NaOH	0.03

The inhibiting effect of the layer is explained in camphor as compared to the cellulose nitrate itself. Camphor, being the less polar of the two, would not be as good a solvent. The reactive order KOH > NaOH > LiOH follows the same order as the normal solubility of these reagent inorganic media. Diffusion of etch products through the camphor layer must also be considered. If their diffusion is greatly retarded, they would build up at the surface and this might also inhibit further etching. This does not mean that the buildup of the colloidal layer on the surface of the detector during etching consists of only plasticizer (camphor) but for the main part, it consists of the plasticizer and the rest is degraded cellulose nitrate. This is confirmed by the observed levelling out of the bulk etching rate with increasing etchant concentration at a given temperature for both plasticizer and unplasticized cellulose nitrate, as shown in Figures 6.10, 6.12, 6.13 and 6.14. From these figures it is clear that the influence of plasticizer on the bulk etching rates is dominant. It governs the nature of the etching for a given set of conditions.

The enhancing effect of KSCN on the etch rate can be explained by the assumption that it dissolves or reduces the colloidal layer

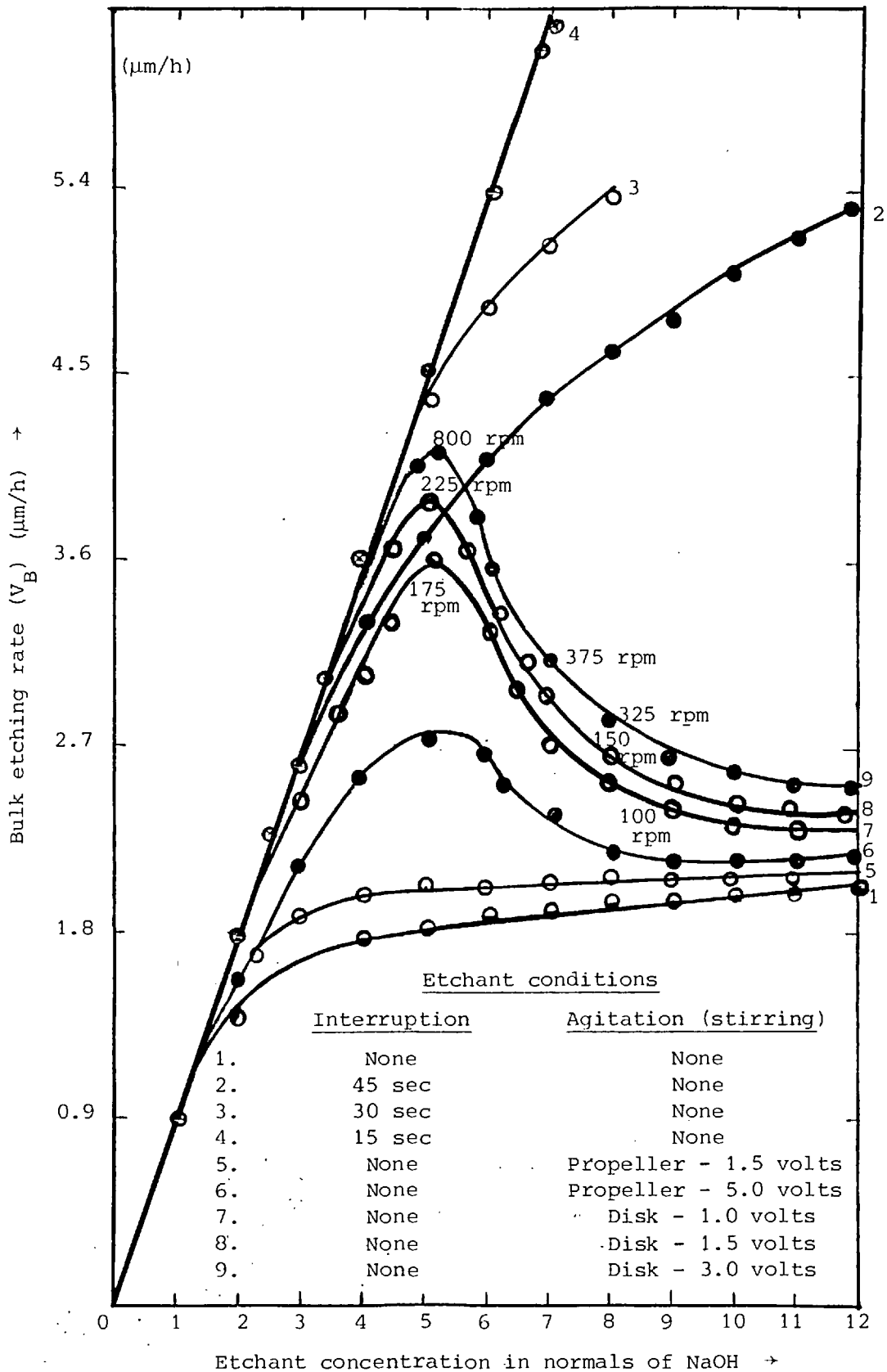
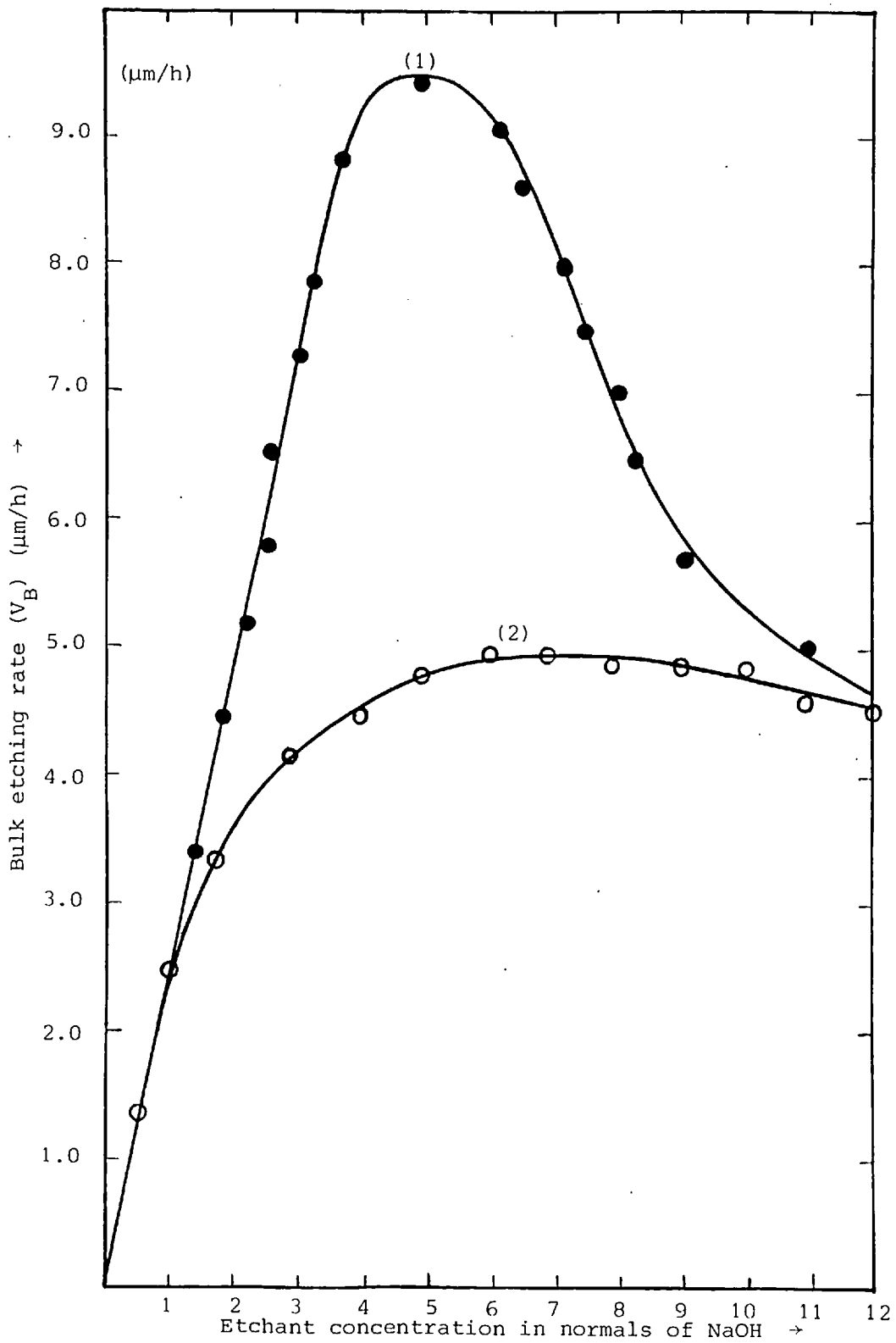


Figure 6.12 Bulk etching rate (V_B) of CA 80-15 cellulose nitrate versus NaOH concentration (normals) at 50°C with varying interruption periods and stirring speeds



(1) With stirring (~ 100 rpm)
 (2) Without stirring

Figure 6.13 Bulk etching rate of unplasticised cellulose nitrate versus NaOH concentration (normals) at 40°C

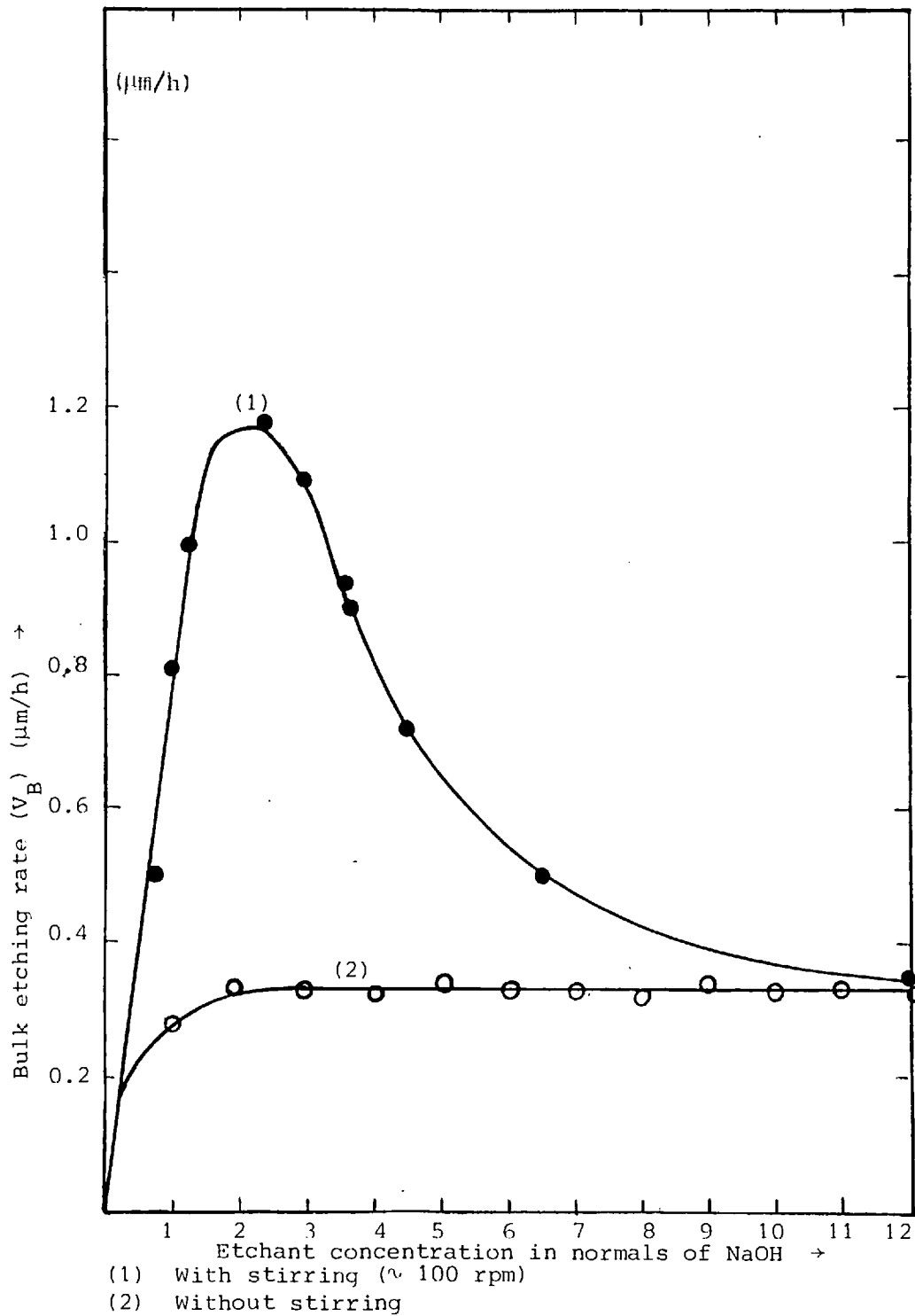
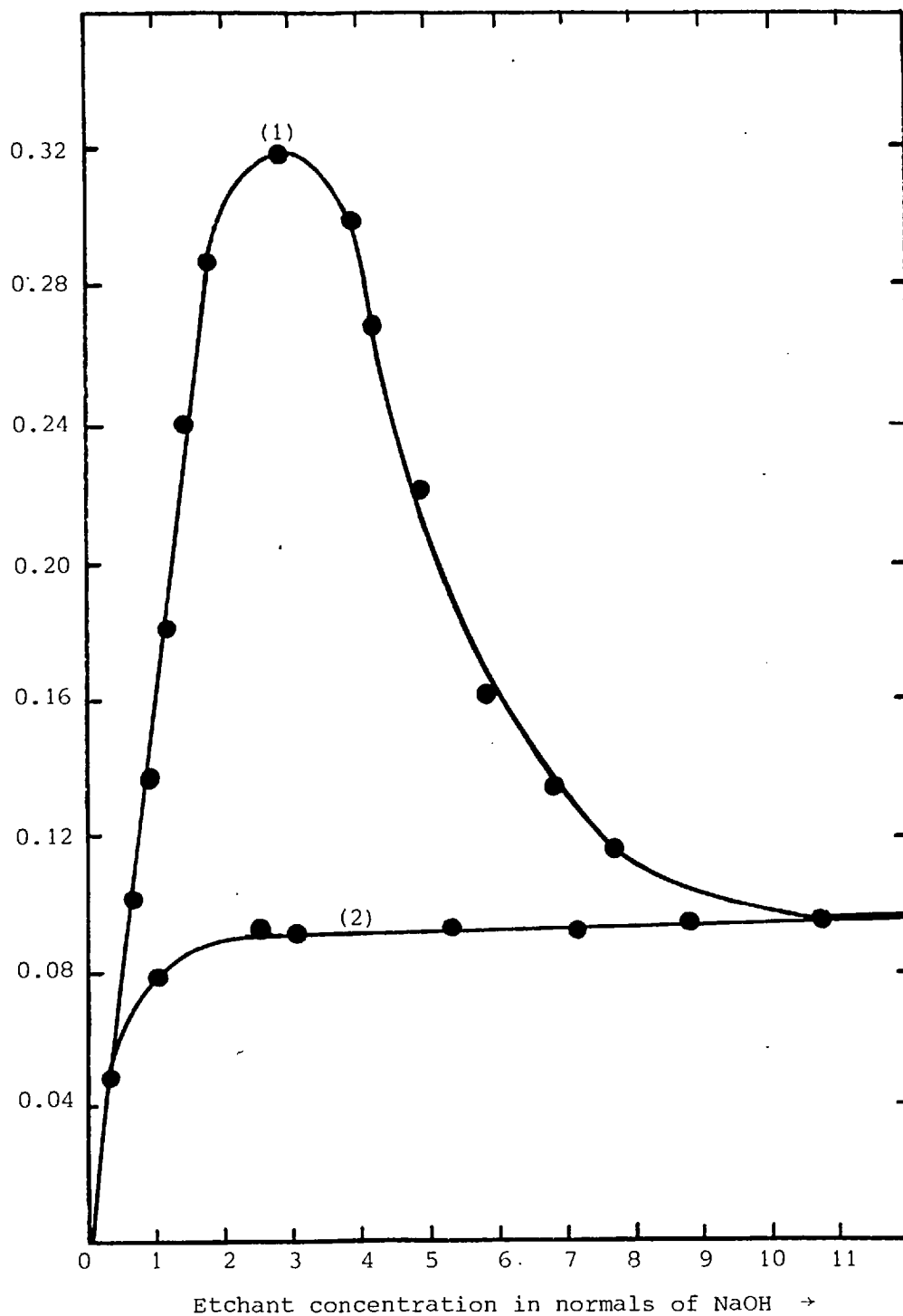


Figure 6.14 Bulk etching rate of CA 80-15 cellulose nitrate partly plasticized (stored in high vacuum) vs normality for NaOH at 40°C



(1) With stirring (~ 100 rpm)
 (2) Without stirring

Figure 6.15 Bulk etching rate of CA 80-15 cellulose nitrate partly plasticized (stored in high vacuum) versus normality of NaOH at 15°C

which has been formed on the surface of the plastic during etching, thus reducing the barrier between the cellulose nitrate and the hydroxide, resulting in a faster reaction. But in fact our studies revealed that the KSCN solution is an excellent swelling agent for cellulose nitrate and does not react with either cellulose nitrate or camphor; it probably swells the cellulose nitrate, loosening the lattice structure for an easier penetration of the hydroxide which results in a degradation of cellulose nitrate by the hydroxide. The thiocyanate ion is a good nucleophile (133). However, sodium thiocyanate is not nearly as effective a swelling agent as the potassium salt (the bulk etching rate 4 N KSCN in 6 N NaOH is 3.11 times larger than the bulk etching rate of 4 N NaSCN in 6 N NaOH), indicating that the effect is not just due to the thiocyanate ion.

It was also assumed that mechanical stirring will wash away or decrease the buildup of the colloidal layer on the surface of the plastic. In fact we believe the major contribution of the stirring is to prevent the exhaustion of the solution near the surface, which accounts for the major increase of bulk etching rate due to stirring. During the etching process, a concentration gradient of hydroxyl ions is expected to build up at the surface due to etchant exhaustion in the bulk. Also the surface is analogous to that of a membrane, with a dipole layer of charge leading to a potential difference. Stirring will decrease the concentration gradient significantly, thereby aiding the passage of hydroxyl ions from the solution to the bulk. Clearly, stirring will have little effect on the fluid inside a narrow track, so the track etching rate is practically unaffected. Thus stirring decreases the sharpness and length of etched tracks.

It is evident from these discussions that intermediate rinsing is the only reliable method for washing away the colloidal layer during etching, and the only procedure that gives an accurate measurement of the decrease in bulk etching rates due to the buildup of the colloidal layer of partially degraded cellulose nitrate.

It is evident from Figure 6.10 (a, b and c) that the temperature is by far the most influential parameter on the bulk etching rate of cellulose nitrate. An increase of etching temperature from 15°C up to 30°C and up to 50°C (Figure 6.10 a, b and c) results in about a sevenfold and an eighty-three-fold increase in etching rate respectively,

at an etchant concentration of 6 N NaOH. Measurements of the bulk etching rates for LR-115 type II and CA 80-15 plasticized cellulose nitrate etched in 2.5 N and 6 N NaOH, 2.5 N KOH and 2.5 N LiOH solutions at different temperatures are given in Figure 6.16, and LR-115 type II and CA 80-15 partly plasticized (stored in a high vacuum) cellulose nitrate etched in 2.5 N NaOH solution are given in Figure 6.17.

It is clear that the rate of chemical attack is highly temperature dependent. This reflects the importance of maintaining a constant temperature during etching if reproducibility and quantitative measurements are required.

In Figures 6.16 and 6.17 the natural logarithm of the bulk etching rate (microns/hour for a single surface) is plotted as a function of $1/T$, where T is the temperature of the etching solution in $^{\circ}\text{K}$. The slope of the curve gives the activation free energy (ΔF_B) of the bulk etching rate, being 1.01 eV for the CA 80-15 and 0.96 eV for the LR-115 type II plasticized cellulose nitrate etched in 5 N NaOH. The activation free energy of the bulk etching rate of the partly plasticized (stored in high vacuum) material is slightly higher. It is clearly noted from Figure 6.16 that all measurements fall on a straight line up to a definite temperature, ($\approx \sim 55^{\circ}\text{C}$ for 2.5 N NaOH), above which a break occurs probably due to the anisotropic bulk etching rate at high temperatures, where swelling of cellulose nitrate is very small and accessibility of the hydroxide to the bulk will be non-uniform rather than isotropic. At these temperatures, reactions of the hydroxide with the bulk will be rapidly degrading rather than gently etching. This is shown by the observation that at higher etching temperatures the etching rates for both LR-115 type II and CA 80-15 approach each other. Measurements of V_B for LR-115 type II and CA 80-15 plasticized and partly plasticized (stored under high vacuum) plastics etched in 2.5 N NaOH solutions at different temperatures are given in Table 6.7.

It should also be noted that a break of the linearity of Figure 6.10 occurs at lower temperatures ($\approx \sim 34^{\circ}\text{C}$) for higher etchant concentration (~ 5 N NaOH). This is due (in addition to the previously discussed contributions) to the preferential absorption of alkali by the cellulose nitrate in contact with solutions containing more than 3.7 N NaOH.

NaOH

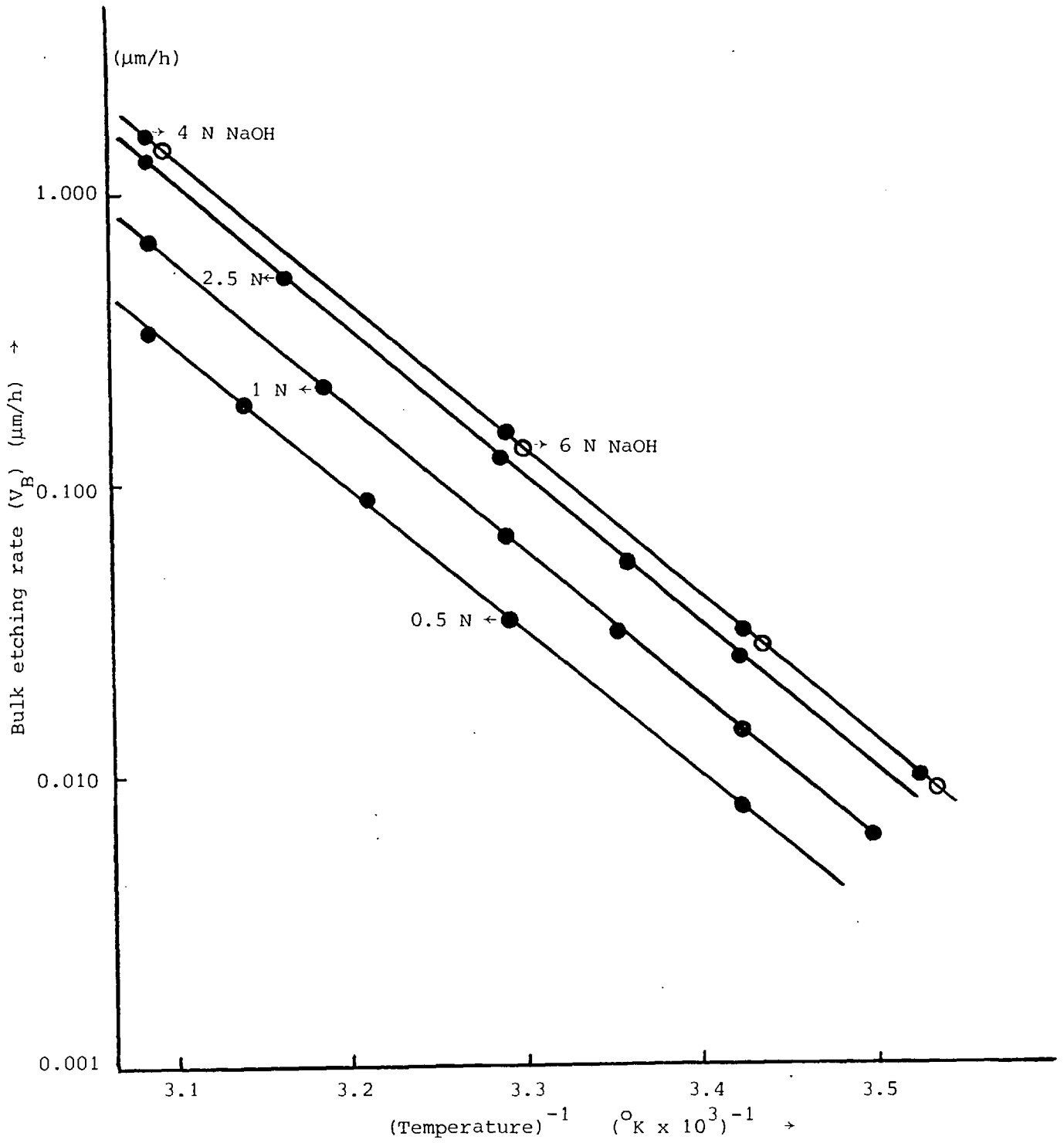


Figure 6.16 Bulk etching rate of CA 80-15 cellulose nitrate versus temperature at different concentrations of NaOH, without interruption or agitation

KOH

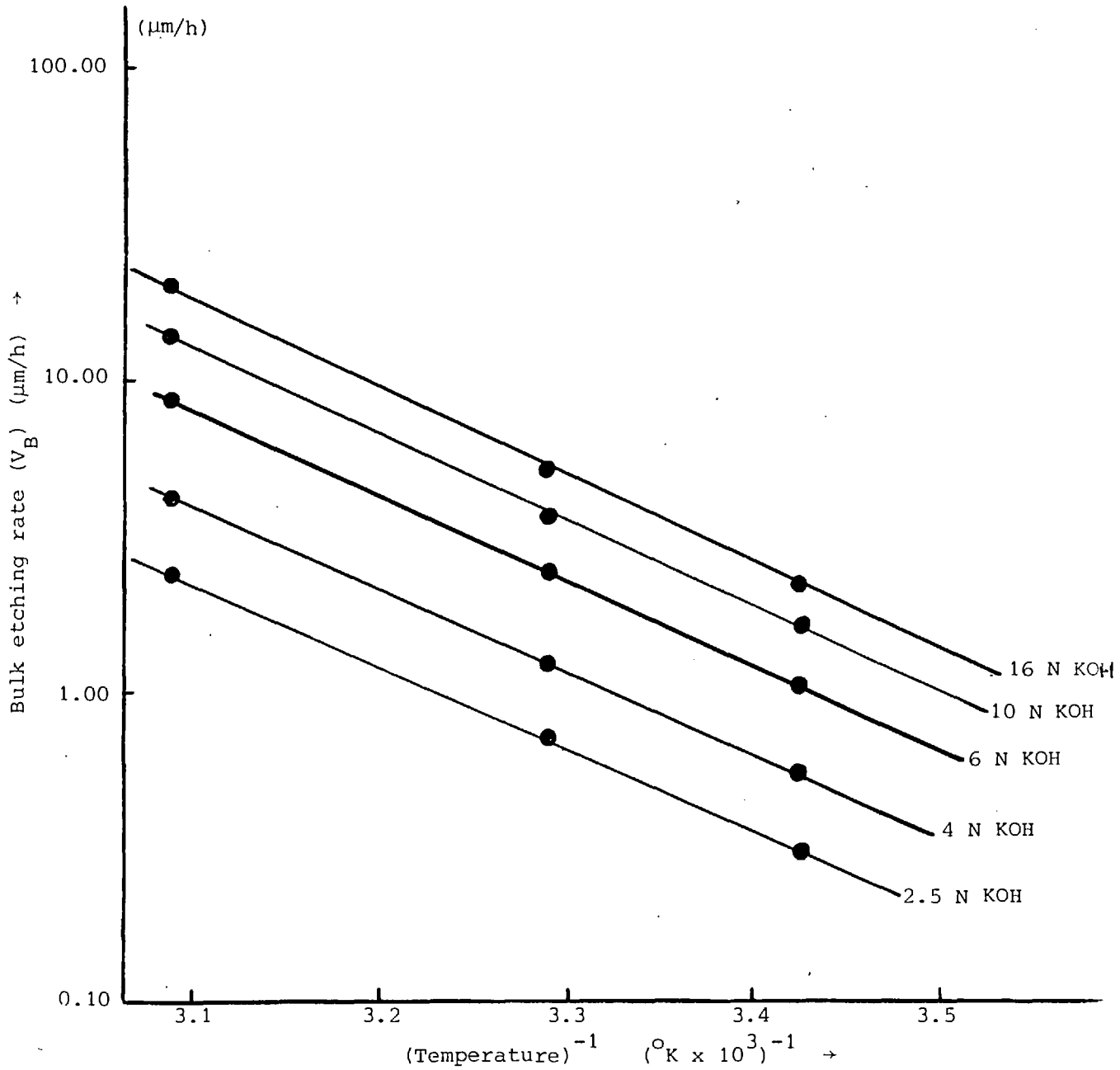
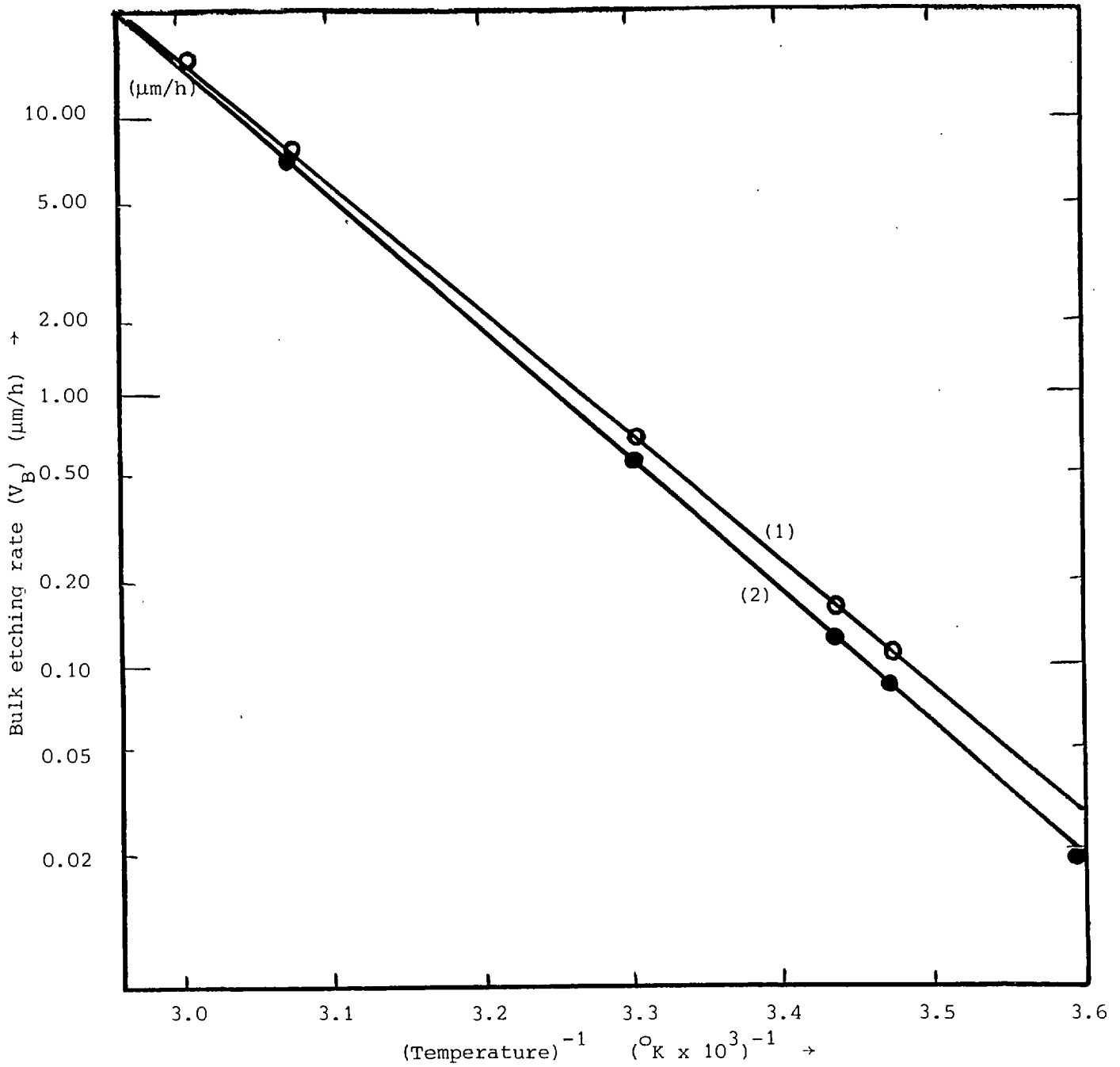


Figure 6.16b Bulk etching rate of CA 80-15 cellulose nitrate versus temperature at different concentrations of KOH, without interruption or agitation



- (1) For LR-115 type-II cellulose nitrate
- (2) For CA 80-15 cellulose nitrate

Figure 6.17 Bulk etching rate of partly plasticized CA 80-15 and LR-115 type-II (stored in high vacuum) as a function of temperature, without interruption or agitation

TABLE 6,7

Bulk Etching Rate (micron/hour for a single surface) as a Function of Temperature for LR-115 type II and CA 80-15 Plasticized and Partly Plasticized (stored under a high vacuum) Cellulose Nitrate Etched in 2.5 N NaOH.

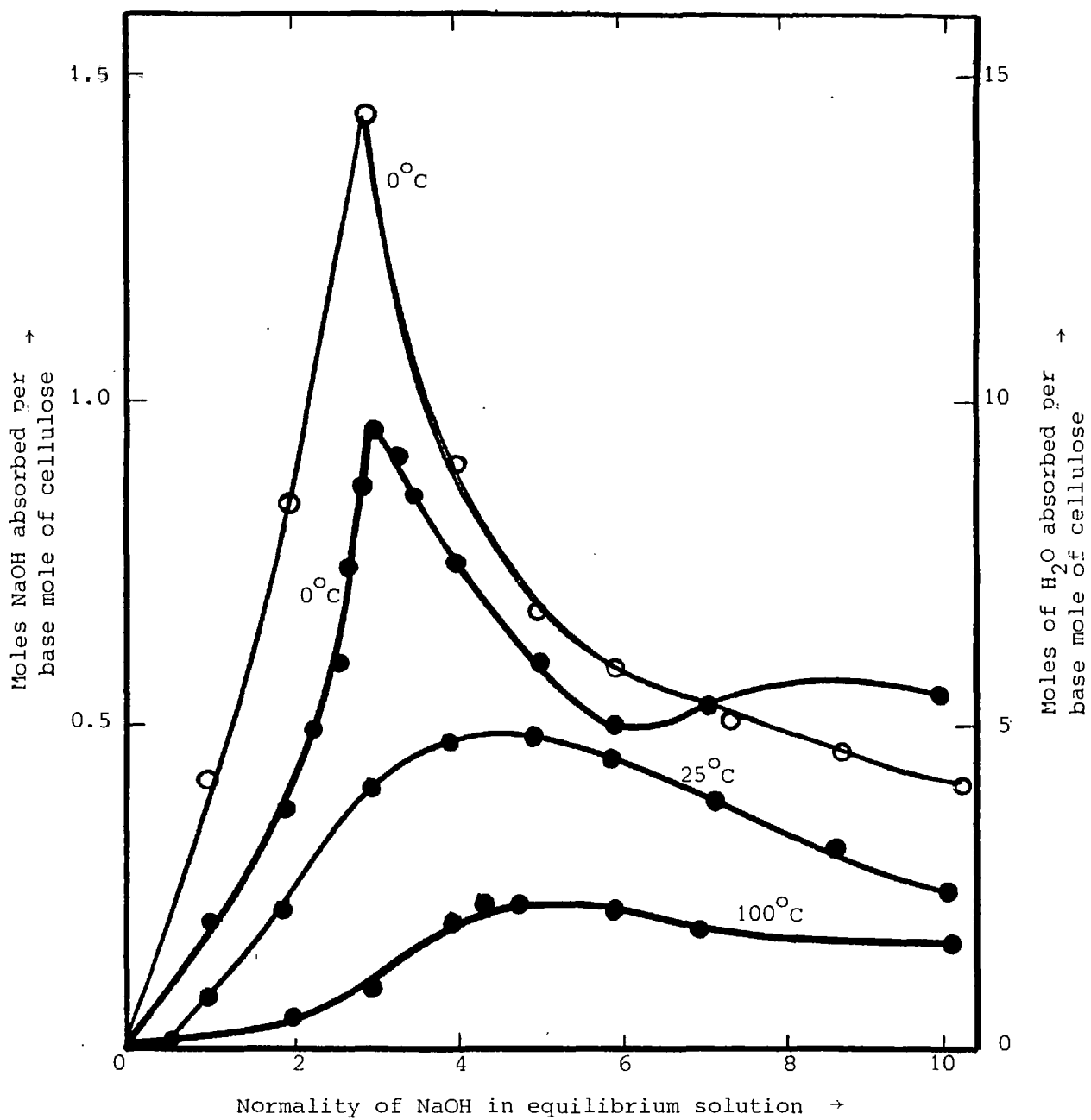
T(°C)	(V _B) LR-115 Type II Plasticized	(V _B) CA 80-15 Plasticized	(V _B) LR-115 Type II Partly Plasticized	(V _B) CA 80-15 Partly Plasticized
15	0.028	0.021	0.125	0.082
30	0.135	0.115	0.555	0.525
50	1.65	1.64	6.75	5.88
70	4.52	4.48	69.4	67.6

So far, no attention has been given to the swelling, hydration and the preferential absorption of alkali by cellulose nitrate during etching. Most early investigators disregarded swelling phenomena and the role played by water in the etching process of cellulose nitrate, and explained unusual observations as contributions from the colloidal layer formed at the surface of the plastic.

6.7.1.1 Method for Determining alkali absorbed in Cellulose Nitrate and its effect on Bulk Etching

Cellulose nitrate films were treated with various concentrations of NaOH, KOH and LiOH (a ratio of 10:1 by weight for alkali solution to cellulose nitrate was used) at various etchant temperatures. The change in alkali concentration is determined by titrating a known weight of cellulose nitrate placed in a known weight or volume of alkali solution. The method requires careful standardization of the experimental conditions in order to obtain reproducible results.

Figure 6.18 shows the effect of temperature and concentration on the total alkali and water absorbed by plasticized (CA 80-15) and un-plasticized cellulose nitrate. These experiments and their results (Figure 6.18) show that, for temperatures between 5°C and 40°C, points of maximum hydration and maximum alkali absorption occur, and that



Unplasticized CA 80-15 cellulose nitrate
 Plasticized CA 80-15 cellulose nitrate

Figure 6.18 The effect of temperature and concentration on the total alkali and water absorbed by CA 80-15 plasticized and unplasticized cellulose nitrate

these maxima are greater at lower temperatures. For solutions of concentrations 0.75N NaOH to 2.25N NaOH, the effects of temperature on hydration and on caustic soda absorbed bear a close resemblance to each other, indicating that under these conditions the solutions in which the cellulose nitrate was immersed were absorbed without change in composition. For the more concentrated solutions, (> 2.5N NaOH) the curves are not similar, and this has been taken to indicate preferential absorption or the occurrence of chemical reaction.

Figure 6.19 shows NaOH and H₂O absorbed by cellulose nitrate at 25°C. Curves: 1, total alkali absorbed; 2, preferentially absorbed alkali; 3, water absorbed. On close study, it is found that, if the amounts of alkali preferentially adsorbed as indicated by the curve 2 of Figure 6.19 are deduced from the total absorption (Curve 1), the remaining quantities of alkali and water are present in cellulose nitrate in almost exactly the proportions as in the mother liquors. The differences in total absorption may be assumed, therefore, to represent mainly difference in degree of swelling.

6.7.1.2 Swelling of Cellulose Nitrate in Alkali Hydroxide Solutions and its effect on Bulk Etching

Cellulose nitrate undergoes considerable swelling when treated with a solution of an alkali hydroxide. The network of cellulose nitrate chains and crystallites is most highly oriented in the direction of the fibre axis. The alkali solution, entering the network, pushes the units apart and loosens interconnecting secondary bonds, thus allowing the structure to assume a less oriented condition. However, the rupture of the secondary bonds is probably incomplete, so that the structure is still held together at certain points, and the shape of the fibre must change anisotropically, that is, more in one direction than the other. In principle swelling always precedes dissolution.

Swelling measurements of cellulose nitrate were performed on the thickness of films before and after treating the plastics with various concentrations of alkali hydroxide solutions. The time of exposure to alkali solution is not a critical factor in the swelling of cellulose nitrate, provided the cellulose nitrate is in the form of loose fibres or thin sheets. Under most conditions, swelling takes place almost instantaneously, with penetration but this is not necessarily true in thick sheets.

Under the latter conditions, air may be entrapped between the fibres in the sheets, and it is important that it be expelled in order to obtain rapid and uniform swelling. In this work the time of exposure to alkali solution is long enough to swell the cellulose nitrate without dissolving it. Figure 6.20 shows the alkali absorbed by cellulose nitrate at 25°C and the swelling produced in cellulose nitrate at 25°C on treatment with the solutions of various alkali metal hydroxides. In the case of lithium and potassium hydroxides, the compounds are strictly analogous to those formed with sodium hydroxide. With rubidium and cesium hydroxides, the indicated compounds contain 3 moles of cellulose nitrate for each mole of hydroxide. The concentrations of alkali in solution required for the formation of these compounds increase in the same order as the atomic weights of the alkali metals, which is: $\text{Li} < \text{Na} < \text{K} < \text{Rb} < \text{Cs}$. It is also to be noted that for the first three hydroxides, the normal concentration at which the break in the absorption curve occurs is almost identical, although the percent concentration increases.

Etching conditions should be determined in order to obtain an even bulk etching rate over the whole surface of the detector with a smoothly finished surface. This means that a low concentration of the etchant should be employed so that no preferential absorption of alkali by cellulose nitrate is obtained during etching. The temperature of the etchant should be maintained to satisfy the conditions of maximum swelling of cellulose nitrate during etching. The ideal bulk etching condition according to Figures 6.18, 6.19 and 6.20 would be (2-3)N NaOH at temperatures of $< 25^\circ\text{C}$. (See Figures 6.21, 6.22, 6.23, 6.24, 6.25 and 6.26.)

6.7.2 Measurement of Track Etching Rates

The measurements of track etching rates were made by irradiating CA 80-15 and LR-115 type II cellulose nitrate films with alpha particles of energies 0.6 - 6.0 MeV and angles of incidence of 10° , 20° and 30° to the surface of the plastics (see Chapter Five, Table 5.2). V_T was then determined by measuring the projected length of the tracks at various etching times and a correction was made for the loss of the bulk material during etching. V_T was measured for the same concentrations of NaOH and KOH and over the same temperature range as for the measurement of V_B . The coordinates of the etched cones of

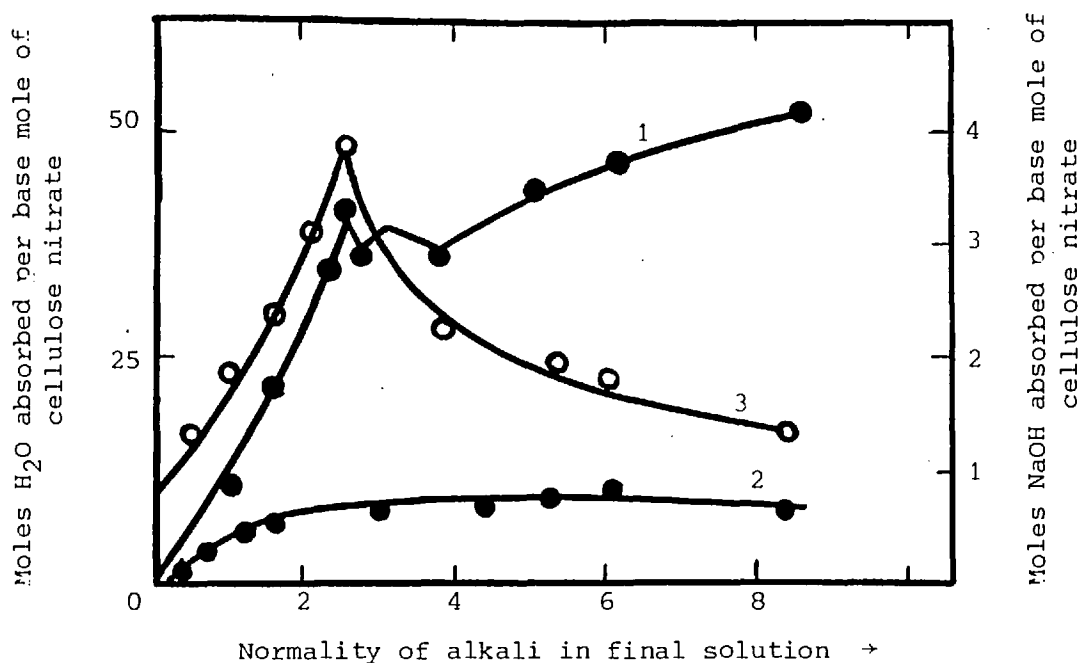


Figure 6.19 NaOH and H₂O absorbed by cellulose nitrate at 25°C
 Curves: 1. total alkali; 2. preferentially absorbed alkali; 3. water absorbed

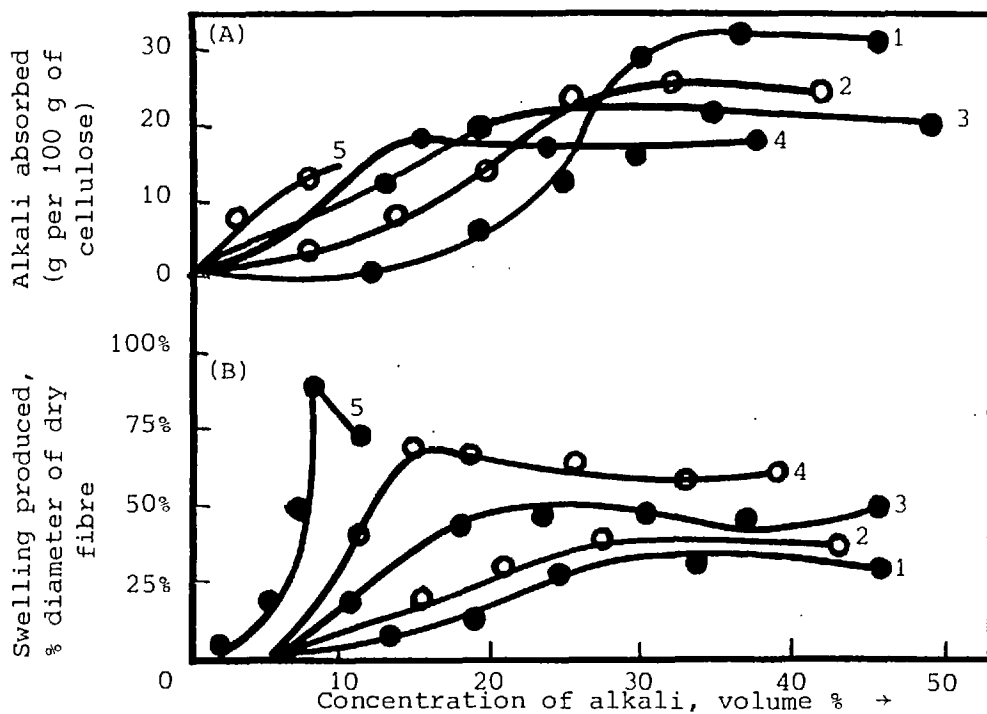


Figure 6.20 Comparison of (A) the alkali absorbed by and (B) the swelling produced in cellulose nitrate on treatment with solutions of various alkali metal hydroxides

Curve	Alkali	Concentration of maximum swelling	Pseudostoichiometric ratio
1	CsOH	40%	(C ₆ H ₁₀ O ₅) ₃ .CsOH
2	RbOH	38%	(C ₆ H ₁₀ O ₅) ₃ .RbOH
3	KOH	32%	(C ₆ H ₁₀ O ₅) ₂ .KOH
4	NaOH	18%	(C ₆ H ₁₀ O ₅) ₂ .NaOH
5	LiOH	9.5%	(C ₆ H ₁₀ O ₅) ₂ .LiOH

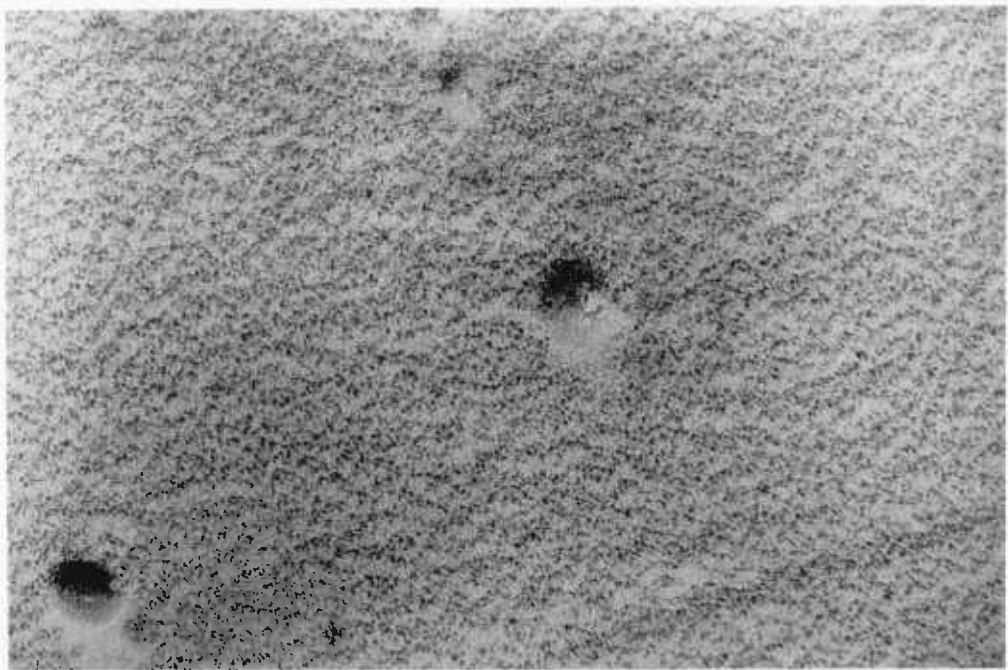


Figure 6.21 Electron micrograph of cellulose nitrate detector, CA80-15 (Kodak-Pathe, France) unirradiated, etched with 2.5 N sodium hydroxide at 18°C for 20 hours, (25 K x 3).



Figure 6.22 Electron micrograph of cellulose nitrate detector, CA80-15 (Kodak-Pathe, France) unirradiated, etched with 5 N sodium hydroxide at 50°C, for 1 hour (25 K x 3).

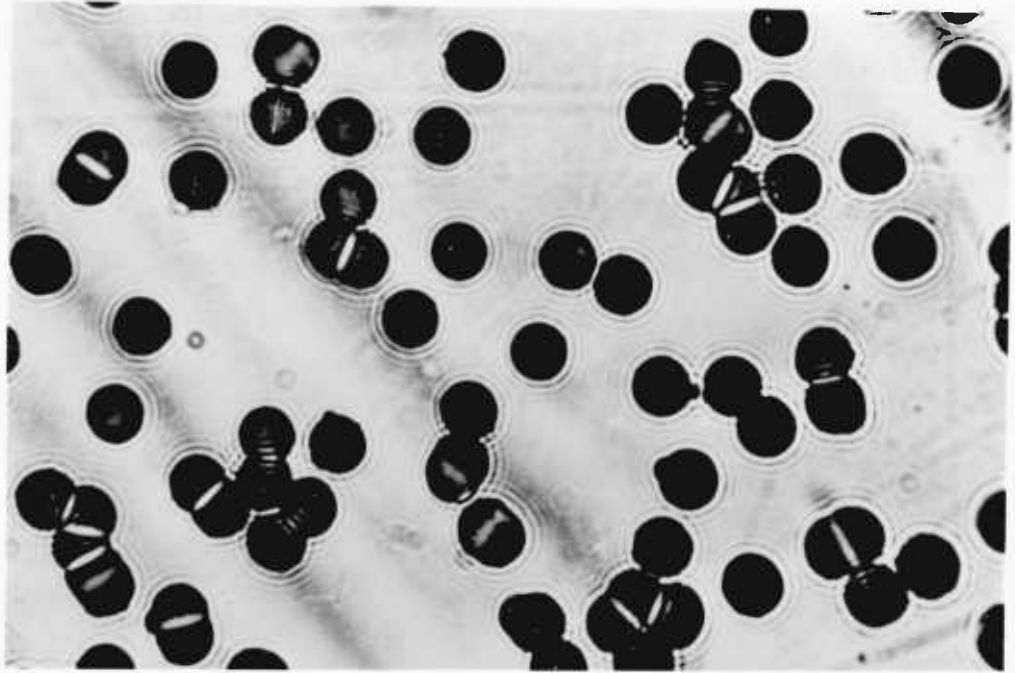


Figure 6.23 Photomicrograph of 2.0 MeV alpha tracks in LR115 Type 2 (Kodak-Pathe, France) at 90° incidence, etched in 5N sodium hydroxide at 50°C , for 1 hour.

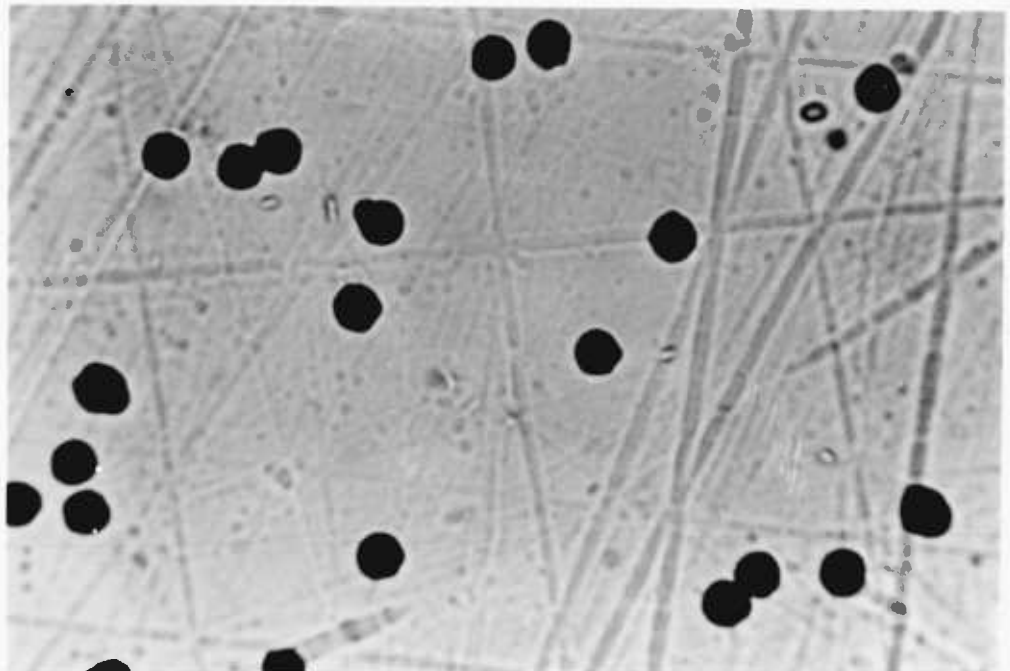


Figure 6.24 Photomicrograph of 2.0 MeV alpha tracks in LR115 Type 2 (Kodak-Pathe, France) at 90° incidence, etched in 2.5 N sodium hydroxide at 18°C , for 20 hours.

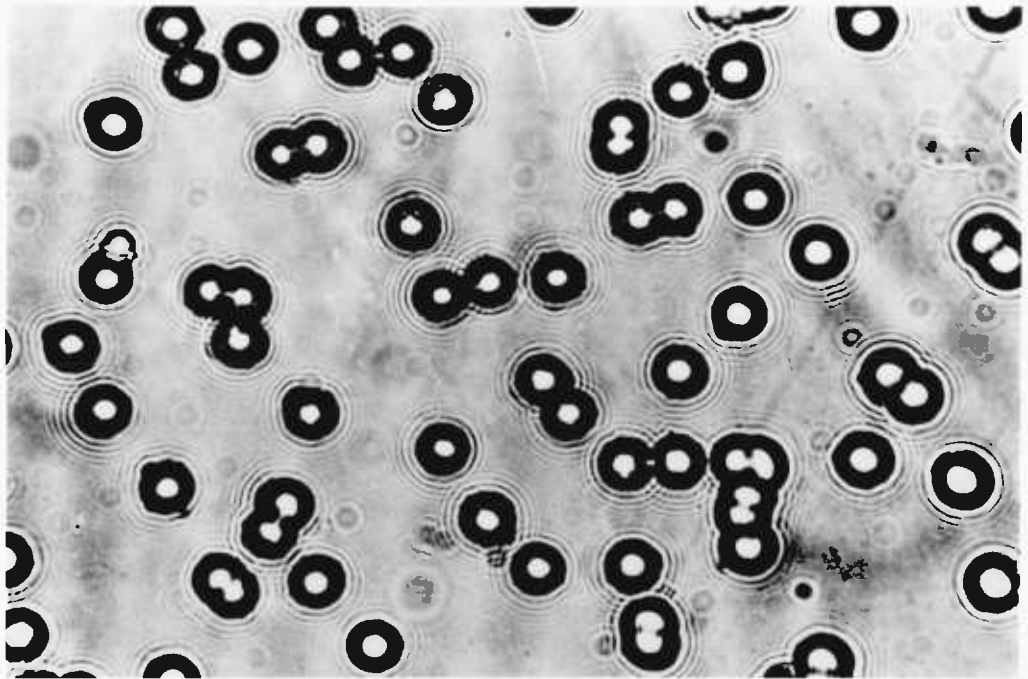


Figure 6.25 Photomicrograph of 2.0 MeV alpha tracks in LR115 Type 2 (Kodak-Pathé, France) at 90° incidence, pre-swollen in 65% zinc chloride solution for two hours at 18°C , then etched in 5 N sodium hydroxide at 50°C , for 1 hour.

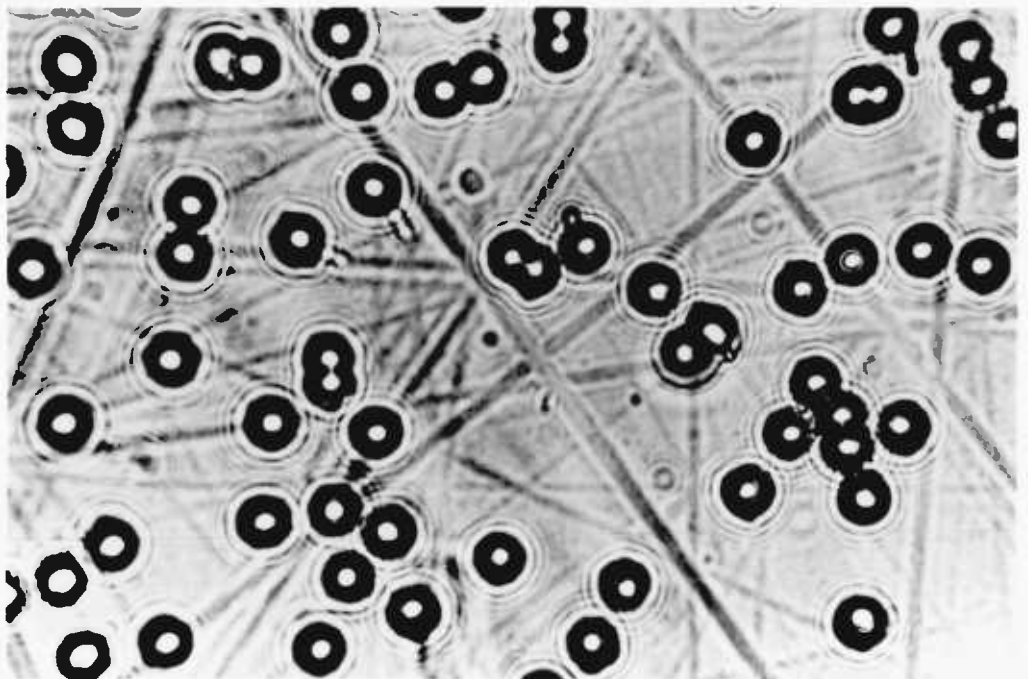


Figure 6.26 Photomicrograph of 2.0 MeV alpha tracks in LR115 Type 2 (Kodak-Pathé, France) at 90° incidence, pre-swollen in 65% zinc chloride solution for 2 hours at 18°C , then etched in 2.5 N sodium hydroxide at 18°C for 18 hours.

Figure 6.27 were measured and recorded with a Reichert (Model MEF 2) microscope with oil immersed objectives (140X and 150X) together with 12.5X and 20X eye pieces and with a Phillips EM 301 electron microscope operated at 100 kV (see Section 6.64). The rate of track attack was found to vary with the concentration of the OH^- ions and the etching temperature. This is demonstrated in Figure 6.28 where the time in minutes needed to completely etch out 4 MeV alpha particle track in CA 80-15 plastic is given as a function of concentration of NaOH at etching temperature of 55°C and 15°C . It is evident from Figure 6.28 that linearity of the curve breaks down at low temperatures with increasing concentration of the etching solution. This is probably due to the decrease in the diffusion rate of etching products which inhibits the etching velocity. Moreover at low etchant temperature and concentration, swelling of the plastic makes it possible for the basic solution to penetrate deeply and attack the radiation damaged area of the plastic, thus increasing the track etching rate. This effect is shown in Figures 6.29, 6.30, 6.31, 6.32 and 6.33. At an etchant temperature of 15°C , there is an increase in track etching rate with increasing etchant concentration up to a point after which any further increase will result in a decrease in the track etching rate. This hump behaviour is believed to be mainly due to the specimen swelling.

As the bulk etching rate depends on etchant stirring, it is necessary to investigate whether the track etching rate depends on it too. These investigations were carried out, and the track etching rate was found not to be dependent on etchant stirring; the track etching rate was found to be constant (within the standard deviation) with and without etchant stirring, although the bulk etching rates are very different. The implications of this behaviour will be dealt with later in this chapter.

6.7.3 Comparison of Track and Bulk Etching Rates

If tracks are to be quantitatively analysed then it is important to establish the variation of the ratio V_T/V_B as a function of etchant concentration and temperature. The ratio V_T/V_B was found to vary with etchant temperature and concentration, since the track cone angles θ ($\sin\theta = V_B/V_T$, Eqn.6.1) were seen to increase with increasing etchant temperature (Figure 6.34) and concentration (Figure 6.35). It is possible to predict this dependence by applying the activation complex

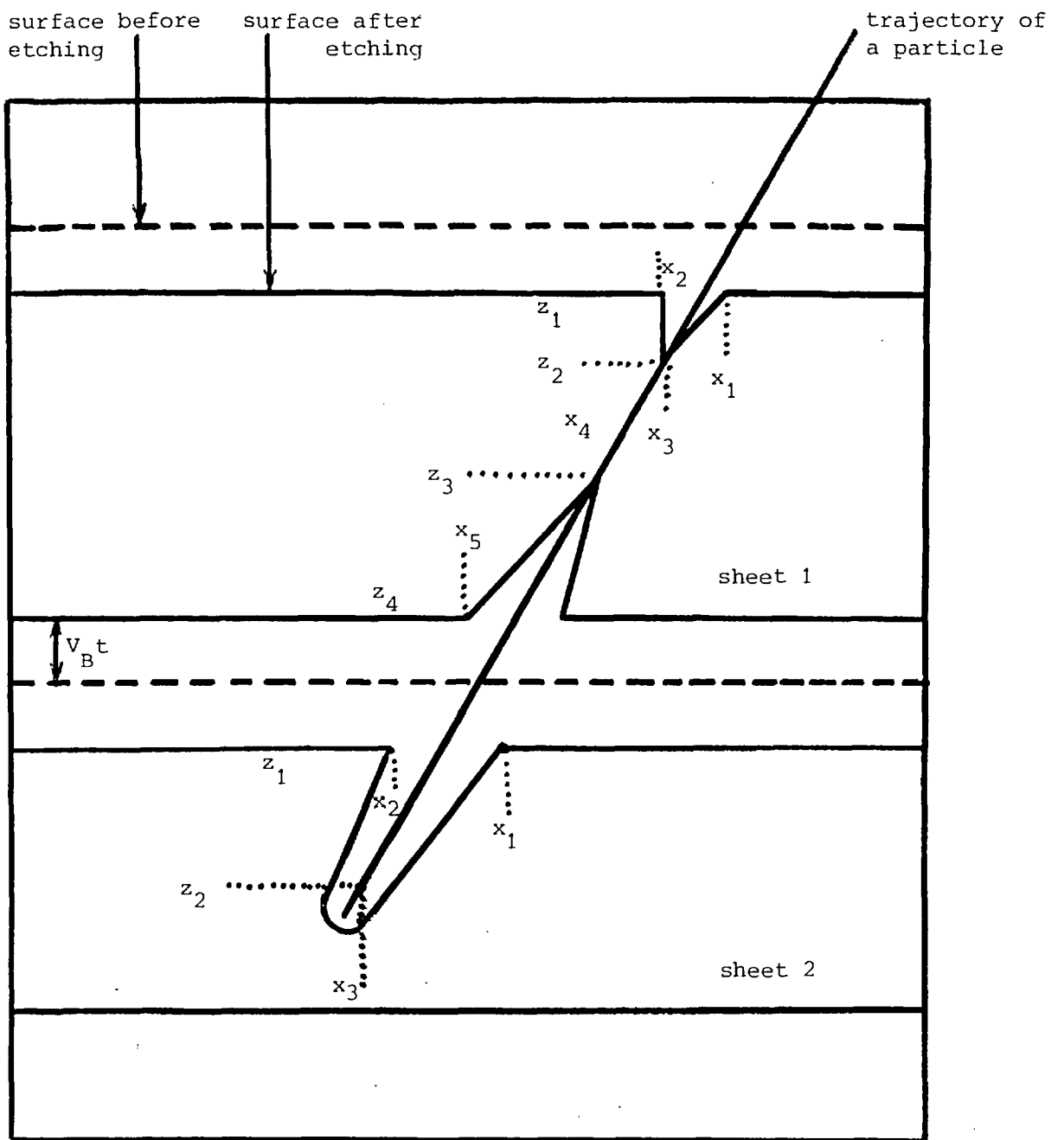
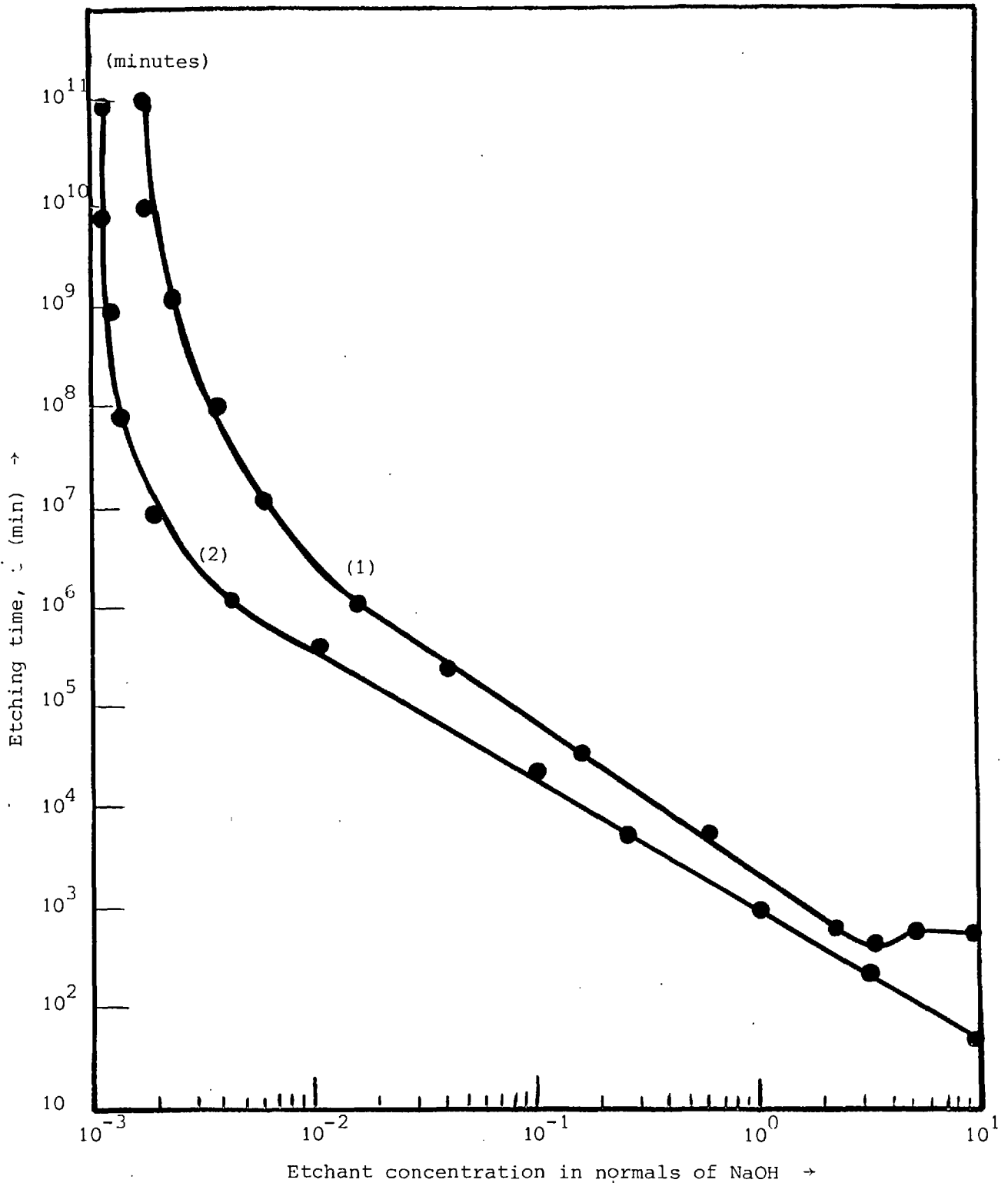
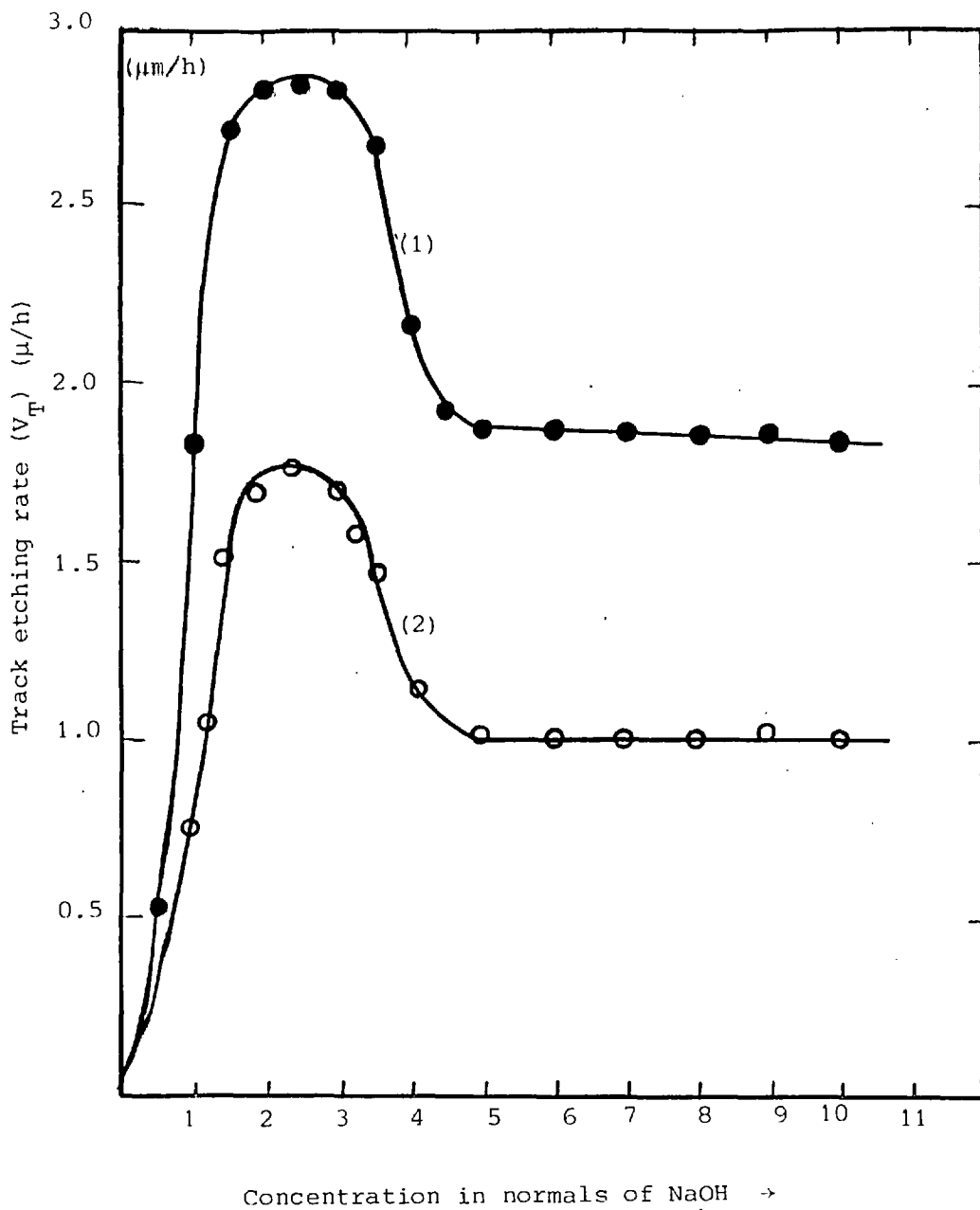


Figure 6.27 Plot of the measurements of the cone-coordinates



- (1) Etched in NaOH at 15°C
- (2) Etched in NaOH at 50°C

Figure 6.28 The time required to etch out fission fragment tracks in CA 80-15 cellulose nitrate plastic as a function of NaOH concentration (normals), without interruption or agitation



- (1) CA 80-15 plasticized cellulose nitrate
 (2) CA 80-15 partly plasticized cellulose nitrate (stored in high vacuum)

Figure 6.29 Track etching rate (V_T) of CA 80-15 cellulose nitrate as a function of NaOH concentration (normals) at a temperature of 15°C , without interruption or agitation

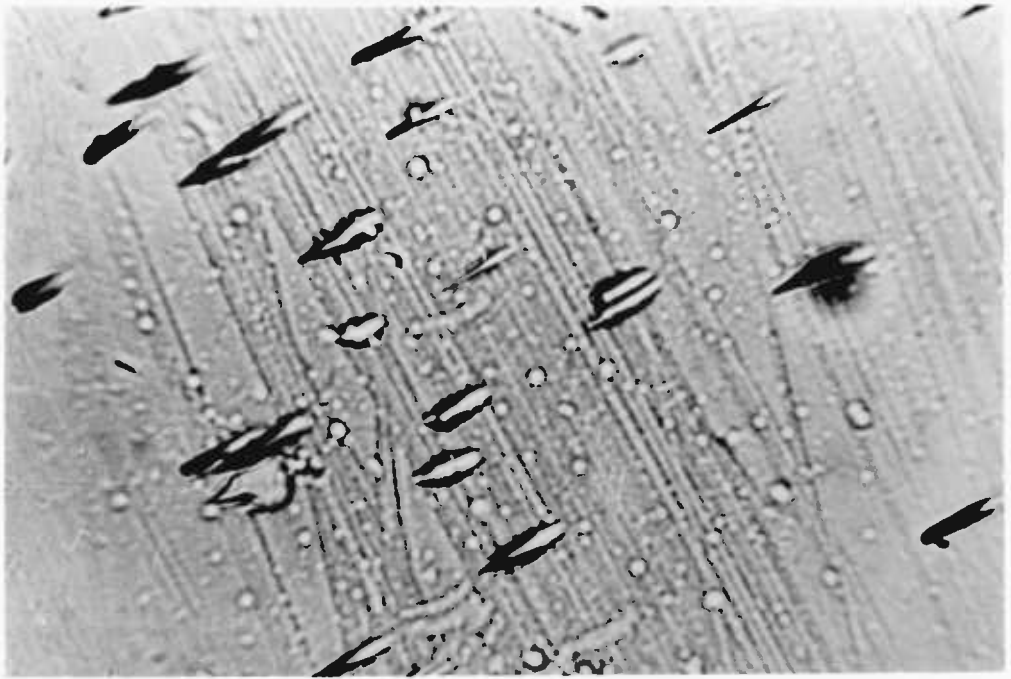


Figure 6.30 Photomicrograph of 2.0 MeV alpha tracks in LR115 Type 2 (Kodak-Pathe, France) at 30° incidence, etched in 5 N sodium hydroxide at 50°C , for 1 hour.

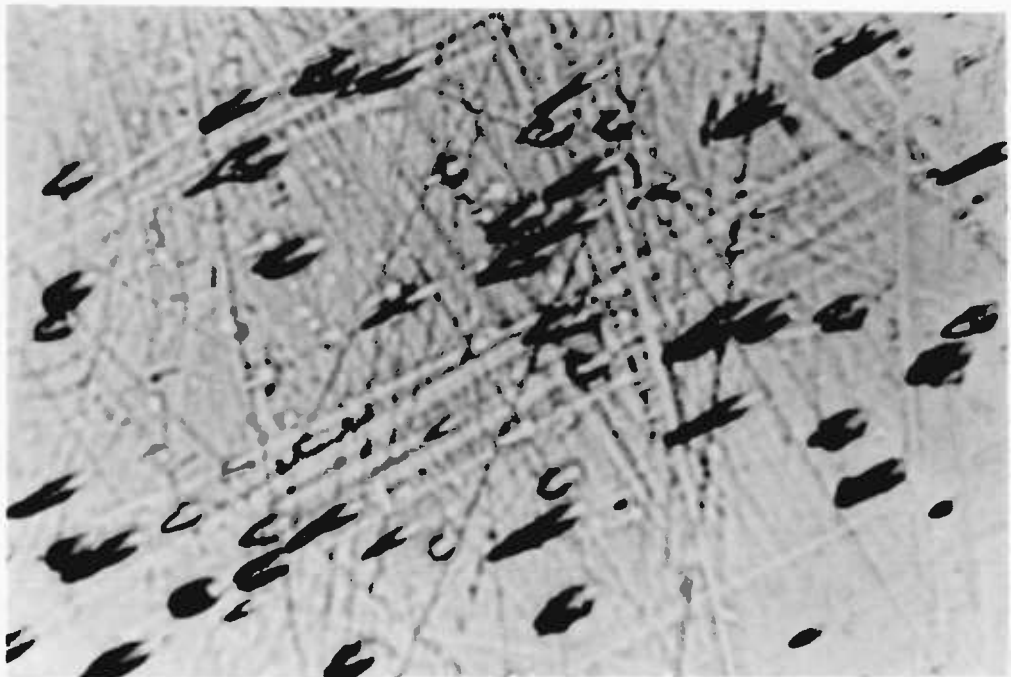


Figure 6.31 Photomicrograph of 2.0 MeV alpha tracks in LR115 Type 2 (Kodak-Pathe, France) at 30° incidence, pre-swollen in 65% zinc chloride solution for 2 hours, then etched in 5 N sodium hydroxide at 50°C for 1 hour.

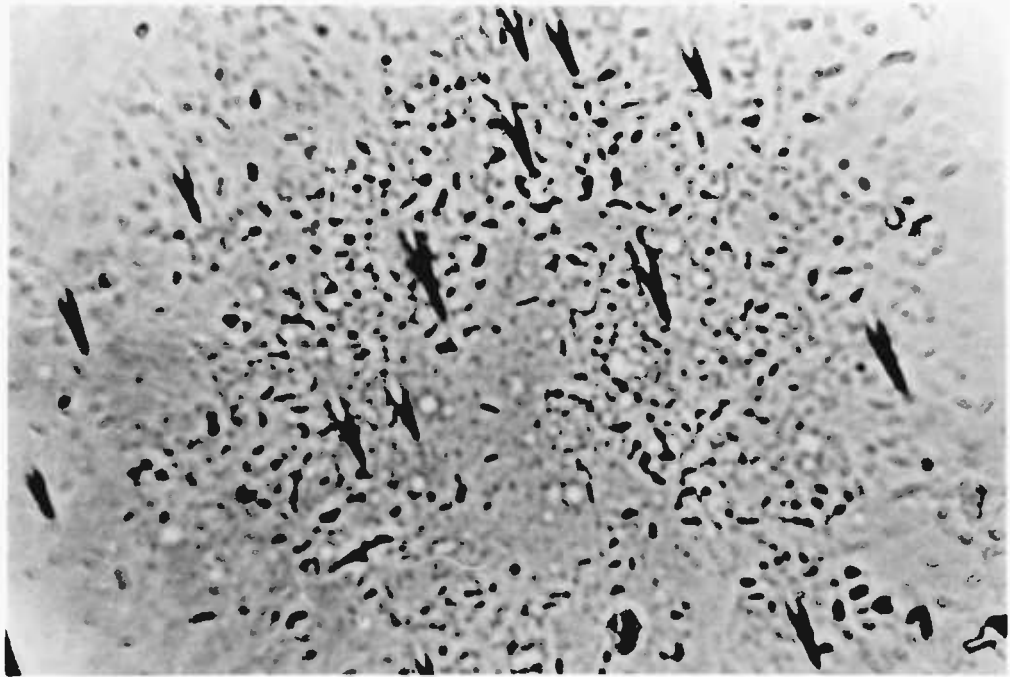


Figure 6.32 Photomicrograph of 2.0 MeV alpha tracks in LR115 Type 2 (Kodak-Pathe, France) at 30° incidence, etched in 2.5 N sodium hydroxide at 18°C , for 20 hours.

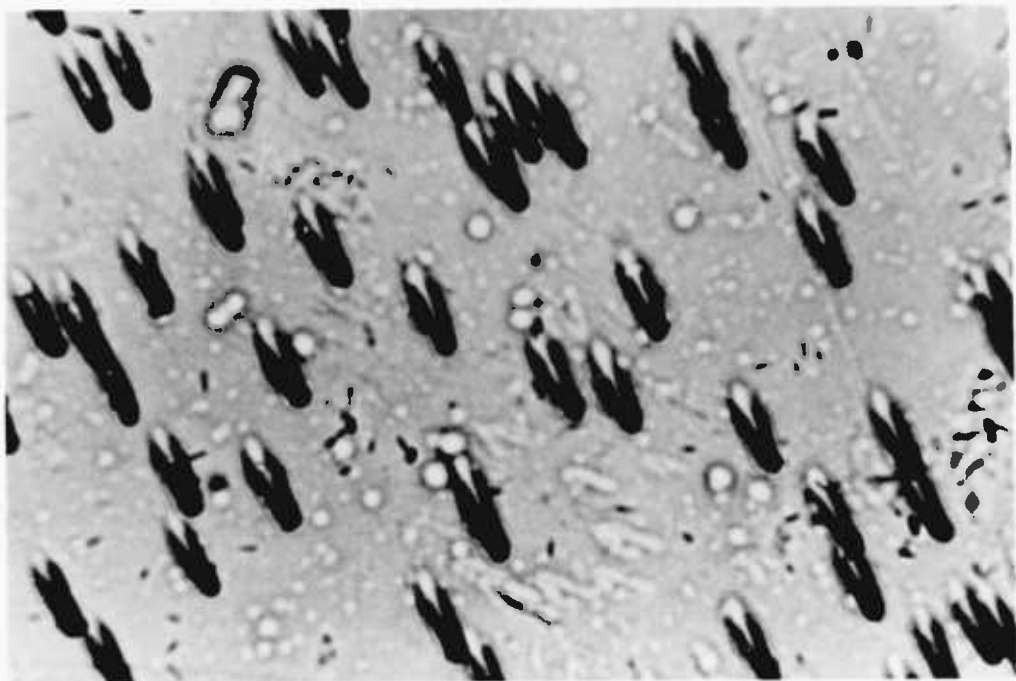
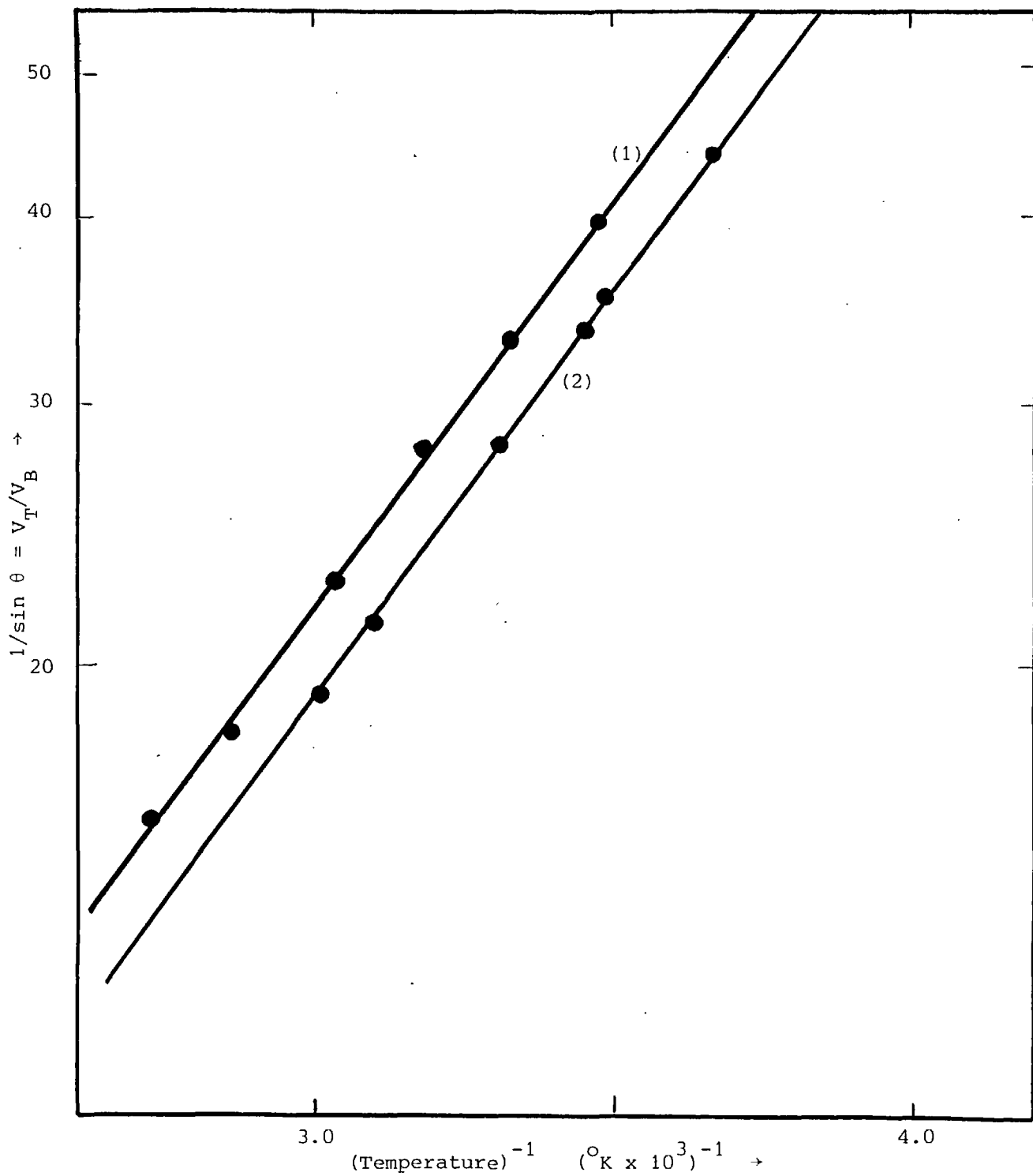
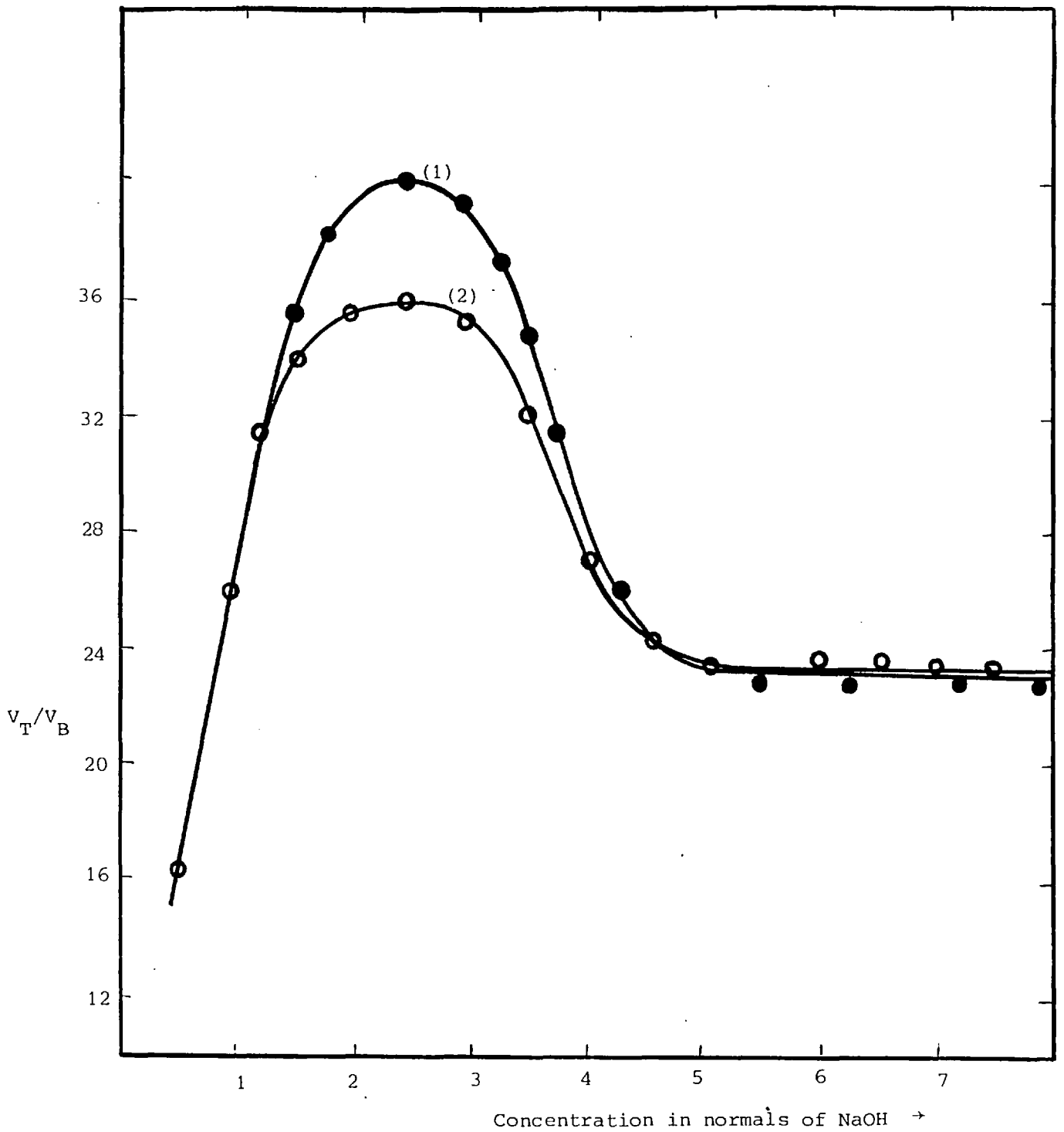


Figure 6.33 Photomicrograph of overetched 2.0 MeV alpha tracks in LR115 Type 2 (Kodak-Pathe, France) at 30° incidence, pre-swollen in 65% zinc chloride solution for 2 hours, then etched in 2.5 N sodium hydroxide at 18°C , for 18 hours.



- (1) CA 80-15 (plasticized)
- (2) CA 80-15 (partly plasticized)

Figure 6.34 V_T/V_B of CA 80-15 cellulose nitrate as a function of temperature for 2.5 N NaOH, without interruption or agitation



- (1) CA 80-15 cellulose nitrate (plasticized)
- (2) CA 80-15 cellulose nitrate (partly plasticized)

Figure 6.35 V_T/V_B of CA 80-15 cellulose nitrate as a function of NaOH etchant concentration (normals) at 15°C, without interruption or agitation

theory of chemical reaction rates; the free energies of the reactants and products are plotted in Figure 6.36. It is possible to determine the quantities ΔF_T and ΔF_B which are the activation energies for track etching and bulk etching respectively. Let us define F_T and F_B as the free energies associated with the track region and etchant together with the bulk polymer and etchant respectively. Also if F_A is the free energy of the activated complex then ΔF_T and ΔF_B may be written as follows:

$$\Delta F_T = F_A - F_T \quad (6.48)$$

$$\Delta F_B = F_A - F_B \quad (6.49)$$

The free energy associated with the region of the polymer traversed by a highly ionizing particle is greater than that of the bulk material, $F_T > F_B$. From statistical mechanics we know that the probability that an atom undergoing thermal vibration will have a value of free energy equal to or greater than any value ΔF above its ground state is given by $P = \exp(-\Delta F/kT)$, where ΔF is the reaction free energy and that the rate of this reaction will be proportional to $\exp(-\Delta F/kT)$. The overall rate of this reaction can be simply expressed as:-

$$v = A e^{-\Delta F/kT} \quad (6.50)$$

where T = absolute temperature of the chemical
 k = Boltzmann's Constant (8.67×10^{-5} eV/ $^{\circ}$ K)
 A = constant

Thus, the ratio v_T/v_B is given by the following expression:-

$$\frac{v_T}{v_B} = B e^{\left(\frac{F_T - F_B}{kT}\right)} \quad (6.51)$$

where B = another constant

Equation 6.51 predicts that as T is decreased v_T/v_B will increase; also as the difference between F_T and F_B is increased v_T/v_B will increase, and if $F_T = F_B$ and $B = 1$ then $v_T = v_B$. These predictions agree with experiment.

By noting from Equation 6.1 that $\sin\theta = v_B/v_T$ Equation 6.51 can be written in the following form,

$$\ln(1/\sin\theta) = (F_T - F_B)/kT + \ln B \quad (6.52)$$

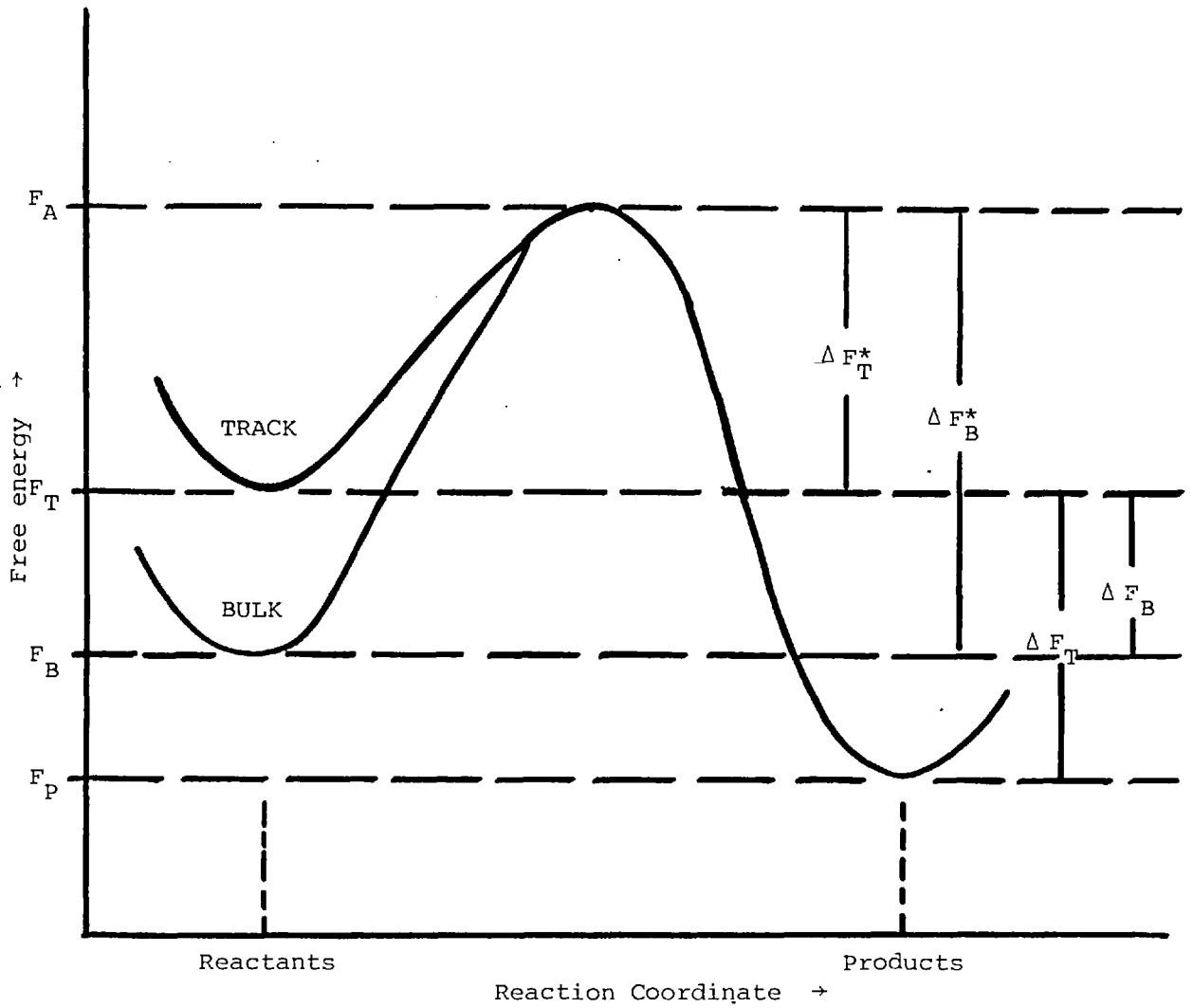


Figure 6.36 A free energy diagram of irradiated and unirradiated CA 80-15 cellulose nitrate

The above equation shows a linear relationship between $\ln(1/\sin\theta)$ and $1/T$, with a slope of $(F_T - F_B)/k$. This predicted linear dependence is observed in Figure 6.34. The slope shows that $(F_T - F_B) = 0.3$ eV. Measurement of the slope of Figure 6.16 curve 2 for CA 80-15 gives $\Delta F_B = 1.01$ eV, hence the activation free energy for track etching, ΔF_T is found to be equal 1.31 eV.

The above observed phenomenon of variation of the cone angle (θ) with the temperature of etchant has an important practical significance, namely, by etching at low temperatures a considerable increase in V_T/V_B is achieved. It should be noted that the plateau bulk etching rates observed in Figure 6.10 are proportional to $\exp(-F_B/kT)$, as may be expected from simple chemical kinetics.

Discussion

It can be seen from Figure 6.35 that for NaOH the optimum concentration is 2.5 N. Furthermore, small variations of concentration about 2.5 N will not have any significant effect on the ratio V_T/V_B . Thus for all the work with NaOH a concentration of 2.5 N was used and this concentration controlled to within $\pm 1.0\%$. Similar work with KOH showed that the concentration required for optimum V_T/V_B was also 2.5 N.

The ratio V_T/V_B for 2.5 N NaOH was plotted against the inverse of the etchant temperature and is shown in Figure 6.34. All the measurements were performed on both CA 80-15 and LR 115. It can be seen from Figure 6.34 that the results are well predicted by Equation 6.51 with $(F_T - F_B)$ differing by 4% between CA 80-15 and LR 115.

The cone angle was measured for tracks etched in various concentrations of NaOH and at a number of temperatures. The cone angle at each concentration and temperature was taken from the mean of 60 individual measurements. The ratios of V_T/V_B determined from cone angles (Eqn.6.1), was compared with those from the previous method and agreement was excellent and within the experimental errors.

The choice of etchant temperature depends on the final use of the SSTR. For reaction rate measurements etching at high temperatures (50°C) will reveal tracks within a few minutes. These tracks are of acceptable quality for counting but control of the etchant temperature to within $\pm 0.2^\circ\text{C}$ is necessary to prevent errors of greater than $\pm 1\%$ in the track density.

However, if the shape of tracks are to be measured, in order to determine particle energies, then very careful control over the etching process is required. It is not satisfactory to etch at high temperatures (50°C) since the time of etching must be accurately known which is not possible since etching takes place when the SSTR is removed from the etchant. The SSTR is always washed in water to neutralise the etchant after etching is completed, but if etching takes place at 50°C then only a few seconds in transferring the SSTR to the water is sufficient for etching to continue and cause a significant error in analysing track dimensions.

Etching at low temperatures (18°C), although time consuming, does permit precise control over the etching process. A few seconds in transferring an SSTR into water at the end of 11 hours of etching will result in an insignificant effect on the track dimensions. Furthermore, etching at low temperatures ensures that the SSTR suffers very little damage and that the resulting tracks are of a very high quality. A variation of $\pm 0.5^{\circ}\text{C}$ at 18°C will result in a $\pm 1.0\%$ change in V_T/V_B for a 2.5 N NaOH etchant while at 50°C a $\pm 0.5^{\circ}\text{C}$ variation will result in more than a 4.0% change in V_T/V_B .

6.8 Latent Track Annealing

The thermal repair of the damage track created by a charged particle in a solid is a complicated process on the atomic scale. Useful information about tracks can be learned by measuring the kinetics of track repair. Usually tracks in a solid are heated to various temperatures, and the time for total track fading is measured at each temperature. Partial removal of tracks is the result of heating for times that are less than times of complete track removal. If quantitative measurements of the fraction of tracks remaining are made at a fixed temperature, a series of activation energies are inferred. Low activation energies are measured in the initial stages of annealing, and monotonically higher values are found as more complete track removal occurs.

In crystalline solids, the observed activation energies have the same magnitude as those for atomic diffusion, suggesting that annealing corresponds to diffusive motion of displaced atoms back to proper lattice positions. Tracks corresponding to less severe damage anneal out at lower temperatures.

In polymers, the situation is more complicated. Diffusion and reaction of free radicals and of new molecular species including trapped gases is probably the relevant process, since it is hard to see how a broken chain could repair itself. This diffusive motion away from the track centre together with recombination of reactive species will reduce the concentration of "chemical activation centres" and hence the rate of track etching V_T . Diffusion of free radicals is known to be sensitively temperature dependent. When diffusion is low, as in polycarbonate plastic, the substance retains tracks on heating until it becomes a viscous fluid.

Kodak-Pathé CA 80-15 cellulose nitrate plastic exposed to 2.5 MeV alpha particles and processed after 12 months storage at room temperature (22° - 25° C) showed remarkable thermal stability. No evidence of track fading was observed. A series of annealing experiments were carried out using 2.5 MeV alpha particles and fission fragments from Californium 252 (see Table 5.2) in order to investigate the latent track fading phenomenon. The exposed specimens were annealed at various temperatures (50° - 120° C) for various times (1-8640 minutes) then etched for 15 hours in a 2.5 N NaOH solution at 18° C. The data are shown in Figure 6.37, where the rate of fading (reciprocal of the fading time) is plotted as a function of $1/T$ ($^{\circ}$ K) $^{-1}$. The degree of fading is represented by the fraction of the circle that is filled. Closed points indicate a lack of fading, the open circles indicate essentially complete fading. It was observed that greater etching times revealed tracks in samples which failed to show tracks at 15 hours etching time. Latent tracks of fission fragments required an order of magnitude greater annealing times.

To summarize, annealing reduces the track etch rate V_T . The rate of reduction of V_T is a function of the dE/dX of the particle, the annealing temperature and the time. Since the activation free energy for the annealing process is of the order of 1 eV, the process involves atomic motion which is in agreement with our earlier predictions.

6.9 Critical Angle of Etching and its Effect on the Detection Efficiency of Cellulose Nitrate

The process of etching introduces an important phenomenon. This consists of the fact that there exists a minimum angle of incidence

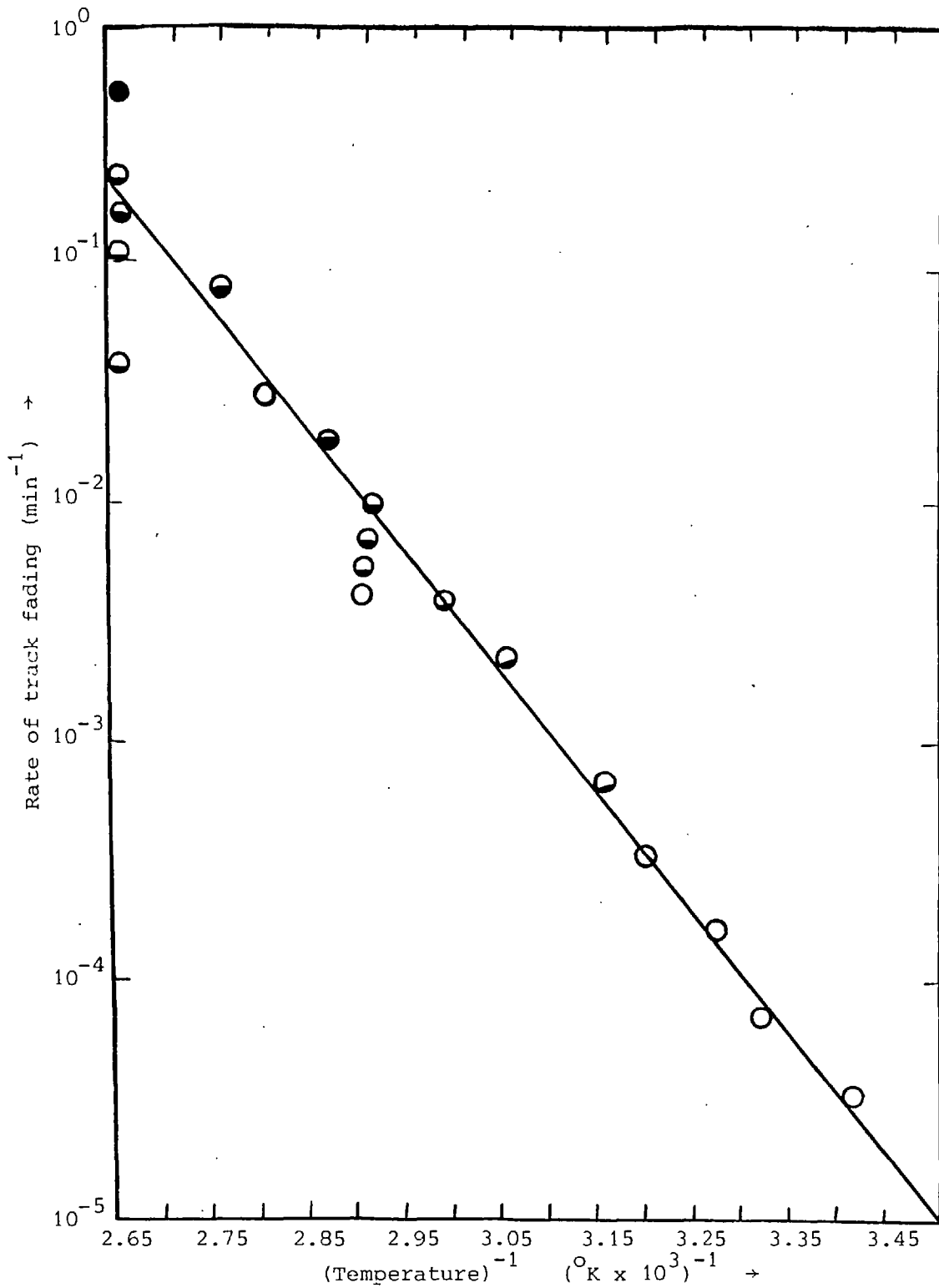


Figure 6.37 The temperature dependence of latent track fading for 2.5 MeV alpha particles in CA 80-15 cellulose nitrate plastic etched for 15 hours in 2.5 N NaOH solution at 18°C, without interruption or agitation. The degree of fading is represented by the fraction of the circle that is filled.

of a particle to the surface of the detector which will leave an observable track after etching, below which the tracks either fail to register or even register but fail to leave an observable track after etching. This critical angle, besides being dependent on the nature of the medium, the etching conditions, and the optical microscope resolution, is an important factor which controls the detection efficiency of all track storing mediums.

6.9.1 Critical Angle of Etching

In Figure 6.38 a track lies at an incident angle θ to the horizontal surface of the detector. In t seconds of etching, the etchant travels a distance $V_T \cdot t$ along the track, and $V_B \cdot t$ vertically. Thus a layer $V_B \cdot t$ thickness of the medium is dissolved away in time t . If, then, the vertical component of $V_T \cdot t$ is smaller than $V_B \cdot t$ the track will fail to leave an etch pit on the final layer. On the other hand if the vertical component of $V_T \cdot t$ is larger than $V_B \cdot t$ but not large enough to be resolved by the microscope employed we also will consider that the track fails to leave an etched track. This happens at all angles lower than a critical angle θ_c such that $V_B/V_T = \sin \theta_c$ together with a vertical component of the residual track length $R'_p \geq$ the optical resolution of the microscope.

Consider a track shown in Figure 6.39 which is obtained after etching for time t .

Let R' = residual track length

R'_p = projected residual track length (horizontal component)

L' = the vertical component of R'

Now $R = V_T t$ (6.53)

$$\begin{aligned} L' &= L - V_B t \\ &= R \sin\theta - V_B t \\ &= R (\sin\theta - V_B/V_T) \end{aligned} \quad (6.54)$$

$$R' = L'/\sin\theta$$

and $R'_p = L'/\tan\theta$

For small angles $\tan\theta = \sin\theta$

$$\therefore R'_p = L'/\sin\theta \quad (6.55)$$

Equation 6.54 must be positive if a track is to be registered.

\therefore The critical condition for track registration is:-

$$\sin \theta_c = V_B/V_T \quad (6.56)$$

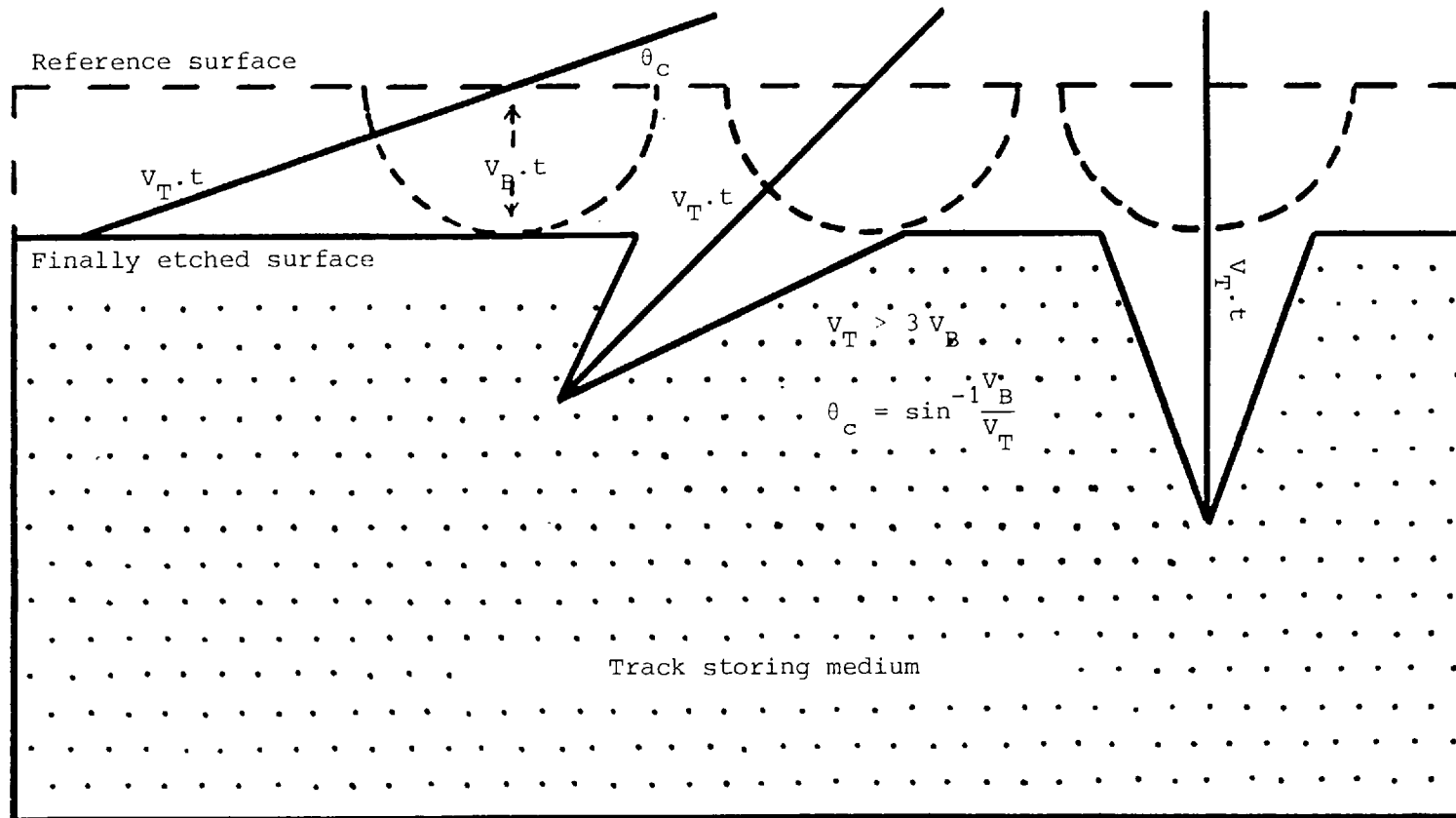
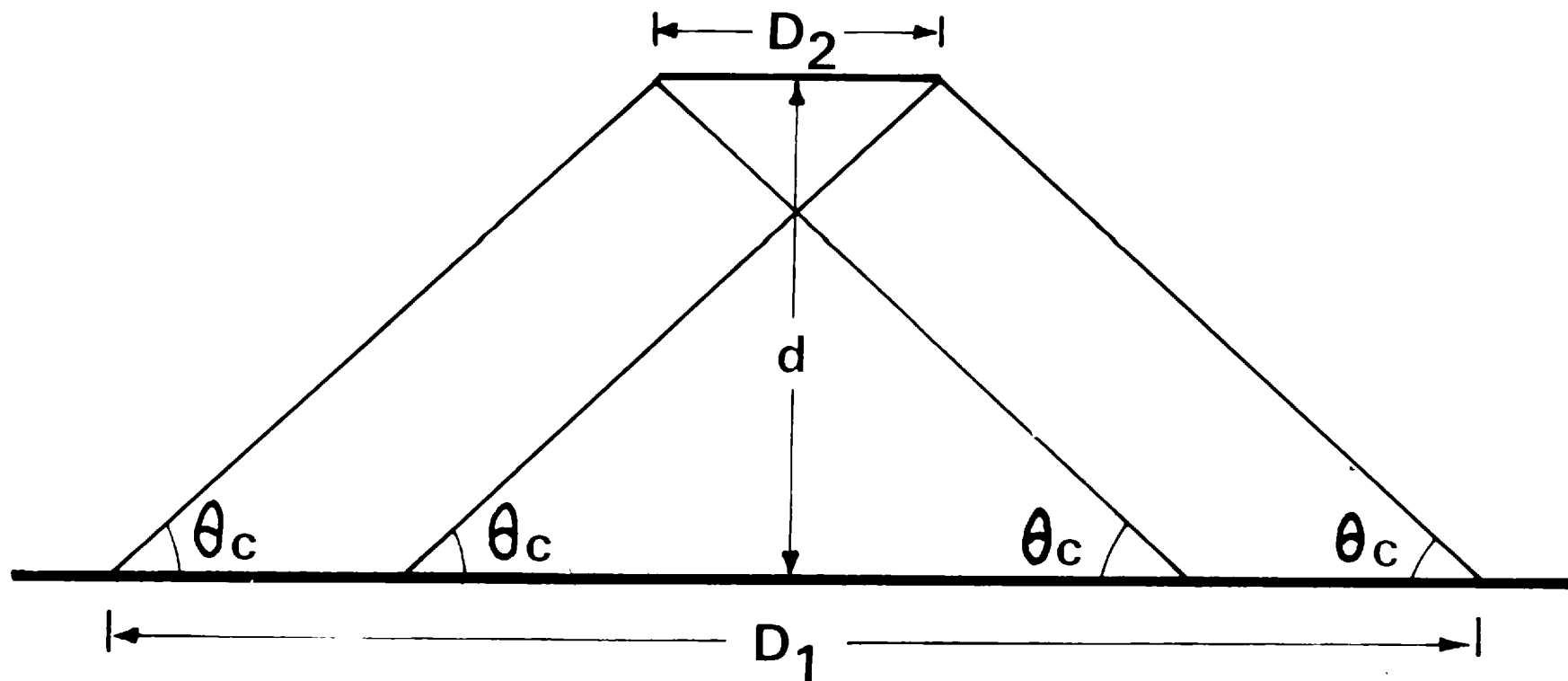


Figure 6.38 The critical angle of etching (θ_c)

THIN CHARGED PARTICLE SOURCE



SOLID STATE NUCLEAR TRACK DETECTOR
(SSNTD)

Figure 6.38

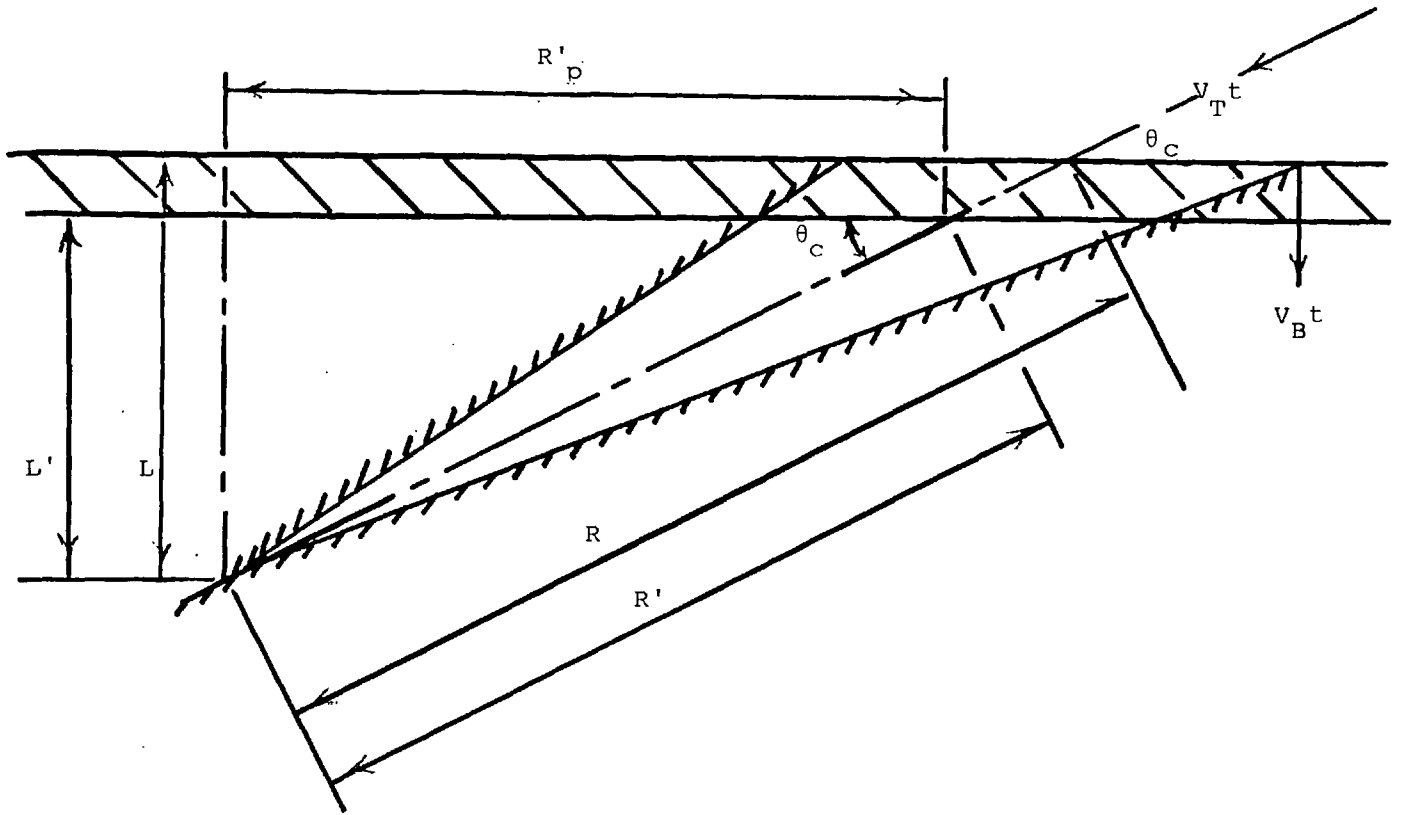


Figure 6.39 Diagrammatic representation of an etched track

However, if the track is to be observed R'_p must be greater than the optical resolution of the microscope.

$$\therefore R'_p \geq \frac{1.22\lambda}{2n}$$

where n = Index of refraction of the objective

λ = Wavelength of the light being used

In the present case, $n = 1.3$ and $\lambda = 0.6\mu$

$$\therefore R'_p \geq 0.28\mu \quad (6.57)$$

Thus for tracks to be observed both $\theta > \theta_c$ and Equation 6.57 must be satisfied.

From Equations 6.57 and 6.55 we obtain

$$L'/\sin\theta > 0.28\mu$$

or from (6.54)

$$\frac{R}{\sin\theta} (\sin\theta - V_B/V_T) \geq 0.28\mu$$

$$\therefore \sin\theta \geq V_B/V_T \cdot \frac{1}{1 - 0.28/R} \quad (6.58)$$

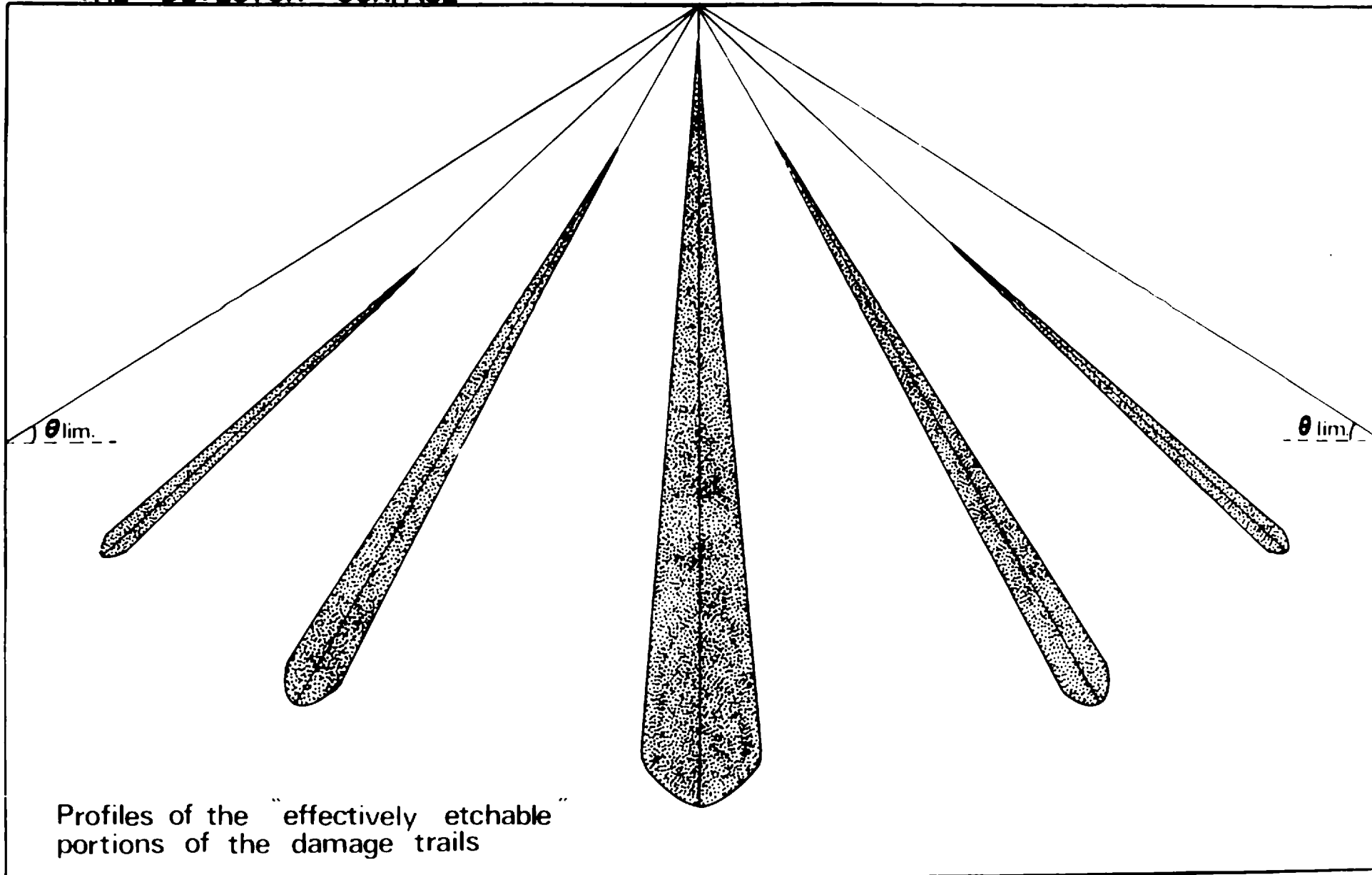
The critical angle of etching for cellulose nitrate and the type of incident charged particle is measured by varying the angle of incidence (with the surface of the detector) of an external beam of particles until the tracks fail to etch out. Both collimated and uncollimated beams of varying energies have been employed (see Chapter Five). In most cases, the particles used are alpha particles from an accelerator or an americium 241 source, though protons and fission fragments have also been used (see Table 5.2).

To find the exact critical angle of etching sets of careful measurements are made within the angular interval around the critical angle. Particular emphasis was given to angles in the region 0 to 10° since the critical angle for obtaining an observable track lies in this region. Figure 6.40 shows the variation of etchable volume (lengths and widths) of latent tracks with dip angles or angles of impact with regard to the surface of the detector.

Equation 6.58 gives the critical angle for observable tracks, θ_c , in terms of V_B , V_T and the range R . For 2.5 N NaOH the ratio V_T/V_B is 36 and in the present experiments on CA 80 the range of alpha particles varied from 2.2μ to 36.13μ corresponding to alpha

Figure 6.40

THE DETECTOR SURFACE



particle energies of 0.6 and 6 MeV respectively. Equation 6.58 gives values of θ_c of 1.8° and 1.6° corresponding to alpha particle energies of 0.6 and 6 MeV respectively.

The observed critical angle for tracks etched in 2.5 N NaOH at 18°C for 21 hours was 5° . However, for small amounts of etching, so that tracks were just observed, the critical angle was found to be 2° which is in good agreement with the values given by Equation 6.58. It should be noted that the experiments were performed with CA 80-15 at 1° increments in angle of incidence between 0 and 10° . And that the observed track density falls suddenly to zero just below the critical angle which reflects the precision of incident angle.

6.9.2 Detection Efficiency and Counting Techniques

An important consequence of the existence of a critical angle, and of the fact that the smaller it is the greater the efficiency of registration of a given particle, is that it over rides the ordinary solid angle considerations in detection efficiency. Thus consider two different types of track detectors, A and B (Figure 6.41), situated on either side of, and equidistant from, a point source of radiation, S. Assume B to be physically larger than A, so that the solid angle presented by detector B at S is larger than that by A. If, however, the critical angle $(\theta_c)_A$ is smaller than $(\theta_c)_B$, detector A will register more tracks per unit of exposure than will B, contrary to the normal situation. The ratio of the efficiencies in the case cited can be easily shown to be $\cot^2(\theta_c)_A / \cot^2(\theta_c)_B$, being in proportion to the base areas of the two cones defined by the critical angles of incidence (assuming the detectors to be larger than these areas).

The detection efficiency in the case of a point source lying on a detector (i.e. seemingly ' 2π geometry') is given by the solid angle subtended by the detector on the source (circumscribed by the critical angle limitation) expressed as a fraction of the total solid angle (2π). The detection efficiency is found to be:-

$$f = \frac{\int_{\theta_c}^{\pi/2} d\Omega}{\int_{\theta}^{\pi/2} d\Omega} = \frac{\int_{\theta_c}^{\pi/2} 2\pi \cos\theta d\theta}{2\pi} = 1 - \sin\theta_c \quad (6.59)$$

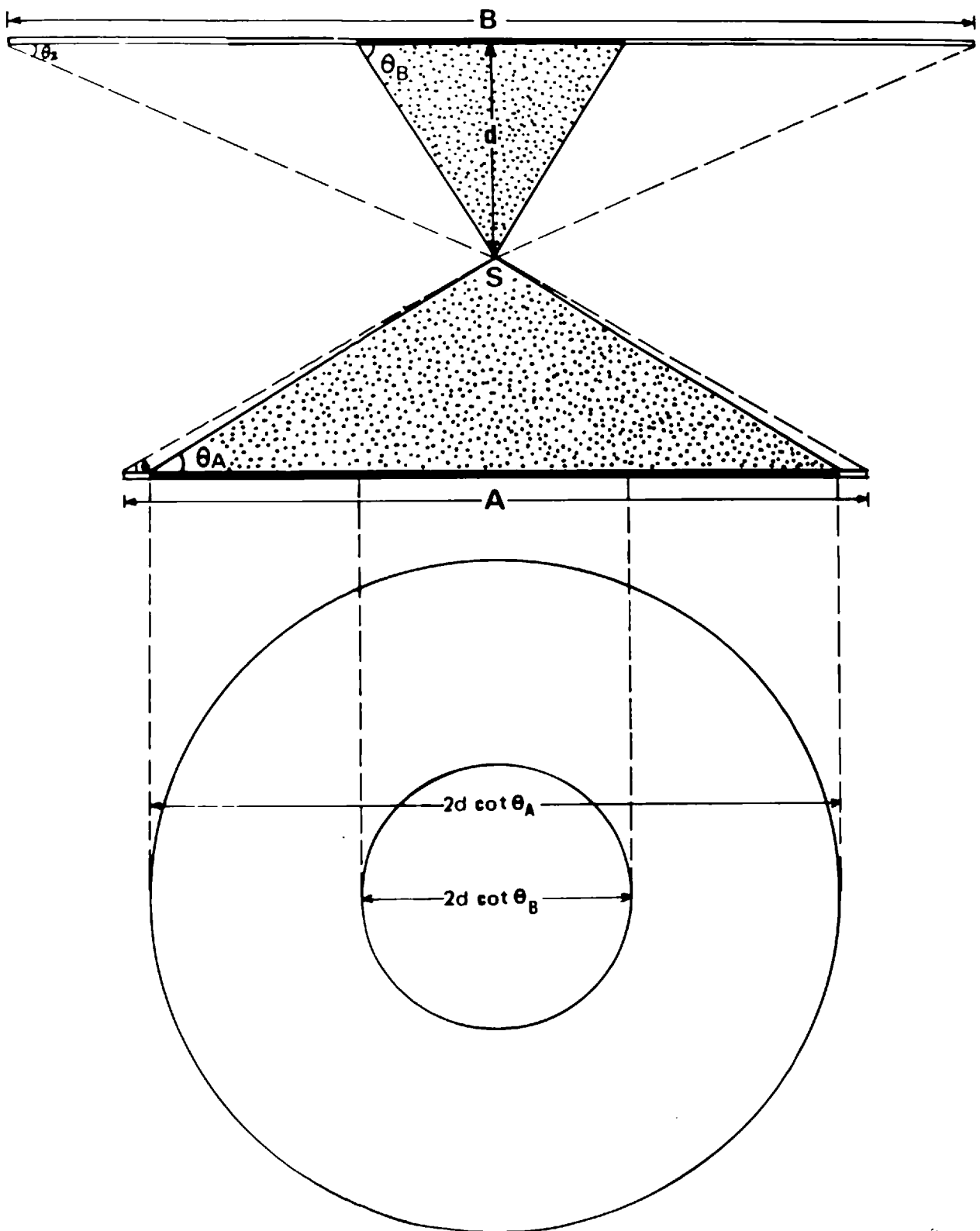


Figure 6.41 The importance of the critical angles of etching in the determination of solid angles subtended by SSTRs on a point source

The above result is also true for thin extended sources which may be considered to be made up of a superposition of point sources.

It is, thus, of great importance in determining the registration efficiencies of solid state nuclear track detectors to measure their critical angles of etching in relation to particles of different charge and energy, and to conditions of prevailing temperatures etc.

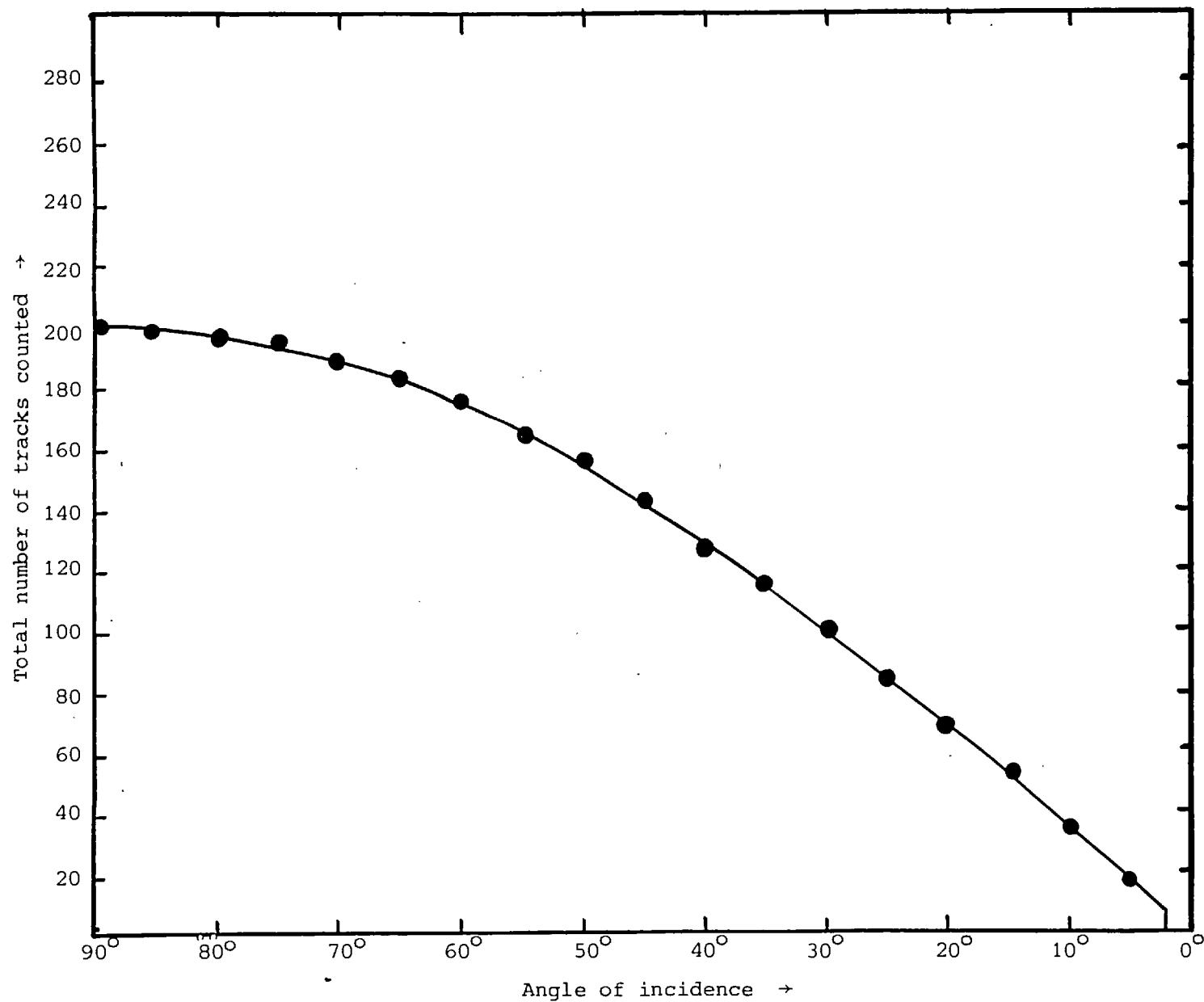
Both CA 80 and LR 115 films were irradiated and etching was initially performed on two sets of SSTR, one for 20 hours for 2.5 N NaOH and the other for 11 hours for 2.5 N KOH. The recorders were washed in distilled water immediately after etching. Tracks were counted manually for each recorder, by the method described previously. For angles of incidence of 90° , 80° , 70° , 60° , 50° , 45° , 40° , 30° counting statistics were better than $\pm 1\%$. whilst those for angles of 20° , 10° , 7° and 5° were counted to better than $\pm 3\%$.

The efficiency for track registration was determined by taking the monitor count density and dividing into the measured track density. The efficiency of CA 80 at various alpha particle energies at angles of incidences of 90° , 70° , 50° , 30° and 10° is given in Table 6.8. A summary of measurements on CA 80-15 at all measured angles is given in Table 6.9 where the energy range of observed tracks is shown together with the mean efficiency of registration. It should be noted that in many cases the range of observed tracks was limited by the accelerator energy limits of either 0.6 or 6 MeV.

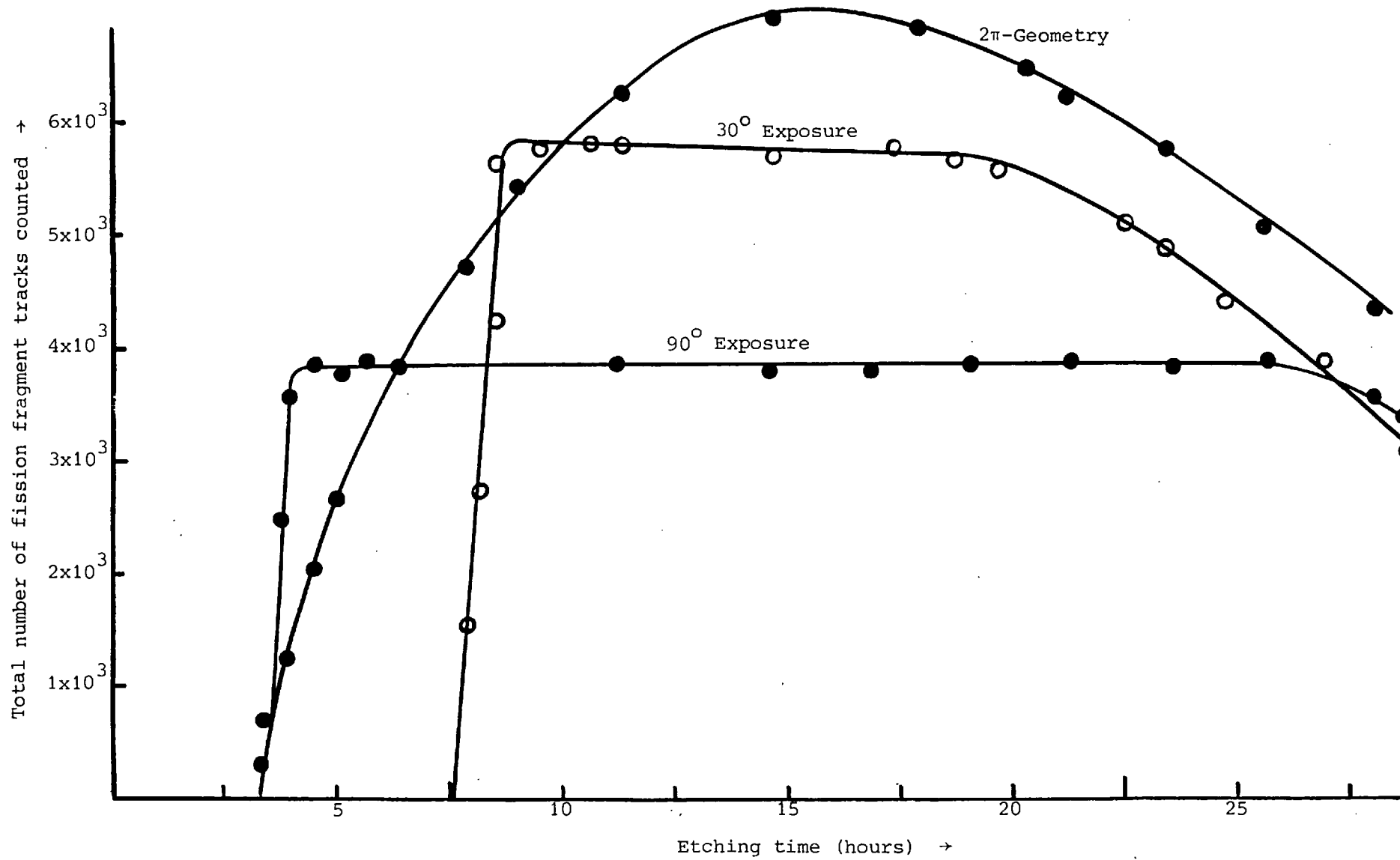
The critical angle for observed tracks was found to be 5° for etching in 2.5 N NaOH at 18°C for 20 hours. It was subsequently found that etching for shorter times permits the critical angle to be reduced. For example etching for 5 hours gives a critical angle of 2.5° . This topic will be discussed later.

The experiments were repeated using KOH as the etchant and efficiency values agreed with those found using NaOH to within the experimental errors $\pm 1\%$.

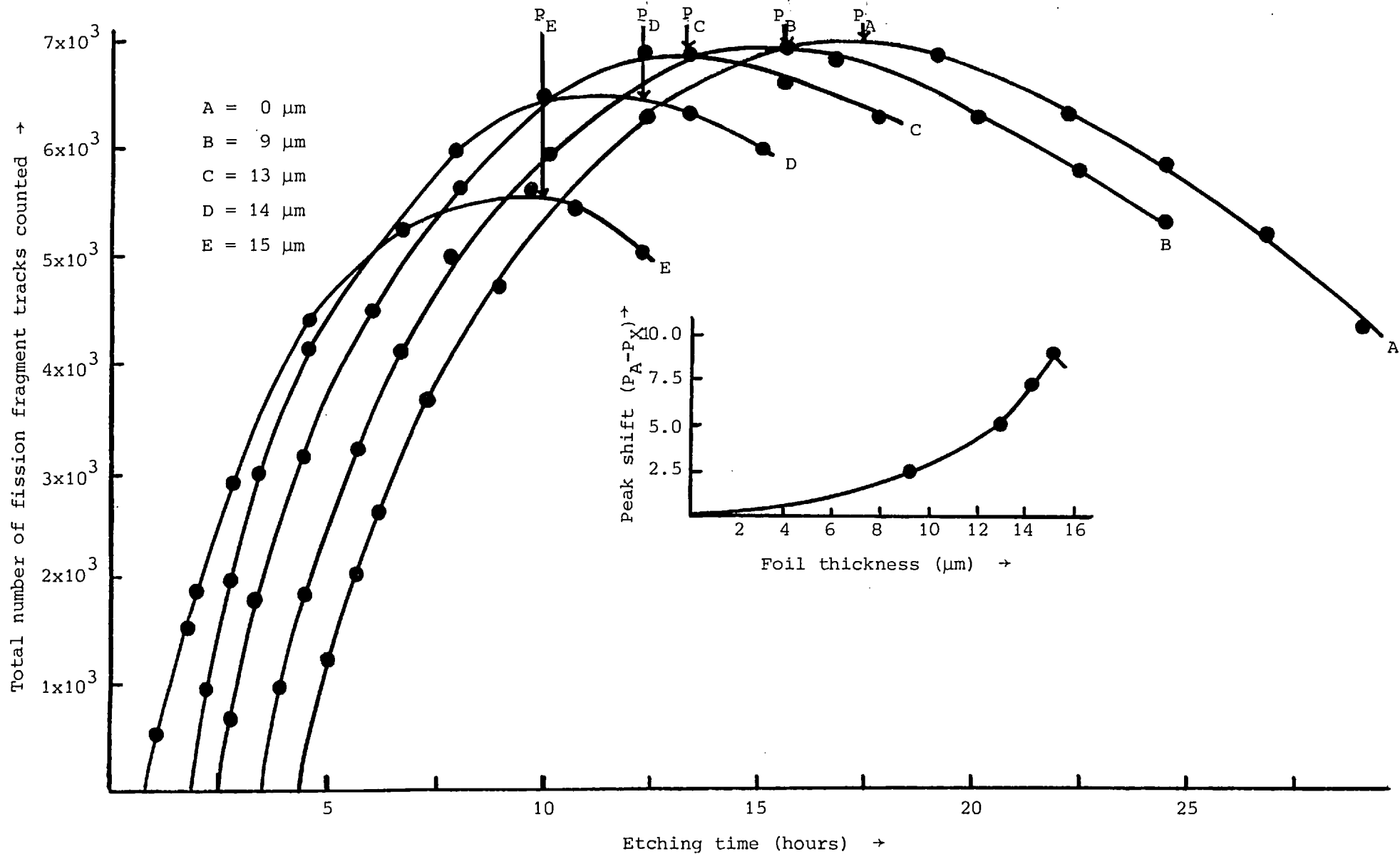
The measurements for LR 115 were similar to those performed with CA 80-15 and the results are summarised in Table 6.10. It can be seen that the efficiency values for LR 115 are slightly lower than for CA 80-15 and that the energy range of observed tracks is smaller for LR 115 as the angle of incidence is decreased. These differences between CA 80-15 and LR 115 are to be expected since LR 115 is thin (10μ) compared to CA 80-15 and also to the track ranges.



Registration efficiency of CA 80-15 cellulose nitrate in relation to 3.5 MeV alpha particle incident angles. Detector was etched in 2.5 N NaOH at 18°C.



Variation of the registration efficiency of fission fragment tracks in CA 80-15 cellulose nitrate as a function of etching time.



Variation of the peak of fission fragment (slowed down by aluminium foil) track registration as a function of etching time of cellulose nitrate and fission fragment energy

TABLE 6,8

EFFICIENCY OF CA 80 AT VARIOUS ALPHA PARTICLE ENERGIES FOR ANGLES OF INCIDENCE OF 90, 70, 50, 30 and 10°. ETCHING CONDITIONS 2.5 N NaOH AT 18°C FOR 20 HOURS.

Energy MeV	Angles of Incidence				
	90	70	50	30	10
0.60	99.22 \pm 1.00	99.21 \pm 0.97	99.22 \pm 0.87	99.28 \pm 0.71	0
0.65	99.29 \pm 0.87	99.19 \pm 0.86	99.15 \pm 0.77	99.32 \pm 0.63	0
0.70	99.01 \pm 0.96	99.09 \pm 0.93	99.39 \pm 0.84	99.34 \pm 0.68	0
0.75	98.84 \pm 0.93	98.90 \pm 0.90	99.28 \pm 0.82	99.02 \pm 0.66	0
0.80	99.20 \pm 0.88	99.20 \pm 0.87	99.15 \pm 0.79	99.32 \pm 0.64	0
0.85	99.01 \pm 0.88	99.12 \pm 0.86	99.25 \pm 0.77	99.24 \pm 0.62	0
0.90	99.16 \pm 0.89	99.21 \pm 0.87	99.15 \pm 0.78	99.30 \pm 0.63	0
0.95	99.09 \pm 0.85	99.26 \pm 0.83	99.46 \pm 0.75	99.46 \pm 0.60	0
1.00	99.12 \pm 0.86	99.17 \pm 0.83	99.37 \pm 0.75	99.34 \pm 0.61	0
1.25	98.96 \pm 0.87	99.03 \pm 0.84	99.35 \pm 0.76	99.28 \pm 0.61	0
1.50	98.89 \pm 0.85	98.97 \pm 1.00	99.18 \pm 0.74	99.30 \pm 0.60	99.40 \pm 0.81
2.00	99.04 \pm 1.06	99.13 \pm 1.03	99.15 \pm 0.93	99.24 \pm 0.75	97.44 \pm 1.01
2.50	99.26 \pm 0.85	99.11 \pm 0.82	99.28 \pm 0.74	99.28 \pm 0.60	99.40 \pm 0.81

TABLE 6.8 (cont.)

Energy MeV	Angles of Incidence				
	90	70	50	30	10
3.00	99.11 \pm 0.85	99.13 \pm 0.82	99.17 \pm 0.74	99.38 \pm 0.60	99.40 \pm 0.81
3.50	99.10 \pm 1.00	99.10 \pm 0.97	99.22 \pm 0.87	99.30 \pm 0.71	99.49 \pm 0.97
3.60	99.29 \pm 0.78	99.06 \pm 0.75	99.25 \pm 0.68	99.26 \pm 0.55	99.34 \pm 0.74
3.70	98.91 \pm 1.05	98.99 \pm 1.02	99.12 \pm 0.92	98.98 \pm 0.74	99.17 \pm 1.01
3.80	0	99.04 \pm 1.05	99.72 \pm 0.95	99.14 \pm 0.76	96.98 \pm 1.04
3.90	0	99.09 \pm 0.80	99.13 \pm 0.72	99.28 \pm 0.58	97.50 \pm 0.78
4.00	0	99.12 \pm 0.82	99.09 \pm 0.74	99.32 \pm 0.60	99.40 \pm 0.81
4.25	0	99.01 \pm 0.93	99.22 \pm 0.84	99.00 \pm 0.68	98.99 \pm 0.92
4.50	0	99.16 \pm 0.83	99.25 \pm 0.73	98.76 \pm 0.59	99.11 \pm 0.80
4.75	0	0	99.13 \pm 0.86	99.28 \pm 0.69	99.34 \pm 0.94
5.00	0	0	99.16 \pm 0.82	99.26 \pm 0.66	99.45 \pm 0.90
5.50	0	0	99.15 \pm 0.75	99.28 \pm 0.61	99.34 \pm 0.83
6.00	0	0	99.02 \pm 0.73	99.18 \pm 0.59	99.40 \pm 0.81

TABLE 6.9
MEAN DETECTOR EFFICIENCY AT VARIOUS ANGLES
OF INCIDENCE USING CA 80
ETCHING TIME 20 HOURS IN 2.5 N NaOH AT 18°C

Angle of Incidence θ°	Energy Range of Observed Tracks (MeV)	Mean Efficiency at Angle of Incidence θ°
90	0.6 - 3.80	99.09
80	0.6 - 4.50	99.05
70	0.6 - 4.75	99.11
60	0.6 - 5.50	99.16
50	0.6 - 6.0	99.28
45	0.6 - 6.0	99.16
40	0.6 - 6.0	99.18
30	0.6 - 6.0	99.20
20	0.8 - 6.0	98.98
10	1.5 - 6.0	98.94
7	1.8 - 6.0	98.84
5	2.5 - 6.0	99.21

GRAND MEAN 99.10 \pm 0.40

NOTE: The error on the mean efficiency is less than \pm 0.5% in each case.

TABLE 6.10
MEAN DETECTOR EFFICIENCY AT VARIOUS ANGLES
OF INCIDENCE USING LR 115
ETCHING TIME 20 HOURS IN 2.5 N NaOH AT 18°C

Angle of Incidence θ°	Energy Range of Observed Tracks (MeV)	Mean Efficiency at Angle of Incidence θ°
.90	0.6 - 3.8	98.35
80	0.6 - 4.0	98.61
70	0.6 - 4.0	98.45
60	0.6 - 4.0	98.18
50	0.6 - 4.0	98.20
45	0.6 - 4.25	98.27
40	0.6 - 4.25	98.09
30	0.6 - 4.25	97.98
20	0.75 - 5.0	97.42
10	1.5 - 6.0	97.91
7	2.5 - 6.0	97.89
5	3.5 - 6.0	98.34

GRAND MEAN 98.14 \pm 1.04

NOTE: The error on the mean efficiency is less than \pm 0.5% in each case.

6.9.3 Effect of Temperature and Ultra-Violet Light on Detection Efficiencies

It may be required in some experiments to operate the detectors at a temperature higher than the normal room temperature. It has already been mentioned in Section 6.8 that at higher temperatures the number density of the etched tracks decrease. This fact makes the apparent registration efficiency become somewhat smaller. Heating produces an apparent reduction of particle track length as well, presumably, as its (latent) diameter. This causes a decrease in V_T , which results in an increase in the critical angle of etching, θ_c . The application of very high temperatures makes θ_c become almost 90° and the apparent etchable range R_{ap} reduces to almost zero; thus the tracks are not etchable even at normal incidence of particles. In other words, the latent damage is effectively cured by heating the detectors to very high temperatures. Thus, for accurate track analysis, proper temperature-dependent corrections to the efficiency factors must be applied.

To find the track registration efficiency of an SSTR for a specific particle of a specific energy, when it is operated at a certain temperature for a certain period of time, one has to find the θ_c corresponding to the temperature and duration of annealing.

Values of θ_c for alpha particles in CA 80-15 cellulose nitrate were determined at different temperatures in the case when the detectors operated for ten minutes each. The materials were exposed to alpha particle beams at various angles in the manner previously described. The exposed materials were then annealed at a number of different temperatures for 10 min each. The annealing temperatures were varied between room temperature and slightly lower than the softening temperature of the material concerned. The samples were then etched in 2.5 N NaOH solution at 18°C and the angular interval containing θ_c determined. A second set of precise determinations of angle yielded the critical angle, from which the particle registration efficiency was obtained by using Equation 6.59. Some typical results are shown in Figure 6.42, which are based on experimental observations, the room temperature values of efficiency having been calculated from the previously determined values of θ_c (Section 6.92). It is clear that the registration efficiency reduces progressively as the detectors are operated at higher and higher

Change of θ_c with Temperature

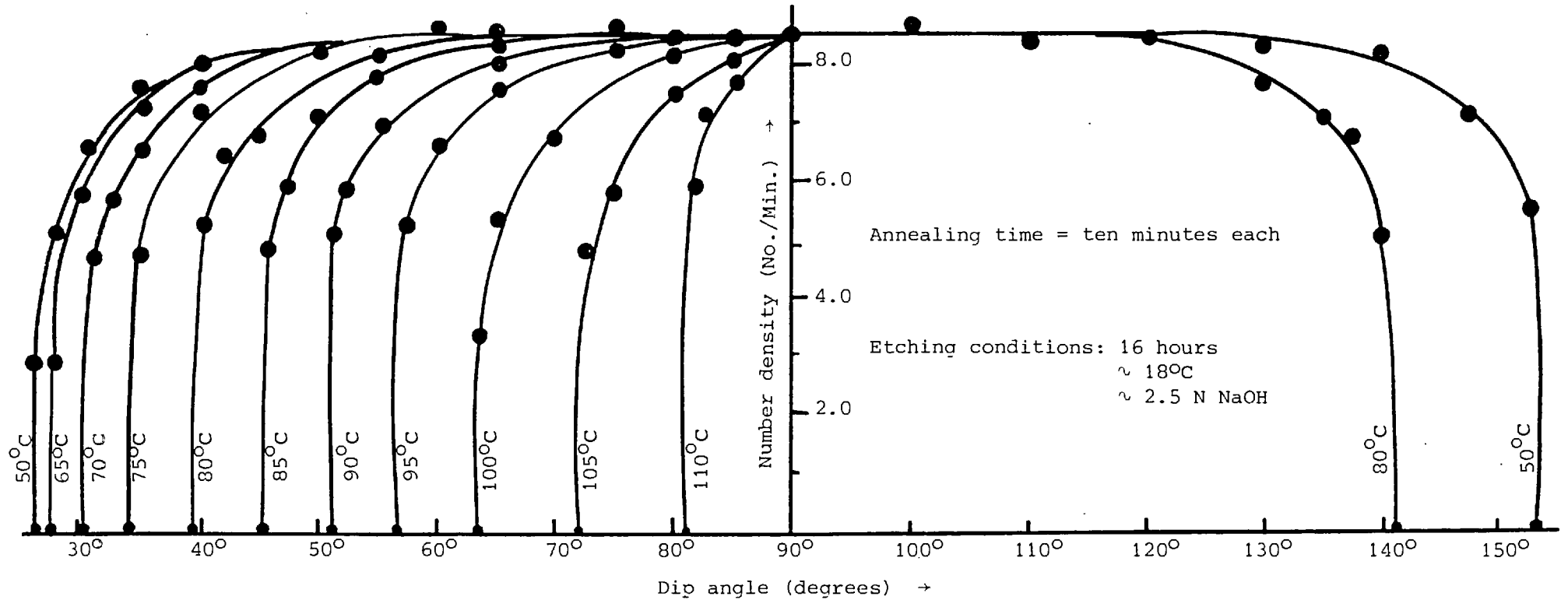


Figure 6.42 The variation of the critical angle of track revelation (θ_c) with annealing temperature for CA 80-15 cellulose nitrate etched in 2.5 N NaOH at 18°C for 16 hours without interruptions or stirring. The critical angle of track revelation (θ_c) was $5^\circ \pm 2^\circ$. No change in θ_c took place when the CA 80-15 cellulose nitrate was annealed between 25°C and 40°C, at 5°C intervals, for an annealing time of ten minutes at each temperature.

temperatures for constant annealing times. Table 6.11 gives the θ_c and registration efficiencies of CA80-15 cellulose nitrate when operated at different temperatures for ten minutes each.

As for the ultra-violet effect, it has been shown that the exposure of plastics to uv light reduces the etching time needed to reveal tracks. It is difficult to give a detailed interpretation of the photo-oxidation enhancement effect and only a plausible qualitative description can be made. One may speculate that a bombarding particle creates new chemical species along its path in plastics as a result of energy deposition. The electronic configuration of these new chemical species in the damaged region is such that they absorb longer uv wavelengths at a much higher rate than the surrounding material. This extra energy absorbed, first excites the electrons, which on deexcitation probably share it with the adjacent chemical bonds of the main polymeric chain. This situation may result in the formation of free radical, which in the presence of oxygen combines with it, thus producing a permanent scission. Thus it may be inferred that the exposure of plastics to ultra-violet light increases the extent of damage in the latent damage trail, which in turn increases the etching velocity V_t along the track. This implies that $\theta_c \left[= \sin^{-1}(V_B/V_t) \right]$ decreases, assuming V_B to increase by a lesser amount than does V_t .

As already mentioned, θ_c for plastics is increased (or the registration efficiency is decreased) when they are annealed at high temperatures. A CA 80-15 sample annealed at 125°C for ten minutes was expected to yield a decrease of about 38% in registration efficiency. But before etching it, the same piece was exposed to ultra-violet light (Hanovia chromatol lamp of 30 W) for 240 h at a temperature of 22°C at a distance of 0.5 cm from the uv source. On etching the sample a few hours after the end of exposure a decrease of only 9% in untreated registration efficiency was observed. This means that a decrease in the efficiency of a plastic SSTR caused by annealing can be partially, or in some cases totally, counter-balanced if, subsequent to irradiation, the specimen is exposed to ultra-violet light for a calculable length of time.

TABLE 6.11

The Registration Efficiencies for ^{252}Cf Fission Fragments and
3 MeV Alpha Particles in CA80-15 Cellulose Nitrate SSTR
Annealed at Different Temperatures for Ten Minutes each
after Irradiation

Temperature of annealing ($^{\circ}\text{C}$) ($\pm 1^{\circ}\text{C}$)	Registration efficiencies (%) ^a of CA80-15 cellulose nitrate SSTR	
	^{252}Cf fission fragments	3 MeV alpha particles
10	100.0	100.0
20	100.0	99.8
40	99.6	99.3
50	99.1	98.7
60	98.4	94.4
70	94.8	93.7
80	91.7	94.1
90	93.2	93.4
100	92.6	92.8
110	89.3	86.9
120	81.7	87.1
130	76.9	79.7
140	71.4	65.5
150	64.5	60.8
160 ^b	19.9	29.1
165	19.1	14.3
166 ^b	0.0	0.0

^a The efficiencies have been normalised against a surface-barrier semi-conductor detector placed in vacuum in the same (2π) geometry as SSNTD, the detection efficiency of the former having been assumed to be unity for the fission fragments and alpha particles falling on it.

^b Extrapolated values.

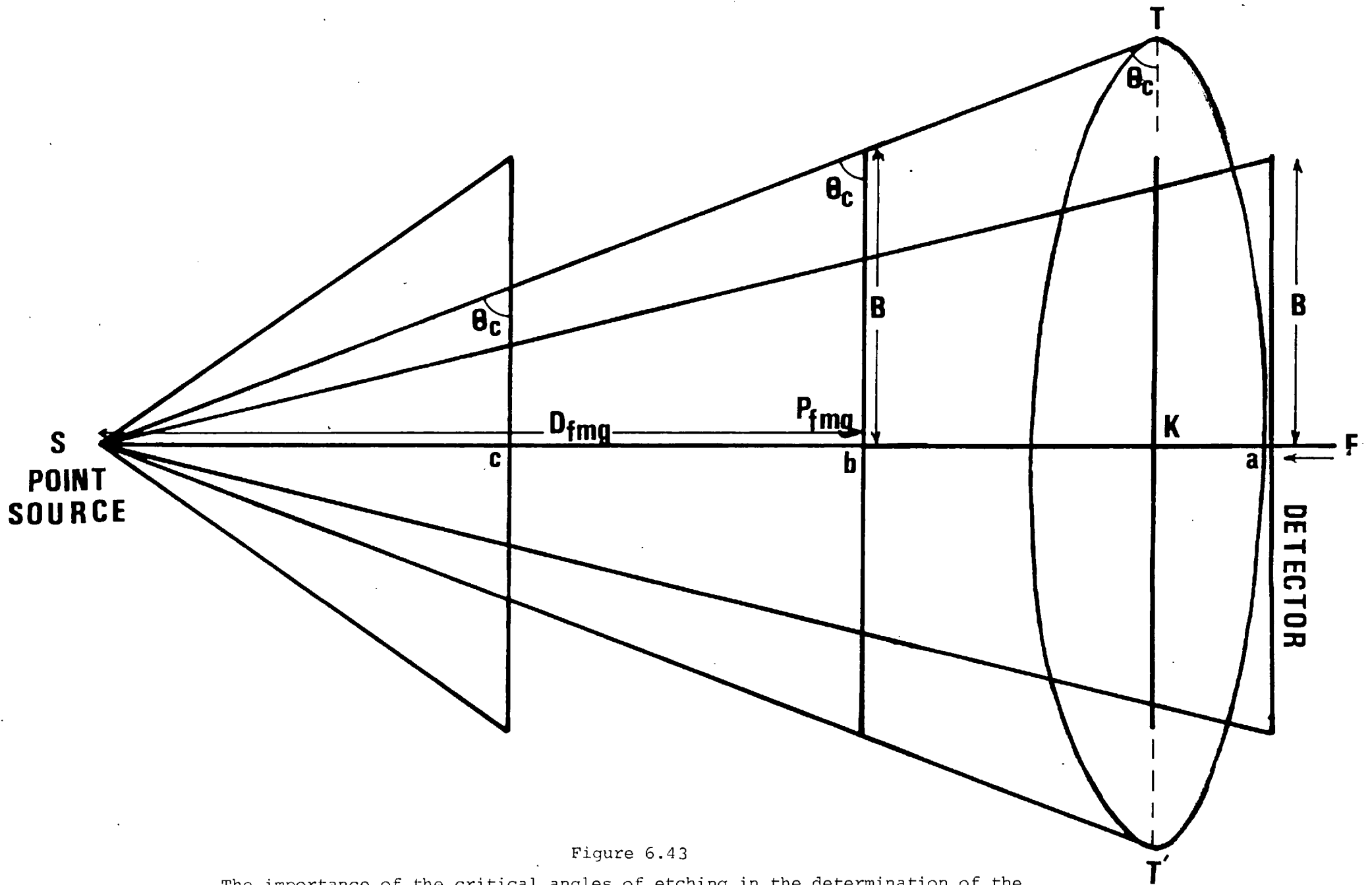


Figure 6.43

The importance of the critical angles of etching in the determination of the efficiency of SSTRs on a point source

6.9.4 Modifications in Geometry Factors for SSTR's

The 'geometry factor' G_p of a circular disc for a point source is defined as the solid angle subtended at the point source by the disc expressed as a fraction of the total solid angle, i.e.

$$G_p = \Omega_p / (4\pi) \quad (6.60)$$

Jaffey (134) has shown that in the case of a point source lying at a distance D from, and on the axis of, a circular detector of radius B the 'geometry factor' is given by

$$G_p = \frac{1}{2}(1 - D/T) = \frac{1}{2}B^2/[T(T + D)] \quad (6.61)$$

where T is the distance from the point source to the periphery of the detector.

If instead of a point source, a uniformly spread source with radius A, situated parallel to and coaxially with the circular detector of radius B, is considered, the 'geometry factor' of the detector is given by (134):-

$$G_d = G_p - \frac{3}{16} A^2 (B^2 D/T^5) + \frac{5}{32} A^4 (B^2 D/T^9) \times (D^2 - \frac{3}{4} B^2) + \dots \quad (6.62)$$

where T is now the distance from the centre of the extended source to the periphery of the detector.

These formulas, which are applicable to conventional detectors, need certain modifications when applied to SSTR's. The reason for the modification is that, the critical angle of etching θ_c now becomes the over-riding factor. If any particles arrive at the detector (and proceed unscattered) at an angle of incidence less than θ_c , they fail to produce etchable tracks in SSTR's.

The situation can be visualised by reference to Figure 6.43 which depicts the point source case. SST' is the maximum cone within which particles emitted from an isotropic point source situated at S can form etchable tracks on a detector (lying in a plane perpendicular to, and coaxially with, SK), the base angle being θ_c for the detecting material. Imagine a circular detector of radius B approaching the source S from a point F, and being exposed successively at points, b, c and d at decreasing distances from the source, the solid angle subtended (or the cone cut) by it increasing all the while. At

position c, the cone cut by the detector equals the 'maximum cone'; the geometry at this 'critical point' P_c is the maximum possible geometry of the system. The distance of this critical point P_c from the source is the 'critical distance' D_c , which for an SSTR of radius B is given by

$$D_c = B \tan \theta_c \quad (6.63)$$

At distances smaller than D_c , for instance at position d, and down to zero, the 'geometry factor' remains constant but is no longer given by Equation 6.61. It is then given, instead by

$$G'_p = \text{constant} = \frac{1}{2}(1 - \sin \theta_c), \quad \text{for } D < B \tan \theta_c \quad (6.64)$$

At distances $D \geq B \tan \theta_c$, Equation 6.61 of course continues to apply.

Similar considerations apply to extended sources. So long as no angles of incidence, from any point on the extended source and subtended on any point on the detector, are less than θ_c , the conventional formulas for geometry factor apply; as soon as any angle falls below θ_c modifications become necessary. Thus the 'geometry factor' is given by Equation 6.62 for $D \geq (A + B) \tan \theta_c$, where A is the radius of the source. The value of G'_d increases with a decrease in D for $(B - A) \tan \theta_c < D \leq (A + B) \tan \theta_c$, but becomes constant for $D < (B - A) \tan \theta_c$, for the case treated (where $B > A$). Modifications necessary for other situations can be easily derived, bearing in mind the supremacy of the critical angle of etching in the case of SSTR's.

The existence of the human element in the present measurements can represent a source of serious systematic error. For precision work, a great deal of effort has been concentrated on the method of track counting to ensure the elimination of personal bias which can lead to mistaken observations. The results of different observers must be repeatedly tested and compared in order to remedy faulty techniques. This process of trial and error has provided the necessary experience needed to establish the present alpha particle track observations on an objective basis.

One crucial assumption employed in these tests has been the applicability of Poisson statistics. It is not immediately evident, however, that this assumption holds for human track counting observations. Hence, the validity of this assumption was experimentally tested with data obtained from a measurement of the americium-241 source. In this measurement, CA 80-15 and LR 115 type II

cellulose nitrate detectors were scanned over equal areas (0.024 cm²) strips. There were 690 such strips, and a total of 12159 tracks were observed, corresponding to a mean value of 17.622 tracks/strip. The frequency histogram for these data is displayed in Figure 6.44 and compared with the Poisson distribution.

$$P_n = \frac{690 (m)^n e^{-m}}{n!} \quad (6.65)$$

Here the normalization constant is 690, the total number of strips, and m is the mean value of the distribution. As can be seen from this figure, the Poisson distribution obtained with $m = 17.622$ is in excellent agreement with the frequency histogram. Moreover, the standard deviation obtained directly from the histogram is 4.135, whereas the value from Poisson statistics is $(m)^{\frac{1}{2}} = (17.622)^{\frac{1}{2}} = 4.198$. One can therefore conclude that Poisson statistics can be employed in the present counting experiments. The agreement was observed, in fact, to be well within the random error predicted by Poisson statistics in the track density region bounded by 4×10^5 tracks/cm².

6.10 Particle Identification and Energy Measurement

Until now it has been assumed that the track etching rate is constant along the trajectory of the incident charged particle, independent of the particle's energy loss rate. The optimal etching condition which was established in Sections 6.71, 6.72 and 6.73, did not take into account the stopping power of the target medium. In actual fact, the track etching rate varies significantly with the stopping power. It is immediately observed that tracks of heavy particles etch faster. The faster preferential etching rate for a given etching time results in the tracks having correspondingly smaller cone angles and longer track lengths. As a result, measurements of the dependence of the track etching rate on the particle REL rate can be used for particle identification and energy measurement. While the REL criterion (the point where $V_T = V_B$) predicts which portion of the particle trajectory in the plastic has $V_T > V_B$ and whether a latent track will be produced.

It was observed in Figure 6.45 that the track etching rate (V_T) rapidly approaches V_B for small values of REL. This very rapid decrease in V_T is the key to the threshold characteristic of the detector (see the registration data for protons and alpha particles

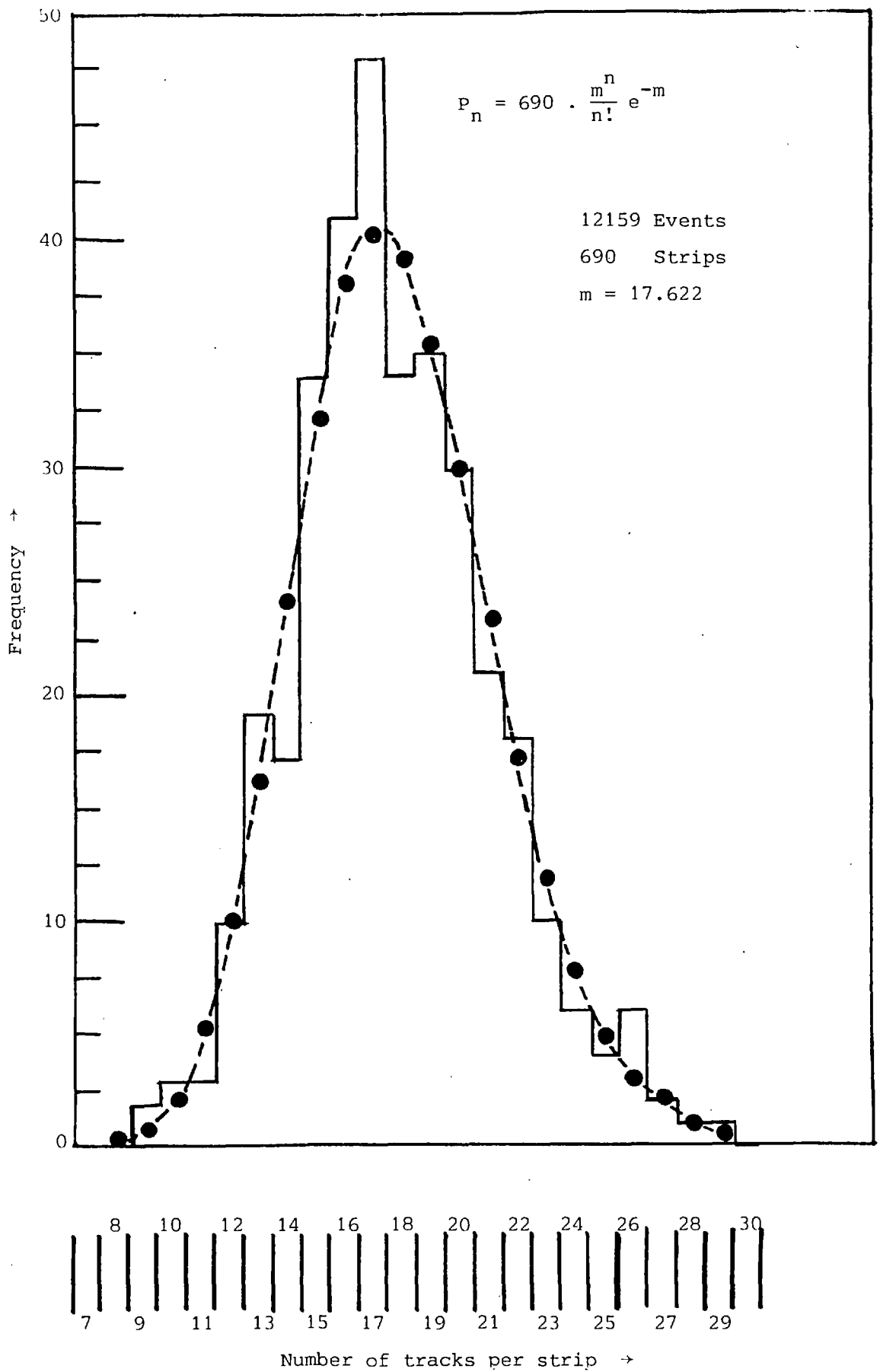


Figure 6.44 Comparison of the frequency histogram of observed number of tracks per strip with the Poisson distribution, P_n , corresponding to the observed mean value ($m=17.622$)

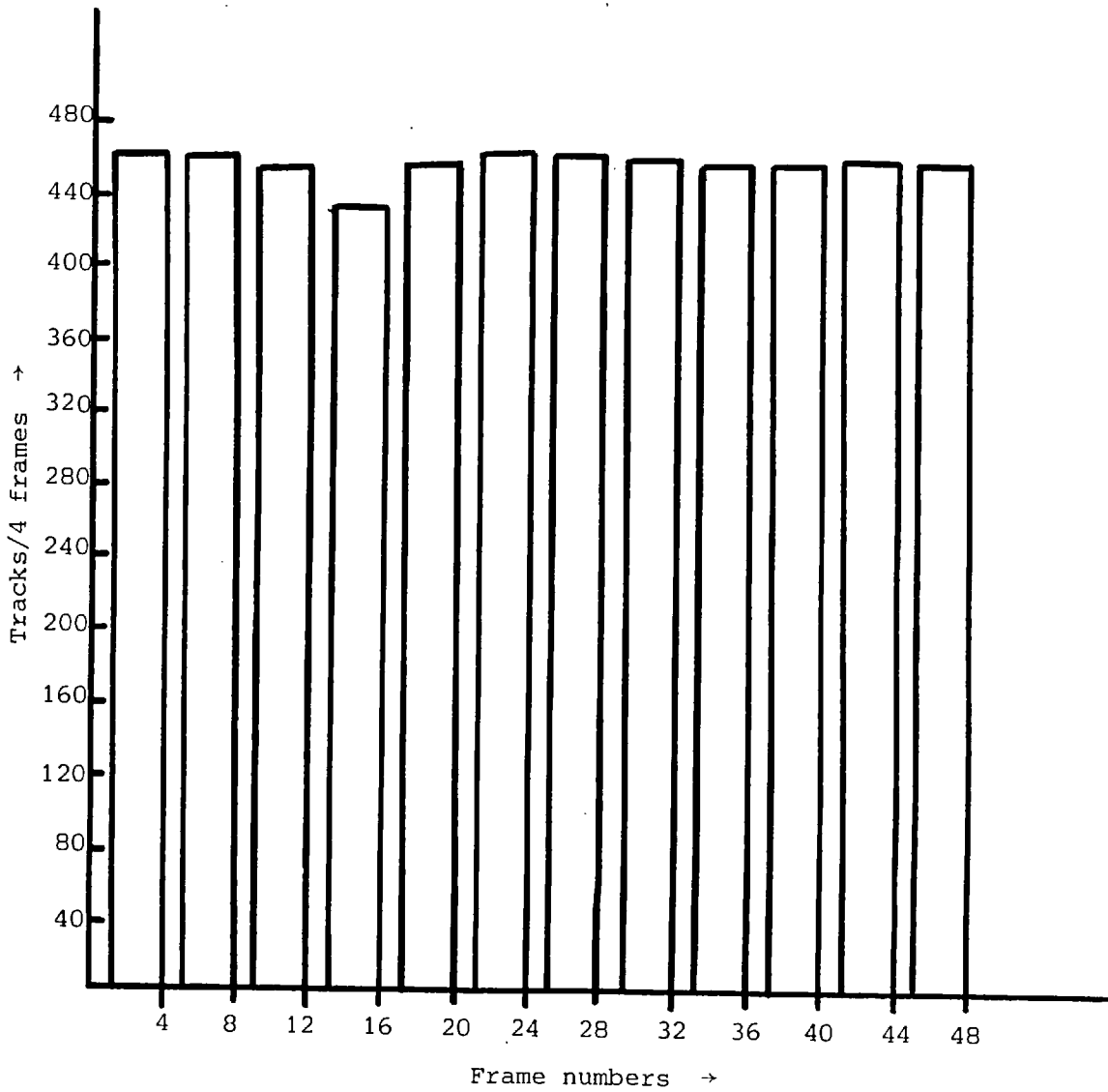


Figure 6.44b Track density as a function of SSTR radius

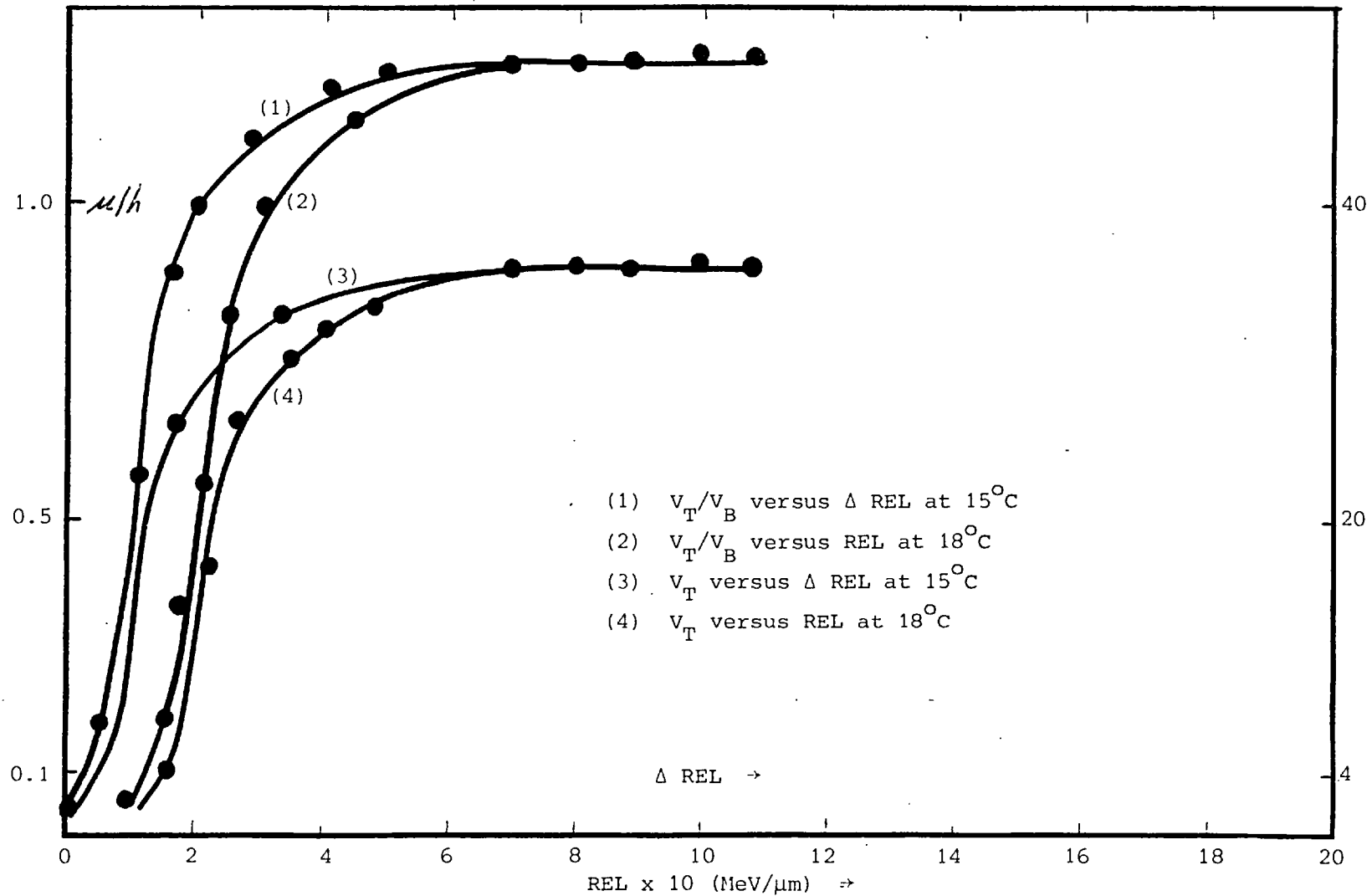


Figure 6.45 Measurements of the track etching rates and the ratio of the track etching rates to the bulk etching rates as a function of the particle restricted energy loss rates (REL) and Δ REL (REL of the incident particle - REL critical of the detector) for CA 80-15 cellulose nitrate etched in 2.5 N NaOH at 15°C and 18°C , without interruptions or stirring

in Figure 3.4). Figure 6.46 shows how dE/dx varies along the range (R) of an alpha particle incident normal to the surface of the detector. The threshold (REL critical) of track registration of the detector is a function of:

- (a) the energy of the incoming particle
 - (b) the molecular structure of the plastic detector used
- and
- (c) pre- and post-etching treatments of the plastic and etching conditions used.

The energy E_{\max} at stage B of Figure 6.46 and E_{\min} at Stage C of the same figure are two limiting energies for the revelation of the damaged trail by etching. Only the 'dotted' portion (BC) of the original latent trail is etchable and parts AB and CD cannot be revealed by etching. This, coupled with the fact that the part AB of a lower energy alpha particle will be smaller than that of a higher energy alpha particle, can explain the threshold characteristics of SSRS.

The behaviour of the track etching rate (V_T) as a function of the restricted energy loss (REL) for a specific etching condition should be investigated. An optimal etching condition with a low registration threshold and a measurable etched track parameter should be established, and compared with the previously determined optimal etching conditions, along with a simple reproducible relationship between the track etching rate and the restricted energy loss (REL) or the total energy loss (dE/dx). Since the REL takes into account secondary electrons of energy only less than 1 keV (31), the REL is a more suitable parameter to describe the detector's etching property than the total energy loss. This relationship will enable identification of particles, resolve energies and separate isotopes of small mass differences.

6.10.1 Dependence of the Track Etching Rate on the Restricted Energy Loss

Measurements of the track etching rate as a function of the particle's restricted energy loss are presented in Figure 6.47. The data were obtained by bombarding CA 80-15 cellulose nitrate films with heavy and light charged particles from the Harwell and Oxford accelerators (see Table 5.2). The bombarded specimens were etched in various etchant (NaOH) concentrations, temperatures and etching time

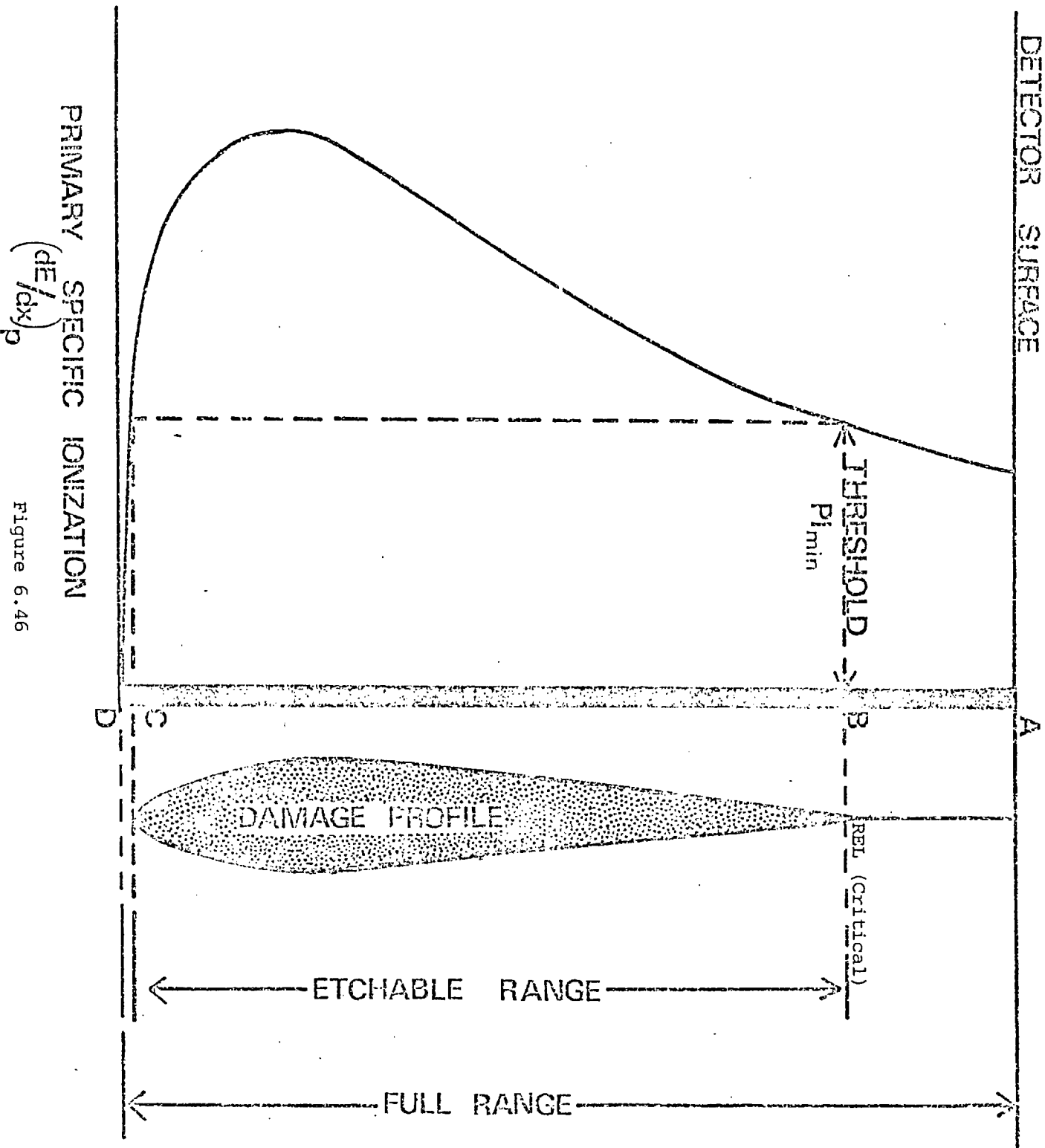


Figure 6.46

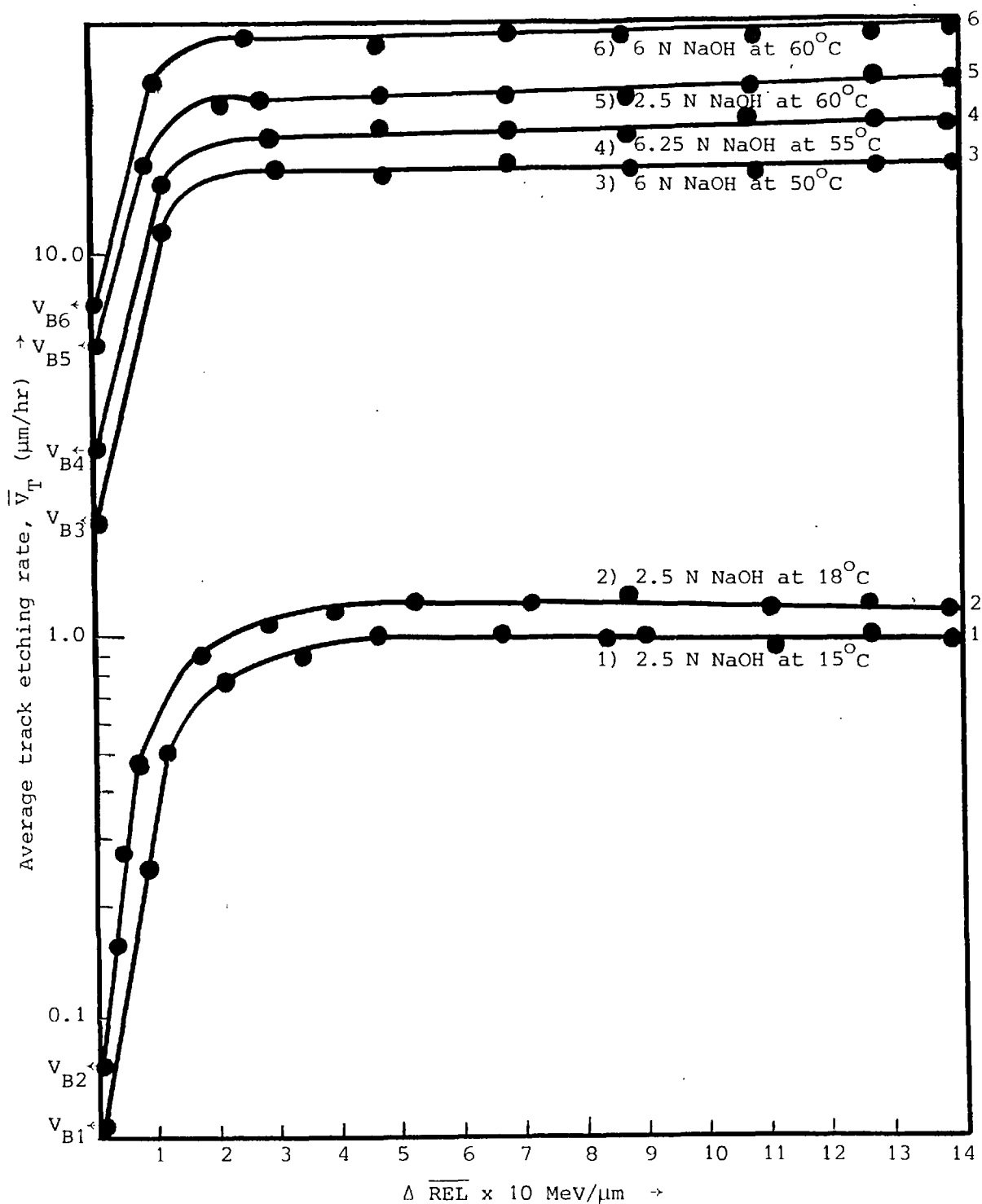


Figure 6.47a Measurements of the average track etching rate, \bar{V}_T , as a function of $\Delta \overline{\text{REL}}$ (the difference between the particle average REL and the detector's critical REL (REL_{crit})) in CA 80-15 cellulose nitrate plastic etched with various concentrations of NaOH and at different etching temperatures, without interruptions or stirring

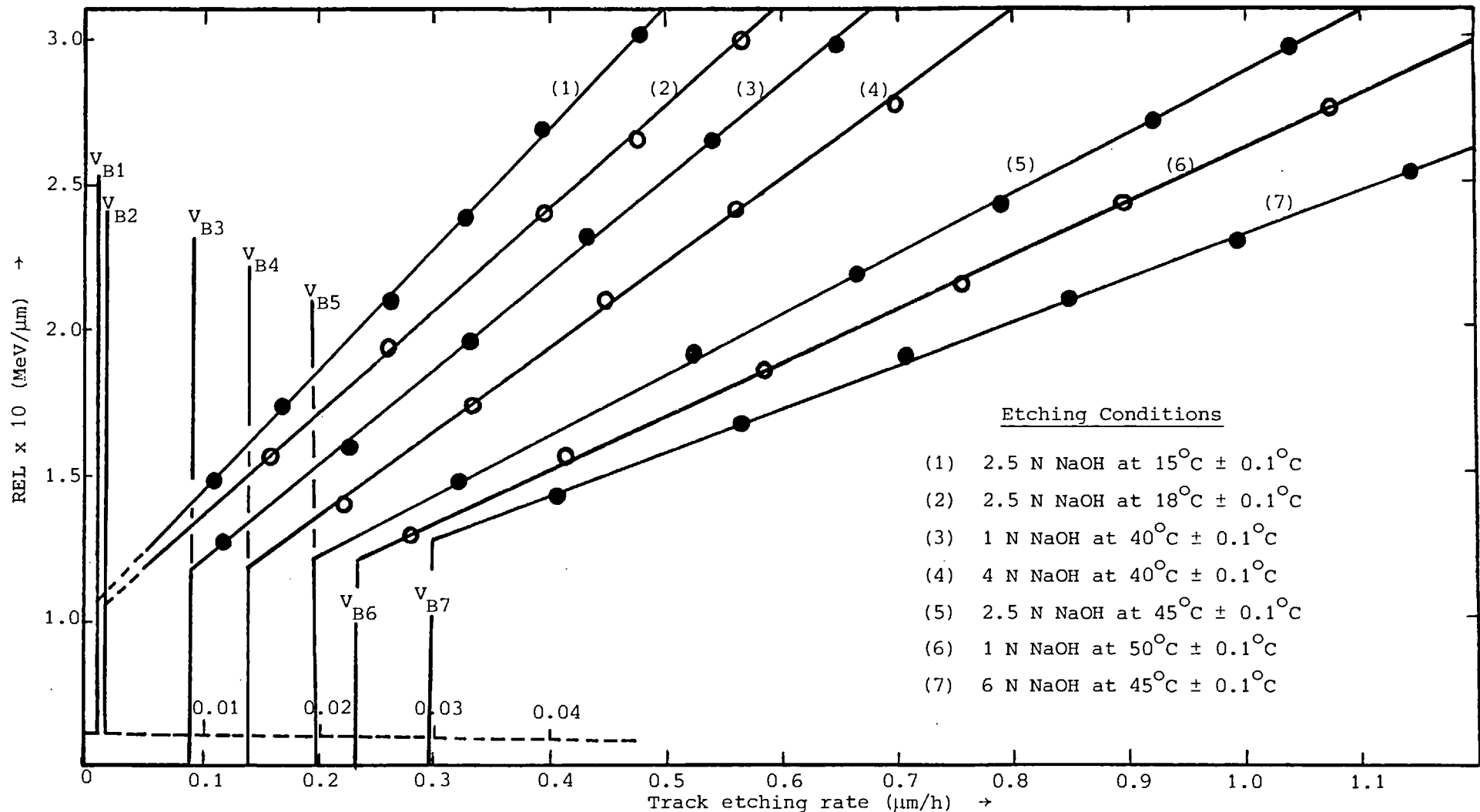


Figure 6.47b Measurements of track etching rate (V_T) versus REL for CA 80-15 cellulose nitrate plastic pre-treated in a concentrated solution of zinc chloride (swelling agent) and etched with different etchant concentrations and temperatures, without interruptions or stirring

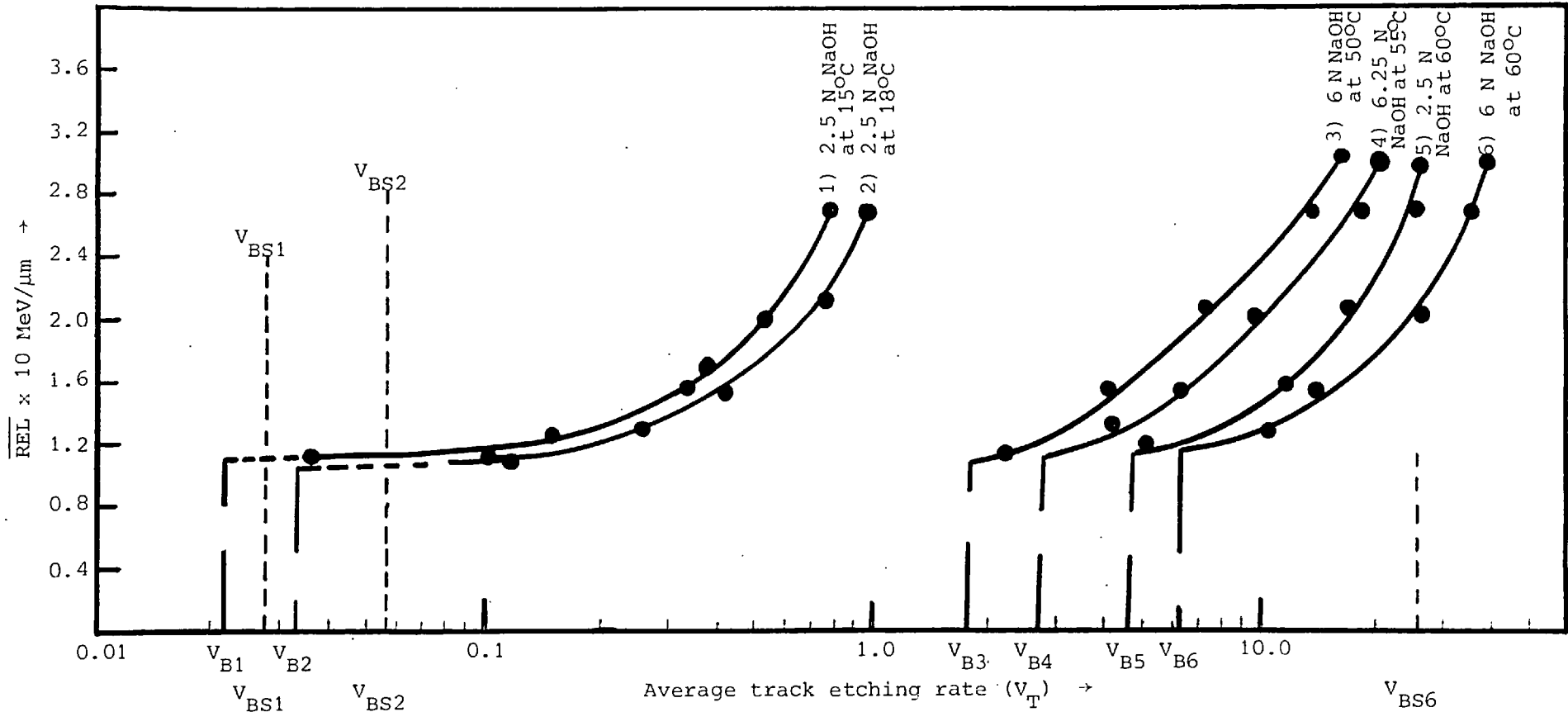


Figure 6.47c Measurements of the particle average \overline{REL} as a function of the average track etching rate, V_T , in CA 80-15 cellulose nitrate plastic etched with various concentrations of NaOH at different etching temperatures, without interruptions or stirring, except where indicated (by V_{BS})

intervals. Measurements of track lengths were performed with charge particles incidental 5° , 10° , 20° , 30° and 90° to the surface of the detectors. The normal incident particles were observed at 30° from the normal by tilting the electron microscope stage $\pm 30^\circ$. This technique will enable accurate measurements (better than $0.025 \mu\text{m}$) of the diameter and the projected track length of the incident charged particles normal to the surface of the detector as shown in Figures 6.48 and 6.49.

The plots of the track etching rates against their corresponding restricted energy loss of CA 80-15 cellulose nitrate under various etching conditions (Figures 6.45 and 6.47) show a large value of V_T/V_B at high REL. The REL at which the track etching rate equals the bulk etching rate is taken as the critical restricted energy loss under which no etchable tracks can be produced (REL criterion). The critical energy loss for etchable track revelation was found to be dependent on the etchant concentration and etching temperature. Neither the track etching rate nor the critical energy loss criterion for etchable track revelation depend on agitation of the etchant. On the other hand the bulk etching rate is highly sensitive to stirring of the etchant as shown in Figure 6.47c. The linearity of the track etching rate against their corresponding restricted energy loss of CA 80-15 cellulose nitrate fails at low values of REL if induction time is not taken into consideration; alpha particles of energies higher than 3.8 MeV reach the detector's critical values of energy loss at some distance below the surface of the detector, so at first the etchant has to remove a certain layer of material with a normal bulk etching rate before it reaches the preferential etching region of the latent tracks. Alpha particles between 3.5 and 3.8 MeV have an energy loss rate about the critical registration value of the detector's surface, these are attacked immediately. Particles of lower energy create smaller etchable tracks as shown in Figure 6.50. This phenomenon will enable identification of particles and energy discrimination by measuring etched track diameters and induction times, as will be discussed later in this chapter.

The combination of restricted energy loss-energy (135) curves and range-energy curves (135) has been used to measure etching rates as a function of the corresponding restricted energy loss rate (Figures 6.45 and 6.47). The important conclusion to be drawn from

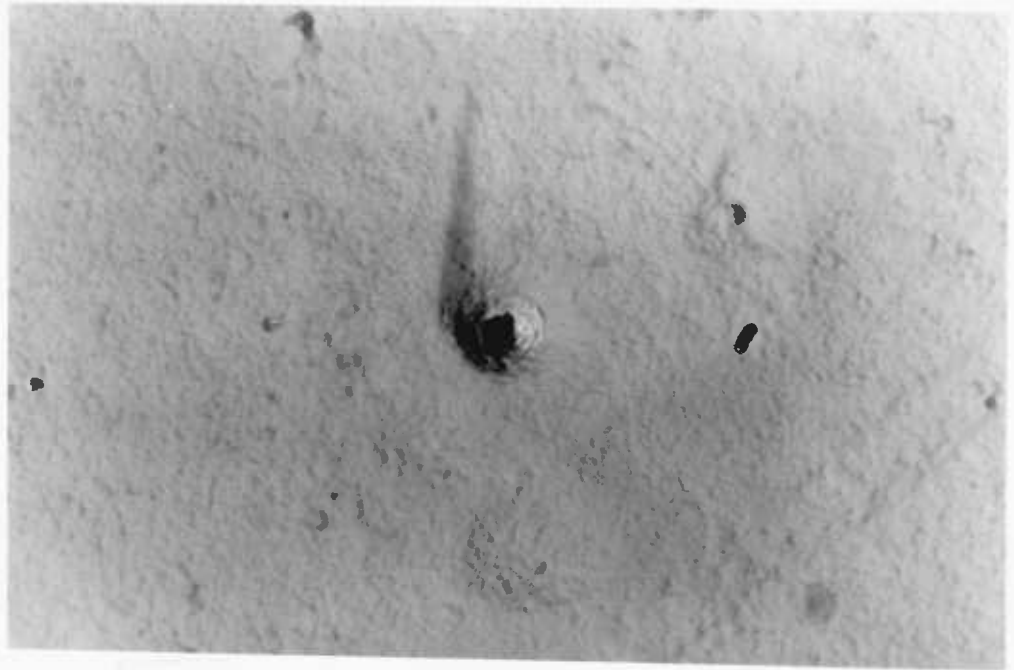


Figure 6.48 Electron micrograph of 1.1 MeV proton track in CA80-15 (Kodak-Pathe, France) at 90° incidence, pre-swollen in 65% zinc chloride solution for 2 hours, then etched in 2.5 N sodium hydroxide at 18°C , for 4 hours (25 K x 3).



Figure 6.49 Electron micrograph of 1.1 MeV underetched proton tracks in CA80-15 (Kodak-Pathe, France) at 60° incidence, pre-swollen in 65% zinc chloride solution for 2 hours, then etched in 2.5 N sodium hydroxide at 18°C , for 4 hours (25 K x 3).

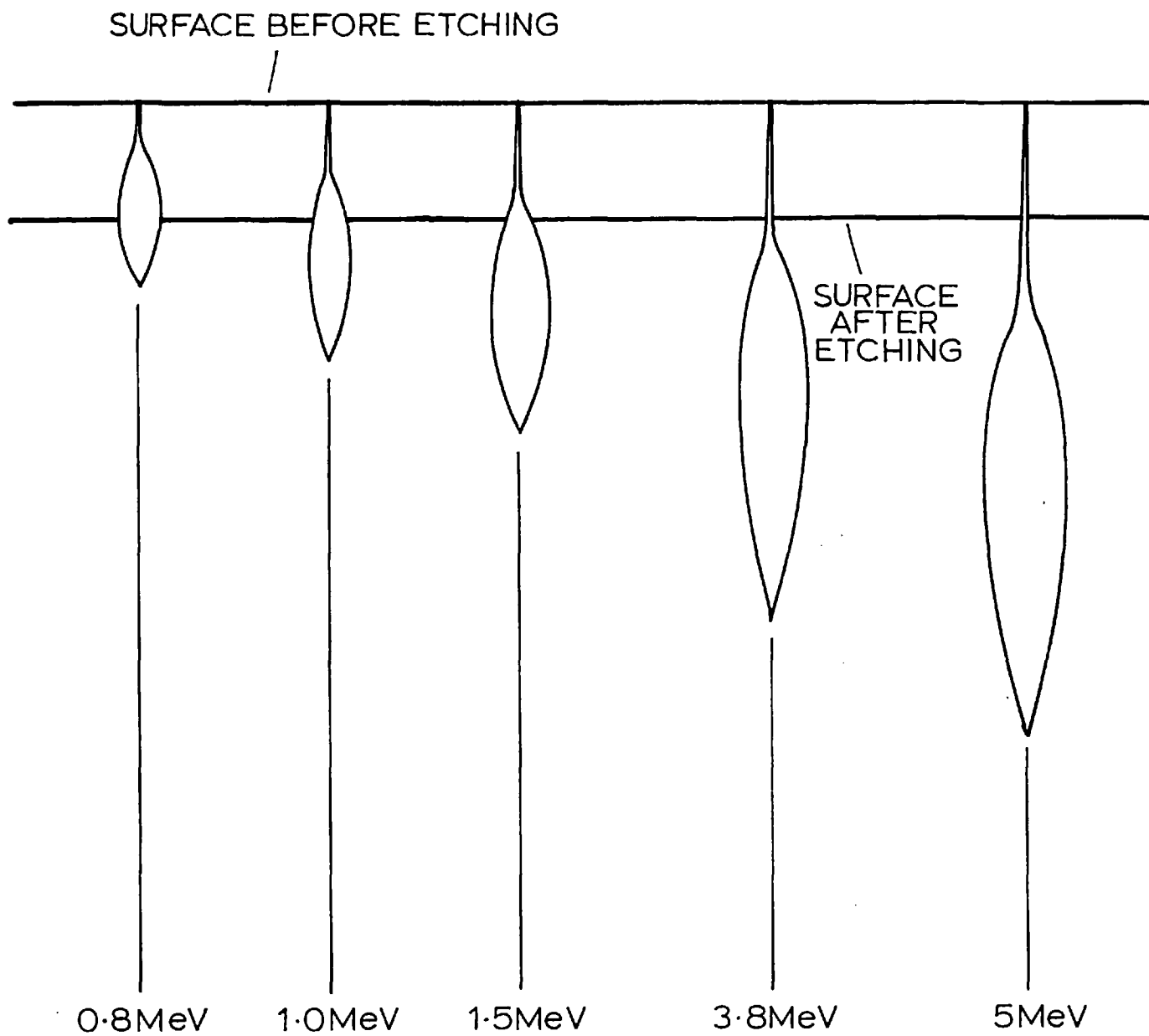


Figure 6.50 Diagrammatic representation of alpha particle tracks in CA 80-15 at various particle energies for etching in 2.5 N NaOH for 20 hours at 18°C

these measurements and Figure 6.46 is that etching rate increases with increasing restricted energy loss. Also a relationship is deduced for a given etching condition based on first order chemical kinetics; a track is due to irradiation induced changes in the relative concentration of the chemically etchable species.

The relationship below has been developed.

$$V_T = V_B + a(1 - \exp b \cdot \Delta \text{REL}) \quad (6.66)$$

where

V_B = bulk etching rate in $\mu\text{m}/\text{h}$ as in Equations 6.50 and 6.51,

= 0.022 $\mu\text{m}/\text{h}$ for 2.5 N (NaOH) and 15°C,

= 0.034 $\mu\text{m}/\text{h}$ for 2.5 N (NaOH) and 18°C,

a = a proportionality constant for a given etching condition. It is a function of OH^- ion concentration, mobility and the effective swelling of bulk material,

= 0.98 for 2.5 N (NaOH) and 15°C,

= 1.2 for 2.5 N (NaOH) and 18°C,

b = a constant for a given etching condition. It is proportional to the etchant temperature ($T^\circ\text{K}$);

$$b_1/b_2 = T_1^\circ\text{K}/T_2^\circ\text{K},$$

= 0.752 μ/MeV for 2.5 N (NaOH) at 15°C,

= 0.760 μ/MeV for 2.5 N (NaOH) at 18°C,

ΔREL = REL critical - REL along the trajectory of the particle,

REL critical \approx 0.108 MeV/ μm for 2.5 N (NaOH) and 15°C up to 20°C,

\approx 0.124 MeV/ μm for 2.5 N (NaOH) and 50°C up to 60°C.

This is a useful empirical fit to the experimental points and can be used to calculate curves for the true cone length (L) versus the residual range (R) and $\Delta L/\Delta R$ versus the particle's charge (z) in order to identify z, M and energy (E) of particles.

We can see from Equation 6.66 that CA 80-15 cellulose nitrate has a sudden increase in track etching rate (v_T) at REL $\approx 11 \times 10^{-2}$ MeV/ μm , while it levels off at REL $0.8 \sim 10 \times 10^{-1}$ MeV/ μm and seems to form a plateau. The meaning of this may be best illustrated by

showing the registering power of CA 80-15 cellulose nitrate allows detection of protons, helium and lithium particles. Protons and helium particles cannot be detected by Lexan, since Lexan has a sudden increase in track etching rate (V_T) at higher REL ($3 \sim 5 \times 10^{-1}$ MeV/ μ m). Therefore Lexan has better characteristics for the study of heavier particles. It should also be noted from Equation 6.66 that the sudden increase in V_T for lower etching temperature is produced at lower values of REL and the levelling off of V_T at these lower temperatures occurs at higher values of REL. This implies that etching at lower temperatures will produce higher energy resolution and better track geometry (sharper cone angles).

6.10.2 Information Content of Particle Etched Tracks

The damaged region along the trajectory of the incident charged particle in the SSTR contains all the information required concerning that individual incident particle. The problem is to determine what information exists, and to find ways of extracting this information.

In this chapter it was shown that the chemical etching development of tracks is composed of two independent processes, namely,

- (a) the track etching rate along the incident particle's trajectory (V_T),

and

- (b) the material bulk etching rate (V_B).

Here it is assumed that the entire information content of a track is contained in the track etching rate and its variation over the entire length of the incident particle's trajectory in the detector. Table 6.12 is a summary of the incident charged particle information possibly accessible from the etched tracks.

TABLE 6.12

Measurable Track Parameter	Detector Variable	Particle Parameters
The residual range (R)	$I_{adj}, A/Z$	E, z, M
The cone angle (θ)	V_B/V_T	} REL (z, β)
The true track length (L)	\bar{V}_T	
$d\theta/dR$ dL/dR	} $dV_T/d(REL)$	$d(REL)/dR$
The registration range R_{reg}		

From the above table the following relationships are observed:

- (a) The residual range (R) of the stopping particle in the detector is a function of the particle's kinetic energy (E), charge (z) and mass (M).
- (b) The track etching rate (V_T) is a measure of the particle's restricted energy loss (REL).
- (c) The rate of change of the cone angle (θ) or the true track length (L) (L includes the portion removed by the bulk etching process) with the range is a measure of the rate of change of the REL with the particle's range, $d(REL)/dR$.
- (d) The registration range (the region where $V_T > V_B$) of the slowing particle in the detector is a function of the particle's charge (z) and mass (M).

The measure of the particle track etching rate (V_T) can be determined from the relationship between the cone angle (θ) and the track etching rate (V_T), as demonstrated in Equation 6.1 ($\sin\theta = V_B/V_T$). The cone angle (θ) is a measure of the track etching rate (V_T) at every point along the particle trajectory. For many tracks, V_T is larger than or equal to $10 V_B$, and the corresponding θ is less than or equal to 6° . Here, the determination of V_T through θ involves the measurements of small cone angles, and errors in the measurement may become significant. In these situations the true track length (L) is a better measure of V_T where:

$$L_i = \int_0^t V_T(i) dt = \int_0^t V_T(REL) dt \quad (6.67)$$

The measurement of the true track length yields an average value V_T for that part of the trajectory where:

$$\bar{V}_T = L/t \quad (6.68)$$

At the other extreme, for tracks where $V_T \approx 2V_B$, the cone angles are large ($\theta = 30^\circ$). The observation of a track segment with a large cone angle is an immediate visual indication that the REL of the particle is approaching the REL registration criterion of the material. However, the observation of a short track means the range of the particle is small. The decision of whether θ or L , or both, should be measured must be individually assessed in every situation.

6.10.3 Particle Identification Techniques and Particle Energy Measurements

The residual range (R) of a charged particle with a charge (z) and mass (M) is given by

$$R = \int_E^0 dE' / (dE'/dx) \quad (6.69)$$

where E is the kinetic energy at that point corresponding to a velocity $V = \beta c$. The rate of energy loss (dE/dx), as well as the restricted rate of energy loss (dE'/dx), are functions of the particle's charge and velocity. Conversely, the particle's charge may be determined by measuring two quantities such as E and dE'/dx (or REL); the variation in dE'/dx (or REL) over an interval of range may also be used. If the particle's velocity is known, z may be determined by a single measurement dE'/dx . Also if the particle's charge (z) is known, E may be determined by the registration range or the true cone length (L) measurements (range-energy relation).

Here we are concerned with two categories of particles:

- (a) Those particles that stop in the detector stack (see Figure 6.51), where the range and REL can be used to determine z .
- (b) Those particles that show appreciable slowing down, but do not stop in the stack. Here the REL and its variation over the available portion of the trajectory can be used. Very fast particles whose velocity remains essentially constant during traversal of the stack, or particles that undergo nuclear interactions are not considered.

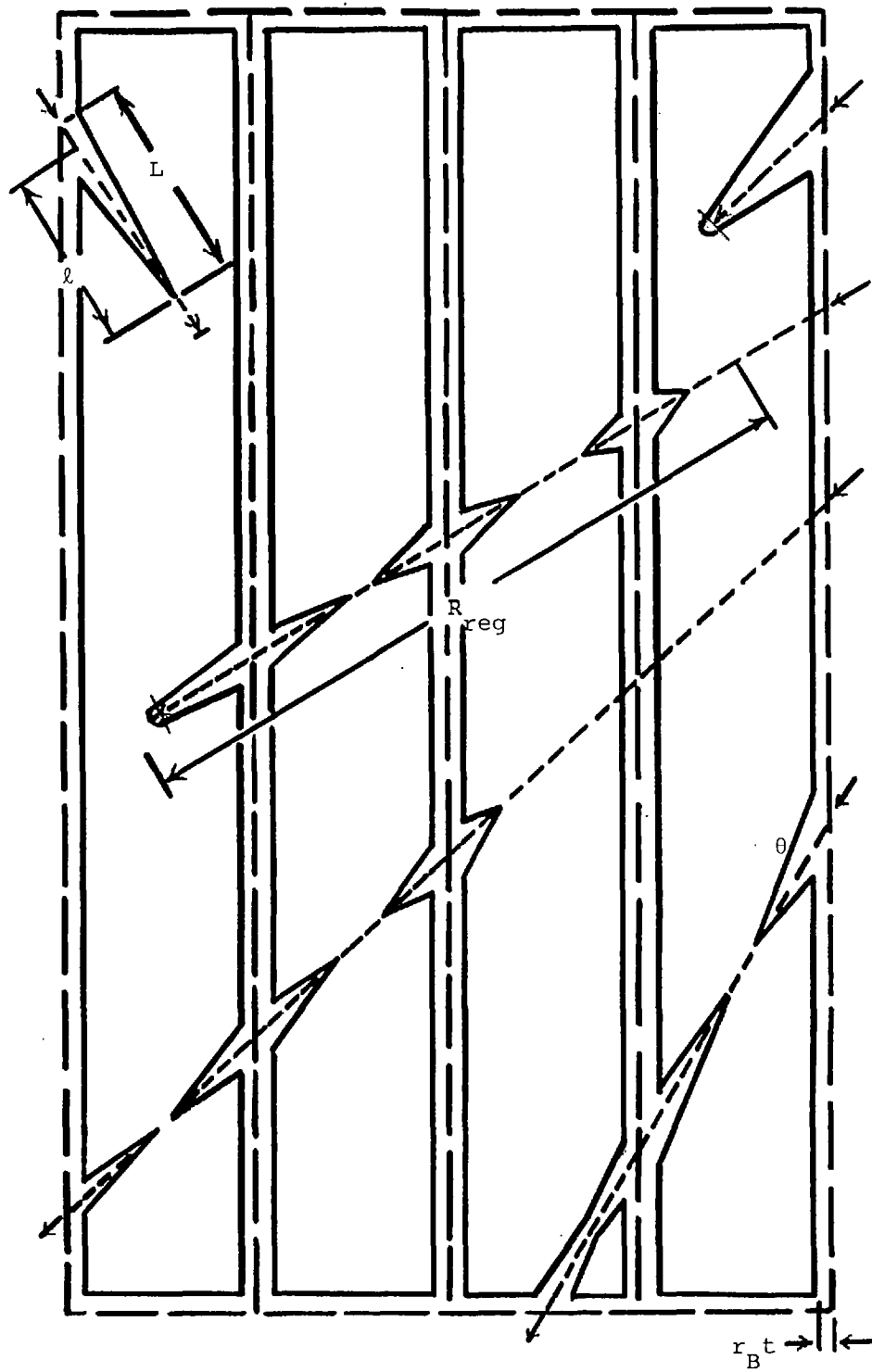


Figure 6.51 The various observed categories of etched tracks in a stack of cellulose nitrate plastic layers

A charged particle penetrating a stack of dielectric track detectors produces a series of co-linear, etchable track segments over the part of its range where REL of the particle is above the critical value required by the material. A subsequent partial etch treatment of duration t , reveals a series of etched tracks, each of length L and having a cone angle θ (see Figure 6.51). The entire information content of such a track ensemble resides in the following track parameters:

- (a) the length of each track segment (L),
- (b) the variation of L as a function of R ,
- (c) the cone angle (θ) of each track segment, and
- (d) the variation of θ as a function of R .

The cone angle is a function of the REL of the particle, decreasing with increasing REL, and quickly becoming large when the REL approaches the critical value of the material. The track length of an individual segment of the entire track is defined for specific etching conditions. For an etching time (t) L is given by Equations 6.66 and 6.67. The quantity L will approach zero where β is sufficiently high such that the REL drops below the REL criterion.

Each decelerating particle of sufficient energy traversing a stack of sufficient dimensions will produce etchable tracks at every plastic surface between the point where the REL equals the REL criterion and the point where the particle comes to rest. The length of this region of the particle trajectory is the registration range (R_{reg}). In Figure 6.52 the predicted R_{reg} is given for CA 80-15 cellulose nitrate as a function of z for the most abundant isotope of each element.

6.10.4 Evaluation of z and E for particles whose Entire Registration Range is Contained within the Plastic Film

The precision of the z or E determination is governed by the ability to locate both ends of the registration range or the true cone length (L) and to determine the range-energy relation in cellulose nitrate. For particles with range \geq the plastic thickness etching should be performed by floating the irradiated surface of the detector on the etchant, rather than immersing the detector completely in the etchant (immersed etching is valid only for detection of particles with range \leq three-quarters the plastic thickness). Otherwise the stopping end of the particle trajectory can be determined only to

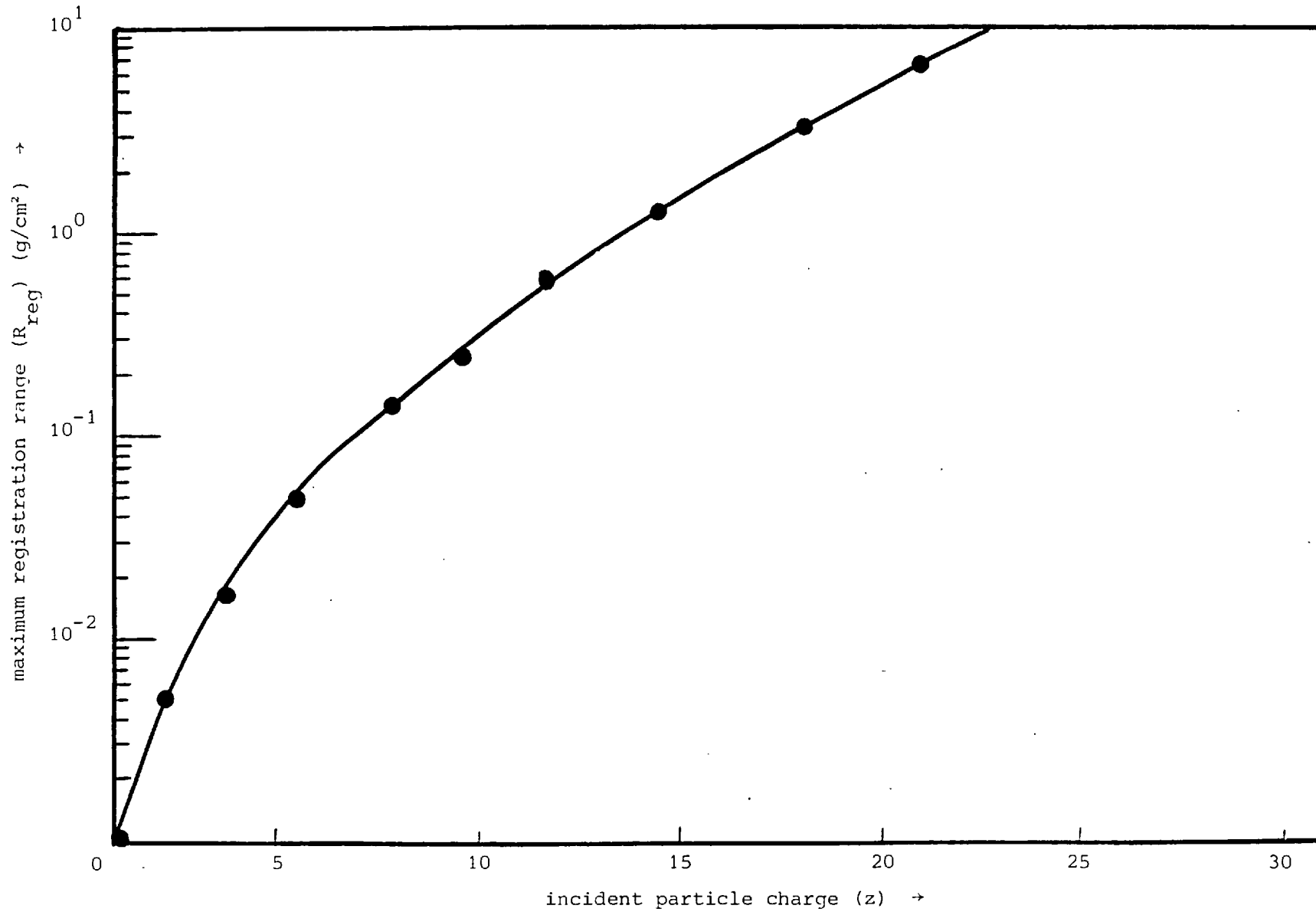


Figure 6.52 The predicted maximum registration range, R_{reg} , in CA 80-15 cellulose nitrate (density of CA 80-15 cellulose nitrate is 1.52 g/cm³)

+ one-half the distance from the point where the particle is expected to stop and the other plastic surface. However, if the track in the stopping layer of the plastic is etched to the stopping end (indicated by the tracks rounding off), this end of the registration range is quite precisely determined. The point where REL equals the REL critical value can also be precisely determined. The uniqueness of the REL = REL critical point is the key to the accurate determination of z or E, by the measurement of the registration range or the true cone length. If this point is unique, the very critical dependence of the registration range on z or E implies that z or E can be determined to ± 1 or possibly with complete confidence provided that the calculation of the range-energy relationship in cellulose nitrate is adequate.

6.10.4.1 Determination of range-energy relation in Cellulose Nitrate

The method of Barkas and Berger (135) was used as a basis for estimating the range of α -particles in cellulose nitrate, as a function of energy. The method is based on a semi-empirical relation where the range of an ion is represented by the range of an 'ideal' proton together with a range extension related to the effective charge of the ion.

Thus the range of a charged particle in matter can be expressed as follows:

$$R(\beta) = M/z^2 \{ \lambda(\beta) + B_z(\beta) \} \quad (6.70)$$

where M = mass of the incident charged particle in units of protons
z = charge of the incident particle in units of protons
 $\lambda(\beta)$ = range of an 'ideal' proton with velocity βc
 $B_z(\beta)$ = the range extension in the same material, caused by the neutralisation of the moving ion's positive charge by electron capture when its velocity decreases.

The range can be calculated in g/cm^2 from Equation 6.70 as a function of five parameters, A/Z, I_{adj} , z, M and E. The ratio A/Z is the atomic mass number per electron of the stopping material, I_{adj} is the mean value of the excitation energy (eV) for the stopping material adjusted by assuming that the shell correction for relativistic particles is zero and z, M, E are the atomic number, mass and energy of the incident ion respectively.

The rate of energy loss dE/dx , can be defined as $(dR/dE)^{-1}$ where dR/dE can be obtained from Equation 6.70.

$$E = Mm_p c^2 (\gamma - 1) = Mm_p c^2 \left\{ (1 - \beta^2)^{-1/2} - 1 \right\} \quad (6.71)$$

where m_p = the rest mass of a proton.

The proton range, λ , is expressed in terms of the energy of a proton, τ . This is the kinetic energy of a proton of the same velocity as the particle of mass Mm_p and is given by:-

$$\tau = E/M \quad (6.72)$$

$$\therefore \frac{dE}{dx} = z^2 \left[\left(\frac{d\lambda}{d\tau} \right) + \left\{ \frac{(1 - \beta^2)^{3/2}}{(m_p c^2 \beta)} \right\} \frac{dB_z}{d\beta} \right]^{-1} \quad (6.73)$$

where $M = A/1.008$ and $m_p c^2 = 938.59$ MeV.

A is the atomic weight of the ion and E is the kinetic energy of the ion.

I_{adj} for a given stopping material is computed from the I_{adj} 's of the individual constituents.

$$(I_{adj})_i = (12 Z_i + 7) \text{ eV} \quad \text{for } Z \leq 13 \quad (6.74)$$

I_{adj} for the individual constituents is given by:-

$$\ln I_{adj} = \left\langle \frac{A}{Z} \right\rangle \sum_i \left\{ \frac{f_i Z_i}{A_i} \right\} \ln (I_{adj})_i \quad (6.75)$$

where

$$f_i = \frac{\mu_i A_i}{\sum_j \mu_j A_j} \quad (6.76)$$

f_i is the fraction by weight of the i^{th} component of the stopping material.

μ_j is the formula number of the i^{th} component.

$$\left\langle \frac{A}{Z} \right\rangle = \frac{\sum_i \mu_i A_i}{\sum_i \mu_i Z_i} \quad (6.77)$$

The ideal proton range, λ , is obtained from the range-energy data of Barkas and Berger. The data is fitted to the following expression:-

$$\ln \lambda = \ln \langle A/Z \rangle + \sum_{n=0}^N \sum_{m=0}^M a_{mn} \{\ln I_{adj}\}^m \{\ln \tau\}^n \quad (6.78)$$

where a_{mn} are the coefficients used to fit λ . Thus λ is a smooth function of I_{adj} .

The quantity $d\lambda/d\tau$ is obtained by differentiating Equation 6.78:-

$$\frac{d\lambda}{d\tau} = \left(\frac{\lambda}{\tau}\right) \sum_{n=1}^N \sum_{m=0}^M n a_{mn} \{\ln I_{adj}\}^m \{\ln \tau\}^{n-1} \quad (6.79)$$

The range extension $B_z(\beta)$ was determined using the range extension for emulsion by Heckman et al (69), $C_z(137\beta/z)$, scaled to an arbitrary material. The scaling is such that $B_z(\beta)$ has the same asymptotic value given by Barkas and Berger (135).

$$(7.0 + 0.85 I_{adj}^{5/8}) \langle A/Z \rangle 10^{-6} z^{8/3}$$

Thus, the range extension, $B_z(\beta)$ is given by

$$B_z(\beta) = (31.8 + 3.86 I_{adj}^{5/8}) \langle A/Z \rangle 10^{-6} z^{8/3} C_z(137\beta/z) \quad (6.80)$$

where $C_z(137\beta/z)$ was obtained using the data of Heckman et al (69).

Comparison between the calculated range-energy curves of alpha particles in CA 80-15 cellulose nitrate, using Equation 6.70, and the measurements of etched track lengths (points), is shown in Figure 6.53. The true cone lengths are calculated by correcting the observed cone lengths for the portions $\Delta L = V_B t \csc\theta$ (θ is the incident angle; between the trajectory of the particle and the surface of the detector) that were lost in the bulk etching process. Values of z for given particle energies (E) and vice versa were determined with complete confidence by using Equation 6.70 and the direct measurements of etched track lengths, whose entire registration range were contained in the plastic film (see Figure 6.54). Track length can be used for accurate determination of particle energy or charge.

Thus a particle's energy (E) for a known charge (z) or vice versa can be determined either by direct measurement of the observed cone length (range-energy relation in CA 80-15 cellulose nitrate for incident charge particles), or by determining the change in REL as a function of distance along the particle trajectory. REL, z or E can

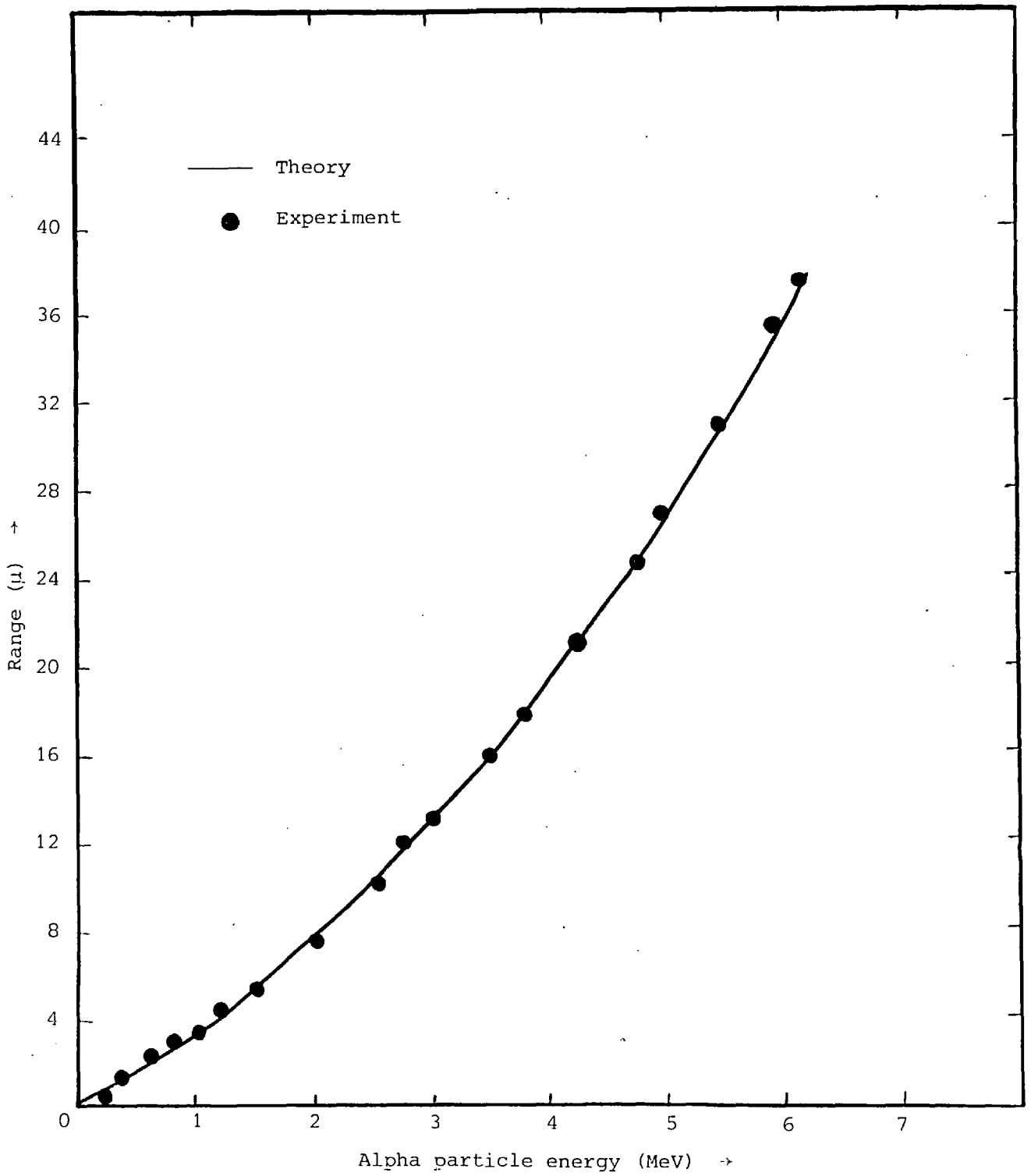


Figure 6.53 Alpha particle ranges in CA 80-15 using 2.5 N NaOH at 18°C

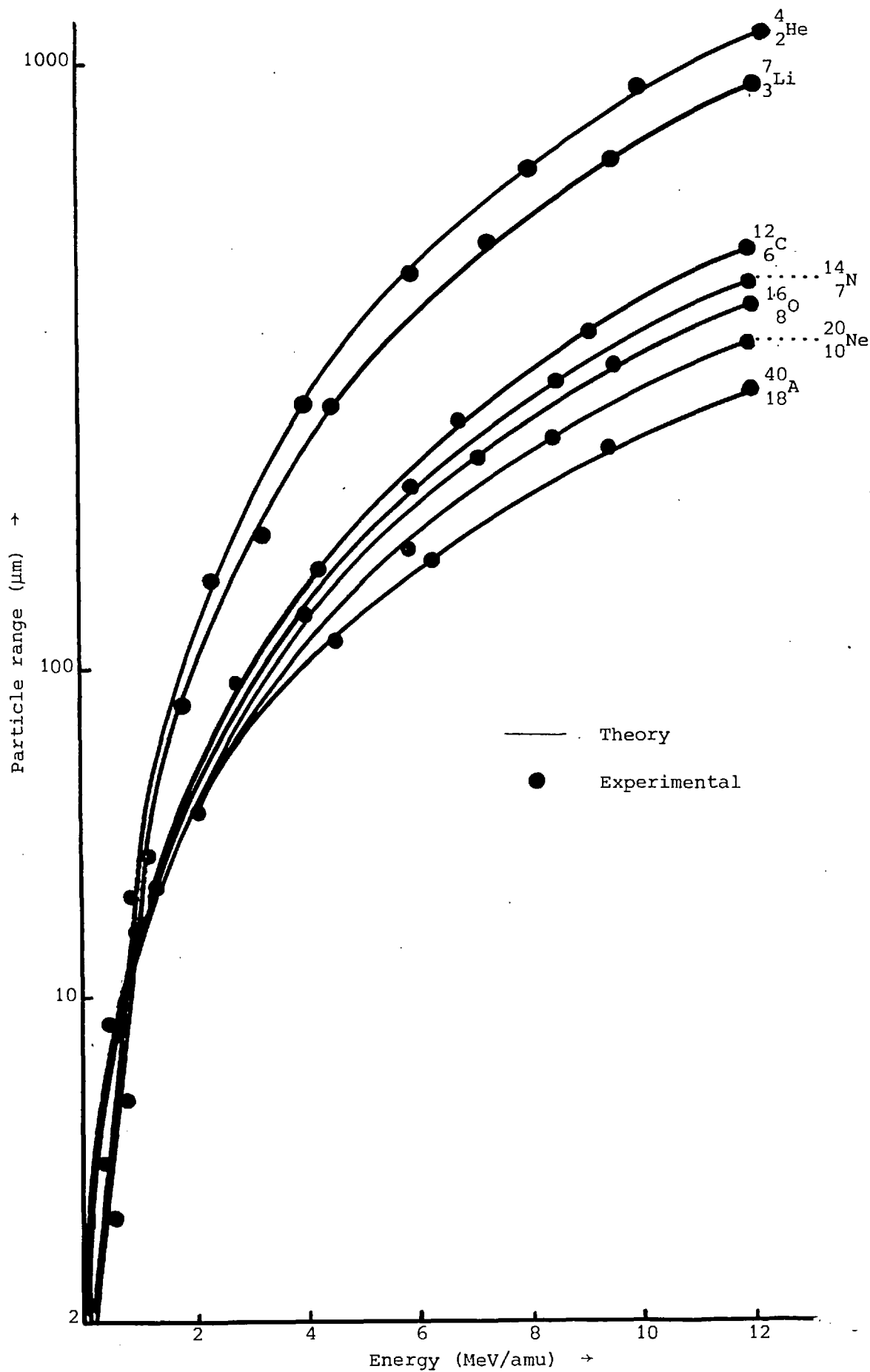


Figure 6.53b Graph showing the ranges of various charged particles measured in CA 80-15 cellulose nitrate using 2.5 N NaOH at 18°C .

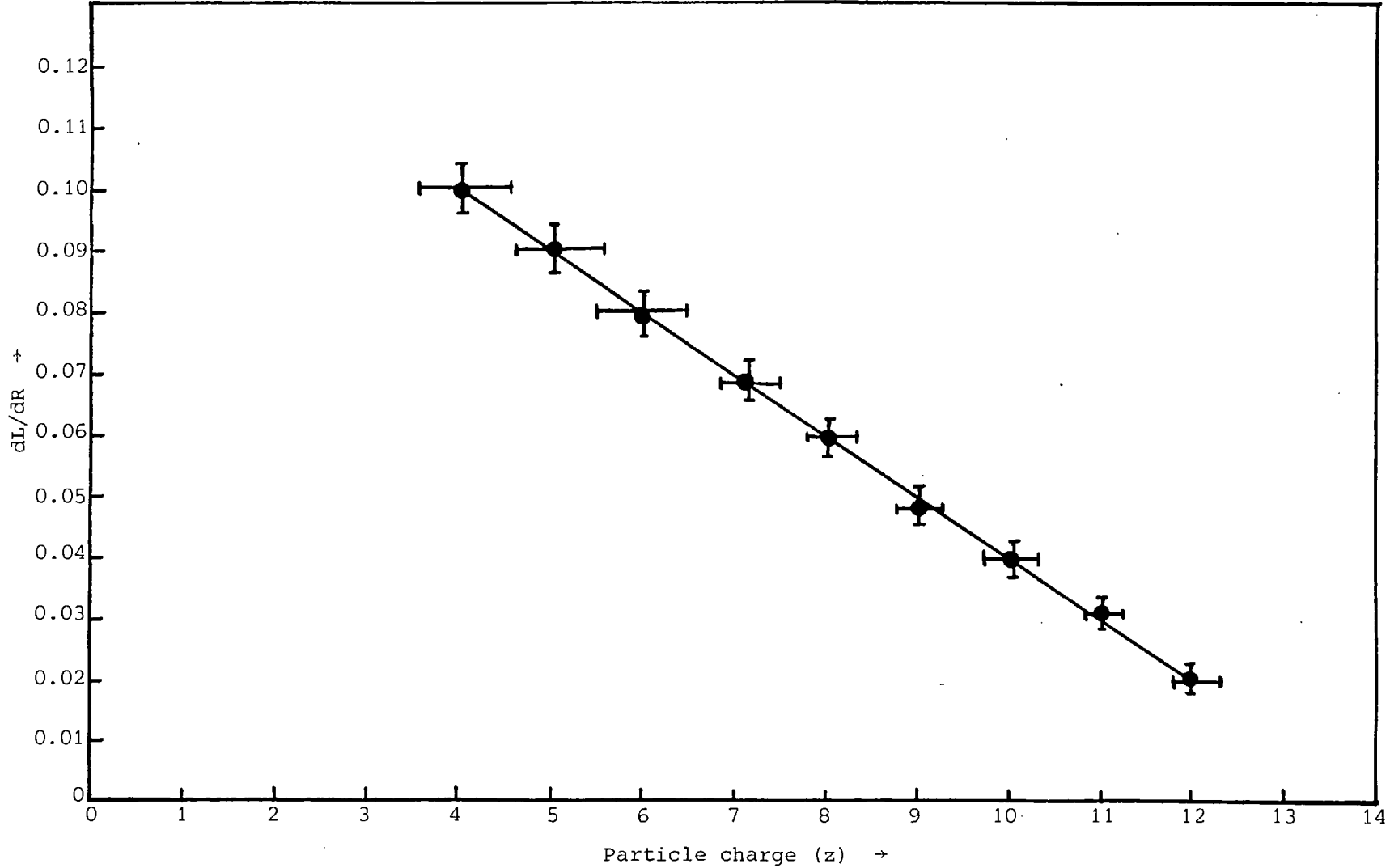


Figure 6.54 Measurements of the rate of change of etched track length with respect to particle residual range as a function of the particle charge (z) for stacks of CA 80-15 cellulose nitrate irradiated with ions of maximum energy 12.6 MeV/amu and etched in 2.5 N NaOH at 18°C for 100 hours, without interruptions or stirring

be derived from the range (R) and the cone length (L) which are calculated from V_T and V_B by Equation 6.67, if the etching time is given. Thus the relation between R and L can be obtained, starting from the following formulae (6.81) and (6.82)

$$\text{(etching time) } T = \int_R^{R+L(R)} dR/V_T(R) \quad (6.81)$$

Knowing the function $V_T(R)$ and REL (R,z) the etching along tracks of given ions can be calculated from

$$R(t) = \int_0^t V_T(R) dt \quad (6.82)$$

For this calculation it is assumed that the etching starts at time $t = 0$ from the stopping end $R = 0$ of the trajectory. The $L(R)$ curve for a given etching time T is then obtained from Equation 6.83

$$L(R_0) = R(t_0 + T) - R_0(t_0) \quad (6.83)$$

Figure 6.55 shows the set of curves for cone length versus residual range with $z = (1 - 10)$. The etching times are 100 and 6 hours, the temperature is as mentioned before 18°C , and the solution used is 2.5 N NaOH. Thus measuring the cone length and the residual range gives an estimate of the charge. The accuracy of this method is the determination of the charge of an incident particle depends on two factors. The first factor is how much the curves are separated for a unit charge difference. It is obvious that the separation is smaller for higher charges, and the charge identification becomes thus less accurate. The second factor is the number of points available along the track for measurements. This number of points increases for heavier particles at a given energy, because it gives longer etchable range. These two factors compensate each other and the accuracy of charge identification remains approximately the same throughout the charge spectrum.

From the experiments it was found the standard deviation of ΔZ was 0.3 charge units, in the case where the number of points is about 9 for z equals. However the standard deviation becomes $\Delta Z = 0.2$ charge units for tracks somewhat steep and number of points about 20.

The measured charge spectrum gives a picture of good separation of charge (z) between 2 and 30 (Figure 6.56).

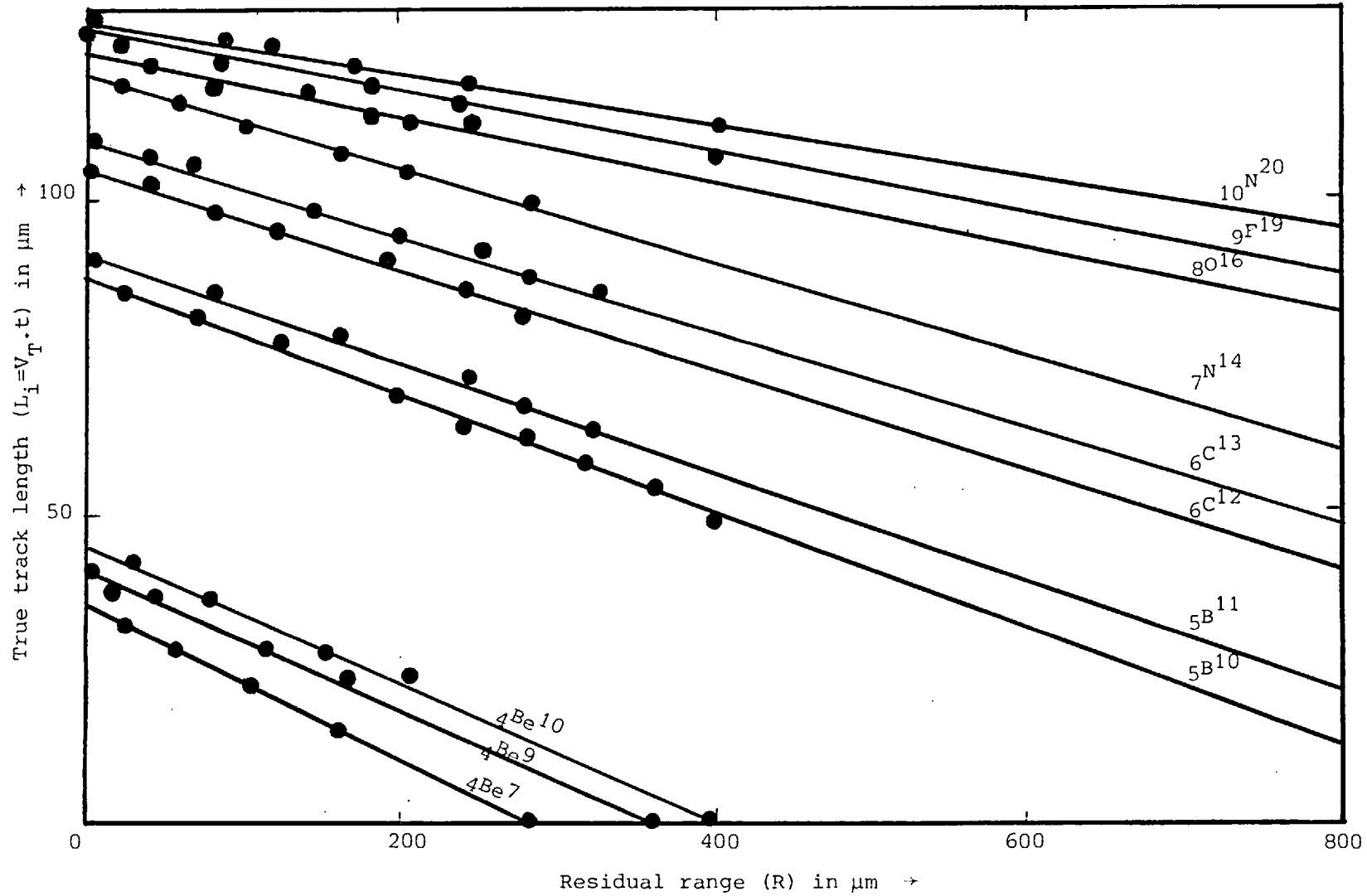


Figure 6.55a Measurements of true track length (L_i) as a function of residual range (R) for stacks of CA 80-15 cellulose nitrate irradiated with ions of maximum energy 12.6 MeV/amu and etched in 2.5 N NaOH at 18°C for 100 hours without interruptions or stirring

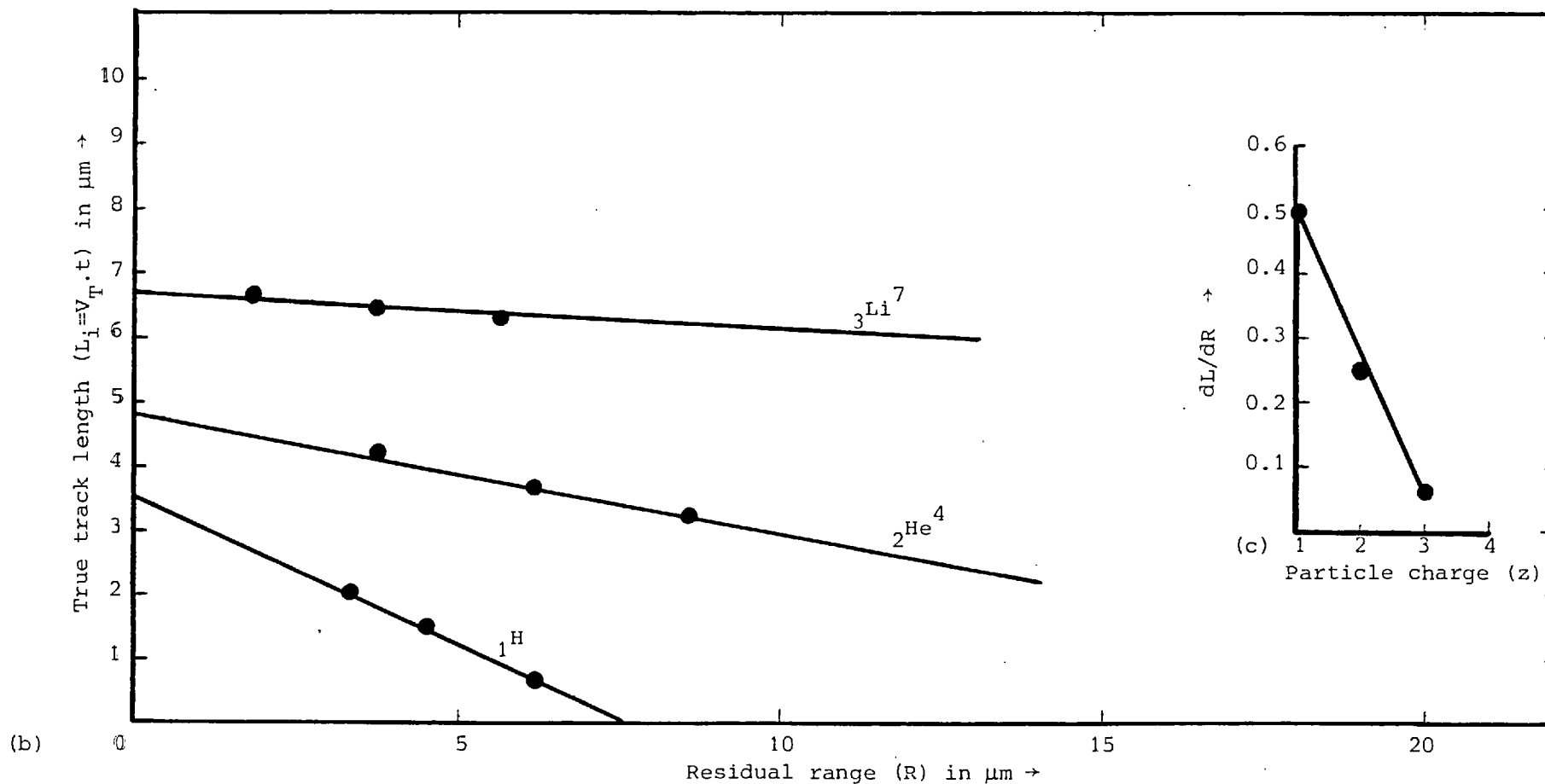


Figure 6.55b,c (b) Measurements of the true track length (L_1) as a function of residual range (R) for CA 80-15 cellulose nitrate films irradiated with charged particles of maximum energy 0.70 MeV/amu and etched in 2.5 N NaOH at 18°C for 6 hours, with no interruptions or stirring.

(c) Measurements of the rate of change of etched track length with respect to particle range as a function of the particle charge (z) for CA 80-15 cellulose nitrate films irradiated and etched as in (b).

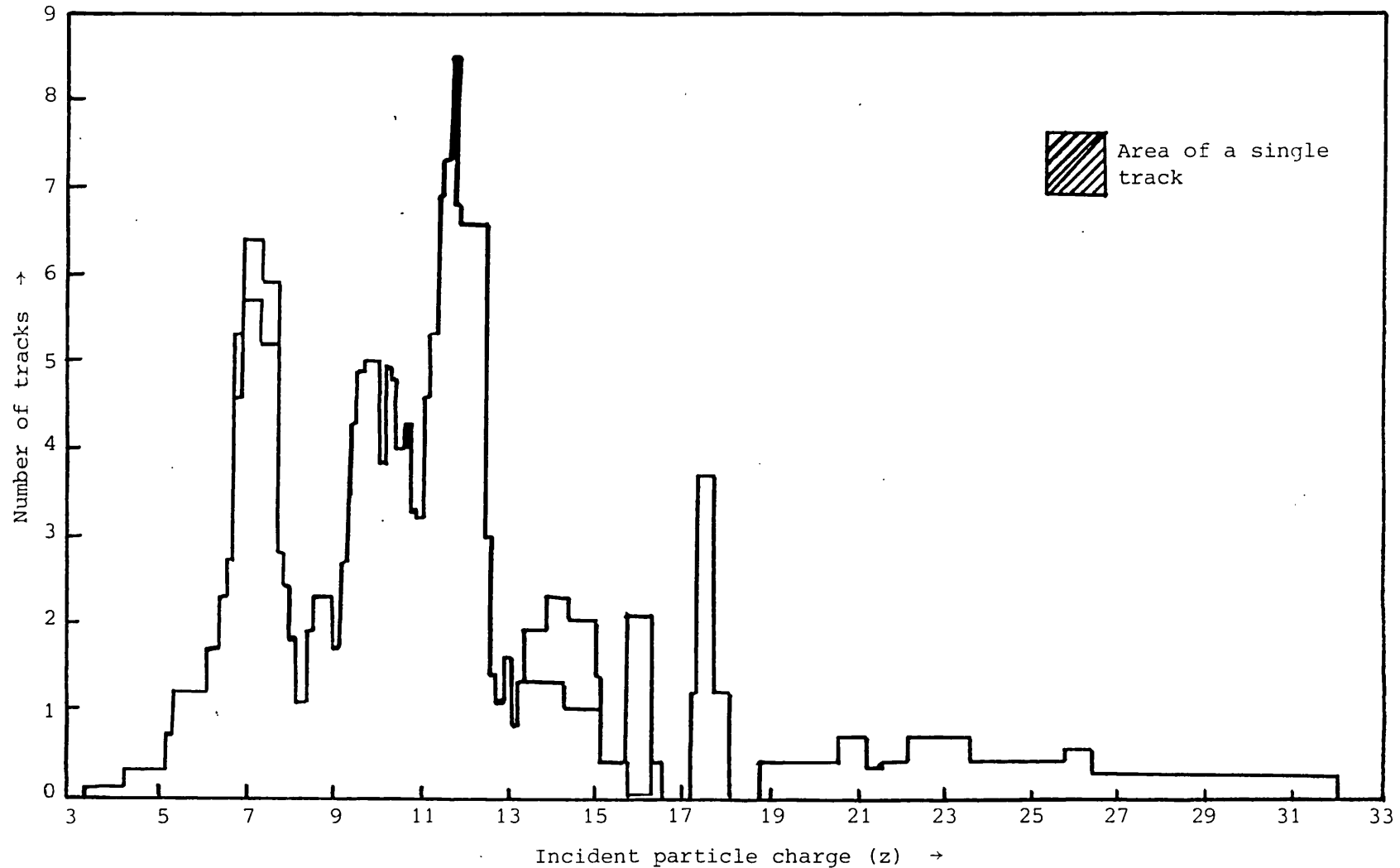


Figure 6.56 The measured charge distribution of cosmic ray particles in CA 80-15 cellulose nitrate at an altitude of 145,000 ft over Manitoba, Canada. The peaks observed in the figure indicate that charge discrimination is being achieved. The precision in the z determination varies from approximately ± 0.3 for $z=18$ to ± 3 for some of the particles measured at $z=7$

6.10.5 Evaluation of z for Particles whose Entire Registration Range is not contained within the Stack

If the entire registration range is not contained within the stack, z cannot be determined by the method described in the previous section. However, if a sufficient fraction of the registration range can be observed, z identification can be achieved by determining the change in REL as a function of distance along the particle trajectory.

Assuming that the track etching rate, V_T is only a function of REL, i.e.

$$V_T = F_n (\text{REL}) \quad (6.84)$$

then the rate of change of V_T with respect to the distance along the trajectory, R, is a constant times a function of z determined from the range energy relationships of the ion, i.e.

$$\left(\frac{dV_T}{dR}\right)_{\text{REL}} = \left(\frac{dV_T}{d(\text{REL})}\right)_{\text{REL}} \left(\frac{d(\text{REL})}{dR}\right)_{\text{REL}} \quad (6.85)$$

If dV_T/dR is measured at a particular value of V_T a specific value of REL is implied and $dV_T/d(\text{REL})$ evaluated at this point is a constant for all the particles measured. For a given value of REL, $d(\text{REL})/dR$ is only a function of z. In CA 80-15 cellulose nitrate at $\text{REL} \approx 1.9 \times 10^{-1} \text{ MeV}/\mu\text{m}$, a value not far above the critical value, $d(\text{REL})/dR$ can be represented approximately by

$$d(\text{REL})/dR = C Z^{-3.6} (\text{MeV}/\mu\text{m}^2) \quad \text{for } 5 < z < 40 \quad (6.86)$$

Therefore

$$dV_T/dR = \frac{C_1 Z^{-3.6}}{M} \quad \text{for } 5 < z < 40 \quad (6.87)$$

where C_1 is a function of the chemistry of the stopping material and of the etching conditions. The $Z^{-3.6}$ dependence of $d(\text{REL})/dR$ is found to hold over the entire useful range of the particle's REL (see Equation 6.66 and Figure 6.45), up to about $\text{REL} \approx 1 \text{ MeV}/\mu\text{m}$. From Equation 6.87 it is observed that as in the case of registration range (R_{reg}) the rate of change of V_T with R is quite a sensitive function of z. A sufficient length of the particle's trajectory must be contained within the stack for an accurate determination of dL/dR or $d\theta/dR$.

6.10.6 Isotopic Mass Separation of Particles

In the previous discussions it was stated that R_{reg} varies approximately as Mz^2 for carbon through $z^{3.8}$ for iron. Since the quantity of R_{reg} is proportional to the particle's mass, the heavy isotopes of a given element will have greater R_{reg} values than the lighter isotopes. Thus, if R_{reg} can be measured precisely, isotopic mass separation for individual particles may be possible. The measurement of R_{reg} for different mass particles within a given z group would yield discrete values of R_{reg} . The different z groups are well separated in R_{reg} so that overlapping of light isotopes of charge z and heavy isotopes of charge $(z + 1)$ is not expected to be a problem. It may also be possible to determine the mass by noting that dV_T/dR is proportional to $\frac{1}{M} z^{-3.6}$. Charge separation for two particles with a given energy (E) is performed by measurement of either track etching rate, at two known points on its trajectory in a stack of plastic sheets (V_T versus R plots) or measurements of true track length (L) and residual range (R) ($L = V_T \cdot t$ versus R) plots or range-energy relation (maximum etchable track length). For nuclei having the same charge, the residual ranges for a given velocity are proportional to their masses. Hence, the etching rate along their paths expressed as a function of the residual range will be different for each mass number. In principle, therefore, it is feasible to distinguish between the isotopes of certain nuclei by measuring the etching rate (in practice the etched track length or the cone angle θ) at a point on the trajectory of each isotope, and its residual range from that point.

L versus R plots or V_T versus R plots for CA 80-15 cellulose nitrate bombarded with various ions and isotopes, can resolve individual masses and charges of lightest elements (up to $z \approx 31$).

Measurements of L_i for ${}^7_4\text{Be}$, ${}^9_4\text{Be}$, ${}^{10}_4\text{Be}$, ${}^{10}_5\text{B}$, ${}^{11}_5\text{B}$, ${}^{12}_6\text{C}$ and ${}^{13}_6\text{C}$ ions in different sheets of cellulose nitrate as a function of R_i are plotted in Figure 6.55. At maximum energy of 12.6 MeV/amu all ions penetrate four sheets of thickness 100 μm each and part of a fifth 100 μm sheet. There is a clear tendency for tracks of heavier ions (${}^{11}_5\text{B}$) to be longer than tracks of lighter ions (${}^{11}_5\text{B}$) with the same residual range. The straight lines through the ${}^{11}_5\text{B}$ and ${}^{10}_5\text{B}$ data (Figure 6.55), (calculated by the method of least squares) intersect the abscissas at values of residual range having the ratio

of their masses 11/10 as is expected. Any differences between the positions of the least squares lines fitting different measurements of the same particles which do not arise from statistical uncertainties may arise from small differences in conditions of etching and in microscope optics. This observation may indicate that reproducibility remains to be established.

Etching at low temperatures (15-20°C) and etchant concentrations (2-3N NaOH) will establish reproducible results and minimise the above mentioned differences. These etching conditions were successfully used to distinguish between isotopes of energetic ions differing in mass by 9%. Reproducibility was established simply by measuring the two parameters L_1 and R_1 . Additional measurements L_2, R_2, L_3, R_3 , etc. will provide further information and may make it possible to distinguish isotopes with a smaller mass difference for particles that come to rest in the cellulose nitrate stack.

Even if the particle completely penetrates the stack without coming to rest in it - it may still be possible to identify the particle if the change in etching rate from one side of the stack to the other side is detectable. One simply adds a constant amount to the residual range for each etch pit so that the resulting L versus R or V_T versus R curve gives the best fit to one of the family of its corresponding L versus R or V_T versus R curves. The procedure is discussed in detail in (136,137).

The charge resolution for nuclei with $3 \leq z \leq 30$ in CA 80-15 cellulose nitrate is $\Delta z \pm 0.5$ and the mass resolution (ΔA) is about 0.4 amu for beams from the accelerator. Figures 6.55 and 6.56 illustrate the kind of resolution that was obtained from particles that come to rest in CA 80-15 cellulose nitrate films.

6.10.7 Particle Identification by Measurements of Induction Time and Etched Pit Diameter

To study the detailed development of etched tracks in CA 80-15 cellulose nitrate it was necessary to use the high resolution of an electron microscope. Films of CA 80-15 irradiated perpendicularly with protons, alpha particles and other heavy charged particles of energies from 0.15 - 1.5 MeV/amu were stored for three months in a high vacuum and etched with 2.5 N NaOH at 18°C for various times. Carbon replicas were prepared as described in Section 6.64 and

examined on a Philips EM 301 electron microscope. After one hour of etching a feature was observed which might indicate a track. After three hours of etching the replicas are rigid cones. The etching time, the base diameter and height of cones as measured on electron micrographs are shown in Figures 6.57, 6.58, 6.59 and 6.60.

(i) Induction time

In the course of the experimental program to determine the etching rates, track diameters and the lengths of fully etched tracks of heavy ions in CA 80-15 cellulose nitrate track detectors, it was observed that track detectors do not start to etch for some small but discernible period of time following the beginning of etching. This delay has been noted as the "incubation" or "induction" time. It also became apparent that the latent damage trails of charged particles of known kinetic energy (E) had their visible etched pits initiated only after a period of time proportional to $\exp \Delta REL$. z^* value of the incident charged particle, where z^* is the effective ion charge of the incident particle $\approx z(1 - \exp(-130\beta z^{2/3}))$ (67) and $\Delta REL = REL$ critical of the detector - REL of the incident charged particle.

Induction time could be explained by Figure 6.50. The latent tracks are imbedded in the bulk material to a depth inversely proportional to the ΔREL of the incident charged particle. The bulk material has to be etched to a sufficient depth to expose the etchable portion of the track. For latent tracks that interface the surface of the detector, the track etching rate (v_T) is drastically reduced at the surface of the cellulose nitrate films by any of a number of effects. It may not be commonly realised that conventional stopping power theory does not take vacuum-to-solid motion or its reverse into account, but assumes a uniform stopping medium. There are several fundamental considerations which suggest that both stopping power and REL, and hence v_T , should probably be reduced. However, other parameters, such as variations in chemical composition at the surface may be a contributing factor. If the v_T reduction is sufficiently large, the bulk etch velocity, v_B , will exceed v_T until the bulk etch process has reached such a depth that v_T exceeds v_B . At this time the tracks appear. A large value of REL will be associated with a low value of the depth at which the tracks begin to appear and vice versa. It is also clear that the etch induction

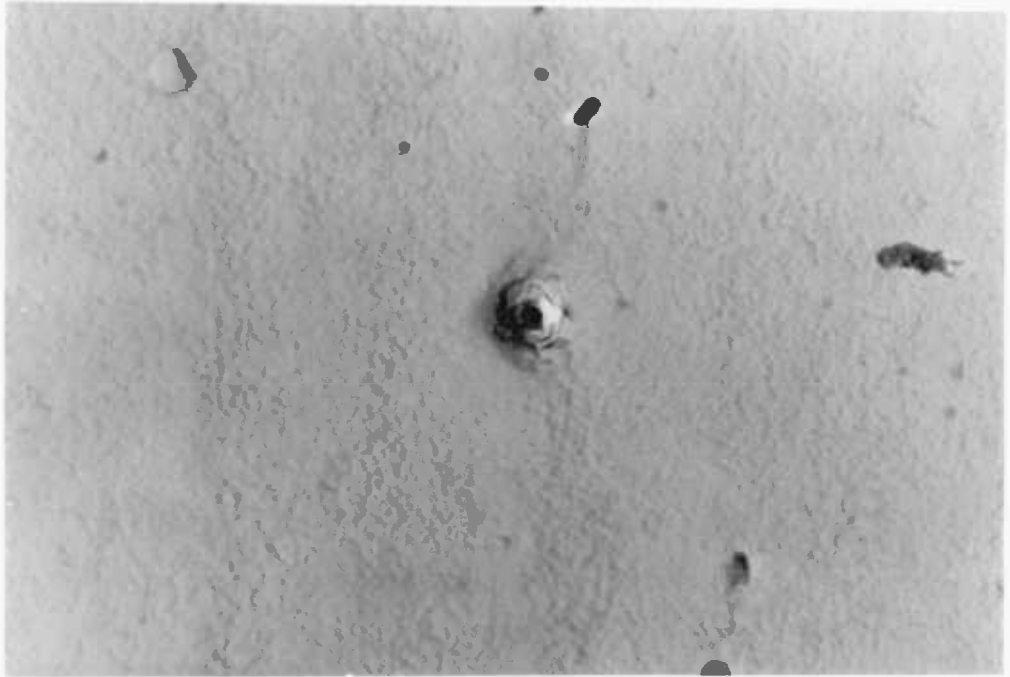


Figure 6.57 Electron micrograph of 0.8 MeV alpha track in LR115 type 2 (Kodak-Pathe, France) at 90° incidence, etched in 2.5 N sodium hydroxide at 18°C for 2 hours (25 K x 31).

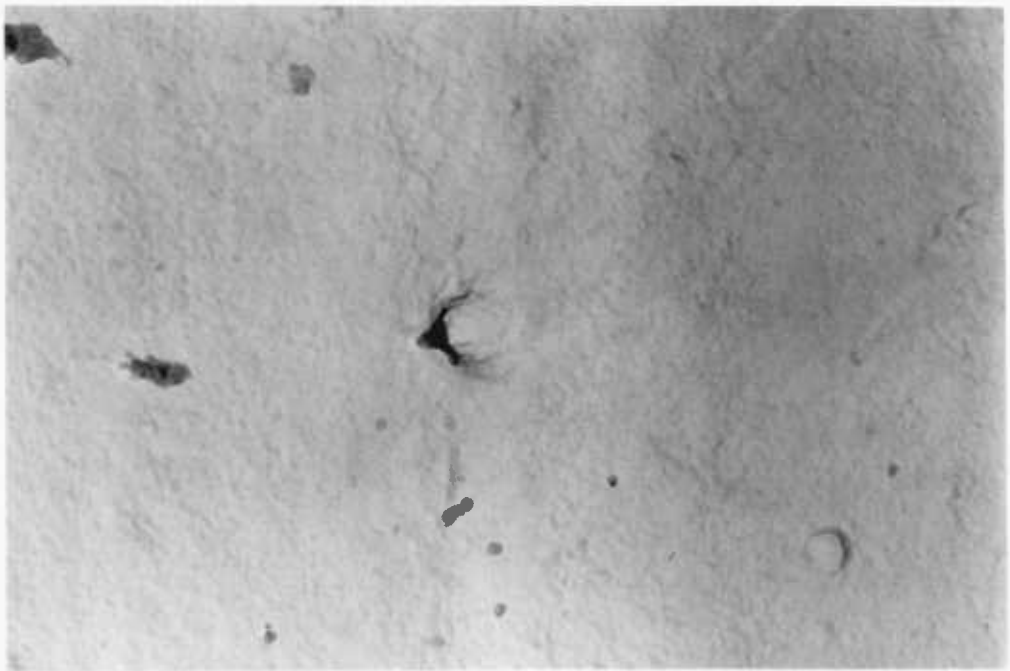


Figure 6.58 Electron micrograph of 0.8 MeV alpha track in LR115 type 2 (Kodak-Pathe, France) at 30° incidence, etched in 2.5 N sodium hydroxide at 18°C for 2 hours (25 K x 3).

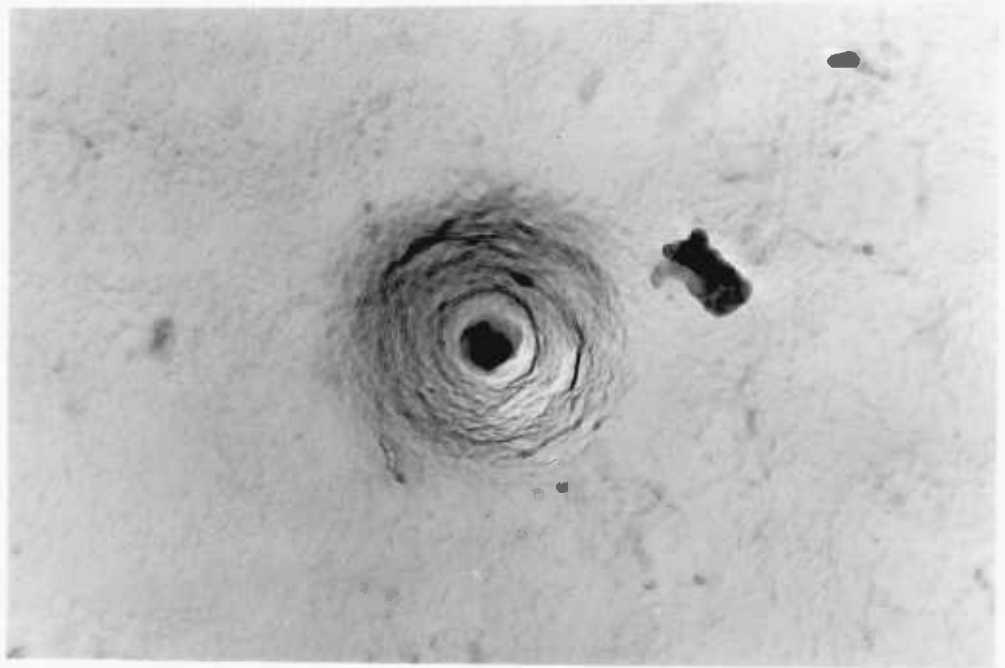


Figure 6.59 Electron micrograph of 1.1 MeV proton track in CA80-15 (Kodak-Pathe, France) at 90° incidence, pre-swollen in 65% zinc chloride solution for 2 hours, then etched in 2.5 N sodium hydroxide at 18°C , for 16 hours (25 K x 2).

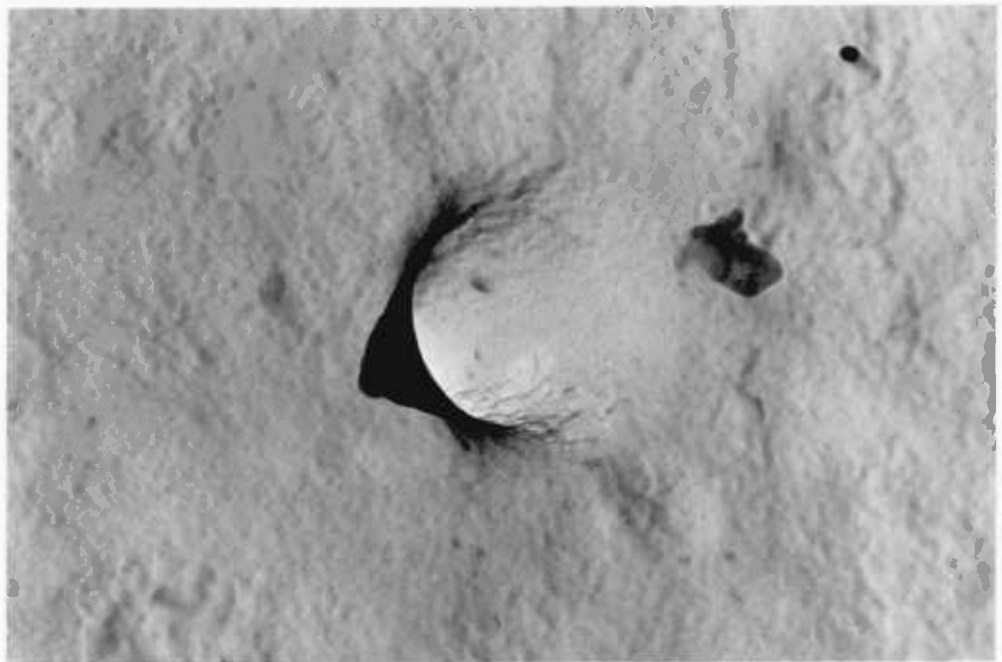


Figure 6.60 Electron micrograph of 1.1 MeV proton track in CA80-15 (Kodak-Pathe, France) at 60° incidence, pre-swollen in 65% zinc chloride solution for 2 hours, then etched in 2.5 N sodium hydroxide at 18°C , for 16 hours (25 K x 2).

time will decrease reciprocally as V_B increases, as would be expected if one had a thermally damaged cellulose nitrate detector. Finally, from elementary range theory, it can be shown that the critical depth at which induction time is measured must be inversely proportional to particle charge (z) and the (normal) stopping power at the surface. By geometry, the induction time or the critical depth can be shown to be directly proportional to the sine of the particle incident angle to the surface of the detector. Limited data support an approximate sine dependence of the particle incident angle and the induction time. Moreover, the data in Figure 6.61 are approximately consistent with a variation of the induction time with the quantity $\exp \Delta REL z^*$. This proportionality can be utilized for particle identification provided that the continuous etching and observation method is employed. It should be possible to identify any one of the following parameters (z , E , θ) if the other two parameters are given (θ is the particle incident angle to the surface of the detector).

The following formula can be employed for particle identification.

$$t_o = a \sin \theta_o (\exp + b. \Delta REL_o z_o^*) \quad (6.88)$$

where t_o is the induction time in hours (an experimentally determined parameter for a given particle and given etching condition).

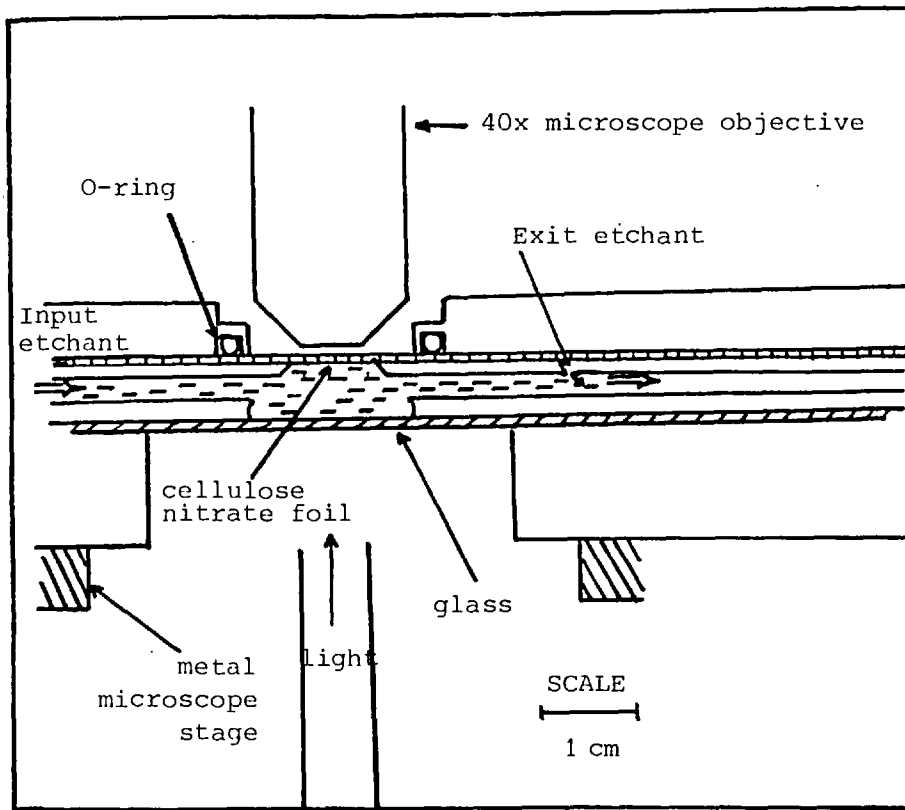
a is a proportionality constant,

b is another constant.

An experimental plot of $\ln t_o$ versus ΔREL_o or z_o^* for a given incident angle θ_o could be established for particle identification.

(ii) Etched track diameter

As we noted earlier that track length (L), diameter (D) and cone angle (θ) are all functions of V_T/V_B , hence are related to the ionization rates (L , D and θ are functions of ΔREL , t and V_B), and therefore possible particle identification. Where values of θ are small tracks are long and narrow, and consequently any of L , dL/dR versus z or L versus residual range (R) along the track is the most sensitive and easily measured parameter and all have been used in earlier work. Where values of θ are large, as in many glasses and in plastics (for very light particles), and in cases where particles enter at right angles to the detector surface, D becomes the preferred parameter. Figure 6.62 shows how the diameter of a fission track in glass of initial cone angle 26° varies with etching time (t).



The Continuous Etch Apparatus for Induction Time Measurements

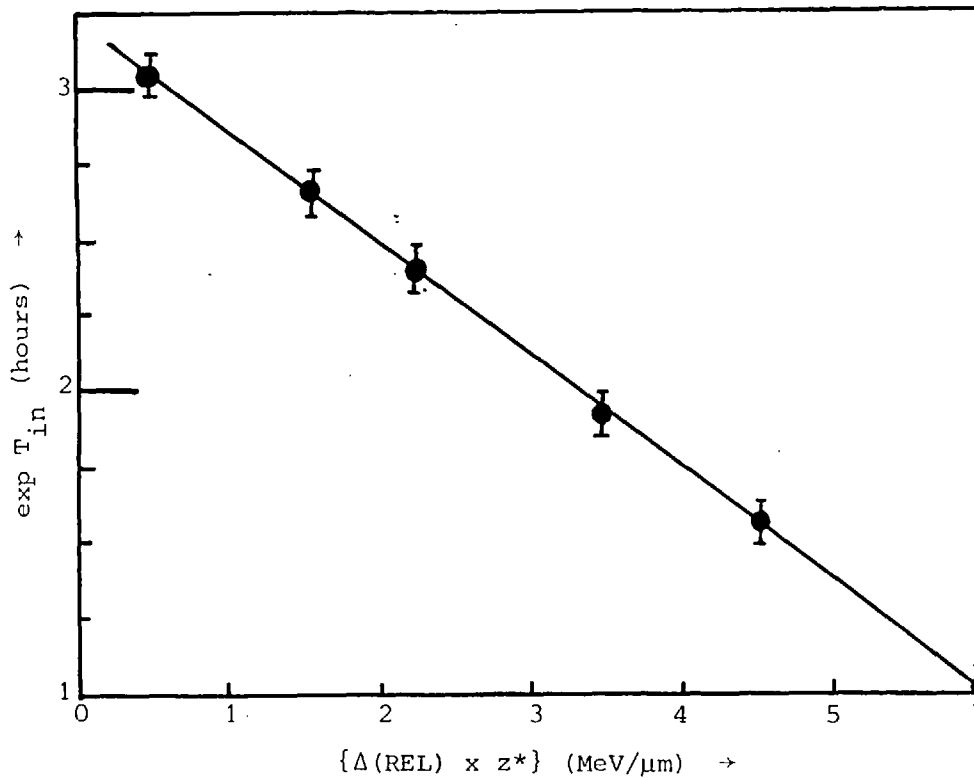
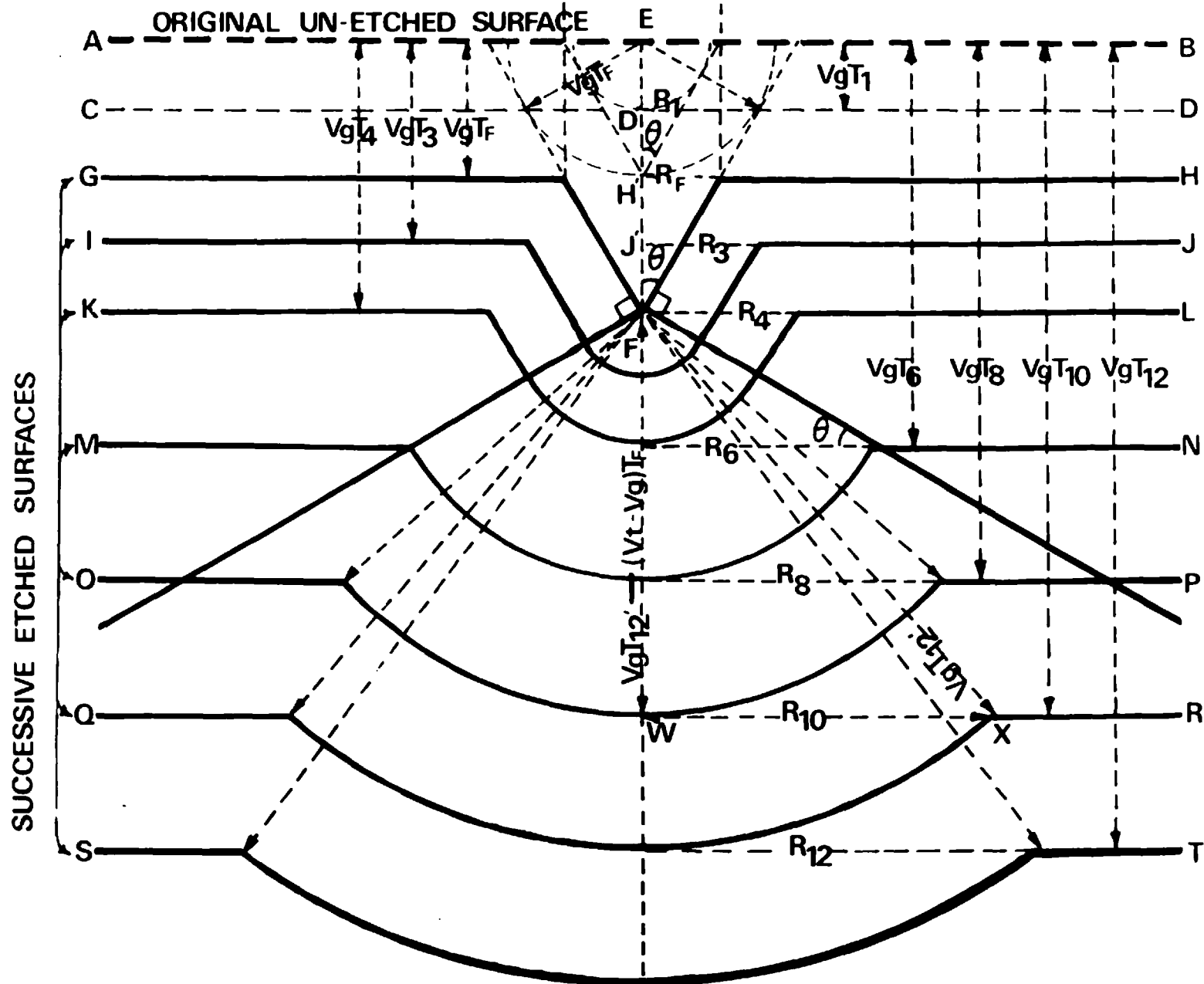


Figure 6.61 The induction time (T_{in}) versus the particle's $|\Delta(\text{REL}) \times z^*|$. These measurements were obtained using the apparatus shown above.

Figure 6.62



It is of interest to know how the diameter of the normal incident particle will vary with etching time and with the energy of the incident charged particle or restricted energy loss i.e. for the variation of track etching rates with position along the track.

From Figure 6.63 the etching time needed to reach the point (x_o, y_o) of a particle entering normal to the detector surface with zero induction time is given by:-

$$t = \frac{dy}{v_T(y)} + \frac{(y_o - y')^2 + x_o^2}{v_B}^{-\frac{1}{2}} \quad (6.89)$$

where twice the value of x_o ($x_o = v_B t$) gives the diameter as a function of time ($D = 2 x_o$).

Equation 6.89 is composed of two terms. The time to etch along the track from $(0,0)$ to $(0,y')$ given by

$$\int_0^{y'} \frac{dy}{v_T(y)} \quad (6.90)$$

and the time to etch from $(0,y')$ to (x_o, y_o) given by $((y_o - y')^2 + x_o^2)^{\frac{1}{2}}/v_B$. Since the actual path from $(0,0)$ to (x_o, y_o) corresponds to least time, taking the derivative of time with respect to y' and set it equal to zero gives the relation:

$$y' = y_o - x_o / (v_T(y')/v_B)^2 - 1)^{\frac{1}{2}} \quad (6.91)$$

which together with Equation 6.89, define x_o and y_o for a given t , y' and $v_T(y)$. By noting that $\tan\theta = (y_o - y')/x_o$ (see Figure 6.63) we can write Equation 6.89 and Equation 6.91 in a more useful parameter in y' as follows:

$$x_o = ((y_o - y')^2 + x_o^2)^{\frac{1}{2}} \cos \theta \quad (6.92)$$

$$y_o = y' + ((y_o - y')^2 + x_o^2)^{\frac{1}{2}} \sin \theta \quad (6.93)$$

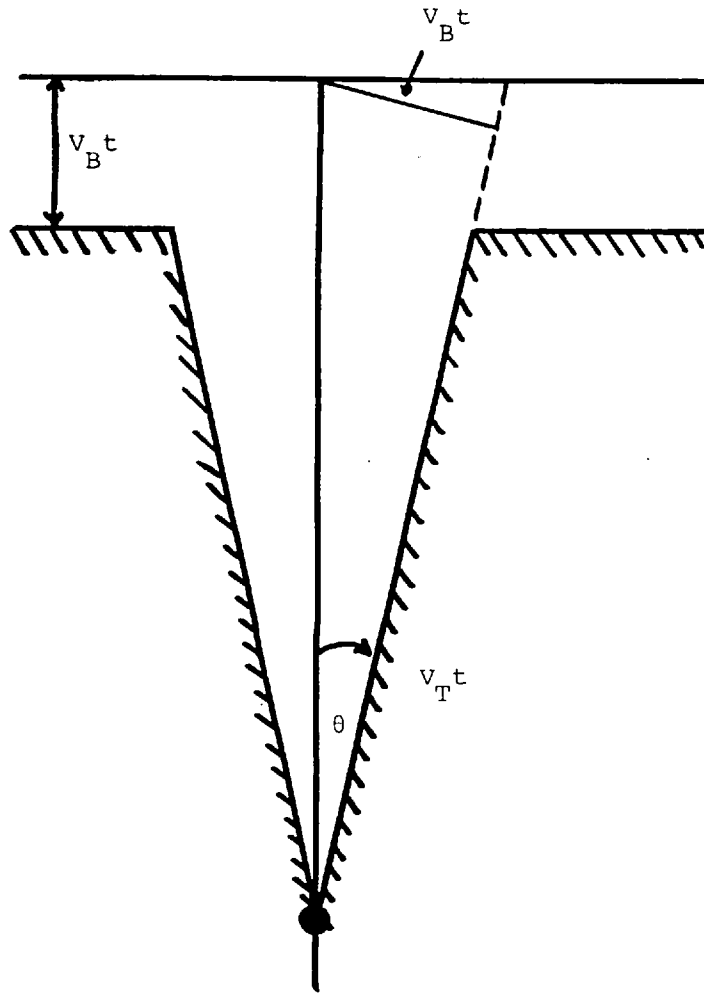
which can be re-written as

$$x_o = v_B \left(t - \int_0^{y'} \frac{dy}{v_T(y)} \right) \left(1 - \frac{v_B^2}{v_T^2(y')} \right) \quad (6.94)$$

$$y_o = y' + \frac{v_B^2}{v_T(y')} \left(t - \int_0^{y'} \frac{dy}{v_T(y)} \right) \quad (6.95)$$

where $\sin\theta = v_T/v_B$ and $\cos\theta = \left(1 - \frac{v_T^2}{v_B^2} \right)^{\frac{1}{2}}$

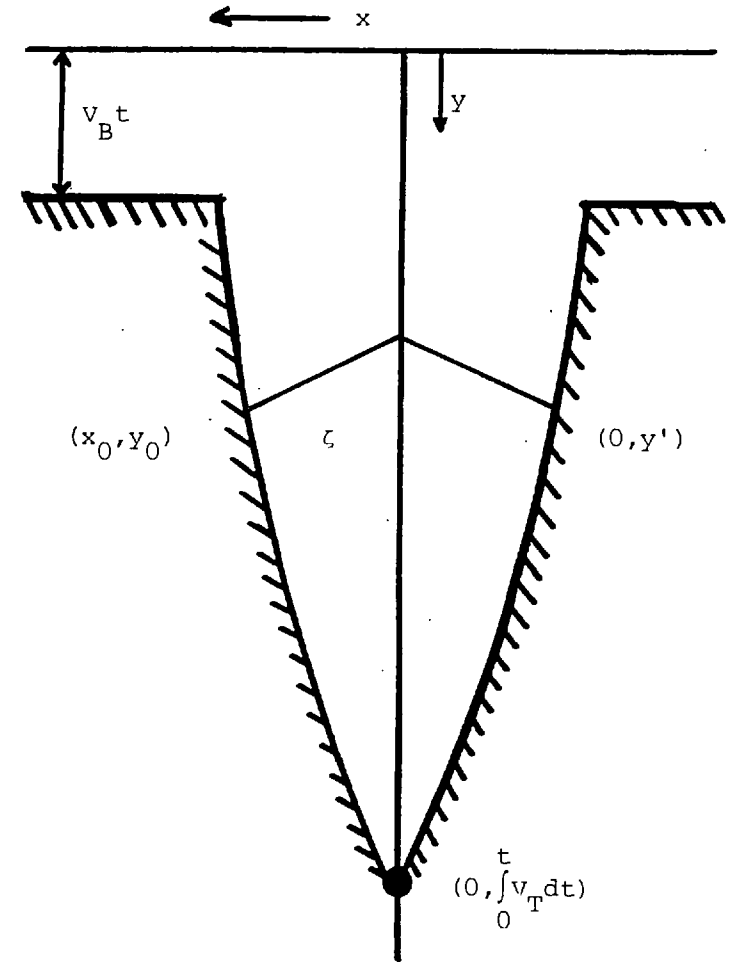
These equations are valid for all y' and t .



(a)

Original surface

Surface at time 1



(b)

Figure 6.63 Track geometry: (a) with v_T constant, the cone angle is $\sin^{-1}(v_0/v_T)$. (b) with v_T decreasing as etching continues, the shape of the etched track is more complicated

Equations 6.96 and 6.97 are obtained by substituting Equation 6.66 for etching conditions, 2.5 N NaOH and 18°C $V_T(y') = V_B (1 - 1.2 \exp 7.6 \Delta REL(y'))$,

$$x_o = (V_B T - \int_0^{y'} \frac{dy}{1-1.2 \exp 7.6 \Delta REL(y')}) \left(1 - \frac{1}{(1-1.2 \exp 7.6 \Delta REL(y'))}\right) \quad (6.96)$$

$$y_o = y' + \left(\frac{V_B}{1-1.2 \exp 7.6 \Delta REL(y')}\right) \left(t - \int_0^{y'} \frac{dy}{V_B (1-1.2 \exp 7.6 \Delta REL(y))}\right) \quad (6.97)$$

Values of y' are obtained from Equation 6.97 for $y_o = V_B \cdot t$ and this value is substituted for y' in Equation 6.96 to give x_o which is half the diameter of the track.

It follows from the above treatment (Equations 6.96 and 6.97) that particles, incident normal to the surface of the detector, with a given charge and different energies (different ΔREL) have different track diameters at a given etching time and particles with a given energy and different masses or charges should also have different track diameters, since they have different ionization loss and consequently different track etching rates.

So far we have considered particles with $REL \geq REL$ critical, where induction time is zero. If particles with $REL < REL$ critical were to be considered, latent tracks embedded under the surface of the detector as shown in Figure 6.50, the tracks will appear only after induction time

$$t(REL) = \frac{a}{\Delta REL \cdot \Delta z^*} + b \quad (\text{see Equation 6.88}) \quad (6.98)$$

or

$$t(REL) = (Y(REL \text{ critical}) - Y(REL)) / V_B \quad (6.99)$$

where $Y(REL \text{ critical})$ is the range of the particle of energy E equals the energy of critical registration of the detector or resitrcited energy loss equals the critical REL of the detector, $Y(REL)$ is the range of the particles of energy E or restricted energy loss REL . It follows from this effect that particles of different energy $E > E$ critical have different diameters of track holes at a given etching

time. If this effect Equation 6.98 or 6.99 is added to Equations 6.93 and 6.94 the resulting equations will be quite complicated but the effect of variation of diameters with REL will be enlarged since experimentally confirmed that induction time is not zero. It is substantially large even at REL = 1.2. REL critical and increases fast with small increase of energy (small decrease in REL).

Figure 6.64 shows the variation of diameters of track holes versus etching time for ${}^1_1\text{H}$, ${}^2_1\text{D}$, ${}^3_1\text{T}$, ${}^3_2\text{He}$ and ${}^4_2\text{He}$ particles in CA 80 cellulose nitrate, irradiated with particles of energy (0.15 - 1.5 MeV/amu) normal to the surface of the detector. It is evident from this Figure 6.64 that there is a correlation between the diameter of the track holes and the particle's energy, and between the diameter of track holes and the particles charge or mass. Also, it should be noted that a measurement of diameter (D), after only one etching time, is not sufficient to allow one to determine z and E, but it is adequate to determine E for a given charge and vice versa. Figure 6.65 shows the variation of track diameter with the corresponding particle energy and charge. This Figure 6.65 is used for energy (E) or charge (z) identification when only one (point (E_1, D_1)) measurement track diameters, for a given etching time and etching condition is available. While Figure 6.64 is used for both energy (E) and charge (z) identification when two or more measurements (Points $(D_1, t_1, D_2, t_2, \dots)$) of track diameter, for given etching times and etching conditions are available.

The high resolution of this technique is demonstrated by the ability to resolve diameters of 1.5 MeV proton tracks. While the maximum proton energy can be resolved with the full etchable track length technique is about 0.9 MeV. The drawback in this technique is that particles must enter the detector normal to the surface in order to obtain maximum charge and energy resolution. If irradiation occurs under 2π geometry, only round etched pits with accurate concentric configurations are evaluated.

Figure 6.66 shows diameter distribution of etch pits initiated by protons of different energies (keV) incident normal to the surface of the detector. Values of the removed layer thickness are noted in each right corner. The energy distribution was made by determining the diameter distribution. The sizes of etch pits were measured by electron and optical microscopes.

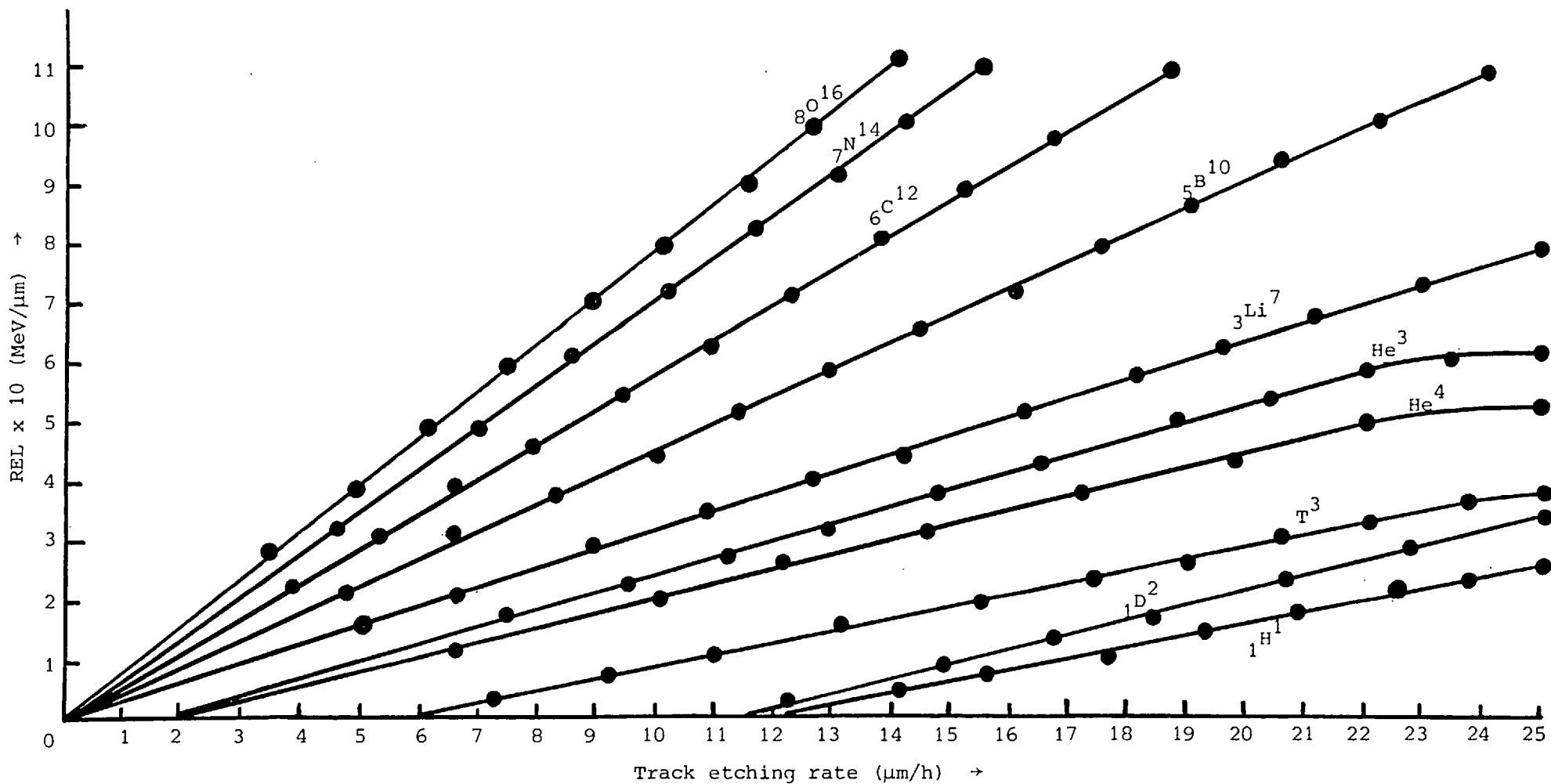


Figure 6.64a Diameter of etched tracks as a function of etching time for charged particles with incident energy 0.5 MeV/amu and with an incident angle normal to the surface of the CA 80-15 cellulose nitrate detector.

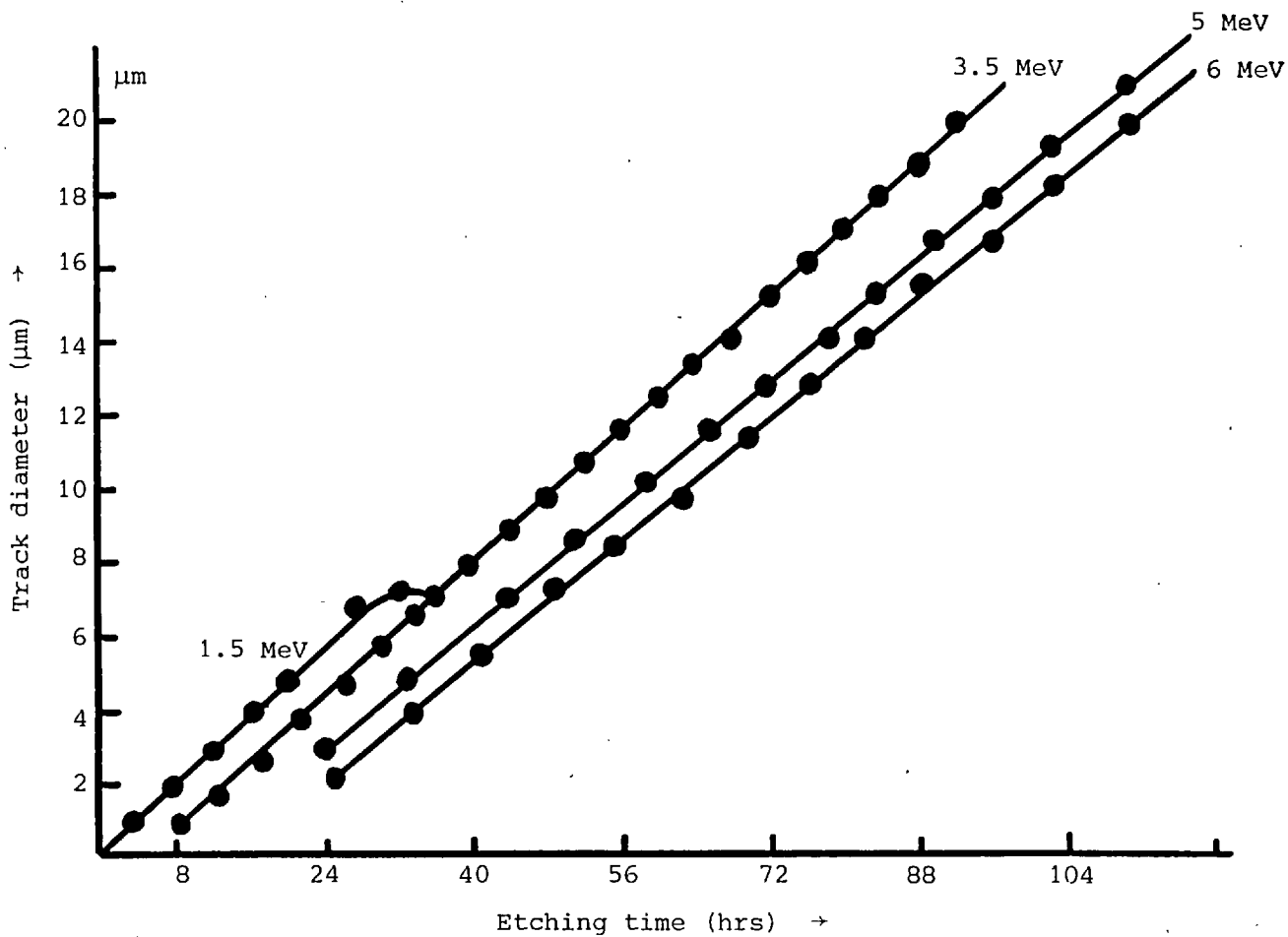


Figure 6.64b Track diameter as a function of etching time for particles at 1.5 and 3.5 MeV with an angle of incidence of 90° using 2.5 N NaOH at 18°C

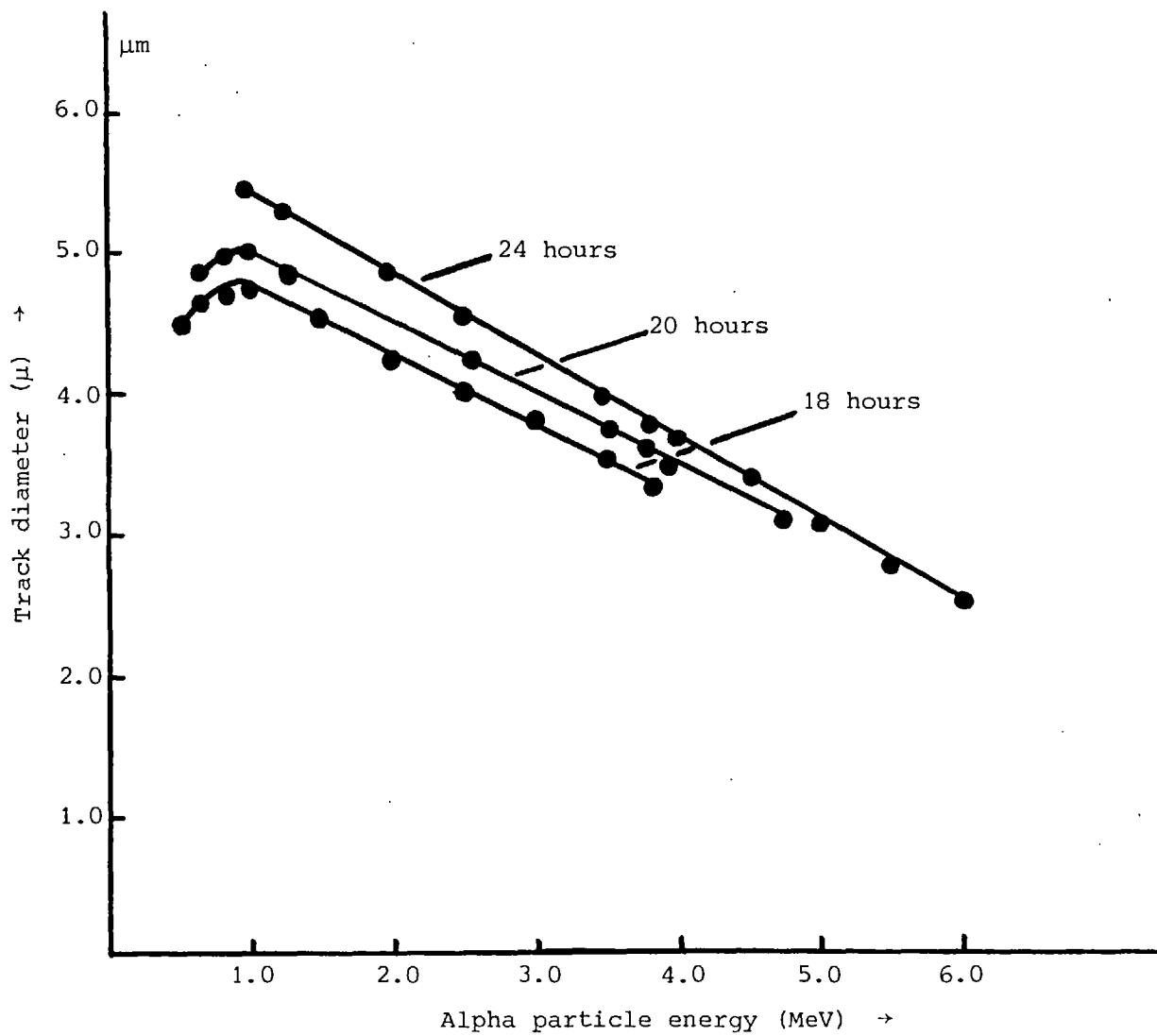


Figure 6.65 Variation of track diameter with alpha particle energy for particles at 90° incidence, with etching times of 18, 20 and 24 hours in 2.5 N NaOH at 18°C

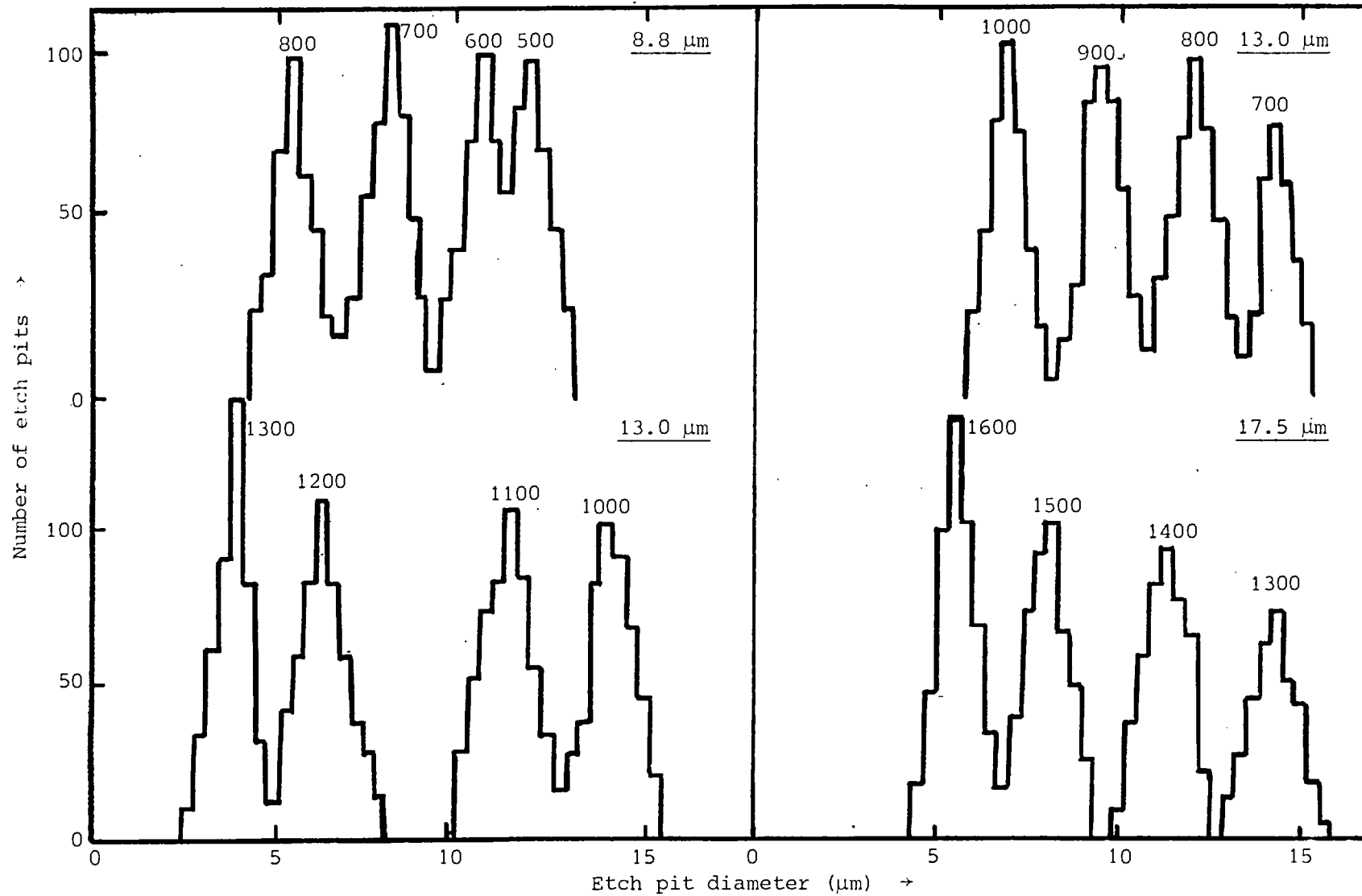


Figure 6.66 Diameter distribution of etch pits initiated by protons of different energies (in keV). Values for the removed layer thickness are noted in each right upper corner.

It is evident from Figure 6.66 that the energy resolution increases with increasing energy. The useful energy range that may be covered in a single etching process rises from about 150 keV for the lowest energy group to about 700 keV for the higher energy.

The diameter distribution results from the range straggling effect. At high energies, range straggling of the protons can exceed this effect. The optimum energy resolution has been found somewhere in the middle of the various measuring ranges. In Figure 6.67 a few optimal values are given for the full width at half-maximum fwhm as a function of energy; 25 keV is reached for the fwhm at 1400 keV.

The lower energy limit for the application of this method depends on the range at which linearity is maintained between the difference of radii and the difference of ranges and the residual thickness up to which the etched sheets may be safely handled.

Figures 6.68, 6.69 shows respectively, etched pit diameter and maximum etchable track length (range) distributions initiated by alpha particles normal to the surface of the detector.

The fwhm of the range determinations by track diameter and maximum etchable track length measurements are given in Figure 6.70 as a function of range and energy. Values of the fwhm of the energy determination calculated by multiplying with the values of specific energy loss were also plotted. The value of the measuring error etching and microscopic measurement is given at an energy of zero. As may be seen range straggling has an influence on the fwhm at energies above 4 MeV only. This influence is fully compensated for by the decreasing energy loss up to 6 MeV so that the energy resolving power average for track diameters is nearly constant at 48 keV and for maximum etchable track length is about 78 keV. For energies above 6 MeV the energy resolution is expected to deteriorate slowly due to increasing range straggling.

It is established that this kind of energy resolution is applicable to ${}^1_1\text{H}$, ${}^2_1\text{D}$, ${}^3_1\text{T}$, ${}^3_2\text{He}$ and ${}^4_2\text{He}$ particles if diameter measurements are obtained under etching conditions similar to those described (2.5 N NaOH, at 18°C). It is also possible to discriminate them according to their energies, masses or charges on the basis of the diameter of track holes as shown in Figure 6.64 (D versus t).

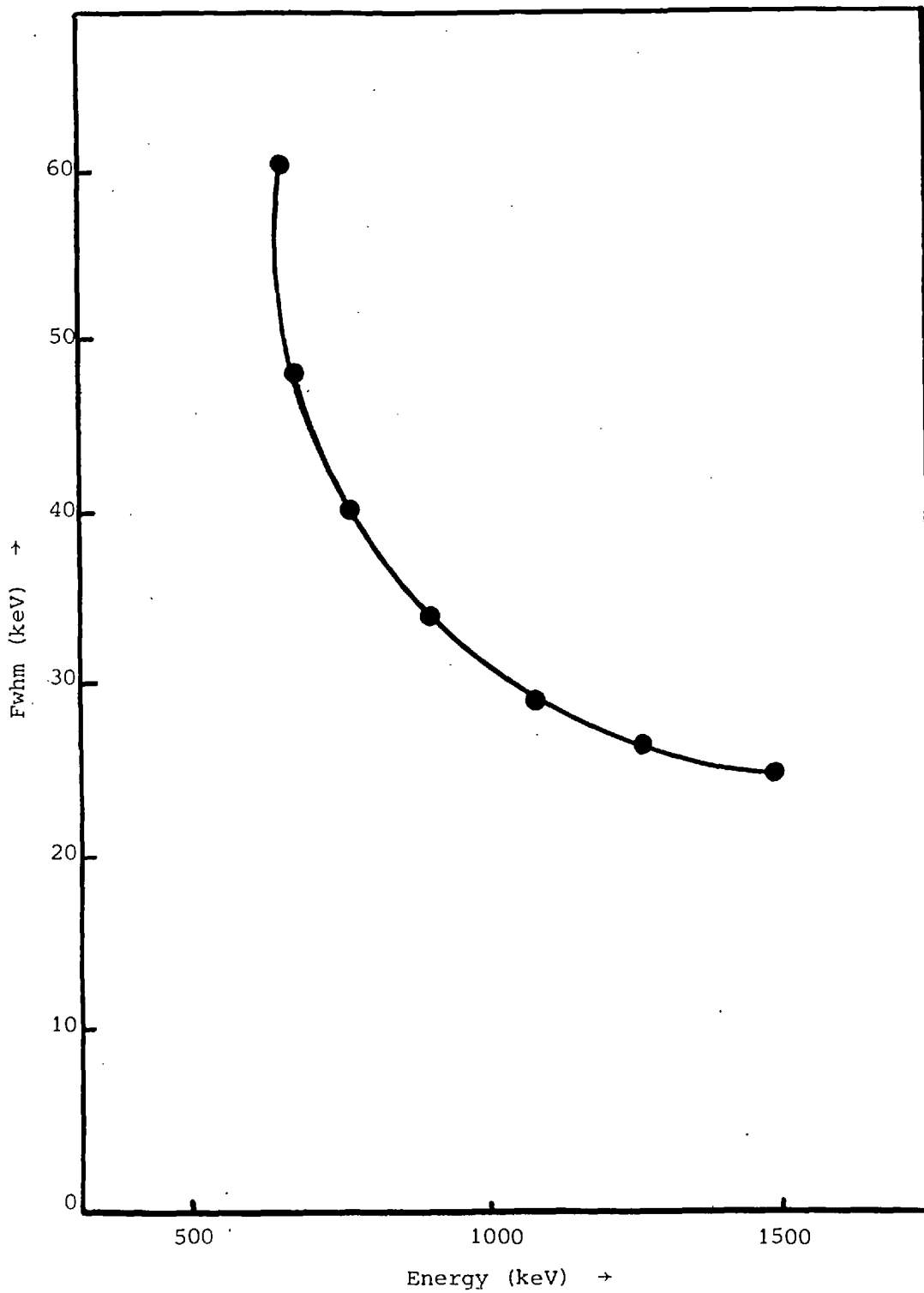


Figure 6.67 A few optimum values for the full width at half-maximum (fwhm) as a function of proton energy, as shown in Figure 6.66

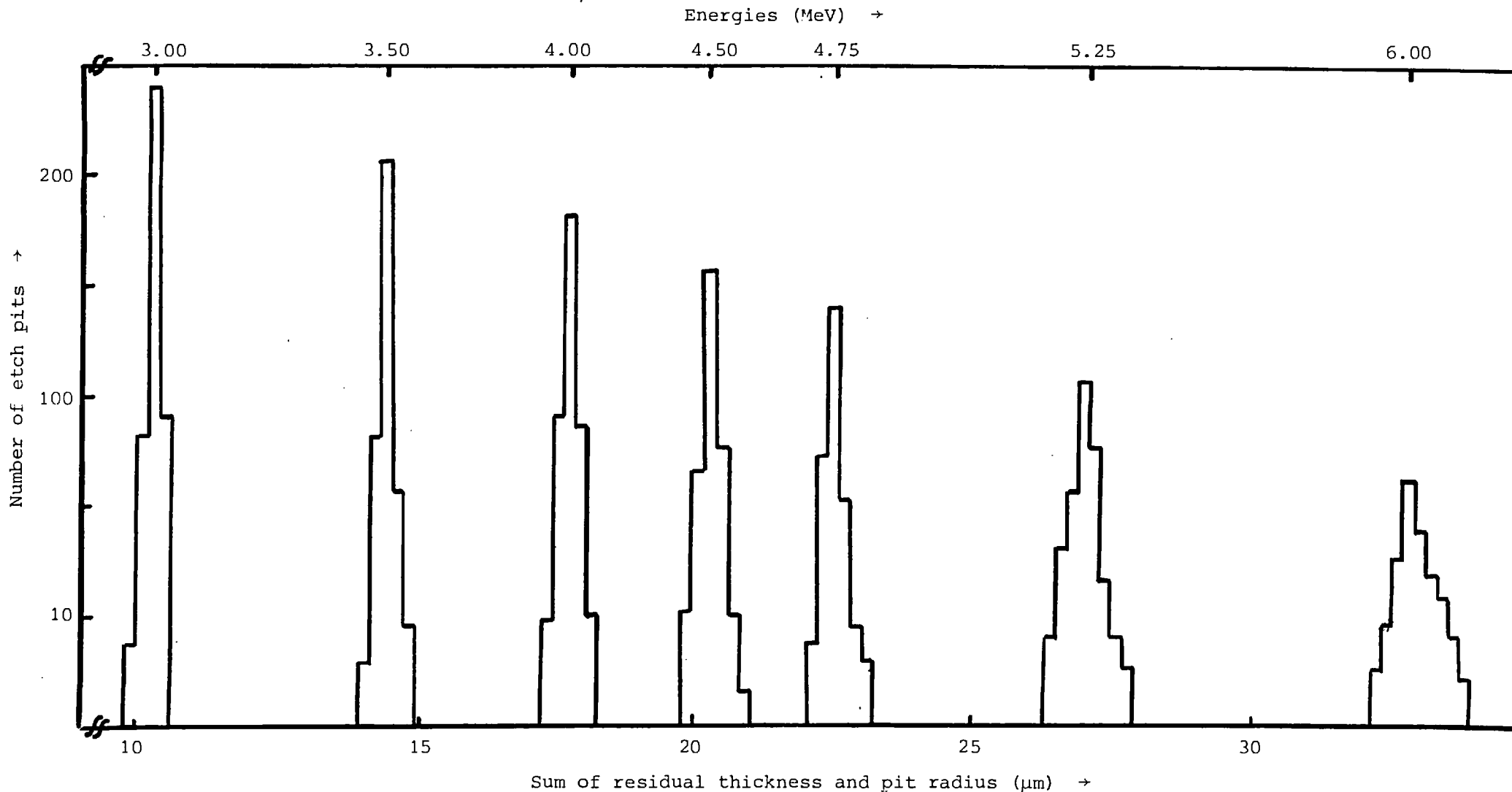


Figure 6.68 Summary of different spectra obtained from alpha particles. Distribution of etch pit radii versus sum of residual thickness and etch pit radius. All the etchings were carried out at the rear of the detector sheets.

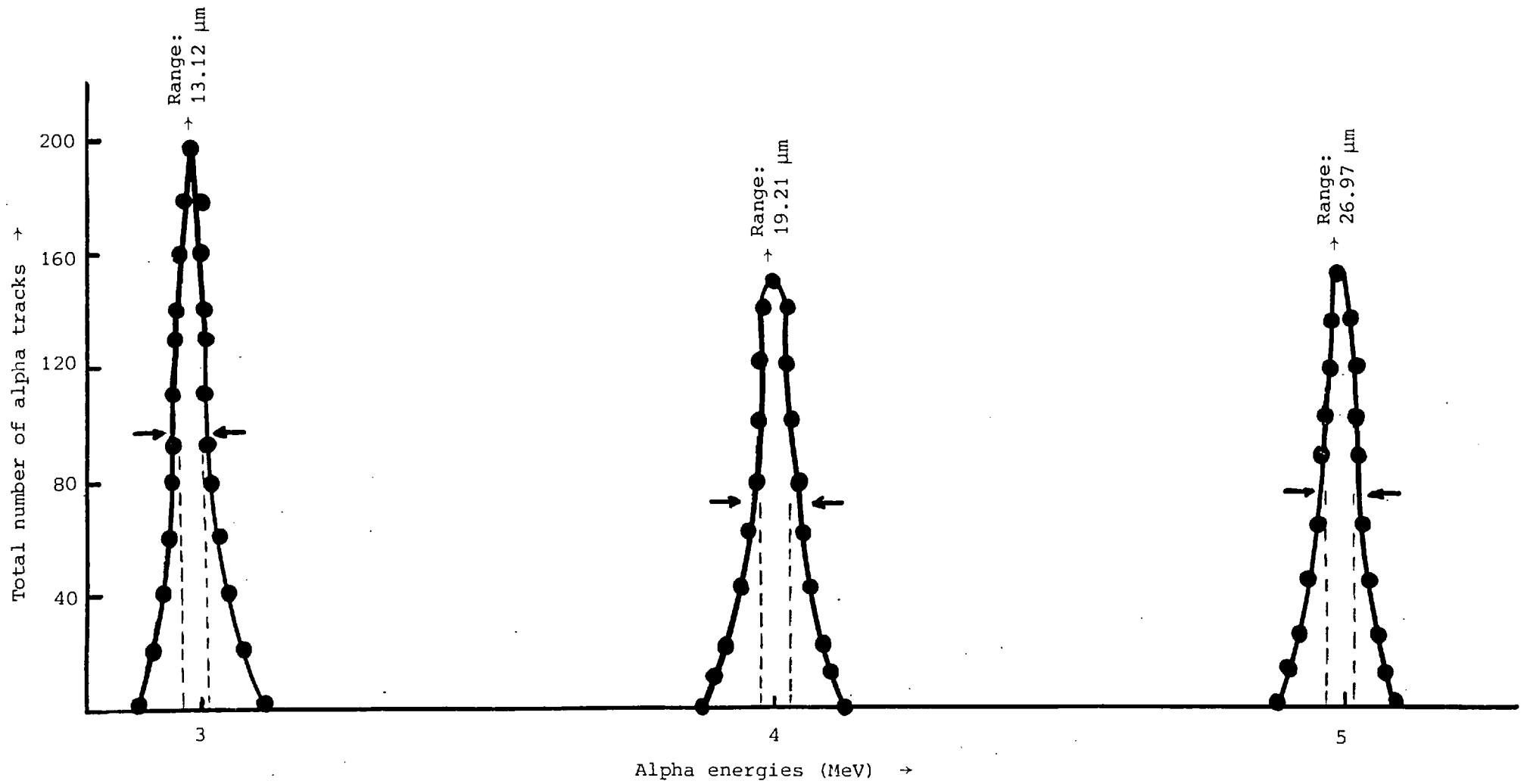


Figure 6.69 Distribution of the range (maximum etchable track length) of alpha particles incident normal to the surface of the detector CA 80-15 cellulose nitrate

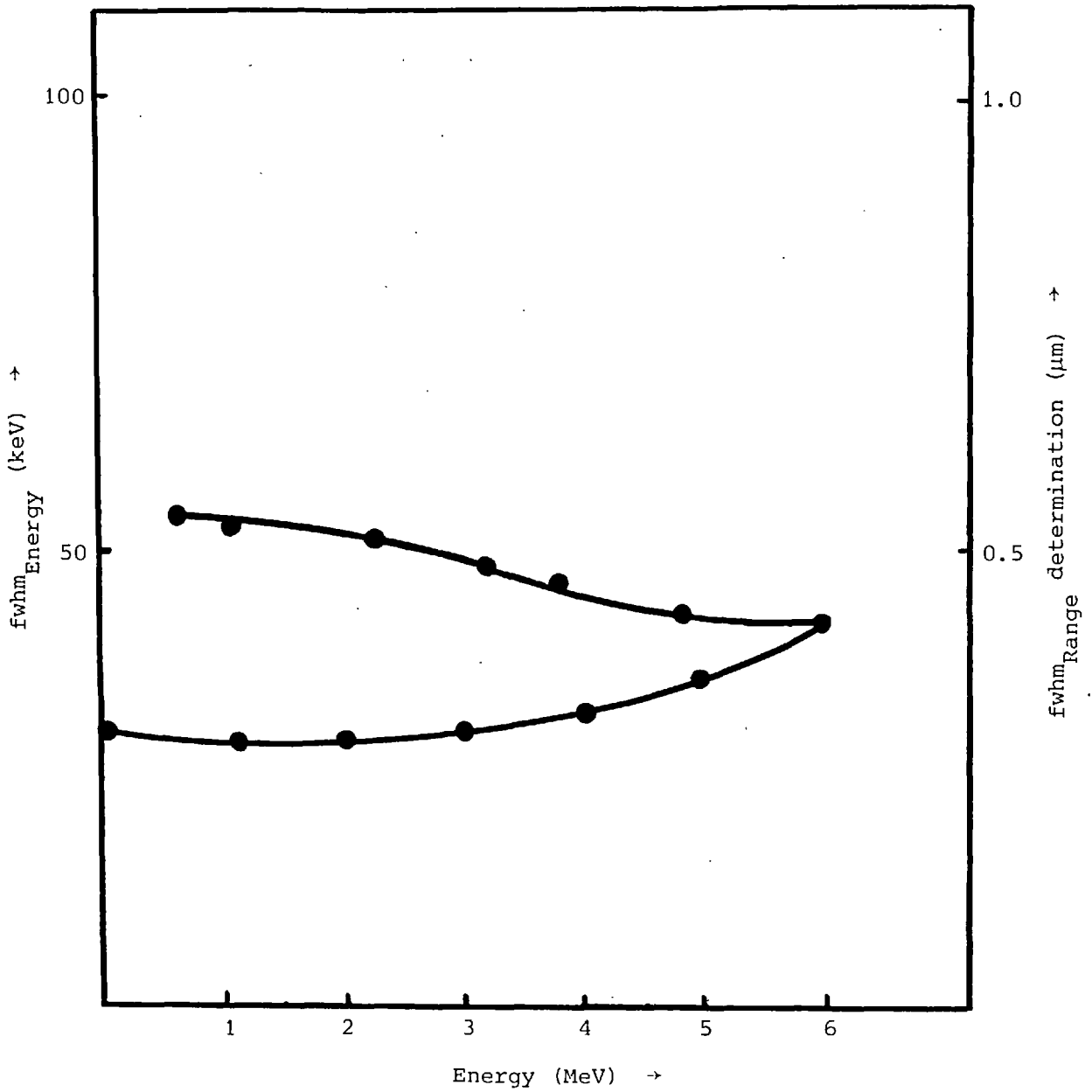


Figure 6.70 The full width at half-maximum of the range (lower curve) and the energy determination (upper curve) as a function of particle range and energy. The error of etching and microscopic measurement is given at 0 MeV

Discussion

Regarding the chemical etch development of tracks in cellulose nitrate plastics, the main conclusions were the following: the geometry of etched tracks can be well approximated by that of mathematical cones. This approximation gives the relationships between the various useful track parameters; the track etch rate ratio, V_T/V_B , can be substantially increased through the reduction of the bulk etch rate (V_B); the bulk etch rate, V_B , was found to vary inversely with the degree of polymerization of the nitrocellulose and inclusion of plasticizers; the etch rate ratio, V_T/V_B , can be increased by etching at lower temperatures or with increasing REL.

Simple theoretical arguments are presented to explain this behaviour.

Figures 6.45-6.47 show how V_T/V_B varies with the incident particle REL and V_T varies with Δ REL in CA80-15 cellulose nitrate films etched at different temperatures and etchant concentrations. It is evident from these figures that for this cellulose nitrate, V_T/V_B increases for higher REL. This and sharp pits are registered. When the REL < 0.108 MeV/ μ m it falls below the detector threshold of track registration, and no longer registers tracks. Alternatively, for lower etching temperatures and etchant concentrations CA80-15 has lower values of REL in order to reach the threshold of minimum track registration and larger values of V_T/V_B for the same values of REL. This is probably due to the preferential swelling of cellulose nitrate; the damaged area swells faster, due to the presence of broken and weakened bonds, loosening and stretching preferentially the lattice structure of the plastic. This preferential swelling will allow the OH^- ions to penetrate deeper and attack the damaged area more efficiently. This increases remarkably the sensitivity of the detector.

Figure 6.47b shows V_T versus REL for CA80-15 plastic pre-treated in a concentrated solution of zinc chloride (swelling agent) and etched with different etchant concentrations and temperatures.

1. V_T/V_B is larger in pre-swollen cellulose nitrate than the non-swollen for the same values of REL;
2. The preferential swelling is more highly sensitive to temperatures than to etchant concentrations;
3. The linearity of the curves V_T versus V_B is improved considerably

by the pre-swelling treatment. This is due to the minimizing of the induction time of latent tracks by preferentially swelling the plastic and allowing the OH^- ions to penetrate deeply into the loose structure of the damaged plastic. The imbedded latent tracks are attacked simultaneously as the bulk etching process is taking place, rather than waiting for the bulk etching process to remove certain layers of the plastic until the OH^- ions come physically in contact with the damaged region where $\text{REL} > \text{REL}_{\text{critical}}$.

4. The detector minimum threshold of track registration varies considerably with the etching conditions. Etching at high temperatures and high etchant concentration will shrink the plastic preferentially, reducing the detector's sensitivity and threshold of track registration. This effect is demonstrated in Table 6.13a and 6.13b, where etching was performed in 5N KOH at 50°C for a period of an hour. Particles with restricted energy loss rates less than 0.163 MeV/amu or larger than 0.259 MeV/amu were not revealed; alpha tracks with restricted energy loss rates larger than 0.259 MeV/amu were etched away by the bulk etching process and alpha tracks with energy loss rates less than 0.163 were below the detector minimum threshold of track registration.

Figure 3.4 also demonstrates the influence of etching conditions on the detector threshold of track registration, where pre-swelling the detector by treatment in zinc chloride solution followed by etching at low temperatures and etchant concentrations improves the detector threshold of track registration twofold.

5. Agitation of the etchant solution works against improvement of track resolution. This is due to an increase in the bulk etching rates without affecting the track etching rates. This results in reduction of the observed residual range (V_T/V_B is reduced).

From the above it is concluded that CA80-15 cellulose nitrate can be made more sensitive to a lower change of ionization rate or ΔREL at the same energy either by pre-swelling the plastic followed by etching or simultaneously swelling with the etching process (treatment in zinc chloride solution followed by etching or etching at low temperatures and concentrations) without stirring the solution.

A relationship is established between the track etching rate (V_T) and the restricted energy loss rates (REL) for two optimal etching conditions. This relationship is experimentally derived using H, He,

TABLE 6.13a

TRACKS FROM α -PARTICLES INCIDENT ON THE LR 115 FILMS AT 90° (1).

Counting was performed by a QTM-720 Image Analysing Computer

Energy (MeV)	1.0	1.5	2.0	2.5	3.0	3.5	4.0
Monitor Dose ² (in α -particles)	41822	52050	41922	42036	43243	46570	45800
Expected Track Density ³ (in tracks/frame)	248	309	250	250	257	276	271
Observed Track Density by QTM-720 ⁴ (in tracks/frame)	-	266 \pm 2.17%	238 \pm 1.95%	227 \pm 2.35%	244 \pm 1.71%	529 \pm 1.44%	The films are mostly destroyed
C _{eff} (Counting Efficiency)	-	86.1%	95.2%	90.8%	94.9%	191.7%	
Area of α -tracks ⁵ (in pp ²)	-	456.9 \pm 1.07%	377.0 \pm 1.59%	344.2 \pm 1.21%	178.5 \pm 1.66%	127.1 \pm 2.03%	
Horizontal Projection of α -tracks ⁴ (in pp)	-	24.8 \pm 3.35%	22.6 \pm 1.32%	20.6 \pm 2.48%	15.6 \pm 1.67%	13.2 \pm 3.71%	
Vertical Projection of α -tracks ⁴ (in pp)	-	25.6 \pm 2.27%	21.4 \pm 2.00%	22.2 \pm 3.31%	14.3 \pm 2.16%	13.0 \pm 2.43%	

Footnote for Table 6.13a.

- (1) LR 115 films were etched in 6.5N NaOH solution at 50°C (completely submerged).
- (2) The monitor dose corresponds to the absolute dose of α -particles. The wheel was rotating at $\approx 120 \text{ rev/min}^{-1}$ and the irradiation lengths were of the order of a few minutes.
- (3) The area to find the track density (i.e. area of the monitor cover hole) is: $A = \pi(3/2)^2 \text{ mm}^2 \approx 7.069 \text{ mm}^2$.
- (4) The QTM-720 frame at x1030 magnification is:
Frame = $0.181 \times 0.232 \text{ mm}^2 \pm 1\%$.
- (5) $1\mu \approx 3.45 \text{ pp}$ at x982 magnification (= x8 eyepiece; x4.91, x25 objective).

TABLE 6.13 b

TRACKS DUE TO α -PARTICLES INCIDENT ON LR 115 FILMS AT VARIOUS ANGLES*. MEASUREMENTS WERE MADE WITH A QTM 720 IMAGE ANALYSING COMPUTER. THE TRACK AREA CORRESPONDS TO pp^2 WHILE THE HORIZONTAL AND VERTICAL TRACK PROJECTIONS CORRESPOND TO pp (picture points)

θ° \ T	1.5 MeV		2.0 MeV		2.5 MeV		3.0 MeV		3.5 MeV	
	Area		Area		Area		Area		Area	
90°	456.9 ± 1.07 %		377.0 ± 1.59 %		344.2 ± 1.21 %		178.5 ± 1.66 %		127.1 ± 2.03 %	
70°	465.7 ± 1.80 %		382.5 ± 2.08 %		380.0 ± 2.03 %		294.8 ± 2.39 %		162.3 ± 3.4 %	
50°	467.0 ± 1.19 %		517.9 ± 1.73 %		464.1 ± 2.48		431.1 ± 3.23 %		272.5 ± 5.41 %	
30°	376.7 ± 3.51 %		518.3 ± 1.52 %		520.9 ± 1.20 %		497.7 ± 3.14 %		382.3 ± 4.45 %	
	Hori- zontal	Vertical	Hori- zontal	Vertical	Hori- zontal	Vertical	Hori- zontal	Vertical	Hori- zontal	Vertical
90°	24.8 ± 3.35%	25.6 ± 2.27%	22.6 ± 1.32%	21.4 ± 2.00%	20.6 ± 2.48%	22.2 ± 3.31%	15.6 ± 1.67%	14.3 ± 2.16%	13.2 ± 3.71%	13.0 ± 2.43%
70°	26.2 ± 2.23	24.6 ± 1.62%	23.6 ± 2.16%	21.0 ± 3.69%	25.6 ± 2.34%	18.6 ± 2.15%	24.0 ± 5.1%	15.8 ± 3.04%	16.3 ± 3.03%	12.5 ± 1.79%
50°	29.7 ± 2.07%	23.5 ± 1.82%	31.4 ± 0.78%	22.4 ± 3.03%	33.2 ± 1.48%	17.6 ± 3.41%	37.2 ± 1.98%	16.0 ± 4.42%	36.5 ± 2.59%	14.0 ± 4.87%
30°	29.8 ± 5.35%	18.2 ± 4.04%	34.3 ± 0.61%	21.2 ± 3.74%	40.4 ± 2.01%	19.4 ± 2.06%	46.0 ± 1.37%	17.0 ± 3.22%	48.8 ± 2.71%	14.0 ± 7.14%

*LR 115 films were etched in 6.5 N NaOH solution at 50°C.

Li, Be, B, C, N, O, Ne, fission fragments and other heavy ion sources from either the University of London reactor or the Oxford and Harwell accelerators. The maximum energy for the nuclei is 12.6 MeV/amu. Track etching rates at various REL values are obtained by slowing down the nuclei in an appropriate absorber.

The relationship between the track etching rate (V_T) and the corresponding REL is established for two etching conditions E_1 and E_2 • E_1 is 2.5N NaOH at 15°C and E_2 is 2.5N NaOH at 18°C. The REL is in the range of (8.8-0.1) MeV/μm. This is expressed in Equation 6.66 by a simple exponential function:

$$V_T(R) = V_B + a(1 - \exp b \cdot \Delta REL(R)) \quad (6.118)$$

Since the track etching rate is related to the restricted energy loss rate, the value of V_T is a possible particle identification parameter.

The range of alpha particles and other heavy particles of various energies was determined for CA80-15 cellulose nitrate by measuring the maximum etchable track length of the particle. The true cone length (range) is calculated by correcting the observed cone length for the portion that was lost in the bluk etching process. The result shows that by applying the calculated range-energy relationship in cellulose nitrate, energies of alpha particles can be resolved with a resolution better than 70 keV over the energy range of 0.60-6.0 MeV. The particle track diameter measurements also show that alpha particle and proton energies can be resolved with a resolution better than that of the track length (range) measurements.

Since the particle range or REL of a given energy (E) is related to z, the charge of particles is also determined by measuring either the particle's track diameter or the particle's true cone length (range). This implies that identification may be made if the energy (or residual range) and energy loss rate (or ionization rate) of the particles are known at any position along their path. It follows, as has been shown, that for known particles, curves such as those given in Figures 6.53, 6.54, 6.64 and 6.65 allow the energy to be determined. Where both the particle and its energy are unknown they were determined by performing length measurements or diameter measurements at two or more points along the trajectory of the particle or at two or more etching times; cone-length measurements together with measurements of track range provide for each event two independent values of ionization rate at a known

residual range. Thus there are two independent ways of identifying each particle.

The standard deviation of the charge resolution (Δz) was found to be 0.3 charge units in the case where the number of pits measured along the trajectory of the particle is about 9 and Δz was 0.2 charge units for about 20 pits.

Isotopic mass separation for individual particles was obtained in a similar way to that used for charge identification. The relation between the cone length and the residual range for isotopes was calculated from Equation 6.66. Figure 6.55a shows the curves calculated for various isotopes of Be, B and C, with the experimental points indicated. The mass resolution (ΔA) is found to be 0.4 amu for beams from the accelerator.

The energy and charge resolution was found to be influenced by the specific energy loss, range straggling, evenness of the plastic thickness, the etching process and the microscopic measurements.

The efficiency of the SSTR as a function of α -energy is shown in Table 6.8. It can be seen that the response is flat to better than $\pm 1\%$ between the limits 0.6-3.8 MeV for etching parameters of 2.5N NaOH at 18°C and for particles at 90° incident to the SSTR surface. The response range is increased for particles at 30° incidence to 0.6-6.0 MeV. This is to be expected since as the angle of incidence is decreased so the etched track becomes closer to the surface. The response is further increased as the angle of incidence is decreased since the tracks are brought within the optical resolution of the microscope.

Tables 6.9 and 6.10 show the energy range of observable tracks at various angles of incidence for CA80 and LR115 respectively. It should be noted that limits of either 0.6 or 6.0 MeV were the limits of the Van de Graaff and the energy range of alpha particles must be extended beyond these limits to obtain the correct energy range of observable tracks at all angles.

The efficiency measurements were based on the assumption that the track density was uniformly distributed across each recorder since only a limited number of frames were analysed for tracks. In order to check this assumption, a scan was made across a number of the plastic recorders and the track density was found to remain constant with the radius of the detector to within $\pm 1\%$. A typical density distribution across a recorder is shown in Figure 6.44b.

A graphical representation of induction times for alpha particles in cellulose nitrate, with energies ranging from 0.6 to 6.0 MeV, incident normal to the surface of the detector, is shown in Figure 6.50. It can be seen that the bulk material has been etched to a sufficient depth to expose the etchable portion of tracks at 0.6, 1.0 and 1.5 MeV while the tracks at 3.8-4.0 MeV are on the threshold of observation and those above 4.0 MeV are below the surface with only a very small tunnel extended to the surface. If the microscope is focused on the surface of the recorder then the small tunnels leading from the surface for tracks at 4.0 MeV, are below the optical resolution of the microscope. Furthermore the etched position of the track is sufficiently far below the surface to be outside the focal length of the microscope, thus preventing the observation of tracks. These tracks can only be observed if either further etching takes place so that the surface is lowered by bulk removal or the tracks are at a sufficiently low angle of incidence to the surface to bring them within the range of the focal length of the microscope. It is possible to refocus the microscope to a point below the surface but contrast then becomes a problem since observation is then through the plastic and not on or near the surface.

Figures 6.71, 6.72, 6.73, 6.74 and 6.75 show tracks of alpha particles and protons at various energies, angles of incidence and etching times. In each case, the microscope was focused at the entrance of the track. The importance of using the correct etching conditions is clearly demonstrated in Figures 6.76, 6.77, 6.78 and 6.79, where the effect of over etching is shown.

Systematic studies have been made concerning the effect of high doses of gamma rays on the track-registration properties of CA80-15 and LR-115 type II plastic SSTRs. The detectors were first exposed to ²⁵²Cf fission fragments and then to gamma doses ranging between 1 and 20 megarads.

Etching the detectors with low etchant concentrations and temperatures results in the following characteristics:-

1. Both the length and the width of the latent damage trail are affected for detectors exposed to gamma doses of the order of a few megarads.
2. The bulk etching rate (V_B) increases with increasing gamma dose.
3. The track registration efficiency is not affected by high doses of gamma rays.

(This subject is discussed in detail in Section 6.11.1.)

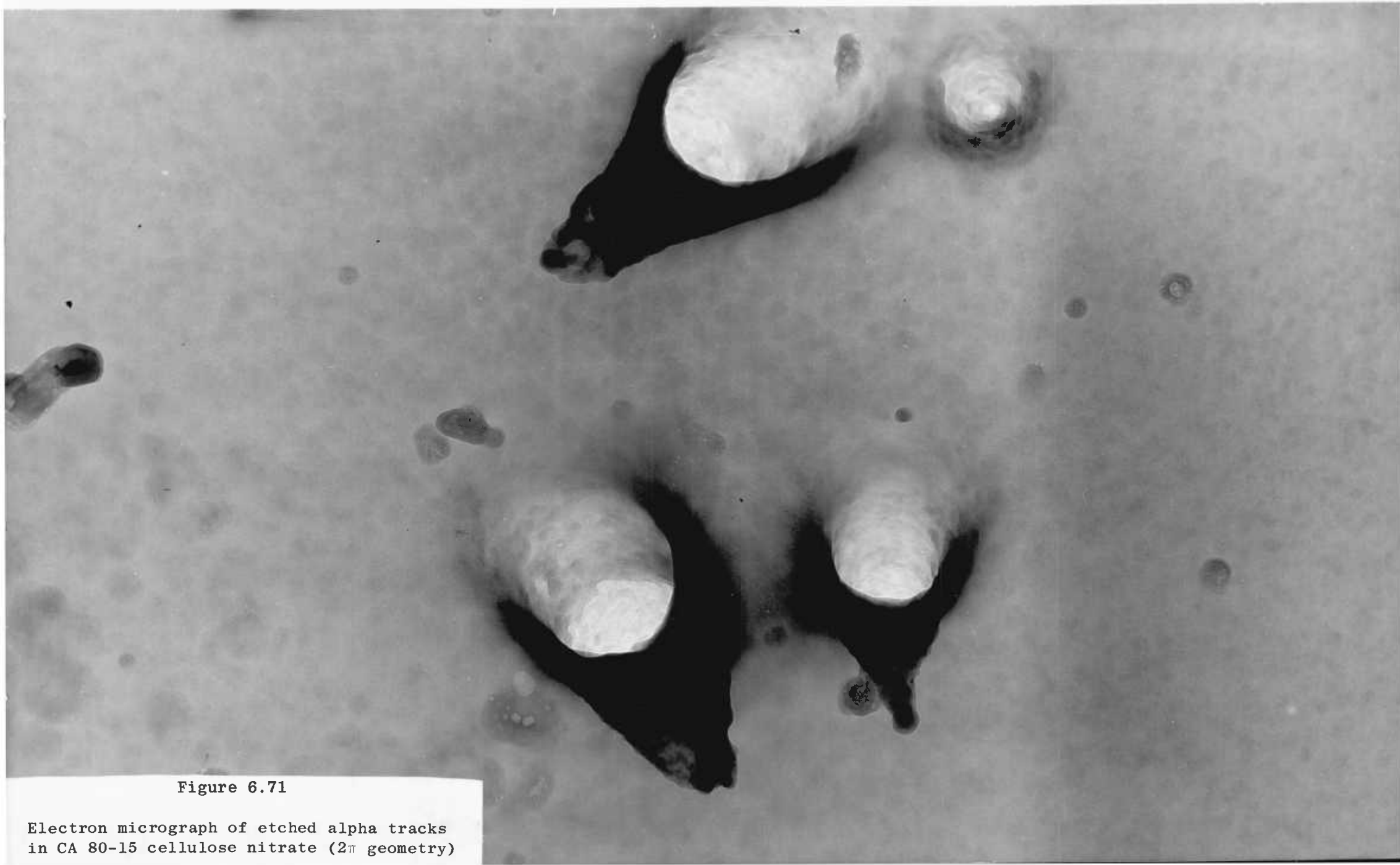


Figure 6.71

Electron micrograph of etched alpha tracks
in CA 80-15 cellulose nitrate (2π geometry)

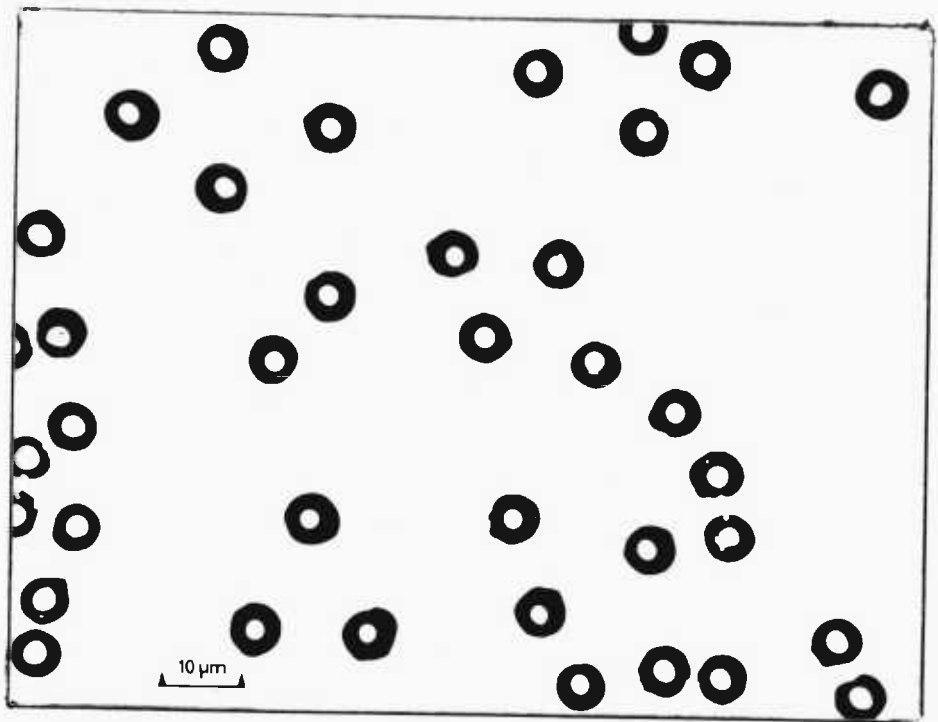


Figure 6.72 Photomicrograph of 4.0 MeV alpha tracks in CA80-15 (Kodak-Pathe, France) at 90° incidence, pre-swollen in 65% zinc chloride solution for 2 hours at 18°C , then etched in 2.5 N sodium hydroxide at 18°C for 20 hours.



Figure 6.73 Photomicrograph of 4.0 MeV alpha tracks in CA80-15 (Kodak-Pathe, France) at 30° incidence, pre-swollen in 65% zinc chloride solution for 2 hours at 18°C , then etched in 2.5 N sodium hydroxide at 18°C for 20 hours.

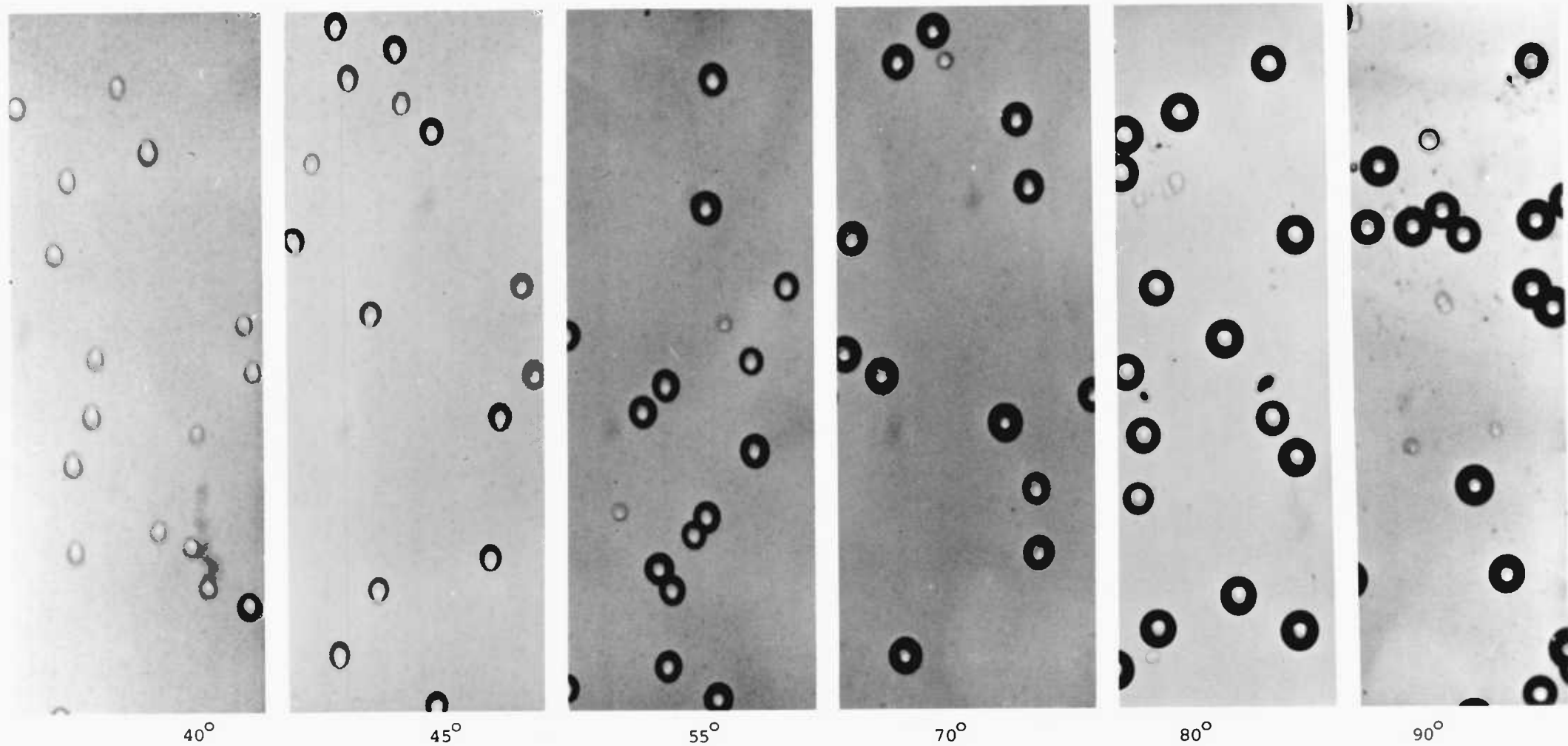


Figure 6.74 Photomicrograph of 6.0 MeV alpha tracks in CA80-15 (Kodak-Pathe, France) at 40°, 45°, 55°, 70°, 80° and 90° incidence, etched in 2.5 N sodium hydroxide at 18°C for 26 hours.

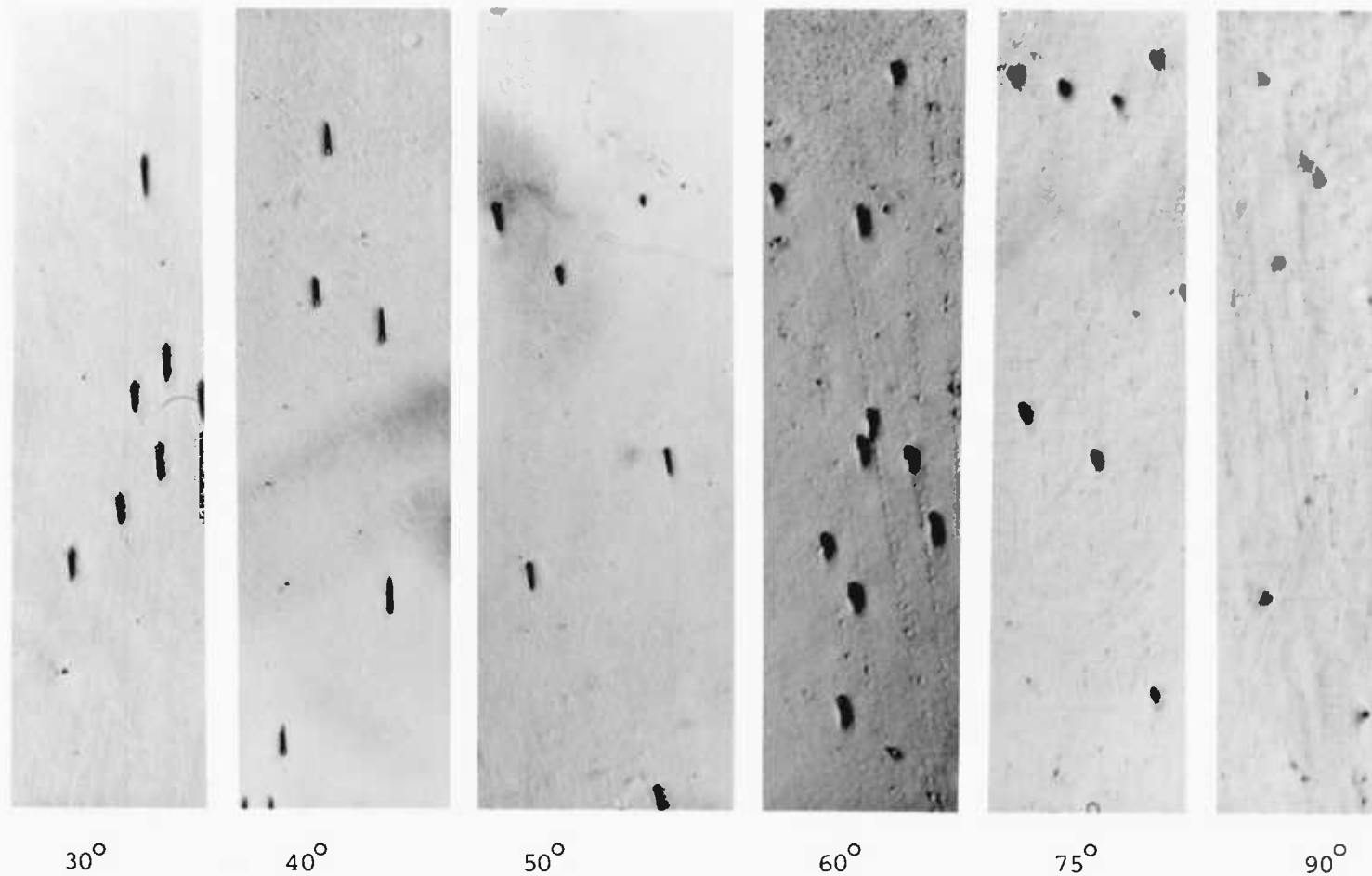


Figure 6.75 Photomicrograph of 1.50 MeV proton tracks in CA80-15 (Kodak-Pathe, France) at 30°, 40°, 50°, 60°, 75° and 90° incidence, pre-swollen in 65% zinc chloride solution for 2 hours, then etched in 2.5 N sodium hydroxide at 18°C for 22 hours.

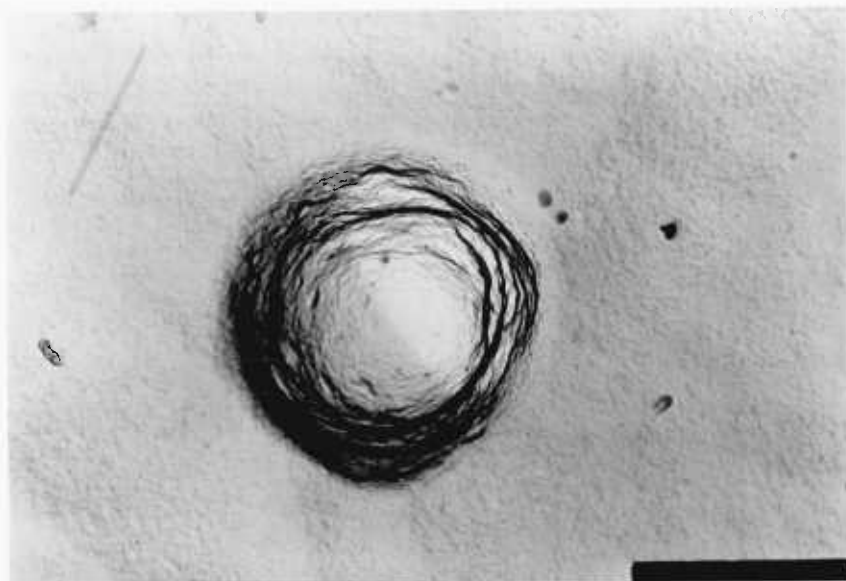


Figure
6.76

Electron micrograph of 1.1 MeV proton track in CA80-15 (Kodak-Pathe, France) at 90° incidence, pre-swollen in 65% zinc chloride solution for 2 hours, then etched in 2.5 N sodium hydroxide at 18°C for 24 hours (25 K x 2).

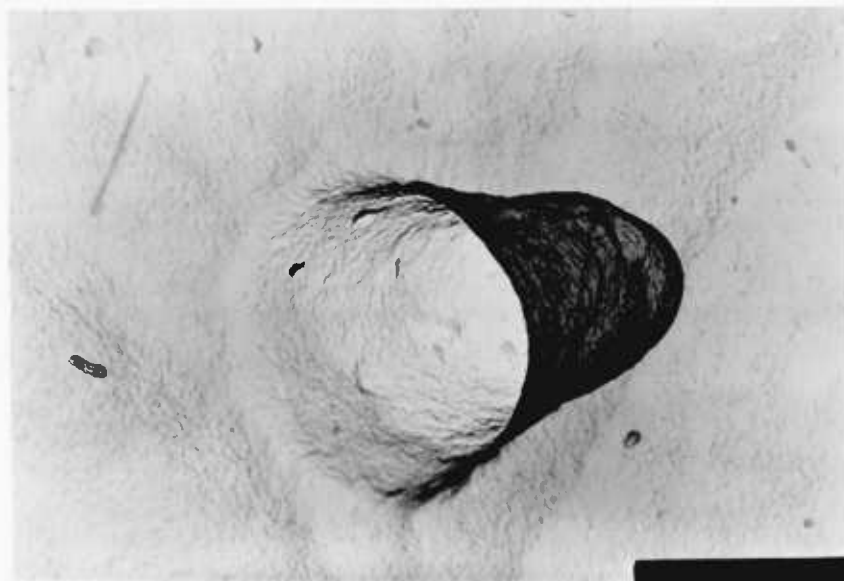


Figure
6.77

Electron micrograph of 1.1 MeV proton track in CA80-15 (Kodak-Pathe, France) at 60° incidence, pre-swollen in 65% zinc chloride solution for 2 hours, then etched in 2.5 N sodium hydroxide at 18°C , for 16 hours (25 K x 2).

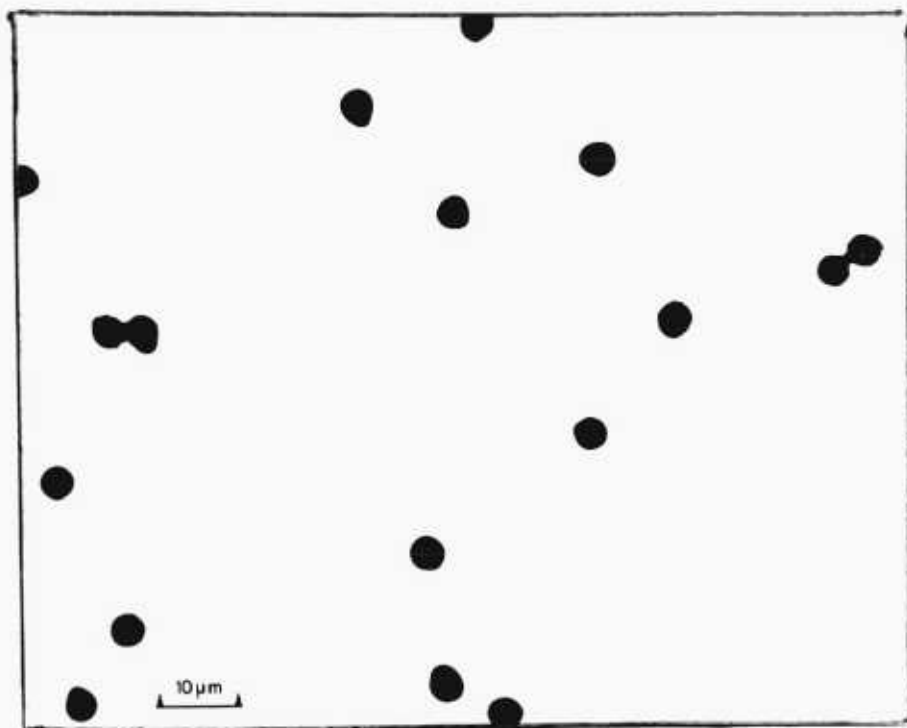


Figure 6.78 Photomicrograph of 3.90 MeV alpha tracks in CA80-15 (Kodak-Pathe, France) at 90° incidence, etched in 2.5 N sodium hydroxide at 18°C , for 26 hours.

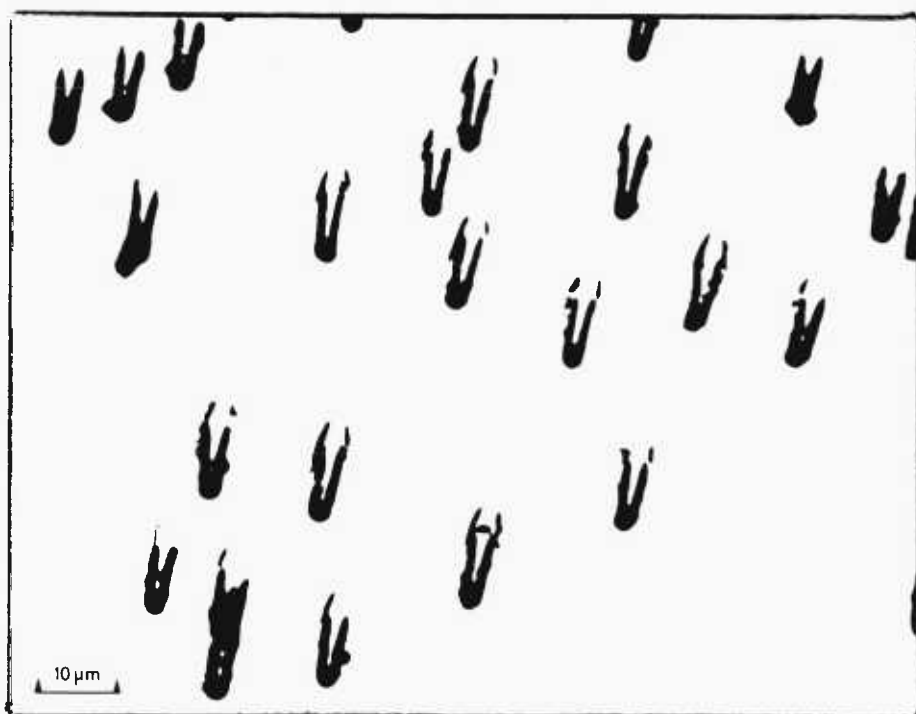


Figure 6.79 Photomicrograph of 3.90 MeV alpha tracks in CA80-15 (Kodak-Pathe, France) at 30° incidence, etched in 2.5 N sodium hydroxide at 18°C for 26 hours.

6.11 Reactor Physics Applications

Before considering the application of these detectors to the core of the reactor, we should consider the influence of the reactor environment on the basic parameters of the detector and its registration efficiency.

The main factors of importance in the reactor which may influence track registration properties of SSTRs and geometry of tracks are:-

(a) Fast neutrons which produce recoil nuclei; these can easily be accounted for by applying our knowledge from the experiments discussed in Sections 6.10-6.107.

(b) High doses of γ -radiation; their effects should be investigated in detail.

6.11.1 The Effect of High Gamma Doses on the Etching Characteristics of Cellulose Nitrate Plastic

It is sometimes assumed that high doses of gamma radiation, such as found in a core of a nuclear reactor, leave unaffected the charged particle track registration properties of plastic detectors (109). However, the validity of this assumption must be experimentally verified for the purpose of reactor applications, since it is known that γ -rays and electrons cause significant radiation damage in all organic polymers.

To check the influence of γ -rays on track registration properties, the following questions must be investigated:

- (1) The effects of high γ -ray doses on track etching parameters: the track etching rate V_T , the bulk etching rate V_B , the threshold of track registration (the minimal value of energy loss or restricted energy loss REL), and the registration efficiency.
- (2) The limit of γ -ray dose below which the basic detector properties remain practically unchanged, so that the effect of γ -rays may be neglected.
- (3) The etching conditions which minimize and which maximize the influence of γ -rays on the track registration properties of a given plastic detector.
- (4) Whether the change in bulk or track etch rate (V_B or V_T respectively) can be used as an accurate measure of the γ -ray dose.
- (5) The appropriate correction factors, depending on the γ -ray dose,

which must be introduced in interpreting track measurements (length, diameter, track revelation time).

To investigate these questions, four sets of plastic film detectors, each consisting of CA80-15 and LR-115 Type II cellulose nitrate, were exposed to varying doses of fission fragments from ^{252}Cf (2π geometry) and to varying doses of γ -rays from ^{60}Co . Set A was exposed first to fission fragments and then to γ -rays, and set B was exposed in reverse order. Set C was exposed only to fission fragments, while set D was exposed only to γ -rays. After the irradiations, the four sets were etched simultaneously under the same etching conditions.

The observed track length l , track width W and cone-angle θ of the etched fission fragment tracks were measured at various stages. The bulk etch rate V_B was measured as a function of γ -ray dose.

Figures 6.80 and 6.81 show the variation of \bar{W}_D/\bar{W}_0 as a function of dose D , for eight etching conditions E_1 to E_8 . E_1 was 2.5 N NaOH at 18°C ; E_2 was 2.5 N NaOH at 50°C ; E_3 was 6 N NaOH at 18°C ; E_4 was 6 N NaOH at 50°C ; E_5 was 2.5 N KOH at 18°C ; E_6 was 2.5 N KOH at 50°C ; E_7 was 6 N KOH at 18°C and E_8 was 6 N KOH at 50°C . \bar{W} denotes the average observed width of etched fission fragment tracks, with the subscript indicating the dose in megarads.

There is a notable increase in the ratio \bar{W}_D/\bar{W}_0 with increasing dose D , for etching conditions E_1 , E_3 , E_5 and E_7 (low etching temperature (18°C)) and the increase is greater for set A than for set B, i.e. for the set which was exposed first to fission fragments. On the other hand, there is practically no increase in the ratio \bar{W}_D/\bar{W}_0 under conditions E_2 , E_4 , E_6 and E_8 (50°C); these etching conditions are insensitive to γ -ray doses.

Figures 6.84 and 6.85 show $V_{B,D}/V_{B,0}$ versus γ -ray dose D for set D (exposure to γ 's only). The influence of γ -rays in this ratio is observed to be the same as for the previous ratio \bar{W}_D/\bar{W}_0 .

These results indicate that the radiochemical changes in the bulk cellulose nitrate, due to γ -rays, may be detected easily under certain "optimal" etching conditions (E_1 , E_3 , E_5 and E_7) but not under certain other conditions (E_2 , E_4 , E_6 and E_8). This suggests the possible employment of cellulose nitrate as a γ -ray dosimeter in the megarad range, by using the ratio $V_{B,D}/V_{B,0}$ or \bar{W}_D/\bar{W}_0 as a measure of the dose D under etching conditions E_1 , E_3 , E_5 or E_7 , i.e. appropriate ratio is measured for a detector film and compared against the calibrated curve. At the same time, if one wishes to avoid consideration of γ -rays on track properties, etching conditions E_2 , E_4 , E_6 and E_8 are to be used.

NaOH

$18^{\circ}\text{C} \pm 0.1^{\circ}\text{C}$

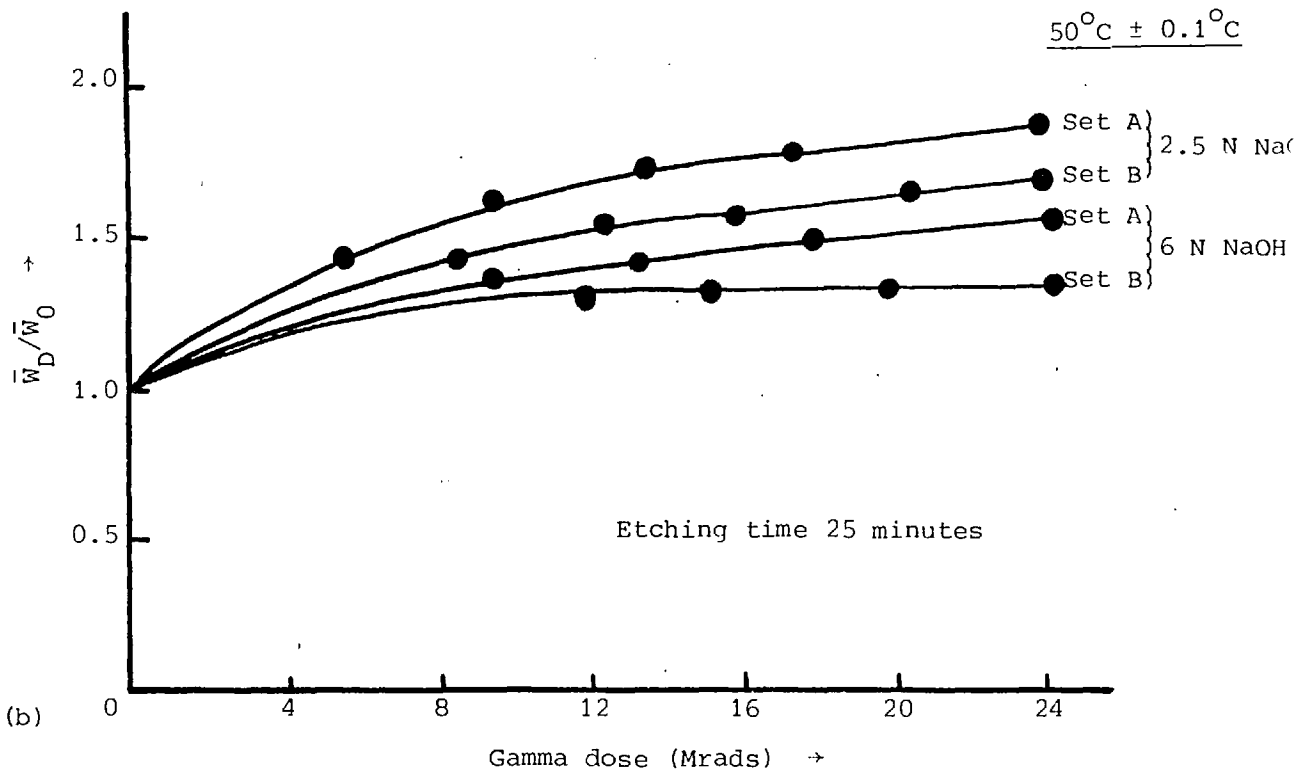
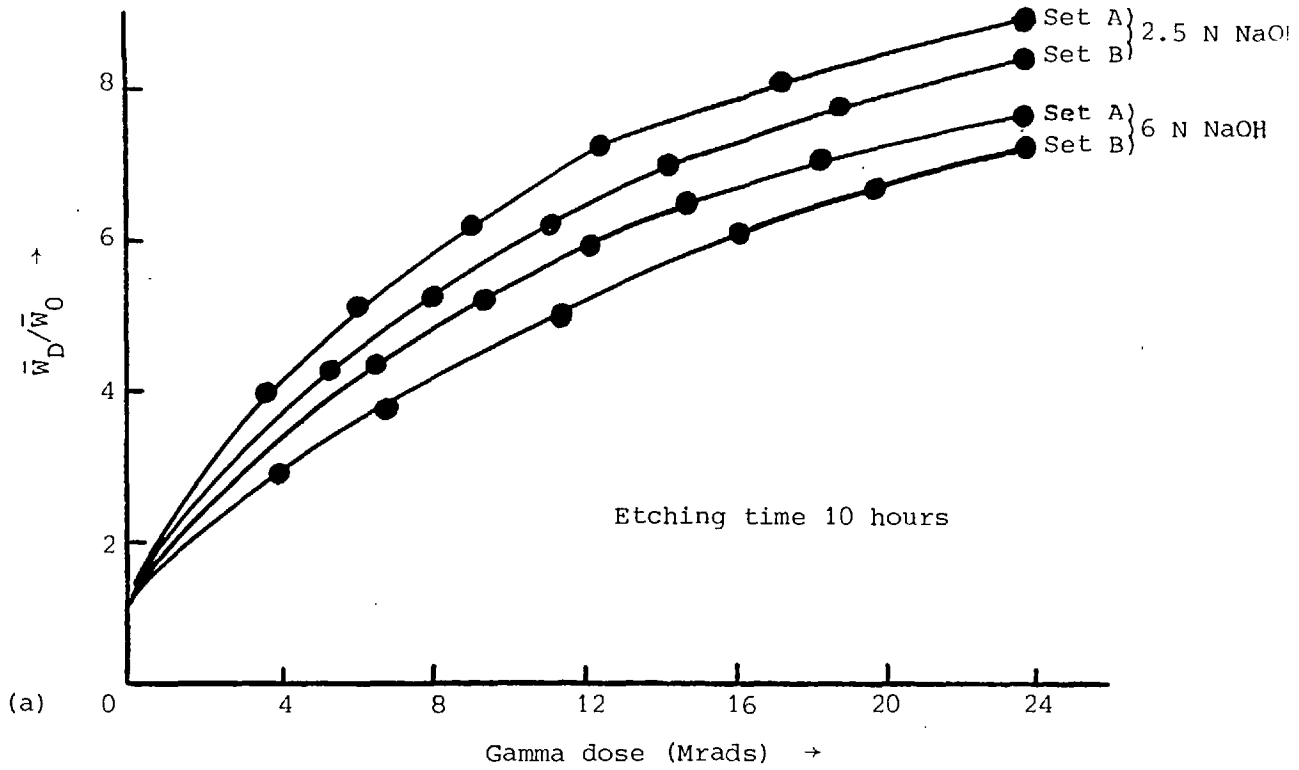


Figure 6.80 The ratio of \bar{W}_D/\bar{W}_0 (the average width of etched fission fragment tracks at gamma doses of "D-megarads" and "zero-megarads") of CA 80-15 cellulose nitrate versus gamma dose, etched in 2.5 N and 6 N NaOH at (a) 18°C and (b) 50°C , without interruptions or stirring

KOH

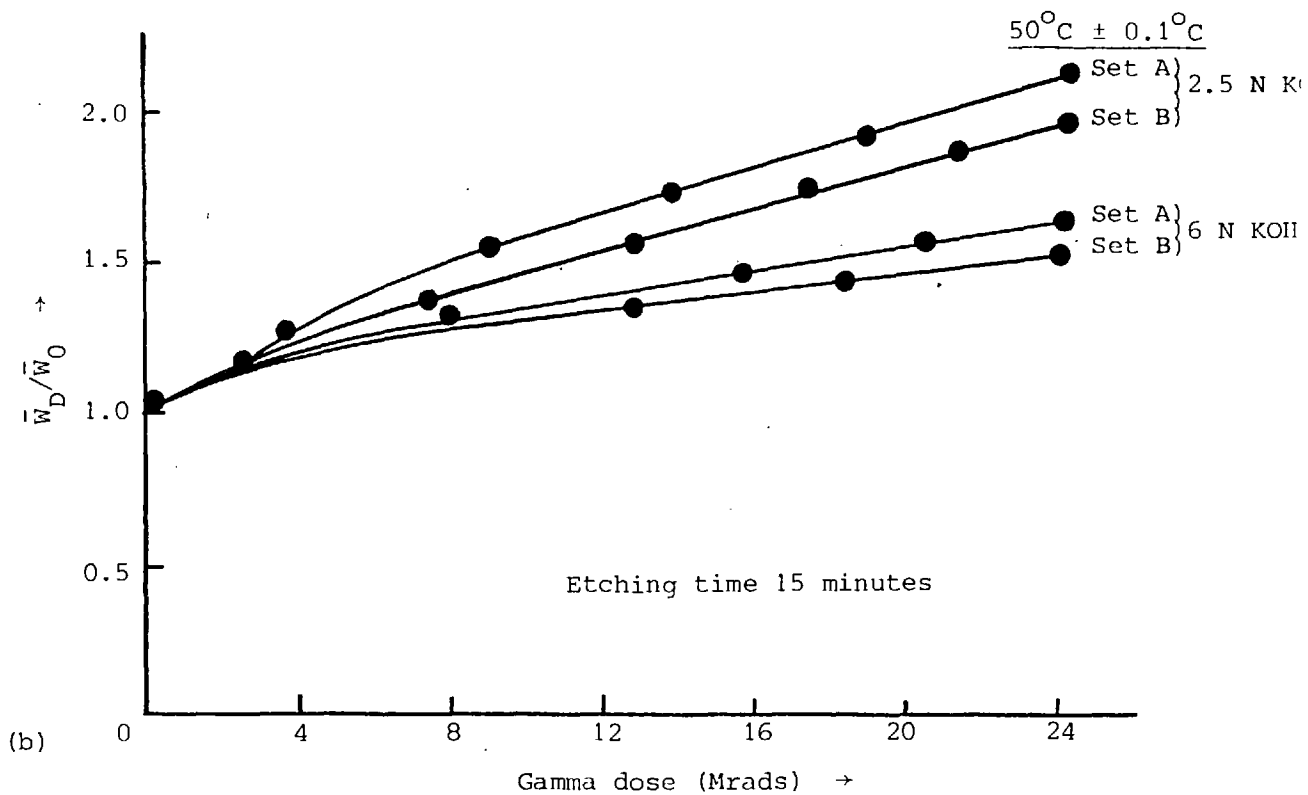
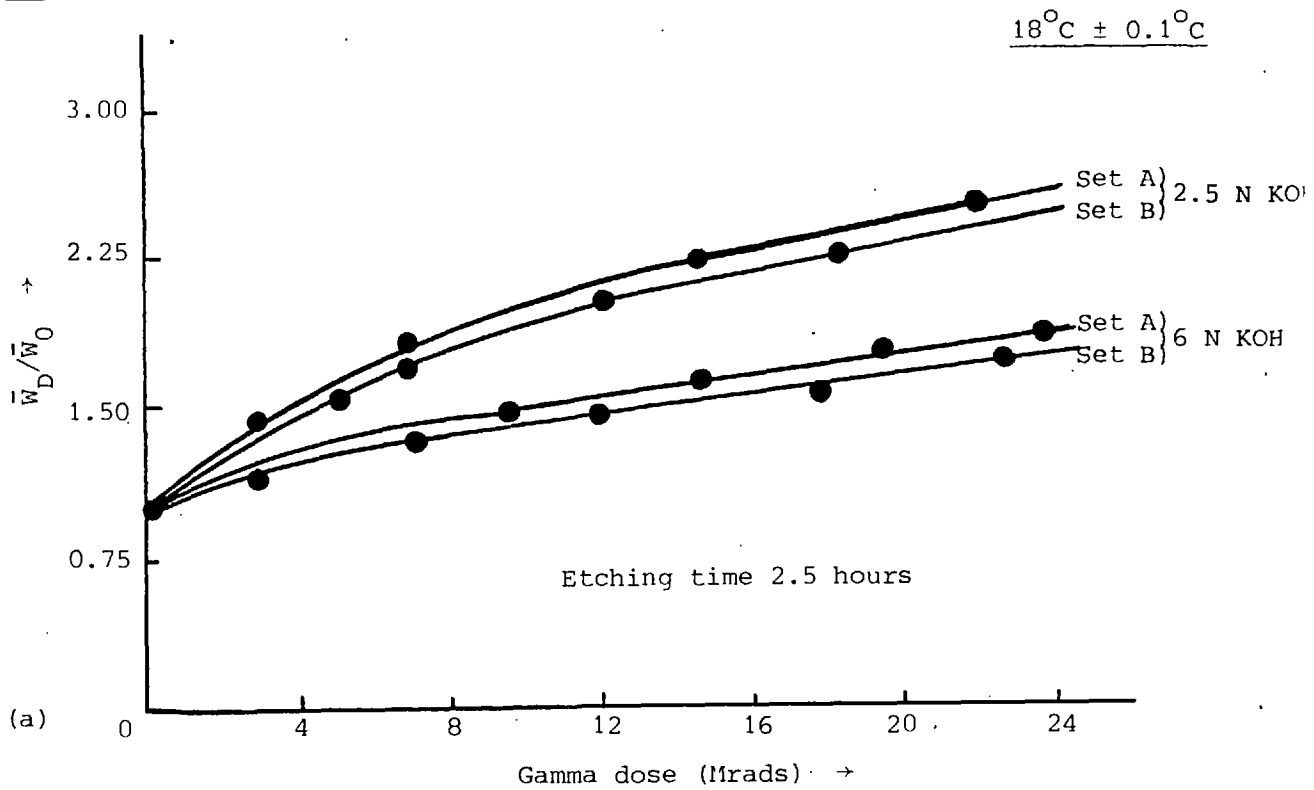


Figure 6.81 The ratio of \bar{W}_D/\bar{W}_0 (the average width of etched fission fragment tracks at gamma doses of "D-megarads" and "zero-megarads") of CA 80-15 cellulose nitrate versus gamma dose, etched in 2.5 N and 6 N KOH at (a) 18°C and (b) 50°C , without interruptions or stirring

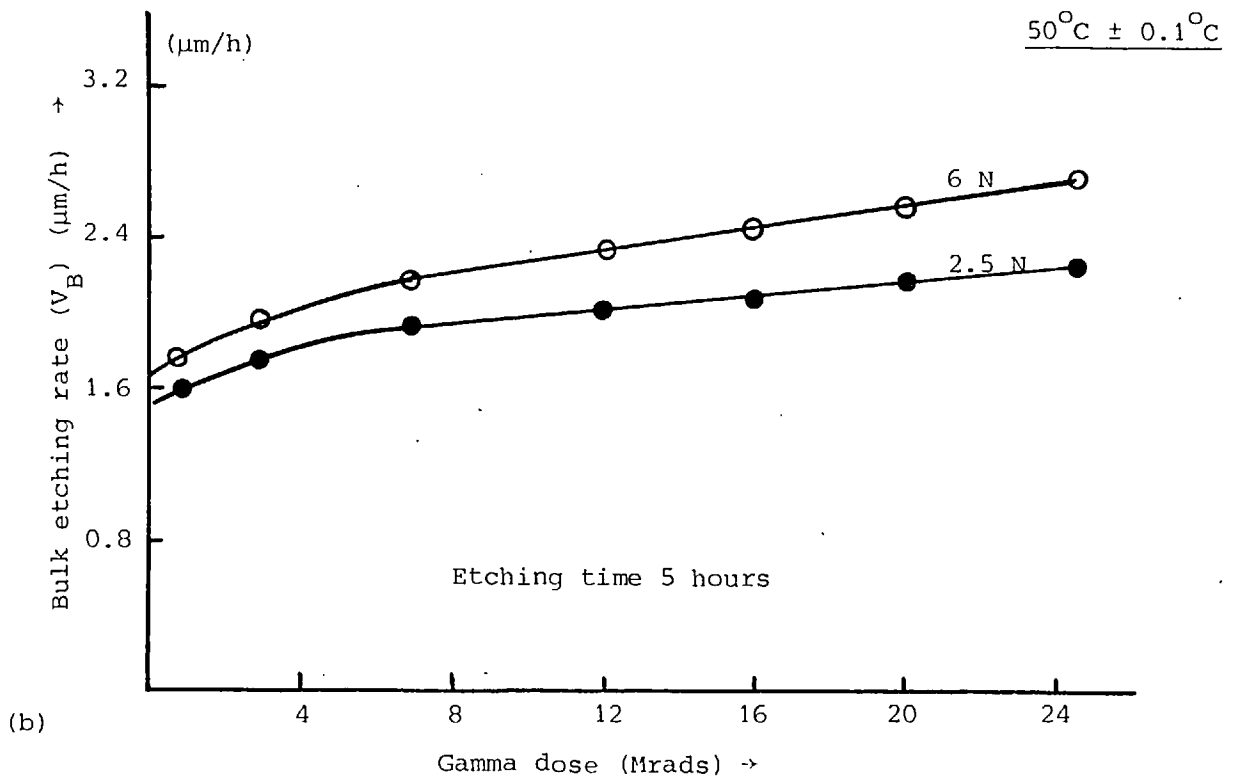
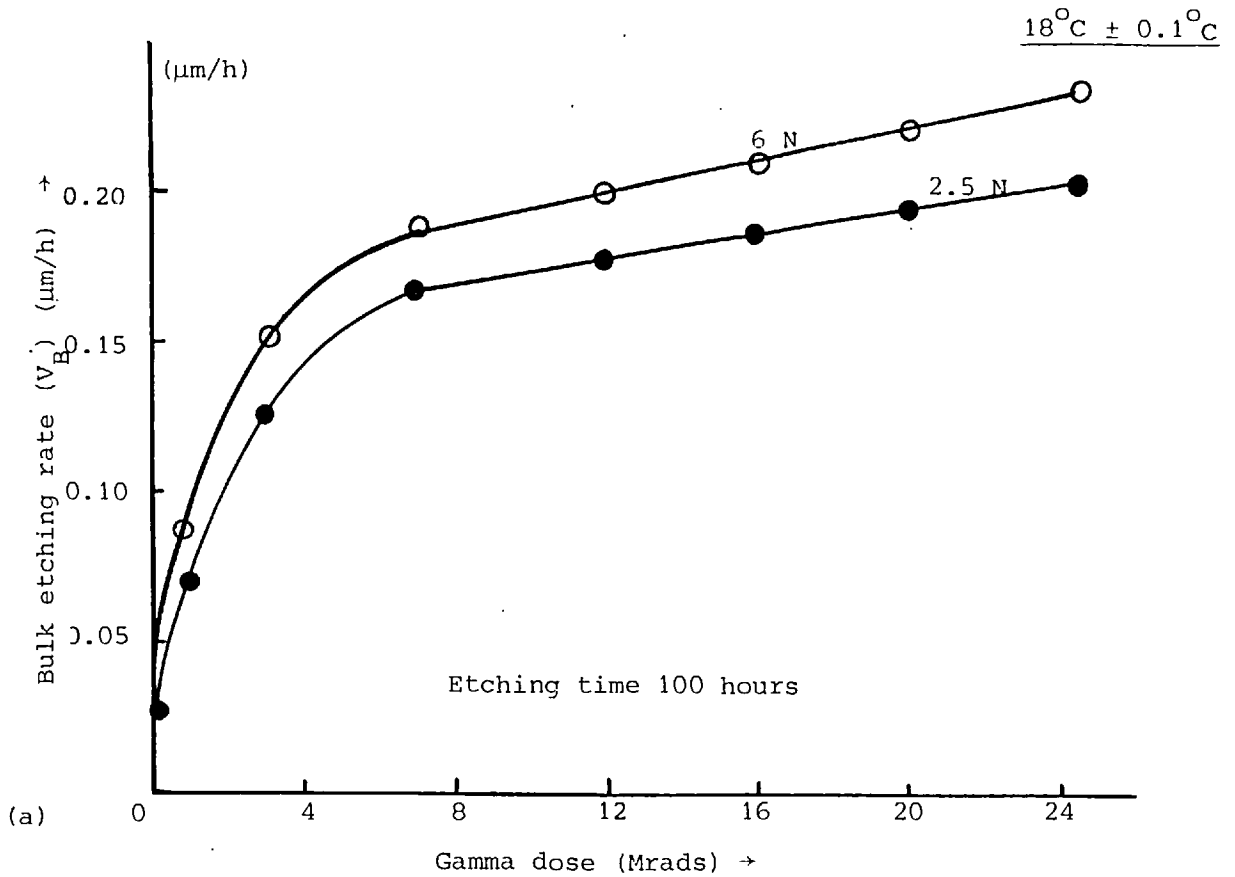


Figure 6.82 Bulk etching rate of CA 80-15 cellulose nitrate versus gamma dose (a) etched in 2.5 N and 6 N NaOH at 18°C without interruption or stirring, and (b) etched in 2.5 N and 6 N NaOH at 50°C without interruption or stirring.

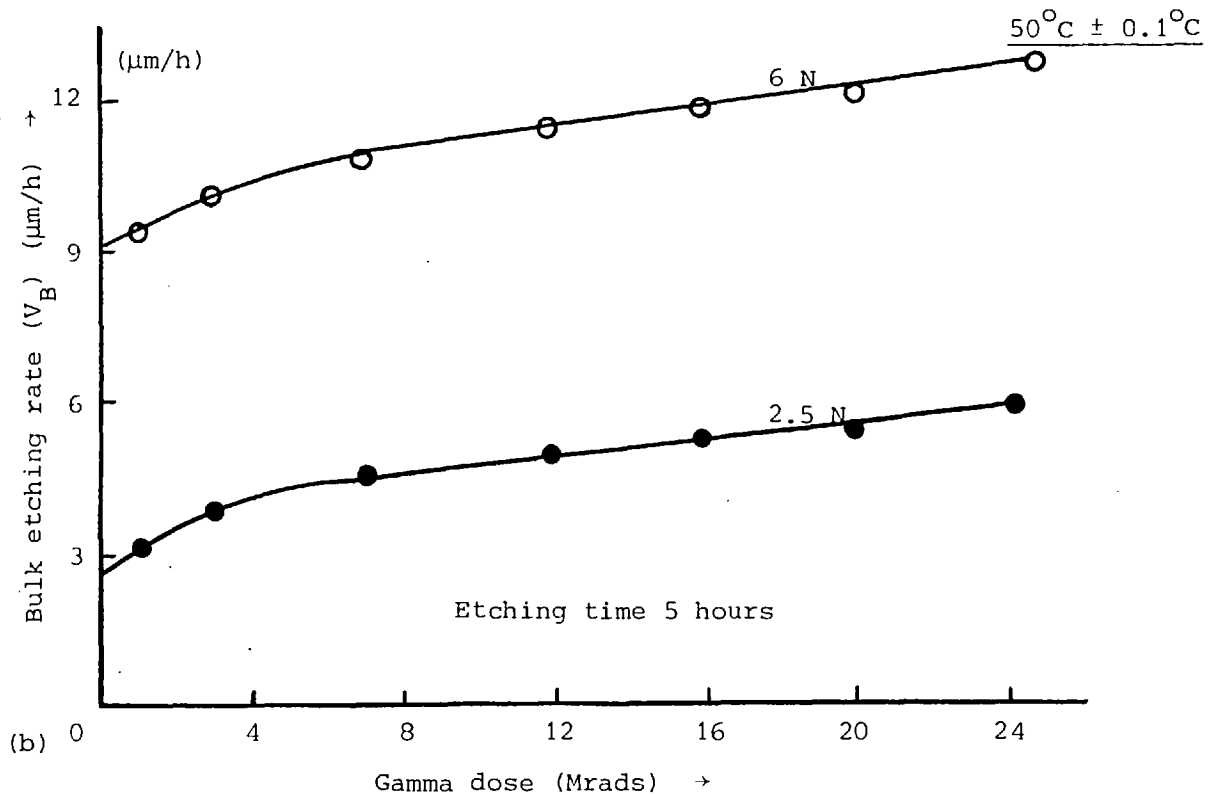
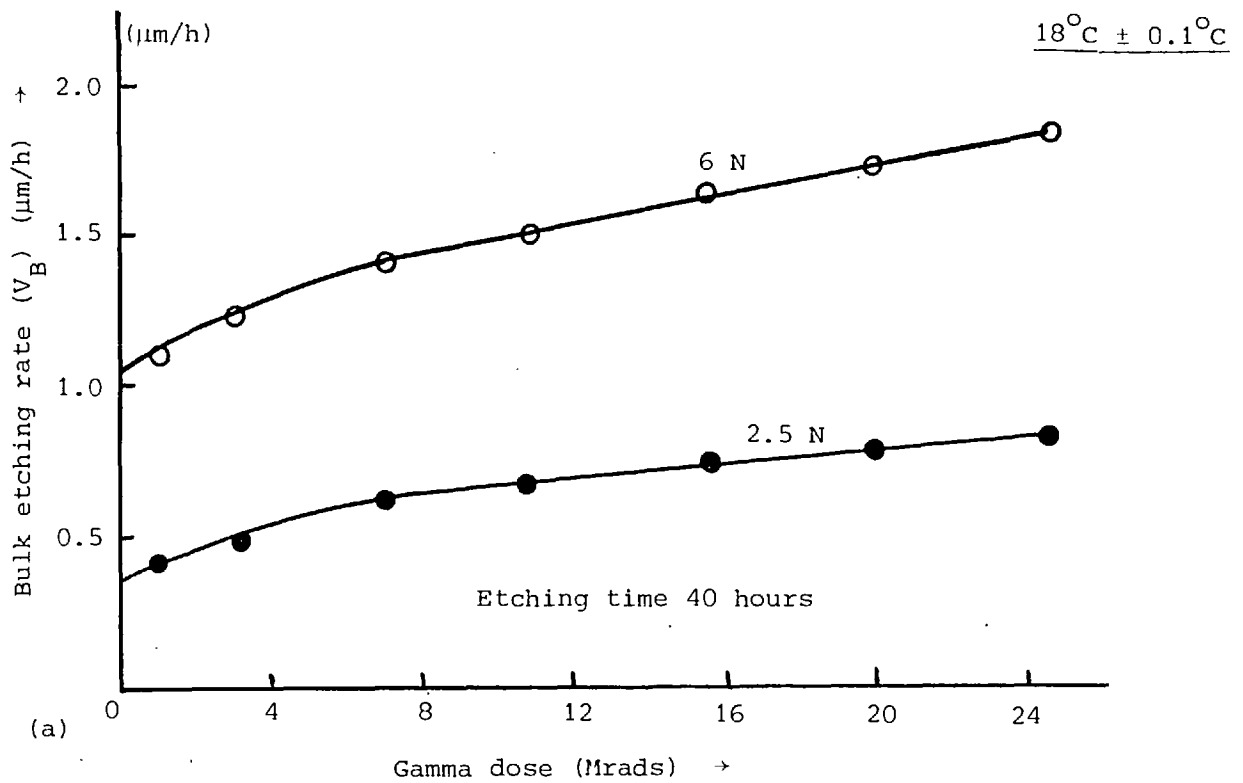


Figure 6.83 Bulk etching rate of CA 80-15 cellulose nitrate versus gamma dose (a) etched in 2.5 N and 6 N KOH at 18°C without interruptions or stirring, and (b) etched in 2.5 N and 6 N KOH at 50°C without interruption or stirring.

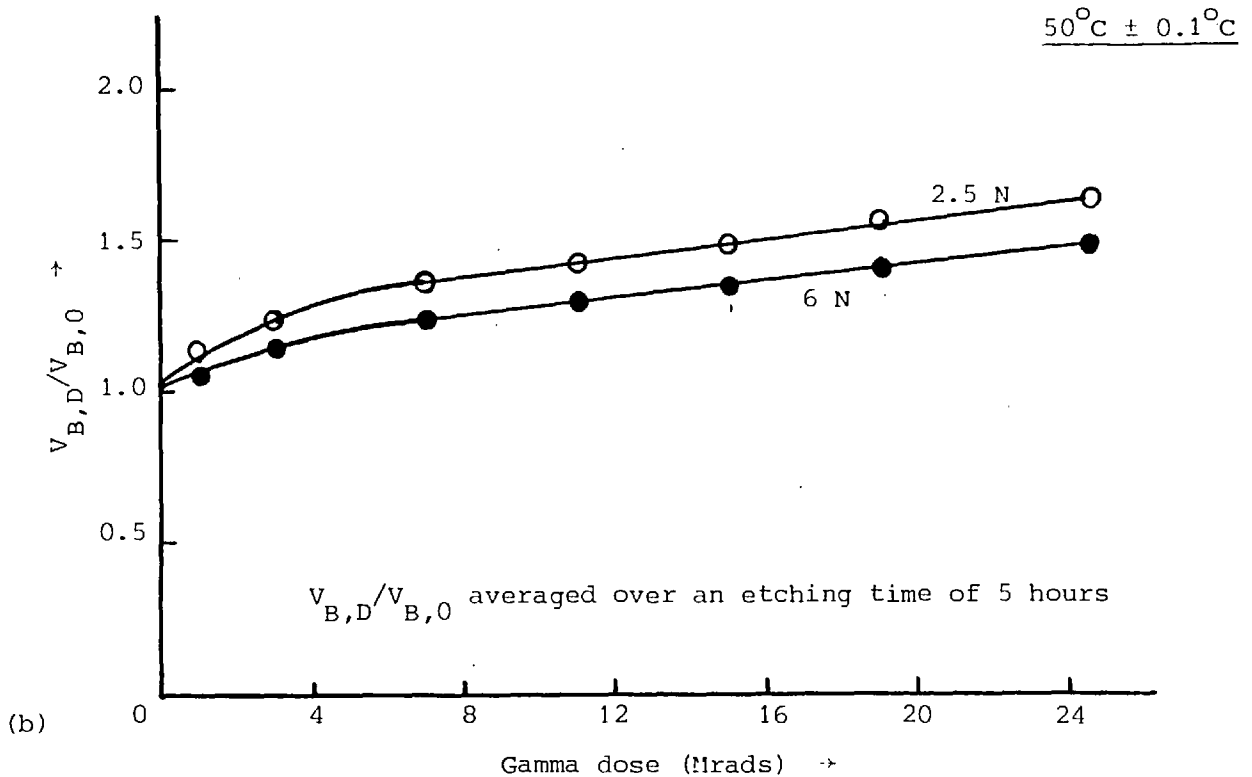
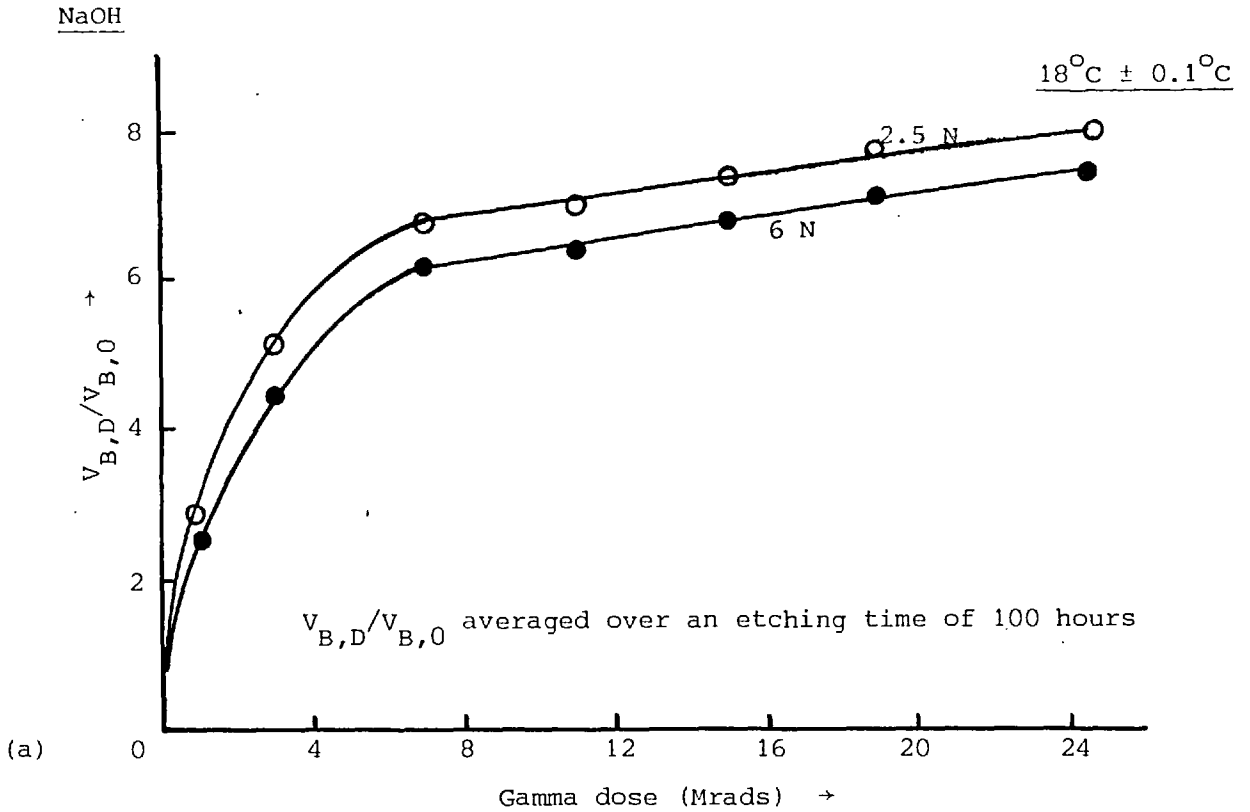


Figure 6.84 The ratio of $V_{B,D}/V_{B,0}$ (the ratio of the bulk etching rate at gamma doses of "D-megarads" and zero-megarads) of CA 80-15 cellulose nitrate versus gamma doses, etched in 2.5 N and 6 N NaOH at (a) 18°C , and (b) 50°C , without interruptions or stirring

KOH

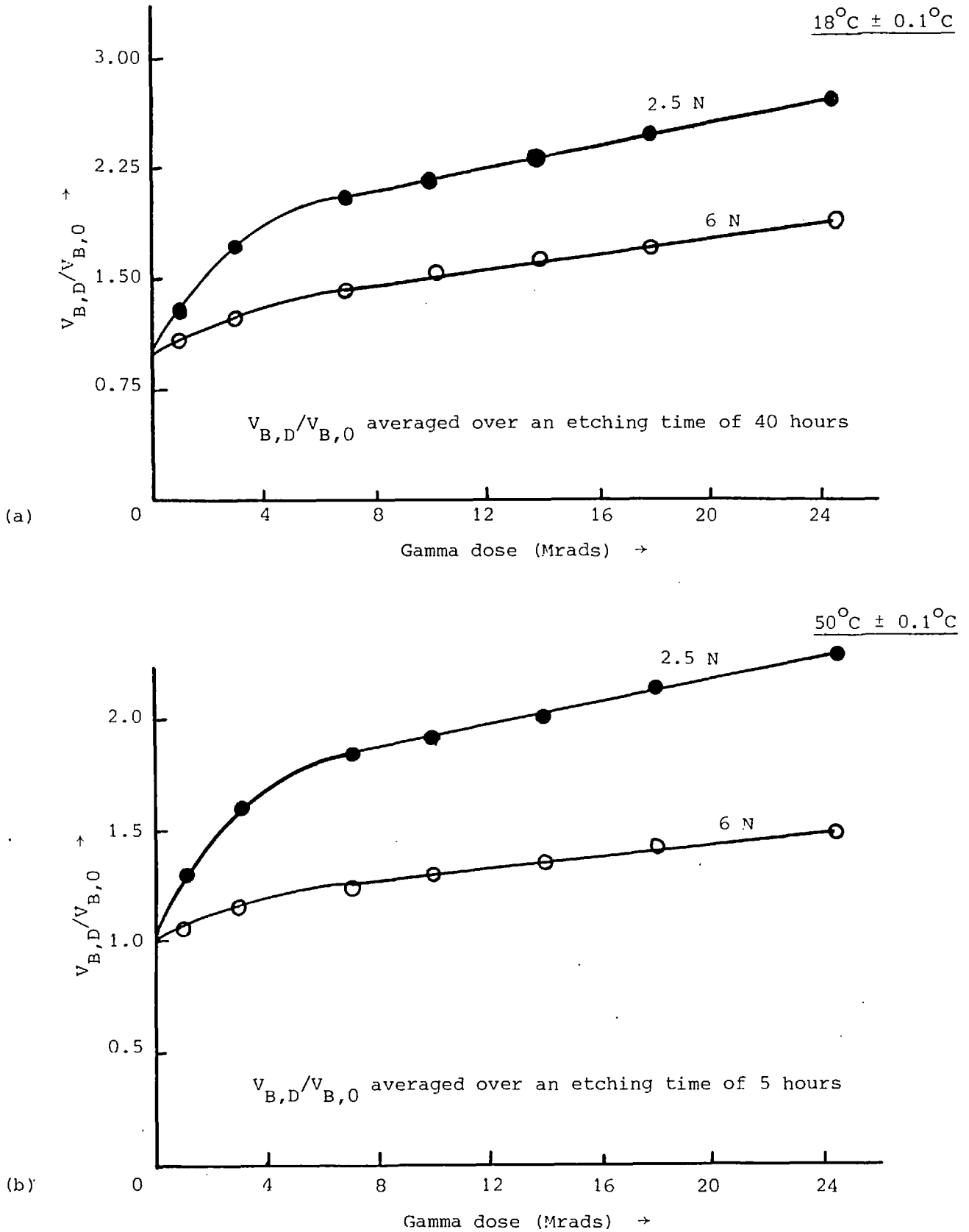


Figure 6.85 The ratio of $V_{B,D}/V_{B,0}$ (the ratio of the bulk etching rate at gamma doses of "D-megarads" and zero-megarads) of CA 80-15 cellulose nitrate versus gamma doses, etched in 2.5 N and 6 N KOH at (a) 18°C, and (b) 50°C, without interruptions or stirring

A possible explanation of these results is the phenomenon of swelling observed in cellulose and its derivatives in alkaline solutions at low temperatures. Swelling is known to be quite large below 20°C (101), but negligible above 30°C. At the same time, swelling is maximized at an ion concentration of about 2.5N, which is the "optimal" etching condition E₁ and E₃. The swelling is related to the diffusion of ions into the cellulose due to ion-exchange with acidic (carboxyl) groups. Since radiation damage involves the creation of such groups in cellulose nitrate, the swelling is considerably increased, and hence the bulk etching rate V_{B,D} as well, since the more rapid penetration of the surface by ions will increase the rate of reaction and of dissolution of the surface.

It should be noted that the efficiency of the detectors etched under conditions E₁ and E₃ is higher than under E₂ and E₄, as shown by the capability of the etchant to reveal tracks at smaller angles of incidence and smaller linear energy transfer. Thus, for track counting purposes, it is advisable to use etching conditions E₁ or E₃.

6.11.2 Measurement of Fast Reactor Reaction Rates using Solid State Track Recorders

The knowledge of the reaction rate in all the constituent materials in a reactor is of fundamental importance to understand the neutron balance. Measuring these reaction rates usually necessitates a small detector, to avoid the perturbations in the neutron flux on insertion in the reactor.

It is of interest to the reactor physicist and nuclear engineer to develop a solid state track recorder technique capable of accurate quantitative detection of relative and absolute (n,α) reaction rates; solid state track recorders made up of CA80-15 films in contact with a suitable source material are irradiated in the required positions within a reactor.

After irradiation the films are etched, and the tracks left by alpha and lithium particles are counted by eye or by a device coupled to an analysing computer. The (n,α) reaction rate is then determined.

Preliminary experiments (138) showed that the Kodak-Pathé LR-115 Type II cellulose nitrate film is a good material for alpha and ⁷Li particle detection. Also in this work, it was shown that CA80-15 cellulose nitrate is considerably better than LR-115 Type II for

detecting alpha and ${}^7\text{Li}$ particles and an etching condition was established which minimizes the influence of high γ -ray doses encountered in the reactor core, on the properties of these detectors. Thus it was decided to measure the (n,α) reaction rates in boron carbide pellets using CABO-15 cellulose nitrate irradiated in different neutron spectra.

Major emphasis was given to the ${}^{10}\text{B}(n,\alpha){}^7\text{Li}$ reaction and measurements of (n,α) reaction rates have been made in boron, as used for fast reactor control rods. The SSTR consisted of a boron carbide pellet covered with an appropriate plastic. It should be noted that the surface of the pellet was carefully polished before applying the film to ensure that the plastic was evenly in good contact with the pellet over its entire surface.

The predominant reason for choosing an SSTR geometry as above was that the target of the present work included a feasibility study on an SSTR technique for measuring the variation of neutron absorption, i.e. the (n,α) reaction rate through a large boron control rod of the type which has been proposed for fast breeder reactor systems. In this case, it was important that the reaction rate should be measured throughout the cross-section of the control rod and that the detector should not result in any perturbation within the rod.

6.11.2.1 Relative (n,α) Reaction Rate Ratios

It was decided to compare (n,α) reaction rates, measured using an SSTR technique as described previously, with (n,α) reaction rates measured with a BF_3 counter. The latter makes an ideal monitor since it measures the reaction rate in ${}^{10}\text{B}$.

In order to establish if the detector was spectrum dependent, a range of reaction rates was measured in a number of different neutron spectra from thermal up to that similar to a fast reactor.

The NISUS facility (see Reference (110)) installed in the reactor CONSORT of London University provides an intermediate neutron spectrum having mean neutron energies from a few KeV up to mean neutron energies somewhat "harder" than those appearing in a typical fast breeder reactor.

Thermal spectra exist in any position of the graphite stack of the thermal column extension of the reactor. To economise in the overall number of irradiations, it was decided to utilise the same experiments for both purposes, i.e. measuring at the same time relative (n,α) reaction rate ratios and also (n,α) reaction rate ratios in two different neutron

spectra. One spectrum was a thermal neutron spectrum produced in the thermal column of the University of London Reactor CONSORT and is denoted as Spectrum 1. The second spectrum denoted Spectrum 8, was a neutron spectrum similar to that of a fast breeder reactor and was produced in the NISUS facility on CONSORT. Hence, it became necessary to assemble the SSTR and the BF₃-counter together so that the centre of the pellet and the centre of the BF₃-counter active-volume were on the same radius of a common cross-section and equally distant from the centre of the NISUS cavity (110). The dimensions of the NISUS facility dictated the use of a miniature BF₃-monitor.

The arrangement of the B₄C pellets and SSTR is shown in Figure 6.86. A film, protected from the B₄C pellet, was also irradiated for background detection. Finally, a BF₃-counter and a fission chamber were used for monitoring purposes.

The details of the irradiations performed in the NISUS cavity and thermal column and given in Table 6.14.

The quantity to be determined with a target accuracy of ± 3% was:

$$\begin{aligned} \text{Ratio} &= \frac{(\alpha + {}^7\text{Li}) - \text{tracks per unit area}}{\text{BF}_3\text{-dose}} \\ &= \frac{\text{TCRPUA}}{\text{BF}_3\text{CR}} \end{aligned} \quad \left. \vphantom{\begin{aligned} \text{Ratio} &= \frac{(\alpha + {}^7\text{Li}) - \text{tracks per unit area}}{\text{BF}_3\text{-dose}} \\ &= \frac{\text{TCRPUA}}{\text{BF}_3\text{CR}} \end{aligned}} \right\} (6.100)$$

TCRPUA is the track count rate per unit time per unit area; time refers to the irradiation length at a reference reactor power and area refers to the surface of the plastic in contact with the pellet (e.g. (α + ⁷Li) - tracks/100 kW.min/mm²).

BF₃CR is the BF₃-count rate referred to the same reactor power (e.g. BF₃-counts/100 kW.s).

It should be noted here that the target accuracy for the relative reaction rates was specified to be of the order of ± 3% following a suggestion made by WINFRITH ATOMIC RESEARCH ESTABLISHMENT.

The tracks of concern should be due to α and ⁷Li particles emerging from (n,α) reactions (i.e. ¹⁰B(n,α)⁷Li) taking place inside the B₄C-pellet only. It was therefore necessary for allowance to be made for any possible background of tracks that might impair the measurements. To check the performance of the present SSTR and the reproducibility of the whole experimental procedure, various reactor

powers were used. Thus, when determining the quantity ratio of equation (6.100), reference was made to a standard reactor power. It should be noted that the track count rate in equation (6.100) corresponds to the actual number of tracks detected by the counting method, which by no means can be considered to be equal to the number of tracks registered in the plastic (i.e. the number of particles leaving damage trails on the plastic).

6.11.2.2 Reaction Rate Ratios in Several Neutron Spectra

Measuring reaction rate ratios in several neutron spectra, using SSTRs implies comparisons of the ratios of the respective track densities (or the respective values of the TCRPUA when several reactor powers are employed). In other words, if two SSTRs are irradiated in two different neutron spectra, the ratio of the respective track densities (or TCRPUAs) gives an estimate of the ratio of the corresponding actual reaction rates.

A theoretical model (109) was developed to relate the TCRPUA (i.e. track count rate per unit area per unit irradiation length) with the actual reaction rate, RR, inside the particle-generating material, through a factor predominantly dependent on the neutron spectrum. This factor was called the "response" of the film and is calculated separately for each particle and each neutron energy, so that \bar{R}_p (S) corresponds to particles p and represents an average value characterised by the neutron spectrum and the reaction under consideration.

To create the model, it was necessary to know:

- (a) Geometry of the system,
- (b) Initial energy spectrum of the particles of interest,
- (c) Ranges, stopping powers and removal cross-sections for charged "proton-like" particles,
- (d) Neutron spectra or mean neutron energies weighed over the cross-sections of the reaction of concern,
- (e) "Particle energy limits for track detection" and "critical angle of particle incidence relative to the film surface for track detection". (N.B. This terminology implies that these magnitudes are different in concept with regard to the respective magnitudes "energy limits for track formation" and "critical angle for etching",

(f) Detection efficiency,

(g) Absolute neutron fluxes of the respective neutron spectra.

The geometry employed by this model is $-2\pi-$ in the sense that particles strike only one of the film-recorder surfaces out of the present SSTR arrangement. Provision has been made in the model to simulate two major experiments, i.e.:

(i) The SSTR is subjected to an isotropic neutron flux.

(ii) The SSTR is bombarded by a collimated neutron beam.

Case (i) pertains to the actual reactor experiment simulated by the CONSORT reactor experiments. Case (ii) was considered mainly because the absolute calibration of the detector together with a point-to-point examination of the model's credibility might dictate the use of well controlled neutron beams.

Considering the neutron spectra 1, 8 and 1', 8', the following equations may be written for reaction rates in two different types of detectors:

SSTR

$$\text{TCRPUA}_1 = \{\bar{R}_\alpha(S_1) + \bar{R}_{\text{Li}}(S_1)\} \cdot N_{\text{B}_4\text{C}}^{10} \cdot K_1 \cdot \int_0^\infty \phi_1(E) \sigma(E) dE \quad (6.101)$$

$$\text{TCRPUA}_8 = \{\bar{R}_\alpha(S_8) + \bar{R}_{\text{Li}}(S_8)\} \cdot N_{\text{B}_4\text{C}}^{10} \cdot K_8 \cdot \int_0^\infty \phi_8(E) \sigma(E) dE \quad (6.102)$$

BF₃-counter

$$\text{BF}_3\text{CR}_1 = C \cdot N_{\text{BF}_3}^{10} \cdot K_{1'} \cdot \int_0^\infty \phi_{1'}(E) \sigma(E) dE \quad (6.103)$$

$$\text{BF}_3\text{CR}_8 = C \cdot N_{\text{BF}_3}^{10} \cdot K_{8'} \cdot \int_0^\infty \phi_{8'}(E) \sigma(E) dE \quad (6.104)$$

where $\text{TCRPUA}_1, \text{TCRPUA}_8$ are the track count rates per unit area in spectra 1 and 8 respectively;

$\text{BF}_3\text{CR}_1, \text{BF}_3\text{CR}_8$, are the BF₃-count rates in spectra 1' and 8';

$N_{\text{B}_4\text{C}}^{10}, N_{\text{BF}_3}^{10}$ pertain to the corresponding numbers of ¹⁰B atoms per cm³ in the B₄C-pellet and BF₃-counter gas;

$K_1, K_8, K_{1'}, K_{8'}$, pertain to the respective spectra normalisation factors over the total absolute fluxes;

C is a constant referring to the discrimination level and analog to digital conversion of the electronics related to the BF_3 -counter.

Supposing now that the two detectors have been mounted in the same position so that spectrum 1 \equiv 1' and 8 \equiv 8', the following can be obtained:

$$\begin{aligned} \text{Ratio}_1 &= \frac{\text{TCRPUA}_1}{\text{BF}_3\text{CR}_1} \\ &= \{ \bar{R}_\alpha(S_1) + \bar{R}_{\text{Li}}(S_1) \} \frac{N_{\text{B}_4\text{C}}^{10}}{C N_{\text{BF}_3}^{10}} \end{aligned} \quad (6.105)$$

$$\begin{aligned} \text{Ratio}_8 &= \frac{\text{TCRPUA}_8}{\text{BF}_3\text{CR}_8} \\ &= \{ \bar{R}_\alpha(S_8) + \bar{R}_{\text{Li}}(S_8) \} \frac{N_{\text{B}_4\text{C}}^{10}}{C N_{\text{BF}_3}^{10}} \end{aligned} \quad (6.106)$$

$$\frac{\bar{R}_\alpha(S_1) + \bar{R}_{\text{Li}}(S_1)}{\bar{R}_\alpha(S_8) + \bar{R}_{\text{Li}}(S_8)} = \text{RATIO} = \frac{\text{Ratio}_1}{\text{Ratio}_8} \quad (6.107)$$

$$\frac{\text{TCRPUA}_1}{\text{TCRPUA}_8} = \frac{\bar{R}_\alpha(S_1) + \bar{R}_{\text{Li}}(S_1)}{\bar{R}_\alpha(S_8) + \bar{R}_{\text{Li}}(S_8)} \cdot \frac{\text{RR}_1}{\text{RR}_8} \quad (6.108)$$

where RR_1 , RR_8 correspond to actual reaction rates inside the particle generating material.

It is already apparent that equations (6.105) and (6.106) pertain to relative reaction rate ratios (see also equation (6.100)) in two different neutron spectra, and equation (6.106) can be used to estimate the respective ratio of the actual reaction rates in these spectra. Moreover, the quantity RATIO of equation (6.107) can be determined both theoretically and experimentally and can be used in a first approximation, to cross-examine the model's reliability.

Checking the theoretical calculations in the manner indicated by equation (6.107) has two major advantages:

- (a) Absolute neutron fluxes do not enter the comparison. This is very important when considering the difficulty to determine with a good accuracy absolute neutron fluxes, especially in fast neutron spectra.
- (b) The "detection efficiency" and "critical angle for particle detection" appear in the calculations as constants of very minor dependence on neutron spectrum. On the other hand, probable errors (within reason) in these values and in the values of the "particle energy limits for track detection" do not significantly alter the value of the quantity RATIO, as will become explicit in due course.

6.11.2.3 Absolute Reaction Rates and Absolute Neutron Fluxes

The basic relation for reaction rates, given by the model for the SSTR is:

$$\text{TCRPUA} = \{ \bar{R}_{\alpha}(S) + \bar{R}_{\text{Li}}(S) \} \cdot \text{RR} \quad (6.109)$$

where RR is the $^{10}\text{B}(n,\alpha)$ reaction rate. $\bar{R}_{\alpha}(S)$, $\bar{R}_{\text{Li}}(S)$ are the mean responses of the SSTR for α and ^7Li particles, respectively, as functions of the neutron spectrums.

or,

$$\text{TCRPUA} = \{ \bar{R}_{\alpha}(S) + \bar{R}_{\text{Li}}(S) \} \cdot N^{10} \cdot K \cdot \int_0^{\infty} \phi(E) \sigma(E) dE \quad (6.110)$$

with $K = \text{AF} / \int_0^{\infty} \phi(E) dE$, AF = absolute neutron flux, RR = the reaction rate.

Hence:

$$\text{TCRPUA} = \{ \bar{R}_{\alpha}(S) + \bar{R}_{\text{Li}}(S) \} \cdot \bar{\Sigma}_{\alpha} \cdot \text{AF} \quad (6.111)$$

where $\bar{\Sigma}_{\alpha}$ is an estimate of the average macroscopic absorption cross-section for the $^{10}\text{B}(n,\alpha)^7\text{Li}$ reaction.

It is apparent that equation (6.109) can be used for absolute reaction rate measurements, while equation (6.111) can be utilised in measuring absolute neutron fluxes. However, to enable this type of measurement to be performed with a "good" degree of accuracy, the values of $\bar{R}_{\alpha}(S)$ and $\bar{R}_{\text{Li}}(S)$ must be known as precisely as possible. The latter can only happen if the parameters involved with the calculation of the absolute value of the "response" of the SSTR can be determined with confidence.

These parameters are:

- (i) Particle energy limits for track detection.
- (ii) Particle angle of incidence relative to the film surface for

track detection.

(iii) Counting-detection efficiency.

Determination of the above conditions necessitates complete understanding of all the factors involved. This requires knowledge of the track formation mechanism and the effects of the etching procedure on the respective damage trails.

The geometry of the detector is shown in Figure 6.86 and a computer programme was written (109) to calculate $\bar{R}_\alpha(S)$ and $\bar{R}_{Li}(S)$ for this geometry. The actual variation of detection efficiency with alpha (and lithium) particle energy and angle of incidence has been measured previously, and a sine function and a flat function were assumed as shown in Figure 6.87 (in fact both functions gave identical results when used in the model). The detection efficiency is, in fact, the counting efficiency defined as the number of tracks counted divided by the number of particles incident on the SSTR surface. The efficiency of the detector is shown in Figure 6.87 to have an upper and lower limit. The limits used for the CA80-15 film were as follows: $E_U = 4$ MeV and $E_L = 150$ KeV for α particles and $E_U = 8.5$ MeV and $E_L = 250$ KeV for ${}^7\text{Li}$ particles.

6.11.2.4 Counting Techniques

(a) Counting by Eye

Counting by eye was performed using a gridded graticule ocular in a transmitted light microscope. The grid-frame with a 40x objective was calibrated to be 0.057×0.057 mm².

When tracks intersected the grid-frame counts were taken only when the upper and left sides were intersected. Track overlap corrections were performed by eye, discriminating double, triple, etc., overlapping by the size of the track.

Eye-counting was found to be extremely laborious and time-consuming. However, considering the eye as the best possible detector, it was decided to use eye-counts as bench-mark observations for the optimisation of automatic counting techniques.

(b) Automatic Counting

Automatic counting was performed using a Quantimet QTM-720 Image Analysing Computer at the Fulmer Research Laboratories.

The overall magnification from the microscope stage to the Vidicon

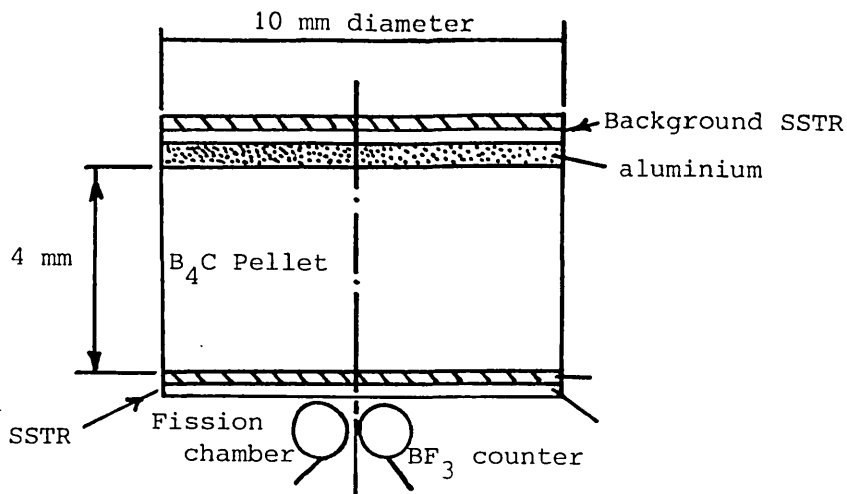


Figure 6.86 Experimental geometry used in the irradiation of boron carbide pellets for the measurement of $^{10}B(n,\alpha)$ reaction rates

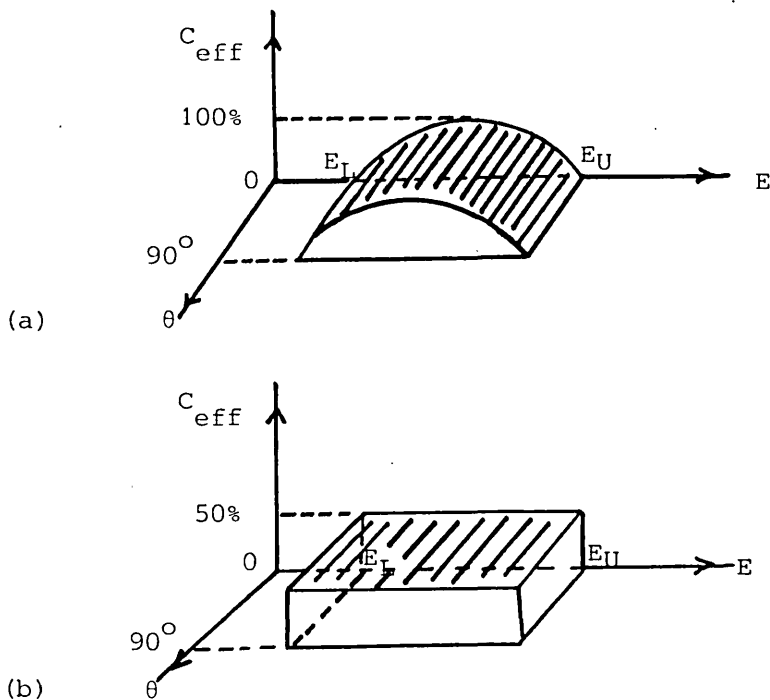


Figure 6.87 Functions assumed for the variation of particle detection efficiency as a function of particle energy and angle of incidence. E_L , E_U are the lower and upper energy limits for track registration respectively, C_{eff} is the counting efficiency, E is the particle energy and θ is the particle angle of incidence relative to the SSTR surface. a. Sinusoidal efficiency, b. Flat efficiency between the sensitivity-energy range limits of 100%.

camera-screen was 1030X and the full QTM frame was used, i.e. 0.237 x 0.185 mm². The overlapping correction was performed by setting two boundary numbers in the form-separator corresponding to the track-area in picture points (p.p.) and separating the track-area universe in three regions, as follows:

Region	Description
3 1100 p.p.	Triple overlapping Equivalent area, circle diameter = 10.3 μm
2 630 p.p.	Double overlapping Equivalent area, circle diameter = 7.8 μm
1	Single Tracks

Hence the number of tracks per frame was:-

$$\text{TPF} = (\text{Number of singles}) + 2(\text{Number of doubles}) + 3(\text{Number of triples})$$

The numbers 1100 and 630 were found by a trial and error procedure by having as a reference real overlaps as counted by eye from the screen. These numbers fit realistic requirements with a better than 2% accuracy, except for extremely high track overlap where agglomeration of four and five tracks becomes significant. This procedure ensures a secure and standard overlap correction, since there is no problem associated with the area measurement or the sort of tracks counted (whether white or black or inbetween) as long as the modified QTM mode is used (i.e. darkening of the area enclosed by the perimeter of the track).

Scanning of the film is automatic on the QTM 720 using the programmable stage control system. Repeatability of positioning of the field of view is essential to ensure correct scanning. Repeatability of the stage position was checked by counting the same field of view several times, after the stage had been moved and repositioned. The field count was exactly the same each time a field of view was repeated.

6.11.2.5 Statistical Analysis of the Counting

The major consideration here is that the experimental set-up is precisely the same, between experiments of the same series (i.e. irradiations

in the same positions and in the same neutron-spectrum) and that the etching process is absolutely reproducible.

Hence, the stochastic variables TPF (tracks per frame) and TCRPF (($\alpha + {}^7\text{Li}$) track count rate per frame) must belong to a statistical population of the same universe, having the same distribution parameters, between all the count-samples of the same experimental series.

When the variable TCRPF is employed, allowance must be made for different reactor powers (Table 6.14) and track background. The first is performed by always normalising to 100 kW minutes whilst the second (i.e. background subtraction) is performed as follows:

Films 503* and 307* in Table 6.14 constitute the background measurements. The track density on the film 503* was found to be about 10 times smaller than that on the film 307*.

The tracks on the film 503* were considered to constitute a permanent background (due to irregularities) though the tracks on the film 307* were considered to consist of the permanent background, plus a time varying background. The latter was attributed to neutron reactions that may occur at high neutron energies (like those of spectrum 8) inside the cellulose nitrate of the CA80-15 ($\text{C}_6\text{H}_8\text{N}_2\text{O}_9$). Reactions of this sort are mainly knock-on protons, ${}^{12}_6\text{C}(n,n')\ 3\alpha$ and ${}^8\text{O}(n,\alpha)$.

The following two different methods of background subtraction were therefore obtained:

Thermal Neutron Spectrum 1

$$\bar{x}'_i = (\bar{x}_i - \bar{x}_{\text{Bp}})/T_i \quad (6.112)$$

$$s'_i = \sqrt{s_i^2 + s_{\text{Bp}}^2}/T_i \quad (6.113)$$

Fast Neutron Spectrum 8

$$\bar{x}'_i = (\bar{x}_i - \bar{x}_{\text{Bp}})/T_i - (\bar{x}_B - \bar{x}_{\text{Bp}})T_B \quad (6.114)$$

$$s'_i = \sqrt{(s_i/T_i)^2 + (s_B/T_B)^2 + \{s_{\text{Bp}}(T_B - T_i)/T_i \cdot T_B\}^2} \quad (6.115)$$

where:

\bar{x}_i , \bar{x}_B , \bar{x}_{Bp} and s_i , s_B , s_{Bp} are the mean values and standard deviations of the variable tracks per frame for the i^{th} film count-sample, background and permanent background respectively (in tracks per frame).

T_i , T_B are the irradiation lengths for the i^{th} film count-sample and background respectively (in 100 kWmin).

TABLE 6.14

NISUS Cavity - Spectrum 8

Film No.	Reactor Power (kW)	Irr. Time (Min)	BF ₃ -counts x10 ⁶	FC-counts x10 ⁶
307	100	10	3.92	1.72
409	50	20	3.90	1.68
407	50	10	2.02	0.858
309	100	5	1.96	0.866
307*	100	10	3.92	1.72
501	100	40	1.69	0.473
503	100	20	0.849	0.236
505	50	20	0.428	0.112
507	100	30	1.29	0.342
503*	100	20	0.849	0.236

* Films for Background measurements

\bar{x}'_i and s'_i are the mean value and the standard deviation of the variable TCRPF for the i^{th} film count-sample in $(\alpha + {}^7\text{Li})$ tracks/100 kW.min/frame.

The present statistical analysis employs the following tests.

(a) χ^2 - Test of Quality of Fitting

The stochastic variable, TPR, is employed. The quality of fitting of every count-sample population versus the theoretical Poisson distribution is examined. Several numbers of classes were used so that the whole region of sample sizes of the present work was safely covered.

This test is mainly a check against the randomness of counting, (sampling) and high unbalanced systematic errors of the counting machine.

High confidences of fitting should be expected only under good random-sampling conditions and limited balanced systematic errors (on the ground that the randomness of the track distribution is guaranteed by the uniformity of track registration properties of the CA80-15 film and uniformity of ${}^{10}\text{B}$ distribution in the B_4C pellet).

(b) Two-Mean Value Tests

The mean value of the stochastic variable TCRPF is employed. Combinations by two, from a given set of count-samples of the irradiated films, are examined.

In this way, systematic counting and experimental errors can be checked.

(c) Several Mean Values Tests

The confidence of the best estimate of the joint mean value of the variable TCRPF is tested.

Before deducing which count-sample combination is the most reliable, tests (b) and (c) are repeated after the replacement of the stochastic TCRPF by the stochastic variable Ratio as follows:-

$$\text{Ratio}_i = \bar{x}'_i / \text{BF}_3 \text{CR}_i \quad (6.116)$$

$$s_{R_i} = s'_i / \text{BF}_3 \text{CR}_i \quad (6.117)$$

where:

Ratio_i and s_{R_i} are the mean value and standard deviation of the variable Ratio = TCRPF/ BF_3CR (relative reaction rate), for the i^{th} film which after appropriate allowance for the area units, are given in

$$\frac{(\alpha + {}^7\text{Li}) \text{ tracks/100 kW.min/mm}^2}{\text{BF}_3 \text{ counts/S}}$$

Consideration of the variable (Ratio) as only one stochastic variable can be justified by the very small statistical error in the BF_3 counting. Under these conditions tests (b) and (c) should result in better confidences when the variable (Ratio) is checked on the grounds that the counting is consistent with the track densities encountered.

The data processing and statistical analysis has been fully automated. The data from sample counts, using the QTM 720, were output onto punched paper tape and subsequently fed into the Imperial College CDC-6400 computer, via a teletype terminal, and stored in data files. A computer program (109) was written to perform the statistical analysis.

Results

Examples of the experimental data, for the χ^2 and mean value tests described in the previous section, are shown in Tables 6.15, 6.16 and 6.17. The most reliable sample counts were then selected from the mean value tests and the confidence determined for the experimental track count rate per unit are (TCRPUA) and $(\text{TCRPUA}/\text{BF}_3\text{CR})$, these being shown in Table 6.18. It can be seen from Table 6.18 that the confidence for sets 1 and 2 have been improved by omitting sample 3090P from set 1 and 5030P from set 2 (see sets 3 and 4). This type of selection is fully justified on examining the mean value tests. For example, sample 3090P is shown in Table 6.17 to be unreliable compared to the other samples.

Finally, the most reliable experimental results are determined from the several mean value tests (c), illustrated by Table 6.18, and are shown in Table 6.19.

The results summarised in Table 6.18 show that relative (n,α) reaction rate ratio measurements can be made to an accuracy of better than $\pm 3\%$ using the SSTR technique. The experimental values for reaction rate RATIO between the two different spectra show that eye and automatic counting agree to within 1% which is well within experimental error. The theoretical value for Ratio is 5% high compared to the experimental values which is only 2% outside the experimental errors.

However, measurements of the track count rate per unit area show that the Quantimet is consistently overcounting the number of tracks by 9% as compared to eye counting. This indicates that the size discrimination level for track recognition is not being correctly set on the Quantimet 720. Further work is currently being done to improve the quality of tracks, particular emphasis being given to the contrast of

TABLE 6.15

χ^2 -Test (%) Confidence in Quality of Fitting

	Sample code	K1	K2	Confidence in fitting to a Poisson distribution (%)					
				K=3	K=4	K=5	K=6	K=K ₁	K=K ₂
QTM 720 counting	307P5C	10	8	1.2	4.2	8.3	13.2	25.5	33.7
	409P4C	10	9	19.2	31.9	58.9	64.4	-	16.3
	407P5C	10	8	16.0	35.2	37.2	58.1	-	66.1
	309P5C	13	9	0	0	0	0	-	0
	307P4B	12	9	71.6	93.3	34.4	77.2	-	51.9
Eye counting	3070P	8	8	76.2	95.2	92.2	80.1	-	-
	4090P	8	8	0.5	1.4	0.4	0.4	-	-
	4070P	10	8	50.9	69.4	88.2	82.5	46.2	90.4
	3090P	11	8	29.6	40.4	75.5	30.0	-	46.2
	3070PB	12	9	44.6	41.3	60.8	59.5	-	41.6

Note: K = Number of equal width classes

$$K_1 = \sqrt{N}$$

$$K_2 = 2 + 3.3 \ln(N)$$

N = Sample size

Confidences have been omitted for classes with an observed frequency below 5.

Sample Code: First three numbers denote the sample.

Letters P or OP denotes QTM 720 or Eye Counting respectively.

A number after P denotes day of counting.

C indicates that the overlap correction described in Section 4 has been used.

B denotes a background count.

TABLE 6.16

Mean Value Tests on the Track Count Rate Per Frame (TCRPF)
 Eye Counting - Spectrum 8

Confidence (%) for no difference							
Sample	3070P	4090P	4070P	3090P	TCRPF	N	TPF
3070P	100	84.0	24.5	6.0	2.26 ± 0.47	69	25.54 ± 0.57
4090P	84.0	100	15.2	2.7	2.25 ± 0.36	76	25.40 ± 0.40
4070P	24.5	15.2	100	49.7	2.38 ± 0.71	110	13.46 ± 0.34
3090P	6.0	2.7	49.7	100	2.44 ± 0.68	128	13.77 ± 0.30
307P2B	Background (Time Varying + Const.)					157	2.88 ± 0.05
503P2B	Background (constant only)					238	0.26 ± 0.01
Note: Stochastic variable employed TCRPF = Track Count per frame in ($\alpha + {}^7\text{Li}$) tracks/frame.100kW min. TPF = Tracks per Frame. N = Sample size QTM 720 Frame = 0.22 x 0.17 = 0.0374 mm ² Eye Frame = 0.057 x 0.057 = 0.00325 mm ²							

TABLE 6.17

Mean Value Tests on Ratio (TCRPUA/BF₃CR)

Eye Counting - Spectrum 8

Confidence (%) for no difference							
Sample	3070P	4090P	4070P	3090P	Ratio	N	Y/X
3070P	100	97.1	65.2	6.0	0.107 ± 0.022	69	0.91
4090P	97.1	100	60.0	3.8	0.107 ± 0.017	76	0.87
4070P	65.2	60	100	14.1	0.109 ± 0.032	110	1.07
3090P	6.0	3.8	14.1	100	0.115 ± 0.032	128	1.01
307P2B	Background (Time varying + Const.)					157	
503P2B	Background (Constant)					238	
<p>Note: Stochastic variable employed Ratio = Track Count Rate per unit area $\frac{(TCRPUA)/BF_3}{\text{Count Rate}(BF_3CR)}$</p> <p>Y = QTM 720 Track Count Rate per Frame (TCRPF)</p> <p>X = EYE-TCRPF</p>							

TABLE 6.18

Best Sample Count Combinations Using Tests (a) and (b)

Technique	Eye counting				QTM 720	Counting
	Nisus	Thermal	Nisus	Thermal	Nisus	Thermal
Experiment Set	1	2	3	4	5	6
Best Samples	3070P	5010P	3070P	5010P		
	4090P	5030P	4090P			503P5C
	4070P	5050P	4070P	5050P	407P5C	505P5C
	3090P	5070P		5070P	309P4C	507P5C
Background Samples	307P2B		307P2B		307P4BC	
	503P2B	503P2B	503P2B	503P2B	503P4B	503P4B
Confidence of the joint mean value for: <TCRPUA> and $\frac{\langle \text{TCRPUA} \rangle}{\text{BF}_3\text{CR}}$	4.2%	7.4%	26.7%	56.5%	2.4%	44.9%
	9.1%	9.0%	83.5%	56.4%	85.6%	23.7%

TABLE 6.19

Final Results Obtained from the Statistical Tests and
 Model for the following Parameters

(a) Track Count Rate per Unit Area <TCRPUA>

(b) Ratio = <TCRPUA/BF₃CR>

(c) $RATIO = \frac{\text{Ratio for Spectrum 1}}{\text{Ratio for Spectrum 8}}$

Method	Spectrum	<TCRPUA>	Ratio = $\frac{\text{TCRPUA}}{\text{BF}_3\text{CR}}$	RATIO = $\frac{\text{Ratio 1}}{\text{Ratio 8}}$
Eye Counting	1	68 ± 1	0.0957 ± 0.0017	0.893 ± 0.019
	8	702 ± 9	0.1071 ± 0.0015	
QTM 720 Counting	1	74 ± 1	0.1071 ± 0.0011	0.888 ± 0.012
	8	774 ± 6	0.1164 ± 0.0009	
Theoretical Model	1	89	-	0.934
	8	838	-	

tracks against background effects.

The automatic counting of tracks with the QTM 720 is certainly reproducible within error limits of $\pm 3\%$ and the system is easy to use, especially with the automatic focusing unit. However, the results showed that problems were encountered with counting track densities in excess of 5000 per mm^2 showing that the overlap correction is no longer valid above this track density.

The theoretical model is at present over-predicting the track count rate per unit area by about 20%. This is probably due to an incorrect assumption of the upper and lower limits of the theoretical detection efficiency of the detector (equation 2.2 or Reference (109)).

The influence of gamma radiation on the track parameters can be discriminated by varying the chemical etching conditions as discussed earlier.

Etching the detectors with low etchant concentrations and temperatures results in the following characteristics, as can be seen in Figures 6.80-6.85:-

1. Both the length and the width of the latent damage trail are affected for detectors exposed to gamma doses of the order of a few megarads.
2. The bulk etching rate (V_B) increases with increasing gamma dose.
3. The track registration efficiency is not affected by high doses of gamma rays.
4. Gamma doses below the megarad region do not affect the track-registration characteristics.
5. The change in track parameters (in the megarad region) or bulk etching rates can be employed as an index of gamma dose.
6. The small size of the detector can be advantageously used in odd locations like a reactor core (in core gamma dosimetry).

None of the above-mentioned points (with the exception of point 3.) was observed, when etching the detectors at high etchant concentrations and etching temperatures.

CHAPTER SEVEN

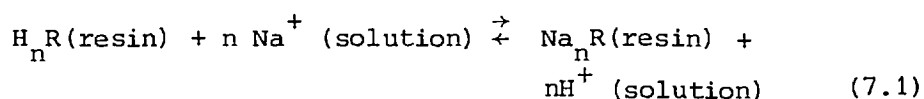
TRACK REVELATION BY BASE-EXCHANGE
AND FREE RADICAL TECHNIQUES

7.1 Introduction

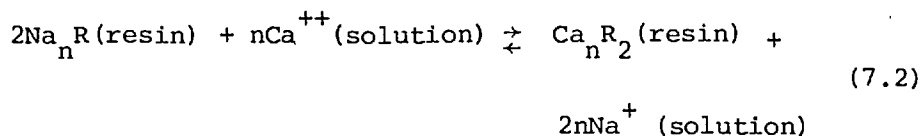
In this chapter, a general discussion of the base-exchange and free radical scavenging phenomena is presented, followed by consideration of their nature in cellulosic materials and their importance for track revelation in cellulose nitrate. The relationship of base-exchange and free radicals to the swelling of the track by etchants as well as various other chemical reagents is discussed and used to elucidate the phenomenon of preferential track etching. Base-exchange and free radicals are then treated in their own right as new track revelation techniques and appropriate experiments are discussed. Some conclusions are drawn on methods which could be used to improve track revelation by either etching, base-exchange or free radicals.

7.1.1 The Base-Exchange Phenomenon

Soils, certain minerals and synthetic resins (specially modified polymers) are able to exchange the cations they contain (which are loosely linked to an insoluble framework) for others in solution. These substances are called cation exchangers. Synthetic cation-exchange resins are organic polymers containing acidic groups such as -COOH (carboxyl), -OH (hydroxyl) and -SO₃H (sulphonyl), which are fixed onto the framework of the insoluble, cross-linked resin structure. These acidic groups contain mobile, exchangeable hydrogen ions ("counter-ions") which are attached to the fixed, negative ions by a kind of adsorption via relatively weak electrical forces. This adsorption may be considered as a "surface" phenomenon since the interior of the resin is accessible to water. The fixed, negative ions are permanently attached to the resin network by strong covalent bonds. When placed in a solution of salt, some of the hydrogen ions of the resin enter the solution, and the electrically equivalent quantity of cations of the dissolved salt become adsorbed on the resins as indicated by the reaction



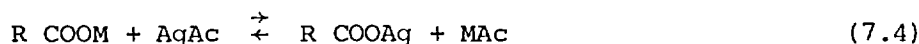
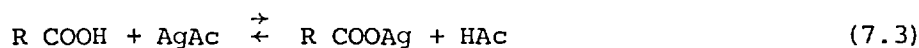
The sodium containing resin can undergo further exchange with other ions such as calcium.



The ability of a resin to adsorb different cations and its affinity for them is determined by their charge and their ionic size in solution (hydrated ion). Under equivalent conditions, affinity increases with the ionic charge and decreases with the hydrated ion size. It seems that the adsorption is essentially electrostatic in nature, but the size of the spaces between the networks of atoms in the resin exerts a large effect on the ease of adsorption (140).

Cellulosic materials engage in cation-exchange reactions in a manner similar to the inorganic zeolites (a large group of hydrated alumino-silicates). The absorption of metals from solutions of their salts by oxidized celluloses was recognized as early as 1883 by Witz as being an outstanding property of such materials. These exchange reactions are limited to cations, of which many are exchanged for one another with a rapidity characteristic of inorganic reactions (141). They are readily reversible although cations vary considerably in their affinity for cellulosic material. The exchange property is believed to be due to the acidic groups (such as carboxyl) which are present as a result of oxidation (57).

The exchange reaction may be illustrated with silver acetate (AgAc):



In the first reaction, the cellulosic material is in the "free-acid" form and exchanges a (hydrated) proton for a silver ion, to form acetic acid (HAc). In the second reaction a bound metallic ion exchanges for a silver ion.

Not all the carboxyl groups bind a silver ion when the cellulosic material is immersed in a solution of silver acetate. Complete

reaction is opposed by the competition of previously attached metal ions (left side of Equation 7.4) and by dissolved protons (right side of Equation 7.3) (142). The first source of competition can be minimized by prior elimination of metallic cations via a preliminary acid wash; this changes carboxyl groups into the free-acid form. The competition of dissolved protons is minimized by increasing the pH of the solution to reduce their concentration, for example by using a large excess of the silver salt of an acid weaker even than acetic acid, such as silver m-nitrophenate (142).

The extent of exchange between cations on the fibre and those in solution depends on their concentration and relative affinities for the acidic groups (141). Tightly bound Ca^{++} ions may be replaced by less tightly bound Na^+ ions provided the latter are in a sufficiently high concentration, and if the drop in solution pH is limited either by a large solution volume or by buffering. On the other hand, Ca^{++} and Mg^{++} exchange readily without a pH change. Since the carboxyl group is only weakly acidic, it has a very strong affinity for the proton, and exchange proceeds readily only in a strongly basic solution whose proton concentration is small (57).

The order of increasing affinity for the carboxyl groups of oxidised cellulose by various ions was found to be (142) $\text{Li}^+ < \text{Na}^+ < \text{K}^+ < \text{Ag}^+ < \text{Ca}^{++} = \text{Ba}^{++}$ at fairly low concentration (0.01 N), whereas at higher concentration (0.1 N) the order is the same except for Ag^+ , which now displays a greater affinity than Ca^{++} and Ba^{++} . The amount of cation bound at a fixed pH increases with concentration, reaching a constant value above about 0.2 N.

The observed affinity of an ion for the carboxyl groups of oxidized cellulose depends on several factors. Since the carboxyls are relatively fixed in their positions, an exchanging ion must fit into a fairly definite volume between chains, which however, are flexible to a certain extent. The Coulomb attraction is greater the closer two charges approach, depending approximately inversely on the size of the hydrated ion. Evidently a bivalent ion is more tightly bound than a monovalent one, although it must neutralize two adjacent positive groups simultaneously. The order of affinities observed can then be understood as follows: the alkalis occupy positions depending inversely on the size of the hydrated ions; the high affinities of Ca^{++} and Ba^{++} depend on the double charge; the high affinity of Ag^+ depends on its particularly small size (57).

7.1.2 Base-Exchange in the Latent Track: Swelling and Etching

Until now the discussion has concerned the base-exchange properties of oxidized celluloses, although it was shown in Chapter Two that radiation damage in cellulose (and especially in cellulose nitrate) leads to oxidative reactions along the latent track, and the consequent formation of acidic groups. Turning now towards the specific effects of radiation, experiments on irradiated cotton cellulose have demonstrated the occurrence of base-exchange, probably due to the acidic groups formed (143). By use of radioisotopes, the exchange of H^+ with Ca^{++} has been shown to be proportional to the radiation dose and to be dependent on the pH of the solution. The amount exchanged is maximum in alkaline solution and minimum in acidic. The relative affinity of the irradiated cellulose for the metal ions examined was $Mg^{++} < Na^+ < Co^{++} < Ca^{++}$, in agreement with the experiments on oxidized celluloses (143).

The general importance of the swelling phenomenon and of swelling agents in cellulose chemistry was already discussed in Chapter Two. One of the explanations for the swelling phenomenon when it is caused by ionic solutions relies on considerations similar to those which explain base-exchange. According to the theory of Neale (144), the action of an alkali on cellulosic material can be represented as an osmotic effect, based on the assumption that the material may be regarded as a weak monobasic acid which forms salts approximately according to the laws of mass action. During swelling caused by e.g, sodium hydroxide, the hydrogens of certain acidic groups are replaced by sodium cations, and a state of dynamic equilibrium is reached between sodium and hydrogen ions and undissociated acid groups. The sodium cations are mobile within the solid, being only weakly attached and continually hopping from site to site via exchange processes (145). This causes an osmotic pressure, approximately according to the ideal gas law, and the alkali solution diffuses inward until the osmotic pressure is balanced by forces arising from the cohesion of the chains. Thus initially the swelling increases with sodium ion concentration; however, at higher alkali concentration (above 3N) the sodium ions become attached to particular sites, and hopping ceases, thereby reducing the osmotic pressure and the associated swelling (145).

On the basis of the above theory of swelling, a latent track in cellulose nitrate, with its high density of acidic (mainly carboxyl) groups should absorb a much greater number of cations and associated water than the bulk material, thereby leading to preferential swelling of the track. The bulk cellulose nitrate, being a fairly tight structure, is relatively impermeable to foreign molecules (its accessibility is very small). The latent track, with its broken chain ends allows for easy penetration (and reaction) thereby acting as a "wick" for entry of the solution. The swelling phenomenon facilitates the penetration and the further chemical reactions by increasing the accessibility of cellulose molecules to the reagents. The chemical attack which leads to preferential track etching (e.g. by sodium hydroxide) in cellulose nitrate probably involves the base-exchange process in an essential manner. In the first stage of etching, the same kind of dynamic penetration by sodium ions occurs along the latent track as envisaged in Neale's theory of swelling, the acidic groups formed by radiation along the track attracting the cations. In the second stage, osmotic forces cause swelling and facilitate further etchant penetration. In the third stage, the high alkali concentration leads to alkaline cleavage as discussed in Chapter Two, and consequent dissolution of the material along the track, thus initiating the visible process of etching.

7.1.3 Revelation by Etching and Swelling

As experimental evidence to support the connection between etching and swelling, one may cite the remarkable similarity between the track etching rate in cellulose nitrate as a function of concentration of sodium hydroxide (146) and the graph of swelling in bulk cellulose versus NaOH concentration (147) (both at a fixed temperature). Both graphs (Figures 6.20 and 6.29) show a pronounced maximum at 2.5 N at a temperature of 18°C; the reason for the existence of such a maximum was discussed above. Further experimental evidence connecting etching with base-exchange is given below.

Charged particle tracks can be revealed in cellulose nitrate by employing certain swelling agents alone. Radiation weakens the structure through scission (148) and the reduction of crystallinity (149) with a consequent increase of chemical accessibility along the track. Tracks of 1.1 MeV protons at 30°C in CA-80 were revealed as fine lines by swelling in saturated zinc chloride solution for two

days, and measured with a high magnification microscope. The track length was $15 \pm 1 \mu$ as compared to the calculated range (31) of 19.3μ . Tracks of fission fragments near 90° in CA-80 were revealed by swelling for 18 days as above, thereby becoming so large that they were easily seen with a low magnification microscope. Zinc chloride is a particularly effective swelling agent since it is extremely soluble and the zinc ion is doubly charged and large; a saturated solution corresponds to 63.5 N. The swollen tracks are visible as regions of lighter colour under the microscope, probably because of the reduced concentration of colouring dye as well as a reduced index of refraction. Potassium thiocyanate is another effective swelling agent, which was used to reveal 1 MeV proton tracks in CA-80. A saturated solution corresponds to 18.2 N (150). However, this reagent also etches tracks very slowly since its pH is fairly high (unlike zinc chloride).

To verify that swelling increases the accessibility to chemical reagents, latent tracks were swollen and subsequently etched; this procedure enhanced the etch rate considerably and gave very sharp, conical tracks. The track length of 1.1 MeV protons at 30° first swollen and then etched for 5 hours in 2.5 N sodium hydroxide at 20°C was 6.9μ , as compared to 4.6μ for the unswollen specimen. The addition of potassium thiocyanate to potassium hydroxide also increases the bulk etching rate of cellulose nitrate by a considerable factor (151).

The connection between etching and base-exchange was studied by examining tracks etched in sodium hydroxide together with calcium hydroxide and comparing them with tracks etched only in NaOH as a control. It has been noted that the calcium ion has a much greater affinity for the acidic groups in cellulosic material than the sodium ion; as a result, a small fraction of calcium ions should have a significant effect on the track etching rate. These calcium ions should enter the track in preference to the sodium ions; since the former do not attack and decompose the cellulose nitrate, their entry should slow down the overall track etching rate. This was indeed found to be the case: tracks of 3.5 MeV alphas at 30° were etched for 20 hours in 2.5 N NaOH solution saturated with calcium hydroxide; the resulting tracks were 25% shorter than in the control specimen. Since the solubility of calcium hydroxide corresponds to

an 0.05 N solution, (150) fifty times smaller than the sodium ion normality, it can be seen that the calcium ions have a proportionately large effect on the etching. Water purity is therefore an important factor in controlling and standardizing etching conditions; distilled water should be used, especially if tap water is hard. To obtain a more striking comparison, 3.9 MeV alphas at 40° were etched in 0.5 N NaOH with saturated calcium hydroxide for 13 days at 18°C. The control specimen showed a high density of large, uniform tracks, which were visible as well-defined points of light under the microscope, using transmitted light. The specimen etched in the presence of calcium ions had a smaller density of small, uneven holes which were indistinct and seemed to consist of calcium deposits without the presence of a point of light to indicate a well-defined hole. As long as the calcium ion concentration is not much smaller than that of the sodium ion, it enters the latent track preferentially, due to its greater affinity, and reduces or prevents the subsequent alkaline degradation and the chemical etching of the track. Calcium hydroxide does not etch cellulose since its pH is not high enough; calcium ions deposit in the tracks without leading to further breakdown of the molecules.

7.1.4 Revelation by Base-Exchange Alone

Both high and low LET tracks (fission fragments and protons) have been revealed in CA-80 by use of the base-exchange phenomenon alone, without the complicating side effects of simultaneous chemical etching. The cations used for revelation included Ca^{++} , Ba^{++} and a cobaltammonium ion (Co^{++} in ammonia solution forming a complex ion).

Tracks of 350 KeV protons were revealed by treatment in saturated calcium hydroxide solution at 50°C in one and a half hours, with an efficiency comparable to that of alkaline etching. Although the solubility of calcium hydroxide is smaller at higher temperatures, the calcium ions diffuse more rapidly into the latent tracks, which are revealed under the microscope as white lines of deposited calcium. Tracks of 1.2 MeV protons were revealed by pre-swelling in zinc chloride and subsequent treatment in calcium hydroxide for 7 days at room temperature. The measured track length was $16 \pm 1 \mu$ as compared to a theoretical range (31) of 21.9 μ . Tracks of 4.5 MeV alphas at 40° were revealed by base-exchange in calcium chloride over a period of 1 day at room temperature; CaCl_2 has a high solubility (150) (13 N at 20°C) although its pH is about neutral, i.e. 7.

Barium hydroxide gave fast revelation of latent tracks; the affinity of acidic groups is about the same for Ba^{++} as for Ca^{++} , but the solubility of barium hydroxide (150) (0.3 N at $15^{\circ}C$) is considerably higher than that of calcium hydroxide. Barium acetate is particularly effective in revealing tracks via base-exchange; it has a relatively high pH and also a high solubility (150) (4.6 N at $0^{\circ}C$). The tracks of 4 MeV alphas at 90° were revealed in saturated barium acetate solution within less than 30 minutes at $30^{\circ}C$; under these conditions etching in 2.5 N NaOH did not reveal the tracks.

The visibility of tracks revealed by depositing calcium (or barium) in them via base-exchange can be dramatically increased by treating the specimens containing the revealed tracks in dilute (1%) sulphuric acid (152). The ensuing chemical reaction rapidly forms small crystals of sulphate along the track, which when viewed under the microscope using either reflected or transmitted light become clearly visible as centres of strong light scattering. Fission fragment tracks in thin, 10 μ Makrofol (a polycarbonate plastic) were treated in calcium hydroxide. The small amount of calcium deposited in the tracks via base-exchange became clearly visible under the microscope after treatment in dilute sulphuric acid.

An attempt was made to reveal alpha tracks using methylene blue, which is a basic dye (the colouring group is contained in the cation) known to have a very strong affinity for carboxyl groups, even stronger than calcium or barium (142). The attempt failed because the dye gradually coloured the whole specimen. This overall colouring is due to the smaller affinity of the methylene blue cation for the hydroxyl groups on the surface of the cellulose nitrate specimen. Methylene blue has a cation which is probably too large to be able to penetrate readily into the latent tracks; its large size is due to the presence of two aromatic rings in the cation.

7.1.5 Increasing the Sensitivity of Track Revelation

The previous considerations suggest ways of improving the sensitivity of track revelation in cellulose nitrate detectors. Evidently the concentration of acidic groups along the latent track is an important factor in track revelation; if a way could be found to increase this concentration, tracks of lower LET could be revealed. For example, one could hope to extend the revelation of complete

proton tracks above the present limit of about 1 MeV. As pointed out in Chapter Two, radiation in cellulosic materials produces many kinds of groups including aldehydes, ketones and acidic groups. In fact, the presence of aldehyde groups of the type shown in Figure 7.1 was explicitly demonstrated by revealing 1 MeV alpha tracks at 90° via Schiff's reagent which is specific for "dialdehydes", yielding a red-coloured compound (152). By employing various gentle

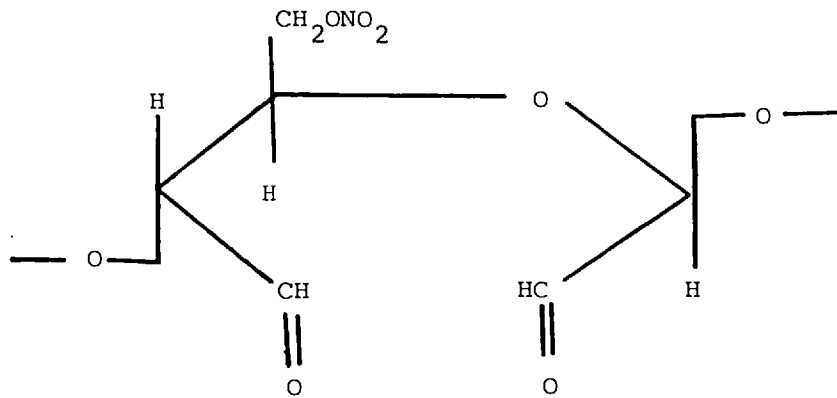


Figure 7.1

oxidising agents to transform some of the products or radiation degradation (such as aldehydes) into acidic groups, it should be possible to increase the concentration of the latter considerably. This would increase the sensitivity of track revelation, both by the etching process and by base-exchange. The "dialdehyde" cellulose of Figure 7.1 is converted by mild oxidation via chlorous acid (153), acidic sodium chlorite (153) or barium hypoiodite (12) into the corresponding "dicarboxyl" cellulose as shown in Figure 7.2. Preliminary experiments with dilute hydrogen peroxide acting as the

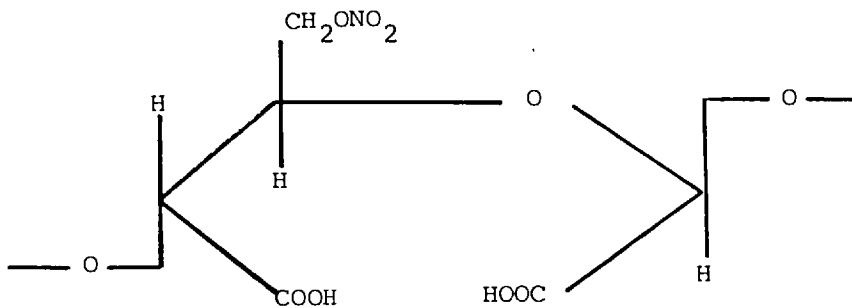


Figure 7.2

mild oxidizing agents of the latent track have been encouraging - a subsequent etching in 2.5 N sodium hydroxide produces tracks which are finer, thinner and more uniform than for the control specimen. This type of oxidative reaction may also explain the observed increased sensitivity of cellulose nitrate detectors when irradiated in the presence of oxygen (12).

7.2 Free Radicals in Nuclear Tracks

Free radicals are exceedingly common radiation products whose widespread existence in all irradiated organic solids has been demonstrated by EPR (electron paramagnetic resonance) techniques (47). They arise from the decomposition of the ions and the excited molecular states which are produced by the radiation; the breaking of a chemical bond results primarily in the formation of free radicals. The essential property of free radicals is their possession of one or more unpaired electrons, therefore the measurement of electron spin resonance (i.e. EPR) is the most conclusive demonstration of their existence in a system. Some free radicals may however be detected by characteristic absorption spectra. Most organic materials become coloured when irradiated; a combination of EPR and optical spectroscopy has established a relationship between radicals and colour centres (47). This colour change is the basis of some cheap plastic dosimeters.

Except for naturally occurring free radicals (e.g. O_2 or NO) and those considerably stabilized by resonance (e.g. DPPH, see below), radicals are in general very reactive entities, which are capable only of transient existence (154). Their transient existence may nevertheless be ascertained by trapping them with reagents for which they have high affinity and with which they combine to give stable products which can then be isolated and identified. At low concentrations, free radicals tend to react with other molecules to produce new and more stable radicals in the system. At higher concentrations they may react with each other to give a stable molecule (155). However, several examples of radical longevity are known: spins have remained unpaired in glycerine at room temperature for over a year; ethanol has been stored over three years at $77^{\circ}K$ without a substantial loss of radicals (47). Most radicals are stable in a sufficiently rigid matrix up to about 0.6 times the

melting point of the pure matrix material (47). The rigid solid structure prevents large radicals from diffusing away and from reacting with solutes or with each other ("cage effect"), however, small radicals such as H (from a broken C-H bond) tend to diffuse away rapidly. In addition, gas molecules may still be able to reach large radicals by diffusion. For example, oxygen promotes the radiolysis of polymers, apparently by the formation of peroxy species, which prevent the recombination of the geminate radical ends of cleaved chains. Thus, polystyrene crosslinks when irradiated in vacuum, but degrades when irradiated in air (93).

Free radicals formed in crystalline materials are much more stable than those formed in similar amorphous media. A twofold change in crystallinity can change the rate of radical destruction by ~ 1000 by changing the activation energy for destruction (149). Recombination may occur by radical migration or by interaction with trapped electrons, as well as by interaction with diffusing gases or solutes.

The importance of free radical intermediates in reactions initiated by heat, light, high-energy radiation and oxidation-reduction reactions has often been invoked in cellulose chemistry (41). UV-irradiated cellulose contains stable free radicals formed by chain cleavage (41). The long-lived radicals created by ionizing radiation are probably located in the crystallites of fibrous cellulose, since they do not interact with aqueous solutions of zinc chloride; however, they do participate in graft copolymerization reactions with vinyl monomers, (52) as shown by the large decrease in the EPR signal. Under conditions of maximum swelling of cellulose by zinc chloride (69-75% solution) the concentration of free radicals decreases due to solvent action to about 35% of the initial concentration; the 65% drop probably represents the free radicals in the amorphous regions (52). The method of grafting for decorating tracks (discussed in Chapter Five) depends on the existence of free radicals along the latent tracks.

7.2.1 Scavengers

Scavengers are substances which react with free radicals to form relatively stable compounds. Radical yields from radiation are often found by measuring the amount of such stable compounds

formed, or the amount of scavenger which has disappeared in such reactions. For example, during the radiolysis of hexane, the disappearance of dissolved iodine (in dilute solution) depends on the dose, independent of the initial iodine concentration (155).

Two types of scavenging effects occur. In the first, the scavenger is accessible during the formation of the radicals e.g. where irradiation is performed in an oxygen or water containing atmosphere. In the second, radicals are generated in an outgassed sample and scavenged later. The bleaching of green colour centres in Lexan was studied as oxygen diffused in from the surface; the diffusion coefficient can be inferred from the rate of recession of the colour boundary (47). In polyethylene, the diffusion of oxygen and the associated spin destruction occur more readily in the amorphous regions; the oxygen mobility is very low in the crystallites (47).

A scavenging technique of the first type has been used to study the formation of free radicals in cellulose triacetate by recoil nuclei and γ -rays (12). The scavenger used was DPPH (diphenyl picryl hydrazyl), which is often employed in polymer work. This odd-electron substance occurs as almost black crystals which dissolve in organic solvents to produce a deep purple solution. The DPPH radicals do not react with each other, but they do react with other active radicals (156). The product of such a reaction is colourless or light yellow, thus the amount of scavenged radicals can be measured by examining the reduction of optical density in the optical absorption bands of DPPH at 3300 \AA or 5300 \AA . The scavenging process proceeds slowly at room temperature after irradiation, due to slow diffusion of the radicals and the DPPH; however diffusion increases rapidly with increasing temperature (12). The radical yields in cellulose triacetate were found to be 17 per 100 eV of γ -ray dose and 5.6 per 100 eV of high LET recoil nuclei dose. The reduction of yield at high LET is probably due to the high radical concentration and the thermal effects in the tracks (Chapter Three), leading to recombination reactions.

7.2.2 Free Radicals in Latent Tracks

The role of free radicals in track formation has been studied in polymethyl methacrylate by both heavy ion irradiation (Kr or Ar)

and electron irradiation (157). The latter leads to a single EPR signal S_1 (due to a radical R_1) while the former gives a complex signal $S_1 + S_2$. The signal S_2 disappears on annealing of specimens at 180°C , (S_1 already disappears at 70°C), after which etching no longer reveals latent tracks; therefore it is suggested that the corresponding radical R_2 is responsible for latent track formation. It is further proposed that in high LET tracks the high concentration of R_1 radicals leads to their rapid exothermic recombination, and the elevated temperature forms R_2 radicals, which are more stable, being of the type formed during pyrolysis. This lends further support to the thermal spike mechanism of track formation (at least for high LET tracks), which was selected as the most reasonable mechanism in Chapter Three.

There have been several explicit suggestions as to the structures of radicals in irradiated celluloses. The apparent equivalence between the yields of scission and the destruction of glucose units suggests that radiation causes splitting mainly of the $\text{C}_1\text{-O}$ and $\text{C}_4\text{-O}$ bonds (158). However, the nitrate groups of cellulose nitrate probably play an important role in radical formation; this does not appear to have been studied yet by EPR.

7.2.3 Track Revelation via Free Radicals

The decoration of polymer tracks by graft copolymerization was discussed in Chapter Five. The grafting occurs onto radicals or onto the peroxide compounds which are formed by the reaction of oxygen with the radicals (159). Hydroperoxides decompose easily into radicals, especially at slightly elevated temperatures (149). Grafting yields in cellulose have been increased by soaking in H_2O_2 before irradiation (159). Oxygen acts to stabilise chain cleavage, thereby increasing grafting yield.

Grafting of acrylic acid to tracks in cellulose acetate had been previously successful (11), but not in cellulose nitrate. It is well known that a swelling agent is an important aid during graft copolymerization (159). Grafting in irradiated CA-80 was performed by first swelling in saturated aqueous zinc chloride and subsequently reacting with 15% acrylic acid monomer in the swelling solution. Grafted tracks of 600 keV protons at 30° had a measured length of $8.5 \pm 1 \mu$ as compared to a calculated range of 9.6μ .

Particle tracks have recently been revealed by the scavengers DPPH and iodine. These are dissolved in solvents such as n-hexane, dioxan and diethyl ether which are able to penetrate the cellulose nitrate by solvent action (swelling). When the DPPH radical reacts with a free radical present inside a latent track, it loses its strong violet colour; tracks are decorated as lines of light colour in a dark background. It is important to control the concentration of DPPH, for if it is too high the specimen becomes too dark. The process of revelation is aided by heating the specimens for several days at 50°C; the reaction rate of DPPH with radicals increases (more diffusion) and peroxide bonds are broken to create more radicals.

Tracks of 4.5 MeV alphas from a ^{241}Am source were revealed in CA-80 using DPPH in dioxan, with good efficiency. Tracks of 1.5 MeV alphas (obtained by slowing the above 4.5 MeV alphas in an Al foil) were revealed clearly by using iodine in hexane. The same agent was used on 800 keV proton tracks giving small tracks of a light colour which were visible under the plastic film surface. Tracks of 1 MeV alphas at 40°C in LR 115 were revealed via DPPH in diethyl ether. Some of the alpha tracks revealed via DPPH were over half a micron wide, indicating that there is a considerable amount of free radical diffusion away from the path of the charged particle.

This new revelation technique is still in its infancy. It remains to discover its advantages. Nevertheless, its success in track revelation demonstrates that free radicals remain present inside particle tracks, which are stored in conditions of low temperature and humidity, for many months.

CONCLUSION

It is evident from this chapter that different methods of nuclear track revelation exist, but better understanding of the chemistry of the detector and the mechanism of the revelation is still required. In fact the advantages techniques such as base-exchange and free radicals (scavengers) have over the chemical etching technique are that these methods are more sensitive to small REL, have better optical contrast and true track length can be visualised rather than only the residual track length, which is the case in chemical etching technique, where part of the track length is lost by the bulk etching process and has to be accounted for.

CHAPTER EIGHT

SOLID STATE TRACK RECORDERS IN NUCLEAR MEDICINE

8.1 Introduction

Several types of fast particles including protons, neutrons, pions and heavy charged particles are currently being evaluated for applications in the radiation therapy and diagnosis of cancer. There is already evidence to indicate that some of these particles will prove superior to conventional x-rays and γ -rays in certain applications (166). Almost all studies with these new techniques are utilizing nuclear detectors, counters and photographic plates originally designed and constructed for nuclear reactor physics and engineering applications. For a variety of reasons these detectors and counters are not appropriate for adoption in widespread medical applications. It appears likely that as the clinical evaluation programmes reach near completion, a demand will be created for medically practical particle detectors and counters. Consequently it is desirable to examine cellulose nitrate track recorders, which we propose to use as a charged particle radiograph for the investigation and location of tumours and regions of abnormal density in soft tissues and to assist in investigations of radiation dose for radiation therapy purposes.

One of the major drawbacks in extending the application of the solid state track recorders to nuclear medicine has been the low optical contrast between the irradiated and un-irradiated regions of the SSTR. This has been overcome by colouring of the acidic group by methylene blue, which was very successful for revealing a charged particle radiograph as well as for the reaction rate measurements in nuclear reactor applications.

The usefulness of this technique lies in the ability to observe the individual tracks produced by the charged particles in the SSTR with a high optical contrast and resolution compatible with the atomic and molecular scales of the detector. This technique is still in its infancy and needs better understanding and more quantitative data.

8.2 Charged Particle Radiography

Current methods in nuclear medicine employing gamma emitting radio-nuclides impose three major limitations on the usefulness of these methods, namely:-

- (i) Image contrast is severely reduced by activity contained in tissues surrounding the regions of interest. This activity which contributes noise to the image, may vary spatially and temporally and

is often so pronounced that only structures with a high radionuclide concentration can be differentiated from their surroundings.

- (ii) In spite of the relatively high inherent resolution capabilities of certain nuclear medicine imaging devices, their effective resolution is limited by that of the collimator whose improvement must be weighed against the concomitant severe loss in detection efficiency. Since the resolution and sensitivity (for the imaging of sources in tissues) of collimators vary with distance, the perceptibility of small or low contrast structures is usually reduced with depth.
- (iii) The widespread use of ^{99m}Tc in nuclear medicine limits the scope of this discipline. Although ^{99m}Tc is readily available, inexpensive, has a low energy-high photon yield and possesses some desirable chemical properties; there are two serious drawbacks to its use:-
 - (a) Because of the low energy gamma radiation from ^{99m}Tc , detection efficiency varies significantly with depth and may be affected by the presence of bone overlying the organ of interest.
 - (b) The chemical properties of ^{99m}Tc are less akin to physiological processes than those of many other radionuclides.

As a consequence of the above limitations and due to the failure of x-ray diagnostic techniques to accurately detect tumours and other regions of abnormal density in soft tissues, imaging in nuclear medicine has been primarily limited to morphological examinations; while rewarding physiological studies which should be possible in this field have been greatly restricted.

Conventional x-ray imaging does well in the evaluation of the chemical composition and large differences in density, such as bone, soft tissue and air. Artificial differences can be made by introducing air or iodine compounds. However, the diagnostic information of conventional x-rays is limited because the tissues of interest are obscured by superposition of over- or underlying tissues in the projected radiograph (Figure 8.1). Also the response of the x-ray photographic films has unwanted halo effects due to the recording of unwanted electrons and charge secondaries.

In order to circumvent these problems and to increase the scope of nuclear medicine, methods have been developed, such as the EMI scanner,

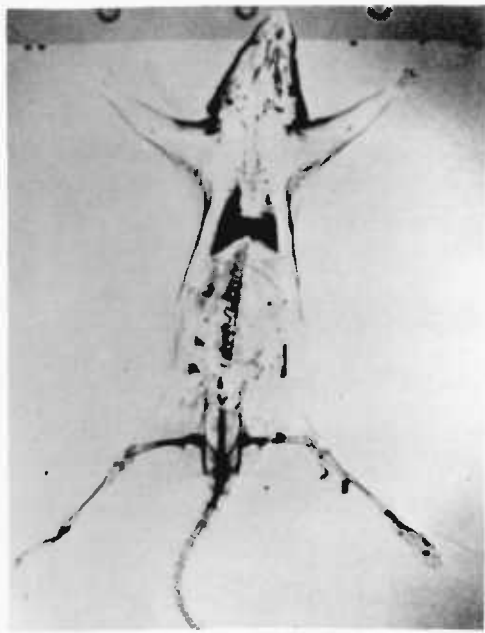


Figure 8.1 Details of a long tailed rodent

a) with X-rays

b) with 400 MeV/nucleon neon ions

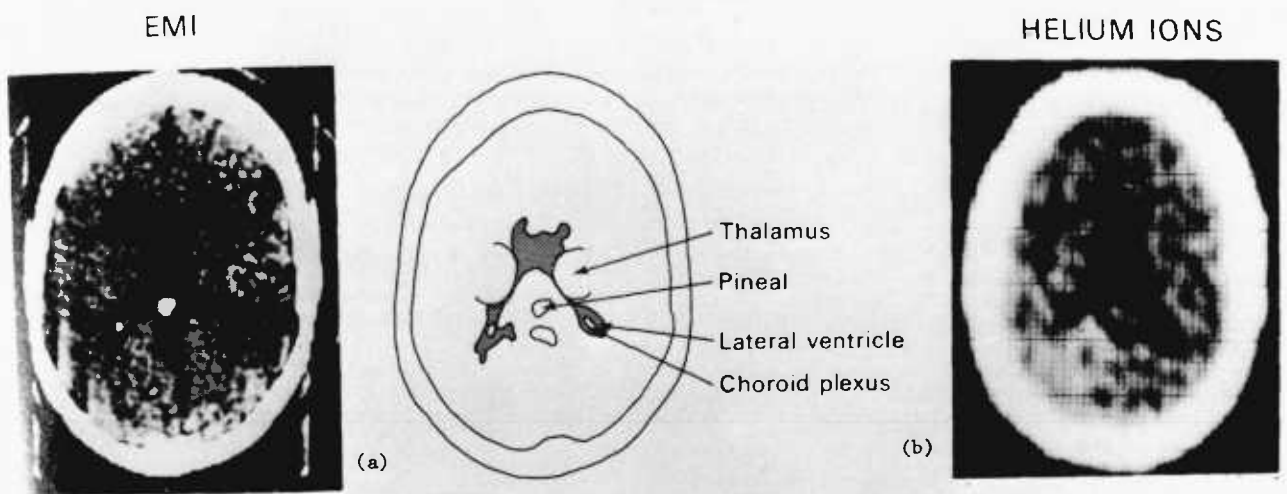


Figure 8.2

a) EMI scan of the brain consisting of 180 views and requiring a 1600 mrad dose to the subject

b) Helium ion image of the same subject on SSTR consisting of 64 sheets of CA 80-15 cellulose nitrate requiring only a 30 mrad dose

which is currently being used. Present research with alpha particles is an attempt to improve on spatial resolution and density sensitivity (Figure 8.2).

8.3 The Technique

A beam of monoenergetic charged particles (e.g. ^{16}O ions) is directed down a beam channel to a facility which houses the detection equipment and the biological object or patient (Figure 8.3). The beam is brought to rest in a stack of plastic sheets; which in the present work were cellulose nitrate films. Particles traverse about the same mass thickness (g/cm^2) before coming to rest in a particular sheet; which gives information about the mass density along their path. The damaged regions in the plastics may either be preferentially etched using a suitable chemical to render the tracks visible under an optical microscope or these tracks may be revealed using methylene blue, which was highly successful for heavy ions.

Proton and alpha radiography is also of interest due to smaller radiation doses as compared to the radiation doses in the methods currently being used such as EMI. Present x-ray and EMI techniques deliver doses of 1000 mrad and 1600 mrad respectively, and probably would not detect a compressed breast or skull tumour directly, compared to a 30 mrad dose from alpha particles with good resolution of the tumour area. As a result of straggling and scattering, radiographs of higher resolution can be produced with heavy ions. The usefulness of this technique lies in the track revelation with a high optical contrast which has been achieved using methylene blue and is discussed in the next section. However, the application of heavy ion radiography is restricted up to some extent by the need for high energy particles (several hundreds of MeV/nucleon).

8.4 Radiograph Development by Methylene Blue

The damage left by a charged particle in a SSTR consists of acidic groups (carboxyl) among the other radiation products. In the present work it was found that the acidic groups in the tracks can be coloured by a basic dye (methylene blue); thereby leading to a direct and convenient method of track revelation in a radiograph.

In a basic dye the colouring group (chromophore) is contained in the cation. Methylene blue is commonly used in histology for staining acidic structures of cells. It is particularly effective since its affinity for basic groups is very high. However, because of the relatively large size of the cation ($\sim 10 \text{ \AA}$); it will not be able to penetrate easily cellulosic

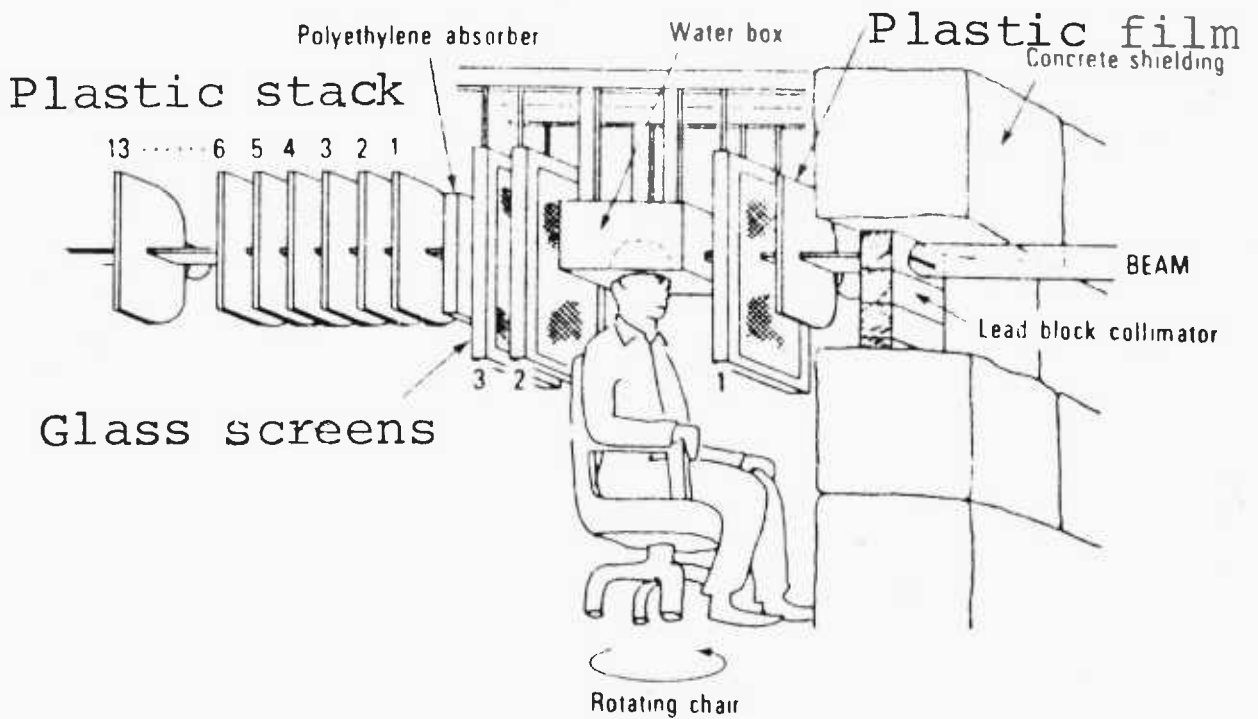


Figure 8.3 Schematic diagram of helium ion transverse section imaging (the Alpha Radiography Facility)

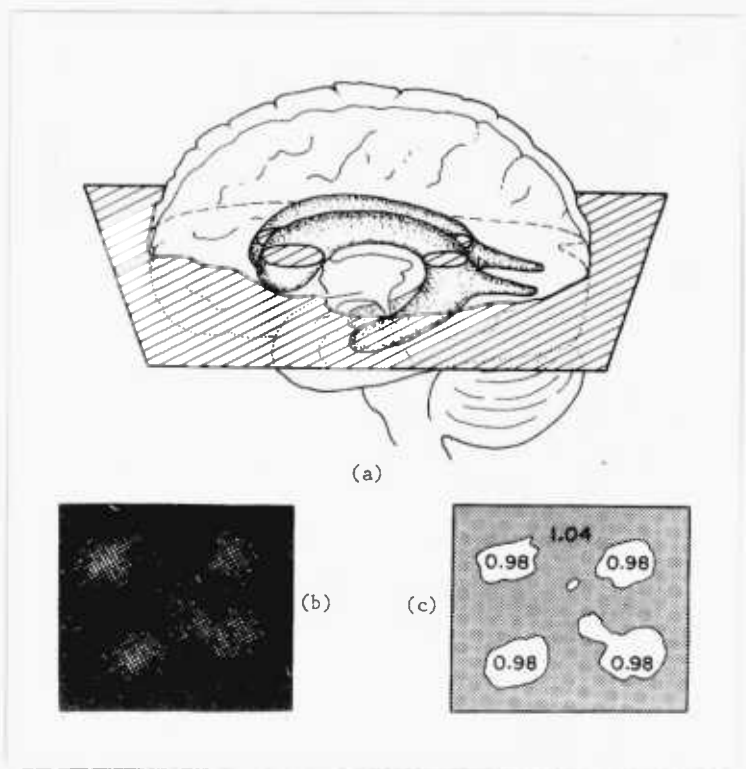


Figure 8.4 a) A plane intersecting the ventricles in the human brain for imaging the cross-section
 b) Reconstructed image of the brain
 c) Densities of the brain and the surrounding bones and tissues

materials, where ions of up to $\sim 8 \text{ \AA}$ diameter are easily admitted. Thus a swelling agent must be employed to expand the spaces between the molecules along the latent tracks in order to aid penetration. In the case of cellulose nitrate, it was found that an aqueous solution of methylene blue with constituents as given in the following formula (1) was quite effective. Formulae (2) and (3) still require better understanding.

(1) Acidic

Methylene Blue	1 g
Glacial Acetic Acid	1 ml
Ethyl Alcohol	20 ml
Distilled Water	80 ml

(2) Basic

Methylene Blue	0.3 g
Ethyl Alcohol	30 ml
0.01% KOH	100 ml

(3) Basic

Methylene Blue	1 g
Borax	1 g
Distilled Water	100 ml

Kodak-Pathé CA80-15 plastic was irradiated by heavy ions at various angles of incidence and various doses. The specimens were immersed in a solution of methylene blue for various lengths of time. Short times are preferable since the plastic becomes uniformly coloured blue due to the weaker affinity of methylene blue for the hydroxyl groups in the cellulose nitrate. The carboxyl groups absorb methylene blue much more rapidly.

The profile of the charged beam was revealed by a very short treatment (~ 5 minutes). Experiments were done to find the minimal dose which could be revealed to the human eye by an immersion in methylene blue. This minimal dose was found to be $\sim 10^5$ particles/cm² at an energy of ~ 35 MeV, which corresponds to a dose of ~ 11.3 mrad at the surface of the plastic.

Further experiments were done on charged particle tracks at 30° to determine the amount of penetration of methylene blue dye into the tracks. This was found to depend on the swelling of the latent track. By using effective swelling agents such as choline chloride, the penetration could be increased by a factor of 2 to a distance of 64μ .

The radiograph can be etched in sodium or potassium hydroxide after colouring, so that the results of dyeing can be checked by a post-etching

Conclusions

This work shows that the SSTRs can be successfully used in nuclear medicine and the resulting tracks can be revealed by dyeing with high efficiency. The major advantage of the method is the high contrast achieved between irradiated and unirradiated regions of the radiograph, which permits easy revelation of a beam profile or a diagnostic beam. Previously, dyes were used to fill etched tracks to achieve higher contrast. Also this work shows that techniques of histological staining are useful in charged particle radiography.

CHAPTER 9

SUMMARY OF CONCLUSIONS AND PROPOSALS FOR FUTURE WORK

9.1 Summary of Conclusions

Considerable discrepancies occurred between the experimental observations and the theoretical calculations of etched track parameters with no acceptable explanation, mainly because no accurate quantitative data and description of the etching rate or detailed knowledge of its mechanism, or the mechanism of track formation and the chemical dissociation, is well known.

In order to carry the solid-state track recorders from the experimental stage to industrial and research applications, these quantitative measurements have to be absolutely resolved and the theories behind them have to be explained well enough to back them.

It was necessary to study the chemistry of cellulose and its derivatives in order to understand the possible latent track formation and preferential chemical etching mechanisms. This led us to introduce a new concept of latent track formation mechanism in solids and preferential chemical etching mechanism in polymers. Some aspects of these concepts were supported by experimental evidence.

The outstanding sensitivity of cellulose and cellulose derivatives among all other plastic detectors was investigated. From the base of purely structural considerations, the following factors were found to contribute to the superior sensitivity of cellulose and its derivatives:-

- (a) Conjugation of monomers with each other through a relatively weak acetal bond.
- (b) Presence of oxygen in a six-membered ring, leading to a displacement of electron densities and thus decreasing the bond-break energy.
- (c) A significantly greater number of easily substituted hydroxyl group in cellulose monomers than in monomers of any other plastic used for detecting ionizing particles.
- (d) Correspondingly greater possibilities for introducing various groups of high reactivity into macromolecules through substituting hydrogen in hydroxyl groups.
- (e) The possibility of introducing such groups, whose great polarizability enables an easier main-chain break as well as groups, whose products of oxidizing and decomposition possess an oxidizing action themselves. The first applies to nitrogroups to the greatest degree,

but also applies to acetyl groups, while the second applies to nitrogroups only, thus this makes it clear why cellulose nitrate is the first in sensitivity among all cellulose derivatives and cellulose acetate comes next.

- (F) The low thermal and electrical conductivities make it more susceptible to localized thermal damage and hence a thermal spike is induced by heavy charged particles of high LET.

Investigations were carried out on the detector's composition parameters such as molecular weight, plasticizer and residual solvent, the latent track chemical etching techniques and the chemical etching conditions such as temperature, hydroxide concentration and solution agitation. Their effect on the detector's (CA 80-15) latent track registration and revelation, reproducibility and efficiency were verified.

Various optimal etching conditions were found by lowering the minimum threshold of latent track revelation by chemical etching techniques. This resulted in improving the detector's latent track revelation sensitivity, reproducibility and efficiency. A reliable track registration and revelation criterion was also established in order to determine which particle produces etchable tracks.

The study of the characteristic dimensions of latent and etched tracks of heavy charged particles by electron microscope in cellulose nitrate revealed information about the mechanism of etchable radiation damage in polymers and about the charge, energy and REL of the particles. This information was utilized for particle identification, energy measurement and separation of isotopes with small mass differences.

Measurements of the bulk etch rate of cellulose nitrate exposed to gamma radiation showed little change in V_B for absorbed doses below 10^6 rad. Above 10^6 rad V_B varies in an approximately linear fashion with gamma radiation dose (see Figures 6.71-6.76). In the dose range from 10^6 to 10^9 rad, this phenomenon can be used to measure the gamma radiation dose. The gamma radiation bulk etch rate dosimeter developed in Chapter 6 has a number of advantages over other gamma dosimeters in the 10^6 to 10^9 gamma dose region. It can be made as compact as desirable, the exposed dosimeters are easily read by a simple measurement of V_B , the "latent image" stability is very high and the dosimeter may be utilized for the measurement of gamma dose in nuclear reactor cores and high doses of soft x- or gamma-rays (such as occur during weapons tests) that have very small penetration depths in matter. By successively etching each time removing only a few microns of the specimen surface, a

depth-dose profile may be measured.

Increased precision coupled with the unmatched spatial resolution available with SSTRs permitted investigation of high resolution studies and measurements of reaction rates in several neutron spectra such as are found in thermal as well as fast reactors, with an accuracy of $\pm 3\%$.

As a result of the above work and better understanding of the chemistry of cellulose and its derivatives, new techniques of track revelation, based on the nature of the latent tracks, have been discovered.

These techniques utilize the following:-

(a) Base-Exchange

It was shown in Chapter 2 that radiation damage in cellulose (and especially in cellulose nitrate) lead to oxidative reactions along the latent tracks and consequent formation of acidic groups. The exchange of the H^+ ion of the irradiated cellulose with the larger Ca^{++} ion from the base exchange solution has also been shown to be proportional to the radiation dose and to be dependent on the pH of the solution. The amount exchanged is maximum in alkaline solution and minimum in acidic. Latent tracks are identified by the contrast of colour between the bulk plastic (a rosy colour) and the Ca^{++} ion which is white (in fact this is similar to the grafting technique).

(b) Free Radicals (Scavengers)

Free radicals are exceedingly common radiation products whose widespread existence in all irradiated organic solids has been demonstrated by EPR (electron paramagnetic resonance) techniques. Scavengers are substances which react with free radicals giving away their colour to form relatively stable compounds. Latent tracks are seen by this distinct colour contrast given by the scavengers, with the rosy bulk plastic background.

(c) Colouring of the Acidic Group by Methylene Blue

Large molecules of methylene blue will anchor themselves, giving away their colour, to the acidic group which had been formed in the bulk plastic due to irradiation.

Latent tracks are recognised, counted and measured by the blue conical damaged trails embedded in a rosy background.

One of the major drawbacks in extending the application of solid-state track recorders via etching technique to nuclear medicine has been the low optical contrast between the irradiated and un-irradiated regions of the SSTR. This has been overcome by colouring of the acidic

group by methylene blue, which was very successful for revealing a charged particle radiograph as well as for the reaction rate measurements in nuclear reactor physics applications.

The usefulness of this technique lies in the ability to observe the individual tracks produced by the charged particles in the SSTR with a high optical contrast and resolution compatible with atomic and molecular scales, which permits easy revelation profiles of a diagnostic beam using charged particle radiograph techniques. This technique is still in its infancy and needs better understanding and more quantitative data.

9.2 Proposals for Further Study

The following domains are recommended for further study.

(a) Thermal Neutron Spectrometer

The development of SSTR techniques as a thermal neutron spectrometer will most probably have to allow for only one type of incident particle and some sort of particle collimation, so that the confounding influence of tracks for several particles incident at various angles can be avoided. This may be achieved by inserting a spacer between the plastic detector and a thin boron film ((n, α) reaction).

(b) Fast Neutron Dosimetry

In spite of the presence of hydrogen in cellulose and cellulose derivatives, such SSTRs have a poor response for fast neutrons. The sensitivity of CA 80-15 and LR 115 Type-II cellulose nitrate for fast neutrons is 5×10^{-8} , 10^{-7} , 10^{-6} , 10^{-5} and 3×10^{-5} recoil proton tracks per cm^2 per unit of neutron fluency for incident neutron energies of 1, 2, 5, 10 and 20 MeV respectively. Accurate counting and measuring of the recoil proton tracks are also difficult due to their small physical size.

We suggest here the use of SSTRs in contact with a foil of U^{238} , U^{235} or Th^{232} , where the fast neutron fission cross-section of each (n,f) is large. Accurate counting and measuring of the large fission fragment tracks are possible.

(c) The Chemistry of Cellulose and Cellulose Derivatives

A better understanding of the chemistry of cellulose and cellulose derivatives, as well as the chemical breakdown of cellulose chains due to charged particle irradiations, may lead to an improvement in the new latent track revelation techniques, i.e. base-exchange, free radicals

(scavengers) and colouring of the acidic group by methylene blue or some other dye. This improvement may be employed in nuclear medicine to achieve a better diagnostic system for cancer using charged particle radiograph techniques and in reactor physics for reaction rate and neutron flux measurements.

REFERENCES

1. Young, D.A. Etching of Radiation Damage in Lithium Fluoride, *Nature*, 182, 375, (1958).
2. Amelinckx, S. The Direct Observation of Dislocations, Academic Press, New York, (1964).
3. Silk, E. and Barnes, R. *Phil. Mag.*, 4, 970, (1959).
4. Price, P.B. and Walker, R.M. *J. Appl. Phys.*, 33, 3407, (1962).
5. Fleischer, R. and Price, P.B. *J. Appl. Phys.*, 34, 2903, (1963).
6. Fleischer, R. and Price, P.B. *Science*, 140, 1221, (1963).
7. Fleischer, R., Price, P.B. and Walker, R.M. Nuclear Tracks in Solids, University of California Press, Berkeley, (1975).
8. Amelinckx, S. "The Direct Observation of Lattice Defects by Electron Microscopy" in The Interaction of Radiation with Solids, ed. R. Strumane et al, North-Holland, Amsterdam, (1964).
9. Childs, C.B. and Slifkin, L. *Phys. Rev. Letters*, 9, 354, (1962).
10. Schopper, E. et al. Proc. 8th Int. Conf. Nuclear Photography and Solid State Detectors, Bucharest, (1972).
11. Monnin, M. and Blanford, G. *Science*, 181, 743, (1973).
12. Boyett, R., Johnson, D. and Becker, K. *Rad. Research*, 42, 1, (1970).
13. Price, P.B. et al. *Phys. Rev.*, 164, 1618, (1967).
14. Benton, E.V., Henke, R. and Tobias, C. *Science*, 182, 474, (1973).
15. Becker, K. *Health Phys.*, 12, 769, (1966).
16. Fleischer, R.L. Particle Dosimetry by Track Etching. General Electric Co. Rep. No. 74 GRD-197, August, (1974).
17. Rago, P. et al. *Nucl. Applic.*, 8, 302, (1970).
18. Kohler, W. *Rad. Effects*, 3, 231, (1970).
19. Roberts, J.H. et al. *Rad. Effects*, 3, 283, (1970).
20. Frank, A.L. and Benton, E.V. Proc. 7th In. Colloq. Corpuscular Photography and Visual Detectors, Barcelone, (1970).
21. Becker, K. Dosimetric Applications of Track Etching in Topics in Radiation Dosimetry, ed. by F. Attix, Academic Press, New York, (1972).
22. Frank, A.L. and Benton, E.V. *Radiation Effects*, 3, 33, (1970).
23. Tuyn, J.W. *Nucl. Applic.*, 3, 372, (1967).
24. Roberts, J.H. et al. *Nucl. Applic.*, 5, 247, (1968).
25. Tuyn, J.W. *Rad. Effects*, 5, 75, (1970).
26. Besant, C.B. and Ipson, S.S. Measurement of Fission Ratios in Zero Power Reactors using Solid-State Track Recorders. *J. Nucl. Energy*, 24, pp 59-69, (1970).

27. Besant, C.B. Proc. 7th Int. Colloq. Corpuscular Photography and Visual Detectors, Barcelona, (1970).
28. Besant, C.B. and Truch, E.R. Automatic Image Analysis in Track Counting. *Microscope*, 20, January (1972).
29. Lambert, M. et al. *Rad. Effects*, 3, 155, (1970).
30. Dartyge, E. and Lambert, M. *Rad. Effects*, 21, 71, (1974).
31. Benton, E.V. A Study of Charged Particle Tracks in Cellulose Nitrate. USNRDL-TR168-14, (1968).
32. Schlenk, B., Somogyi, G. and Valek, A. *Rad. Effects*, 24, 247, (1975).
33. Frank, A.L. and Benton, E.V. University of San Francisco Report, No. DASA 2573 (November 30, 1970).
34. Nicolate, M. *Rev. Roum. Phys.*, 15, 881, (1970).
35. Mark, H. Interaction and Arrangement of Cellulose Chains, in *Cellulose and Cellulose Derivatives, Part I*, ed. E. Ott, H. Spurlin, and M. Grafflin, Interscience, New York, (1954).
36. Howsmon, J.A. and Sisson, W.A. Microscopic Structure, in *Cellulose and Cellulose Derivatives, Part I*, *ibid.*
37. Miles, F.D. *Cellulose Nitrate*, Oliver and Boyd, London, (1955).
38. Nitrocellulose - Chemical and Physical Properties, Hercules Powder Company, Wilmington, Delaware, (1963).
39. Kilzer, F.J. Thermal Degradation, in *Cellulose and Cellulose Derivatives, Part V*, *ibid.*
40. Benton, E.V. and Henke, R.P. Heavy Cosmic Ray Exposure of Apollo-17 Astronauts, *Health Phys.*, 27, 79, (1974).
41. Arthur, J.C. ESR Studies, in *Cellulose and Cellulose Derivatives, Part V*, ed. N. Bikales and L. Segal, Interscience, New York, (1971).
42. McBurney, L.F. Degradation of Cellulose Derivatives, in *Cellulose and Cellulose Derivatives, Part II*, ed. E. Ott, H. Spurlin and M. Grafflin, Interscience, New York, (1954).
43. *Handbook of Chemistry and Physics*, Chemical Rubber Co., (1965).
44. Trogris, C., Tomonari, T. and Hess, K. *Z. Physik Chem.*, B16, 351, (1932): B17, 241, (1932).
45. Dienes, G. and Vineyard, G. *Radiation Effects in Solids*, Interscience, New York, (1957).
46. Lawton, J. and Nason, H.K. *Ind. Eng. Chem.*, 36, 1128, (1944).
47. Alger, R.S. Radiation Effects in Polymers, in *Physics and Chemistry of the Organic Solid State*, ed. by D. Fox, M. Labes and A. Weissberger, Interscience, New York, (1965).
48. Burton, M. Experimental Techniques and Current Concepts - Organic Substances, in *the Effects of Radiation on Materials*, J.J. Harwood, H.H. Hausner, J.G. Morse and W.G. Rauch, editors Reinhold Pub. Co., New York (1958).

49. Carrol, J.G. and Bolt, R.O. Radiation Effects on Organic Materials, Academic Press, New York, (1963).
50. Swallow, A.J. Radiation Chemistry of Organic Compounds, Pergamon Press, Oxford, (1960).
51. Myers, L.S. Radiation Chemistry of Nucleic Acids, Proteins and Polysaccharides, in The Radiation Chemistry of Macromolecules, Vol. II, ed. M. Dole, Academic Press, New York, (1973).
52. Arthur, J.C. Reactions Induced by High-Energy Radiation, in Cellulose and Cellulose Derivatives, Part V, *ibid.*
53. Baugh, P.J. and Phillips, G.O. Photochemical Degradation, in Cellulose and Cellulose Derivatives, Part V, *ibid.*
54. Bolker, H.I. Natural and Synthetic Polymers, M. Dekker, New York, (1974)
55. Nevell, T.P. Oxidation, in Methods in Carbohydrate Chemistry, Vol. III, ed. R. Whistler, Academic Press, New York, (1963).
56. Fantini, M. (Kodak-Pathé), private communication.
57. McBurney, L. Oxidative Degradation, in Cellulose and Cellulose Derivatives, Part I, ed. E. Ott, H. Spurlin and M. Grafflin, Interscience, New York, (1954).
58. Kenyon, W. and Gray, H. J. Am. Chem. Soc., 58, 1422, (1936).
59. Hiller, L.A. Jr. J. Polymer Sci., 385, (1953).
60. Sherman, P.A. and Goldman, I.O. J. Appl. Chem. (USSR), 25, 87, (1952).
61. Bohr, N. Mat. Fys. Medd. Dan. Vid. Selsk., 18, 8, (1948).
62. Chadderton, L.T. Radiation Damage in Crystals, Methuen, London, (1965).
63. Seeger, A. Radiation Damage in Solids, IAEA (Vienna), I, 101, (1962).
64. Bethe, H.A. Ann. d. phys., 5, 325, (1930).
65. Bloch, F. Ann. d. phys., 16, 285, (1933).
66. Bohr, N. Phil. Mag., 25, 10, (1913).
67. Fleischer, R.L. and Price, P.B. Glass Dating by Fission Fragment Tracks, J. Geoghs. Res., 69, 331, (1964).
68. Barkas, W.H. Nuclear Research Emulsions, Academic Press, New York, (1963).
69. Heckman, H.H., Perkins, B.L., Simon, W.G., Smith, F.M. and Barkas, W.H. Phys. Rev., 117, 544, (1960).
70. Fleischer, R.L., Price, P.B., Walker, R.M. and Hubbard, E.L. Criterion for Registration in Dielectric Track Detectors. Phys. Rev., 156, 353, (1967).
71. Fleischer, R.L., Price, P.B. and Walker, R.M. Ann. Rev. Nucl. Sci. 15, 1, (1965).

72. Lambert, M. et al. J. Intern. d'Energ. des Traces dans les Solides Isolans. Clermont-Ferrand, (1969).
73. Benton, E.V. Radiation Effects, 2, 273, (1970).
74. Benton E.V. and Nix, W.D. Nucl. Instr. and Methods, 67, 343, (1969).
75. Katz, R. and Kobetich, E.J. Phys. Rev., 170, 401, (1968).
76. Monnin, M. Report PNCf, 68-RI9., (1968).
77. Felder, R.M. J. Phys. Chem. Sol., 28, 1383, (1967).
78. Maurette, M. Track Formation Mechanisms in Minerals. Report, Laboratory Space Physics, Washington Univ., St. Louis, Missouri, 63130, May (1969).
79. Fleischer, R.L., Price, P.B. and Walker, R.M. J. Appl. Phys., 36, 3645, (1965).
80. Vineyard, G. Energia Nucleare, 8, 9, (1961).
81. Seitz, F. and Koehler, J.S. Solid State Physics, 2, 305, (1956).
82. Bonfiglioli, G., Ferro, A. and Mongi, A. J. Appl. Phys., 32, 2499, (1961).
83. Varley, J.H.O. Nature, 174, 886, (1954).
84. Chadderton, L.T., Morgan, D.V., Torrens, I. MCC, Solid State Comm., 4, 391, (1966).
85. Chadderton, L.T. Radiation Damage in Crystals, Methuen (London), (1965).
86. Brinkman, J.A. J. Appl. Phys., 25, 96, (1954).
87. Brinkman, J.A. Nuclear Met., VI, 1, (1959).
88. Chadderton, L.T. and Torrens, I. Fission Damage in Crystals, Methuen, London, (1969).
89. Fano, U. Ann. Rev. Nucl. Sci., 13, 1, (1963).
90. Mozumder, A. and Magee, J.L. J. Chem. Phys., 47, 939, (1967).
91. Bethe, H.A. and Ashkin, J. Passage of Radiations through Matter, in Experimental Nuclear Physics, Vol. 1, ed. E. Segre, Wiley, New York, (1953).
92. Mozumder, A. Charged Particle Tracks and their Structure, in Advances in Radiation Chemistry, Vol. I, ed. M. Burton and J. Magee, Interscience, New York, (1969).
93. O'Donnell, J.H. and Sangster, D. Principles of Radiation Chemistry, Arnold, London, (1970).
94. Mozumder, A., Chatterjee, A. and Magee, J.L. Advan. Chem. Ser., 81, 27, (1968).
95. Bowden, F.P. and Yoffe, A.D. Fast Reactions in Solids, Butterworths, London, (1958).
96. Young, D.A. J. Chem. Soc., p.4533, (1960).

97. Montagu-Pollock, H.M. Proc. Roy. Soc. A269, 219, (1962).
98. Tubbs, M.R. and Forty, A.J. Phil. Mag., 7, 709, (1962).
99. Brostrom, K.J., Baggilel, J.K. and Lauritsen, T. Phys. Rev., 58, 651, (1940).
100. Deb, S.K. and Yoffe, A.D. Trans. Farad. Soc., 55, 106, (1959).
101. Qaqish, A.Y.K. Science Research Council Application (September 1976).
102. Fantini, M. (Kodak-Pathé, Vincennes, France), private communication.
103. Goland, A.N. Charged Particle Tracks in Solids in Studies in Radiation Effects, Vol. I, ed. G. Dienes, Gordon and Breach, New York, (1966).
104. Merkle, K.L. Bull. Am. Phys. Soc., 8, 236, (1963).
105. Goland, A.N. and Paskin, A. J. Appl. Phys., 35, 2188, (1964).
106. Monnin, M. Rad. Effects, 5, 69, (1970).
107. Macfarlane, R.D. and Torgerson, D.F. Phys. Rev. Letters, 36, 486, (1976).
108. Fraser, J.S., Milton, J.C.D., Bowman, H.R. and Thompson, S.G. Can. J. Phys., 41, 2080, (1963).
109. Lycos, T.A. PhD Thesis, Imperial College, University of London (1976).
110. Petr, J. PhD Thesis, Imperial College, University of London, (1973).
111. Besant, C.B., Truch, E.R.R. Automatic Image Analysis in Nuclear Track Detection. Int. Conf. on Microscopy (Inter Micro 71), Imperial College, September (1971).
112. Becker, K. Radiation Research, 36, 107, (1968).
113. Peterson, D.D. PhD Thesis, Revselaer Polytechnic Institute, (1970).
114. Crawford, W.T., Desorbo, W. and Humphreys, J.S. Jr. Nature, 220, 1313, (1968).
115. Cohen, W.D. Rec. Trav. Chim., 40, 433, (1920).
116. Berthoud, A. and Porret, D. Helv. Chem. Acta, 17, 494, (1934).
117. Taylor, H.S. and Gould, A.J. Phys. Chem., 37, 367, (1933).
118. Blaisdel, B.E. J. Soc. Dyers Colourists, 65, 618, (1949).
119. Race, E. J. Soc. Dyers Colourists, 65, 56, (1949).
120. Block, J., Humphrey, J.S. Jr. and Nichols, G.E. Detection in Polymer Films and in Plastic Track Detectors. Rev. Sci. Inst., 40, 509, (1969).
121. Lark, N.L. Spark Scanning Fission Fragment Tracks in Plastic Foils. Nuc. Inst. Methods, 67, 137, (1969).
122. Cohn, C.E. and Gold, R. Computer Controlled Microscope for Automatic Scanning of Solid State Nuclear Track Recorders. Rev. Sci. Inst., 43, 12, (1972).

123. Quantimet 720 Image Analysing Computer Instruction Manual, Image Analysing Computers Ltd., (IMANCO), Melbourne, Royston, Herts., England.
124. Gunther, G. The Measurement of Fission Rate Microstructure with Plastic Foils, Leitz Scientific and Technical Information, Suppl. 1,2, Wetslar, (July 1972).
125. Schultz, W. and Warner, W. Track Density Measurement in Dielectric Track Detectors with Scattered Light, Knolls Atomic Power Laboratory, Schenectady, N.Y. NSA:22-37990, (January 1968).
126. Congel, F.J., Roberts, J.H., Dreis, D., Kastner, J., Oltman, B.G., Gold, R. and Armani, R.J. Automatic System for Counting Etched Holes in This Dielectric Plastics. Nucl. Inst. Methods, 100, 247, (1972).
127. Oosterkamp, W.J., Schaar, J. and Van Velze, P.L. Automatic Counting of Solid-State Fission Track Recorders. Trans. Amer. Nucl. Soc., 13, 526, (1970).
128. Leitz. T.A.S. Leitz Brochure.
129. Hughes, J., Dewey, M. and Briers, G. Boron Autoradiography with the Electron Microscope. Nature, 223, 489, (1969).
130. Instruction Manual for Folding Mirror Stereoscope. BY-123, Hilger and Watts Ltd.
131. Lycos, T. and Besant, C.B. Measurement of Fast Reactor Reaction Rates using Solid-State Track Recorders. Vol. 24, No. 2, (1976).
132. Guerrero and Black, Trans. Am. Soc. Mech. Eng., B.94, 1087, (1972).
133. Davidson, E.A. Carbohydrate Chemistry, Holt, Rinehart and Winston, Inc., New York, P.202, (1967).
134. Jaffey, A.H. Rev. Sci. Instr., 25, 349, (1954).
135. Barkas, W.H. and Berger, M.J. National Academy of Sciences - National Research Council Publication 1133, 103, (1964).
136. Benton, E.V. and Henke, R.P. High-z Particle Cosmic Ray Exposure of Apollo 8-14 Astronauts. Air Force Weapons Laboratory, TR-72-5, (1972a).
137. Shirk, E.K., Price, P.B. Kobetich, E.J., Osborne, W.Z., Pinsky, L.S., Eandi, R.D. and Rushing, R.B. Charge and Energy Spectra of Trans-Iron Cosmic Rays. Phys. Rev. D., 7, 3220-3232, (1973).
138. Rickard, I.C., Besant, C.B., Lycos, T. and Truch, E.R. The Quantitative Detection of Alpha Particles in Certain Dielective Materials. Microscope Vol. 22, 141, April (1974).

139. Qaqish, et al. The Effects of High Gamma Doses on the Registration Efficiency of Cellulose Nitrate Detectors, (1977), unpublished.
140. Glasstone, S. and Lewis, D. Elements of Physical Chemistry, Second Edition, MacMillan, New York, (1960).
141. Sookne, A. and Harris, M. Base-Exchange Properties, in Cellulose and Cellulose Derivatives, Part I, loc. cit.
142. Davidson, G. J. Text. Inst., 39, T87, (1948).
143. Demint, R. and Arthur, J.C. Textile Res. J., 29, 276, (1959).
144. Neale, S. J. Text. Inst., 20, T373, (1929); 21, T225, (1930); 22, T320, T349, (1931).
145. Peters, R.H. Textile Chemistry, Vol. I and II, Elsevier, Amsterdam, (1967).
146. Qaqish, A.Y.K. and Besant, C.B. Nucl. Instr. and Meth., 138, 493, (1976).
147. Warwicker, J. Swelling, in Cellulose and Cellulose Derivatives, Part IV, ed. N. Bikales and L. Segal, Interscience, New York, (1971).
148. Charlesby, A. Atomic Radiation and Polymers, Pergamon Press, Oxford, (1960).
149. Makhlis, F.A. Radiation Physics and Chemistry of Polymers, Wiley, New York, (1975).
150. Handbook of Chemistry and Physics, 57th Edition, ed. R.C. Weast, CRC Press, Cleveland, (1976).
151. Enge, W. et al. Proc. 8th Int. Conf. on Nuclear Photography and SSNTD's, Bucharest, (1972).
152. Carleton's Histological Technique, Fourth Edition, revised by R. Drury and E. Wallington, Oxford University Press, London, (1967).
153. Galbraith, L. and Rogovin, Z. Derivatives with Unusual Functional Groups, in Cellulose and Cellulose Derivatives, Part V, ed. N. Bikales and L. Segal, Interscience, New York, (1971).
154. Huuang, R.L., Goh, S. and Ong, S. The Chemistry of Free Radicals, Arnold, London, (1974).
155. Hughes, G. Radiation Chemistry, Clarendon Press, Oxford, (1973).
156. Parker, D.B. Polymer Chemistry, Applied Science Publishers, London, (1974).
157. Bernas, A., Chambaudet, A. and Roncin, J. Int. J. Radiat. Phys. Chem., 7, 447, (1974).
158. Florin, R. and Wall, A. J. Polymer Sci., 1A, 1163, (1963).

159. Stannett, V. And Hopfenberg, H. Graft Copolymers, in Cellulose and Cellulose Derivatives, Part V, *ibid.*
160. Ozeroff, J. AEC Research Rep. No. AECD, 2973, (1949).
161. Brooks, H. AEC Research Rep. No. TID-10033, (1950).
162. Dekker, A.J. Phys. Rev., 94, 1179, (1954).
163. Dekker, A.J. Solid State Physics, 6, 251, (1958).
164. Seitz, F. Phys. Rev., 73, 550, (1948).
165. Seitz, F. Phys. Rev., 76, 1376, (1949).
166. Teem, J. Basic Research in Energy Research and Development Administration. IEEE Transactions on Nuclear Science, NS-22, 3, pp. 910-917, June (1975).

APPENDIX A-I

THE ENERGY INTERCHANGE BETWEEN ELECTRONS AND LATTICE

This problem has been considered in some detail for the case of uranium by (160) and (161). The treatments which they give, however, can be applied more generally to insulators, metals and semiconductors. The model is idealized and is treated classically.

A Maxwellian gas of electrons at a temperature T_1 is homogeneously mixed with a second Maxwellian gas of heavy atoms at a lower temperature T_2 . This then represents the state of affairs which is assumed to prevail after passage of the fission fragment. The rate of energy interchange between the electrons themselves, and between the gas atoms, is assumed to be large compared with the rate of interchange between electrons and gas atoms, so that each of the component gases is maintained at equilibrium. The energy interchange may then be computed by considering a pair of particles, one of each type. In the centre of mass system it is:

$$I(\gamma) = \frac{3m_1m_2}{(m_1 + m_2)^2} (kT_1 - kT_2) (1 - \cos\gamma) \quad (\text{A-1.1})$$

where γ is the angle of scattering and m_1 and m_2 are the relevant masses. If in addition to averaging over the two Maxwellian velocity distributions we also average over all values of γ , assuming isotropic scattering, we obtain:

$$(\Delta E)_{av} = \frac{3m_1m_2}{(m_1 + m_2)^2} (kT_1 - kT_2) \quad (\text{A-1.2})$$

The temperatures T_1 and T_2 then satisfy the equations:

$$\frac{d}{dt} \left(\frac{3}{2}kT_1 \right) = - \frac{3m_1m_2}{(m_1 + m_2)^2} \frac{1}{\tau} (kT_1 - kT_2) \quad (\text{A-1.3})$$

$$\frac{d}{dt} \left(\frac{3}{2} kT_2 \right) = \frac{3m_1 m_2}{(m_1 + m_2)^2} \frac{1}{\tau} (kT_1 - kT_2) \quad (\text{A-I.4})$$

where τ is the time between electron/atom collisions.. This may be written:

$$r \frac{(m_1 + m_2)^2}{4m_1 m_2} \frac{d}{dt} (\tau_1 - \tau_2) = - (\tau_1 - \tau_2) \quad (\text{A-I.5})$$

so that the relaxation time is:

$$\tau_R = \frac{(m_1 + m_2)^2}{4m_1 m_2} \tau = \frac{m_2}{4m_1} \tau \quad (\text{A-I.6})$$

The problem of coupling may be represented by the pair of differential equations:

$$K_1 \frac{\partial^2 T_1}{\partial x^2} = C_1 \frac{\partial T_1}{\partial t} + b(T_1 - T_2) \quad (\text{A-I.7})$$

$$K_2 \frac{\partial^2 T_2}{\partial x^2} = C_2 \frac{\partial T_2}{\partial t} - b(T_1 - T_2) \quad (\text{A-I.8})$$

where K_1 and K_2 are conductivities of electrons and atoms respectively, C_1 and C_2 are heat capacities per unit volume, and b is a coefficient of heat transfer between electrons and atoms. For a mixture of perfect gases at two temperatures $C_1 = C_2 = C$, so that we may let:

$$K_1/C = D_1 \quad (\text{A-I.9})$$

$$K_2/C = D_2 \quad (\text{A-I.10})$$

$$b/C = \mu \quad (\text{A-I.11})$$

Solutions to Equations A-I.7 and A-I.8 may be derived by substitutions of the form:

$$T_1 = \alpha_1 \exp(ikx) \exp(\theta t) \quad (\text{A-I.12})$$

$$T_2 = \alpha_2 \exp(ikx) \exp(\theta t) \quad (\text{A-I.13})$$

whence:

$$\theta = -\mu - \frac{(D_1 + D_2)}{2} k^2 \pm \sqrt{\left\{ \left(\frac{D_1 - D_2}{2} \right)^2 + \mu^2 \right\}} \quad (\text{A-I.14})$$

which determines θ as a function of the Fourier transform variable k . For an instantaneous line source produced initially entirely in the electron gas, corresponding to a fission fragment track with uniform heating along its length, the solution for the lattice temperature T_2 becomes:

$$T_2 = \frac{Q_1}{2\pi C_1} \exp(-\mu t) \int_0^\infty \exp(-D_1 + D_2) k^2 t/2) \frac{\sinh(\mu t \sqrt{(1 + \delta^2)})}{\sqrt{(1 + \delta^2)}} J_0(kr) k dk$$

(A-I.15)

where:

$$\delta = \frac{(D_1 - D_2)}{2\mu} k^2$$

(A-I.16)

and Q_1 is the heat generated per unit length of the source.

APPENDIX A-II

THE RANGES OF SECONDARY ELECTRONS IN THE LATTICE

It is assumed that the secondary electron essentially follows a random Brownian-motion path through the crystal before being reduced to the general background energy through collision processes. It is also assumed that only interactions with lattice vibrations are permitted. This then allows us to draw on a theory due to (162) and (163) who has considered the case of the temperature dependence of the secondary electron emission from crystals under primary bombardment. The average energy loss of the secondary in each interaction is independent of the initial energy and is only a function of temperature (164) and (165). Denoting the average energy loss per collision by $\alpha(T)$, the energy of the secondary as a function of the number of collisions n it has suffered since it was energized by a δ -particle is given by:

$$E(n) = E_s - n\alpha(T) \quad (A-II.1)$$

Also, the mean-free-path for collisions with lattice vibrations for electrons with several electron volts of energy is proportional to the energy multiplied by a function of the temperature $\beta(T)$. We may therefore write for the mean-free-path:

$$\lambda(E,T) = \lambda_0 E \beta(T) \quad (A-II.2)$$

where λ_0 is a constant. According to (A-II.1) the energy decreases linearly with n , and therefore so does λ . The 'lifetime' of a secondary in falling to an energy E' is hence limited to a maximum number of scattering collisions n_m such that

$$n_m \alpha(T) = E_s - E' \quad (A-II.3)$$

If we now radically simplify the problem further and assume that the Brownian-motion is one-dimensional we may write the mean square displacement of a secondary during its 'lifetime' of n_m collisions as follows:

$$\langle \chi^2 \rangle_{av} = n_m \langle \lambda^2 \rangle_{av} = n_m \lambda_0^2 \left[\beta(T) \right]^2 \langle E^2 \rangle_{av} \quad (A-II.4)$$

where the averages must be taken over the n_m collisions. The quantity $\langle \chi^2 \rangle_{av}$ may then be considered as the square of a secondary range χ_s' .

Now according to (A-II,1) we may write;

$$\langle E^2 \rangle_{av} = E_s^2 + \alpha^2 \langle n^2 \rangle_{av} - 2\alpha E_s \langle n \rangle_{av} \quad (\text{A-II.5})$$

The average value of n is simply $n_m/2$, and if $n_m \gg 1$ we have:

$$\langle n^2 \rangle_{av} = \int_0^{n_m} \frac{n^2}{n_m} dn = \frac{n_m^2}{3} \quad (\text{A-II.6})$$

Making use of (A-II.3) one readily finds that $\langle E^2 \rangle_{av}$ is independent of temperature and is only determined by the constants E_s and E' :

$$\langle E^2 \rangle_{av} = \frac{1}{3} (E_s^2 + E'^2 + E_s E') \quad (\text{A-II.7})$$

Hence the mean square displacement may be expressed by:

$$\langle \chi^2 \rangle_{av} = \frac{\lambda^2}{3} (E_s - E') (E_s^2 + E'^2 + E_s E') \frac{[\beta(T)]^2}{\alpha(T)} \quad (\text{A-II.8})$$

and the incremental effective range of a secondary electron on this simple model becomes:

$$\chi'_s = k\beta(T) / [\alpha(T)]^{1/2} \quad (\text{A-II.9})$$

where k is a constant factor.

ETCHING CONDITIONS FOR FISSION FRAGMENTS

Note: Because of chemical variations within most minerals, glasses, or plastics of a given type, optimum conditions may vary somewhat from those given. Only the preferred etchant is listed.

A. ETCHANTS FOR MINERALS

Mineral	Etching Conditions	Reference
allanite ($H_2O.4(Ca,Fe)0.3(Al,Fe)_2O_3$.6SiO ₂)	50N NaOH, 2-60 min, 140°C	Naeser and Dodge (1969)
apatite ($Ca_5(F,Cl)(PO_4)_3$)	0.25% HNO ₃ , 1 min, 23°C, or olivine etch without oxalix acid	Bhandari et al (1971b) Lal (unpub.)
aragonite (CaCO ₃)	same as for calcite	
autinite ($Ca(UO_2)_2P_2O_8.8H_2O$)	1% HCl, 10-30 sec, 23°C	Fleischer and Price (1964b)
barite (BaSO ₄)	70% HNO ₃ , 3 h, 100°C	Fleischer and Price (1964b)
barysilite (Pb ₃ Si ₂ O ₇)	glacial acetic acid, 5-70 sec, 23°C	Haack (1973)
bastnasite (CeFCO ₃)	20% HCl, 20-150 min, 155°C	Fleischer and Naeser (1972)
benitoite (CaTiSi ₃ O ₉)	1 ml 40% HF:1 ml 65% HNO ₃ , 5 min, 230°C	Haack (1973)
beryl (Be ₃ Al ₂ Si ₆ O ₁₈)	19N KOH, 9 h, 150°C	Fleischer and Price (1964b)
bismutite (Bi ₂ O ₃ .CO ₂ .H ₂ O)	1g NaOH:1g H ₂ O, 50 min, 140°C	Fleischer, Price and Woods (unpub.)
brewsterite (Sr,Ba,Ca)O.Al ₂ O ₃ .6SiO ₂ .5H ₂ O)	2 ml 48% HF:1 ml 95% H ₂ SO ₄ : 4 ml H ₂ O 3 sec, 230°C	Haack (1973)

APPENDIX B-I (cont.)

Mineral	Etching Conditions	Reference
calcite (CaCO_3)	olivine etch with NaOH added for pH 12, 30 min, 23°C	Lal (unpub.)
celsian ($\text{BaAl}_2\text{Si}_2\text{O}_8$)	19N NaOH, 20 min, boiling	Haack (1973)
cerussite (PbCO_3)	glacial acetic acid, 10-30 min, 23°C	Fleischer et al (1965a)
chlorite ($(\text{Mg,Fe})_5(\text{Al,Fe})_2\text{Si}_3\text{O}_{10}(\text{OH})_8$)	48% HF, 10 min, 23°C	Debeauvais et al (1964)
clinopyroxene (augite, $\text{Ca}(\text{Mg,Re,Al})(\text{Al,Si})_2\text{O}_6$)	2 ml 48% HF: 1 ml 80% H_2SO_4 : 4 ml H_2O , 5-20 min, 23°C	
clinopyroxene (diopside, $\text{CaMgSi}_2\text{O}_6$) (pigeonite, $(\text{Mg,Fe})\text{SiO}_3$) $\cdot (\text{CaMg}(\text{SiO}_3)_2)_{1-x}$	3 g NaOH: 2 g H_2O , 90 min, boiling	Lal et al (1968)
clinopyroxene (diopside, $\text{CaMgSi}_2\text{O}_6$) (pigeonite, $(\text{Mg,Fe})\text{SiO}_3$) $\cdot (\text{CaMg}(\text{SiO}_3)_2)_{1-x}$	3g NaOH: 2 g H_2O , 80 min, boiling	Lal et al (1968)
cryolite (Na_3AlF_6)	50% HI, 3 min, 23°C	Haack (1973)
epidote ($\text{Ca}_2(\text{Al,Fe})_3(\text{SiO}_4)_3\text{OH}$)	50N NaOH, 0.5-2 h, 140°C	Naeser and Doge (1969)
eulytite ($\text{Bi}_4(\text{SiO}_4)_3$)	5% HCl, 60 sec, 23°C	Fleischer, Price and Woods (unpub.)
	33% HNO_3 , 15 min, 23°C	Haack (1973)
feldspar (albite, $\text{NaAlSi}_3\text{O}_8$)	3 g NaOH: 4 g H_2O , 85 min, boiling	Lal et al (1968)
feldspar (anorthite, $\text{CaAl}_2\text{SiO}_2\text{O}_8$)	3 g NaOH: 4 g H_2O , 14 min, boiling	Lal et al (1968)
feldspar (bytownite, An_8Ab_2)	3 g NaOH: 4 g H_2O , 19 min, boiling	Lal et al (1968)
feldspar (labradorite, An_6Ab_4)	3 g NaOH: 4 g H_2O , 40 min, boiling	Lal et al (1968)
feldspar (microcline; orthoclase KAlSi_3O_8)	5 g KOH: 1 g H_2O , 80 min, 190°C	Fleischer, Price and Woods (unpub.)

APPENDIX B-I (cont.)

Mineral	Etching Conditions	Reference
feldspar (oligoclase, An_2Ab_8)	3 g NaOH: 4 g H ₂ O, 75 min, boiling	Lal et al (1968)
fluorite (CaF ₂)	98% H ₂ SO ₄ , 10 min, 23°C	Fleischer and Price (1964b)
garnet (pyrope, Mg ₃ Al ₂ (SiO ₄) ₃)	50N NaOH, 0.5-2 hr, 140°C	Naeser and Dodge (1969)
garnet (almandine-pyrope, (Fe _{1-x} Mg _x) ₃ .Al ₂ (SiO ₄) ₃)	5 to 30 min 50N NaOH, boiling	Haack and Gramse (1972)
garnet (spessartine, Mn ₃ Al ₂ (SiO ₄) ₃)	10 min, 50N NaOH, boiling	Haack and Gramse (1972)
garnet (andradite-grossular; Ca ₃ (Fe _{1-x} Al _x) ₂ .(SiO ₄) ₃)	1 to 6 h, 75N NaOH, boiling	Haack and Gramse (1972)
gillespite (FeO.BaO.4SiO ₂)	19 N NaOH, 12 min, boiling	Haack (1973)
glass (see separate list of etchants for glasses)		
gypsum (CaSO ₄ .2H ₂ O)	5% HF, 5-10 sec, 23°C	Fleischer and Price (1964b)
halite (NaCl)	1 g/l HgCl ₂ in ethanol, 30 sec, 23°C*	Komarov (unpub.)
harmotome (a ₅ (NaK)Al ₁₁ Si ₂₉ O ₈₀ .25H ₂ O)	2.4% HF, 30 sec, 23°C	Haack (1973)
hardystonite (Ca _{1.99} Pb _{.01} ZnSi ₂ O ₇)	1 g NaOH: 1 g H ₂ O, 20-70 min, 140°C	Price et al (1970b)
heulandite (a zeolite, (Ca,Na ₂)O. Al ₂ O ₃ .9SiO ₂ .6H ₂ O)	10 ml aqua regia: 1 ml 48% HF, 30 sec, 23°C	Fleischer (unpub.)
huebnerite (MnWO ₄)	5 g NH ₄ Cl: 5 g Na ₄ P ₂ O ₇ : 5 ml H ₃ PO ₄ : 20 ml H ₂ O, 110 min, boiling	Haack (1973)
kleinite (Hg ₂ N(Cl,SO ₄).nH ₂ O)	37% HCl, 7 min, 23°C	Fleischer, Price and Woods (unpub.)
leuchtenbergite (low-iron clinocllore)	49% HF, 10 min, 23°C	Debeauvais et al (1964)

APPENDIX B-I (cont.)

Mineral	Etching Conditions	Reference
lithium fluoride (LiF)	H ₂ O + .13 gm/liter LiF + 0.5 ppm Fe, ~ 1 min, 23°C*	Johnston (unpub.)
margarite (CaAl ₄ Si ₂ O ₁₀ (OH) ₂)	48% HF, 2 min, 23°C	Fleischer and Price (1964b)
mica (biotite, K(Mg,Fe) ₃ AlSi ₃ O ₁₀ (OH) ₂)	20% HF, 1-2 min, 23°C	Price and Walker (1962a)
mica (lepidolite; zinwaldite, K ₂ Li ₃ Al ₄ Si ₇ O ₂₁ (OH,F) ₃)	48% HF, 3-70 sec, 23°C	Fleischer and Price (1964b)
mica (muscovite, KAl ₃ Si ₃ O ₁₀ (OH) ₂)	48% HF, 10-40 min, 23°C	Price and Walker (1962a)
mica (phlogopite; lepidomelane, KMg ₂ Al ₂ Si ₃ O ₁₀ (OH) ₂)	48% HF; 1-5 min, 23°C	Price and Walker (1962a)
microlite (Ca ₂ Ta ₂ O ₇)	1 ml 48% HF; 1 ml 65% HNO ₃ , 6 min, 23°C	Haack (1973)
mimetite (Pb ₅ Cl(AsO ₄) ₃)	33% HNO ₃ , 3 sec, 23°C (1010 planes)	Haack (1973)
monazite ((Ce,La,Th)(PO ₄ ,SiO ₄))	98% H ₂ SO ₄ , 6-8 min, 23°C*	Muralli and Rajan (unpub.)
mullite (Al ₆ Si ₂ O ₁₃)	25N NaOH, 100°C, 4-5 h	Fleischer (unpub.)
nasonite (Pb ₄ (PbOH) ₂ Ca ₄ (Si ₂ O ₇) ₃)	1 g NaOH: 1 g H ₂ O, 10 min 137°C	Fleischer, Price and Woods (unpub.)
nickel chloride; nickel bromide (NiCl ₂ ,NiBr ₂)	air (40% humidity), 10 min, 20°C (submicroscopic)	Caspar (1964)
olivine ((Mg,Fe) ₂ SiO ₄)	1 ml H ₃ PO ₄ : 1 g oxalic acid: 40 g EDTA: 100 ml H ₂ O: ~ 4.5 g NaOH+, 2-3 h, 125°C ² (or 6 h, 95°C)	Krishnaswami et al (1971)

APPENDIX B-I (cont.)

Mineral	Etching Conditions	Reference
orpiment (As_2S_3)	0.25N NaOH, 10-15 min, 23°C	Perelygin and Otgonsuren (unpub.)
orthopyroxene (bronzite, $\text{Mg}_{1-f}\text{Fe}_f\text{SiO}_3$, (.1<f<.2)	3 g NaOH: 2 g H_2O , 40 min, boiling	Lal et al (1968)
orthopyroxene (enstatite, MgSiO_3)	3 g NaOH: 2 g H_2O , 35 min, boiling	Lal et al (1968)
orthopyroxene (ferrohypersthene, $\text{Mg}_{1-f}\text{Fe}_f\text{SiO}_3$, f>.5)	3 g NaOH: 2 g H_2O , 70 min, boiling	Lal et al (1968)
orthopyroxene (hypersthene, $\text{Mg}_{1-f}\text{Fe}_f\text{SiO}_3$, (.2<f<.5)	3 g NaOH: 2 g H_2O , 42 min, boiling	Lal et al (1968)
pennine (a chlorite)	48% HF, 5 min, 23°C	Fleischer and Price (1964b)
pollucite ($\text{H}_2\text{O}.2\text{Cs}_2\text{O}.2\text{Al}_2\text{O}_3.9\text{SiO}_2$)	5-8% HF, 35 sec, 23°C	Haack (1973)
pucherite (BiVO_4)	5% HCl, 90 sec, 23°C	Fleischer, Price and Woods (unpub.)
pyromorphite ($\text{Pb}_5\text{Cl}(\text{PO}_4)_3$)	33% HNO_3 , 5 sec, 23°C, (on (10 $\bar{1}$ 0) planes)	Haack (1973)
quartz (SiO_2)	KOH(aq), 3 h, 150°C, or 48% HF, 24 h, 23°C	Fleischer and Price (1964b)
raspite (PbWO_4)	6.25N NaOH, 4 min, 23°C	Fleischer, Price and Woods (unpub.)
sanbornite (BaSi_2O_3)	19N NaOH, 60 min, boiling	Haack (1973)
scheelite (CaWO_4)	6.25N NaOH, 90 min, 95°C	Fleischer, Price and Woods (unpub.)
sphene (CaTiSiO_5)	conc HCl 0.5-1.5 h, 90°C 6N NaOH, 20-30 min, 130°C	Naeser and Faul (1969) Calk and Naeser (1973)
spodumene ($\text{LiAlSi}_2\text{O}_6$)	48% HF, 24 h, 23°C	Fleischer and Price (1964b)

APPENDIX B-I (cont.)

Mineral	Etching Conditions	Reference
stilbite ((Ca,Na ₂)).Al ₂ O ₃ .65SiO ₂ .6H ₂ O), a zeolite)	1% HF, 60 sec, 23°C	Fleischer (unpub.)
stibiotantalite ((SbO) ₂ (Ta,Nb) ₂ O ₆)	1 ml 48% HF: 1 ml 65% HNO ₃ , 6 min 23°C	Haack (1970)
talc (Mg ₃ Si ₄ O ₁₀ (OH) ₂)	48% HF, 15 min 23°C	Walker (1963)
thorite (ThSiO ₄)	H ₃ PO ₄ , 1 min, 250°C	Fleischer et al (1965a;1966b)
torbernite (Cu(UO ₂) ₂ P ₂ O ₈ .12H ₂ O)	10% HCl, 10 min, 23°C	Fleischer et al (1965a)
tridymite (SiO ₂)	10% HF, 1 h, 23°C	Fleischer et al (1965a)
topaz (Al ₂ SiO ₄ (F,OH) ₂)	KOH(aq), 100 min, 150°C	Fleischer and Price (1964b)
tourmaline (complex silicate)	KOH(aq), 20 min, 220°C	Fleischer and Price (1964b)
vanadinite (Pb ₅ Cl(VO ₄) ₃)	33% HNO ₃ ; 1 sec, 23°C	Haack (1973)
vermiculite (biotate-derived)	48% HF, 5-10 sec, 23°C	Fleischer and Hart (unpub.)
whitlockite (Ca ₃ (PO ₄) ₂)	0.25% HNO ₃ , 10 sec to 2 min, 23°C or olivine etch without oxalic acid	Fleischer et al (1965a) Lal (unpub.)
willemite (Zn ₂ SiO ₄)	33% HNO ₃ , 10 sec, 23°C	Haack (1973)
zircon (ZrSiO ₄)	H ₃ PO ₄ , few sec, 375-500°C, or NaOH(aq), .25 to 5 h, 220°C, or 2 ml 48% HF: 1 ml 80% H ₂ SO ₄ at 180°C in a pressure bomb	Fleischer et al (1964a) Naeser (1969) Krishnaswami et al (1973)

*shallow pits †to adjust pH to 8.0

APPENDIX B-I (cont.)

ETCHANTS FOR GLASSES

Type	Etching Conditions (at 23°C if not otherwise noted)	Reference
alumino-silicate (Corning 1720)	5.7% HF, 6 min	Fleischer and Hart (1972c)
andesitic glass (Ab ₆₀ An ₄₀)	5% HF, 3-5 min 29% HBF ₄ : 5% HNO ₃ : 0.5% acetic acid, 50 min	Fleischer et al (1969a) Macdougall (1971)
basaltic glass	20% HF, 1 min 25% HBF ₄ : 5% HNO ₃ : 0.5% acetic acid, 10 min	Fleischer et al (1968b) Macdougall (1971)
borate glass	H ₂ O 1 min	Fleischer and Price (1963b)
flint (lead-silicate) glass	5.7% HF, 3 min	Fleischer et al (1971a)
germania glass (GeO ₂)	48% HF, 6 sec	Fleischer (unpub.)
lead phosphate glass	1 ml 70% HNO ₃ : 3 ml H ₂ O, 2-20 min	Lal (unpub.)
obsidian	48% HF, 30 sec	Fleischer and Price (1964c)
phosphate glass	48% HF, 5-20 min	Fleischer and Price (1963b)
pumice	5% HF, 500 sec	Fleischer et al (1965e)
silica glass (fused quartz; Vycor; Libyan Desert Glass)	48% HF, 1 min	Fleischer and Price (1963b)
soda-lime (microscope slide; cover slip; window glass)	48% HF, 5 sec (better: 5% HF, 2 min) 24% HBF ₄ : 5% HNO ₃ : 0.5% acetic acid, 1 h	Fleischer and Price (1963b) Macdougall (1971)

APPENDIX B-I (cont.)

Type	Etching Conditions	Reference
tektite	48% HF, 30 sec 24% HBF ₄ : 5% HNO ₃ : 0.5% acetic acid 90 min	Fleischer and Price (1964a) Macdougall (1971)
uranium-soda glass	48% HF, 5 sec	Brill et al (1964)
uranium phosphate glass	50% HF, 30 min	Hart (unpub.)
V ₂ O ₅ ·(P ₂ O ₅) ₅ (semiconducting)	48% HF, 10 sec	Fleischer et al (1965d)

ETCHANTS FOR PLASTICS

Plastic (Trade Names)	Etching Conditions	Reference
amber	30 g K ₂ Cr ₂ O ₇ : 50 ml conc. H ₂ SO ₄ , 40 h, 28°C	Uzgiris and Fleischer (1971)
cellulose acetate (Kodacel; Triafol T; Cellit)†	1 ml 15% NaClO: 2 ml 6.25N NaOH, 1 h, 40°C 25g NaOH: 20 g KOH: 4.5 g KMnO ₄ : 90 g H ₂ O, 2-30 min, 50°C	Price et al (1971) Somogyi et al (1968)
cellulose acetate butyrate†	6.25N NaOH, 12 min, 70°C	Fleischer et al (1965d)
cellulose nitrate (Diacell; Nixon-Baldwin)†	6.25N NaOH, 2-4 h, 23°C	Fleischer et al (1965b)
cellulose nitrate (Kodak-Pathe)	2.5N NaOH, 15-20 h, 22°C	Qaqish et al (1976)(146)

APPENDIX B-I (cont.)

Plastic (Trade Names)	Etching Conditions	Reference
cellulose propionate (Cellidor)	28% KOH, 100 min, 60°C	Becker (1969)
cellulose triacetate (Kodacel TA401, unplasticized; Bayer TN)†	1 ml 15% NaClO: 2 ml 6.25N NaOH 1 h, 40°C	Price et al (1970a)
dimethyl siloxane (crosslinked)	25N NaOH, 3 min, 115°C	Fleischer and Bergeron (unpub.)
formophenol (ambrolithe, phenoplaste)	6N NaOH, 1 h, 40°C; 48% HF, 30 sec, 40°C, in sequence	Monnin et al (1966)
HBpaIT (polyester, C ₁₇ H ₉ O ₂)	6.25N NaOH, 8 min, 70°C	Fleischer et al (1965a)
ionomeric polyethylene (Surlyn)†	10 g K ₂ Cr ₂ O ₇ : 35 ml 30% H ₂ SO ₄ , 1 h 50°C	Besson et al (1967)
polyamide (H-Film)	KMnO ₄ (25% aq), 1.5 h, 100°C 6N NaOH solution	Besson et al (1967) Fleischer (unpub.)
polyimide	KMnO ₄ in H ₂ O	Monnin and Isabelle (1970)
poly 1-4 butylene terephthalate	1 ml 6.25N NaOH: 1 ml ethanol, 24 h, 23°C	Fleischer (unpub.)
polycarbonate (Lexan; Makrofol; Merlon; Kimfol)†	6.25N NaOH, 20 min, 50°C 6.25N NaOH + 0.4% Benax*, 20 min, 70°C	Fleischer and Price (1963a)
polyethylene	10 g K ₂ Cr ₂ O ₇ : 35 ml 30% H ₂ SO ₄ , 30 min, 85°C	Monnin et al (1967)
polyethylene terephthalate (Mylar; Chronar; Melinex; Terphane)	6.25N NaOH, 10 min, 70°C KMnO ₄ (25%,aq), 1h 55°C	Fleischer and Price (1963a) Monnin et al (1967)
polymethyl methacralate (Flexiglas; Lucite)†	sat. KMnO ₄ , 8 min, 85°C	Monnin et al (1966)

APPENDIX B-I (cont.)

Plastic (Trade Names)	Etching Conditions	Reference
polyoxymethyl (Delrin)	5% KMnO_4 , 10 h, 60°C	Monnin et al (1966)
polyphenoxide	KMnO_4 , (25% aq.), 4 min, 100°C	Besson et al (1967)
polyphenylene oxide (PPO)	KMnO_4 aq., sat., 24 h, 93°C	Fleischer (unpub.)
polypropylene (Cryovac-Y)†	35 ml 30% H_2SO_4 : 10 g, $\text{Cr}_2\text{K}_2\text{O}_7$, 5 min, 94°C	Besson et al (1967)
polystyrene	sat. KMnO_4 , 2.5 h, 85°C	Monnin et al (1966)
	10 g $\text{K}_2\text{Cr}_2\text{O}_7$: 35 ml, 30% H_2SO_4 , 3 h, 85°C	Monnin et al (1967)
polyvinyl acetate (Formvar)	6.25N NaOH, 200 h, 23°C	Fleischer (unpub.)
polyvinylaceto-chloride	KMnO_4 (25% aq.) 30 min, 100°C	Besson et al (1967)
polyvinylchloride	sat. KMnO_4 , 2.5 h, 85°C	Monnin et al (1966)
polyvinylidene chloride (Saran)	KMnO_4 (25% aq.), 2 h, 35°C	Besson et al (1967)
polyvinyl toluene	KMnO_4 , sat., aq., 30 min, 100°C	Fleischer and Price (unpub.)
silicone-polycarbonate copolymer	6.25N NaOH 20 min, 50°C	Fleischer et al (1972b)
siloxane-cellulose copolymer	8N NaOH + ~ 0.1% Dowfax, 3 h, 85°C	Fleischer, Viertl and Holub (unpub.)

*Dow surfactant 2A1, Dowfax, Dow Corning: presaturated with etch products (Peterson, 1970).

†Tracks of low-energy alpha particles can be revealed by etching this plastic.

TRACK ANNEALING CHARACTERISTICS

Note- Data given here pertain (except as noted) to fission fragment tracks, which in general will have different annealing characteristics from other tracks. Unless noted differently, all data are for annealing in air at atmospheric pressure. For extensive annealing data for tracks of Kr, Zn, Fe and Cl ions in various silicate minerals, see Price et al (1973).

Material	Activation Energy (Electron Volts)			1 Hour Annealing Temperature (°C)			Reference
	Total Fading	50% Track Loss	Start of Track Loss	Total Fading	50% Track Loss	Start of Track Loss	
Amber (Baltic)	-	3.0	-	-	110	-	Uzgiris and Fleischer (1971)
Apatite	-	-	-	530	-	400	Fleischer and Price (1964b)
	-	2.2	-	-	336	-	Wagner (1968)
	2.8	2.1	1.62	375	322	275	Naeser and Faul (1969)
Aragonite (CaCO ₃)	-	-	-	150	-	130	Fleischer et al (1968a)
Autinite	-	-	-	60	-	40	Fleischer and Price (1964b)
Barysilite	-	3.3	-	-	440	-	Fleischer, Price & Woods (unpub)
Calcite (CaCO ₃)	-	-	-	-	200(g)	-	MacDougall (unpub.)
Cellulose acetate (Cellit-T)	-	-	-	165	~160	>100	Somogyi (1972b)
Cellulose nitrate (Kodak- Pathe)	-	-	-	-	~125	-	Qaqish et al (1976)

APPENDIX B-II (cont.)

Cellulose nitrate (Nixon-Baldwin)	-	-	-	-	85	-	Fleischer et al (1965d)
(Daicel; fission frag)	-	-	-	147	~140	>110	Somogyi (1972b)
(Daicel; alpha particles)	-	-	-	138	~130	<110	Somogyi (1972b)
Epidote	18.2(a)	12.5	6.0	715	680	575	Naeser and Dodge (1969)
	-	8	-	-	650	-	Wagner (1972)
Feldspar (Albite)	~5	-	-	775(b)	-	-	Fleischer et al (1967)
Feldspar (Anorthite)	-	-	-	~680(b)	550(b)	350(b)	Crozaz et al (1970)
Feldspar (Bytownite)	-	6.6	-	790	750	690	Fleischer et al (1965d)
Garnet (Ca _{2.91} Fe _{.09} .Fe _{.82} Al _{1.18}).(SiO ₄) ₃)	8.4	5.4	2.1	690	665	560	Haack and Potts (1972)
Glass (Aluminosilicate Corning 1720)	-	-	-	500	320	100	Fleischer and Hart (1972c)
Glass (Andesitic impact glass)	2.5	-	1.1	250	-	190	Fleischer et al (1969a)
Glass (Basaltic, tachy- litic impact glasses)	-	2.6	-	-	190-225	-	Fleischer et al (1969a)
Glass (Basaltic)	1.9	1.6	1.3	240	190	140	Macdougall (1973)
Glass (Basaltic, tholeitic)	-	2.2	-	300	-	280	Fleischer et al (1968b)
	-	2.2	-	-	275	-	Fleischer et al (1971c)
	-	2.3	-	-	275	-	Aumento (1969)
Glass (Borosilicate, pyrex)	>2.5	1.2	-	380	302	-	Fleischer (unpub.)
	-	-	-	-	275	-	Fleischer et al (1965d)
Glass (Lunar black, Apollo 12)	-	1.3	-	-	250	-	Fleischer et al (1971b)

APPENDIX B-II (cont.)

Glass (Feldspathic)	-	-	-	235	-	200	Fleischer et al (1968c)
Glass (Lunar green, Apollo 15, >2.6 g/cc)	-	3.5(b)	-	417(b)	337(b)	321(b)	Fleischer and Hart (1972b)
Glass (Lunar green, Apollo 15, <2.6 g/cc)	-	5.3(b)	-	372(b)	307(b)	285(b)	Fleischer and Hart (1972b)
Glass (Libyan desert, 98% SiO ₂)	3.6(c)	1.9	1.2(d)	570(c)	460	330(d)	Storzer and Wagner (1971)
	-	-	1.3(e)	-	-	335(e)	Gentner et al (1969)
Glass (Obsidian)	-	1.8	-	-	390	-	Suzuki (1970)
Glass (Obsidian, .3% H ₂ O)	-	2.3(f)	-	-	262(f)	-	Lakatos and Miller (1972b)
Glass (Obsidian, .8% H ₂ O)	-	2.0(f)	-	-	250(f)	-	Lakatos and Miller (1972b)
Glass (Obsidian, 2.2%, H ₂ O)	-	1.5(f)	-	-	190(f)	-	Lakatos and Miller (1972b)
Glass (Ryolite)	-	1.9	-	-	262	-	Aumento and Souther (1973)
Glass (Phosphate)	-	-	-	300	-	150	Perelygin et al (1969)
(Phosphate)	-	-	-	190	130	90	Fleischer and Hart (1972c)
Glass (Pitchstone)	-	1.6	-	-	450	-	Storzer (1970)
	-	-	-	700	-	-	Fleischer and Price (1963b)
Glass (Silica)	-	-	-	>500	290	100	Fleischer and Hart (1972c)
	-	-	-	370	-	-	Fleischer and Price (1963b)
Glass (Soda lime)	-	-	-	-	190	-	Fleischer and Hart (1972c)
Glass (NBS soda lime) (4 glasses)	-	1.5-2.0	0.7-1.2	-	230	110	Reimer et al (1972)
Glass (Australian tektite)	2.8	1.7	1.05	510	380	225	Storzer and Wagner (1969)
Glass (Bediasite tektite)	3.5(a)	1.6	.94(d)	510(c)	370	220(d)	Storzer and Wagner (1971)
	2.8(g)	1.6	1.15(e)	490(g)	360	235(e)	Durrani and Khan (1970)

APPENDIX B-II (cont.)

Glass (Indochina tektite							
1 atm	-	2.51	-	-	500	-	Fleischer and Price (1964a)
10 kbar	-	1.7	-	-	360	-	Fleischer et al (1965c)
60 kbar	-	.75	-	-	100	-	Fleischer et al (1965c)
Glass ($V_2O_5 \cdot 5P_2O_5$)	-	1.2	-	-	95	-	Fleischer et al (1956d)
Hardystonite	-	5.7	-	-	450	-	Fleischer, Price & Woods (unpub.)
Hornblende	-	-	-	630	590	530	Fleischer et al (1968a)
	-	-	-	750	720	650	Maurette (1970), Crozaz et al (1969)
	-	-	-	500(h)	315(h)	100(h)	Maurette (1970), Crozaz et al (1969)
Mica (Biotite)	-	1.7	-	-	-	-	Shukolyukov & Komarov (1966)
Mica (Lepidolite)	-	2.0	-	-	-	-	Shukolyukov & Komarov (1966)
Mica (Muscovite)	-	-	-	540	510	450	Fleischer et al (1964b)
	-	2.8	-	680	-	510	Fleischer et al (1964b)
	-	-	-	550	-	275	Perelygin et al (1969)
	-	-	-	700	670	550	Maurette (1970)
	-	-	-	600(h)	520(h)	290(h)	Maurette (1970)
	-	1.0	-	-	-	-	Shukolyukov et al (1965)
	-	-	-	>600	540	400	Mehta and Rama (1969)
Mica (Phlogopite)	-	1.8	-	550	-	350	Maurette et al (1964) Fleischer et al (1964b)
Monazite	-	0.3-0.7	-	-	300	-	Shukolyukov & Komarov (1970)
Mullite	-	-	-	270(+130)	525(+25)	625(+75)	Fleischer, Hart & Giard (unpub.)
Nasonite	-	5.3	-	450	-	-	Fleischer, Price & Woods (unpub.)

APPENDIX B-II (cont.)

Olivine (1 atm and at 80 kbar)	3.3	-	-	500	-	-	Fleischer et al (1965c)
Pollucite	-	1.3	-	-	670	-	Fleischer, Price and Woods (unpub.)
Polycarbonate (Lexan)	-	-	-	>185	-	-	Fleischer & Price (1963a)
	-	-	-	-	-	< 40	Hart, Giard & Fleischer (unpub.)
	-	-	-	-	170	110	Khan & Durrani (1972a)
(Makrofol)	-	-	-	200	~190	100	Somogyi (1972b)
Pyroxene (Augite)	-	-	-	560(b)	480(b)	300(b)	Crozaz et al (1970)
Pyroxene (Diopside)	-	~10	-	-	875	-	Fleischer et al (1967)
	-	-	-	880	850	820	Fleischer et al (1968c)
Pyroxene (Enstatite)	-	~ 5(b)	-	-	450(b)	-	Fleischer et al (1967)
Pyroxene (Hypersthene)	-	-	-	475(b)	-	-	Fleischer et al (1968c)
	-	-	-	600	-	525	Naurette (1970)
	-	-	-	500(b)	330(b)	300(b)	Maurette (1970)
Pyroxene (Pigeonite)	-	-	-	530	-	500	Fleischer et al (1968a)
Quartz (SiO ₂) (b)	-	-	-	1050	-	1000	Fleischer et al (1968a)
	4.0	-	-	-	-	-	Kosanke (1972)
Sphene (HCl etch)	5.5	4.0	3.0	637	620	520	Naeser & Faul (1969)
(NaOH etch)	5.5	4.8	4.3	780	740	680	Calk and Naeser (1973)
Zircon (1 atm)	-	3.6	-	-	700	-	Fleischer et al (1964a)
(80 kbar)	-	3.6	-	-	675	-	Fleischer et al (1965c)

(a) No fading observed at T < 600°C. (b) Fe-group cosmic ray tracks. (c) 95% loss. (d) 5% loss.
(e) 10% loss. (f) 30% loss. (g) 90% loss. (h) Alpha interaction tracks. (i) Synthetic quartz has lower track
retentivity.

CHEMICAL EFFECTS ON PARTICLE TRACKS

Track Detector	Chemical	Environmental Effect	Reference
<u>Plastics</u>			
cellulose acetate	ozone	v_G^* and v_T increased	Somogyi (1972a)
cellulose acetate	oxygen	v_G and v_T increased	Kartuzhanskii et al (1970)
cellulose triacetate	humid air	v_T/v_G increased	Becker (1968)
cellulose triacetate	nitrogen	v_T/v_G decreased	Becker (1968)
cellulose triacetate	H ₂ O ₂	v_T/v_G increased	Becker (1968)
cellulose nitrate	high electric field (ozone?)	v_T/v_G increased	Crannell et al (1969)
cellulose nitrate	oxygen	v_T/v_G increased	Boyett et al (1970)
cellulose nitrate	oxygen	v_T or v_G increased	Kartuzhanskii et al (1970)
cellulose nitrate	camphor added	v_T/v_G increased	Vepruk et al (1970)
cellulose nitrate	ozone	v_G increased	Somogyi (1972a)
cellulose nitrate	water at 50°C	v_G and v_T increased	Enge et al (1970)
cellulose nitrate	swelling	v_T/v_G REL critical	Qaqish et al (1977), (101)
polycarbonate	nitrogen	v_T decreased	Crawford et al (1968)
polycarbonate	products of spark discharge (a nitrogen oxide?)	v_T increased	Blanford et al (1970b)

APPENDIX B-III (cont.)

Track Detector	Chemical	Environmental Effect	Reference
polycarbonate	Cl replacement of H	v_T/v_G decreased	Pai (1973)
polycarbonate	oxygen	v_T increased	Monnin (1968)
polycarbonate	oxygen	v_T increased	Henke et al (1970)
polycarbonate	ozone	v_G and v_T increased	Somogyi (1972a)
<u>Minerals</u>			
muscovite mica	H ₂ O pressure	increases fading rate	Lakatos and Miller (1970,1973), Miller and Lakatos (1970)
volcanic glass	H ₂ O pressure	increases fading rate	Lakatos and Miller (1972a,b)

* $v_G = v_B$ (Bulk etching rate of the detector)

PHOTO-OXIDATION EFFECTS ON PARTICLE TRACKS

Material	Exposure	Effect	Reference
cellulose nitrate	O ₂ + UV	sensitivity increased (plus bulk damage)	Henke et al (1970)
polycarbonate	O ₂ + UV	v _T increased (max. increase at 3040 (+ 100) Å)	Crawford et al (1968) DeSorbo and Humphrey (1970)
polycarbonate	O ₂ + UV	v _T increased (max. increase at 3130 Å)	Henke et al (1970)
polycarbonate	N ₂ O + UV	v _T decreased	DeSorbo and Humphrey (1970)
polycarbonate	NO + UV	v _T increased	DeSorbo and Humphrey (1970)
polycarbonate	H ₂ O ₂ + UV	v _T increased; sensitivity increased	Caputi and Crawford (1970), Henke et al (1970)
polyethylene terephthalate	O ₂ + UV	sensitivity increased	Henke et al (1970)

IRRADIATION EFFECTS ON PARTICLE TRACK ETCHING

Material	Irradiation	Effect	Reference
cellulose nitrate (Daicell)	1.5 MeV electrons, 16 MR (Megarads)	* v_G doubled	Price, Fleischer and Miller, (1969 unpub.)
cellulose nitrate (Daicell)	thermal neutrons 10^{14} nvt	v_G increased factor of 6	R. Scanlon (unpub.)
cellulose nitrate (Hercules)	5 MR, γ -rays	10% increase in v_G	Boyett and Becker (1970)
cellulose nitrate (Hercules)	.006 MR, fast neutrons	10% increase in v_G	Boyett and Becker (1970)
cellulose triacetate (Triafol T)	6 MR, γ -rays	1% increase in v_G	Boyett and Becker (1970)
cellulose triacetate (Triafol T)	.008 MR, fast neutrons	0.5% increase in v_G	Boyett and Becker (1970)
cellulose triacetate (Kodacel)	1.5 MeV electrons, 12 MR	v_G doubled	Price, Fleischer and Miller, (1969 unpub.)
dimethyl siloxane	1.5 MeV electrons 20 MR	v_G decreased	Fleischer, Hart & Nichols, (1972, unpub.)
polycarbonate (Lexan)	1.3 MeV γ -rays 200 MR	v_G doubled	Frank and Benton (1970)
polycarbonate (Lexan)	1.5 MeV electrons 25 MR	v_T increased	DeSorbo (1968, unpub.)
polycarbonate (Lexan)	alpha particles 100 MR	v_G increased by recoil pits	Stone (1969)
polycarbonate (Kimfol)	.006 MR fast neutrons	10% increase in v_G	Boyett and Becker (1970)
polycarbonate (Kimfol)	8 MR γ -rays	<0.1% increase in v_G	Boyett and Becker (1970)

APPENDIX B-V (cont.)

Material	Irradiation	Effect	Reference
polyethylene terephthalate (Mylar)	.007 MR, fast neutrons	1% increase in v_G	Boyett and Becker (1970)
polyethylene terephthalate (Mylar)	7 MR, γ -rays	1% increase in v_G	Boyett and Becker (1970)
phosphate glass	UV, 2×10^{11} ergs/cm ²	v_G or v_T decreased	Hart et al (1973, unpub.)
natural micas	100 keV electrons	track fading	Silk and Barnes (1959)
olivine, muscovite, biotite, phlogopite, tektite glass	1.5 MeV electrons 2×10^3 MR	no effect	Fleischer et al (1965c)
silica glass	20 keV electrons, 3×10^5 MR	v_G doubled	Krättschmer (1971)
silica glass	UV, 2×10^{11} ergs/cm ²	no effect	Hart et al (1973 unpub.)
soda glass	UV, 2×10^{11} ergs/cm ²	no effect	Hart et al (1973 unpub.)
soda glass	1.4×10^{17} protons of 3 MeV	v_G doubled, v_T increased 50%	Durrani (1973 unpub.)

* $v_G = v_B$ (Bulk etching rate of the detector).

METHODS OF LOCATING OR ENLARGING TRACKS

Technique	Track Density where useful	Limitations or Special Features	Reference
Etch aluminium-backed plastic from front, transmits light where metal removed.	< 100/cm ²	Oblique tracks require longer etch, non-uniform hole sizes (but see text).	Fleischer et al (1966a)
Apply potential; (a) observe spark location, (b) scan enlarged holes.	< 10/cm ² < 10 ⁴ /cm ²	High voltage can enlarge holes, including ones that were not quite open.	Flemons (1968), Cross and Tommasino (1968) Lark (1969)
Apply potential, scan holes evaporated in thin aluminium coating by discharge.	<3000/cm ²	Alters etched tracks	Cross and Tommasino (1970,1972)
Press dye through holes onto filter paper	< 10/cm ²	Separate sheet shows track location	Price (1963 unpub.), Alter (1968), Sherwood (1970), Khan (1971)
Blow NO ₃ through holes, thus staining sensitive paper.	< 1/cm ²	Gives separate sheet showing track location, rapid scanning rate (10 ³ cm ² /min)	Blok et al (1969)
Measure resistance of track etched across membrane in electrolyte.	(1 to 10 tracks total)	Can give etching rates v_T and v_G	Walker et al (1965), DeSorbo and Humphrey (1970), Bean et al (1970), DeBlois and Bean (1970)
Enlarge images using slide projector.	10 ⁴ to 5 x 10 ⁶	Individually counted on projection screen.	Khan and Durrani (1972b)
Measure UV light transmission in Mylar, which strongly absorbs	10 ³ to 10 ⁷	Detects light when hole not quite through sheet.	Pretre et al (1968)

AUTOMATED OR INTEGRATING SCANNING METHODS

Technique	Scanning Rate cm ² /min	Track Density cm ⁻²	Comments	Reference
Optical scanning	.15		Pulse height discrimination	Bitter et al (1967)
Optical scanning (Quantimet)			Signal characteristic can be selected	Besant and Ipson (1970), Abmayr et al (1969), Ruegger et al (1969), Jowitt (1971)
Optical scanning (with automatic focussing)	.002	10 ³ - 10 ⁵	Works well on Makrofol polycarbonate, less well on mica	Cohn et al (1969), Cohn and Gold (1972), Gold and Cohn (1972), Goel and Eggmann(1972)
D.C. spark counting with scaler	10	0-3000	D.C. Voltage develops some flaws	Lark (1969), Cross and Tommasino (1968,1970,1972), Abmayr et al (1969), Congel et al (1970), Johnson et al (1970), Somogyi and Gulyas (1972), Paretzke (1972)
A.C. spark counting with scaler	100 to 200 (up to 100 counts/sec)		Avoids most flaws	Geisler and Phillips (1972)
Light scattering		10 ⁴ to 10 ⁶		Becker (1966), Tuyn (1967), Schultz (1968), Khan (1971)
Light transmission through opaque plastic		4 x 10 ⁴ to 3 x 10 ⁶	Ultraviolet light through Mylar	Pretre et al (1968)

APPENDIX B-VII (cont.)

Technique	Scanning Rate cm ² /min	Track Density cm ⁻²	Comments	Reference
Electrical conductivity through membrane Surface barrier detector plus membrane detector Intensity of scattered coherent light Automatic digitising	 1.75 x 10 ⁻³	1 to 10 ¹¹ 10 ² - 10 ⁵ 5 x 10 ⁴ to 10 ⁶ 10 ⁵ - 10 ⁶	 Detects alpha particles transmitted through holes in membrane Linear for scattering at 54°C Signal characteristic can be selected	Walker et al (1963), DeSorbo and Humphrey (1970) Khan and Durrani (1972b) Platzer et al (1972) Qaqish et al (1977)*

*Automatic Digitising System, Imperial College, Department of Mechanical Engineering (unpublished).

APPENDIX C

ALPHA TRACKS (PARTICLES INCIDENT AT ANGLE $\theta = 90^\circ$)

TO THE SURFACE OF THE SEMI CONDUCTOR DETECTOR

Alpha Particle Energy in MeV	0.60	0.65	0.70	0.75	0.80	0.85	0.90	0.95
Monitor Dose in Alpha Particles (normal to detector)	20280 46990	15990 51321	18595 48411	17690 44341	16394 43489	15829 51241	16299 54322	14686 42127
Track Density in Tracks/mm ² (expected) (normal to detector)	2868.46 6646.39	2261.67 7258.98	2630.13 6847.38	2502.12 6271.71	2318.81 6151.20	2238.90 7247.67	2305.37 7683.45	2077.23 5958.56
Track Density in Tracks/Frame (expected) (normal to detector)	114.74 265.86	90.47 290.36	105.21 273.90	100.08 250.87	92.75 246.05	89.56 289.91	92.21 307.34	83.09 238.34

APPENDIX C (cont.)

ALPHA TRACKS (PARTICLES INCIDENT AT ANGLE $\theta = 90^\circ$ TO THE SURFACE OF THE SEMI CONDUCTOR DETECTOR)

1.00	1.25	1.50	2.00	2.50	3.00	3.50	3.60	3.70
14898 54850	15198 41401	14614 49950	22777 46930	14646 41709	14689 41900	20189 44359	12255 40000	22282 47433
2107.21 7758.13	2149.65 5855.87	2067.04 7065.06	3221.64 6637.91	2071.57 5899.43	2077.65 5926.45	2855.59 6274.26	1733.38 5657.71	3151.63 6709.05
84.29 310.33	85.99 234.23	82.68 282.60	128.87 265.52	82.86 235.98	83.11 237.06	114.22 250.97	69.34 226.31	126.07 268.36

APPENDIX C (cont.)

ALPHA TRACKS (PARTICLES INCIDENT AT ANGLE $\theta = 90^\circ$ TO THE SURFACE OF THE SEMI CONDUCTOR DETECTOR)

3.80	3.90	4.00	4.25	4.50	4.75	5.00	5.50	6.00
23679	13840	14610	18605	13997	19480	17780	14978	14031
42741	47601	54970	54970	50470	48413	50105	49902	51460
3349.22	1257.57	2066.48	2631.54	1979.77	2755.30	2514.85	2118.53	1984.58
6045.40	6732.81	7258.59	7775.11	7138.61	6847.67	7086.99	7058.27	7278.64
133.97	78.30	82.66	105.26	79.19	110.21	100.59	84.74	79.38
241.82	269.31	290.30	311.00	285.54	273.91	283.48	282.23	291.15

ALPHA TRACKS (PARTICLES INCIDENT AT ANGLE $\theta = 90^\circ$ TO THE SURFACE OF THE PLASTIC DETECTOR)*

	0.60	0.65	0.70	0.75	0.80	0.85	0.90	0.95
Total tracks counted								
(1) tracks/88 frames	(1) 9980	(1) 7861	(1) 9168	(1) 8707	(1) 8089	(1) 7799	(1) 7998	(1) 7241
(2) tracks/44 frames (observed)	(2) 11465	(2) 13034	(2) 11861	(2) 10836	(2) 11037	(2) 12519	(2) 13283	(2) 10379
Track density in tracks/frame (observed)	(1) 113.41 (2) 260.57	(1) 89.33 (2) 296.23	(1) 104.18 (2) 269.57	(1) 98.94 (2) 246.27	(1) 91.92 (2) 250.84	(1) 88.63 (2) 284.52	(1) 90.89 (2) 301.89	(1) 82.28 (2) 235.89
Efficiency of detector	(1) 98.84 ± 0.82	(1) 98.74 ± 0.75	(1) 99.02 ± 0.72	(1) 98.86 ± 0.75	(1) 99.11 ± 0.64	(1) 98.96 ± 0.69	(1) 98.57 ± 0.81	(1) 99.03 ± 0.64
Tracks/frame (observed)	(2) 98.01	(2) 102.02	(2) 98.42	(2) 98.17	(2) 101.95	(2) 98.14	(2) 98.23	(2) 98.97
Tracks/frame x 100 (expected) Normal to the detector	± 1.01	± 1.65	± 0.85	± 0.81	± 1.15	± 0.92	± 0.93	± 0.98

*Films were etched in 2.5 N NaOH at 18°C (completely submerged).

ALPHA TRACKS (PARTICLES INCIDENT AT ANGLE $\theta = 90^\circ$ TO THE SURFACE OF THE PLASTIC DETECTOR)

1.00	1.25	1.50	2.00	2.50	3.00	3.50	3.60	3.70
(1) 7353	(1) 7486	(1) 7196	(1) 11233	(1) 7229	(1) 7245	(1) 9958	(1) 6049	(1) 10974
(2) 13531	(2) 10158	(2) 12229	(2) 11814	(2) 10261	(2) 10328	(2) 10859	(2) 9787	(2) 11630
(1) 83.56	(1) 85.07	(1) 81.77	(1) 127.65	(1) 82.15	(1) 82.33	(1) 113.16	(1) 68.74	(1) 124.70
(2) 307.52	(2) 230.86	(2) 277.93	(2) 268.50	(2) 233.20	(2) 234.73	(2) 246.80	(2) 222.43	(2) 26.432
(1) 99.13	(1) 98.93	(1) 98.90	(1) 99.05	(1) 99.14	(1) 99.06	(1) 99.07	(1) 99.13	(1) 98.91
± 0.60	± 0.68	± 0.85	± 0.73	± 0.85	± 0.85	± 0.79	± 0.55	± 0.83
(2) 99.09	(2) 98.56	(2) 98.35	(2) 101.12	(2) 98.82	(2) 99.02	(2) 98.34	(2) 98.29	(2) 98.49
± 0.91	± 0.88	± 0.87	± 1.13	± 0.89	± 0.95	± 0.86	± 0.79	± 0.74

ALPHA TRACKS (PARTICLE INCIDENT AT ANGLE $\theta = 90^\circ$ TO THE SURFACE OF THE PLASTIC DETECTOR)

3.80 (a)*	3.90 (a)*	4.00 (a)*	4.25 (a)*	4.50 (a)*	4.75 (a)*	5.00 (a)*	5.50 (a)*	6.00 (a)*
(1) 11666	(1) 6814	(1) 7164	(1) 9115	(1) 6897	(1) 9604	(1) 8756	(1) 7380	(1) 6909
(2) 10472	(2) 11651	(2) 12537	(2) 13410	(2) 12336	(2) 11880	(2) 12262	(2) 12210	(2) 12556
(1) 132.57	(1) 77.43	(1) 81.41	(1) 103.58	(1) 78.38	(1) 109.14	(1) 99.50	(1) 83.86	(1) 78.15
(2) 238.00	(2) 26.480	(2) 284.93	(2) 304.78	(2) 280.36	(2) 270.00	(2) 278.68	(2) 277.50	(2) 285.36
(1) 98.95	(1) 98.89	(1) 98.49	(1) 98.40	(1) 98.98	(1) 99.03	(1) 98.92	(1) 98.96	(1) 98.90
± 0.84	± 0.66	± 0.79	± 0.92	± 0.64	± 0.73	± 0.74	± 0.66	± 0.66
(2) 98.42	(2) 98.33	(2) 98.15	(2) 98.00	(2) 98.19	(2) 98.57	(2) 98.31	(2) 98.29	(2) 98.01
± 0.76	± 0.87	± 0.84	± 0.80	± 0.90	± 0.96	± 0.85	± 0.81	± 0.72

+ a Etching was carried for another 12 hours to reveal a well shaped round etch pit.

ALPHA TRACKS (PARTICLE INCIDENT AT ANGLE $\theta = 80^\circ$ TO THE SURFACE OF THE PLASTIC DETECTOR)

Alpha Particle Energy in MeV	0.60	0.65	0.70	0.75	0.80	0.85	0.90	0.95
Total tracks counted (1) tracks 188 frames (2) tracks 144 frames	(1) 9830 (2) 11240	(1) 7744 (2) 12710	(1) 9034 (2) 11693	(1) 8576 (2) 10621	(1) 7965 (2) 10685	(1) 7683 (2) 12354	(1) 7877 (2) 13015	(1) 7133 (2) 10229
Track density in tracks/frame counted	(1) 111.70 (2) 225.45	(1) 88.00 (2) 288.86	(1) 102.66 (2) 265.75	(1) 97.45 (2) 241.39	(1) 90.51 (2) 242.84	(1) 87.31 (2) 280.77	(1) 89.51 (2) 295.80	(1) 81.06 (2) 232.48
Efficiency of detector = $\frac{\text{Tracks/Frame (observed)}}{\text{Tracks/Frame (expected)}}$ normal to the surface of the detector	(1) 97.35 ± 0.81 (2) 96.08 ± 0.79	(1) 97.27 ± 0.57 (2) 99.48 ± 1.01	(1) 97.58 ± 0.47 (2) 97.02 ± 0.65	(1) 97.37 ± 0.60 (2) 96.22 ± 0.63	(1) 97.58 ± 0.44 (2) 98.70 ± 0.93	(1) 97.49 ± 0.48 (2) 96.85 ± 0.71	(1) 97.07 ± 0.65 (2) 96.25 ± 0.83	(1) 97.56 ± 0.43 (2) 97.54 ± 0.74

ALPHA TRACKS (PARTICLES INCIDENT AT ANGLE $\theta = 80^\circ$ TO THE SURFACE OF THE PLASTIC DETECTOR)

1.00	1.25	1.50	2.00	2.50	3.00	3.50	3.60	3.70
(1) 7242	(1) 7374	(1) 7088	(1) 11060	(1) 7112	(1) 7136	(1) 9811	(1) 9811	(1) 10814
(2) 13126	(2) 10006	(2) 12051	(2) 11622	(2) 10095	(2) 10172	(2) 10647	(2) 9667	(2) 11445
(1) 82.30	(1) 83.80	(1) 80.55	(1) 125.68	(1) 80.82	(1) 81.09	(1) 111.49	(1) 67.48	(1) 122.89
(2) 298.32	(2) 227.41	(2) 273.89	(2) 264.14	(2) 229.43	(2) 231.18	(2) 241.98	(2) 219.70	(2) 260.11
(1) 97.64	(1) 97.45	(1) 97.42	(1) 97.52	(1) 97.54	(1) 97.57	(1) 97.61	(1) 97.32	(1) 97.48
± 0.39	± 0.48	± 0.49	± 0.55	± 0.44	± 0.42	± 0.48	± 0.49	± 0.57
(2) 96.13	(2) 97.09	(2) 96.92	(2) 99.48	(2) 97.22	(2) 97.52	(2) 96.42	(2) 97.08	(2) 96.93
± 0.89	± 1.03	± 0.61	± 1.24	± 0.96	± 0.75	± 0.59	± 1.02	± 0.52

ALPHA TRACKS (PARTICLES INCIDENT AT ANGLE $\theta = 80^\circ$ TO THE SURFACE OF THE PLASTIC DETECTOR)

3.80	3.90	4.00	4.25	4.50	4.75	5.00	5.50	6.00
(1) 11430 (2) 10249	(1) 6710 (2) 11497	(1) 6993 (2) 12467	(1) 9036 (2) 12980	(1) 6792 (2) 12260	(1) 9448 (2) 11702	(1) 8638 (2) 12078	(1) 7278 (2) 12040	(1) 6774 (2) 12370
(1) 129.89 (2) 232.93	(1) 76.25 (2) 261.30	(1) 79.47 (2) 283.34	(1) 102.68 (2) 295.00	(1) 77.18 (2) 278.64	(1) 107.36 (2) 265.95	(1) 98.16 (2) 274.50	(1) 82.70 (2) 273.64	(1) 76.98 (2) 281.14
(1) 96.95 ± 0.84 (2) 96.32 ± 0.64	(1) 97.38 ± 0.49 (2) 97.03 ± 1.01	(1) 96.14 ± 0.88 (2) 97.60 ± 0.76	(1) 97.55 ± 0.49 (2) 94.86 ± 0.83	(1) 97.46 ± 0.46 (2) 97.58 ± 0.77	(1) 97.41 ± 0.57 (2) 97.09 ± 0.49	(1) 97.58 ± 0.46 (2) 96.83 ± 0.55	(1) 97.59 ± 0.42 (2) 96.92 ± 0.53	(1) 96.98 ± 0.64 (2) 96.56 ± 0.50

ALPHA TRACKS (PARTICLE INCIDENT AT ANGLE $\theta = 70^\circ$ TO THE SURFACE OF THE PLASTIC DETECTOR)

Alpha Particle Energy in MeV	0.60	0.65	0.70	0.75	0.80	0.85	0.90	0.95
Monitor Dose in Alpha Particles Normal to Detector	(1) 9377 (2) 10841	(1) 7381 (2) 11880	(1) 8621 (2) 11172	(1) 8187 (2) 10186	(1) 7603 (2) 10151	(1) 7337 (2) 11809	(1) 7520 (2) 12481	(1) 6816 (2) 9769
Track Density in Tracks/mm ² expected Normal to detector	(1) 106.56 (2) 246.39	(1) 83.88 (2) 270.00	(1) 97.97 (2) 25.391	(1) 93.03 (2) 231.50	(1) 86.40 (2) 230.70	(1) 83.38 (2) 268.39	(1) 85.45 (2) 283.66	(1) 77.45 (2) 222.02
Track Density in Tracks/Frame (expected) Normal to detector)	(1) 93.23 ± 0.70 (2) 92.68 ± 0.68	(1) 92.72 ± 0.76 (2) 92.99 ± 0.39	(1) 93.12 ± 0.68 (2) 92.70 ± 0.41	(1) 92.96 ± 0.72 (2) 92.28 ± 0.50	(1) 93.15 ± 0.63 (2) 93.76 ± 0.54	(1) 93.10 ± 0.63 (2) 92.58 ± 0.45	(1) 92.67 ± 0.78 (2) 92.30 ± 0.61	(1) 93.21 ± 0.57 (2) 93.15 ± 1.00

ALPHA TRACKS (PARTICLE INCIDENT AT ANGLE $\theta = 70^\circ$ TO THE SURFACE OF THE PLASTIC DETECTOR)

1.00	1.25	1.50	2.00	2.50	3.00	3.50	3.60	3.70
(1) 6913	(1) 7039	(1) 6767	(1) 10565	(1) 6782	(1) 6809	(1) 9357	(1) 5671	(1) 10321
(2) 12523	(2) 9561	(2) 11500	(2) 10919	(2) 9638	(2) 9715	(2) 10214	(2) 9253	(2) 10936
(1) 78.56	(1) 79.99	(1) 76.90	(1) 120.06	(1) 77.07	(1) 77.38	(1) 106.33	(1) 64.44	(1) 117.28
(2) 289.61	(2) 217.30	(2) 261.36	(2) 248.15	(2) 219.05	(2) 220.80	(2) 232.14	(2) 210.30	(2) 248.55
(1) 93.20	(1) 93.02	(1) 93.01	(1) 93.16	(1) 93.01	(1) 93.11	(1) 93.09	(1) 92.93	(1) 93.03
± 0.58	± 0.65	± 0.64	± 0.73	± 0.64	± 0.61	± 0.72	± 0.61	± 0.78
(2) 91.71	(2) 92.77	(2) 92.48	(2) 93.46	(2) 92.83	(2) 93.14	(2) 92.50	(2) 92.93	(2) 92.16
± 0.82	± 0.42	± 0.72	± 0.85	± 0.57	± 1.01	± 0.50	± 1.10	± 0.68

ALPHA TRACKS (PARTICLE INCIDENT AT ANGLE $\theta = 70^\circ$ TO THE SURFACE OF THE PLASTIC DETECTOR)

3.80	3.90	4.00	4.25	4.50	4.75	5.00	5.50	6.00
(1) 10974 (2) 9860	(1) 6407 (2) 11038	(1) 6673 (2) 11896	(1) 8620 (2) 12429	(1) 6493 (2) 11715	(1) 8933 (2) 11169	(1) 8240 (2) 11518	(1) 6943 (2) 11481	(1) 6498 (2) 11817
(1) 124.70 (2) 224.09	(1) 72.81 (2) 250.86	(1) 75.83 (2) 270.36	(1) 97.95 (2) 282.48	(1) 73.78 (2) 266.25	(1) 101.51 (2) 253.84	(1) 93.64 (2) 261.77	(1) 78.90 (2) 260.93	(1) 73.84 (2) 268.57
(1) 93.08 ± 0.78 (2) 92.67 ± 0.65	(1) 92.99 ± 0.63 (2) 93.15 ± 0.48	(1) 91.74 ± 0.97 (2) 93.13 ± 0.49	(1) 93.06 ± 0.71 (2) 90.83 ± 0.81	(1) 93.17 ± 0.57 (2) 93.24 ± 0.47	(1) 93.11 ± 1.02 (2) 92.67 ± 0.65	(1) 93.09 ± 0.68 (2) 92.34 ± 0.57	(1) 93.11 ± 0.61 (2) 92.05 ± 0.51	(1) 93.02 ± 0.62 (2) 92.24 ± 0.42

ALPHA TRACKS (PARTICLE INCIDENT) AT ANGLE $\theta = 60^\circ$ TO THE SURFACE OF THE PLASTIC DETECTOR

Alpha Particle Energy in MeV	0.60	0.65	0.70	0.75	0.80	0.85	0.90	0.95
Total tracks counted	(1) 8647	(1) 6809	(1) 7953	(1) 7533	(1) 7010	(1) 6763	(1) 6934	(1) 6286
(1) tracks 188 frames	(2) 9949	(2) 10977	(2) 10314	(2) 9398	(2) 9338	(2) 10901	(2) 11518	(2) 9008
Track density in tracks/frame counted	(1) 98.26 (2) 226.77	(1) 77.38 (2) 249.48	(1) 90.38 (2) 234.41	(1) 85.60 (2) 213.59	(1) 79.66 (2) 212.23	(1) 76.85 (2) 247.75	(1) 78.80 (2) 261.77	(1) 71.43 (2) 204.73
Efficiency of detector = tracks/ frame (observed)	(1) 85.64 ± 0.74	(1) 85.53 ± 0.82	(1) 85.90 ± 0.76	(1) 85.53 ± 0.86	(1) 85.89 ± 0.72	(1) 85.81 ± 0.73	(1) 85.46 ± 0.84	(1) 85.97 ± 0.66
Tracks/frame expected normal to the surface of the detector	(2) 85.05 ± 0.70	(2) 85.92 ± 0.58	(2) 85.58 ± 0.40	(2) 85.14 ± 0.59	(2) 86.25 ± 0.96	(2) 85.46 ± 0.47	(2) 84.17 ± 0.75	(2) 85.90 ± 0.68

ALPHA TRACKS (PARTICL INCIDENT) AT ANGLE $\theta = 60^\circ$ TO THE SURFACE OF THE PLASTIC DETECTOR

1.00	1.25	1.50	2.00	2.50	3.00	3.50	3.60	3.70
(1) 6327	(1) 6496	(1) 6241	(1) 9724	(1) 6243	(1) 6296	(1) 8617	(1) 5225	(1) 9525
(2) 11426	(2) 8820	(2) 10642	(2) 10018	(2) 8888	(2) 8993	(2) 9453	(2) 8534	(2) 10134
(1) 71.90	(1) 73.82	(1) 70.92	(1) 110.50	(1) 70.94	(1) 71.55	(1) 97.92	(1) 59.38	(1) 108.24
(2) 259.68	(2) 200.45	(2) 241.86	(2) 227.68	(2) 202.00	(2) 204.39	(2) 214.84	(2) 193.95	(2) 230.32
(1) 85.30	(1) 85.85	(1) 85.78	(1) 85.75	(1) 85.61	(1) 86.09	(1) 85.73	(1) 85.64	(1) 85.86
± 0.85	± 0.70	± 0.71	± 0.90	± 0.76	± 0.61	± 0.85	± 0.69	± 0.85
(2) 83.68	(2) 85.58	(2) 85.58	(2) 85.75	(2) 85.60	(2) 86.22	(2) 85.60	(2) 85.70	(2) 85.83
± 0.83	± 0.41	± 0.41	± 0.57	± 0.40	± 0.96	± 0.40	± 0.52	± 0.53

ALPHA TRACKS (PARTICLE INCIDENT) AT ANGLE $\theta = 60^\circ$ TO THE SURFACE OF THE PLASTIC DETECTOR

3.80	3.90	4.00	4.25	4.50	4.75	5.00	5.50	6.00
(1) 10173 (2) 9132	(1) 5900 (2) 10159	(1) 6168 (2) 11006	(1) 7252 (2) 11372	(1) 5981 (2) 10779	(1) 8309 (2) 10305	(1) 7599 (2) 10667	(1) 6401 (2) 10626	(1) 5989 (2) 10908
(1) 115.60 (2) 207.55	(1) 67.05 (2) 230.89	(1) 70.09 (2) 250.14	(1) 82.41 (2) 258.45	(1) 67.97 (2) 244.98	(1) 94.42 (2) 234.20	(1) 86.35 (2) 242.43	(1) 72.74 (2) 241.50	(1) 68.06 (2) 247.91
(1) 86.29 ± 0.69 (2) 85.83 ± 0.53	(1) 85.63 ± 0.73 (2) 85.73 ± 0.55	(1) 84.79 ± 0.96 (2) 86.17 ± 0.48	(1) 78.29 ± 0.90 (2) 83.10 ± 0.89	(1) 85.83 ± 0.68 (2) 85.80 ± 0.43	(1) 85.67 ± 0.86 (2) 85.50 ± 0.44	(1) 85.84 ± 0.76 (2) 85.52 ± 0.45	(1) 85.84 ± 0.70 (2) 85.54 ± 0.42	(1) 85.74 ± 0.71 (2) 85.15 ± 0.77

ALPHA TRACKS (PARTICLE INCIDENT) AT ANGLE $\theta = 50^\circ$ TO THE SURFACE OF THE PLASTIC DETECTOR

Alpha Particle Energy in MeV	0.60	0.65	0.70	0.75	0.80	0.85	0.90	0.95
Total tracks counted	(1) 7645	(1) 6014	(1) 7050	(1) 6699	(1) 6193	(1) 5989	(1) 6126	(1) 5568
(1) tracks 188 frames	(2) 8892	(2) 9719	(2) 9157	(2) 8403	(2) 8219	(2) 9722	(2) 10224	(2) 7989
Track density in tracks/frame counted	(1) 86.88	(1) 68.34	(1) 80.11	(1) 76.13	(1) 70.38	(1) 68.06	(1) 69.61	(1) 63.27
	(2) 202.09	(2) 220.89	(2) 208.11	(2) 190.98	(2) 186.80	(2) 220.95	(2) 232.36	(2) 181.57
Efficiency of detector = tracks/ <u>frame (observed)</u>	(1) 75.72	(1) 75.54	(1) 76.14	(1) 76.07	(1) 75.88	(1) 75.99	(1) 75.49	(1) 76.16
	± 0.71	± 0.81	± 0.67	± 0.68	± 0.72	± 0.67	± 0.83	± 0.60
<u>Tracks/frame expected</u> normal to the surface of the detector	(2) 76.01	(2) 76.07	(2) 75.98	(2) 76.13	(2) 75.92	(2) 76.21	(2) 75.60	(2) 76.18
	± 0.41	± 0.68	± 0.65	± 0.60	± 0.53	± 0.74	± 0.71	± 0.73

ALPHA TRACKS (PARTICLE INCIDENT) AT ANGLE $\theta = 50^\circ$ TO THE SURFACE OF THE PLASTIC DETECTOR

1.00	1.25	1.50	2.00	2.50	3.00	3.50	3.60	3.70
(1) 5647	(1) 5757	(1) 5529	(1) 8614	(1) 5539	(1) 5554	(1) 7638	(1) 4632	(1) 8424
(2) 10047	(2) 7833	(2) 9392	(2) 8867	(2) 7859	(2) 7961	(2) 8348	(2) 7556	(2) 9015
(1) 64.17	(1) 65.42	(1) 62.83	(1) 97.89	(1) 62.94	(1) 63.11	(1) 86.80	(1) 52.64	(1) 95.73
(2) 228.34	(2) 178.02	(2) 213.45	(2) 201.52	(2) 178.61	(2) 180.93	(2) 189.73	(2) 171.73	(2) 204.89
(1) 76.13	(1) 76.08	(1) 75.99	(1) 75.96	(1) 75.96	(1) 75.94	(1) 75.99	(1) 75.92	(1) 75.93
± 0.61	± 0.63	± 0.65	± 0.82	± 0.66	± 0.67	± 0.76	± 0.61	± 0.82
(2) 73.58	(2) 76.00	(2) 75.53	(2) 75.90	(2) 75.69	(2) 76.32	(2) 75.60	(2) 75.88	(2) 76.35
± 1.11	± 0.40	± 0.42	± 0.50	± 0.65	± 0.90	± 0.71	± 0.72	± 0.93

ALPHA TRACKS (PARTICLE INCIDENT) AT ANGLE $\theta = 50^\circ$ TO THE SURFACE OF THE PLASTIC DETECTOR

3.80	3.90	4.00	4.25	4.50	4.75	5.00	5.50	6.00
(1) 9007	(1) 5226	(1) 5438	(1) 7042	(1) 5299	(1) 7347	(1) 6725	(1) 5664	(1) 5299
(2) 8087	(2) 8993	(2) 9706	(2) 10081	(2) 9564	(2) 9116	(2) 9440	(2) 9406	(2) 9655
(1) 102.35	(1) 59.39	(1) 61.80	(1) 80.02	(1) 60.22	(1) 83.49	(1) 76.42	(1) 64.36	(1) 60.22
(2) 183.80	(2) 204.39	(2) 220.59	(2) 229.11	(2) 217.36	(2) 207.18	(2) 214.55	(2) 213.77	(2) 219.43
(1) 76.40	(1) 75.85	(1) 74.76	(1) 76.02	(1) 76.04	(1) 75.76	(1) 75.97	(1) 75.95	(1) 75.86
± 0.64	± 0.67	± 0.96	± 0.72	± 0.61	± 0.83	± 0.79	± 0.67	± 0.67
(2) 76.01	(2) 75.89	(2) 75.99	(2) 73.67	(2) 76.12	(2) 75.64	(2) 75.68	(2) 75.72	(2) 75.37
± 0.41	± 0.48	± 0.67	± 1.19	± 0.43	± 0.71	± 0.76	± 0.61	± 0.70

ALPHA TRACKS (PARTICLE INCIDENT) AT ANGLE $\theta = 45^\circ$ TO THE SURFACE OF THE PLASTIC DETECTOR

Alpha Particle Energy in MeV	0.60	0.65	0.70	0.75	0.80	0.85	0.90	0.95
Total tracks counted (1) tracks 188 frames (2) tracks 144 frames	(1) 7059 (2) 8174	(1) 5561 (2) 8953	(1) 6499 (2) 8429	(1) 6166 (2) 7718	(1) 5723 (2) 7589	(1) 5525 (2) 8944	(1) 5662 (2) 9471	(1) 5132 (2) 7366
Track density in tracks/frame counted	(1) 80.22 (2) 185.77	(1) 63.19 (2) 203.48	(1) 73.85 (2) 191.57	(1) 70.07 (2) 175.41	(1) 65.03 (2) 172.48	(1) 62.78 (2) 203.27	(1) 64.34 (2) 215.25	(1) 58.32 (2) 167.41
Efficiency of detector = tracks/ frame (observed) <u>Tracks/frame expected</u> normal to the surface of the detector	(1) 69.91 ± 0.68 (2) 69.88 ± 0.54	(1) 69.85 ± 0.72 (2) 70.08 ± 0.41	(1) 70.19 ± 0.65 (2) 69.94 ± 0.40	(1) 70.01 ± 0.72 (2) 69.92 ± 0.44	(1) 70.11 ± 0.64 (2) 70.10 ± 0.42	(1) 70.10 ± 0.64 (2) 70.11 ± 0.68	(1) 69.78 ± 0.75 (2) 70.04 ± 0.49	(1) 70.19 ± 0.58 (2) 70.24 ± 0.51

ALPHA TRACKS (PARTICLE INCIDENT) AT ANGLE $\theta = 45^\circ$ TO THE SURFACE OF THE PLASTIC DETECTOR

1.00	1.25	1.50	2.00	2.50	3.00	3.50	3.60	3.70
(1) 5207	(1) 5296	(1) 5095	(1) 7948	(1) 5103	(1) 5118	(1) 7038	(1) 4266	(1) 7766
(2) 9272	(2) 7201	(2) 8697	(2) 8188	(2) 7262	(2) 7355	(2) 7731	(2) 6973	(2) 8316
(1) 59.17	(1) 60.18	(1) 57.90	(1) 90.32	(1) 57.99	(1) 58.16	(1) 79.98	(1) 48.48	(1) 88.25
(2) 210.73	(2) 163.66	(2) 197.66	(2) 186.09	(2) 165.05	(2) 167.16	(2) 175.70	(2) 158.48	(2) 189.00
(1) 70.20	(1) 69.98	(1) 70.03	(1) 70.09	(1) 69.99	(1) 69.98	(1) 70.04	(1) 69.92	(1) 70.00
± 0.58	± 0.66	± 0.63	± 0.77	± 0.65	± 0.65	± 0.75	± 0.61	± 0.79
(2) 67.91	(2) 69.87	(2) 69.94	(2) 70.09	(2) 69.94	(2) 70.51	(2) 70.01	(2) 70.03	(2) 70.43
± 0.86	± 0.55	± 0.42	± 0.41	± 0.42	± 0.76	± 0.72	± 0.75	± 0.88

ALPHA TRACKS (PARTICLE INCIDENT) AT ANGLE $\theta = 45^\circ$ TO THE SURFACE OF THE PLASTIC DETECTOR

3.80	3.90	4.00	4.25	4.50	4.75	5.00	5.50	6.00
(1) 8313	(1) 4818	(1) 5018	(1) 6494	(1) 4893	(1) 6786	(1) 6209	(1) 5231	(1) 4896
(2) 7479	(2) 8302	(2) 8964	(2) 9298	(2) 8812	(2) 8301	(2) 8609	(2) 8701	(2) 8916
(1) 94.47	(1) 54.75	(1) 57.02	(1) 73.80	(1) 55.60	(1) 77.11	(1) 70.56	(1) 59.44	(1) 55.64
(2) 169.98	(2) 188.68	(2) 203.73	(2) 211.32	(2) 200.27	(2) 188.66	(2) 195.66	(2) 197.75	(2) 202.64
(1) 70.52	(1) 69.92	(1) 68.98	(1) 70.11	(1) 70.21	(1) 69.97	(1) 70.15	(1) 70.14	(1) 70.09
± 0.57	± 0.65	± 0.91	± 0.68	± 0.56	± 0.75	± 0.66	± 0.60	± 0.60
(2) 70.29	(2) 70.06	(2) 70.18	(2) 67.95	(2) 70.14	(2) 68.88	(2) 69.02	(2) 70.07	(2) 69.60
± 0.93	± 0.39	± 0.53	± 0.43	± 0.52	± 0.94	± 0.89	± 0.50	± 0.56

ALPHA TRACKS (PARTICLE INCIDENT) AT ANGLE $\theta = 40^\circ$ TO THE SURFACE OF THE PLASTIC DETECTOR

Alpha Particle Energy in MeV	0.60	0.65	0.70	0.75	0.80	0.85	0.90	0.95
Total tracks counted	(1) 6416	(1) 5040	(1) 5896	(1) 5617	(1) 5198	(1) 5008	(1) 5135	(1) 4641
(1) tracks 188 frames	(2) 7459	(2) 8141	(2) 7660	(2) 7045	(2) 6897	(2) 8137	(2) 8600	(2) 6675
(2) tracks 144 frames								
Track density in tracks/frame counted	(1) 72.91	(1) 57.27	(1) 67.00	(1) 63.83	(1) 59.07	(1) 56.91	(1) 58.35	(1) 52.74
	(2) 169.52	(2) 185.02	(2) 174.09	(2) 160.11	(2) 156.75	(2) 184.93	(2) 195.45	(2) 151.70
Efficiency of detector = tracks/ frame (observed)	(1) 63.84	(1) 63.30	(1) 63.68	(1) 63.78	(1) 63.69	(1) 63.54	(1) 63.28	(1) 63.47
	± 0.65	± 0.56	± 0.41	± 0.33	± 0.54	± 0.45	± 0.58	± 0.47
Tracks/frame expected normal to the surface of the detector	(2) 63.76	(2) 63.72	(2) 63.56	(2) 63.82	(2) 63.71	(2) 63.79	(2) 63.59	(2) 63.65
	± 0.83	± 0.64	± 0.78	± 0.47	± 0.60	± 0.55	± 0.79	± 0.65

ALPHA TRACKS (PARTICLE INCIDENT) AT ANGLE $\theta = 40^\circ$ TO THE SURFACE OF THE PLASTIC DETECTOR

1.00	1.25	1.50	2.00	2.50	3.00	3.50	3.60	3.70
(1) 4731	(1) 4827	(1) 4640	(1) 7224	(1) 4649	(1) 4262	(1) 6412	(1) 3886	(1) 7086
(2) 8404	(2) 6575	(2) 7927	(2) 7429	(2) 6602	(2) 6619	(2) 7042	(2) 6349	(2) 7490
(1) 53.76	(1) 54.85	(1) 52.73	(1) 82.09	(1) 52.83	(1) 48.43	(1) 72.86	(1) 44.16	(1) 80.52
(2) 191.01	(2) 149.43	(2) 180.16	(2) 168.84	(2) 150.05	(2) 150.43	(2) 160.05	(2) 144.30	(2) 170.23
(1) 63.78	(1) 63.79	(1) 63.78	(1) 63.70	(1) 63.76	(1) 58.27	(1) 63.79	(1) 63.69	(1) 63.87
± 0.30	± 0.30	± 0.30	± 0.44	± 0.32	± 1.22	± 0.35	± 0.33	± 0.29
(2) 61.55	(2) 63.80	(2) 63.75	(2) 63.59	(2) 63.59	(2) 63.46	(2) 63.77	(2) 63.76	(2) 63.43
± 1.11	± 0.49	± 0.59	± 0.74	± 0.70	± 0.80	± 0.53	± 0.52	± 0.87

ALPHA TRACKS (PARTICLE INCIDENT) AT ANGLE $\theta = 40^\circ$ TO THE SURFACE OF THE PLASTIC DETECTOR

3.80	3.90	4.00	4.25	4.50	4.75	5.00	5.50	6.00
(1) 7501	(1) 4386	(1) 4570	(1) 5915	(1) 4449	(1) 6170	(1) 5648	(1) 4757	(1) 4452
(2) 6747	(2) 7546	(2) 8143	(2) 8451	(2) 8005	(2) 7663	(2) 7938	(2) 7928	(2) 8113
(1) 85.24	(1) 49.84	(1) 51.93	(1) 67.22	(1) 50.56	(1) 70.11	(1) 64.18	(1) 54.06	(1) 50.59
(2) 153.34	(2) 171.50	(2) 185.07	(2) 192.07	(2) 181.93	(2) 174.16	(2) 180.41	(2) 180.18	(2) 184.39
(1) 63.63	(1) 63.65	(1) 62.82	(1) 63.86	(1) 63.85	(1) 63.61	(1) 63.80	(1) 63.80	(1) 63.73
± 0.50	± 0.37	± 0.70	± 0.27	± 0.25	± 0.46	± 0.31	± 0.29	± 0.33
(2) 63.41	(2) 63.68	(2) 63.75	(2) 61.76	(2) 63.71	(2) 63.58	(2) 63.64	(2) 63.82	(2) 63.33
± 0.84	± 0.66	± 0.60	± 0.95	± 0.64	± 0.76	± 0.71	± 0.47	± 0.99

ALPHA TRACKS (PARTICLE INCIDENT) AT ANGLE $\theta = 30^\circ$ TO THE SURFACE OF THE PLASTIC DETECTOR

Alpha Particle Energy in MeV	0.60	0.65	0.70	0.75	0.80	0.85	0.90	0.95
Total tracks counted	(1) 4993	(1) 3932	(1) 4599	(1) 4361	(1) 4049	(1) 3912	(1) 4005	(1) 3634
(1) tracks 188 frames	(2) 5778	(2) 6345	(2) 5987	(2) 5461	(2) 5361	(2) 6319	(2) 6704	(2) 5219
Track density in tracks/frame counted	(1) 56.74	(1) 44.68	(1) 52.26	(1) 49.56	(1) 46.01	(1) 44.45	(1) 45.51	(1) 41.30
	(2) 131.32	(2) 144.20	(2) 136.07	(2) 124.11	(2) 121.84	(2) 143.61	(2) 152.36	(2) 118.61
Efficiency of detector = tracks/ frame (observed)	(1) 49.45	(1) 49.39	(1) 49.67	(1) 49.52	(1) 49.61	(1) 49.63	(1) 49.65	(1) 49.71
	± 0.56	± 0.53	± 0.42	± 0.49	± 0.43	± 0.41	± 0.55	± 0.35
Tracks/frame expected normal to the surface of the detector	(2) 49.39	(2) 49.66	(2) 49.68	(2) 49.47	(2) 49.52	(2) 49.54	(2) 49.57	(2) 49.77
	± 0.90	± 0.70	± 0.66	± 0.81	± 0.77	± 0.82	± 0.81	± 0.53

ALPHA TRACKS (PARTICLE INCIDENT) AT ANGLE $\theta = 30^\circ$ TO THE SURFACE OF THE PLASTIC DETECTOR

1.00	1.25	1.50	2.00	2.50	3.00	3.50	3.60	3.70
(1) 3685	(1) 3755	(1) 3613	(1) 5628	(1) 3615	(1) 3632	(1) 4989	(1) 3024	(1) 5481
(2) 6561	(2) 5098	(2) 6175	(2) 5799	(2) 5139	(2) 5172	(2) 5481	(2) 4944	(2) 5858
(1) 41.88	(1) 42.67	(1) 41.06	(1) 63.95	(1) 41.08	(1) 41.27	(1) 56.69	(1) 34.36	(1) 62.28
(2) 149.11	(2) 115.86	(2) 140.34	(2) 131.80	(2) 116.80	(2) 117.55	(2) 124.57	(2) 112.36	(2) 133.14
(1) 49.69	(1) 49.62	(1) 49.66	(1) 49.62	(1) 49.58	(1) 49.66	(1) 49.63	(1) 49.55	(1) 49.40
± 0.36	± 0.40	± 0.37	± 0.49	± 0.42	± 0.38	± 0.46	± 0.39	± 0.61
(2) 48.05	(2) 49.46	(2) 49.66	(2) 49.64	(2) 49.50	(2) 49.59	(2) 49.64	(2) 49.65	(2) 49.61
± 0.82	± 0.79	± 0.69	± 0.69	± 0.77	± 0.70	± 0.68	± 0.63	± 0.72

ALPHA TRACKS (PARTICLE INCIDENT) AT ANGLE $\theta = 30^\circ$ TO THE SURFACE OF THE PLASTIC DETECTOR

3.80	3.90	4.00	4.25	4.50	4.75	5.00	5.50	6.00
(1) 5845	(1) 3416	(1) 3558	(1) 4586	(1) 3442	(1) 4803	(1) 4394	(1) 3702	(1) 3464
(2) 5276	(2) 5879	(2) 6347	(2) 6555	(2) 6224	(2) 5965	(2) 6176	(2) 6160	(2) 6341
(1) 66.42	(1) 38.82	(1) 40.43	(1) 52.11	(1) 39.11	(1) 54.58	(1) 49.93	(1) 42.07	(1) 39.36
(2) 119.91	(2) 133.61	(2) 144.25	(2) 148.98	(2) 141.45	(2) 135.57	(2) 140.36	(2) 140.00	(2) 144.11
(1) 49.58	(1) 49.58	(1) 48.91	(1) 49.51	(1) 49.39	(1) 49.52	(1) 49.64	(1) 49.65	(1) 49.58
± 0.53	± 0.41	± 0.67	± 0.51	± 0.49	± 0.51	± 0.30	± 0.39	± 0.41
(2) 49.59	(2) 49.61	(2) 49.69	(2) 47.90	(2) 49.54	(2) 49.49	(2) 49.51	(2) 49.59	(2) 49.50
± 0.71	± 0.72	± 0.67	± 0.94	± 0.81	± 0.83	± 0.83	± 0.75	± 0.86

ALPHA TRACKS (PARTICLE INCIDENT) AT ANGLE $\theta = 20^\circ$ TO THE SURFACE OF THE PLASTIC DETECTOR

Alpha Particle Energy in MeV	0.60	0.65	0.70	0.75	0.80	0.85	0.90	0.95
Total tracks counted (1) tracks 188 frames (2) tracks 144 frames	(1) 3421 (2) 3970	(1) 2683 (2) 4347	(1) 3143 (2) 4078	(1) 2978 (2) 3736	(1) 2757 (2) 3689	(1) 2676 (2) 4325	(1) 2742 (2) 4582	(1) 2470 (2) 3548
Track density in tracks/frame counted	(1) 38.88 (2) 90.23	(1) 30.49 (2) 98.15	(1) 35.72 (2) 92.68	(1) 33.84 (2) 84.91	(1) 31.33 (2) 83.84	(1) 30.41 (2) 98.30	(1) 31.16 (2) 104.14	(1) 28.07 (2) 80.64
Efficiency of detector = tracks/ frame (observed)	(1) 33.89 ± 0.26	(1) 33.70 ± 0.37	(1) 33.95 ± 0.16	(1) 33.81 ± 0.31	(1) 33.78 ± 0.32	(1) 33.95 ± 0.14	(1) 33.79 ± 0.31	(1) 33.78 ± 0.30
Tracks/frame expected normal to the surface of the detector	(2) 33.94 ± 0.28	(2) 34.03 ± 0.66	(2) 33.84 ± 0.47	(2) 33.85 ± 0.44	(2) 34.07 ± 0.61	(2) 33.91 ± 0.37	(2) 33.88 ± 0.42	(2) 33.83 ± 0.84

ALPHA TRACKS (PARTICLE INCIDENT) AT ANGLE $\theta = 20^\circ$ TO THE SURFACE OF THE PLASTIC DETECTOR

1.00	1.25	1.50	2.00	2.50	3.00	3.50	3.60	3.70
(1) 2513	(1) 2557	(1) 2468	(1) 3831	(1) 2467	(1) 2474	(1) 3407	(1) 2067	(1) 3758
(2) 4469	(2) 3404	(2) 4218	(2) 3948	(2) 3517	(2) 3522	(2) 3746	(2) 3375	(2) 3990
(1) 28.56	(1) 29.06	(1) 28.05	(1) 4353	(1) 28.03	(1) 28.11	(1) 38.72	(1) 23.49	(1) 42.70
(2) 101.57	(1) 77.36	(2) 95.86	(2) 89.73	(2) 79.93	(2) 80.05	(2) 85.14	(2) 76.70	(2) 90.68
(1) 33.88	(1) 33.79	(1) 33.93	(1) 33.78	(1) 33.83	(1) 33.82	(1) 33.90	(1) 33.88	(1) 33.87
± 0.22	± 0.30	± 0.17	± 0.38	± 0.27	± 0.27	± 0.24	± 0.21	± 0.29
(2) 32.73	(2) 33.03	(2) 33.02	(2) 33.79	(2) 33.87	(2) 33.77	(2) 33.92	(2) 33.89	(2) 33.79
± 1.10	± 0.92	± 0.33	± 0.52	± 0.39	± 0.52	± 0.31	± 0.35	± 0.53

ALPHA TRACKS (PARTICL INCIDENT) AT ANGLE $\theta = 20^\circ$ TO THE SURFACE OF THE PLASTIC DETECTOR

3.80	3.90	4.00	4.25	4.50	4.75	5.00	5.50	6.00
(1) 3965	(1) 2325	(1) 2204	(1) 3135	(1) 2358	(1) 3288	(1) 3014	(1) 2539	(1) 2371
(2) 3587	(2) 4007	(2) 4322	(2) 4479	(2) 4245	(2) 4083	(2) 4230	(2) 4217	(2) 4346
(1) 45.06	(1) 26.42	(1) 25.05	(1) 35.63	(1) 26.80	(1) 37.36	(1) 34.25	(1) 28.85	(1) 26.94
(2) 81.52	(2) 91.07	(2) 98.23	(2) 101.80	(2) 96.48	(2) 9280	(2) 96.14	(2) 95.84	(2) 98.77
(1) 33.63	(1) 33.74	(1) 30.30	(1) 33.85	(1) 33.84	(1) 33.90	(1) 34.05	(1) 34.05	(1) 33.94
± 0.49	± 0.32	± 1.84	± 0.28	± 0.25	± 0.14	± 0.12	± 0.12	± 0.16
(2) 33.71	(2) 33.82	(2) 33.84	(2) 32.73	(2) 33.79	(2) 33.88	(2) 33.91	(2) 33.95	(2) 33.92
± 0.59	± 0.50	± 0.49	± 0.96	± 0.55	± 0.41	± 0.35	± 0.24	± 0.33

ALPHA TRACKS (PARTICLE INCIDENT) AT ANGLE $\theta = 10^\circ$ TO THE SURFACE OF THE PLASTIC DETECTOR

Alpha Particle Energy in MeV	0.60	0.65	0.70	0.75	0.80	0.85	0.90	0.95
Total tracks counted (1) tracks 188 frames (2) tracks 144 frames	(1) 1685 (2) 1960	(1) 1312 (2) 2132	(1) 1527 (2) 1998	(1) 1455 (2) 1854	(1) 1357 (2) 1816	(1) 1320 (2) 2107	(1) 1368 (2) 22.76	(1) 1226 (2) 1761
Track density in tracks/frame counted	(1) 19.15 (2) 44.56	(1) 14.91 (2) 48.46	(1) 17.35 (2) 45.41	(1) 16.53 (2) 42.15	(1) 15.42 (2) 41.26	(1) 15.00 (2) 47.89	(1) 15.55 (2) 51.73	(1) 13.93 (2) 40.02
Efficiency of detector = tracks/ frame (observed)	(1) 16.69 ± 1.01	(1) 16.48 ± 1.76	(1) 16.49 ± 1.15	(1) 16.52 ± 0.57	(1) 16.63 ± 1.21	(1) 16.75 ± 0.91	(1) 16.86 ± 0.43	(1) 16.77 ± 1.04
Tracks/frame expected normal to the surface of the detector	(2) 16.76 ± 1.04	(2) 16.69 ± 1.11	(2) 16.58 ± 1.21	(2) 16.80 ± 1.00	(2) 16.77 ± 1.13	(2) 16.52 ± 1.17	(2) 16.83 ± 0.81	(2) 16.79 ± 0.86

ALPHA TRACKS (PARTICLE INCIDENT) AT ANGLE $\theta = 10^\circ$ TO THE SURFACE OF THE PLASTIC DETECTOR

1.00	1.25	1.50	2.00	2.50	3.00	3.50	3.60	3.70
(1) 1251	(1) 1275	(1) 1198	(1) 1919	(1) 1205	(1) 1225	(1) 1664	(1) 1051	(1) 1823
(2) 2278	(2) 1717	(2) 2102	(2) 1976	(2) 1693	(2) 1736	(2) 1851	(2) 1652	(2) 1991
(1) 14.21	(1) 14.49	(1) 13.61	(1) 21.81	(1) 13.70	(1) 13.92	(1) 18.90	(1) 11.94	(1) 20.71
(2) 51.76	(2) 39.02	(2) 47.77	(2) 44.91	(2) 38.49	(2) 39.45	(1) 42.06	(2) 37.54	(2) 45.25
(1) 16.86	(1) 16.85	(1) 16.46	(1) 16.92	(1) 16.53	(1) 16.75	(1) 16.55	(1) 16.22	(1) 16.43
± 0.61	± 0.71	± 1.15	± 0.44	± 0.35	± 0.35	± 0.92	± 2.32	± 1.14
(2) 16.68	(2) 16.66	(2) 16.90	(2) 16.91	(2) 16.31	(2) 16.64	(2) 16.76	(2) 16.59	(2) 16.86
± 1.02	± 1.02	± 0.28	± 0.41	± 1.67	± 1.02	± 0.64	± 1.69	± 0.88

ALPHA TRACKS (PARTICLE INCIDENT) AT ANGLE $\theta = 10^\circ$ TO THE SURFACE OF THE PLASTIC DETECTOR

3.80	3.90	4.00	4.25	4.50	4.75	5.00	5.50	6.00
(1) 1986	(1) 1165	(1) 1236	(1) 1547	(1) 1175	(1) 1614	(1) 1497	(1) 1251	(1) 1174
(2) 1796	(2) 2008	(2) 2155	(2) 2276	(2) 2072	(2) 2014	(2) 2058	(2) 2070	(2) 2125
(1) 22.57	(1) 13.24	(1) 14.05	(1) 17.58	(1) 13.35	(1) 18.34	(1) 17.01	(1) 14.22	(1) 13.34
(2) 40.82	(2) 45.64	(2) 48.97	(2) 51.73	(2) 47.09	(2) 45.77	(2) 46.77	(2) 47.05	(2) 48.30
(1) 16.85	(1) 16.91	(1) 17.00	(1) 16.70	(1) 16.86	(1) 16.64	(1) 16.91	(1) 16.78	(1) 16.81
± 0.45	± 0.34	± 0.35	± 0.80	± 0.67	± 0.67	± 0.22	± 0.41	± 0.46
(2) 16.88	(2) 16.95	(2) 16.87	(2) 16.63	(2) 16.49	(2) 16.71	(2) 16.50	(2) 16.67	(2) 16.59
± 0.85	± 0.77	± 0.45	± 0.91	± 1.34	± 0.67	± 0.93	± 0.62	± 0.82

ALPHA TRACKS (PARTICLE INCIDENT) AT ANGLE $\theta = 7^\circ$ TO THE SURFACE OF THE PLASTIC DETECTOR

Alpha Particle Energy in MeV	0.60	0.65	0.70	0.75	0.80	0.85	0.90	0.95
Total tracks counted	(1) 1207	(1) 957	(1) 1082	(1) 1051	(1) 948	(1) 928	(1) 968	(1) 862
(1) tracks 188 frames	(2) 1382	(2) 1535	(2) 1415	(2) 1326	(2) 1254	(2) 1482	(2) 1605	(2) 1249
(2) tracks 144 frames								
Track density in tracks/frame counted	(1) 13.72	(1) 10.88	(1) 12.30	(1) 11.94	(1) 10.78	(1) 10.54	(1) 11.00	(1) 9.80
	(2) 31.41	(2) 34.89	(2) 32.16	(2) 30.14	(2) 28.49	(2) 33.69	(2) 36.48	(2) 28.39
Efficiency of detector = tracks/ frame (observed)	(1) 11.96	(1) 12.03	(1) 11.69	(1) 11.93	(1) 11.62	(1) 11.77	(1) 11.93	(1) 11.79
	± 0.74	± 0.63	± 0.91	± 0.76	± 0.91	± 0.91	± 0.76	± 0.75
Tracks/frame expected normal to the surface of the detector	(2) 11.81	(2) 12.02	(2) 11.74	(2) 12.01	(2) 11.58	(2) 11.62	(2) 11.87	(2) 11.91
	± 0.62	± 0.50	± 0.93	± 0.55	± 0.99	± 1.33	± 0.89	± 0.31

ALPHA TRACKS (PARTICLE INCIDENT) AT ANGLE $\theta = 7^\circ$ TO THE SURFACE OF THE PLASTIC DETECTOR

1.00	1.25	1.50	2.00	2.50	3.00	3.50	3.60	3.70
(1) 886	(1) 900	(1) 873	(1) 1354	(1) 848	(1) 876	(1) 1186	(1) 739	(1) 1321
(2) 1602	(2) 1227	(2) 1482	(2) 1376	(2) 1245	(2) 1263	(2) 13 ² 4	(2) 1206	(2) 1406
(1) 10.06	(1) 10.22	(1) 9.92	(1) 15.39	(1) 9.64	(1) 9.96	(1) 13.48	(1) 8.40	(1) 15.01
(2) 36.41	(2) 27.89	(2) 33.68	(2) 31.27	(2) 28.30	(2) 28.70	(2) 29.64	(2) 27.41	(2) 31.95
(1) 11.94	(1) 11.89	(1) 12.00	(1) 11.94	(1) 11.63	(1) 11.98	(1) 11.80	(1) 11.73	(1) 11.91
± 0.56	± 0.39	± 0.57	± 0.73	± 1.04	± 0.65	± 0.99	± 0.43	± 0.72
(2) 11.73	(2) 11.91	(2) 11.92	(2) 11.78	(2) 11.99	(2) 11.81	(2) 11.81	(2) 11.59	(2) 11.91
± 0.92	± 0.85	± 0.69	± 0.82	± 0.44	± 0.43	± 0.62	± 0.43	± 0.72

ALPHA TRACKS (PARTICLE INCIDENT) AT ANGLE $\theta = 7^\circ$ TO THE SURFACE OF THE PLASTIC DETECTOR

3.80	3.90	4.00	4.25	4.50	4.75	5.00	5.50	6.00
(1) 1409	(1) 810	(1) 868	(1) 1104	(1) 811	(1) 1164	(1) 1063	(1) 882	(1) 829
(2) 1255	(2) 1415	(2) 1517	(2) 1555	(2) 1451	(2) 1394	(2) 1466	(2) 1487	(2) 1514
(1) 16.01	(1) 9.20	(1) 9.86	(1) 12.55	(1) 9.22	(1) 13.23	(1) 12.08	(1) 10.02	(1) 9.42
(2) 28.52	(2) 32.16	(2) 34.49	(2) 35.34	(2) 32.98	(2) 31.69	(2) 33.31	(2) 33.80	(2) 34.41
(1) 11.95	(1) 11.75	(1) 11.93	(1) 11.92	(1) 11.64	(1) 12.00	(1) 12.01	(1) 11.83	(1) 11.87
± 0.59	± 0.61	± 0.76	± 0.81	± 0.68	± 0.57	± 0.55	± 0.31	± 0.82
(2) 11.79	(2) 11.94	(2) 11.88	(2) 11.36	(2) 11.55	(2) 11.57	(2) 11.75	(2) 11.97	(2) 11.82
± 0.78	± 0.75	± 0.56	± 1.14	± 0.56	± 1.04	± 0.93	± 0.51	± 0.58

ALPHA TRACKS (PARTICLE INCIDENT) AT ANGLE $\theta = 5^\circ$ TO SURFACE OF THE PLASTIC DETECTOR

Alpha Particle Energy in MeV	0.60	0.65	0.70	0.75	0.80	0.85	0.90	0.95
Total tracks counted	(1) 1150	(1) 901	(1) 1052	(1) 995	(1) 928	(1) 890	(1) 924	(1) 825
(1) tracks 188 frames	(2) 1329	(2) 1439	(2) 1363	(2) 1253	(2) 1218	(2) 1448	(2) 1540	(2) 1193
(2) tracks 144 frames								
Track density in tracks/frame counted	(1) 13.07	(1) 10.23	(1) 11.96	(1) 11.31	(1) 10.54	(1) 10.11	(1) 10.50	(1) 9.38
	(2) 30.21	(2) 32.70	(2) 30.98	(2) 28.48	(2) 27.68	(2) 32.91	(2) 35.00	(2) 27.11
Efficiency of detector = tracks/ frame (observed)	(1) 8.78	(1) 8.84	(1) 8.80	(1) 8.85	(1) 8.80	(1) 8.86	(1) 8.78	(1) 8.86
	± 0.78	± 0.61	± 0.79	± 0.61	± 0.74	± 0.60	± 0.78	± 0.76
Tracks/frame expected normal to the surface of the detector	(2) 8.80	(2) 8.88	(2) 8.84	(2) 8.81	(2) 8.89	(2) 8.81	(2) 8.88	(2) 8.79
	± 0.80	± 0.61	± 0.62	± 0.63	± 0.62	± 0.76	± 0.60	± 0.79

ALPHA TRACKS (PARTICLE INCIDENT) AT ANGLE $\theta = 5^\circ$ TO THE SURFACE OF THE PLASTIC DETECTOR

1.00	1.25	1.50	2.00	2.50	3.00	3.50	3.60	3.70
(1) 845	(1) 853	(1) 832	(1) 1284	(1) 832	(1) 825	(1) 1145	(1) 777	(1) 1262
(2) 1543	(2) 1168	(2) 1402	(2) 1326	(2) 1170	(2) 1191	(2) 1258	(2) 1128	(2) 1336
(1) 9.60	(1) 9.69	(1) 9.46	(1) 14.59	(1) 9.45	(1) 9.38	(1) 13.01	(1) 7.91	(1) 14.34
(2) 35.07	(2) 26.56	(2) 31.86	(2) 30.14	(2) 26.57	(2) 27.06	(2) 28.58	(2) 25.63	(2) 30.36
(1) 8.78	(1) 8.87	(1) 8.74	(1) 8.83	(1) 8.77	(1) 8.86	(1) 8.78	(2) 8.83	(1) 8.79
± 0.79	± 0.65	± 0.92	± 0.70	± 0.69	± 0.65	± 0.81	± 0.83	± 0.76
(2) 8.85	(2) 8.82	(2) 8.87	(2) 8.81	(2) 8.88	(2) 8.76	(2) 8.87	(2) 8.77	(2) 8.84
± 0.67	± 0.81	± 0.63	± 0.75	± 0.64	± 0.86	± 0.63	± 0.76	± 0.67

ALPHA TRACKS (PARTICLE INCIDENT) AT ANGLE $\theta = 5^\circ$ TO THE SURFACE OF THE PLASTIC DETECTOR

3.80	3.90	4.00	4.25	4.50	4.75	5.00	5.50	6.00
(1) 1332	(1) 783	(1) 819	(1) 1052	(1) 793	(1) 1093	(1) 1006	(1) 840	(1) 793
(2) 1215	(2) 1346	(2) 1541	(2) 1426	(2) 1420	(2) 1371	(2) 1408	(2) 1410	(2) 1448
(1) 15.14	(1) 8.90	(1) 9.31	(1) 11.96	(1) 9.01	(1) 12.43	(1) 11.43	(1) 9.54	(1) 9.01
(2) 27.61	(2) 30.60	(2) 35.02	(2) 32.41	(2) 32.26	(2) 31.16	(2) 32.00	(2) 32.04	(2) 32.90
(1) 8.85	(1) 8.80	(1) 8.88	(1) 8.80	(1) 8.79	(1) 8.87	(1) 8.80	(1) 8.88	(1) 8.81
± 0.72	± 0.79	± 0.62	± 0.78	± 0.74	± 0.62	± 0.84	± 0.61	± 0.72
(2) 8.76	(2) 8.86	(2) 8.83	(2) 8.81	(2) 8.85	(2) 8.79	(2) 8.86	(2) 8.81	(2) 8.85
± 0.79	± 0.70	± 0.85	± 0.84	± 0.67	± 0.74	± 0.68	± 0.72	± 0.67

APPENDIX D1

ENERGY-LOSS RATE IN CELLULOSE NITRATE (in MeV mg⁻¹ cm²)*

E/nucl. (MeV/amu)	² He ⁷	³ Li ⁷	⁶ C ¹²	⁷ N ¹⁴	⁸ O ¹⁴	¹⁰ Ne ²⁰	¹² Mg ²⁴	¹⁴ Si ²⁸
0.05	2.162	2.981	5.287	6.074	6.859	8.404	9.910	11.370
0.10	2.053	3.190	5.910	6.808	7.717	9.554	11.400	13.230
0.15	1.989	3.098	6.238	7.200	8.174	10.160	12.180	14.220
0.20	1.881	2.954	6.434	7.454	8.477	10.560	12.700	14.870
0.25	1.788	2.930	6.550	7.629	8.697	10.860	13.080	15.350
0.30	1.705	2.880	6.609	7.750	8.862	11.090	13.380	15.720
0.40	1.560	2.756	6.615	7.878	9.082	11.440	13.830	16.290
0.05	1.426	2.644	6.533	7.906	9.020	11.690	14.170	16.720
0.60	1.303	2.554	6.414	7.871	9.254	11.870	14.450	17.060
0.70	1.207	2.475	6.289	7.798	9.258	12.010	14.670	17.350
0.80	1.133	2.404	6.221	7.708	9.229	12.100	14.850	17.600
0.90	1.075	2.337	6.187	7.615	9.179	12.170	15.010	17.820
1.00	1.027	2.273	6.180	7.527	9.117	12.210	15.140	18.020
1.50	0.735	1.654	5.305	6.620	7.907	11.010	14.190	17.290
2.00	0.568	1.278	4.496	5.727	7.004	9.678	12.830	16.010
2.50	0.466	1.048	3.894	5.011	6.210	8.710	11.570	14.710
3.00	0.420	0.946	3.623	4.696	5.845	8.326	10.960	14.060
4.00	0.337	0.758	3.005	3.961	4.984	7.241	9.701	12.350
5.00	0.290	0.653	2.611	3.503	4.447	6.530	8.865	11.350
6.00	0.259	0.584	2.335	3.169	4.063	6.022	8.232	10.640
7.00	0.237	0.534	2.135	2.906	3.765	5.632	7.733	10.060
8.00	0.220	0.496	1.983	2.699	3.518	5.317	7.330	9.574
9.00	0.207	0.465	1.861	2.533	3.308	5.052	6.997	9.159
10.00	0.196	0.440	1.760	2.396	3.129	4.824	6.708	8.801
11.00	0.186	0.419	1.676	2.281	2.979	4.622	6.456	8.489
12.00	0.178	0.401	1.603	2.182	2.850	4.440	6.233	8.216

APPENDIX D1 (cont).

E/nucl. (MeV/amu)	$^{32}_{16}\text{S}$	$^{40}_{18}\text{A}$	$^{56}_{26}\text{Fe}$	$^{65}_{30}\text{Zn}$	$^{84}_{30}\text{Kr}$	$^{107}_{42}\text{Mo}$	$^{127}_{53}\text{I}$	$^{141}_{56}\text{Ba}$
0.05	12.200	12.750	13.250	13.630	13.970	15.410	18.530	19.160
0.10	15.060	16.870	21.900	23.500	24.060	26.170	26.840	28.540
0.15	16.280	18.330	26.500	29.640	31.260	32.960	35.260	36.620
0.20	17.080	19.300	28.380	32.280	36.220	39.350	42.470	44.940
0.25	17.670	20.020	29.710	34.720	40.630	44.780	49.330	51.850
0.30	18.120	20.570	30.740	36.050	43.640	50.720	55.990	58.020
0.40	18.810	21.400	32.300	38.050	47.070	56.130	65.620	68.930
0.50	19.330	22.020	33.440	39.530	49.130	59.320	74.970	78.670
0.60	19.740	22.510	34.340	40.680	50.750	61.480	82.130	86.180
0.70	20.090	22.920	35.070	41.630	52.070	63.250	85.870	91.620
0.80	20.400	23.280	35.700	42.430	53.190	64.740	88.220	95.180
0.90	20.680	23.610	36.250	43.130	54.150	66.040	90.250	97.450
1.00	20.930	23.900	36.750	43.750	55.010	67.170	92.040	99.440
1.50	20.380	23.500	36.860	44.180	56.040	68.990	95.730	103.800
2.00	19.190	22.380	35.930	43.340	55.390	68.620	96.140	104.400
2.50	17.900	21.110	34.680	42.090	54.150	67.420	95.470	103.600
3.00	17.290	20.560	34.290	41.750	53.890	67.260	95.310	102.800
4.00	15.410	18.620	32.230	39.610	51.580	64.780	92.560	101.000
5.00	14.090	17.180	30.740	37.940	49.760	62.780	90.200	98.550
6.00	13.170	16.060	29.310	36.550	48.240	61.090	88.140	96.380
7.00	12.540	15.170	28.160	35.330	46.900	59.610	86.300	94.430
8.00	12.00	14.550	27.130	34.240	45.710	58.270	84.640	92.660
9.00	11.520	14.040	26.210	33.250	44.610	57.060	83.110	91.030
10.00	11.100	13.570	25.380	32.330	43.610	55.930	81.700	89.520
11.00	19.730	13.150	24.620	31.490	42.660	54.880	80.380	88.110
12.00	10.400	12.770	23.930	30.710	41.780	53.900	79.140	86.790

*Density of Kodak Pathé CA 80-15 cellulose nitrate is 1.52 gm/cm³

APPENDIX D2

RANGE IN CELLULOSE NITRATE (in μm)*

E/nucl. (MeV/amu)	${}^4_2\text{He}$	${}^7_3\text{Li}$	${}^{12}_6\text{C}$	${}^{14}_7\text{N}$	${}^{16}_8\text{O}$	${}^{20}_{10}\text{Ne}$	${}^{24}_{12}\text{Mg}$	${}^{28}_{14}\text{Si}$
0.05	0.86	1.12	1.18	1.25	1.33	1.51	1.72	1.93
0.10	1.50	1.87	1.89	1.98	2.06	2.22	2.40	2.61
0.15	2.16	2.61	2.56	2.65	2.78	2.90	3.07	3.25
0.20	2.86	3.39	3.19	3.29	3.36	3.55	3.72	3.90
0.25	3.59	4.19	3.81	3.91	4.00	4.17	4.35	4.52
0.30	4.36	5.00	4.42	4.52	4.61	4.79	4.95	5.12
0.40	6.00	6.67	5.64	5.72	5.81	5.98	6.14	6.30
0.50	7.80	8.41	6.86	6.91	6.98	7.14	7.29	7.43
0.60	9.77	10.22	8.11	8.10	8.14	8.27	8.41	8.55
0.70	11.92	12.09	9.37	9.30	9.30	9.40	9.52	9.64
0.80	14.22	14.01	10.67	10.51	10.47	10.51	10.61	10.71
0.90	16.65	15.99	11.97	11.74	11.63	11.62	11.69	11.78
1.00	19.21	18.03	13.28	12.98	12.81	12.72	12.76	12.82
1.50	35.17	30.47	20.39	19.74	19.23	18.55	18.28	18.17
2.00	56.12	46.77	28.66	27.38	26.44	25.06	24.25	23.81
2.50	82.36	67.18	38.31	36.17	34.60	32.41	30.86	29.94
3.00	112.36	90.52	48.91	45.75	43.42	40.21	37.96	36.41
4.00	184.49	146.61	73.49	67.68	63.44	57.58	53.69	50.73
5.00	270.81	213.75	102.35	92.99	86.32	77.15	71.09	66.69
6.00	368.95	290.09	135.06	121.24	111.63	98.60	89.97	83.81
7.00	477.37	374.41	171.20	152.24	139.11	121.66	110.18	101.98
8.00	594.94	465.86	210.39	185.83	168.64	146.21	131.59	121.14
9.00	720.86	563.79	252.36	221.81	200.14	172.13	154.09	141.22
10.00	854.45	667.70	296.98	233.54	233.54	199.33	177.61	162.16
11.00	995.21	777.18	343.81	300.19	268.73	227.77	202.10	183.91
12.00	1142.69	891.88	392.98	342.33	306.60	257.41	227.50	206.41

APPENDIX D2 (cont.)

E/nucl. (MeV/amu)	$^{32}_{16}\text{S}$	$^{40}_{18}\text{A}$	$^{56}_{26}\text{Fe}$	$^{65}_{30}\text{Zn}$	$^{84}_{36}\text{Kr}$	$^{107}_{42}\text{Mo}$	$^{127}_{53}\text{I}$	$^{141}_{56}\text{Ba}$
0.05	2.13	2.58	3.08	3.26	3.66	4.07	3.82	3.99
0.10	2.85	3.44	4.27	4.65	5.39	6.11	5.83	6.11
0.15	3.46	4.12	5.07	5.56	6.58	7.58	7.39	7.76
0.20	4.08	4.76	5.72	6.28	7.47	8.72	8.65	9.12
0.25	4.70	5.42	6.31	6.90	8.22	9.65	9.71	10.27
0.30	5.30	6.08	6.86	7.46	8.88	10.44	10.62	11.27
0.40	6.46	7.36	7.93	8.51	10.04	11.81	12.12	12.91
0.50	7.58	8.60	9.02	9.52	11.10	12.99	13.36	14.26
0.60	8.68	9.80	10.12	10.54	12.10	14.08	14.45	15.43
0.70	9.76	10.98	11.21	11.57	13.08	15.12	15.44	16.50
0.80	10.82	12.14	12.27	12.61	14.07	16.11	16.37	17.47
0.90	11.87	13.29	13.31	13.63	15.09	17.09	17.25	18.40
1.00	12.90	14.42	14.34	14.63	16.09	18.07	18.10	19.29
1.50	18.12	20.10	19.46	19.60	21.17	23.18	22.16	23.47
2.00	23.54	25.95	24.62	24.58	26.22	28.40	26.34	27.66
2.50	29.34	32.12	29.94	29.68	31.36	33.67	30.79	32.11
3.00	35.39	38.51	35.35	34.85	36.55	38.98	35.24	36.65
4.00	48.59	52.57	46.67	45.59	47.26	49.87	44.32	45.89
5.00	63.19	67.30	58.64	56.86	58.39	61.13	53.65	55.38
6.00	79.01	83.48	71.19	68.58	69.90	72.73	63.21	65.09
7.00	95.74	100.69	84.28	80.72	81.76	84.63	72.99	75.01
8.00	113.25	118.82	97.88	93.27	93.94	96.82	82.96	85.13
9.00	131.52	137.61	111.98	106.20	106.42	109.28	93.13	95.44
10.00	150.51	157.07	126.55	119.51	119.21	121.99	103.47	105.92
11.00	170.19	177.16	141.59	133.18	132.28	134.95	113.99	116.58
12.00	190.53	197.88	157.08	147.21	145.63	148.16	124.68	127.40

*Density of Kodak Pathé CA 80-15 cellulose nitrate is 1.52 gm/cm³